

UNIVERSITÉ LILLE 1, SCIENCES ET TECHNOLOGIES

Doctoral School ED SMRE

University Department **Unité de Catalyse et Chimie du Solide**

Thesis defended by **Anke SCHÖN**

Defended on **27th March, 2015**

In order to become a Doctor of the Université Lille 1, Sciences et Technologies

Academic Field **Molecules and Condensed Matter**

Speciality **Heterogeneous catalysis**

Development of alternative 3-way catalysts: Fe-based perovskites with low noble metal content

Thesis supervised by Pascal GRANGER Supervisor
Jean-Philippe DACQUIN Advisor
Christophe DUJARDIN Advisor

Committee members

<i>Referees</i>	Anne GIROIR-FENDLER	Professor at the Université Claude Bernard Lyon 1	
	Xavier COURTOIS	Associate professor at the Université de Poitiers	
<i>Examiners</i>	David THOMPSETT	Manager at Johnson Matthey	
	Patrick DA COSTA	Professor at the Université Pierre et Marie Curie (Paris)	
	Pascal ROUSSEL	Senior Researcher (CNRS) at UCCS, Lille	Committee President
<i>Supervisors</i>	Pascal GRANGER	Professor at the Université Lille 1	
	Jean-Philippe DACQUIN	Assistant professor at the Université Lille 1	
	Christophe DUJARDIN	Professor at the École Nationale Supérieure de Chimie de Lille	

UNIVERSITÉ LILLE 1, SCIENCES ET TECHNOLOGIES

École doctorale ED SMRE

Unité de recherche **Unité de Catalyse et Chimie du Solide**

Thèse présentée par **Anke SCHÖN**

Soutenue le **27 mars 2015**

En vue de l'obtention du grade de docteur de l'Université Lille 1, Sciences et Technologies

Discipline **Molécules et Matière Condensée**

Spécialité **Catalyse hétérogène**

Développement d'une nouvelle génération de catalyseurs 3 voies : Perovskites à base de fer à faible teneur en métaux nobles

Thèse dirigée par Pascal GRANGER directeur
Jean-Philippe DACQUIN co-encadrant
Christophe DUJARDIN co-encadrant

Composition du jury

<i>Rapporteurs</i>	Anne GIROIR-FENDLER	professeure à l'Université Claude Bernard Lyon 1
	Xavier COURTOIS	maître de conférences HDR à l'Université de Poitiers
<i>Examineurs</i>	David THOMPSETT	manager chez Johnson Matthey
	Patrick DA COSTA	professeur à l'Université Pierre et Marie Curie (Paris)
	Pascal ROUSSEL	directeur de recherche au CNRS (UCCS, Lille) président du jury
<i>Directeurs de thèse</i>	Pascal GRANGER	professeur à l'Université Lille 1
	Jean-Philippe DACQUIN	maître de conférences à l'Université Lille 1
	Christophe DUJARDIN	professeur à l'École Nationale Supérieure de Chimie de Lille

*To a peaceful Europe and beyond:
May curiosity, reason, fairness,
tolerance, understanding and
friendship reign*

*To my dearest:
To my family
To Philipp*

Stay curious and openminded.
Learn from mistakes.
It's worthwhile.

Das kannst du *noch* nicht.

Acknowledgements

This thesis was only possible due to the support of a lot of different people whom I would like to thank.

First of all, I would like to acknowledge the European Commission for financing the NEXTGENCAT project (FP7 project 280890-NEXT-GEN-CAT) and thereby my thesis. Moreover, my supervisors – Jean-Philippe Dacquin, Christophe Dujardin and Pascal Granger – deserve special thanks for having welcomed me in the DeNO_x group and for having helped and followed my work during these 3 years. Thanks to your knowledge, readiness to impart the latter and constructive criticism I have learnt many things throughout this time.

Furthermore, I would like to thank all the jury members and especially the 2 referees, Anne Giroir-Fendler and Xavier Courtois, for having accepted to judge my work.

I also gratefully acknowledge the interns who I had the opportunity to co-supervise throughout my thesis and who worked with me on this subject: René Herbeaux, Antoine Briand, Lizabeth Rodríguez and Fadila Ait Sidi M'hand – sometimes highlighting very interesting issues. Moreover, I am grateful to Abdelali Zaki who kindly provided the polymer spheres used in this study.

I also thank the different NEXTGENCAT consortium partners for interesting discussions and the good collaboration, especially Jeff Nyalosaso Likoko, Qi Xin and Pegie Cool from the University of Antwerp, the colleagues from the University of Padova and Kerry Simmance and David Thompsett from Johnson Matthey - the latter also for providing the commercial reference catalyst.

Another big thanks goes to the NEXTGENCAT colleagues at the UCCS: Élise Berrier, Dimitri Blanck, Jean-François Paul and Anne-Sophie Mamede as well as in the DeNO_x group: Sylvain Gillot, Abdelali Zaki and Simona Bianca Troncea Ghimis, for fruitful discussions on the subject and others.

Equally, this work would not have been possible if it were not for all those who kindly did various analyses for me and/or trained me in doing them on my own, namely Olivier Gardoll, Nora Djelal, Laurence Burylo and Martine Trentesaux (all UCCS) as well as Sandra Casale (LRS-UPMC). In a different way I would like to acknowledge Denis Bitouzé who elaborated *yathesis*, the LaTeX template used for this thesis.

I'd like to thank the UCCS members in general for the welcoming atmosphere and the good time I spent in the institute and the office 05 members in particular – thanks for the sometimes funny, sometimes serious or even controversial discussions on “God and the world” opening up my horizon a little further and the support during the last months of my writing.

Likewise, I was supported by and spent a good time with a lot of friends near and far. In Lille, the (spicy) soirées and bike tours with our *usual suspects* Karen, Di, Wei, Jenya, Fabio and Ewa will not be forgotten, neither will be the members of¹ and lots of memorable events at the best circus club ever, “Les Intrépides”. The *Feuerzangenbowle* brought together

¹You are (un)fortunately too many who deserve mentioning but I trust that those concerned will know it.

different spheres at times ;) Moreover, some very good long-time friends persist in spite of the distance, a very special thanks therefore goes to Annika, Wei, Lui, Jule F, Alhama and Tatjana for forgiving me my sporadic communication and for just so many happy and intense moments we spent together.

My family – especially my beloved parents, my dearest brother Rolf and my great grandmas – deserves nothing short of a huge, huge thanks for their unconditional support and trust in me throughout all my life and especially whenever most needed. Needless to say that I owe you forever!

Finally, I would like to thank Philipp. With your smile, your everlasting patience – not exclusively but also with my python beginnings, your support – even when you yourself were under loads of pressure, and the wonderful time we spent doing acrobatics and so much more during the last years I am happy to know that we are able to surmount difficulties and accomplish great things together. I am so grateful for having you at my side.

DEVELOPMENT OF ALTERNATIVE 3-WAY CATALYSTS: FE-BASED PEROVSKITES WITH LOW NOBLE METAL CONTENT**Abstract**

This study aims at developing alternative 3-way catalysts (TWC) for the exhaust gas treatment of spark-ignition engines. Petrol engine exhaust comprises carbon monoxide, hydrocarbons and nitrogen oxides (NO_x) which need to be eliminated simultaneously. The partial replacement of platinum group metals (PGM) which are nowadays used as TWC active phase was intended. To this end Fe-based perovskites were investigated.

The main drawback of PGM is their scarcity which leads to high environmental, societal and economic exploitation and usage cost. The stability of PGM nanoparticles which tend to sinter during catalyst operation and the N_2 selectivity during NO_x reduction also deserve improvement. 3-way catalytic reactions have been performed on LaFeO_3 -based perovskites in complex feed streams containing all 3 kinds of pollutants and other naturally present gases such as O_2 and H_2 and high amounts of inhibitors (CO_2 , H_2O). To improve results of the LaFeO_3 perovskite, 2 approaches – textural properties and composition optimisation – were studied. Textural properties could be improved by optimising synthesis parameters such as the employed solvent and the calcination atmosphere. Interesting NO_x reduction results were obtained by changing the calcination atmosphere during LaFeO_3 synthesis. Surface and bulk composition optimisation lead to significantly enhanced catalytic performances. Furthermore, an increased N_2 selectivity is observed compared to a commercial reference catalyst. The doping with low PGM content lead to enhanced performances which were increased by a reductive pre-treatment.

Keywords: 3-way catalyst, perovskite, automotive exhaust gas treatment, denox

DÉVELOPPEMENT D'UNE NOUVELLE GÉNÉRATION DE CATALYSEURS 3 VOIES : PEROVSKITES À BASE DE FER À FAIBLE TENEUR EN MÉTAUX NOBLES**Résumé**

Cette étude vise à développer de nouveaux catalyseurs 3-voies (TWC) pour le traitement de gaz d'échappement issus de moteurs à essence. TWC doivent simultanément éliminer le monoxyde de carbone, les hydrocarbures et les oxydes d'azote (NO_x). Le remplacement partiel des métaux nobles (PGM) qui sont actuellement utilisés comme phase active dans les TWC est l'objectif de cette étude. Afin de parvenir à ce but, des perovskites à base de Fe ont été étudiées.

L'inconvénient majeur des PGM est leur rareté qui cause un coût élevé d'exploitation et d'usage. La stabilité des nanoparticules ayant tendance de fritter lors de l'usage du TWC et la faible sélectivité en N_2 (S_{N_2}) pendant la conversion de NO nécessitent une amélioration. Les réactions 3-voies ont été menées sur les perovskites à base de LaFeO_3 dans des flux complexes contenant les 3 types de polluants et d'autres gaz naturellement présents comme O_2 , H_2 ainsi que de hautes quantités d'inhibiteurs (CO_2 , H_2O). Afin d'améliorer les résultats de la perovskite LaFeO_3 , 2 approches – l'optimisation des propriétés texturales et de la composition – ont été poursuivies. Les propriétés texturales ont pu être améliorées par l'optimisation de paramètres de synthèse comme le solvant ou l'atmosphère de calcination. Le changement de l'atmosphère de calcination a donné des résultats prometteurs sur la réduction des NO_x . L'optimisation de la composition de la surface et du bulk a apporté un gain significatif en performance catalytique. De plus, une S_{N_2} accrue est observée comparé à un catalyseur de référence commercial. Le dopage à faible teneur en métaux nobles amène à une performance élevée qui a été augmenté par un traitement réducteur.

Mots clés : catalyseur 3 voies, perovskite, traitement d'effluents automobile, dénox

Symbols, acronyms and abbreviations

3DOM	3-dimensionally ordered macroporous
A	A-site atom
a	unit cell parameter a (XRD)
A	pre-exponential factor
A/F	air-to-fuel ratio
B	B-site atom
b	unit cell parameter b (XRD)
B. E.	binding energy
BET	Brunauer-Emmett-Teller theory
BJH	Barret-Joyner-Halenda theory
c	unit cell parameter c (XRD)
CA	citric acid
CCM	conventional citrate method
CCM*	conventional citrate method with 1 st part of calcination under stagnant atmosphere
CCT	colloidal crystal templating
CNRS	<i>French</i> Centre National de la Recherche Scientifique, meaning National Institute for Scientific Research
d	diameter
\bar{d}	average diameter
\bar{d}_{pore}	average pore diameter
d_{cryst}	average crystallite diameter
d_{pore}	pore diameter
δ	stoichiometric term describing the difference between the nominally expected and the actual amount of oxygen in a perovskite
ΔE_{split}	multiplet splitting energy difference
ΔT_{50}	difference between temperatures of 50 % conversion
DSC	differential scanning calorimetric analysis
e. g.	<i>Latin</i> exempli gratia, meaning for example
$E_{A, \text{app}}$	apparent activation energy
EDX	energy dispersive X-ray spectroscopy
Eq.	Equation(s)
et al.	<i>Latin</i> et alii, meaning and co-workers

EtOH	ethanol
EU	European Union
$F_{i, \text{inlet}}$	molar flow rate of the gas i at the inlet of the reactor
Fig.	Figure(s)
FWHM	full width at half maximum
GHSV	gas hourly space velocity
GWP	global warming potential
H ₂ -TPR	hydrogen temperature-programmed reduction
HAM	hydroalcoholic method
HAM N ₂	hydroalcoholic method with 1 st part of calcination under N ₂ flow, drying in climate chamber
HAM air	hydroalcoholic method, calcination under air flow
HAM NO	hydroalcoholic method with 1 st part of calcination under NO flow, drying in climate chamber
HAM*	hydroalcoholic method with 1 st part of calcination under stagnant atmosphere, dried in a regular oven
HAM* _{cooling}	hydroalcoholic method with 1 st part of calcination under stagnant atmosphere followed by a cooling before the atmosphere switch, the drying step was performed in a regular oven
HC	hydrocarbons
HTXRD	high temperature X-ray diffraction
i. e.	<i>Latin id est</i> , meaning that is
ICDD	International Centre for Diffraction Data
ICP	inductively coupled plasma atomic emission spectroscopy
IR spectroscopy	infrared spectroscopy
IUPAC	International Union of Pure and Applied Chemistry
IWI	incipient wet impregnation method
k	rate constant
K. E.	kinetic energy
λ	stoichiometric factor (section 1.1) or wavelength of source radiation (XRD)
λ_{exc}	wavelength of excitation (Raman)
m	mass
m_{catalyst}	mass of catalyst
MSM	macro-structuring method
MSM*	macro-structuring method with 1 st part of calcination under stagnant atmosphere
MSM _{cooling}	macro-structuring method with 1 st part of calcination under N ₂ flow followed by a cooling before the atmosphere switch to air flow
n	(molar) amount of substance

n. a.	not available
NAFTA	North American Free Trade Agreement
O_{ads}	adsorbed oxygen species, i. e. O_2^{2-} , O_2^- , surface hydroxyl and carbonate species
O_{lattice}	lattice oxygen, O^{2-}
OSC	oxygen storage capacity
p	pressure
p_0	atmospheric pressure
PDF	powder diffraction file – Hereby are meant the reference files of the ICDD database
PGM	platinum group metals
PMMA	polymethylmethacrylate
p_{N_2}	nitrogen partial pressure
Procedure A	catalytic performance test procedure A conducted for perovskites, s. Fig. 2.7
Procedure B	catalytic performance test procedure B conducted for the commercial reference catalyst, s. Fig. 2.8
Procedure C	catalytic performance test procedure C, conducted for perovskites including a reductive pretreatment, s. Fig. 2.9
Procedure D	catalytic performance test procedure D, conducted for perovskites including a reductive pretreatment, modified stoichiometric conditions, s. Fig. 2.9
PS	polystyrene
Q_0	total flow rate
R	universal gas constant
r	radius
$r_{\text{intrinsic}}$	intrinsic reaction rate
r_{specific}	specific reaction rate
r. h.	relative humidity
RP	Ruddlesden-Popper phase
rt	room temperature
S_{N_2O}	N_2O selectivity during NO reduction
S_{N_2}	N_2 selectivity during NO reduction
S_{NH_3}	NH_3 selectivity during NO reduction
SCA	<i>French</i> service central d'analyse, meaning Central Analyses Service
SEM	scanning electron microscopy
SOFC	solid oxide fuel cell
SSA	specific surface area
stoic1	1 st test ramp under stoichiometric conditions
stoic2	return test = 4 th test ramp under stoichiometric conditions
T	temperature

t	tolerance factor (Goldschmidt)
<i>t</i>	time
T_{25}	temperature of 25 % conversion
T_{50}	temperature of 50 % conversion
TEM	transmission electron microscopy
T_g	glass temperature
TGA	thermogravimetric analysis
θ	Bragg angle (XRD)
T_S	temperature for which the selectivity is listed
TWC	3-way catalysis or 3-way catalyst
USA	United States of America
V_{pore}	cumulative pore volume
$V_{\text{unit cell}}$	unit cell volume
V_{O}	oxygen vacancy
WGS	water-gas shift reaction
WTO	World Trade Organisation
X	conversion
<i>x</i>	mole fraction
XAS	X-ray absorption spectroscopy
X_i	conversion of the gas <i>i</i>
XPS	X-ray photo-electron spectroscopy
XRD	X-ray diffraction
$Y_{\text{N}_2\text{O}}$	N_2O yield
Y_{N_2}	N_2 yield
Y_{NH_3}	NH_3 yield

Table of Contents

Acknowledgements	vii
Abstract	ix
Symbols, acronyms and abbreviations	xi
Table of Contents	xv
Introduction	1
1 Bibliographic study	3
1.1 Automotive exhaust gas treatment of spark-ignition engine operated vehicles	3
1.1.1 Principle of 3-way catalysis (TWC)	4
1.1.2 Composition of a conventional TWC catalysts	7
1.1.3 Parameters influencing the catalytic performances of TWC and catalytic performance evaluation	8
1.1.4 Criteria of a good TWC	11
1.2 Perovskites $ABO_{3\pm\delta}$	12
1.2.1 Structure	12
1.2.2 Properties and (non-catalytic) applications	14
1.2.3 Perovskites in 3-way catalysis	17
1.3 Synthesis methods for obtaining perovskites	29
1.3.1 Solid state methods	29
1.3.2 Wet synthesis methods	30
1.3.3 Macro-structuring methods	34
1.4 Conclusion	37
Bibliography	41
2 Experimental protocols and techniques	49
2.1 Synthesis protocols	49
2.1.1 Conventional Citrate Method (CCM)	49
2.1.2 HydroAlcoholic Method (HAM)	51
2.1.3 Macro-Structuring method (MSM)	51
2.1.4 Calcination procedures	52
2.1.5 Incipient Wet Impregnation (IWI) method for the doping of perovskite catalysts with noble metals	53
2.1.6 Summary of conducted syntheses by parameters	53
2.2 Physico-chemical characterisation conditions	54
2.2.1 Elementary analysis	54

2.2.2	Thermogravimetric and Differential Scanning Calorimetric analysis (TGA/DSC)	54
2.2.3	Hydrogen Temperature-programmed Reduction (H ₂ -TPR)	54
2.2.4	N ₂ physisorption	55
2.2.5	X-ray diffraction XRD	55
2.2.6	Raman spectroscopy	56
2.2.7	Transmission electron microscopy TEM	56
2.2.8	Scanning electron microscopy SEM	56
2.2.9	X-ray photo-electron spectroscopy XPS	57
2.3	Catalytic performance measurements	57
2.3.1	Feed stream composition	57
2.3.2	Experimental setup for catalytic tests	59
2.3.3	Catalytic performance test protocols	60
2.3.4	Estimation of reaction rates and Arrhenius parameters of perovskites	61
	Bibliography	63
3	Reference catalysts LaBO₃ (B = Mn, Fe), La₂CuO₄ and commercial TWC	65
3.1	Bulk/Structural properties	65
3.1.1	Chemical composition in the bulk	65
3.1.2	XRD	65
3.1.3	Raman spectroscopy	67
3.2	Thermal stability and reducibility	68
3.2.1	High Temperature XRD (HTXRD) analyses	68
3.2.2	H ₂ -TPR	73
3.3	Textural properties	75
3.4	Chemical composition at the surface	76
3.4.1	XPS analyses of the calcined samples	76
3.4.2	Ex situ XPS analyses of post-HTXRD samples	79
3.5	Catalytic performance	82
3.5.1	Catalytic performance of the commercial reference catalyst	82
3.5.2	Catalytic performance of the perovskite reference catalysts	86
3.5.3	Physico-chemical properties of the spent perovskite catalysts	90
3.6	Conclusion	91
	Bibliography	93
4	Influence of synthesis parameters on properties of LaFeO₃	95
4.1	Solvent effect	95
4.1.1	Nitrate-citrate precursor decomposition	96
4.1.2	Structural properties	98
4.1.3	Textural properties	99
4.1.4	Chemical composition at the surface	102
4.1.5	Conclusion	103
4.2	Influence of the template	104
4.2.1	Thermal analysis of the template	104
4.2.2	Bulk/Structural properties	108
4.2.3	Reducibility	109
4.2.4	Textural properties	110
4.2.5	Chemical composition	115

4.2.6	Catalytic activity	116
4.2.7	Conclusion	118
4.3	Effect of the calcination atmosphere	119
4.3.1	Effect of calcination under <i>stagnant</i> atmosphere (CCM*, HAM*, MSM*)	120
4.3.2	Effect of the kind of calcination atmosphere on LaFeO ₃ perovskites (HAM)	135
4.3.3	Conclusion	147
4.4	Conclusion	148
	Bibliography	151
5	Composition optimisation of Fe-based perovskite catalysts	153
5.1	Surface composition optimisation	153
5.1.1	Chemical composition in the bulk and at the surface	153
5.1.2	Structural properties	155
5.1.3	Thermal stability and reducibility	157
5.1.4	Textural properties	161
5.1.5	Catalytic activity	163
5.1.6	Conclusion	167
5.2	Influence of substitution in A-site	168
5.2.1	Structural properties	168
5.2.2	Reducibility	169
5.2.3	Textural properties	170
5.2.4	Chemical composition at the surface	171
5.2.5	Catalytic performance	174
5.2.6	Conclusion	177
5.3	Influence of substitution in B-site	177
5.3.1	Bulk/Structural properties	177
5.3.2	Thermal stability and reducibility	180
5.3.3	Textural properties	184
5.3.4	Chemical composition at the surface	185
5.3.5	Catalytic activity	188
5.3.6	Conclusion	193
5.4	Influence of substitution in A- and B-site	193
5.4.1	Bulk/Structural properties	194
5.4.2	Reducibility	196
5.4.3	Textural properties	197
5.4.4	Chemical composition at the surface	198
5.4.5	Catalytic activity	200
5.4.6	Conclusion	204
5.5	Combining surface and bulk composition optimisation approaches	204
5.5.1	Bulk/Structural properties	205
5.5.2	Reducibility	207
5.5.3	Textural properties	209
5.5.4	Chemical composition at the surface	211
5.5.5	Catalytic activity	214
5.5.6	Conclusion	220
5.6	Conclusion	220
	Bibliography	223

6 Fe-based perovskites doped with low loadings of PGM	225
6.1 Influence of the nature of the doping noble metal on $\text{La}_{0.8}\text{Ca}_{0.2}\text{Fe}_{0.8}\text{Cu}_{0.2}\text{O}_3$.	225
6.1.1 Physico-chemical properties	225
6.1.2 Catalytic performance	230
6.2 Rh-doped $\text{La}_{0.67}\text{Fe}_{0.83}\text{Cu}_{0.17}\text{O}_3$	238
6.2.1 Physico-chemical properties	238
6.2.2 Catalytic performance	240
6.3 Conclusion	247
Bibliography	251
Conclusion and Prospects	253
A Synthesis schemes	257
B ICP and XPS results	259
C HTXRD $\text{LaFe}_{1-x}\text{Cu}_x\text{O}_3$ ($x = 0.05, 0.1$)	263
D Additional catalytic activity test results	267
D.1 Influence of synthesis parameters on properties of LaFeO_3	267
D.2 Composition optimisation	271
D.3 PGM-doped perovskites prepared by CCM	278
List of Tables	281
List of Figures	285

Introduction

Motivation Besides the industry and the energy transformation sector, traffic exhaust gases are a major source of local and global pollution. Efforts in science and engineering and the introduction of different regulations throughout the world, such as Euro 6 (European Union and affiliates) and Tier II (North American Free Trade Agreement (NAFTA), Brazil) in the traffic sector, aim to reduce this pollution.

Regarding traffic exhaust, different kinds of pollutants are regulated, namely CO, NO_x, hydrocarbons (HC), particulate matter (soot) and SO₂. While the regulation of the latter lead to the limitation of sulphur content in fuel and is thereby eliminated at the source, the other 4 kinds of pollutants are formed during the combustion process and need to be dealt with by after-treatment systems, i. e. catalytic converters.

In engines fuelled by petrol (spark-ignition engines) all of these pollutants are formed but soot emissions are much lower than for auto-ignition engines (fuelled by diesel) and as a consequence were exempt of the previous petrol vehicle regulation (up to Euro 5). The employed catalyst, therefore, needs to eliminate the following 3 pollutants simultaneously: CO, NO_x, HC. This is why it is generally called a 3-way catalyst (TWC). Such a TWC contains different materials but the active phase commonly consists of platinum group metals (PGM), i. e. Pt, Pd, and Rh. These noble metals are short in supply and demand high environmental and social costs due to their exploitation by mining. This is why the after-treatment system in cars is relatively high in cost.

Indeed, regulation has lead to a significant decrease in pollution caused by traffic since its first implementation in California in the 1960s and limits became more challenging over the decades. This lead to the desulfurisation of the fuel and the ban of known catalyst poisons such as lead. In Europe, the current regulation, Euro 6, just entered into effect in September 2014. Concerning petrol engines, the only change implemented compared to the Euro 5 legislation is the introduction of a soot (“particle number”) regulation. The TWC-pollutants’ regulation remains unchanged.

Even though a high conversion of pollutants can nowadays be achieved via conventional 3-way catalysis (TWC), leading to a significant decrease of individual pollution since the 1960s, the increasing use of cars has globally caused an augmentation of absolute pollutant quantity emitted via road traffic emission, even if this is different from the trend observed in

Europe. This evolution is most striking in *emerging countries*, especially in India and China which generally also have an older car fleet. In order to be able to equip all the vehicles, in those countries included, a way of substituting the rare and also expensive noble metals which are used in today's catalysts is highly needed.

Although challenging, it is therefore evident that a further decrease in price, i. e. in platinum group metals (PGM), in the catalytic converter is necessary and worthwhile.

Objectives The objective of this study is the investigation of Fe-based perovskite catalysts – without or with low PGM content – as alternative to conventional 3-way catalysts. The overall goal is the development of less expensive but catalytically performing and stable 3-way catalysts presenting high N₂ selectivities.

Approach This thesis is divided into 6 chapters. First, a bibliographic study (Chapter 1) on 3-way catalysis and conventional 3-way catalysts as well as perovskites (in 3-way catalysis) is performed.

In Chapter 2 the synthesis protocols, employed conditions of the physico-chemical characterisations and the catalytic activity evaluation are presented.

Chapter 3 focusses on the reference catalysts, i. e. the perovskite references LaBO₃ (B = Mn or Fe) and La₂CuO₄ and the commercial reference catalyst. The choice of the starting system, i. e. Fe-based perovskites, as alternative 3-way catalysts is justified. The results of physico-chemical characterisations of LaBO₃ (B = Mn or Fe) and La₂CuO₄ prepared by conventional citrate method as well as their catalytic performances are shown to illustrate the choice of Fe-based perovskites as a suitable alternative system. In addition, the catalytic performance of a conventional 3-way catalyst containing rare earth, noble metals and promoters is described in Section 3.5.1 for comparison with the later results.

Chapter 4 discusses the different synthesis approaches followed in order to optimise the LaFeO₃ perovskites' textural properties. After investigating the influence of the solvent during synthesis comparing conventional citrate method (CCM) to hydroalcoholic method (HAM) (Section 4.1), the impact of adding a template (macro-structuring method (MSM)) to allow for a controlled structuring of the perovskite is discussed in Section 4.2. Finally, the influence of the calcination procedure and especially its atmosphere is explored in Section 4.3.

In Chapter 5 different approaches to enhance catalytic activity of non-noble metal doped Fe-based perovskites by composition optimisation in B- and A-site are investigated. The interest of tailoring the surface composition of perovskites is laid out in Section 5.1, whereas the substitution in A- and B-sites of the perovskite is treated in Sections 5.2, 5.3, and 5.4. The influence of combining these composition optimisations on the catalysts' properties is investigated in Section 5.5.

Finally, the impregnation with low PGM content on selected promising catalysts is studied in Chapter 6.

Bibliographic study

In general, a catalyst is a compound which accelerates the conversion of reactants to products intervening in intermediate steps and thereby lowering the activation energy for these reactions. This compound is never consumed, however. It acts on the kinetics of a reaction, not its thermodynamics. Heterogeneous catalysts as used in exhaust gas treatment are in a different phase than the reaction takes place in, i. e. the reactants. The 3-way catalyst (TWC) consists of a solid whereas the reactions take place in the gas phase. This catalyst is capable of converting simultaneously 3 main atmospheric pollutants from petrol engine exhausts: CO, NO and unburnt hydrocarbons (HC).

1.1 Automotive exhaust gas treatment of spark-ignition engine operated vehicles

As already stated earlier, automotive exhaust gas treatment depends on the engine (and the fuel) the vehicle runs on. Major differences exist between spark-ignition and auto-combustion engines leading to different amounts of pollutants being formed. Therefore, different after-treatment systems have been developed for both vehicle types. The present study focuses on the investigation of the catalytic converters employed in conjunction with petrol fuelled engines, i. e. spark-ignition engines.

Origin of the pollutants The pollutants CO and HC in the exhaust gas of spark-ignition engines are due to incomplete combustion. There are multiple reasons for the combustion to proceed incompletely. The main reason is the lack of air leading to CO and unburnt HC residues. HC may also end up in the exhaust gas if fuel goes directly through to the exhaust. In addition CO is formed if temperature is too low. NO_x , on the other hand, are formed at high temperature in the presence of excess oxygen.

Effects of the pollutants on (human) health and environment CO is a known toxic gas leading to an oxygen displacement in blood and thereby asphyxiation which may be fatal at high concentrations. But even lower concentrations are still noxious. HC as a class of compounds have different effects on health and environment. Some are carcinogenic, another effect is its contribution in forming ozone and photochemical smog by their reaction with NO_x under sunlight. In addition, ozone and NO_x themselves are known to provoke and deteriorate respiratory problems. Furthermore, NO_x may cause acid rain.^[1]

Regulation in effect (Europe) In September 2014, the Euro 6 regulation came into force in the European Union. While diesel fuelled car emissions were further limited, the main targets for petrol fuelled cars remained the same as for the Euro 5 regulation as shown in Table 1.1. Merely, a particle number limit per kilometre was added.

Table 1.1 – **Euro 5 and 6 regulations for petrol fuelled cars.** Emissions are regulated on a g km⁻¹ basis except for the particle number (P).^[2]

regulation	effective date	CO	THC ^a	NMHC ^b	NO _x	PM ^{c,d}	P (#/km)
Euro 5	September 2009	1.0	0.10	0.068	0.060	0.005	-
Euro 6	September 2014	1.0	0.10	0.068	0.060	0.005	6 · 10 ¹¹ ^e

^a Total hydrocarbon content.

^b Non-methane hydrocarbon content.

^c Particulate matter.

^d Applies only to vehicles with direct injection engines.

^e Limits are set to 6 · 10¹² km⁻¹ during the first 3 years from the effective dates.

Viable ways to reduce pollutant emissions 2 different ways to address the pollutant emissions can be deduced from what has been said before. One possibility is to improve the engine operation in order to reduce incomplete combustion, i. e. emission control at the source. This corresponds to the challenge for engineers. The other possibility is the reduction of the emissions via the optimisation of the catalytic after-treatment devices, the objective of this study.

1.1.1 Principle of 3-way catalysis (TWC)

A major difference between petrol and diesel fuelled engines is the air-to-fuel ratio (A/F) at which the combustion takes place. While the latter engine is operated under highly oxidising, i. e. under so-called lean conditions with a fuel deficiency and oxygen excess, the former is actuated around the so-called stoichiometry (air-to-fuel ratio (A/F) = 14.7/1 kg/kg). As becomes clear from the already discussed origins of the pollutants and can be seen in Fig. 1.1, this is necessary to allow for optimum conversions of all 3 kinds of pollutants. At very high

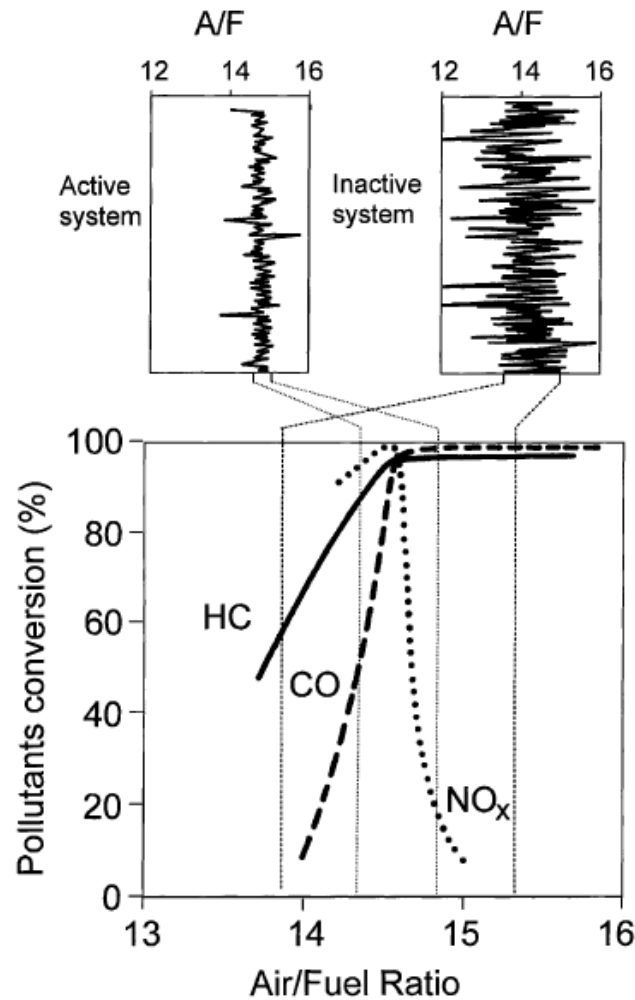


Figure 1.1 – **Ideal operation air-to-fuel ratio (A/F) in TWC.** Optimum conversions of all 3 kinds of pollutants can only be achieved under so-called stoichiometric conditions and therefore stoichiometry-control is constantly required.^[3]

air, i. e. oxygen, excess CO and HC are completely converted, however, NO_x remain or are additionally formed. On the other hand, the deficiency of air (rich conditions) leads to the products of incomplete combustion, i. e. CO and unburnt HC.

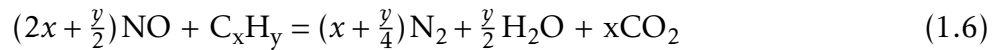
To facilitate the reading and comparisons between different authors the A/F is generally indicated by the stoichiometric factor (λ). It describes the difference between the real and the optimum A/F (Eq. 1.1). For A/F = 14.7, λ corresponds to 1.^[3-6]

$$\lambda = \frac{\text{actual engine A/F}}{\text{stoichiometric engine A/F}} \quad (1.1)$$

Under rich conditions λ is defined to be < 1 , under lean > 1 . Indeed, a λ sensor is employed to adjust the A/F in operating conditions. It measures the partial oxygen pressure in the exhaust and results are used to electronically control the amount of injected fuel.^[4] As a consequence of this, short time lapses between the sensing of an increased or lowered A/F and the corrective reaction occur leading to a fluctuation between slightly rich and slightly

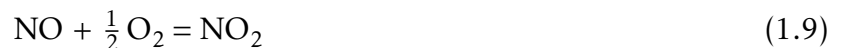
lean conditions.

The reactions which take place over the catalyst correspond to the oxidation of unburnt HC (Eq. 1.2 and 1.6) and CO (Eq. 1.3 and 1.5) and the reduction of NO which may occur via different pathways as shown in Eq. 1.4 to 1.6.



Furthermore, at high temperature steam reforming of different HC may contribute to their conversion as shown in Eq. 1.7. Likewise, CO can be oxidised by the water-gas shift reaction (WGS) as shown in Eq. 1.8. The necessary steam is provided by the combustion in the engine.

Additionally, other side-products as NO₂, nitrous oxide (N₂O) and ammonia (NH₃) may be formed. NO₂ is a toxic gas which may mainly be formed under lean conditions according to Eq. 1.9. Nitrous oxide, even though non-toxic, is also an undesired side-product because it is a very potent greenhouse gas and contributes to the depletion of the ozone layer. Its global warming potential (GWP) of 310 exceeds by far not only the one of CO₂ (1) but also the one of the even more potent methane (21).^[7-9] NH₃, on the other hand, is a corrosive compound which is dangerous for aquatic animals. Typically, N₂O can be generated during the cold start of the engine below the light-off temperature from incomplete NO_x reduction, e. g. according to Eq. 1.10).^[5,8,10,11] Ammonia, on the other hand, is mainly formed in rich conditions, i. e. in a large excess of H₂ (Eq. 1.11).^[5] Such high amounts may be present due to WGS under rich conditions.



1.1.2 Composition of a conventional TWC catalysts

A conventional catalytic converter is a complex system. An example as used in TWC is depicted in Fig. 1.2. A metallic or ceramic (cordierite $2\text{MgO} \cdot 2\text{Al}_2\text{O}_3 \cdot 5\text{SiO}_2$) monolith is generally packed inside a metal casting, protected by a mat out of ceramics or metal wire mesh. This cylindrical monolith has a honeycomb structure with long and narrow channels which allow for a high exchange surface with the gas phase. A cell density of 300 to 600 cpsi (cells per square inch) is generally used in automotive exhaust gas treatment.^[6] The monolith is washcoated by a highly porous oxide layer presenting a high specific surface area (SSA), generally alumina, and incorporating a variety of additives namely the so-called promoters and the (catalytically) active phase.

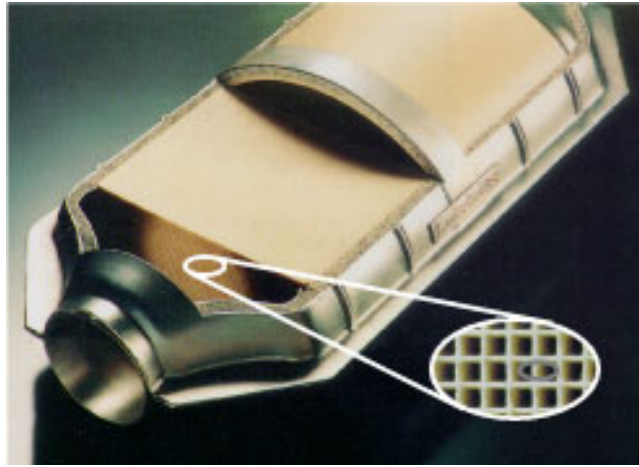


Figure 1.2 – Conventional TWC converter.^[12]

The promoters are mainly rare earth metal oxides (CeO_2 , ZrO_2) as well as La_2O_3 and BaO but other oxides may be added in lower amounts as well. The former are incorporated to allow for a temporary stocking (Eq. 1.13) or release of oxygen (Eq. 1.12), i. e. to enhance the oxygen storage capacity (OSC), in order to stabilise the stoichiometry. Indeed, as already discussed earlier, in 3-way operating conditions the A/F does not meet ideal stoichiometry continuously despite the invention of the λ sensor. Instead, a cycling around the stoichiometry is generally observed. Even though the operating window could be narrowed down in recent years, periods under rich and lean conditions are frequently passed through during the driving cycle. In these cases the promoters allow for buffering the effect of the fluctuation by balancing the oxygen content.^[3,5,13–17] This helps in continuously obtaining acceptable conversions of all 3 pollutants.



La_2O_3 and BaO addition, on the other hand, improves the thermal stability of the alumina.^[3,6] But CeO_2 and ZrO_2 were also shown to enhance this stability.^[18] In fact, it is known, that CeO_2 also stabilises the noble metal dispersion,^[5] and favours WGS and steam reforming reactions by promoting the catalytic activity on the interfacial metal-support sites as well as it enhances CO oxidation by using lattice oxygen.^[3,14]

The active phase itself is dispersed onto the washcoat in the form of small nanoparticles (approximately 1 to 2 nm for the fresh catalyst). It consists of trace amounts of different noble metals of the platinum group metals (PGM). These are mainly Pt, Pd and Rh. Others as Ru and Ir were investigated but proved unsuitable due to their volatility and/or toxicity.^[5,19] While the main function of Pt and Pd is to promote oxidation, the benefit of adding Rh is attributed to its reduction performances.^[3,6,20] The enhanced NO conversion is generally explained by an enhancement of the NO dissociation on Rh.^[3,21,22]

One drawback of the use of PGM nanoparticles, however, is that over the time the active phase nanoparticles tend to sinter due to the high temperature which can reach more than 1000 °C.^[3,6] This leads to a decrease in catalytic activity due to the lower density of active sites.

Table 1.2 – Current market prices of TWC-relevant PGM.

PGM	price (\$·troy ounce ⁻¹) ^a
Pt	1271
Pd	782
Rh	1180

^a Prices as of 20th January, 2015.^[23]

The TWC system has been in use for a long time and optimised over the last decades allowing for very high conversions of all regulated pollutants. Its major inconvenience is its cost, however. This is mainly caused by the expensive PGM (Table 1.2) used as the active phase, and was more recently aggravated due to the price increase for rare earths. This was mainly caused by an export restriction by China, the leading producer. In response to the World Trade Organisation (WTO) ruling against China after a dispute settlement case was launched by the European Union (EU), Japan and the United States of America (USA) this restriction is supposed to be lifted, though.^[24-26]

1.1.3 Parameters influencing the catalytic performances of TWC and catalytic performance evaluation

The catalytic performances of a TWC depend on multiple parameters as illustrated in Fig. 1.3 which can be classified into the following fields: the chemistry and the physics of the catalyst

and the engineering aspects.^[5] In addition, all of these parameters have an impact on the others. This generally complicates an exhaustive investigation.

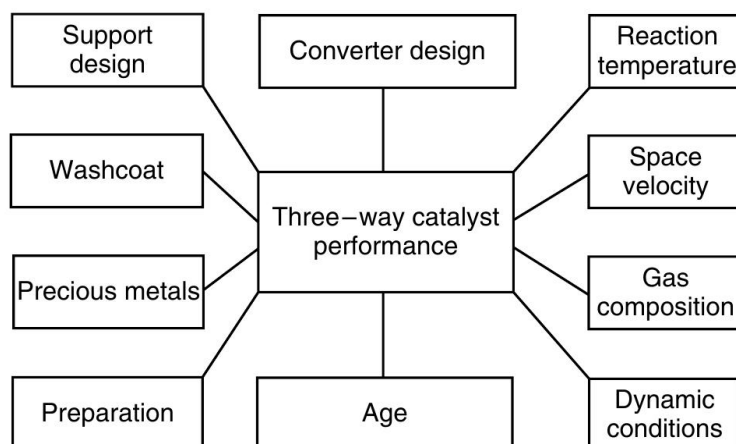


Figure 1.3 – Parameters influencing the performances of a 3-way catalyst (TWC).^[27]

As a chemist, I will not dwell on the challenges of support and converter design, without abnegating the importance and need for elaborate designs, which do influence many of the other parameters.

From the chemist's and material scientist's point of view, the preparation of the coated monolith and the composition of the washcoat and the active phase, i. e. the precious metals or alternative compounds, is primordial. Interactions between the elements of the washcoat with the support are important to allow for proper adhesion of the catalyst. Moreover, positive and negative interferences between components may occur inside the washcoat itself and with the active phase. Additionally, the active phase has to be prepared in a way to satisfy high dispersion and out-standing thermal stability. The durability of a catalyst is much dependent on its age, i. e. its thermal stability. In general, TWC loose in performance during use due to the sintering of the active phase or the support occluding the active phase. Alloying effects can also be detrimental to the intrinsic activity of PGM to convert NO, CO and HC. This sintering as well as deleterious reactions with catalyst poisons need to be prevented as much as possible by catalyst design.

On the other hand, the reaction temperature naturally determines the ease or difficulty for all reactions taking place, e. g. the desorption of exhaust gases and conversion products and the interactions/reactions between the exhaust gases themselves, thereby influencing the conversions of the different compounds, i. e. the catalyst performance.

Depending on the space velocity, the time for interaction between the exhaust gas and the catalyst differs. In a real TWC, gas hourly space velocity (GHSV) of up to $100\,000\text{ h}^{-1}$ reign,^[6] leaving but little time for the catalytically promoted after-treatment reactions. The higher the space velocity, the lower the performance of the TWC.

Finally, the gas composition plays a key role in the performance of TWC. As already

discussed above, TWC are optimised to run in stoichiometric conditions. The influence of fluctuations around this stoichiometry, i. e. dynamic conditions, has been laid out earlier. Moreover, different kinds of HC may be formed in the engine in different temperature ranges and depending on the (in)completion of the combustion higher or lower amounts of inhibiting reaction products (H_2O and CO_2) may be present in the exhaust stream.

This list is non-exhaustive but allows to understand the challenges of performance evaluations. Catalytic evaluations can be performed in a real vehicle (chassis dynamometer tests), in an engine bench test or in model laboratory tests using synthetic gas mixtures. Chassis dynamometer and engine bench tests are generally very expensive and do not allow to study particular aspects of the catalyst performance parameters. In terms of judging the practical applicability of the TWC such tests are indispensable, though, because real life conditions are difficult to mimic in their whole complexity in laboratory tests.

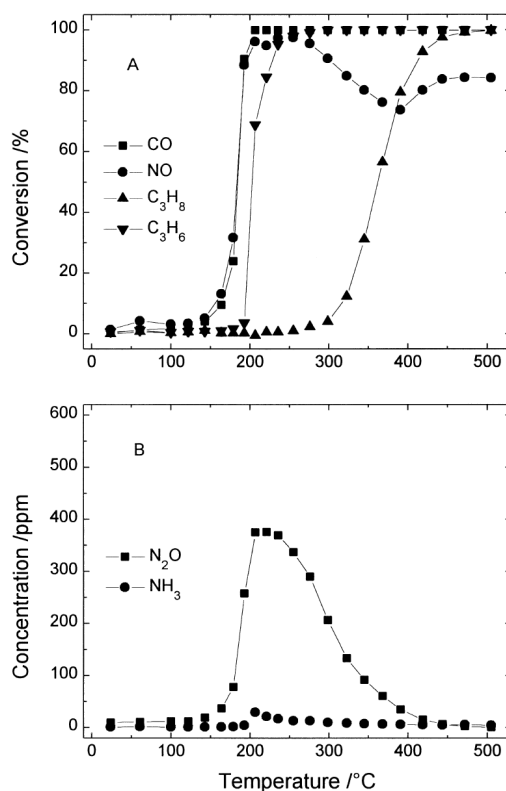


Figure 1.4 – **Light-off curves for Rh/alumina.** Reaction of 10 300 ppm CO, 2680 ppm H_2 , 490 ppm C_3H_6 , 197 ppm C_3H_8 , 1030 ppm NO, 9350 ppm O_2 and 5000 ppm H_2O balanced by He at a total flow rate of $200 \text{ cm}^3 \text{ min}^{-1}$ (GHSV of 7500 h^{-1} , $\lambda = 0.98$) over Rh/ Al_2O_3 : (A) conversions of CO, NO, C_3H_6 and C_3H_8 ; (B) production of N_2O and NH_3 .^[28]

Model laboratory reactions with synthetic gas mixtures, if conducted to evaluate catalytic performances in TWC, should, nonetheless, exhibit an appreciable complexity to resemble real-life conditions. Laboratory evaluations are often performed following a temperature programme. This leads to the typical, generally S-shaped, light-off curve of conversion of the different reactants as shown in Fig. 1.4A.

Some trends are observed for nearly all TWC and listed hereafter. Indeed, CO is generally easier oxidised than any of the HC. Concerning the HC, alkenes and aromatic compounds are more reactive than alkanes and therefore exhibit lower light-off temperatures. The more C atoms are present in an alkane molecule, the easier it will be converted.^[5] Furthermore, NO reduction is more difficult than CO oxidation and generally does not proceed via the CO + NO reaction in realistic exhaust gas.^[8]

However, differences between the activities of different PGM exist. Cant et al. studied the impact of the nature of the noble metal on the production of nitrous oxide for supported Rh, Pd and Pt catalysts at slightly lean conditions.^{[28]¹} The authors showed that most nitrous oxide was formed over the Rh catalyst but that the N₂O production drops at temperatures above 250 °C (Fig. 1.4B). The Pt catalyst, on the other hand, favours the production of ammonia, nitrous oxide formation is only observed in a narrow temperature range. More complex behaviour was evidenced for the Pd catalyst. This catalyst leads to the widest temperature range for N₂O production, starting at low temperatures according to the authors via the catalysis of the NO + H₂ reaction, and persisting even above 350 °C. Differences were also observed concerning the hydrocarbon oxidation conversions.

Therefore, the optimisation of an elaborate combination of different active phases and promoters on suitable supports is required for optimum performances.

1.1.4 Criteria of a good TWC

A 3-way catalyst should ideally exhibit high intrinsic catalytic activity in oxidation and reduction. The oxidation and reduction performances should additionally be as high as possible under stoichiometric conditions in the presence of a complex gas mixture including the pollutants and inhibitors such as high amounts of water and CO₂.

Secondly, high selectivities of non-noxious conversion products are desirable. Especially concerning NO reduction, a high N₂ selectivity during NO reduction (S_{N_2}) is important. Other by-products exhibit harmful effects, N₂O being a non-toxic but extremely potent greenhouse gas, NO₂ and NH₃ being known for their toxicity.

Thirdly, such a catalyst should present a high thermal stability under the described conditions, i. e. withstand as much as possible occurring sintering processes.

To ensure best conditions for TWC, the fluctuations around the stoichiometry should be buffered by a component with a reasonable oxygen storage capacity (OSC).

The stability against catalyst poisons such as SO₂ and Pb is appreciable but is less important nowadays than in the beginnings of automotive exhaust gas treatment. This change is due to the fact that, on the one hand, Pb, formerly present due to the use of tetraethyl lead as anti-knock additive has been forbidden in fuel as a consequence of its toxicity and its deleterious effects on the after-treatment catalysts. The SO₂ content in exhaust gas, on the

¹General conditions of the study are reported in the caption of Fig. 1.4.

other hand, has decreased significantly during the last decades thanks to the limitation by regulation of S in the fuel.

Finally, a good availability and thereby cost is desirable.

As is evident from this list, a good TWC is generally composed of many different components. The interplay of all these components allows for the good overall performance. Interactions between so many components cannot be prevented which can have positive or negative consequences.

Therefore, many different systems such as zeolites or perovskites have been proposed to (partially) replace at least one component of the conventional TWC. Some perovskites, oxides which are easily tunable in composition, were shown to exhibit promising catalytic performances coupled with relatively high thermal stability and present the advantage of being more easily available than the conventionally employed active phase noble metals.

1.2 Perovskites $ABO_{3\pm\delta}$

Compounds of the perovskite family as investigated in this study are mixed oxides of nominal composition ABO_3 with A-site atom (A) being Ca and B-site atom (B) being Ti in the eponymous mineral. They are used in many different domains due to their versatile property to accommodate a wide range of cations. Most of these oxides present a slightly lower or higher oxygen content with respect to the nominally expected amount, the stoichiometric term δ presenting the difference from this theoretical content. However, to allow for easier readability, $ABO_{3\pm\delta}$ will be denoted as ABO_3 hereafter.

1.2.1 Structure

Perovskites

Indeed, the ABX_3 perovskite structure can be formed by a variety of different ions. Non-oxides as $KZnF_3$ and $KNiF_3$, carbides, halides, nitrides and hydrides crystallise in the perovskite structure as well^[4,29] but are not subject of this study.

For a perovskite structure as ABO_3 to be formed 2 main electronic and structural requirements have to be met. The first is the electroneutrality of the compound, i. e. the sum of the valences of the A and B-site cations must equal 6. The other requirement relies on the size of the cations. While one of the cations should present a similar radius as the O^{2-} cation, e. g. Ca^{2+} and La^{3+} , and is generally denoted as A, the other is significantly lower in size (B^{2+}).^[4]

In this structure, for which the ideal crystal lattice is cubic (space group $Pm\bar{3}m$), the A-site cation is coordinated by 12 oxygen anions, while the B-site one is octahedrally coordinated (6-coordinate) as shown in Fig. 1.5. Only few structures of the so-called perovskite family are

²B is a generic term and does not refer to the element boron.

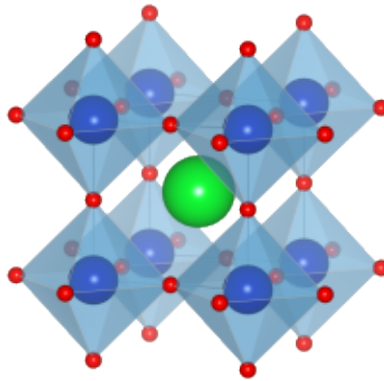


Figure 1.5 – **Perovskite structure.** A green, B blue, O red.^[30]

perfectly cubic, e. g. $SrTiO_3$, $BaSnO_3$. Most display distortions leading to orthorhombic and rhombohedral, less often to tetragonal, monoclinic and triclinic lattices.^[19] Another possible structure consists of the hexagonal lattice.

Considering both conditions, a wide variety of metal cations can be incorporated into the perovskite structure. Following the condition of electroneutrality, compounds of the formulas $A^+B^5+O_3$, $A^{2+}B^{4+}O_3$, and $A^{3+}B^{3+}O_3$ should be allowed. If they additionally meet the geometrical requirement with a tolerance factor, t (Eq. 1.14), being in the limits of $0.75 \leq t \leq 1$, they should form a perovskite structure.^[6,19] The coefficient α initially proposed by Goldschmidt in 1926 to describe the limits of the perovskite structure's accommodation capability^[31] is nowadays generally denoted as the tolerance factor .

$$t = \alpha = \frac{1}{\sqrt{2}} \frac{r_A + r_O}{r_B + r_O} \quad (1.14)$$

A-site elements which meet these requirements are alkaline earths or rare earth metals, e. g. Sr, Ca or La, whereas suitable B-site elements are 3d, 4d or 5d transition metals as Fe, Mn, or Co. This leads to a large variety of possible compound compositions.

In addition to this, partial substitutions of the ions is possible if the above conditions are met. Slight distortions are generally tolerated so that some elements can be accommodated in low amounts which otherwise would not form a perovskite structure, e. g. Cu. This may lead to a certain degree of cation or anion defects, also denoted as non-stoichiometry. This tolerance is the reason why perovskites are widely appreciated for their customisable properties.

Ruddlesden-Popper phase A_2BO_4

The Ruddlesden-Popper phase (RP) (A_2BO_4) can be derived from the perovskite structure. It forms a tetragonal K_2NiF_4 -structure^[32,33] which for the oxides can be described as a layered structure of ABO_3 and AO (rock salt), i. e. $[(AO)(ABO_3)]_m$.

Since Cu cannot form a perovskite as described earlier, its corresponding RP, La_2CuO_4 ,

was studied in comparison to the perovskites. This compound presents an orthorhombic distortion. The A-site cation has a 9-fold, the B-site one a 6-fold coordination.^[34]

Hereafter, the perovskite-like RP will be included whenever it is spoken of perovskites, unless stated otherwise.

1.2.2 Properties and (non-catalytic) applications

Depending on the constituting elements perovskites show very different properties. They may exhibit a large panel of properties such as (ferro)magnetism (e. g. SrRuO₃, LaFeO₃ only weak), ferroelectricity (e. g. BaTiO₃), piezoelectricity, pyroelectricity, thermoelectricity (e. g. La₂CuO₄), and superconductivity (YBa₂Cu₃O₇).^[6,29,35]

LaMnO₃ and LaCoO₃ are used as cathode and LaCrO₃ as interconnect materials in solid oxide fuel cells (SOFCs).^[36,37] This application relies on their good ion mobility. This ion mobility, especially the O₂ mobility can be easily enhanced by creating oxygen vacancies. The formation of anionic vacancies can be inherent to the anion-defective perovskite or can be achieved or enhanced via partial substitution by lower valency cations in A- and/or B-site, the structural tolerance being a perovskite property with great impact on catalysis as well.

Cationic defects, i. e. vacancies, are observed much less often. Especially, B-site defects are not thermodynamically favoured as a consequence of their high charge density.^[29]

Owing to the high electronic and ionic conductivity combined with high electrochemical stability and interesting catalytic activity of some perovskites, e. g. LaFeO₃, they are also investigated for the use in Li-O₂ batteries.^[38] Different conduction properties can be found depending on the composition of the solid. Some perovskites are insulating, some show p- or n-type semiconducting or metallic transport properties.^[39]

Based on the p-type semiconducting properties of certain perovskites as LaFeO₃ which increase if an oxidising gas adsorbs on their surface, they can be used as gas sensors, e. g. LaFeO₃ was shown to be sensible to acetone and methanol, SmFeO₃ to petrol, and EuFeO₃ to formaldehyde.^[40–42]

The perovskites good redox properties rely on oxygen adsorption properties and the reversible oxygen release and uptake of the perovskite structure as depicted in Fig. 1.6.^[39] The reduction to the brownmillerite (ABO_{2.5}) is an extreme example in which a perovskite-type structure is still retained. In most cases, only part of the oxygen is released leading to intermediary structures.

Weidenkaff studied the reactivity of LaBO₃ perovskites (B = Ni, Co, Mn and Fe) during redox cycles by thermogravimetric analysis (TGA).^[39] She observed a dependence of the reaction rates of the solids (weight loss = $f(T)$) on the respective B-site cation. Reactivity was found to increase from ferrites over manganites, and cobaltites to nickelites. This corresponds to an analogous lowering of the reduction temperature from LaFeO₃ to LaNiO₃. Additionally, a dependence on the specific surface area was observed which was not further exposed.

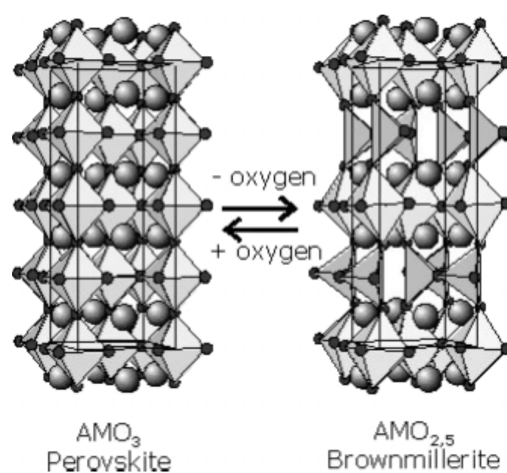


Figure 1.6 – Changes to the perovskite structure during redox reactions.^[39]

Regarding substitutions in the A-site, a higher reactivity was revealed for Ca-substituted cobaltites than for Sr-substituted ones.

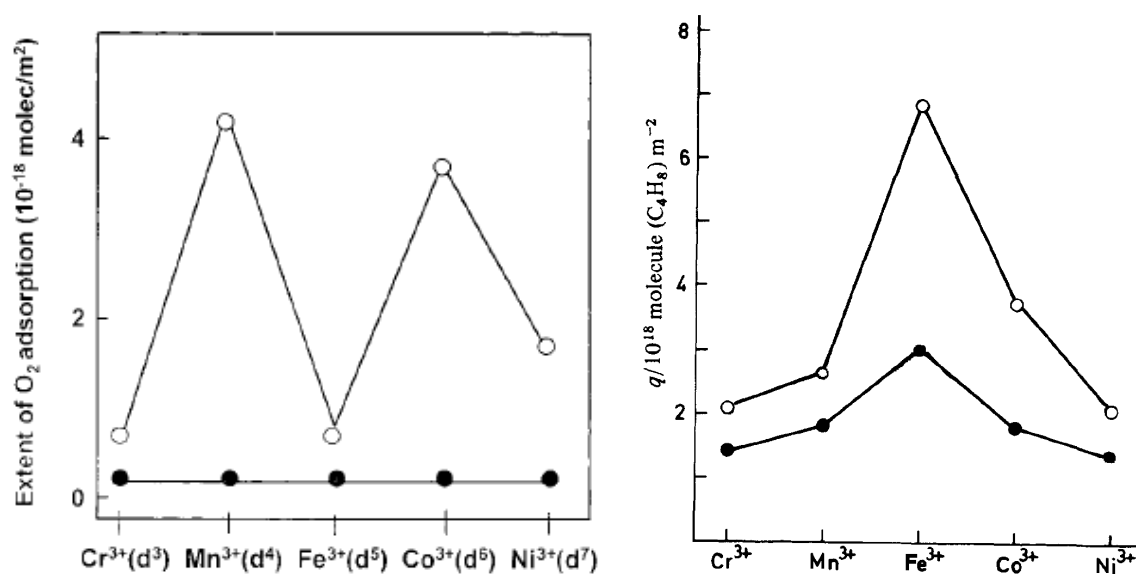


Figure 1.7 – O₂ (left) and isobutene (right) adsorption on LaBO₃. B = Cr, Mn, Fe, Co or Ni. Open circles correspond to the total, filled circles to reversible adsorption.^[29,43] (Adapted from [43].)

Kremenčić et al. investigated the O₂ and isobutene adsorption behaviour of perovskites LaBO₃ with B being a first row transition metal – except V and Ti since their compounds or precursor (in solution) are unstable.^[43] Low reversible O₂ adsorptions were observed on all solids which hints at physisorption. The authors found marked maxima of total adsorbed quantities for LaMnO₃ and LaCoO₃ during O₂ adsorption experiments (Fig. 1.7), on the other hand. The total isobutene adsorption is highest on LaFeO₃, though. Furthermore, for all investigated solids, the O₂ adsorption on clean surfaces was observed to be lower than on the corresponding preadsorbed surfaces with isobutene (not shown). The authors concluded

that no competitive adsorption between isobutene and O_2 takes place, i. e. the adsorption occurs on different sites. No explanation of the observed maximum of isobutene adsorption on $LaFeO_3$ was given.

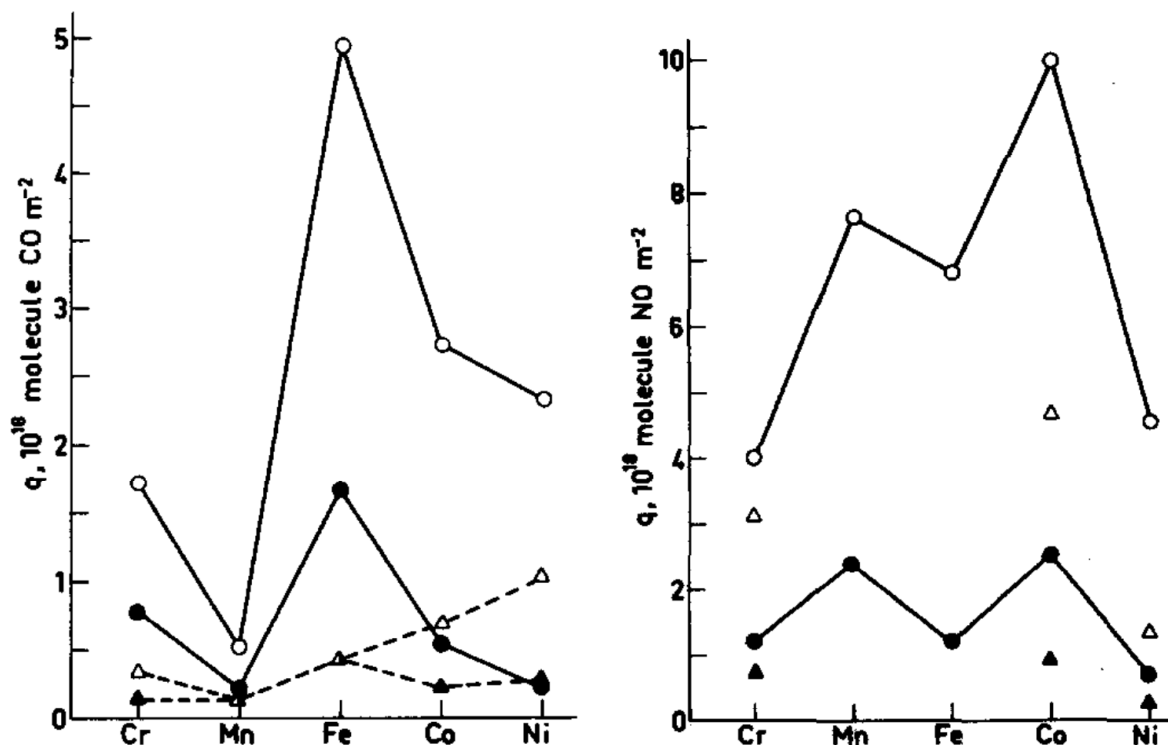


Figure 1.8 – CO (left) and NO (right) adsorption on $LaBO_3$. B = Cr, Mn, Fe, Co or Ni. Open symbols correspond to the total, filled to reversible adsorption. Circles represent adsorptions on clean surfaces, triangles adsorptions on which NO (left) or CO (right) is pre-adsorbed.^[44]

A similar study was conducted by Tascón et al. focussing on the adsorption of CO and NO on $LaBO_3$ (B = Cr, Mn, Fe, Cr, Ni).^[44] Results shown in Fig. 1.8 also reveal a maximum for NO adsorption on $LaMnO_3$ and $LaCoO_3$ solids as previously observed for O_2 . The difference in total adsorption between $LaMnO_3$ and $LaFeO_3$ in the case of NO is lower than for the O_2 adsorption, though. The $LaFeO_3$ sample, on the other hand, exhibits the maximum CO adsorption capacity in analogy to the isobutene results obtained by Kremenčić et al. According to the authors, CO and NO adsorption consist of competitive phenomena, i. e. take place (partially) at the same sites. This investigation also revealed a stronger NO adsorption preventing CO adsorption. Infrared spectroscopy (IR spectroscopy) after simultaneous CO and NO adsorption on $LaFeO_3$ revealed interactions between CO and NO and the surface oxygen of the oxide. Isocyanate species (NCO) could be evidenced as was already observed for conventional alumina-supported Pt TWC and correlated with ammonia production in the case of $CO + NO + H_2$ reactions.^[28]

Acid-base properties were investigated via the adsorption of probe molecules, e. g. pyridine to probe acidic and CO_2 to probe basic sites, monitored by IR spectroscopy. It was found that $LaBO_3$ perovskites (B = Mn, Fe, Cr) present only weak acidity.^[45] Basic properties are

very common for perovskites, on the other hand.^[19] This basicity is the reason why carbonates formed with atmospheric CO_2 are often found on their surfaces.^[29] These carbonates have different stabilities on the perovskite surface since they may be bonded as mono- or bidentate species.^[19]

The adsorptive, acid-base and redox properties of perovskites play an important role in catalysis and caused the interest in this mixed oxide family for this field during the last decades and up to now.^[29]

Another important aspect is the thermal stability of perovskites under reductive atmospheres. Differences depending on the A-site cation occur. For lanthanide cobaltites ($LnCoO_3$), the reducibility increases, i. e. thermal stability decreases, with decreasing lanthanide radius.^[46,47] Consistent results were obtained for $LnFeO_3$ solids by studying their Gibbs free energies of formation ($\Delta_f G^\circ$).^[48,49] Hence, La provides the highest thermal stability for perovskites if the A-site cation is chosen from the lanthanide series as is generally the case in heterogeneous catalysis.^[29] Concerning the B-site cations, thermal stability under reductive atmosphere was found to increase in the following way in $LaBO_3$ perovskites: $Ni < Co < Mn < Fe < Cr \approx V$.^[50] This trend has also been reported for the single oxides of Fe, Co and Ni.^[19,51] Perovskites containing these cations were more stable than the corresponding simple oxides,^[19] though, confirming the enhanced stability of transition metal cations in the perovskite structure.

Generally, perovskites prepared by conventional synthesis methods exhibit a lower specific surface area (SSA) than alumina (1 to $5\text{ m}^2\text{ g}^{-1}$ versus $100\text{ m}^2\text{ g}^{-1}$ for γ -alumina).^[52] The surface area can, however, be increased as shown in Section 1.3. As has been pointed out by Weidenkaff,^[39] textural properties depend very much on the exact compositions and synthesis parameters need to be optimised accordingly.

1.2.3 Perovskites in 3-way catalysis

In this Section, particular attention is paid to perovskites comprising first row transition metals in the B- and lanthanides in the A-site.

Perovskites were indeed already reported to be active in heterogeneous catalysis in the early 1950s, e. g. for CO oxidation in the case of $LaFeO_3$ or $La_{0.55}Sr_{0.35}MnO_3$.^[53,54] However, the interest in their catalytic properties became more evident in the 1970s after Meadowcraft reported on the electrocatalytic activity in oxygen reduction of a cobaltite.^[55] Other reports followed on the gas-phase reactivity of $LaCoO_3$ and $LaMnO_3$ which proved catalytically active for CO oxidation, NO removal and other reactions as the hydrogenation and hydrogenolysis of cis-2-butene.^[56-60]

Nitadori et al. already studied the effects of the A- and B-site cations in a perovskite on heterogeneous catalysis in the late 1980s.^[61] As shown in Fig. 1.9, the authors found that propane oxidation activity is mainly affected by the B-site cation. The A-site cation

plays a minor role in this respect as long as isovalent comparisons are made. Differences depending on the A-site cation occur in the thermal stability under reductive atmosphere as discussed earlier. Since La-containing perovskites are the most stable of the lanthanide series and furthermore present slightly higher catalytic activities than Sm- and Gd-containing perovskites, only LaBO_3 solids will be discussed further.

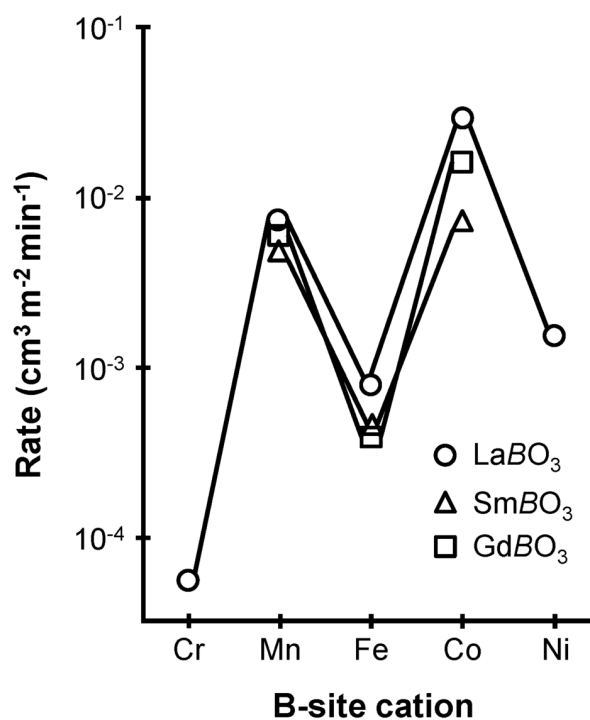


Figure 1.9 – Catalytic activity of ABO_3 for propane oxidation at 227 °C. A = La, Sm or Gd; B = Cr, Mn, Fe, Co or Ni.^[6,61]

Peter et al. performed a study on Ln_2CuO_4 with $\text{Ln} = \text{La, Pr or Nd}$.^[62] The comparison of the low SSA Ln_2CuO_4 ($\approx 0.5 \text{ m}^2 \text{ g}^{-1}$) for the $\text{CO} + \text{NO}$ reaction yielded best results for La. According to the authors, contrarily to the LnBO_3 samples, this enhanced catalytic activity results of the higher reducibility – lower temperature peaks were found in H_2 -TPR measurements – leading to the formation of more and therefore smaller Cu^0 nuclei according to Eq. 1.15.



According to the authors, this higher reducibility resulted itself of the less dense structure because of the higher radius of La^{3+} as compared to Pr^{3+} and Nd^{3+} , leading to more labile oxygen species which make the oxide easier reducible.

From Fig. 1.9,^[6,61] it is evident that the B-site element has a dramatic importance for the catalytic activity. This confirms the results obtained for other oxidation reactions, i. e. CO , propylene and isobutene oxidations, which gave similar results.^[43,63] Indeed, LaMnO_3 and

$LaCoO_3$ show highest oxidation activities compared to Ni-, Fe- and especially Cr-containing perovskites. This correlates with the results obtained for O_2 -adsorption (Fig. 1.7) by Kremenčić et al. as discussed above.^[43]

This leads to the result that mainly Co-, Mn-, Fe-, Ni- and Cu-containing perovskites present interesting oxidative properties. Out of these, Ni and Co perovskites are excluded for the scope of this study as a consequence of doubts concerning resulting environment and health problems of their use – either due to the toxicity of formed compounds or their precursors.^[6,64–67] Therefore, the focus of this study will be laid on $LaMnO_3$, $LaFeO_3$ and La_2CuO_4 perovskites. Comparisons to the $LaCoO_3$ or other perovskite solids are occasionally made since the $LaCoO_3$ perovskite presents one of the most studied systems.

It has to be kept in mind that partial substitutions in the A- and B-site as discussed later can enhance the catalytic activity of different perovskites. Apart from the impact of the composition, other parameters which are determined by the preparation method of the catalyst – discussed in Section 1.3 – e. g. specific surface area (SSA), redox behaviour, and oxygen mobility may also influence the catalytic activity of a perovskite.

CO and HC oxidation

$LaBO_3$ perovskites (B being a 1st row transition metal) are well renowned for their high oxidative catalytic activity which is generally attributed to their good O_2 adsorption as already discussed above.^[29,68] Moreover, the easier reducible the oxide, the better is the catalytic activity for oxidation reactions. For the series of B as 3d transition metal, it was found that perovskites containing Ni, Co or Mn in the B-site were the most reducible and gave the best results.^[29,69]

The catalytic oxidation of HC and CO has been studied for different perovskite-type oxides like cobaltites, manganites and ferrites. Especially Co- and Mn-containing perovskites are considered to be highly catalytically active for oxidation reactions as already stated.^[29,70–72]

The CO oxidation is generally assumed to follow a suprafacial mechanism.^[72] Only chemisorbed oxygen species from gaseous oxygen are involved in such a suprafacial process which occurs at relatively low temperatures. This explains why oxygen adsorption properties play a key role in this reaction. On the other hand, for CH_4 combustion, which only occurs at high temperatures over perovskites, an intrafacial mechanism is preferred.^[72] In this case, migration of bulk oxygen to the surface, filling up the oxygen vacancies, is considered. The necessary oxygen mobility is an additional factor to be considered to allow for high conversions. The mechanisms of other HC oxidations such as alkenes are assumed to follow suprafacial mechanisms.^[72]

The generally observed oxygen non-stoichiometry in $LaMnO_3$, i. e. the presence of low amounts of Mn^{4+} , is assumed to be advantageous for the methane oxidation.

NO reduction

The catalytic reduction of NO_x by the same perovskite compositions as used for oxidation reactions – something which is needed in TWC – requires other operation conditions in order to yield (nearly) complete conversion. This has been stated for LaMnO_3 in the 1970s already.^[73] It was found that oxygen vacancies, $V_{\text{O}}^{\bullet\bullet}$, in the perovskite ($\text{LaMn}_{0.9}\text{V}_{\text{O}0.1}\text{O}_{3-\delta}$) allow for a better reduction activity.^[73] Zhao et al. also investigated the vacancy dependency regarding Ni-based perovskites and stated that for NO reduction oxygen vacancies are needed to allow for a better adsorption and activation of NO as well as an increased lattice oxygen mobility which enables a faster restoration of the active sites.^[74] This correlation was confirmed by Zhu et al. who studied La_2CuO_4 and LaSrCuO_4 phases.^[75] A way to obtain those vacancies is the partial substitution by lower valent metals such as copper or strontium as already discussed before.

A mechanism for NO reduction on perovskites was proposed by Voorhoeve et al. over manganites in 1975^[76] in which oxygen vacancies ($V_{\text{O}}^{\bullet\bullet}$) play a major role as can be seen in Eq. 1.16 to 1.21.



According to the authors, the reaction shown in Eq. 1.17 is favoured at low temperatures while the reaction reported in Eq. 1.20 is actually favoured at high temperatures. The latter finding is explained by the higher availability of active sites and lower NO_{ads} concentration due to the easier desorption at higher temperatures. This explains why N_2 formation is generally mainly observed at high temperatures. Ferri et al. assume that NO reduction by H_2 follows the same mechanism.^[77] In the same study, the authors stressed the importance of the inhibitory effect of stable tetravalent B-site cations. Furthermore, the authors observed a higher N_2 selectivity during NO reduction (S_{N_2}) for manganites and ferrites compared to the tested Co- and Ni-based perovskites.

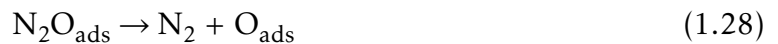
The presence of O_2 , H_2O , and CO_2 as inhibitors has been studied by different groups.^[78,79] Tofan et al. showed that all these compounds have an inhibiting effect on the rate of NO reduction by H_2 over substituted cobaltite, ferrite and nickelite.^[78] CO_2 exhibits an especially strong inhibition. This is presumably due to the formation of carbonates on the basic perovskite surface. All investigated perovskites show a similar inhibiting effect by water

adsorption. Differences between the water inhibition mechanism over the ferrite compared to the nickelite and cobaltite are supposed, though. The degree of the inhibition effect of CO_2 is different for the 3 perovskites. CO_2 inhibition was the strongest on the nickelite and the weakest on the ferrite. Furthermore, an increase of the inhibiting effect of H_2O , and CO_2 with increasing temperature was observed while O_2 inhibition is lowered in the same temperature range. Iwakuni et al. confirmed the highly deleterious effect of CO_2 on NO decomposition over a $BaMnO_3$ -based perovskite.^[79] According to the authors, the inhibition could be attenuated by co-feeding H_2 . H_2 also allows for an easier removal of nitrate species which form on the perovskite surface and are strongly bonded. This surface cleaning helps to enhance the NO conversion.

CO + NO reactions

CO + NO reactions are often performed to get a preliminary notion of TWC reactivity of a catalyst. The test on this reaction implicates, however, much simplified conditions compared to those which reign in TWC, ignoring competitive adsorption and reactions as well as the influence of inhibitors. Due to the simplicity of the test, it cannot be assumed that results obtained by this method could be directly transferable to judge on the activity in TWC applications. Since the test of this reaction is relatively easily feasible however, a large panel of conducted tests has been reported in literature. A recent extensive review of this reaction over perovskites can be found in [72].

The mechanism of CO + NO reactions, as generally described for perovskites,^[72,73,80] follows the elementary surface reactions shown in Eq. 1.22 to Eq. 1.29.



Different groups have reported on the CO + NO reaction over ferrites, manganites and cuprates.^[62,81–83] Peter et al. found that ferrites and cuprates show most interesting results even better than for cobaltites.^[81]

An important feature of a good TWC is the high N_2 selectivity during NO reduction. Cu

ions are presumed very active for the NO reduction and were found to enhance N₂ selectivity during NO + CO reduction.^[83,84] Peter et al. monitored the NO conversion products during the CO + NO reaction catalysed by La₂CuO₄.^[62] Even though, at 200 °C, the N₂O selectivity during NO reduction (S_{N₂O}) is 100 %, it decreases with increasing temperature to favour largely the formation of N₂ at 450 °C. At this temperature, S_{N₂O} is down to 10 %. During the CO + NO reaction, metallic Cu particles are formed as evidenced by XRD after the catalytic test. These metal particles are considered the active species. The RP structure itself, however, is nearly completely destroyed as can be seen from the appearance of strong diffraction peaks ascribed to La(OH)₃ and very weak contributions from the original compound.^[62] In subsequent runs, the light-off temperature drops. It can be assumed that the Cu species which are initially finely dispersed in the perovskite-like structure right after the destruction of the RP are subject to Ostwald ripening processes. This sintering then leads to decreasing activities. Although high reducibility is correlated to high catalytic activity, the retention of the perovskite structure to stabilise the active cations is crucial for the thermal stability.

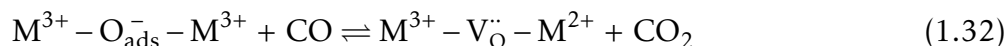
Effect of substitutions in A

The main substitutions in A position, which is most often held by lanthanum, are performed using Sr²⁺ and Ce⁴⁺. The catalytic activity regarding HC oxidation can be increased by doping with Sr²⁺.^[85–88] This effect is mainly attributed to the compensation of charge which leads to partial B⁴⁺-formation and oxygen vacancies, thereby creating defects in the crystal structure and enhanced oxygen mobility. Nonetheless, Voorhoeve stated a decrease in catalytic activity concerning CO oxidation for Sr-doped perovskites.^[73] The substitution with Ce on the other hand promotes the CO oxidation even though it seems that a Ce content of more than 0.2 cannot be overcome because it cannot be stabilized in the structure and therefore leads to the formation of a catalytically inactive CeO₂ phase.^[89] This phase is known on the other hand to form one of the best oxygen storage systems used up to date because of the easy redox process (Eq. 1.13 and 1.12) as already discussed earlier.^[90]

Other mainly divalent substituting ions as Ca²⁺ may also be used in order to form B ions in an unusual oxidation state and/or oxygen vacancies. Pecchi et al. investigated the partial substitution of La by Ca in LaFeO₃ for the methane combustion and found that the formation of Fe⁴⁺ lead to enhanced catalytic activity.^[91] Barbero et al. found similar results for the same system in propane oxidation.^[92]

Different substitution patterns of La₂CuO₄ were proposed to enhance its catalytic activity. Zhu et al. explored the partial substitution by Sr for the NO + CO reaction.^[93] They found a correlation between the Sr content, the molar ratio of Cu³⁺/Cu²⁺ and the non-stoichiometric oxygen. In this study, LaSrCuO₄ gave the best results in the catalytic reaction. The increase in oxygen vacancies, later on written as V_O[•], seemingly enhances the NO adsorption and dissociation ability of the oxide since they intervene in the assumed mechanism, as shown in

the following equations (Eq. 1.30 to 1.32).



The same trend was confirmed for higher surface area oxides in CH_4 oxidation.^[88] The authors could observe Cu^{3+} species by XPS.

Effect of substitutions in B

B-site substitution in perovskites by non-isovalent cations leads to the generation of oxygen vacancies and B cations in unusual oxidation states. This kind of substitution can change the redox behaviour and ion mobility compared to the parent perovskite.^[29,72]

The moderate catalytic activity of LaFeO_3 for different oxidation and reduction reactions including the $\text{CO} + \text{NO}$ reaction was shown to be considerably enhanced by partial Fe substitution with Cu.^[83] In this case, the formation of anion vacancies allowed for easier adsorption of the reactants and dissociation of adsorbed NO. Oxygen mobility in the structure was also increased which led to a faster regeneration of active sites. Furthermore, the N_2 selectivity during NO reduction was higher for the Cu-substituted ferrite than for non-substituted LaFeO_3 .

Even though Mn perovskites show high activity regarding oxidation, it can still be increased via partial substitution. Mizuno et al. investigated the incorporation of copper leading to remarkable results.^[94] Rate constants for CO oxidation and $\text{NO} + \text{CO}$ reaction at 400°C of $\text{LaMn}_{1-x}\text{Cu}_x\text{O}_3$ ($m_{\text{catalyst}} = 10$ to 50 mg, diluted with 250 mg SiC) were determined at $p = 8$ kPa with CO to NO ratio of 1. Rate constants of $\text{LaMn}_{0.6}\text{Cu}_{0.4}\text{O}_3$ obtained in this way were approximately 400 and 5000 times higher than for LaMnO_3 and La_2CuO_4 , respectively. Moreover, a 100-fold higher rate constant than for $\text{La}_{0.8}\text{Sr}_{0.2}\text{CoO}_3$ was observed. At the time of publication, this solid was reported to yield comparable results as $\text{Pt}/\text{Al}_2\text{O}_3$. A synergistic effect of copper facilitating the CO activation and Mn increasing the lattice oxygen reactivity is claimed to be at its origin.

The doping by magnesium was studied by Saracco et al.^[95] Compared to LaMnO_3 , for $0 < x \leq 0.2$ in $\text{LaMn}_{1-x}\text{Mg}_x\text{O}_3$ a higher activity for methane combustion was observed. This is not only but also due to the formation of MgO which helped in the formation of small perovskite crystals and to prevent agglomeration.

3-way catalysis

In the past, mainly cobaltites and manganites were investigated for dual-bed catalysis and TWC.^[6,19,70,96] This is a consequence of the early reports on higher oxidation activities of such ACoO_3 and AMnO_3 solids. As has been discussed above and emphasized by Teraoka et al., however, well chosen substitutions may increase the catalytic activities of less active perovskites to rival those of solids deemed more active.^[97] More recently, perovskites containing other B-site cations such as Fe were studied for this application as well.^[98,99]

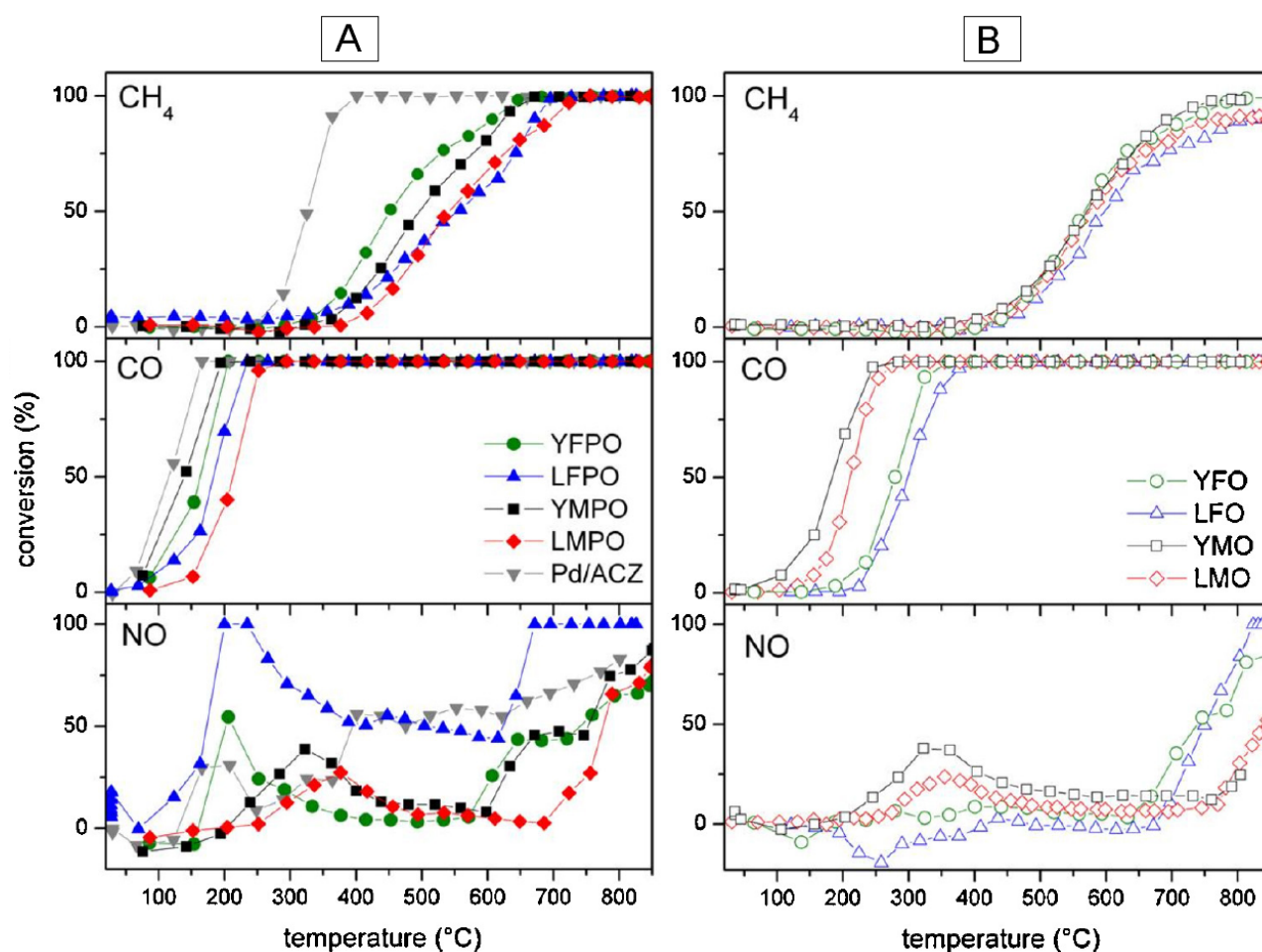


Figure 1.10 – CH_4 , CO and NO conversions of YFeO_3 (YFO), LaFeO_3 (LFO), YMnO_3 (YMO), LaMnO_3 (LMO) (left) and the corresponding Pd-doped perovskites (2 wt.%, YFPO, LFPO, YMPO, LMPO) (right) compared to a conventional TWC catalyst (Pd/ACZ; left) under TWC conditions. The conventional TWC was in powder-form and composed of Pd, alumina and ceria-zirconia ($\text{Pd}/(\text{alumina} + \text{CeO}_2/\text{ZrO}_2) = 1.6 \text{ wt.}\%$). Catalytic evaluations of the powder catalysts (150–200 μm , 100 mg, diluted with the same volume of sieved sea sand) were performed after oxidative pre-treatment in 20 Vol.% O_2/He (50 ml min^{-1}) at 700 $^\circ\text{C}$ for 2 h. Reactions were conducted in the temperature range of 25 $^\circ\text{C}$ to 850 $^\circ\text{C}$ under synthetic gas flow containing 7000 ppm CO , 1300 ppm CH_4 , 1600 ppm NO_x and 5300 ppm O_2 , balanced by He (total flow rate of 100 ml min^{-1} ; GHSV = 60 000 h^{-1}).^[99]

Lu et al. investigated the catalytic performances of LaFeO_3 , LaMnO_3 and the correspond-

ing yttrium ferrite and manganite prepared by flame spray pyrolysis under model 3-way catalytic conditions.^[99] Results are depicted in Fig. 1.10B. The synthetic gas mixture was composed of CO, methane, NO_x and O_2 in He and thus did not contain any inhibitors or other HC than CH_4 . Under these conditions, manganites yielded significantly better results for CO oxidation and slightly better results for methane oxidation than the corresponding ferrites. Regarding low temperature NO conversion, i. e. in the temperature range of 200 °C to 500 °C, the same trend of manganites being more active than ferrites is observed. High temperature NO reduction is significantly higher for the ferrites.

According to the authors, the higher CO oxidation activity of the manganites is caused by their higher oxygen mobility. This argumentation was supported by OSC values which were measured for the solids and yielded the following trend of decreasing values: YMO > LMO > YFO > LFO in agreement with the CO oxidation performance trend.

PGM-doped perovskites The insertion of noble metals into perovskites was investigated since the 1970s. The primarily pursued goal of PGM doping consists of enhancing catalytic activity and preventing catalyst poisoning.^[19,96]

Coming back to the study on yttrium and lanthanum manganites and ferrites performed by Lu et al. (results shown in Fig. 1.10),^[99] a clear enhancement of catalytic performances was observed for samples containing 2 wt.% of Pd (Fig. 1.10A). Again, yttrium-based perovskites showed higher oxidation performances than their lanthanum counterparts. Regarding the differences in catalytic performances observed between ferrites and manganites, a reversed trend is observed for the La-based perovskites, i. e. Pd-doped lanthanum ferrites show higher catalytic performances than Pd-doped lanthanum manganites for CO oxidation and NO reduction (low and high temperature) and approximately the same performances regarding methane oxidation. According to the authors, exposed Pd on the catalyst surface is the main driver for CO oxidation activity, as for the methane conversion. The nature of the perovskite strongly influences the interaction between the noble metal and the perovskite and the nature of the Pd species on the surface, though.^[100,101] Supported PdO nanoparticles are assumed to be the active species for methane oxidation. Concerning NO reduction, the Pd-doped $LaFeO_3$ sample shows the highest NO conversions, even higher than for the conventional TWC. A high low temperature reduction performance is observed for this sample which coincides with the CO light-off curve. This simultaneous conversion hints at an initial CO + NO reaction. A similar observation was made for the Pd-doped $YFeO_3$ sample. The Pd-doped $LaFeO_3$ solid shows a wide activity window with conversions over 50%. The manganites' NO reduction performance, on the other hand, is not as much enhanced by the Pd-doping below 700 °C. An activation of the perovskite samples for the catalytic activity for methane and NO elimination under test conditions was observed. During the 2nd test, methane conversion of the Pd-doped $YFeO_3$ solid yielded equal results as for the conventional TWC. No subsequent deactivation was observed during a 3rd conducted test. This activation is explained by the

formation of (relatively large) Pd⁰ particles (≈ 20 nm) at the surface of the catalysts due to the high maximum temperature of 850 °C.^[99]

Labhsetwar et al. focused on the interaction between a high surface area support and a catalytically active perovskite. They reported on the application of a La_{0.7}Sr_{0.3}Mn_{0.95}Pt_{0.05}O₃ perovskite supported on alumina in TWC.^[96] In contrast to the above discussed example, the authors studied the catalyst performance first in a model laboratory test, and then in engine and chassis dynamometer tests. The authors stressed the importance of increasing the specific surface area of perovskites for catalytic applications. Comparing the solid obtained by co-precipitation method (s. Section 1.3) with an alumina-supported sample – prepared by in-situ synthesis on lanthanum oxide pre-coated alumina – laboratory evaluations revealed significantly enhanced performances for the supported La_{0.7}Sr_{0.3}Mn_{0.95}Pt_{0.05}O₃ perovskite. Subsequently performed engine and chassis dynamometer tests confirmed the high activity of the catalyst. According to the authors, the low Pt-content is not the sole responsible for the high performances. Identical amounts of Pt dispersed on an alumina support yielded lower performances. The thermal stability of the perovskite might, however, be improved by the doping. Furthermore, adhesion of the perovskite to the monolith was improved by the developed preparation route. Research on this subject is important and ongoing but exceeds the scope of this study. A recent review which deals with this topic was written by Keav et al.^[6]

Concerning the B-site substitution by PGM in La₂CuO₄, Guilhaume et al. investigated the use of La₂Cu_{1-x}Pd_xO₄ ($0 \leq x \leq 0.2$) in TWC.^[102] Therein, a relatively small partial substitution of Cu by Pd, $x = 0.1$ yielded the best results consisting in comparable conversions for NO reduction while at the same time CO and propylene oxidation performances appear to be strongly enhanced and therefore higher than by a conventional reference catalyst, Pt-Rh/CeO₂- γ -Al₂O₃ (containing 1.13 wt.% Pt, 0.19 wt.% Rh and 19.3 wt.% Ce) under water-free conditions.

Perovskite-PGM interactions In the last decade, the stabilisation of the noble metal nanoparticle dispersion by the intrinsically catalytically active perovskite as first reported by Tanaka et al. is a supplementary motive for noble metal insertion into the perovskite structure.^[64,98] Indeed, the TWC support materials often consist of ceramic honeycomb structures with an alumina washcoat which does not stabilise well the dispersion of the PGM nanoparticles. As a result, agglomerates form during catalyst use limiting its life span. Therefore, several groups investigated the incorporation of these noble metals in perovskite-type oxides.^[8,98] It has been shown that this incorporation of noble metals in the perovskites' B-site position prevents the noble metal's agglomeration leading to increased catalytic efficiency of these oxides and at the same time higher stability of the catalyst.^[103,104]

Tanaka et al. found that Pd could reversibly segregate and be reincorporated in the B-site position of the perovskite lattice of a ferrite.^[98] This so-called “self-regenerative function”

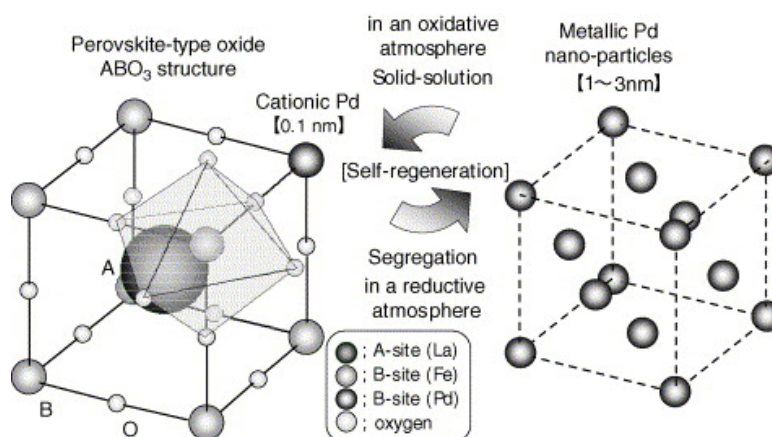


Figure 1.11 – Self-regenerative function of the *intelligent catalyst*.^[64]

of Pd in $LaFe_{0.95}Pd_{0.05}O_3$ prevents sintering of the Pd and thereby enhances the stability of the catalyst. Catalytic activity after ageing was improved significantly compared to a conventional TWC (Pd/ Al_2O_3). Both supported catalysts contained the same amount of Pd (3.24 mg cm^{-3}).

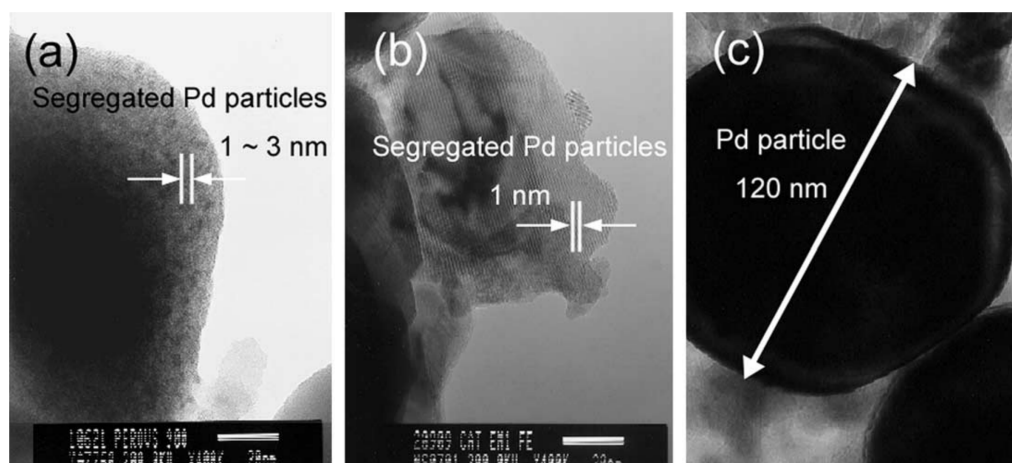


Figure 1.12 – **PGM segregation on ageing.** Transmission electron micrographs of $LaFe_{0.57}Co_{0.38}Pd_{0.05}O_3$ (a), $LaFe_{0.95}Pd_{0.05}O_3$ (b) and Pd/alumina (c), after engine ageing at $900 \text{ }^\circ\text{C}$ for 100 h.^[105]

A stabilising effect of incorporating PGM into the perovskite lattice and thereby increased durability of the catalyst was reported by Nishihata et al.^[105] They investigated the particle size of segregated Pd particles on different catalysts after engine ageing. As depicted in Fig. 1.12, the Pd-doped perovskites also showed segregation of PGM particles just as the Pd/alumina sample. However, particle sizes on the perovskite were much lower than for the alumina-supported Pd. The same group also reported the influence of ageing on the catalytic activity as shown in Fig. 1.13.^[106] The authors revealed that after 100 h of ageing under exhaust gas at $900 \text{ }^\circ\text{C}$, a decrease of 10 % in catalytic performance was observed for the conventional Pd-catalyst, whereas the catalytic performance of the Pd-incorporated

perovskite catalyst remained stable.

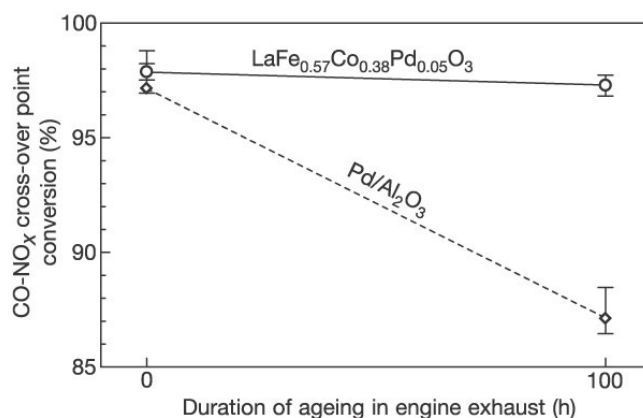


Figure 1.13 – Ageing dependence of CO–NO_x cross-over point conversion ($\lambda = 1$). Depicted for the LaFe_{0.57}Co_{0.38}Pd_{0.05}O₃ perovskite catalyst and a γ -Al₂O₃-supported Pd catalyst. Conversion efficiency was evaluated 3 times for each sample by a cycling test ($0.890 \leq \lambda \leq 1.096$; fluctuation $\Delta\lambda = \pm 3.4\%$ at 0.5 Hz at 400 °C; space velocity = 35 000 h⁻¹). The median of the CO–NO_x cross-over point conversion ($\lambda = 1$) is plotted. Ageing was performed under engine exhaust at 900 °C.^[106]

Eyssler et al. investigated the Pd incorporation in LaCoO₃, LaMnO₃, LaFeO₃ and YFeO₃ by X-ray absorption spectroscopy (XAS), X-ray photo-electron spectroscopy (XPS), and temperature-programmed reduction by hydrogen (H₂-TPR).^[100,101] They revealed that Pd was incorporated into the perovskite structure of the cobaltite and the LaFeO₃ sample but that this was not the case for the LaMnO₃ perovskite. Incorporation of Pd into YFeO₃ was found to depend on the calcination temperature. During a first test, catalytic activity for methane combustion of the LaFe_{0.95}Pd_{0.05}O₃ catalyst was found to equal the non-substituted LaFeO₃ solid, unlike the Pd-impregnated LaFeO₃ sample which exhibited higher performances.^[100] This was attributed to the non-accessibility of the Pd inside the bulk structure. After attaining 900 °C, enhanced methane conversion and drastic changes in the structure were observed and attributed to the self-regenerative function of the catalyst.

The interaction between Pt and LaFeO₃ has been investigated via ageing studies by Dacquin et al.^[107,108] The Pt-doped LaFeO₃ perovskite was compared to Pt dispersed on alumina (both 4 wt.%) for the simultaneous reduction of NO and N₂O. Lower sintering effects of the Pt nanoparticles were observed for the Pt-doped perovskite. According to the authors, this higher thermal stability can be explained by occurring strong metal/support interactions. This hypothesis is backed up by high resolution transmission electron spectroscopy (HRTEM) revealing the epitaxial growth of Pt(1 1 1) planes with the characteristic surface plans of the orthorhombic structure of LaFeO₃.^[107]

The perovskites' catalytic activity is strongly dependent on the composition but also on its textural properties.^[29,72,109] The next Section therefore covers a choice of different preparation methods which have been developed to synthesise perovskites.

1.3 Synthesis methods for obtaining perovskites

Different synthesis methods were developed over the years to prepare perovskites. The main motivation behind this research activity in the field of catalysis has been to improve the textural properties of the solids, i. e. the increase in SSA and a control of their porosity to render the catalytically active components more accessible.

A multitude of different perovskite preparation routes was proposed over the years ranging from solid state reactions, over co-precipitation to reverse micelles microemulsion^[82] and microwave assisted routes.^[110] This non-exhaustive study can address but a limited overview. Additional details can be found in a recent review by Zhu et al.^[109]

A non-exhaustive overview of the surface areas of LaFeO₃ solids prepared by different synthesis methods is given in Table 1.3 in the Conclusion.

1.3.1 Solid state methods

Ceramic method

The oldest preparation route leading to perovskites is the conventional ceramic method by direct annealing.^[111,112] It is based on the equimolar mechanical mixing of the single oxide, hydroxides or carbonate precursors of the constituting metals. This precursor mix is then calcined at very high temperatures up to 1550 °C.^[113] This process has several inconveniences such as the low homogeneity of the obtained solid with impurity phases as well as its low SSA of less than 5 m² g⁻¹ due to the high calcination temperature.^[29,52]

Reactive grinding

A more recent mechano-synthesis route based on a solid state reaction is the reactive grinding proposed by Kaliaguine et al.^[114,115] It consists of 3 steps. First, the oxide precursors are ball milled under oxidising atmosphere to form the perovskite. This solid, however, does not present a high SSA. Introducing a 2nd ball milling step including an additive such as ZnO₂, which is later on eliminated by leaching during a post-treatment, leads to very high SSA of up to 105 m² g⁻¹.^[114] In contrast to the ceramic method, the reactive grinding relies on mechanical not thermal energy to form the crystalline perovskite structure. Therefore, calcination temperatures if conducted at all are well below 1000 °C. However, the right equipment such as carbon tungsten balls and vial is necessary to prevent impurities as they may occur using stainless steel materials. The Fe impurities may also enhance catalytic activity as in the case of N₂O decomposition, though.^[116] Other contamination may arise from the employed additive.^[117]

1.3.2 Wet synthesis methods

In order to generate the perovskite structure at lower calcination temperatures, a better mixing of the precursors is necessary thereby increasing the solid state diffusion. This can be achieved by various wet synthesis techniques as the co-precipitation and especially sol-gel methods. Additionally to the lowered calcination temperature and the more rapid reaction, an improved homogeneity is inherent to solution-based preparation methods. All this leads to smaller particle sizes and enhanced reactivity of the prepared perovskites.

Evaporation to dryness

The simplest wet synthesis route is the evaporation to dryness which consists of dissolving metal precursor salts as nitrates or acetates in an appropriate solvent which is then evaporated before calcination.^[85] Compared to the solid state reaction method the main advantage is a slightly higher homogeneity of the precursor solid and therefore the resulting perovskite. Since calcination temperatures are, nonetheless, very high (850 to 1250 °C), the SSA is not increased compared to the ceramic method.

Spray or freeze drying

The freeze drying method^[112,118,119] also relies on the homogeneous solution of the metal precursors in an appropriate solvent, generally water. However, instead of precipitating the precursors and filtrate the solvent, a rapid freezing step leads to chemically homogeneous droplets. In order to achieve a fast enough freezing, a vaporiser is generally used. The thereby created small droplets are shot into a cooled non-solvent such as hexane or liquid N₂. Afterwards, the droplets are freeze-dried by sublimation under vacuum to give dehydrated salts. Finally, these salts are decomposed under oxidising atmosphere to form the perovskite. SSA are generally in the order of 2 to 12 m² g⁻¹.^[118,119]

Co-precipitation

The co-precipitation method relies on the simultaneous precipitation of metal salts such as hydroxides of the aqueous precursor metal salt solution. The precursors are often metal nitrates, oxalates or carbonates.^[112,120,121] The precipitation is triggered changing the pH, e. g. the addition of diluted ammonia for forming LaAlO₃,^[121] or of a NaOH–Na₂CO₃ buffer solution in the case of (substituted) LaMnO₃.^[122–124] After washing the obtained precipitate with water and ethanol (EtOH), the solid is dried and then calcined at elevated temperature. In order to reduce carbon impurities, triethylamine can be used as precipitating agent in conjunction with methanol as wash alcohol as was done in the case of CeM_xO_y.^[125]

This synthesis method allows to obtain solids with higher SSA of up to 47 m² g⁻¹.^[123] However, it presents several inconveniences. The main one is that depending on the com-

pound to be formed the precursors need to be well-chosen because they influence greatly the synthesis conditions. Indeed, different precursor solubilities may make necessary to change the synthesis parameters as the pH and in some cases may lead to the impossibility of forming a desired mixed oxide.^[52]

Auto-combustion

The auto-combustion route is widely used to produce perovskites and other oxides.^[126,127] It consists of the combustion of a precursor resin to a powder. This solid resin is formed by heating an acidic solution containing the metal precursor salts and a combustible material which is generally moreover a complexing agent. Depending on the compound and the parameters, the ground combustion product may be directly the perovskite^[128] or may need a further calcination step.^[129] The latter is mainly performed to eliminate residual carbon species and achieve a higher crystallinity of the perovskite. However, it can lead to a decreased SSA as well.

Different (polymerisable) combustibles such as glycine,^[124,129,130] saccharose,^[128] urea,^[131] glycerol^[132] and citric acid^[133] have been used. They allow to keep a homogeneous distribution of the precursor cations in the solid matrix during and after the drying step, i. e. in the foam.^[134] The preparation route's main advantage resides in its simplicity. Besides, the precursor salts and the combustible are generally low cost. A rigorous control of the combustible content needs to be observed, though, in order to control the exothermic and potentially explosive reaction.

Flame spray pyrolysis

Another combustion method which becomes more popular recently is the flame spray pyrolysis.^[99,135-138] The perovskite is obtained by vaporising an aqueous solution containing the complexed metal precursor ions, e. g. metal nitrates or acetates, via an atomiser into a hydrogen/oxygen flame. The thereby crystallised solid is in powder form and needs to be collected by electrostatic precipitation. As for the auto-combustion method, different complexing agents such as citric acid can be used. The flame yields a very high temperature of 1600 to 1800 °C in its centre but each droplet passes by very quickly (residence time of about 3 to 10 ms). This is why their SSA are high considering the elevated temperature. Likewise, oxides prepared by this method are well crystallised. This preparation route further allows for obtaining thermally stable perovskites. Some detectable crystalline impurities as La_2O_3 may however be formed.^[99]

One major drawback of this preparation route is the highly specialised equipment, i. e. the flame spray and the collecting apparatus. The need for the electrostatic precipitator has been emphasized by Saracco et al. who prepared LaMnO_3 by this method.^[139] Different parameters such as the flame temperature, the solution flow, the addition of an additive

like citric acid or dimethylformamide may influence the physico-chemical properties of the perovskites. The homogeneity of the solid is improved by adding a complexing additive in agreement with its supposed effect, i. e. leading to stronger interactions between the precursor ions while securing a randomised distribution. But SSA may decrease.^[140]

Sol-gel based methods

The sol-gel method consists of the gel formation out of a metal alkoxide solution. This gel is formed by hydrolysis and inorganic polycondensation. Inhomogeneity might occur if the gel is formed too rapidly. Therefore, temperature and other kinetic factors need to be well controlled. The obtained gel can then be calcined at lower temperatures thanks to the higher interactions of the precursor ions. Via the kinetic control, this method allows to tailor the solid's particle sizes – which depends, nonetheless, on the calcination temperature as well. The major drawback of this method is the high cost of metal alkoxides. Therefore, pseudo sol-gel methods have been developed, hereafter denoted as *sol-gel based methods*.

Sol-gel based methods as the conventional citrate method (CCM)^[141,142] and the so-called Pechini method^[143] are generally based on the dissolution of the corresponding metal precursor salts and a complexing agent, mainly organic acids as citric acid^[52,141,142,144] or other polyhydroxy alcohols.

For the Pechini method, ethylene glycol is added to the acidic precursor solution to yield the gel by moderate heating.^[143] The so-obtained gel is dried at temperatures up to 200 °C and then calcined.

In the case of the conventional citrate method (CCM), the citrate-precursor complex solution is left to form a gel under gentle evaporation. This gel slowly forms a xerogel in an oven at 80 °C before the obtained solid precursor is ground. The amorphous solid thereby obtained is then subjected to a heating treatment in a muffle oven at approximately 150 to 250 °C depending on the constituting ions. This step is generally denoted as the nitrate decomposition step referring to the most common precursors, being metal nitrates. Their decomposition is exothermic and often explosive and therefore separated from the main calcination step. This also allows to grind and homogenise the solid once again in between both steps. The final calcination can then be performed at relatively low temperatures of 550 °C to 750 °C due to the ions close proximity and interactions in the complex.

Many synthesis parameters influence the properties of the obtained perovskite and have been studied in literature.

Various complexing agents have been used over the time. Most of them are organic polyhydroxy alcohols as citric, maleic or tartaric acid.^[52] Rare exceptions excluded, citric acid was found to yield the most stable precursors. The CCM relies on the formation of a complex first formed in solution by the different precursor cations and the polyanionic citrate ions and retained during slow evaporation to a gel. This secures the chemical homogeneity

of the different constituting cations in the following steps until calcination.

Likewise, different metal precursors can be employed.^[52] According to Schwickardi et al., nitrates yield the best results however.^[145] The same authors also emphasized the high solubility of the metal nitrates. Furthermore, as ammonium salts, nitrates do not lead to any residues in the final solid. All these reasons explain why nitrates are the precursors which are used most often.^[75,124,141,144,146,147]

Another important parameter is the ratio of metal ions to employed acid as was already investigated by Courty et al.^[52] The authors found that the residual carbon content decreased for higher citric acid amounts in the case of metal oxides containing metal cations considered little or not active for oxidation reactions. They explained this finding with a lower density and higher porosity due to the higher complexing agent amount facilitating the combustion of residual carbon species. For Fe, Ni, Co, and Cu containing precursors, i. e. containing cations which are active in oxidation catalysis, different, more complicated observations were made. The authors attributed this different behaviour to higher decomposition temperatures leading to particle sintering.

In addition, the solvent plays an important role in the initial dissolution and complexation step. Depending on its boiling point, a different behaviour during the drying step may occur. Krupicka et al. have studied the influence of using either water, ethanol or isopropanol as solvent for the synthesis of LaMnO₃, LaCoO₃, LaNiO₃ and LaFeO₃ nanoparticles.^[144] LaFeO₃ did not form nanoparticles under the investigated conditions and was therefore excluded from further discussions. For LaMnO₃, LaCoO₃, and LaNiO₃, on the other hand, the authors concluded that best results, i. e. highest SSA, were obtained using water as solvent. They attributed this finding to the stabilisation of the complex in solution by strong hydrogen-bonded networks.

As for all combustion methods relying on nitrate-organic complexing agent solutions, e. g. sol-gel, auto-combustion, flame spray pyrolysis, the formation of CO₂ and NO_x cannot be prevented and constitutes the main drawback of these preparation methods. The organic complexing agent can also be a source of carbon which is why carbonates are generally formed at the surface of the perovskites prepared by such methods.

Zhang et al. have recently compared the properties and catalytic activity for toluene oxidation of LaMnO₃ prepared by co-precipitation, auto-combustion and sol-gel citrate method.^[124] The sample prepared by sol-gel synthesis yielded the highest SSA (35 m² g⁻¹) as well as the highest catalytic performance. It also exceeded in stability and durability throughout the catalytic tests, repeated 3 times for each sample. The authors attributed these superior properties to the enhanced SSA, its increased low temperature reducibility as well as a higher content of adsorbed oxygen species at the surface.

1.3.3 Macro-structuring methods

Controlling the porosity of perovskites is difficult by the aforementioned synthesis routes. Even though high SSA porous perovskites can be prepared, for example by auto-combustion method,^[148] only randomly distributed pores can be achieved in this way. Instead, controlled macro-structuration can be yielded by using structuring agents, i. e. templates.

Different templates are known which are generally classified as either hard or soft.^[109] The most common hard structuring agent is silica.^[149–152] The use of such a hard template has one major drawback, its need to be removed in a separate step after the perovskite synthesis. Polymers such as polystyrene (PS) or polymethylmethacrylate (PMMA) spheres^[153,154] and carbon templates,^[145,155] on the other hand, are denoted as soft templates.

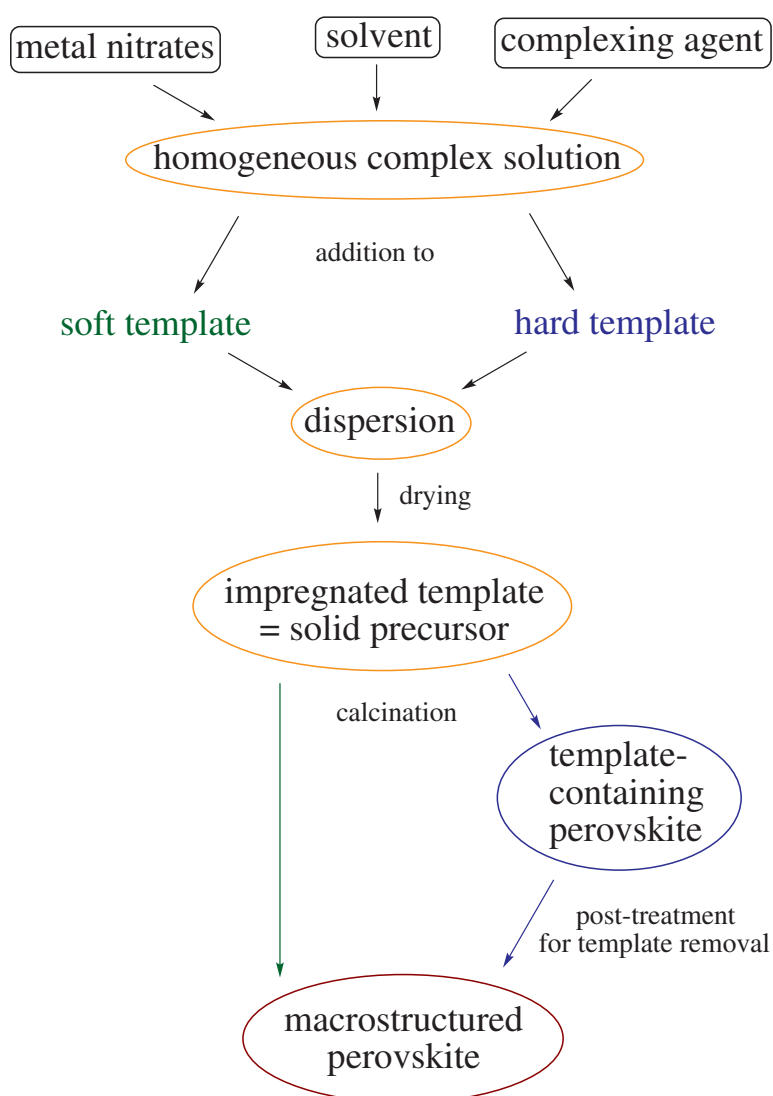


Figure 1.14 – **Generic scheme of macro-structuring methods.**

Fig. 1.14 shows the classical steps followed by all macro-structuring methods based on the sol-gel method. First, the homogeneous complex precursor solution is added to the template. This dispersion left under stirring yields the impregnated structuring agent. This precursor

solid is then calcined. In the case of the soft template, the macro-structured perovskite is obtained directly by this calcination. In the case of the hard template, an additional post-treatment is necessary to remove the structuring agent. This may include a second calcination.

Both kinds of templates have advantages and inconveniences. The hard templates have the advantage of being easily synthesized in the desired shapes and being stable throughout the perovskite synthesis. However, the necessary post-treatment step is their major drawback because it sometimes involves harsh conditions and impurities may prevail. Soft templates, on the other hand, do not need to be removed after the synthesis since they are eliminated during the calcination step. Retaining the shapes of soft templates and thereby of the solid framework of the perovskite, especially during the calcination step, is a challenge, though.

Another way of classifying structuring methods is their division into endo-, exo-templating and colloidal crystal templating (CCT) routes as proposed by Schüth, the CCT method being a special case of an endo-templating route.^[156] This classification relies on the difference between independent template particles or blocks which are incorporated by the forming solid during synthesis and on the other hand, the template being one single scaffold with voids which are filled up by precursors in the course of the synthesis. The former being the case for endo-, the latter for the exo-templating methods.

Active carbon³ and silica templates are most often used as exo-templates.^[145,151,152,155] Polymers, on the other hand, are generally used in the form of nano-scale spheres⁴.^[153,154,156]

The CCT has been used in several fields such as in physics for the preparation of photonic crystals (inverse opals),^[158,159] or materials science for the preparation of electrocatalysts^[38] or gas sensors^[42] as well as heterogeneous catalysts.^[153,154] It relies on the concept depicted in Fig. 1.15. An ordered structures of particles is used as template. This structure is infiltrated by a precursor solution forming a composite which incorporates the endo-template. After removal of the template, either by calcination or by other processing steps, a macroporous solid is obtained.

The CCT is named after a naturally occurring material, the colloidal crystals. The best example is the opal which is formed of silica spheres which exhibit a high periodicity in all 3 dimensions. The silica spheres' interstices are filled by solidified hydrated silica. Mimicking syntheses rely on a highly ordered template to obtain the same periodicity for the final solid. The solids obtained by CCT-based synthesis are often also called 3-dimensionally ordered macroporous (3DOM) solids.^[153,160,161] To obtain the desired periodical order of the resulting perovskite, the template has to be quasi monodisperse and packed most efficiently (in analogy to atoms packed in a crystal). This compacting of the template spheres is generally achieved by prior centrifugation.^[160]

Depending on the characteristics of the template (hard or soft), the materials prepared

³high SSA

⁴Other shapes may also be investigated but are not within the scope of this study.

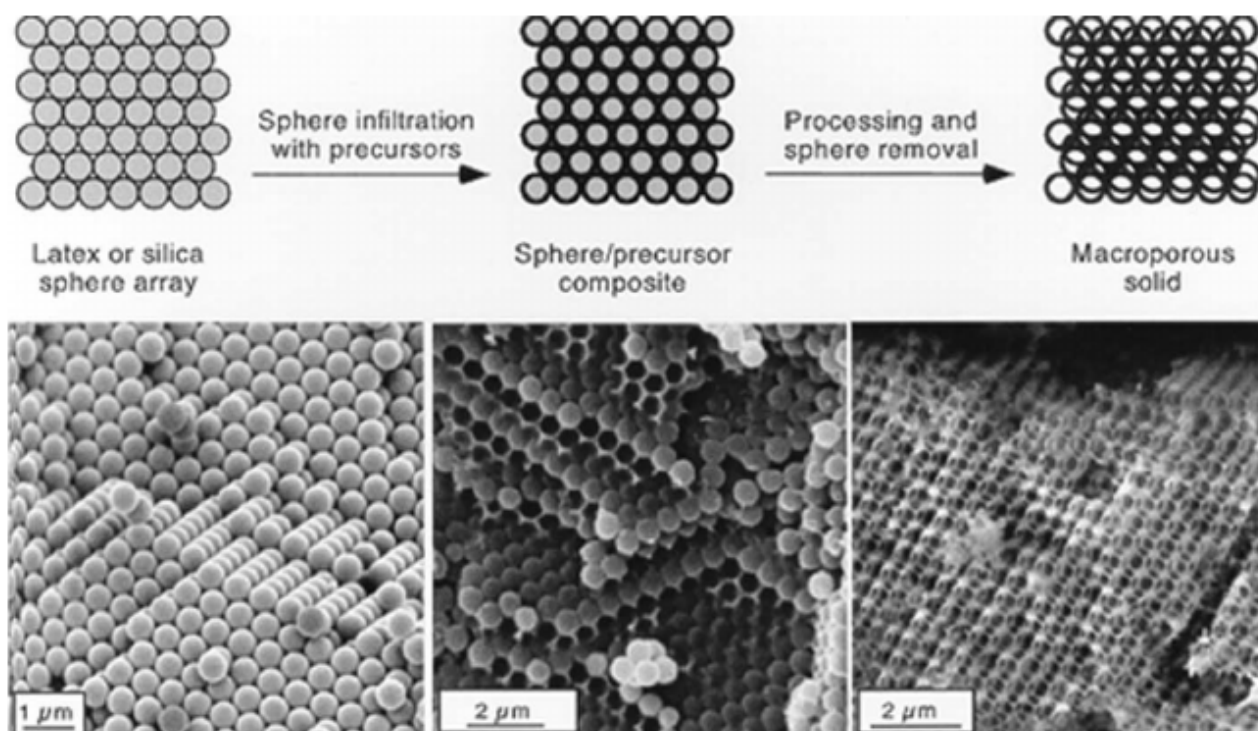


Figure 1.15 – **Colloidal crystal templating (CCT) scheme.** Steps and corresponding scanning electron microscopy (SEM) are shown for a PS/silica system prepared with tetraethyl orthosilicate.^[157]

using templates are generally no exact inverse replicas of the structuring agent.^[157] Exceptions are, however, those solids obtained by nanocasting with hard templates by 3DOM. Soft templates, however, tend to shrink and melt during calcination.

A critical parameter besides the template itself is the employed solvent. It is crucial in connection with the choice of the precursors, i. e. their solubility, as well as for the impregnation and drying steps. Indeed, if ethylene glycol is used, an evaporation becomes difficult due to its high boiling point of 197.3 °C (atmospheric pressure). Therefore, the remaining ethylene glycol solution after impregnation is generally vacuum filtrated.^[153,160,161] This is the reason why relatively high precursor concentrations need to be used for these syntheses and yields are generally low and most often not reported. Ethanolic and hydroalcoholic solutions, as used in conjunction with silica templates by Valdés-Solís et al. and Wang et al. respectively,^[149,150] on the other hand, present the advantage of being highly volatile. This volatility of the solvent allows to use lower concentrations of precursor solids. The whole amount of the employed precursors is retained throughout the synthesis and yields are close to the theoretical ones. Ethanolic and hydroalcoholic solutions are strong polar solvents, however. This polarity presents a challenge if polymer templates are employed. In this case, interactions between solvent and the generally hydrophobic polymer spheres are less strong, especially for polystyrene (PS). On the other hand, the high polarity of these solvents improves the solubility of the precursor salts.

Interactions between the solvent and the polymer template spheres can also be improved by functionalising the polymer surface with less hydrophobic functions. The addition of carboxy functions on the template spheres was already used to increase the glass temperature (T_g) of the polymer as well.^[162] This may be necessary to obtain the desired solid perovskite framework. Indeed, the T_g of commonly used PMMA is below 130 °C. This is close to or lower than the nitrate decomposition temperature of most perovskite precursors and below the solidification temperature of the solid framework.

The low heat resistance of the polymer spheres is the reason why calcinations are generally performed in 2 successive parts.^[162] The first part is conducted under inert atmosphere (Ar or N₂ flow). After yielding a sufficient solidification of the metal oxide framework, the atmosphere is switched to air flow. This second step allows for the elimination of residual carbon species. In addition, calcination is conducted at a low heating rate and quartz sand or quartz wool is employed to prevent hot spots.^[162]

Regarding the specific surface areas, macroporous perovskites generally yield better results (up to 130 m² g⁻¹ for LaFeO₃^[151]) than samples obtained by non-templated methods as shown exemplarily for LaFeO₃ in Table 1.3. Furthermore, LaFeO₃ prepared using hard silica templates exhibit higher SSA than the solids obtained by using soft templates.

1.4 Conclusion

Nowadays TWC are already well developed and performing but present the major inconvenience of relying on some scarce and therefore expensive noble metals. The development of a low(er)-cost alternative based on more available materials would be highly desirable.

Perovskites, especially those with the formula LaBO₃ (B being a 1st row transition metal), have the potential to be interesting TWC based on the criteria developed above, i. e. they show interesting catalytic activity in oxidation and in some cases also for reduction, they present a high thermal stability and precursors are relatively low-cost. Furthermore, the tolerance of the perovskite structure allows to tune the catalytic activity by changing the composition of the perovskite for a wide range of metals.

Since the very potent catalyst poisons SO₂ (and Pb)⁵ are banned from fuel nowadays, perovskites can be tailored to be as stable as PGM or enhance the stability of noble metals under TWC conditions. Out of the 1st row transition metals, Mn, Fe, Co and Cu seem to present the most promising catalytic potential meriting a closer investigation. Keeping in mind that doubts on the environmental and health effects have been expressed, however, Co is excluded from this list for this study.

After choosing a starting LaBO₃ system to be investigated, 2 major pathways can be

⁵Since Pb can be incorporated in the perovskite structure, it never was as deleterious for perovskite catalysts as for Pt for example.^[70]

Table 1.3 – Comparison of SSA of LaFeO_3 perovskites obtained by different synthesis methods.

synthesis method	calcination T (°C)	template	SSA ($\text{m}^2 \text{g}^{-1}$)	reference
ceramic method	1200	-	1	[163]
reactive grinding	550	-	20	[164]
co-precipitation	600	-	30	[165]
co-precipitation	800	-	5	[166]
auto-combustion	900	-	2	[167]
flame-spray pyrolysis	700	-	17	[99]
sol-gel based	700	-	7	[149]
sol-gel based	1000	-	1	[168]
sol-gel based	800	-	5	[168]
sol-gel based	700	-	10	[168]
sol-gel based	600	-	15	[168]
sol-gel based	500	-	22	[168]
sol-gel based (Pechini)	900	-	3	[167]
sol-gel based (Pechini)	800	-	6	[155]
sol-gel based (Pechini)	800	-	17	[166]
sol-gel based (Pechini)	600	-	21	[165]
sol-gel based (CCM)	600	-	22	[165]
exo-templated route	700	active carbon	49	[145]
exo-templated route	800	active carbon	49	[155]
exo-templated route	700	silica xerogel	110	[149]
exo-templated route	900	SBA-16	35	[151]
exo-templated route	800	SBA-16	85	[151]
exo-templated route	700	SBA-16	101	[151]
exo-templated route	600	SBA-16	130	[151]
exo-templated route	700	KIT-6 silica	110	[152]
endo-templated route (3DOM)	600	PS	45-49	[160]
endo-templated route (3DOM)	400	PS	29	[38]
endo-templated route (3DOM)	600	PMMA	26-30 ^a	[169]
endo-templated route (3DOM)	600	PMMA	25	[42]

^a Depending on the polymer sphere diameter. Diameters ranged from 185 nm to 415 nm.

followed in order to exploit this TWC potential. As already laid out above, the choice will be made in between Mn, Fe and Cu (La_2CuO_4 in this case).

The first step will consist of studying the influence of the synthesis method. This should include a study on the employed solvent and the use of a macro-structuring agent – the main goal being to improve the textural properties of the solid for TWC application. Considering the main advantages and inconveniences of the presented known synthesis methods, not limited to but including the obtained specific surface areas (Table 1.3), the investigation will be based on the sol-gel based conventional citrate method (CCM) which allows for the formation of homogeneous perovskites with moderate SSA and generally available equipment.

Concerning the investigation of the influence of using a macro-structured perovskite, the study will be based on using soft polymer templates which do not require post-treatments even though specific surface areas are generally lower than for carbon or silica-templated perovskites. The transfer of the macro-structuring silica sol-gel route in hydroalcoholic solvent to perovskites prepared with soft templates is envisaged.

In parallel, a study on the composition optimisation of the chosen LaBO_3 system is conducted. This includes the optimisation at the surface as well as the bulk composition optimisation. Finally, after combining the most promising results, the addition of low amounts of PGM by impregnation may be considered.

Bibliography

- [1] H. Bosch, F. Janssen, *Catalysis Today* **1988**, 2, 369–379.
- [2] European Commission, Regulation (EC) No 715/2007 of the European Parliament and of the Council of 20 June 2007 on type approval of motor vehicles with respect to emissions from light passenger and commercial vehicles (Euro 5 and Euro 6) and on access to vehicle repair and maintenance information (Text with EEA relevance), **2007**, <http://eur-lex.europa.eu/legal-content/EN/ALL/?uri=CELEX:32007R0715> (visited on 2015-01-20).
- [3] J. Kašpar, P. Fornasiero, N. Hickey, *Catalysis Today* **2003**, 77 (4), 419–449.
- [4] A. F. Holleman, E. Wiberg, N. Wiberg, *Lehrbuch der Anorganischen Chemie*, 101st ed., Walter de Gruyter, **1995**.
- [5] E. S. J. Lox in *Handbook of Heterogeneous Catalysis*, (Eds.: G. Ertl, H. Knözinger, F. Schüth, J. Weitkamp), Wiley-VCH Verlag GmbH & Co. KGaA, **2008**, Chapter Part 11. Environmental Catalysis – 11.2 Automotive Exhaust Treatment.
- [6] S. Keav, S. Matam, D. Ferri, A. Weidenkaff, *Catalysts* **2014**, 4, 226–255.
- [7] J. Pérez-Ramírez, F. Kapteijn, K. Schöffel, J. Moulijn, *Applied Catalysis B: Environmental* **2003**, 44, 117–151.
- [8] G. C. Mondragón Rodríguez, K. Kelm, S. Heikens, W. Grünert, B. Saruhan, *Catalysis Today* **2012**, 184 (1), 184–191.
- [9] Unites States Environmental Protection Agency, Global Warming Potential, <http://www.epa.gov/climatechange/ghgemissions/gases.html> (visited on 2015-01-22).
- [10] P. Granger, J. J. Lecomte, L. Leclercq, G. Leclercq, *Applied Catalysis A: General* **2001**, 208, 369–379.
- [11] P. Granger, P. Malfoy, G. Leclercq, *Journal of Catalysis* **2004**, 223, 142–151.
- [12] Association for Emissions Control by Catalyst, TWC converter, **2015**, <http://www.aecc.be/en/Technology/Catalysts.html> (visited on 2015-01-20).
- [13] J. Kašpar, P. Fornasiero, M. Graziani, *Catalysis Today* **1999**, 50, 285–298.
- [14] R. Di Monte, J. Kašpar, *Catalysis Today* **2005**, 100, 27–35.
- [15] M. V. Twigg, *Philosophical Transactions of the Royal Society A: Mathematical Physical and Engineering Sciences* **2005**, 363, 1013–1033.
- [16] X. Courtois, N. Bion, P. Marécot, D. Duprez in *Past and Present in DeNOx Catalysis From Molecular Modelling to Chemical Engineering*, (Eds.: P. Granger, V. Pârvulescu), Studies in Surface Science and Catalysis, Elsevier, **2007**, pp. 235–259.
- [17] P. Granger, V. I. Pârvulescu, *Chemical Reviews* **2011**, 11 (5), 3155–3207.
- [18] T. Horiuchi, Y. Teshima, T. Osaki, T. Sugiyama, K. Suzuki, T. Mori, *Catalysis Letters* **1999**, 62, 107–111.
- [19] L. G. Tejuca, J. L. G. Fierro, *Advances in Catalysis* **1989**, 36, 237–328.
- [20] D. Duprez, Le pot catalytique, **2015**, www.societechimiquedefrance.fr/img/pdf/fiche_pot_catalytique.pdf.
- [21] K. C. Taylor, J. C. Schlatter, *Journal of Catalysis* **1980**, 63, 53–71.

- [22] S. H. Oh, G. B. Fisher, J. E. Carpenter, D. Goodman, *Journal of Catalysis* **1986**, *100*, 360–376.
- [23] BASF, Engelhard Industrial Bullion (EIB) Prices, <http://apps.catalysts.basf.com/apps/eibprices/mp/>.
- [24] European Commission, EU challenges China's export restrictions on rare earths, <http://europa.eu/rapid/pressReleasesAction.do?reference=MEMO/12/182>.
- [25] European Commission, WTO Appellate Body rules against Chinese restrictions on access to rare earths and other raw materials, **2014**, <http://trade.ec.europa.eu/doclib/press/index.cfm?id=1147>.
- [26] Süddeutsche.de, China gibt Handel mit Seltenen Erden frei, **2015**, <http://www.sueddeutsche.de/wirtschaft/wichtiger-rohstoff-china-gibt-handel-mit-seltenen-erden-frei-1.2291728>.
- [27] D. W. Wendland, W. R. Matthes, Visualization of Automotive Catalytic Converter Internal Flows, tech. rep. SAE Technical Paper 861554, General Motors Research Labs., **1986**.
- [28] N. W. Cant, D. E. Angove, D. C. Chambers, *Applied Catalysis B: Environmental* **1998**, *17*, 63–73.
- [29] M. A. Peña, J. L. G. Fierro, *Chemical Reviews* **2001**, *101* (7), 1981–2018.
- [30] P. Hirel, Perovskite structure, http://pierrehirel.info/recherche-postdoc_KIT.php (visited on 2014-03-20).
- [31] V. M. Goldschmidt, *Die Naturwissenschaften* **1926**, *14*, 477–485.
- [32] D. Balz, K. Plieth, *Z. Elektrochem.* **1955**, *59*, 545.
- [33] S. Ruddlesden, P. Popper, *Acta Crystallographica* **1957**, *10* (8), 538–539.
- [34] J. Longo, P. Raccach, *Journal of Solid State Chemistry* **1973**, *6*, 526–531.
- [35] A. S. Bhalla, R. Guo, R. Roy, *Materials Research Innovations* **2000**, *4*, 3–26.
- [36] R. M. Ormerod, *Chemical Society Reviews* **2002**, *32*, 17–28.
- [37] J. C. Ruiz-Morales, J. Canales-Vázquez, C. Savaniu, D. Marrero-López, P. Núñez, W. Zhou, J. T. S. Irvine, *Physical Chemistry Chemical Physics* **2007**, *9* (15), 1821–1830.
- [38] J.-J. Xu, Z.-L. Wang, D. Xu, F.-Z. Meng, X.-B. Zhang, *Energy & Environmental Science* **2014**, *7*, 2213–2219.
- [39] A. Weidenkaff, *Advanced Engineering Materials* **2004**, *6*, 709–714.
- [40] N. N. Toan, S. Saukko, V. Lantto, *Physica B: Condensed Matter* **2003**, *327*, 279–282.
- [41] T. Chen, Z. Zhou, Y. Wang, *Sensors and Actuators B: Chemical* **2009**, *143* (1), 124–131.
- [42] J. Qin, Z. Cui, X. Yang, S. Zhu, Z. Li, Y. Liang, *Sensors and Actuators B: Chemical* **2015**, *209*, 706–713.
- [43] G. Kremenić, J. M. L. Nieto, J. M. D. Tascón, L. G. Tejuca, *Journal of the Chemical Society Faraday Transactions 1: Physical Chemistry in Condensed Phases* **1985**, *81* (4), 939–949.
- [44] J. M. D. Tascón, L. González Tejuca, C. H. Rochester, *Journal of Catalysis* **1985**, *95*, 558–566.

- [45] L. G. Tejuca, C. H. Rochester, J. L. G. Fierro, J. M. D. Tascón, *Journal of the Chemical Society Faraday Transactions 1: Physical Chemistry in Condensed Phases* **1984**, 80, 1089–1099.
- [46] T. Arakawa, N. Ohara, J. Shiokawa, *Journal of Materials Science* **1986**, 21, 1824–1827.
- [47] M. Futai, C. Yonghua, Louhui, *Reaction Kinetics and Catalysis Letters* **1986**, 31, 47–54.
- [48] T. Katsura, K. Kitayama, T. Sugihara, N. Kimizuka, *Bulletin of the Chemical Society of Japan* **1975**, 48, 1809–1811.
- [49] T. Katsura, T. Sekine, K. Kitayama, T. Sugihara, N. Kimizuka, *Journal of Solid State Chemistry* **1978**, 23, 43–57.
- [50] T. Nakamura, G. Petzow, L. J. Gauckler, *Materials Research Bulletin* **1979**, 14, 649–659.
- [51] R. B. Anderson in *Catalysis, Vol. 4*, (Ed.: P. H. Emmett), Reinhold, New York, **1956**, pp. 29–256.
- [52] P. Courty, H. Ajoy, C. Marcilly, B. Delmon, *Powder Technology* **1973**, 7, 21–38.
- [53] G. Parravano, *The Journal of Chemical Physics* **1952**, 20, 342.
- [54] G. Parravano, *Journal of the American Chemical Society* **1953**, 75, 1497–1498.
- [55] D. B. Meadowcroft, *Nature* **1970**, 226, 847–848.
- [56] W. F. Libby, *Science* **1971**, 171, 499–500.
- [57] R. J. H. Voorhoeve, J. P. Remeika, P. E. Freeland, B. T. Matthias, *Science* **1972**, 177, 353–354.
- [58] R. J. H. Voorhoeve, J. P. Remeika, D. W. Johnson Jr., *Science* **1973**, 180, 62–64.
- [59] R. J. H. Voorhoeve, J. P. Remeika, L. E. Trimble in *The Catalytic Chemistry of Nitrogen Oxides*, **1975**, pp. 215–233.
- [60] R. J. H. Voorhoeve, J. P. Remeika, L. E. Trimble, *Annals of the New York Academy of Sciences* **1976**, 272, 3–21.
- [61] T. Nitadori, T. Ichiki, M. Misono, *Bulletin of the Chemical Society Japan* **1988**, 61, 621–626.
- [62] S. D. Peter, É. Garbowski, V. Perrichon, M. Primet, *Comptes Rendus Chimie* **2004**, 7 (1), 57–61.
- [63] J. M. D. Tascón, L. González Tejuca, *Reaction Kinetics and Catalysis Letters* **1980**, 15, 185–191.
- [64] H. Tanaka, M. Taniguchi, N. Kajita, M. Uenishi, I. Tan, N. Sato, K. Narita, M. Kimura, *Topics in Catalysis* **2004**, 30-31 (1-4), 389–396.
- [65] Erste Allgemeine Verwaltungsvorschrift zum Bundes-Immissionsschutzgesetz (Technische Anleitung zur Reinhaltung der Luft - TA Luft), tech. rep., Bundesministerium für Umwelt, Naturschutz und Reaktorsicherheit (BRD), **2002**.
- [66] ScienceLab.com, MSDS nickel nitrate, English, <http://www.sciencelab.com/msds.php?msdsId=9926215> (visited on 2014-08-05).
- [67] ScienceLab.com, MSDS cobalt nitrate hexahydrate, English, <http://www.sciencelab.com/msds.php?msdsId=9923525> (visited on 2014-08-05).
- [68] N. Yamazoe, Y. Teraoka, *Catalysis Today* **1990**, 8 (2), 175–199.

- [69] T. Seiyama in *Properties and Applications of Perovskite-type Oxides*, (Eds.: L. G. Tejuca, J. L. G. Fierro), Marcel Dekker, New York, **1993**, p. 215.
- [70] R. J. H. Voorhoeve, J. D. W. Johnson, J. P. Remeika, P. K. Gallagher, *Science* **1977**, *195* (4281), 827–833.
- [71] M. F. M. Zwinkels, S. G. Järås, P. G. Menon, T. A. Griffin, *Catal. Rev. Sci. Eng.* **1993**, *35* (3), 319.
- [72] S. Royer, D. Duprez, F. Can, X. Courtois, C. Batiot-Dupeyrat, S. Laassiri, H. Alamdari, *Chemical Reviews* **2014**, *114*, 10292–10368.
- [73] R. J. H. Voorhoeve, *Advanced Materials in Catalysis: Perovskite-related oxides as oxidation-reduction catalysts*, (Ed.: N. Y. Academic Press), ISBN: 012147450X 9780121474508, James Joseph Burton and Robert L. Garten, **1977**.
- [74] Z. Zhao, X. Yang, Y. Wu, *Applied Catalysis B: Environmental* **1996**, *8* (3), 281–297.
- [75] J. Zhu, Z. Zhao, D. Xiao, J. Li, X. Yang, Y. Wu, *Industrial and Engineering Chemistry Research* **2005**, *44* (12), 4227–4233.
- [76] R. J. H. Voorhoeve, J. P. Remeika, L. E. Trimble, A. S. Cooper, F. J. Disalvo, P. K. Gallagher, *Journal of Solid State Chemistry* **1975**, *14*, 395–406.
- [77] D. Ferri, L. Forni, M. A. P. Dekkers, B. E. Nieuwenhuys, *Applied Catalysis B: Environmental* **1998**, *16*, 339–345.
- [78] C. Tofan, D. Klvana, J. Kirchnerova, *Applied Catalysis B: Environmental* **2002**, *36*, 311–323.
- [79] H. Iwakuni, Y. Shinmyou, H. Yano, K. Goto, H. Matsumoto, T. Ishihara, *Bulletin of the Chemical Society of Japan* **2008**, *81*, 1175–1182.
- [80] A. K. Ladavos, P. J. Pomonis, *Applied Catalysis B: Environmental* **1992**, *1*, 101–116.
- [81] S. D. Peter, E. Garbowski, V. Perrichon, M. Primet, *Catalysis Letters* **2000**, *70*, 27–33.
- [82] A. E. Giannakas, A. A. Leontiou, A. K. Ladavos, P. J. Pomonis, *Applied Catalysis A: General* **2006**, *309* (2), 254–262.
- [83] R. Zhang, H. Alamdari, S. Kaliaguine, *Journal of Catalysis* **2006**, *242*, 241–253.
- [84] G. Centi, S. Perathoner, *Applied Catalysis A: General* **1995**, *132*, 179–259.
- [85] H. Arai, T. Yamada, K. Eguchi, T. Seiyama, *Applied Catalysis* **1986**, *26*, 265–276.
- [86] T. Nitadori, S. Kurihara, M. Misono, *Journal of Catalysis* **1986**, *98*, 221–228.
- [87] K. Stephan, M. Hackenberger, D. Kießling, G. Wendt, *Chemical Engineering & Technology* **2002**, *25* (5), 565–571.
- [88] L. Zhang, Y. Zhang, J. Deng, H. Dai, *Journal of Natural Gas Chemistry* **2012**, *21* (1), 69–75.
- [89] Y. Zhang-Steenwinkel, J. Beckers, A. Bliëkv, *Applied Catalysis A: General* **2002**, *235* (1-2), 79–92.
- [90] H. He, H. X. Dai, C. T. Au, *Catalysis Today* **2004**, *90*, 245–254.
- [91] G. Pecchi, M. G. Jiliberto, A. Buljan, E. J. Delgado, *Solid State Ionics* **2011**, *187*, 27–32.
- [92] B. P. Barbero, J. A. Gamboa, L. E. Cadús, *Applied Catalysis B: Environmental* **2006**, *65* (1-2), 21–30.

- [93] J. Zhu, Z. Zhao, D. Xiao, J. Li, X. Yang, Y. Wu, *J. Mol. Catal. A: Chem.* **2005**, *238* (1-2), 35–40.
- [94] N. Mizuno, Y. Fujiwara, M. Misono, *Journal of the Chemical Society Chemical Communications* **1989**, *5*, 316–318.
- [95] G. Saracco, F. Geobaldo, G. Baldi, *Applied Catalysis B: Environmental* **1999**, *20* (4), 277–288.
- [96] N. K. Labhsetwar, A. Watanabe, R. B. Biniwale, R. Kumar, T. Mitsuhashi, *Applied Catalysis B: Environmental* **2001**, *33* (2), 165–173.
- [97] Y. Teraoka, H. Nii, S. Kagawaa, K. Jansson, M. Nygren, *Applied Catalysis A: General* **2000**, *194-195*, 35–41.
- [98] H. Tanaka, I. Tan, M. Uenishi, M. Taniguchi, M. Kimura, Y. Nishihata, J. Mizuki, *Journal of Alloys and Compounds* **2006**, *408-412*, 1071–1077.
- [99] Y. Lu, K. A. Michalow, S. K. Matam, A. Winkler, A. E. Maegli, S. Yoon, A. Heel, A. Weidenkaff, D. Ferri, *Applied Catalysis B: Environmental* **2014**, *144*, 631–643.
- [100] A. Eyssler, P. Mandaliev, A. Winkler, P. Hug, O. Safonova, R. Figi, A. Weidenkaff, D. Ferri, *The Journal of Physical Chemistry C* **2010**, *114*, 4584–4594.
- [101] A. Eyssler, A. Winkler, O. Safonova, M. Nachtegaal, S. K. Matam, P. Hug, A. Weidenkaff, D. Ferri, *Chemistry of Materials* **2012**, *24*, 1864–1875.
- [102] N. Guilhaume, S. D. Peter, M. Primet, *Applied Catalysis B: Environmental* **1996**, *10* (4), 325–344.
- [103] H. Hamada, Novel Catalytic Technologies for Car Emission Reduction, **2009**, <http://www.oecd.org/dataoecd/54/21/44022244.pdf>.
- [104] I. Hamada, A. Uozumi, Y. Morikawa, A. Yanase, H. Katayama-Yoshida, *Journal of the American Chemical Society* **2011**, *133* (46), 18506–18509.
- [105] Y. Nishihata, J. Mizuki, H. Tanaka, M. Uenishi, M. Kimura, *Journal of Physics and Chemistry of Solids* **2005**, *66*, 274–282.
- [106] Y. Nishihata, J. Mizuki, T. Akao, H. Tanaka, M. Uenishi, M. Kimura, T. Okamoto, N. Hamada, *Nature* **2002**, *418* (6894), 164–167.
- [107] J.-P. Dacquin, M. Cabié, C. R. Henry, C. Lancelot, C. Dujardin, S. Raouf, P. Granger, *Journal of Catalysis* **2010**, *270* (2), 299–309.
- [108] J.-P. Dacquin, C. Lancelot, C. Dujardin, C. Cordier-Robert, P. Granger, *Journal of Physical Chemistry C* **2011**, *115* (5), 1911–1921.
- [109] J. Zhu, H. Li, L. Zhong, P. Xiao, X. Xu, X. Yang, Z. Zhao, J. Li, *ACS Catalysis* **2014**, *4*, 2917–2940.
- [110] R. Ran, D. Weng, X. Wu, J. Fan, L. Qing, *Catalysis Today* **2007**, *126* (3-4), 394–399.
- [111] G. J. McCarthy, P. V. Gallagher, C. Sipe, *Materials Research Bulletin* **1973**, *8*, 1277–1284.
- [112] J. Twu, P. K. Gallagher in *Properties and Applications of Perovskite-type Oxides*, (Eds.: L. G. Tejuca, J. L. G. Fierro), Marcel Dekker, New York, **1993**, pp. 1–23.
- [113] U. Berndt, D. Maier, C. Keller, *Journal of Solid State Chemistry* **1975**, *13*, 131–135.

- [114] S. Kaliaguine, A. V. Neste, V. Szabo, J. E. Gallot, M. Bassir, R. Muzychuk, *Applied Catalysis A: General* **2001**, 209 (1-2), 345–358.
- [115] S. Royer, F. Bérubé, S. Kaliaguine, *Applied Catalysis A: General* **2005**, 282 (1-2), 273–284.
- [116] J.-P. Dacquin, C. Lancelot, C. Dujardin, P. Da Costa, G. Djega-Mariadassou, P. Beaunier, S. Kaliaguine, S. Vaudreuil, S. Royer, P. Granger, *Applied Catalysis B: Environmental* **2009**, 91 (3-4), 596–604.
- [117] J.-P. Dacquin, *Molécules et Matière Condensée*, Université de Lille 1, UCCS, **2008**.
- [118] A. González, E. Martínez Tamayo, A. Beltrán Porter, V. Cortés Corberán, *Catalysis Today* **1997**, 33, 361–369.
- [119] N. Nikolic, L. Mancic, Z. Marinkovic, O. Milosevic, M. M. Ristic, *Annales de Chimie Science des Matériaux* **2001**, 26, 35–41.
- [120] J. G. McCarty, H. Wise, *Catalysis Today* **1990**, 8, 231–248.
- [121] W. Li, M. W. Zhuo, J. L. Shi, *Materials Letters* **2004**, 58, 365–368.
- [122] Y. Liu, H. Zheng, J. Liu, T. Zhang, *Chemical Engineering Journal* **2002**, 89, 213–221.
- [123] X. Wu, L. Xu, D. Weng, *Catalysis Today* **2004**, 90, 199–206.
- [124] C. Zhang, Y. Guo, Y. Guo, G. Lu, A. Boreave, L. Retailleau, A. Baylet, A. Giroir-Fendler, *Applied Catalysis B: Environmental* **2014**, 148-149, 490–498.
- [125] C. Lamonier, A. Ponchel, A. D’Huysser, L. Jalowiecki-Duhamel, *Catalysis Today* **1999**, 50, 247–259.
- [126] K. C. Patil, S. Aruna, T. Mimani, *Current Opinion in Solid State and Materials Science* **2002**, 6, 507–512.
- [127] S. T. Aruna, A. S. Mukasyan, *Current Opinion in Solid State and Materials Science* **2008**, 12, 44–50.
- [128] K. Prabhakaran, J. Joseph, N. M. Gokhale, S. C. Sharma, R. Lal, *Ceramics International* **2005**, 31, 327–331.
- [129] N. P. Bansal, Z. Zhong, *Journal of Power Sources* **2006**, 158, 148–153.
- [130] Y. Wang, J. Zhu, L. Zhang, X. Yang, L. Lu, X. Wang, *Materials Letters* **2006**, 60, 1767–1770.
- [131] A. Civera, M. Pavese, G. Saracco, V. Specchia, *Catalysis Today* **2003**, 83, 199–211.
- [132] S. Specchia, A. Civera, G. Saracco, *Chemical Engineering Science* **2004**, 59, 5091–5098.
- [133] R. S. Guo, Q. T. Wei, H. L. Li, F. H. Wang, *Materials Letters* **2006**, 60, 261–265.
- [134] L. Chick, L. Pederson, G. Maupin, J. Bates, L. Thomas, G. Exarhos, *Materials Letters* **1990**, 10, 6–12.
- [135] R. Giacomuzzi, M. Portinari, I. Rossetti, L. Formi, *Studies in Surface Science and Catalysis*, 12th International Congress on Catalysis, Proceedings of the 12th ICC **2000**, 130, 197–202.
- [136] R. Leanza, I. Rossetti, L. Fabbrini, C. Oliva, L. Forni, *Applied Catalysis B: Environmental* **2000**, 28, 55–64.
- [137] I. Rossetti, L. Forni, *Applied Catalysis B: Environmental* **2001**, 33, 345–352.

- [138] C. Oliva, L. Bonoldi, S. Cappelli, L. Fabbrini, I. Rossetti, L. Forni, *Journal of Molecular Catalysis A: Chemical* **2005**, 226 (1), 33–40.
- [139] G. Saracco, F. Geobaldo, D. Mazza, G. Baldi, *Journal of Thermal Analysis and Calorimetry* **1999**, 56, 1435–1442.
- [140] G. Tesquet, PhD thesis, Université Lille 1 – Sciences et Technologies, **2013**.
- [141] M. S. G. Baythoun, F. R. Sale, *Journal of Materials Science* **1982**, 17, 2757–2769.
- [142] H. Taguchi, S. Matsu-ura, M. Nagao, T. Choso, K. Tabata, *Journal of Solid State Chemistry* **1997**, 129 (1), 60–65.
- [143] M. P. Pechini, *Patent*, US3330697 (US), **1967**.
- [144] E. Krupicka, A. Reller, A. Weidenkaff, *Crystal Engineering* **2002**, 5 (3-4 SPEC), Crystal Chemistry of Functional Materials II, Proceedings of Symposium L, E-MRS, 195–202.
- [145] M. Schwickardi, T. Johann, W. Schmidt, F. Schüth, *Chemistry of Materials* **2002**, 14 (9), 3913.
- [146] I. Twagirashema, M. Frere, L. Gengembre, C. Dujardin, P. Granger, *Topics in Catalysis* **2007**, 42-43 (1-4), 171–176.
- [147] J. Zhang, H. Deng, L. Lin, *Molecules* **2009**, 14, 2747–2757.
- [148] S. Specchia, C. Galletti, V. Specchia, *Studies in Surface Science and Catalysis*, Scientific Bases for the Preparation of Heterogeneous Catalysts - Proceedings of the 10th International Symposium, Louvain-la-Neuve, Belgium, July 11-15, 2010 **2010**, 175, 59–67.
- [149] T. Valdés-Solís, G. Marbán, A. B. Fuertes, *Chemistry of Materials* **2005**, 17 (8), 1919–1922.
- [150] Y. Wang, J. Ren, Y. Wang, F. Zhang, X. Liu, Y. Guo, G. Lu, *Journal of Physical Chemistry C* **2008**, 112 (39), 15293–15298.
- [151] H. Su, L. Jing, K. Shi, C. Yao, H. Fu, *Journal of Nanoparticle Research* **2010**, 12 (3), 967–974.
- [152] M. M. Nair, F. Kleitz, S. Kaliaguine, *ChemCatChem* **2012**, 4 (3), 387–394.
- [153] Y. Wei, J. Liu, Z. Zhao, Y. Chen, C. Xu, A. Duan, G. Jiang, H. He, *Angewandte Chemie International Edition* **2011**, 50, 2326–2329.
- [154] J. Zheng, J. Liu, Z. Zhao, J. Xu, A. Duan, G. Jiang, *Catalysis Today* **2012**, 191 (1), 146–153.
- [155] R. K. C. de Lima, M. S. Batista, M. Wallau, E. A. Sanches, Y. P. Mascarenhas, E. A. Urquiza-González, *Applied Catalysis B: Environmental* **2009**, 90 (3-4), 441–450.
- [156] F. Schüth, *Angewandte Chemie International Edition* **2003**, 42, 3604–3622.
- [157] A. Stein, *Microporous and Mesoporous Materials* **2001**, 44-45, 227–239.
- [158] E. Yablonovitch, *Journal of the Optical Society of America B* **1993**, 10, 283–295.
- [159] J. D. Joannopoulos, P. R. Villeneuve, S. Fan, *Nature* **1997**, 386, 143–149.
- [160] M. Sadakane, T. Asanuma, J. Kubo, W. Ueda, *Chemistry of Materials* **2005**, 17 (13), 3546–3551.

- [161] J. Xu, J. Liu, Z. Zhao, C. Xu, J. Zheng, A. Duan, G. Jiang, *Journal of Catalysis* **2011**, *282*, 1–12.
- [162] M. Sadakane, T. Horiuchi, N. Kato, C. Takahashi, W. Ueda, *Chemistry of Materials* **2007**, *19* (23), 5779–5785.
- [163] S. Nakayama, *Journal of Materials Science* **2001**, *36*, 5643–5648.
- [164] B. Levasseur, S. Kaliaguine, *Applied Catalysis A: General* **2008**, *343*, 29–38.
- [165] P. Miquel, PhD thesis, Université de Lille 1, **2009**.
- [166] P. V. Gosavi, R. B. Biniwale, *Materials Chemistry and Physics* **2010**, *119*, 324–329.
- [167] M. Kumar, S. Srikanth, B. Ravikumar, T. C. Alex, S. K. Das, *Materials Chemistry and Physics* **2009**, *113*, 803–815.
- [168] S. Li, L. Jing, W. Fu, L. Yang, B. Xin, H. Fu, *Materials Research Bulletin* **2007**, *42*, 203–212.
- [169] M. Sadakane, T. Horiuchi, N. Kato, K. Sasaki, W. Ueda, *Journal of Solid State Chemistry* **2010**, *183* (6), 1365–1371.

Experimental protocols and techniques

2.1 Synthesis protocols

All synthesis protocols are based on a citrate complexation route from nitrate precursors. An overview of the different parameters adapted from the present method are depicted in Fig. 2.1. They differ in the use of polymer structuring agents, i. e. templates, the employed solvent and finally the atmosphere under which the 1st part of the calcination was performed. The 2nd part was always performed under air flow.

Concerning the calcination atmosphere, selected syntheses were conducted including a calcination part under quasi semi-closed so-called stagnant atmosphere (Fig. A.1) in the absence of an imposed gas flow.

All perovskites of structure $ABO_{3\pm\delta}$ exhibit minor oxygen excess or deficiency, i. e. are non-stoichiometric. For the sake of simplicity, the notation of ABO_3 will be conventionally used instead of $ABO_{3\pm\delta}$.

2.1.1 Conventional Citrate Method (CCM)

The conventional citrate method derived from Taguchi et al.^[1] was used in order to obtain reference solids for later comparison and for composition optimisation.

For each compound, the corresponding metal nitrates (La, Ca, Fe, Mn, Cu) and citric acid (CA) ($n_{CA} = n_{A-nitrate} + n_{B-nitrate}$) were first dissolved separately in minimum volumes of deionised water under stirring for 30 min. After mixing, the resulting solution was kept stirring for 10 min at room temperature (rt).

The solution was then transferred to a flask and evaporated at 60 °C at reduced pressure (progressively lowering the pressure from initially 60 to 5 mbar) until a gel is formed. The gel was poured in a Petri dish and dried in air at 80 °C for 48 h.

The obtained xerogel was ground in a mortar. The nitrates decomposition was carried out in a muffle oven by increasing gradually the temperature according to the corresponding thermal analyses, from room temperature (rt) up to generally 150 to 250 °C. After another grinding step, the solid was calcined under air flow (0.21 min^{-1}) for 8 h at 600 °C (ramp: 2 K min^{-1}). The mixed oxide was ground again before characterisations and tests were conducted.

Different (calcination) conditions were used to obtain the perovskite structure as described in Section 2.1.4.

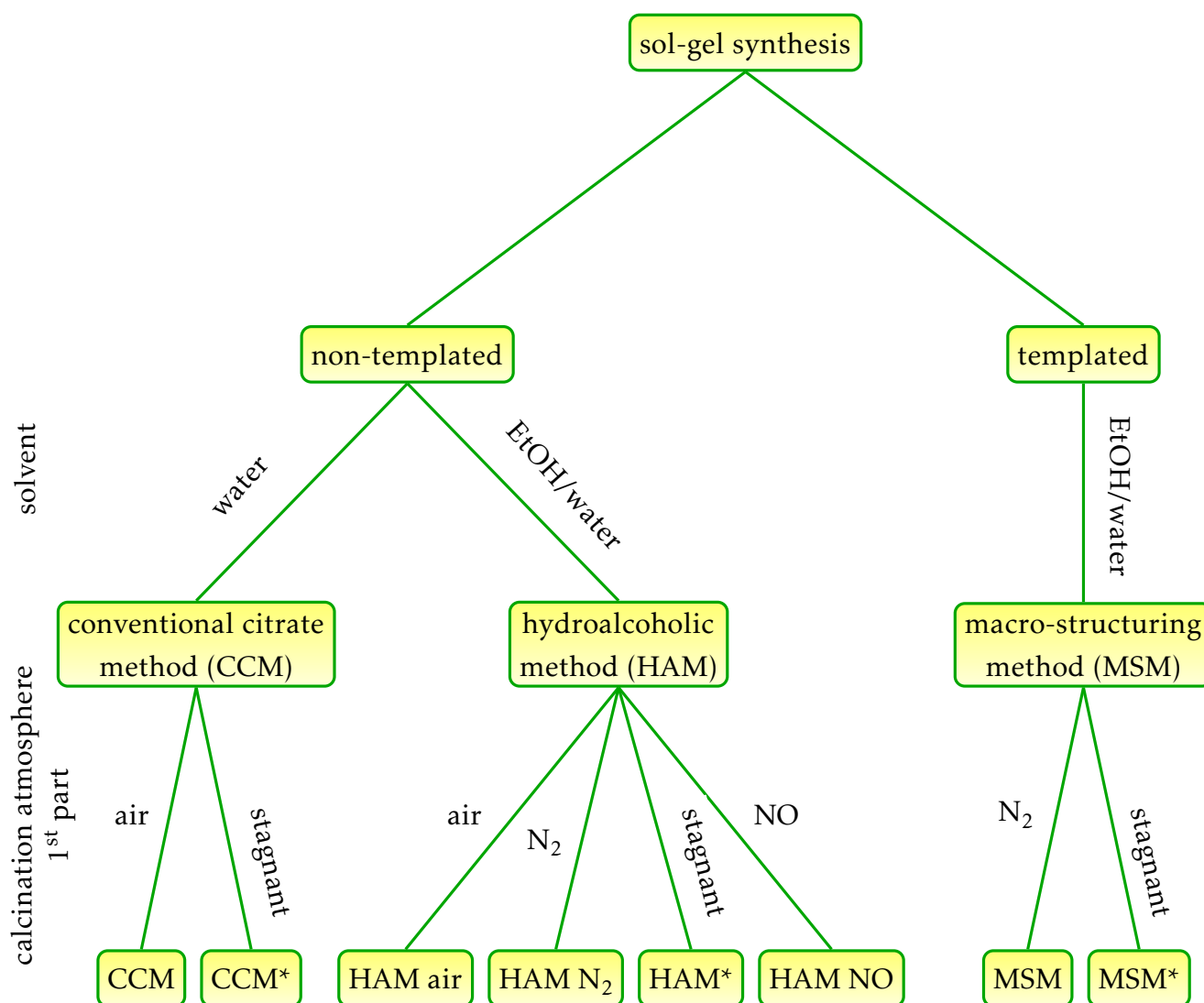


Figure 2.1 – **Overview of different synthesis methods.** A 1st distinction corresponds to the presence or absence of a template during synthesis. Secondly, different solvents, either water (CCM) or a mixture of water in EtOH (hydroalcoholic method (HAM), macro-structuring method (MSM)), were employed. Thirdly, methods are classified depending on the atmosphere of the 1st part of the calcination. The 2nd part of the calcination was always conducted under air flow.

2.1.2 HydroAlcoholic Method (HAM)

The so-called hydroalcoholic method is derived from previous works conducted by Krupicka et al.^[2] and Wang et al.^[3]

For each compound, the corresponding amounts of metal nitrates (La, Fe) and citric acid (CA) ($n_{CA} = n_{A-nitrate} + n_{B-nitrate}$) were dissolved overnight in 15 ml of EtOH and 5 ml of deionised water in a sealed 100 ml beaker under stirring.

After removing the sealing polyethylene/paraffin film, the resulting homogeneous solution containing the metal-nitrate-citrate-complex was placed in a drying chamber at 40 °C. Some samples were placed in a climate chamber at 40 °C and 30 % relative humidity (r. h.) instead of the regular drying chamber. After the drying period for at least 2 days, the solid precursor was ground in a mortar.

No separate nitrate decomposition as for the CCM samples was performed. However, to improve heat transfer and prevent hot spots during calcination, quartz sand (20 - 30 mesh) was added to the sample ($m_{sand}/m_{sample} = 5$). Additionally, the calcination ramp was decreased to 1 K min⁻¹ instead of 2 K min⁻¹ for the CCM.

After calcination at 600 °C, the solid was sieved over 300 µm to separate the catalyst from the quartz sand.

Different calcination procedures were investigated as described in Section 2.1.4.

2.1.3 Macro-Structuring method (MSM)

The macro-structuring method was adapted from Wang et al.^[3] Our goal was to obtain perovskite catalysts with controlled porosity, morphology and higher specific surface areas. The synthesis method was based on the HAM including a supplementary template impregnation step.

Nearly monodisperse polymer spheres (Fig. 2.2) were used as macro-templates. Polymer spheres were spanning diameters between 80 nm and 400 nm (± 20 nm).

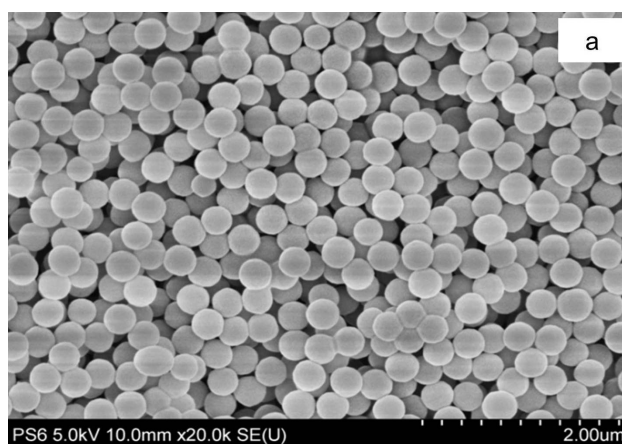


Figure 2.2 – SEM of **polymer spheres employed as structuring agent**. Exemplarily shown for polystyrene (PS) spheres with $d = 200$ nm.^[4]

The impregnation took place after the complete dissolution of the metal nitrates and CA. The chosen template was weighed in a 100 ml beaker and dried at 120 °C for 2 h beforehand. The homogeneous solution was then poured over the template and left for impregnation under stirring for 10 min (sealed by a polyethylene/paraffin film).

The resulting solution containing the metal-nitrate-citrate-complex was placed in a climate chamber at 40 °C with varying relative humidity (r. h.) for controlling the evaporation of the supernatant solution. Experiments were conducted at r. h. of 30, 50, and 80 %. Out of these conditions, 30 % r. h. were retained for the study.

The calcination procedure is described in Section 2.1.4 (Fig. 2.4) and analogous to the one conducted for the HAM N₂ solid. The 1st part of the calcination was always performed under N₂ flow, i. e. inert atmosphere, to prevent a too early deformation/decomposition of the template spheres for which the T_g is generally close to 300 °C.

2.1.4 Calcination procedures

All perovskites which were prepared by CCM were decomposed in a muffle oven prior to calcination which was conducted at a heating rate of 2 K min⁻¹ up to 600 °C which were held for 8 h before cooling down to rt.

Indeed, all perovskite calcinations were conducted at a maximum temperature of 600 °C. If a gas flow was applied, its flow was regulated to 0.2 l min⁻¹.

All HAM-based syntheses and the CCM* synthesis were conducted with a heating ramp of 1 K min⁻¹ to 600 °C and the total time at maximum temperature equalled 10 h.

In the framework of this study, 2 main types of calcination procedures were performed. The continuous air flow calcination was employed to prepare the CCM and the HAM air solids. All other solids were obtained after a calcination in 2 parts which were conducted under 2 different atmospheres as shown exemplarily for the CCM* synthesis in Fig. 2.3 (blue), for which the 2nd part was always performed under air flow.

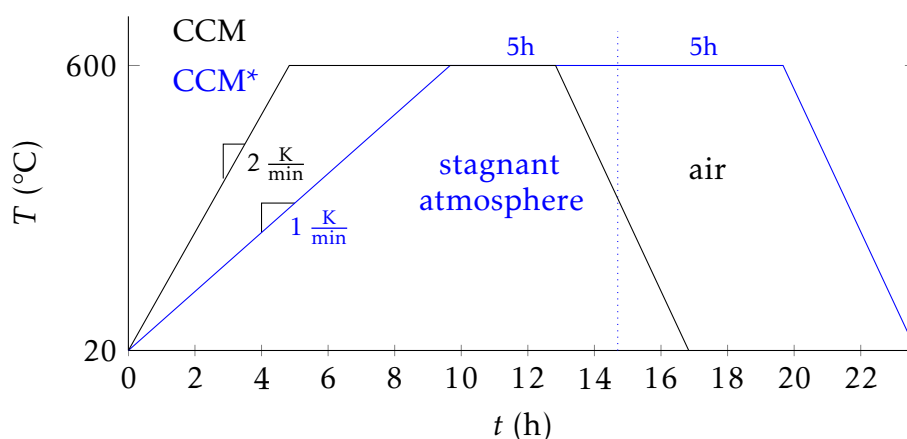


Figure 2.3 – **Temperature profiles of the calcination procedures of the CCM and CCM*.** CCM was conducted under continuous air flow whereas this is only the case for the second part of calcination for CCM*. Its first part was done under stagnant atmosphere.

The 1st part of the calcination consists of the heating ramp and the first 5 h at maximum temperature and was either conducted under inert gas flow, i. e. N₂ flow (HAM N₂, all MSM), diluted NO/He flow (HAM NO) or under so-called *stagnant* atmosphere (CCM*, HAM*, HAM*_{cooling} and MSM*). Stagnant conditions are defined as an atmosphere which is not exposed to any imposed gas flow – but no confined system either – as depicted in Fig. A.1 in Appendix A. The initial atmosphere consisted of air. Regardless of the precursor, samples calcined under stagnant conditions will be denoted with an asterisk *.

Another variant of this 2-part calcination procedure consisted of observing an intermediate cooling before the gas switch was performed as shown in Fig. 2.4. This procedure was followed in order to prevent sintering of the solid due to an exothermic peak at the final calcination temperature. Regardless of the atmosphere employed in the 1st step, these samples will be denoted with the subscript *cooling*.

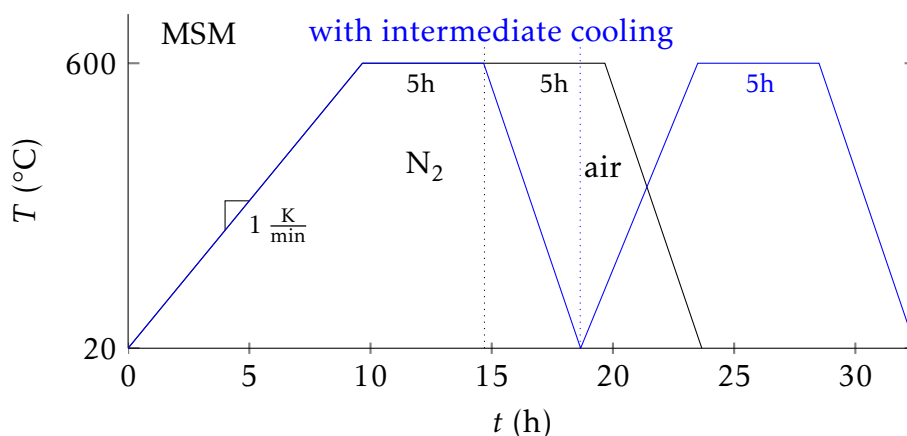


Figure 2.4 – Temperature profile of the calcination procedure of the MSM and MSM_{cooling}. The procedure can be conducted with (blue) and without an intermediate cooling (black) before the gas switch.

A summary of the different parameters and the corresponding notations is given in Section 2.1.6.

2.1.5 Incipient Wet Impregnation (IWI) method for the doping of perovskite catalysts with noble metals

Perovskites doped with low loadings of noble metals were prepared by using an incipient wet impregnation technique. First, aqueous solutions of noble metal nitrates ($\text{Pd}(\text{NO}_3)_2 \cdot x\text{H}_2\text{O}$, $\text{Rh}(\text{NO}_3)_3$, and $\text{Pt}(\text{NH}_3)_4(\text{NO}_3)_2$) were prepared.

The solid to be impregnated was then weighed in an evaporation flask. A precise amount of the corresponding metal solution and deionised water was added (both volumes should add up to a maximum of 10 ml). The solution was then evaporated slowly in a rotative evaporator at 100 mbar to 200 mbar until complete dryness (≈ 5 h).

The obtained solid was calcined at 400 °C for 8 h (heating ramp: 2 K min^{-1}) in a regular oven for allowing the decomposition of the metallic precursor.

2.1.6 Summary of conducted syntheses by parameters

Table 2.1 summarises the conducted differently modified sol-gel based syntheses specifying the employed parameters.

Table 2.1 – Syntheses by parameters.

notation	solvent	calcination atmosphere		cooling? ^a	drying step ^b
		1 st part	2 nd part		
CCM	H ₂ O	air flow		-	drying chamber (80 °C)
CCM*	H ₂ O	stagnant	air flow	-	drying chamber (80 °C)
HAM air	EtOH/H ₂ O	air flow		-	drying chamber (40 °C)
HAM N ₂	EtOH/H ₂ O	N ₂ flow	air flow	-	climate chamber ^d
MSM	EtOH/H ₂ O	N ₂ flow	air flow	-	climate chamber ^d
MSM _{cooling}	EtOH/H ₂ O	N ₂ flow	air flow	+	climate chamber ^d
MSM*	EtOH/H ₂ O	stagnant	air flow	-	climate chamber ^d
HAM* _{cooling}	EtOH/H ₂ O	stagnant	air flow	+	drying chamber (40 °C)
HAM*	EtOH/H ₂ O	stagnant	air flow	-	climate chamber ^d
HAM NO	EtOH/H ₂ O	NO flow ^c	air flow	-	climate chamber ^d

^a Intermediate cooling before calcination atmosphere switch.

^b Drying step performed in regular drying or climate chamber.

^c 5 Vol.% NO/He.

^d 40 °C; 30 % r. h.

2.2 Physico-chemical characterisation conditions

2.2.1 Elementary analysis

Elementary analyses were performed by the central analyses service of the CNRS (SCA, ISA-CNRS) using inductively coupled plasma atomic emission spectroscopy (ICP) to determine the bulk compositions of selected perovskites.

Results of all analysed solids are shown in Appendix B.

2.2.2 Thermogravimetric and Differential Scanning Calorimetric analysis (TGA/DSC)

thermogravimetric analysis (TGA)/differential scanning calorimetric analysis (DSC) measurements were performed on a TA Instruments SDT-Q600 with an alumina reference. Up to 5 mg of sample were exposed to either air flow, N₂ flow or stagnant conditions (air atmosphere but without any gas flow) while being gradually heated from rt to 800 °C. These low amounts were chosen due the highly exothermic decomposition of the nitrate-citrate-precursor complexes.

2.2.3 Hydrogen Temperature-programmed Reduction (H₂-TPR)

H₂-TPR is used to investigate the reducibility of compounds. H₂-TPR experiments were undertaken on a Micromeritics AutoChemII 2920. During the analysis, 50 mg of sample were overflowed by a 25 or 50 ml min⁻¹ flow of 5 Vol.% H₂/Ar. The H₂ consumption was monitored during a heating ramp of 5 K min⁻¹ from room temperature to 1100 °C using a thermal conductivity detector. Produced water was trapped in a cold trap before reaching this detector.

2.2.4 N₂ physisorption

Specific surface areas (SSA) were determined by N₂ physisorption at –196 °C on approximately 0.5 g of sample previously outgassed at 200 °C under vacuum during 2 h using the Micromeritics TriStarII. Single-point SSA were determined by measurements on a micromeritics FlowSorbIII. In both cases, Brunauer-Emmett-Teller theory (BET) was applied to calculate the specific surface areas. Pore size distributions were obtained at the same time from the isotherms based on the Barret-Joyner-Halenda theory (BJH) theory. Desorption branches were used to determine SSA, pore size distributions, V_{pore} and \bar{d}_{pore} . All discussions on pores (average diameters, cumulative volume, pore size distributions) are related to open pores only, closed pores being non-accessible to this analysis method.

The discussion of the thereby determined pore distributions are based on the International Union of Pure and Applied Chemistry (IUPAC) recommendations on classification of pores,^[5,6] i.e. being defined by their respective diameters: micropores with $d < 2$ nm, mesopores with $2 \leq d \leq 50$ nm, and macropores with $d > 50$ nm.

2.2.5 X-ray diffraction XRD

X-ray diffraction (XRD) was used to determine the crystalline phases of the prepared solids. Furthermore, unit cell parameters and the average crystallite size were estimated.

In this study XRD analyses were performed at room temperature with a Bruker AXS D8 Advance diffractometer in Bragg–Brentano geometry. Data was recorded in the 2θ range of 10–80° with a 2θ step of 0.02° and a Cu K α source ($\lambda = 0.154$ nm).

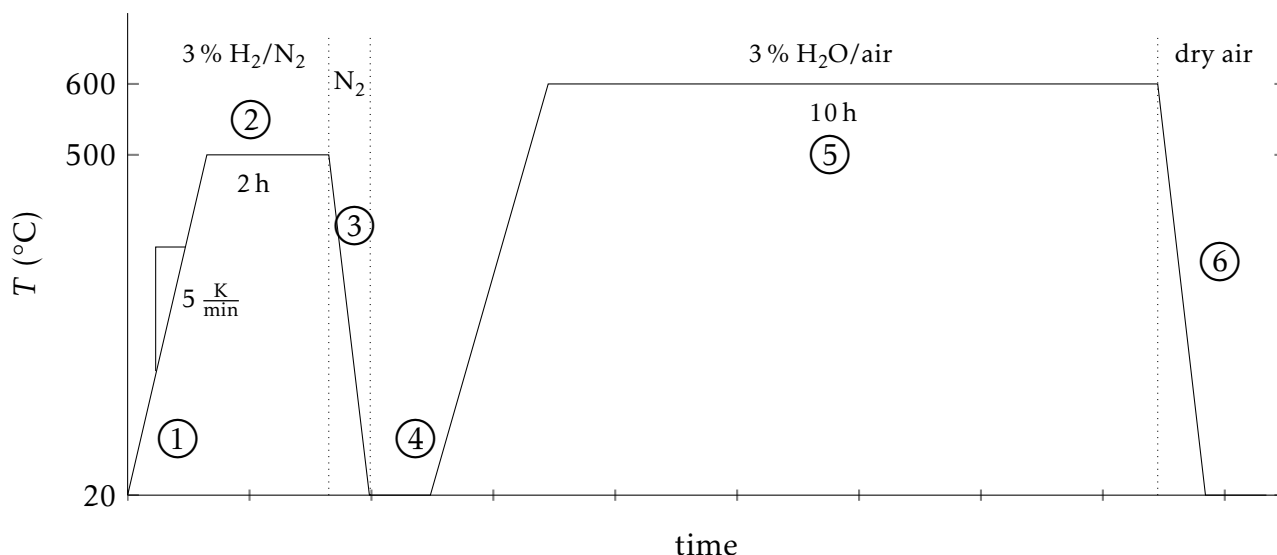


Figure 2.5 – **Temperature profile of the High Temperature XRD analysis.** After a reduction with 3 Vol.% H₂/N₂ at 500 °C for 2 h, the sample is cooled down in N₂ atmosphere. Under humid air (3 Vol.% H₂O/air) flow, the sample is heated to 600 °C and left under these conditions for 10 h before it is cooled down to rt under dry air flow. A last scan is conducted at rt.

Unit cell parameters (a, b, c) as well as apparent average crystallite sizes (d_{cryst}) were estimated by full pattern matching of the corresponding XRD structures using the Fullprof Software Suite.^[7–9] The Thompson-Cox-Hastings pseudo-Voigt function was chosen for

peak profile estimation. Instrument resolution was evaluated by using LaB_6 as standard. Standard deviations were obtained by the Fullprof software after multiplying with the Bérar factor^[10,11] likewise calculated by the Fullprof software.

All diffractograms displayed in this study were normalised.

In situ high temperature X-ray diffraction (HTXRD) experiments were performed to investigate the phase transitions under reductive or humid atmosphere during temperature ramps - if any. They were conducted according to the scheme shown in Fig. 2.5. At first, the temperature (T) was raised to 500 °C under reductive atmosphere (3 Vol.% H_2 in N_2 , step 1). This temperature was held for 2 h (step 2) before cooling down to rt in inert atmosphere (step 3). Then, the sample was exposed to a humid air flow (3 Vol.% H_2O) while being heated to 600 °C (step 4). After 10 h at this temperature (step 5), the sample was cooled down under dry air flow (step 6).

2.2.6 Raman spectroscopy

Raman spectroscopy is a technique which allows to investigate molecular vibrations of a compound. Thereby information on molecular unit structures but also on impurities can be obtained.

The spectra of different grains of sample were recorded on a microdispersive Raman spectrometer (HORIBA HR800 UV) using different excitation sources: a blue ($\lambda_{\text{exc}} = 488 \text{ nm}$, Ar), or a red laser ($\lambda_{\text{exc}} = 633 \text{ nm}$, He-Ne).

In the literature, 2 different symmetry notations are used for the orthorhombic LaFeO_3 structure.^[12] In accordance with the XRD discussions, the orthorhombic LaFeO_3 perovskite was discussed in Pbnm instead of Pnma symmetry. Therefore, all assigned modes which were described as B_{3g} (Pnma) in literature are hereafter written as the corresponding active B_{1g} modes in Pbnm symmetry for the LaFeO_3 type structure.^[12]

2.2.7 Transmission electron microscopy TEM

The transmission electron microscopy (TEM) was conducted to analyse the surface morphology of the perovskites at the nanometric scale.

Transmission electron micrographs were recorded on a JEOL-JEM 2010. Samples were prepared by depositing a suspension of dispersed ground solid in EtOH (dispersion under ultra-sound) on a carbon grid.

Energy dispersive X-ray spectroscopy (EDX) was conducted on selected samples to determine the nature of the elements. No (semi-)quantitative information could be obtained due to the large area covered.

2.2.8 Scanning electron microscopy SEM

SEM analyses were performed to analyse the surface morphology of the perovskites at the micrometre scale.

Scanning electron micrographs were recorded on either a Hitachi S-4700 or a Hitachi SU70 SEM FEG. For the former, samples were prepared including carbon sputtering to prevent/lighten charging phenomena, whereas for the latter samples were prepared by depositing the calcined powder on a conductive double-faced adhesive tape. The scanning electron microscope was operated at about 5 kV and 10 μA .

2.2.9 X-ray photo-electron spectroscopy XPS

X-ray photo-electron spectroscopy (XPS) measurements of the solids were conducted to determine the surface composition of the perovskites, i. e. the relative abundance of the elements. The thereby obtained data was furthermore exploited to specify the oxidation states of the elements and their chemical environment. It has to be kept in mind, that the elementary analysis of the surface is limited to a relative accuracy of about 20 %.

Samples were prepared by depositing the respective solid on an adhesive Cu tape. XPS analyses were then carried out either on an AXIS Ultra DLD Kratos spectrometer equipped with a monochromatised aluminium source (150 W) and charge compensation gun or on a VG Scientific Escalab 220i-XL equipped with a non-monochromatised aluminium source (300 W), the energy of the Al source being 1486.6 eV. All binding energies were calibrated with C 1s core level at 285 eV. Data exploitation was performed using the program CasaXPS. Background corrections were conducted applying a procedure proposed by Shirley^[13] if possible. In most cases, however, a linear background was subtracted before estimating the peak areas.

Spectral decomposition of photopeaks was performed using position constraints as reported in literature and area considerations in agreement with the occupancy of the orbitals. The estimation of Cu⁺ and Cu²⁺ contributions to the Cu 2p_{3/2} signal was conducted using the method proposed by Biesinger et al. relying on the ratio of the intensities of main signal and satellite.^[14,15]

Complete surface compositions obtained by XPS are reported in Appendix B.

2.3 Catalytic performance measurements

Catalytic performance tests were conducted in lab-scale condition experiments with feed gas compositions representative of the exhaust gas. Temperature-programmed tests were performed with different feed compositions corresponding to rich, lean and stoichiometric conditions.

2.3.1 Feed stream composition

The chosen feed compositions contain major pollutants (NO, CO, and CH₄, C₃H₆, and C₃H₈ representing HC pollutants) as well as inhibitors (CO₂ and H₂O) and H₂ naturally present in petrol engine exhaust gas. Indeed, independently of the A/F, the molar CO/H₂ ratio is close to 3:1 in spark-ignition engine exhaust.^[16] This ratio was observed in the present study. The compositions and their corresponding stoichiometry factor, λ , calculated according to Eq. 2.1 are presented in Table 2.2.

$$\lambda = \frac{2 \cdot [\text{O}_2] + [\text{NO}] + [\text{H}_2\text{O}] + 2 \cdot [\text{CO}_2] + [\text{CO}]}{[\text{H}_2] + 2 \cdot [\text{CO}] + 4 \cdot [\text{CH}_4] + 9 \cdot [\text{C}_3\text{H}_6] + 10 \cdot [\text{C}_3\text{H}_8] + [\text{H}_2\text{O}] + 2 \cdot [\text{CO}_2]} \quad (2.1)$$

Based on the observation that most catalysts do not convert CH₄ under the stated “stoichiometric” conditions, i. e. it acts as an inert gas, a modified stoichiometric feed was tested for selected catalysts. It consists of the same composition as the stoichiometric one except for the O₂ content which is reduced by the amount which would be necessary to fully oxidise methane.

Conversions of the corresponding gas *i*, X_{*i*}, were generally calculated by comparing its inlet ([*i*]₀) and outlet concentrations ([*i*]) according to Eq. 2.2. In the case of NO, conversion

Table 2.2 – **Feed compositions for catalytic tests.** Compositions correspond to stoichiometric, lean or rich conditions. The modified stoichiometric composition is obtained by reducing the oxygen content by the amount necessary to oxidise CH₄.

λ [Gas] (Vol.-%)	1.02 lean	1.00 stoichiometric	0.98 rich	modified stoichiometric
NO	0.1000	0.1000	0.1000	0.1000
CO	0.5000	0.7000	0.9000	0.7000
CH ₄	0.0150	0.0225	0.0300	0.0225
C ₃ H ₆	0.0300	0.0450	0.0600	0.0450
C ₃ H ₈	0.0150	0.0225	0.0300	0.0225
CO ₂	15	15	15	15
H ₂	0.1670	0.2330	0.3000	0.2330
O ₂	0.9350	0.7770	0.6090	0.7320
H ₂ O	10	10	10	10
He	balance	balance	balance	balance

was also calculated according to Eq. 2.3 based on the reduction products N₂ and N₂O. Differences between both values should then be attributable to additional NO conversion products such as NH₃.

$$X_i = \left(1 - \frac{[i]}{[i]_0} \right) \quad (2.2)$$

$$X_{\text{NO}} \text{ (formula 2)} = \left(\frac{2[\text{N}_2] + 2[\text{N}_2\text{O}]}{[\text{NO}]_0} \right) \quad (2.3)$$

On the same basis, i. e. assuming that all non-N₂ and non-N₂O converted NO leads to ammonia formation (Eq. 2.4),¹ the N₂ selectivity during NO reduction (S_{N₂}), the S_{N₂O} and the S_{NH₃} were calculated according to Eq. 2.5, 2.6 and 2.7 respectively.

$$[\text{NH}_3]_{\text{estimated}} = [\text{NO}]_0 - ([\text{NO}] + 2 \cdot [\text{N}_2] + 2 \cdot [\text{N}_2\text{O}]) \quad (2.4)$$

$$S_{\text{N}_2} = \frac{[\text{N}_2]}{[\text{N}_2] + [\text{N}_2\text{O}] + 0.5 \cdot [\text{NH}_3]_{\text{estimated}}} \quad (2.5)$$

$$S_{\text{N}_2\text{O}} = \frac{[\text{N}_2\text{O}]}{[\text{N}_2] + [\text{N}_2\text{O}] + 0.5 \cdot [\text{NH}_3]_{\text{estimated}}} \quad (2.6)$$

$$S_{\text{NH}_3} = \frac{[\text{NH}_3]_{\text{estimated}}}{2 \cdot [\text{N}_2] + 2 \cdot [\text{N}_2\text{O}] + [\text{NH}_3]_{\text{estimated}}} \quad (2.7)$$

Additionally, N₂ yield (Y_{N₂}), Y_{N₂O} and Y_{NH₃} were calculated according to Eq. 2.8.

$$Y_i = X_i \cdot S_i \quad (2.8)$$

¹Normally, NO₂ formation should also be taken into account. Since it could not be quantified, however, it was not considered. Since NO conversion mainly occurs under rich i. e. reductive conditions, under which NO₂ formation is less probable, this is nonetheless a good enough approximation.

2.3.2 Experimental setup for catalytic tests

Catalytic measurements were performed with a setup according to the scheme in Fig. 2.6. This setup was equipped with mass flow regulators connected to certified gas mixtures as well as a steam generator combined with a liquid flow meter. This allowed to conduct the tests with a space velocity (Eq. 2.9 with Q_0 standing for the total flow rate, m_{catalyst} for the mass of the catalyst) of $60\,000\text{ ml h}^{-1}\text{ g}^{-1}$ in all conditions.

$$\text{space velocity} = \frac{Q_0}{m_{\text{catalyst}}} \quad [\text{space velocity}] = \left[\frac{\text{ml} \cdot \text{h}^{-1}}{\text{g}} \right] \quad (2.9)$$

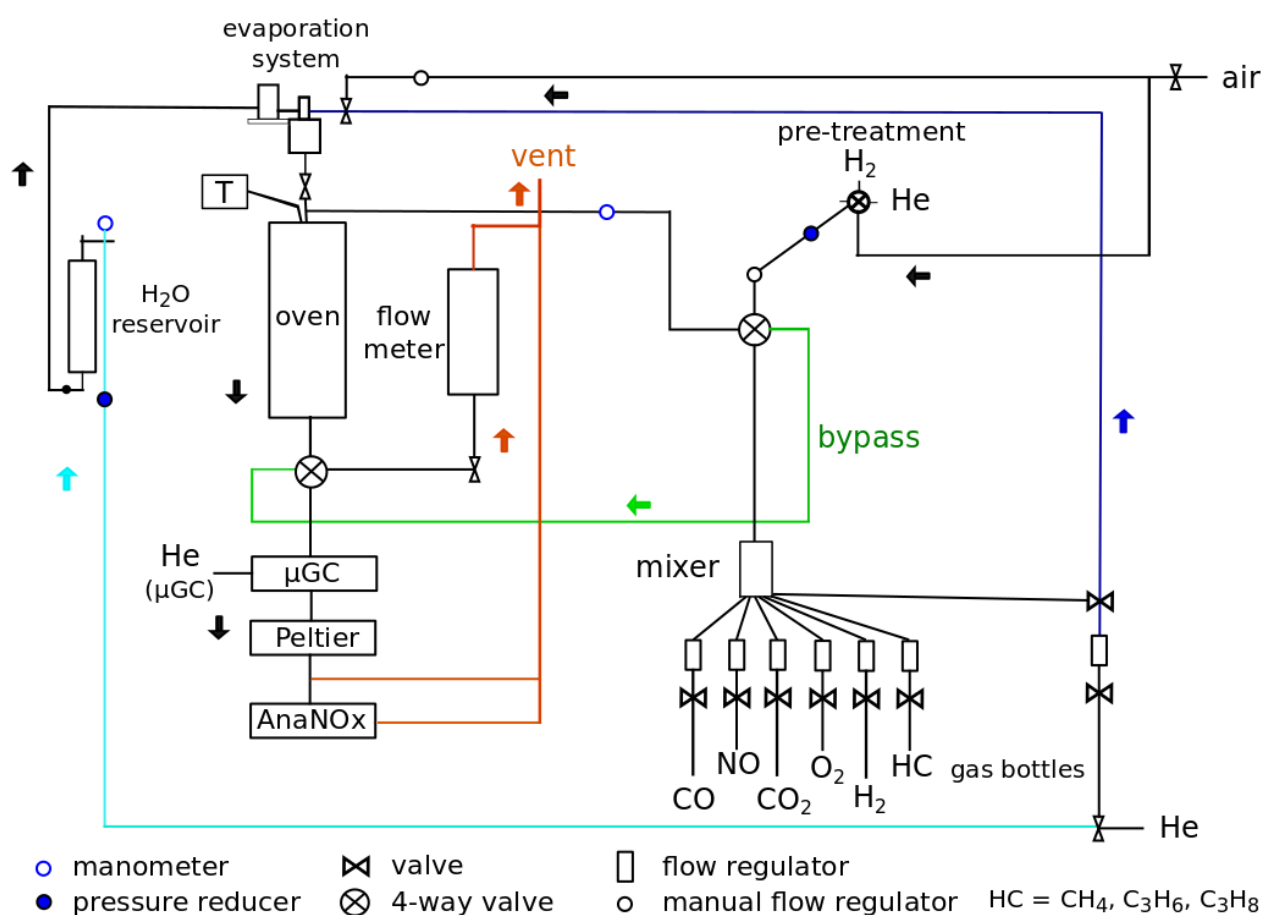


Figure 2.6 – Catalytic test setup scheme. “AnaNO_x” designates the NO_x analyser, “T” the temperature display of the thermocouple.

The quartz fixed bed flow reactor (inner diameter (d) of 18 mm) was heated in an oven. The catalytic bed filter had a porosity of 3.

An NO-NO₂-NO_x analyser (Thermo Scientific Mégatec Model 42*i*-HL) was used in conjunction with a μ GC (Agilent Technologies 490 Micro GC) to monitor the gas phase reactions. All injected gases (H₂, O₂, CO, CH₄, C₃H₆, C₃H₈, CO₂, as well as NO and H₂O²) were detected and separated in the μ GC. Additionally, NO conversion products, N₂ and N₂O, were analysed and quantified. He was used as balance gas in order to be able to analyse N₂. NO was quantified by the NO_x analyser (relying on chemiluminescence). Normally, NO₂ should also

²NO and H₂O could be observed but were not quantified by μ GC.

have been quantified by the same device but this was not working properly. However, if NO_2 has been produced it is considered to have happened only under lean conditions.

2.3.3 Catalytic performance test protocols

NO_x and reductants concentrations were measured in a fixed bed continuous flow reactor during temperature-programmed reactions at a space velocity of $60\,000\text{ ml h}^{-1}\text{ g}^{-1}$ and a total flow rate of 12 l h^{-1} from $110\text{ }^\circ\text{C}$ to $500\text{ }^\circ\text{C}$ ³.

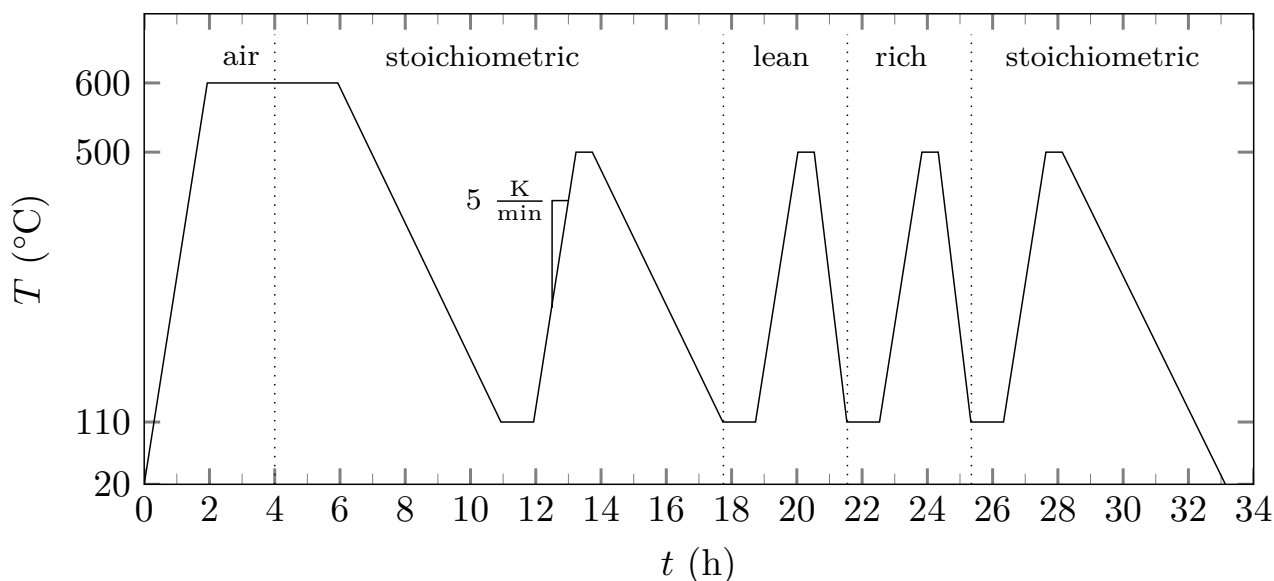


Figure 2.7 – **Procedure A.** Experimental protocol followed for the perovskite catalysts.

For each test, 200 mg of a given sample were sieved in the granulometry of 100-200 μm and mixed with as much inert SiC (210 μm).

All perovskite catalysts were analysed according to the Procedure A as shown in Fig. 2.7. After thermal treatment under air and subsequent activation at $600\text{ }^\circ\text{C}$ under reaction, i. e. stoichiometric, conditions, the catalysts were successively exposed to stoichiometric (also denoted as “stoic1”), lean, and rich conditions and finally to stoichiometric conditions at the end of this sequence to verify the occurrence of deactivation phenomena. This last test run will be denoted hereafter as return test (or “stoic2”).

In contrast to the perovskite catalysts, the commercial reference catalyst was studied according to Procedure B. The only difference being the inversion of the lean and rich test ramps as can be seen in Fig. 2.8. Furthermore, no additional SiC was used in this case since the commercial catalyst consists of a crushed washcoated monolith, i. e. incorporates already enough inert material.

Furthermore, selected catalysts, namely some PGM-doped perovskites were additionally tested according to Procedure C as depicted in Fig. 2.9. This procedure includes a reductive pretreatment during 5 h at $300\text{ }^\circ\text{C}$ instead of the thermal treatment under air followed by an activation under stoichiometric feed at $600\text{ }^\circ\text{C}$. Procedure C also forms the basis of the Procedure D which differs only in the use of the modified stoichiometric feed stream instead of the generally employed stoichiometric one (Table 2.2).

³During the first tests, the rich composition was conducted at the maximum GHSV of $57\,400\text{ h}^{-1}$.

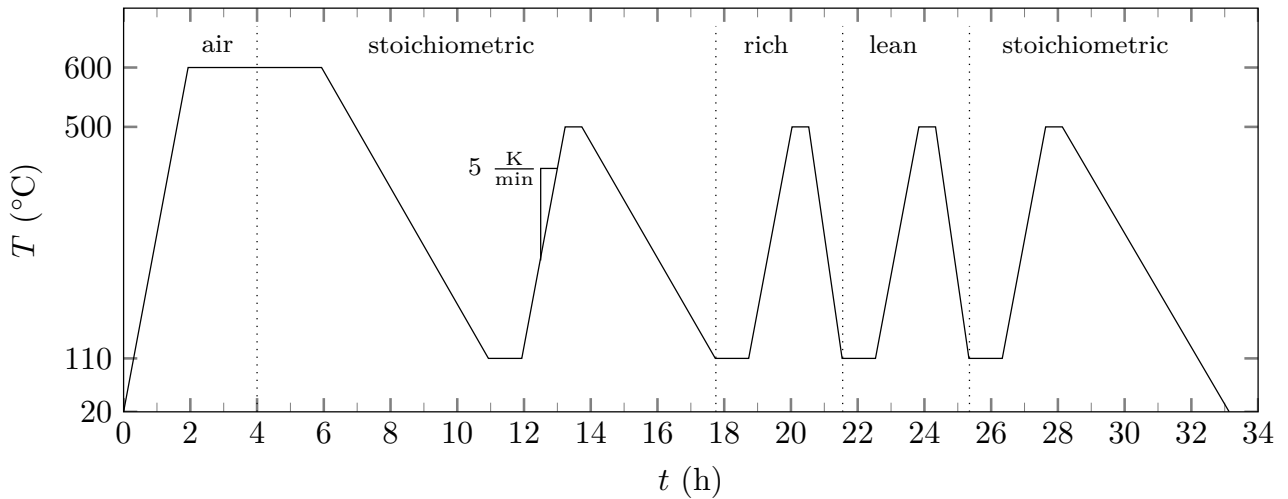


Figure 2.8 – **Procedure B**. Experimental protocol followed for the commercial reference catalyst.

2.3.4 Estimation of reaction rates and Arrhenius parameters of perovskites

In order to calculate the reaction rates and to determine Arrhenius parameters of perovskites, rate constants (k) were calculated from Eq. 2.10 with Q_0 standing for the total flow rate, m_{catalyst} for the mass of the catalyst and X_i for the conversion of the gas of interest.

$$k(T) = \frac{Q_0}{m_{\text{catalyst}}} \cdot \ln\left(\frac{1}{1 - X_i(T)}\right) \quad (2.10)$$

This equation is established for a plug flow reactor and assumed a 1st order kinetic reaction as reported by Hueso et al. for LaCoO_3 ^[17] on the basis of kinetic works of Tascón et al.^[18] or as reported by Parravano for $\text{La}_{0.55}\text{Sr}_{0.35}\text{MnO}_3$.^[19]

The specific reaction rates (r_{specific}) were calculated according to Eq. 2.11 where $F_{i, \text{inlet}}$ stands for the molar flow rate of the gas i at the inlet of the reactor.

$$r_{\text{specific}}(T) = k(T) \cdot \frac{F_{i, \text{inlet}}(1 - X_i(T))}{Q_0} \quad [r_{\text{specific}}] = \left[\frac{\text{mol}}{\text{s} \cdot \text{g}} \right] \quad (2.11)$$

Intrinsic reaction rates ($r_{\text{intrinsic}}$) were calculated according to Eq. 2.12 by dividing the specific reaction rate by the specific surface area of the catalyst (SSA).

$$r_{\text{intrinsic}}(T) = \frac{r_{\text{specific}}(T)}{\text{SSA}} \quad [r_{\text{intrinsic}}] = \left[\frac{\text{mol}}{\text{s} \cdot \text{m}^2} \right] \quad (2.12)$$

Arrhenius plots were then established from CO and C_3H_6 conversions respectively which were obtained during temperature-programmed reactions as described earlier. These plots were used to determine apparent activation energies ($E_{A, \text{app}}$) and pre-exponential factors (A) by linear regression according to Eq. 2.13 and 2.14 respectively, with R being the ideal gas constant.

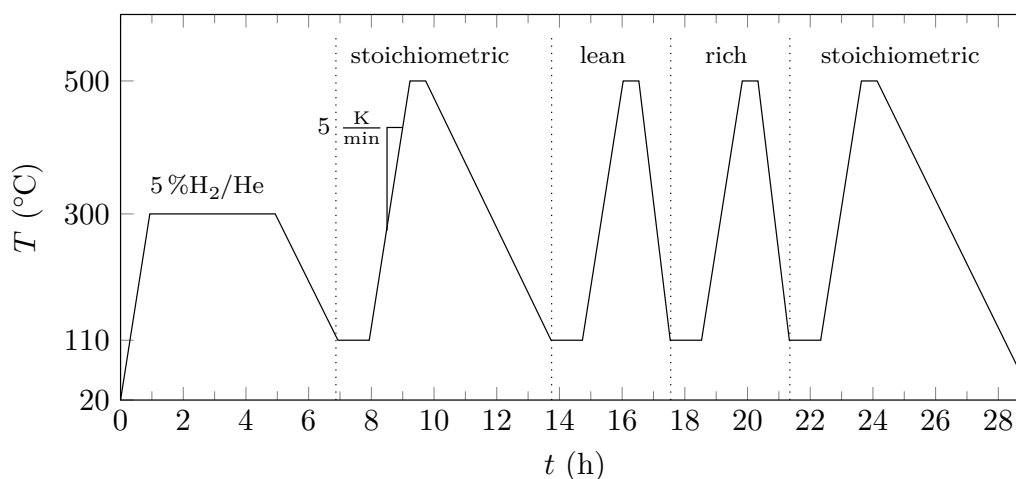


Figure 2.9 – **Procedure C.** Experimental protocol including a reductive pretreatment followed for selected PGM-doped perovskite catalysts. While Procedure C was conducted with the “normal” stoichiometric feed streams, Procedure D follows the same sequence but was performed employing the modified stoichiometric composition.

$$E_{A,app} = -R \cdot \text{slope} \quad \left[E_{A,app} \right] = \left[\frac{\text{kJ}}{\text{mol}} \right] \quad (2.13)$$

$$A = e^{\text{intercept}} \quad [A] = \left[\frac{\text{m}^3}{\text{s} \cdot \text{g}} \right] \quad (2.14)$$

Bibliography

- [1] H. Taguchi, S. Matsu-ura, M. Nagao, T. Choso, K. Tabata, *Journal of Solid State Chemistry* **1997**, *129* (1), 60–65.
- [2] E. Krupicka, A. Reller, A. Weidenkaff, *Crystal Engineering* **2002**, *5* (3-4 SPEC), Crystal Chemistry of Functional Materials II, Proceedings of Symposium L, E-MRS, 195–202.
- [3] Y. Wang, J. Ren, Y. Wang, F. Zhang, X. Liu, Y. Guo, G. Lu, *Journal of Physical Chemistry C* **2008**, *112* (39), 15293–15298.
- [4] A. Zaki, J. Xu, G. Stoclet, S. Casale, J.-P. Dacquin, P. Granger, *Microporous and Mesoporous Materials* **2015**, *208*, 140–151.
- [5] K. S. W. Sing, *Pure and Applied Chemistry* **1985**, *57*, DOI 10.1351/pac198557040603.
- [6] J. Rouquerol, D. Avnir, C. W. Fairbridge, D. H. Everett, J. M. Haynes, N. Pernicone, J. D. F. Ramsay, K. S. W. Sing, K. K. Unger, *Pure and Applied Chemistry* **1994**, *66*, DOI 10.1351/pac199466081739.
- [7] J. Rodríguez-Carjaval, *Physica B* **1993**, *1-2*, 55–69.
- [8] J. Rodríguez-Carjaval, Recent Developments of the Program FULLPROF, in Commission on Powder Diffraction (IUCr), **2001**, Newsletter 26, 12-19.
- [9] Institut Laue-Langevin, Full Prof reference, **2015**, <http://www.ill.eu/sites/fullprof/php/reference.html>.
- [10] J. F. Béar, P. Lelann, *Journal of Applied Crystallography* **1991**, *24*, 1–5.
- [11] J. F. Béar, *Accounts in Powder Diffraction II*, NIST Sp. Pub. 846 **1992**, 63.
- [12] J. Andreasson, J. Holmlund, R. Rauer, M. Käll, L. Börjesson, C. Knee, A. Eriksson, S.-G. Eriksson, M. Rübhausen, R. Chaudhury, *Physical Review B* **2008**, *78*, DOI 10.1103/physrevb.78.235103.
- [13] D. A. Shirley, *Physical Review B: Condensed matter and materials physics* **1972**, 4709.
- [14] M. C. Biesinger, B. R. Hart, R. Polack, B. A. Kobe, R. S. Smart, *Minerals Engineering* **2007**, *20*, 152–162.
- [15] M. C. Biesinger, B. P. Payne, L. W. M. Lau, A. Gerson, R. S. C. Smart, *Surface and Interface Analysis* **2009**, *41*, 324–332.
- [16] E. S. J. Lox in *Handbook of Heterogeneous Catalysis*, (Eds.: G. Ertl, H. Knözinger, F. Schüth, J. Weitkamp), Wiley-VCH Verlag GmbH & Co. KGaA, **2008**, Chapter Part 11. Environmental Catalysis – 11.2 Automotive Exhaust Treatment.
- [17] J. Hueso, D. Martínez-Martínez, A. Caballero, A. González-Elipe, B. Mun, M. Salmerón, *Catalysis Communications* **2009**, *10*, 1898–1902.
- [18] J. M. D. Tascón, J. L. G. Fierro, L. G. Tejuca, *Zeitschrift für Physikalische Chemie* **1981**, *124*, 249–257.
- [19] G. Parravano, *Journal of the American Chemical Society* **1953**, *75*, 1497–1498.

Reference perovskite catalysts LaBO_3 ($\text{B} = \text{Mn}, \text{Fe}$) and La_2CuO_4 and commercial reference 3-way catalyst

Reference catalysts were studied for later comparison. The choice of the starting perovskite system is elucidated by comparing physico-chemical properties and catalytic activities of cheaper transition metal based perovskites and the derived Ruddlesden-Popper phase (La_2CuO_4).

Perovskites, LaBO_3 , were already discussed as an alternative to conventional 3-way catalysts in Section 1.2. Due to the tolerance of the structure to accommodate various cations, different transition metals are possible candidates in the B position. Some catalytically interesting candidates as Ni and Co were excluded due to the toxicity of the final solid or their precursors.^[1,2] Mn, Fe and Cu were selected. The ABO_3 structure cannot be obtained for Cu due to electroneutrality limitations previously discussed in Section 1.2, Cu forming generally mono- or divalent cations. Therefore, the derived Ruddlesden-Popper phase (RP) with A_2BO_4 structure was compared to LaMnO_3 and LaFeO_3 .

Furthermore, the catalytic performances of a commercial reference catalyst containing platinum group metals (PGM) and promoters are shown and discussed to allow for comparison.

3.1 Bulk/Structural properties

3.1.1 Chemical composition in the bulk

The bulk composition was verified for the LaFeO_3 sample only. Elementary analysis yielded a bulk composition of $\text{La}_{1.01}\text{FeO}_{3+\delta}$ confirming the atomic ratio between La and Fe of the nominal composition. It is assumed that the same holds true for the Mn- and Cu-containing mixed oxides.

3.1.2 XRD

The crystalline structures of the calcined LaBO_3 ($\text{B} = \text{Fe}, \text{Mn}$) solids correspond to the orthorhombic and the rhombohedral perovskite structure (LaFeO_3 and LaMnO_3 respectively), as well as the one of the calcined La_2CuO_4 sample to the orthorhombic RP structure as shown

in Fig. 3.1. LaMnO_3 seems to be well-crystallized in spite of the relatively low calcination temperature of 600°C . Additional peaks with low intensity are only observed in the RP diffractogram at 23° , 46° , and 69° . They cannot be attributed to lanthanum dioxycarbonate, lanthanum carbonate hydroxide, LaOH_3 , $\text{La}_2\text{Cu}_2\text{O}_5$ nor the corresponding Cu or La single oxides. The peak at 69° has been reported before but was not attributed either.^[3]

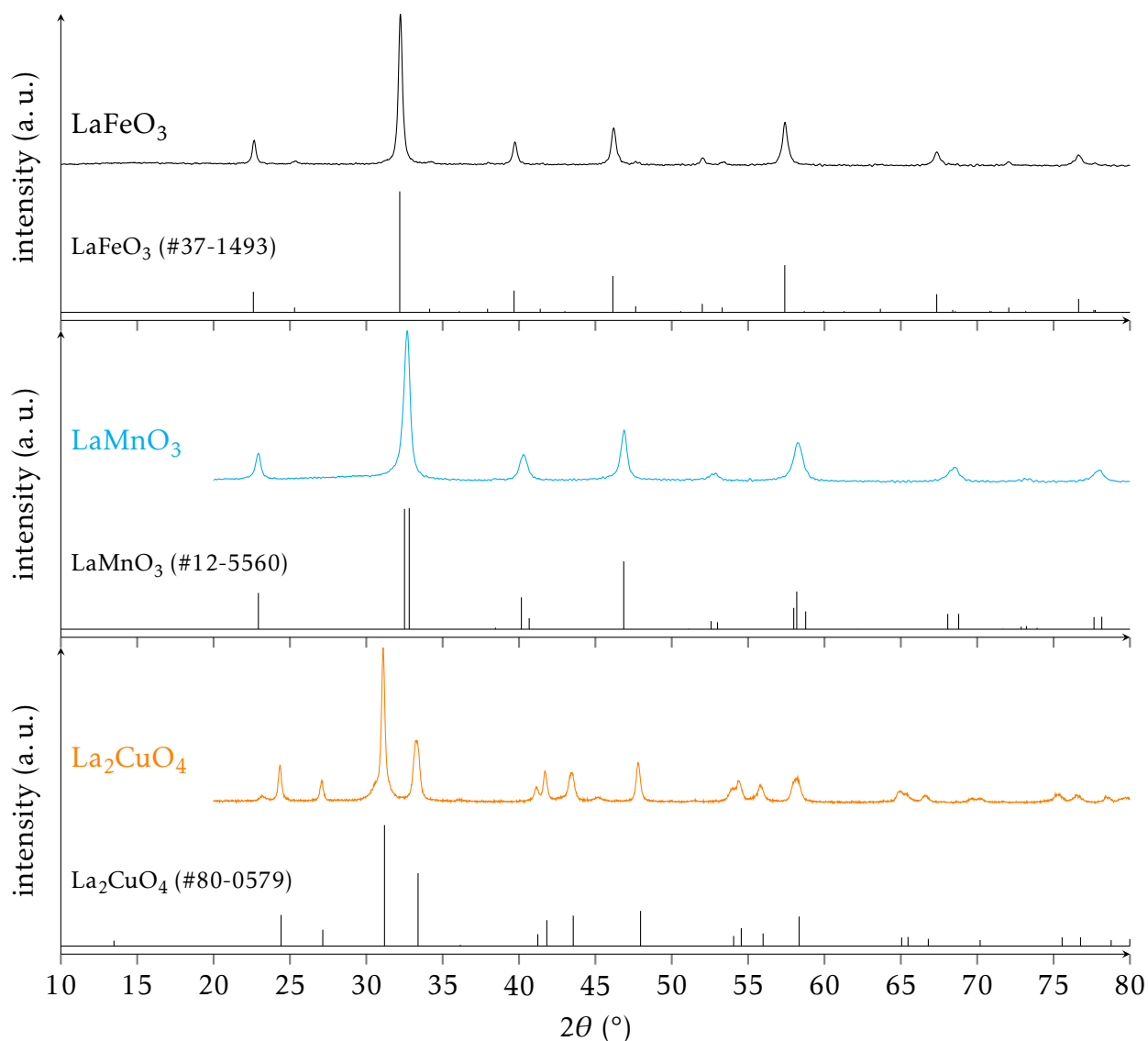


Figure 3.1 – X-ray diffractograms of calcined LaBO_3 ($B = \text{Fe, Mn}$; CCM) and La_2CuO_4 (CCM).

Apparent crystallite sizes and unit cell parameters estimated by full pattern matching are reported in Table 3.1. Lowest crystallite sizes of 14 nm were obtained for LaMnO_3 which is in accordance with the highest specific surface area (Table 3.4).

The unit cell parameters of the calcined catalysts correspond to those of the references for LaFeO_3 and La_2CuO_4 . Only very slight distortions are apparent for the La_2CuO_4 sample compared to the reference (#80-0579). However, the Mn-based perovskite solid seems to present an oxygen excess. Its unit cell parameter a of 5.48 \AA is closer to the reference #78-5235 ($\text{LaMnO}_{3.31}$, $a = 5.48830 \text{ \AA}$) than to #12-5560 (LaMnO_3 , $a = 5.50500 \text{ \AA}$). This oxygen excess has to be compensated by a low fraction of Mn^{4+} to allow for charge neutrality. The

Table 3.1 – Comparison of crystallite sizes, unit cell parameters and volumes derived from full pattern matching of LaBO_3 ($B = \text{Fe}, \text{Mn}$) and La_2CuO_4 (CCM).

		d_{cryst} (nm)	a (Å)	b (Å)	c (Å)	$V_{\text{unit cell}}$ (Å ³)
LaFeO_3	calcined	20.1 ± 0.1	5.561	7.858	5.558	242.85 ± 0.17
LaMnO_3	calcined	14.3 ± 0.1	5.484	5.484	13.369	348.18 ± 0.28
La_2CuO_4	calcined	22.1 ± 0.1	5.376	5.379	13.161	380.63 ± 0.18
References (PDF)						
LaFeO_3	(#37-1493)		5.567	7.855	5.553	242.75
LaMnO_3	(#12-5560)		5.505	5.505	13.301	349.08
$\text{LaMnO}_{3.31}$	(#78-5235)		5.488	5.488	13.311	347.23
La_2CuO_4	(#80-0579)		5.359	5.363	13.127	377.27

presence of this tetravalent Mn species has been reported before for LaMnO_3 .^[4]

3.1.3 Raman spectroscopy

Raman spectroscopy was performed to confirm the purity of the LaFeO_3 perovskite solid since this complementary technique allows to detect amorphous or finely dispersed compounds which are not detectable by XRD.

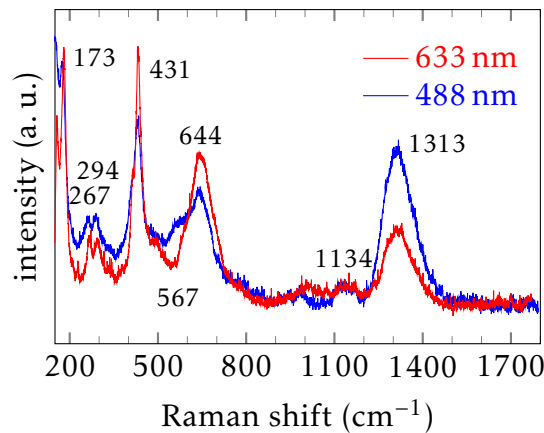


Figure 3.2 – Raman spectra of LaFeO_3 . The powder was excited with $\lambda_{\text{exc}} = 488$ nm (blue) and 632 nm (red) respectively.

Fig. 3.2 shows the Raman spectra of LaFeO_3 recorded on a microdispersive Raman spectrometer using a blue (488 nm) and a red excitation laser (632 nm) respectively. The strongest lines are observed at 173 cm^{-1} , 431 cm^{-1} , 644 cm^{-1} , and 1313 cm^{-1} . The first ones can be assigned to an A-site A_g mode, an oxygen bending B_{1g} mode, and an oxygen stretch mode (B_{1g}) of the lanthanum ferrite respectively.^[5-9] The last (1313 cm^{-1}) was attributed to either a 2-phonon scattering phenomenon or an oxygen stretching vibration before.^[5-9] Furthermore, weak to medium lines were seen at 267 cm^{-1} , 294 cm^{-1} which were formerly assigned to oxygen tilt B_{1g} and A_g modes.

Additionally, a shoulder at 567 cm^{-1} and a weak line at 1134 cm^{-1} are observed. While the latter is presumably a 2nd harmonic of the former, the assignment of this one is not straight-

forward. However, it does not correspond to any reported $\alpha\text{-Fe}_2\text{O}_3$ or Fe_3O_4 lines.^[10,11] It may be assigned to lanthanum hydroxides for which a line at 582 cm^{-1} was observed before.^[12]

In conclusion, the characteristic LaFeO_3 perovskite lines were observed and no significant impurities were detected.

3.2 Thermal stability and reducibility

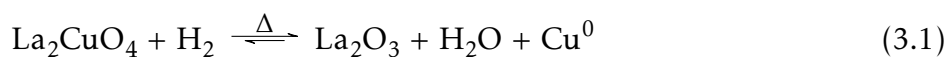
3.2.1 High Temperature XRD (HTXRD) analyses

In situ HTXRD analyses were performed on calcined LaFeO_3 and La_2CuO_4 catalysts prepared by CCM to determine their stability under reductive atmosphere. The analyses were performed in 6 consecutive steps corresponding to a reductive followed by a humid oxidative thermal treatment (See steps in scheme in Fig. 2.5.).

As can be seen in Fig. 3.3 and 3.4, the LaFeO_3 structure is retained during the whole procedure including the heating ramp under reductive atmosphere. Only slight shifts to lower angles are observed which can be attributed to thermal dilatation.

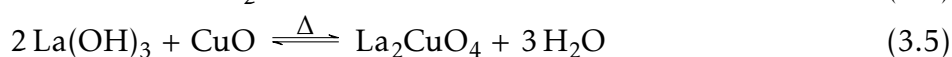
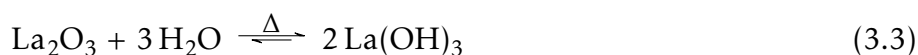
The atomic compositions at the surface of the LaFeO_3 solid after HTXRD analysis were determined by XPS. Results are discussed in Section 3.4.2. The results of full pattern matching performed on the last scan of the procedure are discussed together with the one of the La_2CuO_4 sample.

In contrast to the stability of LaFeO_3 , La_2CuO_4 starts to decompose between 250 and 300 °C under reductive atmosphere, see Fig. 3.5. The reduction ultimately leads to the formation of $\text{La}_2\text{O}_2\text{CO}_3$ and metallic Cu particles via a 2-step process according to the following sequence (Eq. 3.1 and Eq. 3.2).



Low amounts of Cu^0 are detected at $T \geq 250\text{ °C}$. However, no crystalline CuO or Cu_2O phases as possible intermediate phases in the overall reduction process were detected.

The results of the second part of the HTXRD procedure are shown in Fig. 3.6. A full recovery of the RP is observed under humid air and heating up to 600 °C. At this temperature, only dilatation effects cause deviations from the reference (as usual measured at rt) by shifts to lower diffraction angles. This recovery of the La_2CuO_4 structure is in agreement with literature according to which perovskites can be reversibly reduced and oxidised.^[13] The reconstruction of the La_2CuO_4 phase can be achieved following consecutive steps. At first, surface hydroxylation takes place leading to the formation of $\text{La}(\text{OH})_3$ (Eq. 3.3). Then a mix of low amounts of different compounds including La_2O_3 and $\text{La}_2\text{O}_2\text{CO}_3$ is observed between 350 °C and 500 °C. Finally from 550 °C onwards the RP is clearly discernible. One possible pathway could be the combination of Eq. 3.3, 3.4 and 3.5.



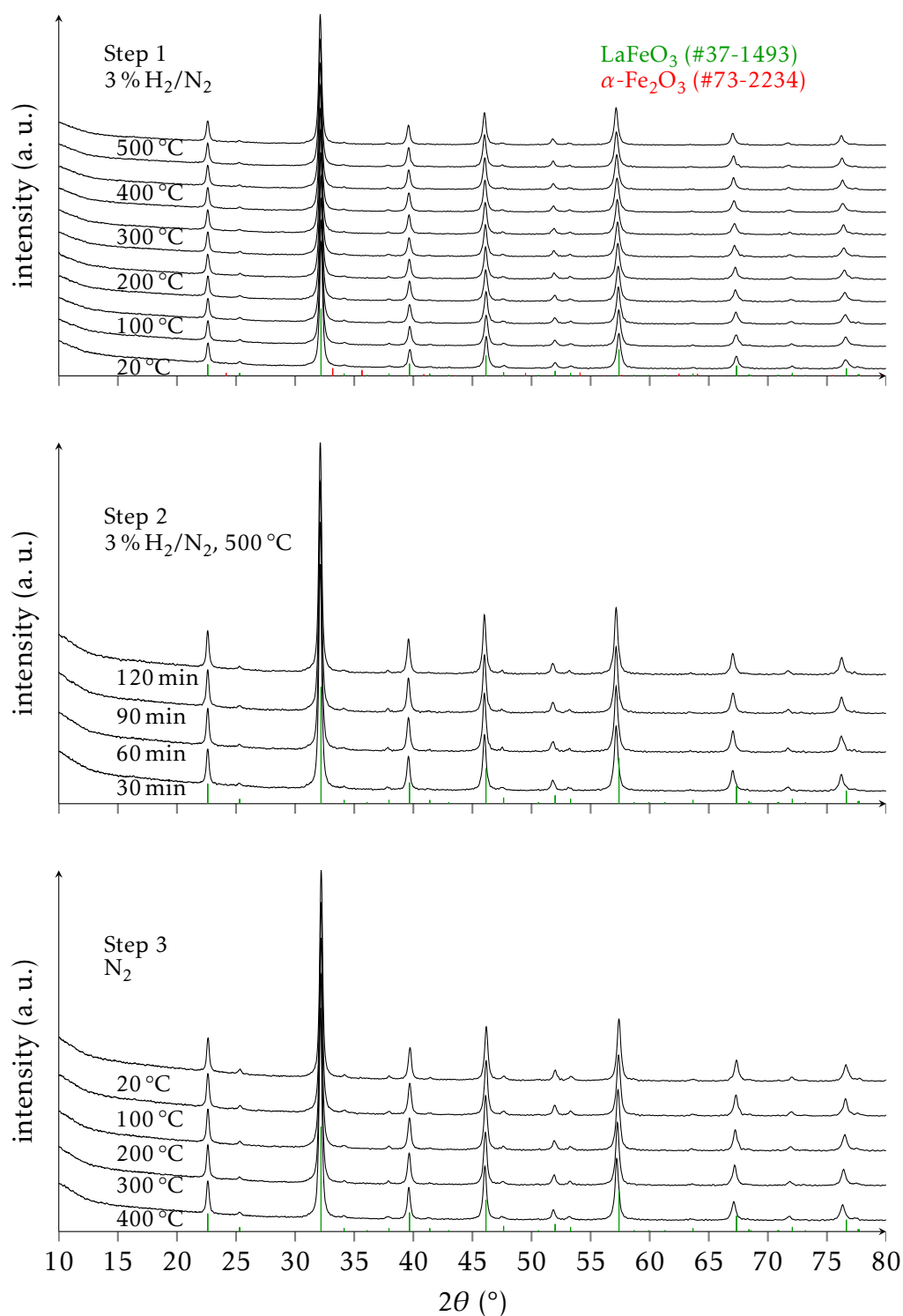


Figure 3.3 – High Temperature X-ray diffractograms of LaFeO_3 prepared by the conventional citrate method (CCM). Step 1 corresponds to a heating ramp under reductive atmosphere (3 Vol.% H_2/N_2), Step 2 to the corresponding plateau and Step 3 to the subsequent cooling under inert atmosphere. Scheme in Fig. 2.5.

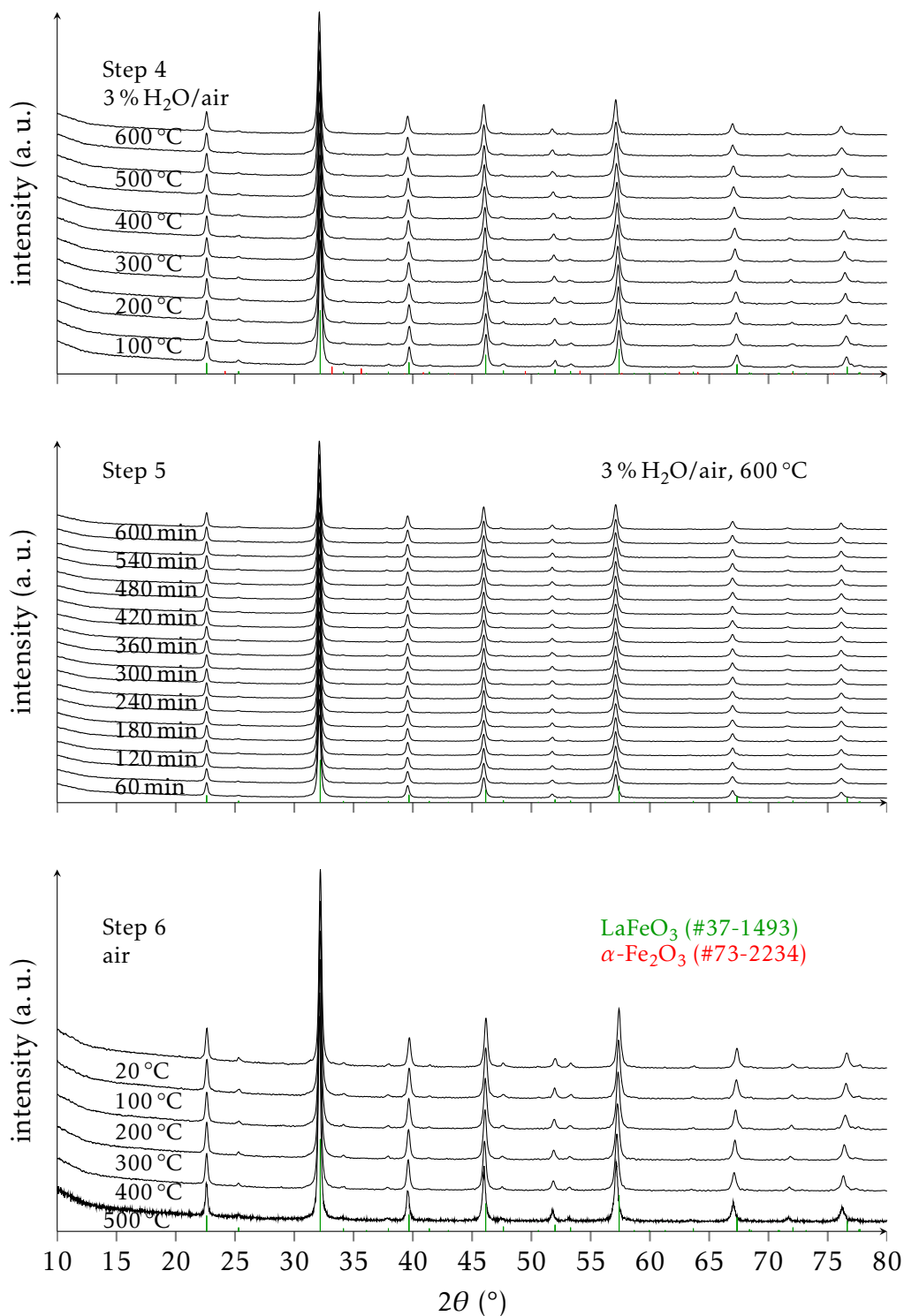


Figure 3.4 – High Temperature X-ray diffractograms of LaFeO_3 prepared by the conventional citrate method (CCM). Step 4 corresponds to a heating ramp under humid air flow up to 600 °C, Step 5 to the corresponding plateau and Step 6 to the subsequent cooling under dry air flow. Scheme in Fig. 2.5.

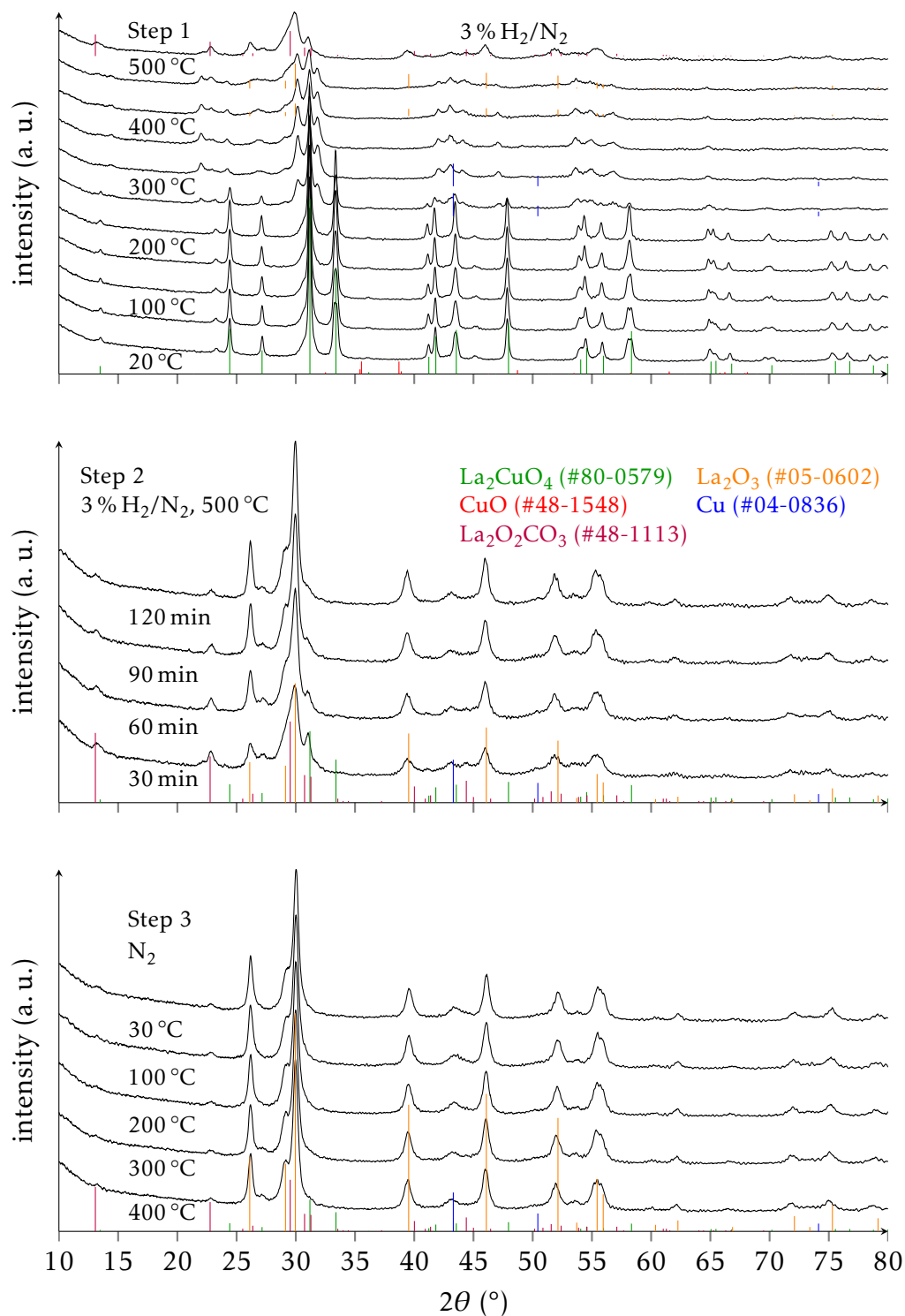


Figure 3.5 – High Temperature X-ray diffractograms of La_2CuO_4 (CCM). Step 1 corresponds to a heating ramp under reductive atmosphere (3 Vol.% H_2/N_2), Step 2 to the corresponding plateau and Step 3 to the subsequent cooling under inert atmosphere. Scheme in Fig. 2.5.

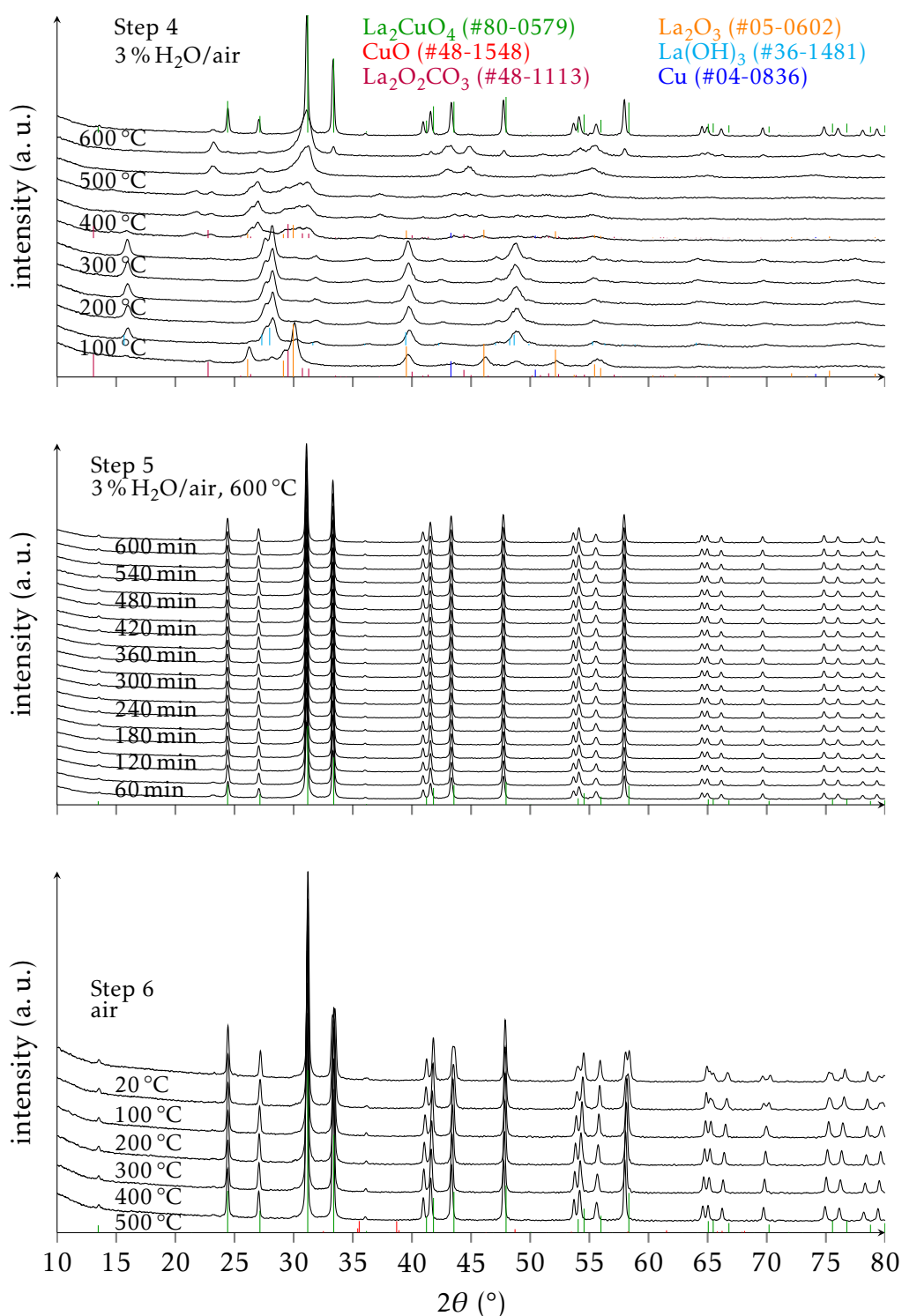


Figure 3.6 – High Temperature X-ray diffractograms of La_2CuO_4 (CCM). Step 4 corresponds to a heating ramp under humid air flow up to 600 $^\circ\text{C}$, Step 5 to the corresponding plateau and Step 6 to the subsequent cooling under dry air flow. Scheme in Fig. 2.5.

After attaining the maximum temperature of 600 °C, while the solid is held under the same conditions for 10 h no major change occurs anymore apart from decreasing La₂O₂CO₃ content (visible by the decrease in intensity of the diffraction peak at approximately 23°). The cooling under dry air does not lead to the detection of any additional crystalline phases but to broader peaks especially at high 2θ, i. e. the formation of smaller crystallites.

As for the LaFeO₃ solid, atomic compositions at the surface of the La₂CuO₄ sample after HTXRD analysis were determined by XPS. Results are likewise discussed in Section 3.4.2.

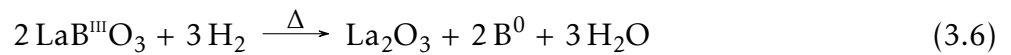
Table 3.2 – Comparison of crystallite sizes, unit cell parameters and volumes derived from full pattern matching of LaFeO₃ and La₂CuO₄ (CCM).

		d_{cryst} (nm)	a (Å)	b (Å)	c (Å)	$V_{\text{unit cell}}$ (Å ³)
LaFeO ₃	calcined	20.1 ± 0.1	5.561	7.858	5.558	242.85 ± 0.17
LaFeO ₃	post-HTXRD	26.1 ± 0.1	5.564	7.850	5.556	242.67 ± 0.14
La ₂ CuO ₄	calcined	22.1 ± 0.1	5.376	5.379	13.161	380.63 ± 0.18
La ₂ CuO ₄	post-HTXRD	43.1 ± 0.1	5.359	5.398	13.155	380.54 ± 0.04

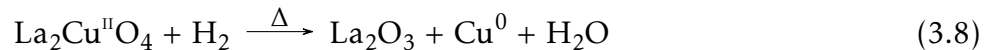
The last diffractograms recorded for LaFeO₃ and La₂CuO₄ after the cooling of step 6 were exploited by using full pattern matching. As shown in Table 3.2, the unit cell parameters still correspond to those obtained for the calcined samples emphasizing the bulk reconstruction of the RP taking place on the in situ reduced sample during the thermal oxidation treatment and the stability of the LaFeO₃ sample. The crystallite sizes for the LaFeO₃ solid are only slightly higher whereas they are much increased for the La₂CuO₄ sample.

3.2.2 H₂-TPR

Full reduction of the B-site cations in the dominant valency of the bulk solid (trivalent Fe and Mn, divalent Cu) is achieved according to the Eq. 3.6 and 3.8 for LaFeO₃, LaMnO₃ and La₂CuO₄ respectively. Based on these equations, the theoretical maximum atomic H/M ratio can be determined considering a complete reduction to the metallic state, equalling 3 for the perovskites (for trivalent B cations) and 2 for the RP phase (Eq. 3.7 and 3.9).



$$(\text{H}/\text{M})_{\text{max}} = (\text{H}/\text{B})_{\text{max}} = (\text{H}/\text{Fe})_{\text{max}} = (\text{H}/\text{Mn})_{\text{max}} = 3 \quad (3.7)$$



$$(\text{H}/\text{M})_{\text{max}} = (\text{H}/\text{Cu})_{\text{max}} = 2 \quad (3.9)$$

The experimental results of H₂-TPR are shown in Fig. 3.7 and Table 3.3.

As was already reported in different studies, the Fe³⁺ in the perovskite is nearly not reducible at temperatures below 700 °C.^[6,13,14] Above this temperature, a weak reduction process with $T_{\text{max}} > 1000$ °C is discernible. This stability toward reducing atmosphere is in agreement with the HTXRD measurements discussed before.

For the The LaMnO₃ solid, the value of the total H/Mn ratio of 1.30 (Table 3.3), much below the theoretical one of 3, is in agreement with an incomplete reduction not proceeding further than Mn²⁺. This lowering of the oxidation state creates a reverse charge imbalance

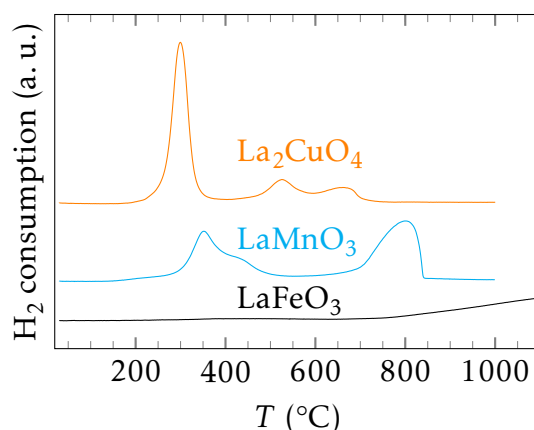


Figure 3.7 – H_2 absorption profiles of calcined LaFeO_3 (50 mg, 50 ml min^{-1} ; CCM), LaMnO_3 and La_2CuO_4 (both 100 mg, 25 ml min^{-1} ; CCM).

compared to the oxygen excess in the starting material. However, the generation of oxygen vacancies can compensate for the Mn^{2+} . This compensation should allow a certain stability of the structure while offering increased reducibility compared to LaFeO_3 . Furthermore, Mn in the LaMnO_3 solid seems to be present in more than the trivalent form in agreement with the results of XRD, i. e. the difference in unit cell parameters derived from full pattern matching to the stoichiometric reference of the structure discussed earlier (Section 3.1). According to Lisi et al.^[15,16] the reduction peaks at low temperature (350 to 420 °C) correspond to the reduction of the Mn^{4+} fraction in the perovskites to Mn^{3+} . The high temperature peak (801 °C) on the other hand is attributed to the reduction of Mn^{3+} to Mn^{2+} . The H_2 consumption corresponding to the 1st and 2nd peak ($\text{H}/\text{Mn} = 0.61$) would correspond to about 60 at.% Mn^{4+} of all Mn in the LaMnO_3 sample. This would furthermore imply that 30 % of trivalent Mn would remain at temperatures above 850 °C.

Table 3.3 – H_2 -TPR results of LaFeO_3 (50 mg, 50 ml min^{-1} ; CCM), LaMnO_3 and La_2CuO_4 (both 100 mg, 25 ml min^{-1} ; CCM).

nominal composition	H_2 consumption ^a (mmol g^{-1})		H/B		T_{max} reduction peaks		
	total	1 st peak	total ^a	1 st peak	(°C)	(°C)	(°C)
LaFeO_3	-	-	-	-	-	-	> 1100
LaMnO_3	2.69	1.26 ^b	1.30	0.61 ^b	351	420	801
La_2CuO_4	2.51	1.81	2.03	1.46	300	525	667

^a H_2 consumption was only integrated for entirely recorded peaks.

^b 1st and 2nd peak were integrated together.

The in situ HTXRD analyses of La_2CuO_4 and its high intensity reduction peak at low temperature during H_2 -TPR confirm the expectation of a higher reducibility of the cuprate compared to the LaMnO_3 and LaFeO_3 perovskites. As reported in Table 3.3, the La_2CuO_4 sample presents a total H/Cu ratio of 2.03. This value is in agreement with a complete reduction of the Cu^{2+} cations. As shown before, the reduction peak at 300 °C can be attributed to the decomposition of the RP via the reduction of Cu^{2+} to Cu^0 accompanied by the formation of mainly La_2O_3 (Eq. 3.1). The 1st reduction peak accounts for an H/Cu ratio of 1.46.

According to Anderson et al.^[17] for bulk CuO, the Cu reduction in the temperature range up to 350 °C takes place in 2 steps via the formation of Cu₂O, and the reduction of Cu²⁺ is delayed until all Cu²⁺ is reduced to Cu⁺. The overlap of both reduction peaks may explain the slight asymmetry and the broadness of the 1st observed reduction peak. The 2 additional peaks at higher temperatures should be attributed to the completion of the reduction of remaining low amounts of perhaps less accessible Cu⁺ species.

3.3 Textural properties

As shown in Fig. 3.8, the isotherms of all reference perovskites are composites of type II and type IV corresponding to macroporous solids with some mesoporous contribution. However, the by far broadest hysteresis is seen for LaMnO₃ (Fig. 3.8A). This is confirmed by the pore size distributions displayed in Fig. 3.8B. For LaMnO₃ a strong contribution of low-sized mesopores is observed, whereas LaFeO₃ only shows a low one and none is observed for La₂CuO₄. Concerning the macropores, La₂CuO₄ shows a predominance of higher diameter pores compared to LaFeO₃ and LaMnO₃. The LaMnO₃ solid generally contains lower diameter pores than the other investigated samples.

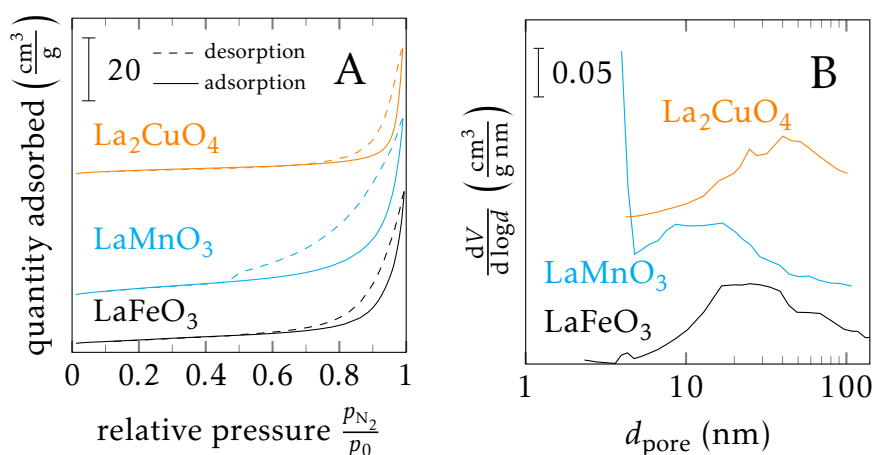


Figure 3.8 – Isotherms (A) and pore size distributions (B) of calcined LaFeO₃, LaMnO₃ and La₂CuO₄ prepared by CCM.

Furthermore, as can be seen in Table 3.4, the specific surface area of 21.9 m² g⁻¹ of LaMnO₃ is significantly higher than for La₂CuO₄ and LaFeO₃ with 12 to 14 m² g⁻¹. The pore volume is lower than 0.1 cm³ g⁻¹ for LaFeO₃ and La₂CuO₄, and little higher for LaMnO₃. These results are in agreement with earlier investigations of simple perovskites.^[16,18,19]

Table 3.4 – Comparison of specific surface area (SSA) and cumulative pore volume (V_{pore}) of LaBO₃ (B = Fe, Mn) and La₂CuO₄ (CCM).

composition	SSA (m ² g ⁻¹)	V_{pore} (cm ³ g ⁻¹)
LaFeO ₃	13.9	0.08
LaMnO ₃	21.9	0.11
La ₂ CuO ₄	12.2	0.07

Overall, the perovskite catalysts prepared by CCM present higher specific surface areas than those obtained by solid state reaction even though considerably lower ones than alumina which is generally used as support for TWC. The perovskites' morphology consists of aggregated particles. The porosity of the solids purely resides on the holes between loose aggregates as can be seen by scanning electron microscopy (SEM) (Fig. 4.5 in Chapter 4).

3.4 Chemical composition at the surface

3.4.1 XPS analyses of the calcined samples

The chemical composition of the surface was investigated by XPS. Table 3.5 lists the binding energy maxima of the photoelectron peaks. The corresponding XP spectra for as-synthesized catalysts are shown in Fig. 3.9.

The La 3d photopeak shows the characteristic multiplet splitting giving rise to 4 photopeaks. However, differences are observed concerning the positions as well as the shape of these multiplet components. For La_2CuO_4 , an additional shoulder appears in the lower binding energy (B. E.) range.

Different shapes of the La 3d photopeak are caused by varying amounts of non-perovskite La species at the surface of the solid. Indeed, lanthanum atoms in species such as La_2O_3 or lanthanum carbonates are in a different chemical environment. The presence of such additional La species leads to a superposition of the photopeaks attributable to the perovskite and other La species and thereby causes a varying multiplet splitting energy difference (ΔE_{split}). This phenomenon can be exploited to determine the presence of different La species.^[20] In this respect, it can be shown that La_2O_3 is not a predominant species at the catalysts' surfaces. Its characteristic ΔE_{split} is expected to be 4.6 eV,^[20] whereas the values for LaFeO_3 and LaMnO_3 solids ($\Delta E_{\text{split}} = 3.8$ eV and 3.7 eV respectively) are close to the 3.9 eV observed for $\text{La}(\text{OH})_3$. This contribution is nonetheless due to surface species only, i. e. low amounts compared to the bulk perovskite, formed by exposure to ambient atmosphere explaining why it is not observed by XRD (Fig. 3.1).

La_2CuO_4 's major splitting energy difference of the La 3d multiplet of 3.5 eV is equal to the carbonate's ($\Delta E_{\text{split}}(\text{La}_2(\text{CO}_3)_3) = 3.5$ eV). The fact that a higher intensity of the component at higher binding energy (B. E.) of La 3d_{5/2} is observed is in agreement with the presence of high amounts of carbonate species. Furthermore, the shoulder discerned at lower B. E. of the La 3d photopeak of the La_2CuO_4 solid (Fig. 3.9) could be assigned to $\text{La}_2(\text{CO}_3)_3$ (834.8 eV).^[20]

The presence of such hydroxides and carbonates on perovskites and cuprates has been described before.^[3,21] It can be explained by the high basicity of the compounds, e. g. strongly adsorbing CO_2 forming carbonates with surface La cations on La_2CuO_4 .^[17]

Table 3.5 – Photopeak maxima of calcined LaBO_3 ($B = \text{Fe, Mn}$; CCM) and La_2CuO_4 (CCM), and corresponding post-HTXRD samples.

B. E. (eV)	La 3d _{5/2}	Fe 2p _{3/2}	Mn 2p _{3/2}	Mn 3s	Cu 2p _{3/2}	O 1s
LaFeO_3	834.3	710.8	-	-	-	529.5
LaMnO_3	834.0	-	642.2	84.0	-	529.7
La_2CuO_4	834.9	-	-	-	933.0	531.6

LaFeO_3 shows the characteristic multiplet splitting and satellites for the Fe 2p photopeak.

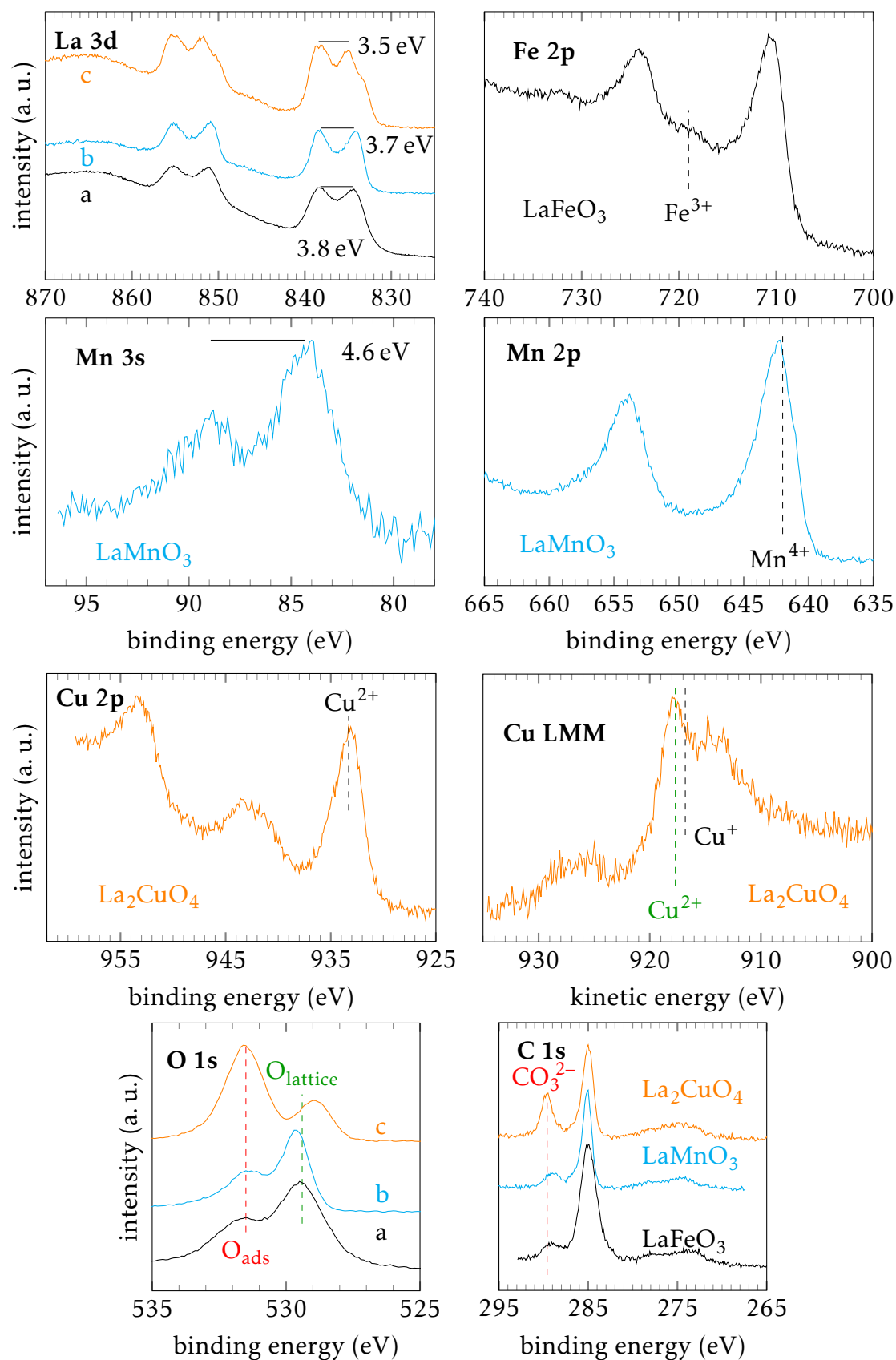


Figure 3.9 – La 3d , Fe 2p , Mn 2p , Cu 2p , O 1s and C 1s photopeaks of calcined LaFeO_3 , LaMnO_3 and La_2CuO_4 solids (CCM). LaFeO_3 (a), LaMnO_3 (b) and La_2CuO_4 (c). LaFeO_3 photopeaks were recorded on a lower resolution and higher intensity XP spectrometer. Their intensities have been divided by 4 (La 3d) or 2 (O 1s , C 1s) in images for better comparison.

The positions of the photopeaks (710.8 eV for Fe 2p_{3/2} and ≈ 719 eV for its satellite) are in agreement with trivalent Fe.^[7,20] Comparing LaFeO₃ and Fe₂O₃, it was reported that this shake-up photopeak is relatively broader and lower in intensity for LaFeO₃ than for Fe₂O₃.^[7,22,23] The O 1s spectrum shows 2 contributions at 529.5 eV (lattice oxygen, O_{lattice}) and at 531.5 eV attributed to adsorbed oxygen containing species (O_{ads}).^[3,20,24]

As for oxygen, the C 1s photopeak also gives evidence of the presence of impurities at the surface of the Fe-based perovskite. The main contribution located at 289.0 eV is ascribed to adventitious carbon contamination. A minor contribution at 289.6 eV corresponding to 13 at.% of the overall signal corresponds to metal carbonate species.^[20,25]

The LaMnO₃ photoelectron spectrum of Mn 3s shows 2 multiplet split components. This splitting is caused by the coupling of non-ionised 3s electrons with 3d valence band electrons.^[26] The splitting energy difference depends on the oxidation state of manganese, i. e. $\Delta E_{\text{split}} = 6.5$ eV is characteristic for Mn²⁺, ≥ 5.5 eV for Mn³⁺ and ≥ 4.5 eV for Mn⁴⁺.^[26] In the case of the studied LaMnO₃ sample, a ΔE_{split} of 4.6 eV is obtained, i. e. surface manganese is predominantly present as Mn⁴⁺ species. From Eq. 3.10, a mean oxidation state of Mn can be estimated.^[27] The calculation for the LaMnO₃ sample yields a value of 3.86 according to Eq. 3.10.

$$\text{mean oxidation degree of Mn} = \frac{7.88 - \Delta E_{\text{split}} (\text{Mn } 3s)}{0.85} \quad (3.10)$$

This average oxidation state is in agreement with the Mn 2p photopeak characteristic of Mn⁴⁺ with a maximum at B. E. = 642.2 eV (Fig. 3.9). Metal oxides with predominant contribution of Mn³⁺ species would exhibit a more symmetric Mn 2p_{3/2} photopeak. For MnO a distinct satellite should appear.^[20] The absence of this satellite confirms the predominance of tetravalent Mn species.

Table 3.6 – Relative abundance of surface species of calcined LaBO₃ (B = Fe, Mn) and La₂CuO₄ (CCM) obtained by spectral decomposition of the corresponding photopeaks.

at.%	Cu ⁺ /Cu _{total}	O _{ads} ^a	C _{CO₃²⁻} ^b
LaFeO ₃	-	45	13
LaMnO ₃	-	53	20
La ₂ CuO ₄	15	75	33

^a O_{ads} + O_{lattice} = 1.

^b C_{CO₃²⁻} + C_{adventitious} = 1.

As for LaFeO₃, lattice oxygen is not the only oxygen species observed at the surface of the LaMnO₃ sample. O_{ads} are present with slightly higher abundance (53 at.%). Furthermore having a look at the C 1s spectrum, as for the LaFeO₃ solid the carbonate photopeak is observed. Its relative intensity is higher than for LaFeO₃, too, as reported in Table 3.6.

Whereas LaFeO₃ and LaMnO₃ show similar features with slight variations only, the cuprate shows significant differences if compared to the former solids. The expected divalence of Cu in La₂CuO₄ is confirmed by the position of the Cu 2p_{3/2} maximum (933.1 eV) which is close to the reported 933.3 eV for Cu²⁺.^[20,28] The presence of a strong Cu 2p_{3/2} shake-up satellite at ≈ 943 eV due to an O→Cu(3d) charge transfer is in agreement with the presence of Cu²⁺.^[3,28–30] This satellite cannot be observed for Cu⁰ or Cu⁺ since their d-shells are completely filled. Only a low contribution of Cu⁺ (15 at.%) was found by deconvolution.

Furthermore, the principal Cu LMM peak (Auger) is observed at 918.0 eV (kinetic energy (K. E.)) which confirms the predominance of Cu^{2+} .^[20]

Concerning the O 1s photopeak, Fig. 3.9 shows a more intense contribution of O_{ads} (75 at.%) than the one assigned to lattice oxygen as already observed by Zhang et al.^[3] Different authors associate these O_{ads} with the presence of oxygen vacancies.^[3,31,32] The presence of carbonate species is also confirmed in the C 1s spectrum by the contribution at 289.6 eV which accounts for 33 at.% of the total C 1s photopeak signal.

Table 3.7 – Atomic ratios $x_{\text{La}}/x_{\text{B}}$ in the bulk (ICP) and at the surface (XPS) and surface compositions of calcined LaBO_3 (B = Fe, Mn) and La_2CuO_4 (CCM).

nominal composition	$x_{\text{La}}/x_{\text{B}}$		surface composition	
	ICP	XPS	based on B	based on La
LaFeO_3	1.01	2.13	$\text{La}_{2.13}\text{FeO}_{4.63}$ ($\text{C}_{3.66}$)	$\text{LaFe}_{0.47}\text{O}_{2.17}$ ($\text{C}_{1.72}$)
LaMnO_3	n. a.	1.91	$\text{La}_{1.91}\text{MnO}_{3.88}$ ($\text{C}_{2.24}$)	$\text{LaMn}_{0.52}\text{O}_{2.04}$ ($\text{C}_{1.18}$)
La_2CuO_4	n. a.	2.98	$\text{La}_{2.98}\text{CuO}_{9.69}$ ($\text{C}_{7.39}$)	$\text{La}_2\text{Cu}_{0.68}\text{O}_{6.52}$ ($\text{C}_{4.96}$)

The surface compositions as determined by X-ray photo-electron spectroscopy (XPS) are different compared to the bulk and nominal composition (Table 3.7). An important excess of lanthanum with respect to B-site cations is observed at the surface of all investigated calcined solids. La enrichment at the surface was already observed before for different perovskites.^[24,33,34] As reported earlier,^[33] La enrichment at the surface can have a detrimental effect on the catalytic properties lowering the accessibility of the active B-site cation.

Concerning the perovskites investigated in this study, the LaFeO_3 perovskite exhibits the highest La enrichment with $x_{\text{La}}/x_{\text{B}} = 2.13$, followed by the LaMnO_3 and La_2CuO_4 samples (Table 3.7). Regarding the surface compositions obtained by XPS, carbon is detected and quantified in addition to the elements which compose the perovskite structure. The presence of (adventitious) carbon on solid surfaces is always evidenced and used as internal reference to calibrate the binding energy (B. E.) values. The contribution of carbon species on the Ruddlesden-Popper phase (RP) surface are relatively high, though, as confirmed by the presence of higher amounts of non-adventitious carbon species such as carbonates.

3.4.2 Ex situ XPS analyses of post-HTXRD samples

The LaFeO_3 solid obtained after the high temperature treatment procedure (labelled as post-HTXRD) was analysed by ex situ XPS after having been exposed to air (Fig. 3.10). Reoxidation processes occurring on the surface due to this exposure cannot be excluded. This analysis revealed that the maximum positions of the photopeaks and the shapes of the La 3d and Fe 2p core levels remained approximately the same as for the calcined sample (Fig. 3.10 and Table 3.8).

Differences were observed for the O 1s and C 1s core levels. In the calcined LaFeO_3 solid both photopeaks could be decomposed into 2 components, namely lattice and adsorbed oxygen species or adventitious carbon and carbonate species, respectively. As shown in Fig. 3.10, for the post-HTXRD sample a 3rd component arises for the O 1s photopeak, i. e. adsorbed water is detected at 533.7 eV ($\text{O}_{\text{ads H}_2\text{O}} = 12$ at.%, Table 3.8). For C 1s the C-O-C component at 286.0 eV – which can be classified as belonging to the adventitious carbon group – becomes more prominent (31 at.% of the overall C 1s signal) after the HTXRD

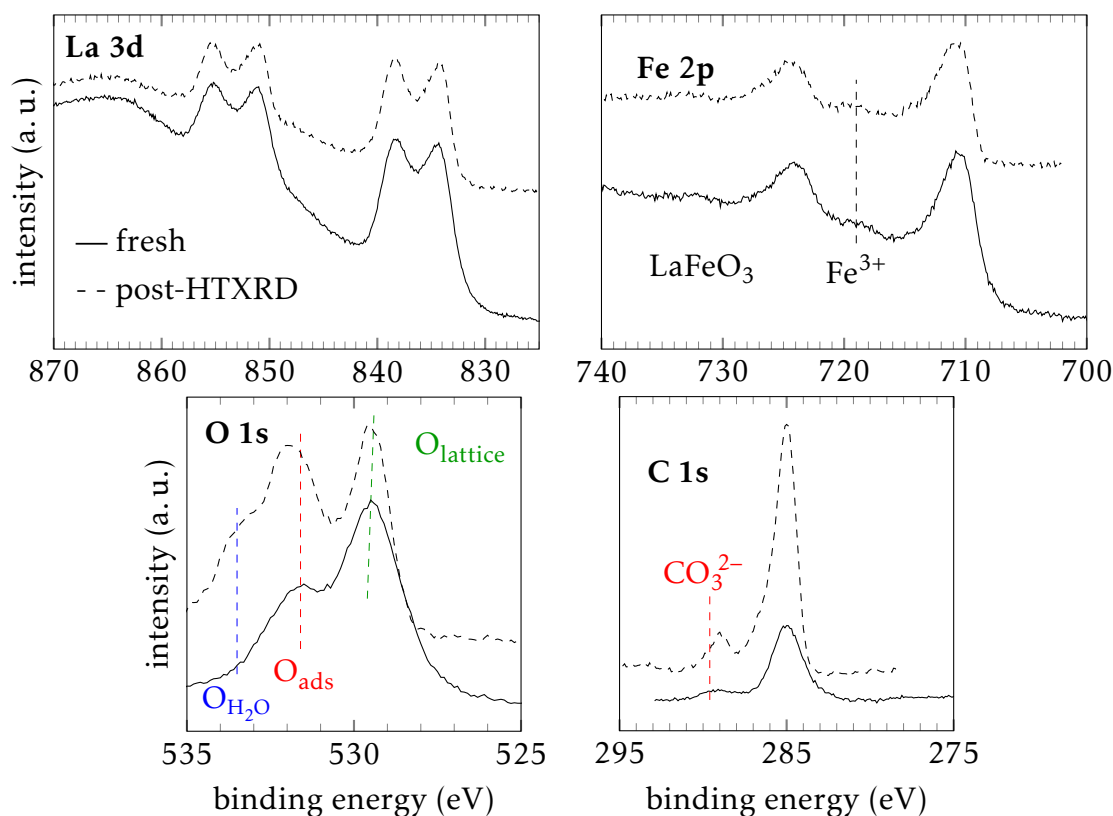


Figure 3.10 – La 3d, Fe 2p, O 1s and C 1s photopeaks of the calcined and post-HTXRD LaFeO_3 samples (CCM). The post-HTXRD sample was analysed on a higher resolution XP spectrometer and its intensities were therefore multiplied by 5 for better comparison.

procedure. This leads to a higher oxygen and carbon content in the post-HTXRD surface compositions (Table 3.9), maybe related to the second heat treatment which is conducted under humid atmosphere except for the cooling step under dry air.

Concerning the atomic La to Fe ratio at the surface, a decrease in La enrichment from 2.13 before HTXRD to 1.64 after this procedure is observed as shown in Table 3.9. The heat treatment therefore yields an LaFeO_3 solid with more accessible Fe cations apart for the adsorbed carbon and oxygen species and does not have a negative impact on the perovskite structure.

In contrast to the post-HTXRD LaFeO_3 sample, XPS measurements on the La_2CuO_4 sample after the HTXRD analysis show an increased La-content at the surface (Table 3.9), presumably due to the still high amorphous content of carbonates. As shown in Fig. 3.11, the relative intensity of the carbonates contribution to the carbon impurities on the surface is still as high as for the as-synthesized solid (Table 3.8). The O 1s photopeak is similar in shape, and equally in its intensity ratio between O_{ads} and the lattice oxygen. The maximum peak position of O 1s is only slightly shifted to lower B. E. The Cu^+ contribution of the Cu $2p_{3/2}$ signal remains similar as for the calcined sample (16 at.%) after the HTXRD procedure.

Having a closer look on the corresponding cation XPS core levels (Fig. 3.11), slight shifts of the photopeaks are observed for the La_2CuO_4 solid after HTXRD. The shoulder at low B. E. of the La photopeak, already seen for the calcined sample, is still clearly discernible for the solid after the HTXRD procedure, consistent with a high carbonate contribution. Even though the maximum of the Cu $2p_{3/2}$ photopeak is shifted to lower binding energies, the

Table 3.8 – Photopeak maxima and relative abundance of surface species on calcined LaFeO_3 and La_2CuO_4 (CCM), and corresponding post-HTXRD samples.

		B. E. (eV)				at.%		
		La 3d _{5/2}	Fe 2p _{3/2}	Cu 2p _{3/2}	O 1s	Cu ⁺ ^a	O _{ads} ^b	C _{CO₃²⁻} ^c
LaFeO_3	calcined	834.3	710.8	-	529.5	-	45	13
LaFeO_3	post-HTXRD	834.4	710.4	-	529.6	-	54 ^d	11 ^e
La_2CuO_4	calcined	835.2	-	933.1	531.7	15	75	25
La_2CuO_4	post-HTXRD	837.7	-	932.7	531.3	16	70	27

^a $\text{Cu}^+/\text{Cu}_{\text{total}}$.

^b $\text{O}_{\text{ads}} + \text{O}_{\text{lattice}} = 1$.

^c $\text{C}_{\text{CO}_3^{2-}} + \text{C}_{\text{adventitious}} = 1$.

^d $\text{O}_{\text{ads}} + \text{O}_{\text{lattice}} + \text{O}_{\text{ads H}_2\text{O}} = 1$. ($\text{O}_{\text{ads H}_2\text{O}} = 12$ at.%)

^e $\text{C}_{\text{CO}_3^{2-}} + \text{C}_{\text{adventitious except C-O-C}} + \text{C}_{\text{C-O-C}} = 1$.

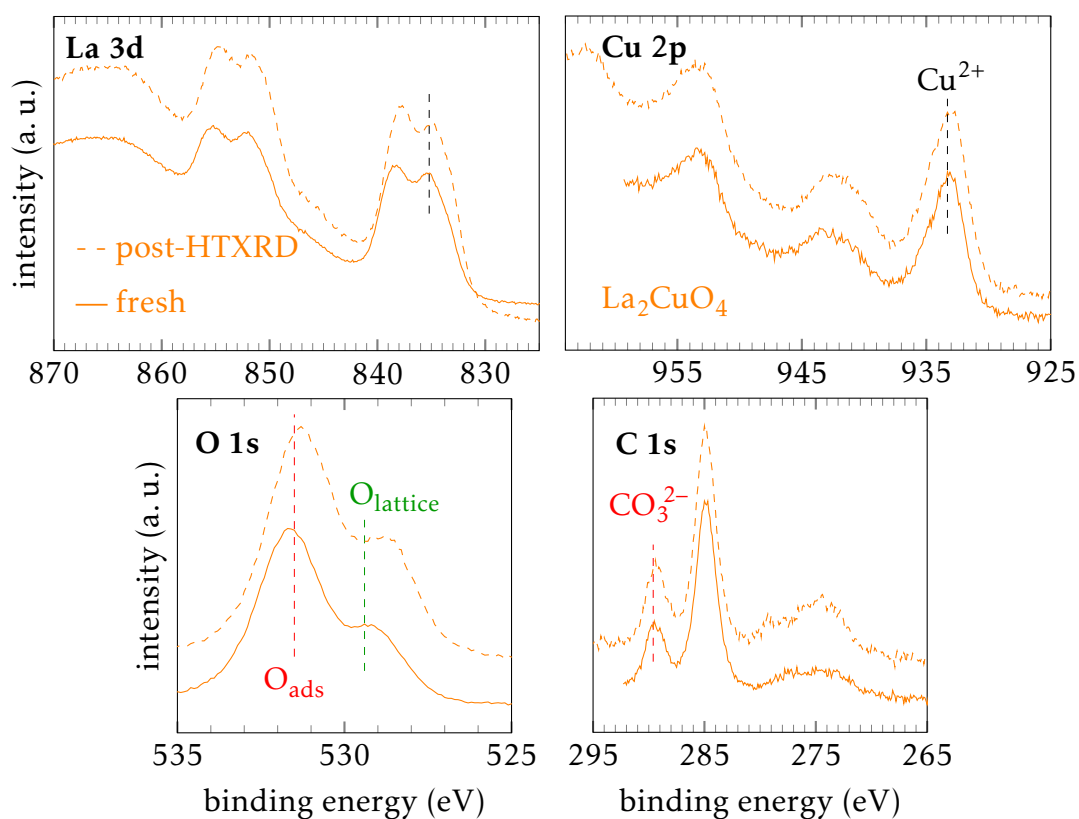


Figure 3.11 – La 3d, Cu 2p, O 1s and C 1s photopeaks of the calcined and post-HTXRD La_2CuO_4 solids (CCM).

predominance of Cu^{2+} is emphasized by a strong satellite. Deconvolution results confirm this with 84 at.% Cu^{2+} in contrast to 16 at.% Cu^+ . The photopeak maximum (932.7 eV) is now close to the one of bulk CuO (932.8 eV).^[17] However, if there might be some CuO extracted at the solid's surface it forms a very finely dispersed or a non-crystalline phase since it is not observed by XRD.

Table 3.9 – Surface atomic ratios $x_{\text{La}}/x_{\text{B}}$ (XPS) and surface compositions of calcined LaFeO_3 and La_2CuO_4 (CCM), and the corresponding post-HTXRD samples.

nominal composition		$x_{\text{La}}/x_{\text{B}}$ XPS	surface composition based on B
LaFeO_3	calcined	2.13	$\text{La}_{2.13}\text{FeO}_{4.63}$ ($\text{C}_{3.66}$)
LaFeO_3	post-HTXRD	1.64	$\text{La}_{1.64}\text{FeO}_{5.20}$ ($\text{C}_{9.36}$)
La_2CuO_4	calcined	2.98	$\text{La}_{2.98}\text{CuO}_{9.69}$ ($\text{C}_{7.39}$)
La_2CuO_4	post-HTXRD	4.75	$\text{La}_{4.75}\text{CuO}_{10.10}$ ($\text{C}_{6.08}$)

3.5 Catalytic performance

3.5.1 Catalytic performance of the commercial reference catalyst

The catalytic performance of a conventional 3-way catalyst was studied for comparison under the same test conditions as the investigated perovskites. The crushed wash-coated monolith sample provided by Johnson Matthey contains an active phase with 0.55 wt.% of noble metals with an atomic ratio of Pd:Rh of 5:1 as well as promoters.

The commercial reference catalyst was studied in 3-way catalysis conditions according to Procedure B (see Section 2.3). The corresponding conversions of all monitored pollutants as well as H_2 and O_2 are shown in Fig. 3.12. The temperatures at half conversion (T_{50}) are reported in Table 3.10.

Table 3.10 – Temperatures corresponding to 50 % conversion of NO , CO , CH_4 , C_3H_6 , C_3H_8 , H_2 , and O_2 of the commercial reference catalyst containing noble metals.

commercial reference catalyst	T_{50} (°C)						
	NO^a	CO	CH_4	C_3H_6	C_3H_8	H_2	O_2
stoichiometric (1 st test ramp)	456	217	464	262	455	149	230
lean	^{-b}	198	^{-b}	213	466	146	231
rich	286	238	^{-b}	336	440	153	215
stoichiometric (return test)	351	228	465	268	457	153	240

^a Based on the conversions calculated by Eq. 3.14.

^b Conversion lower than 50 %.

Typically, conversion vs temperature profiles for the reducing agents and NO and related changes in selectivity towards the production of N_2 , N_2O and ammonia reflect the occurrence of parallel and sequential reaction pathways with the relative rates depending on the operating conditions.

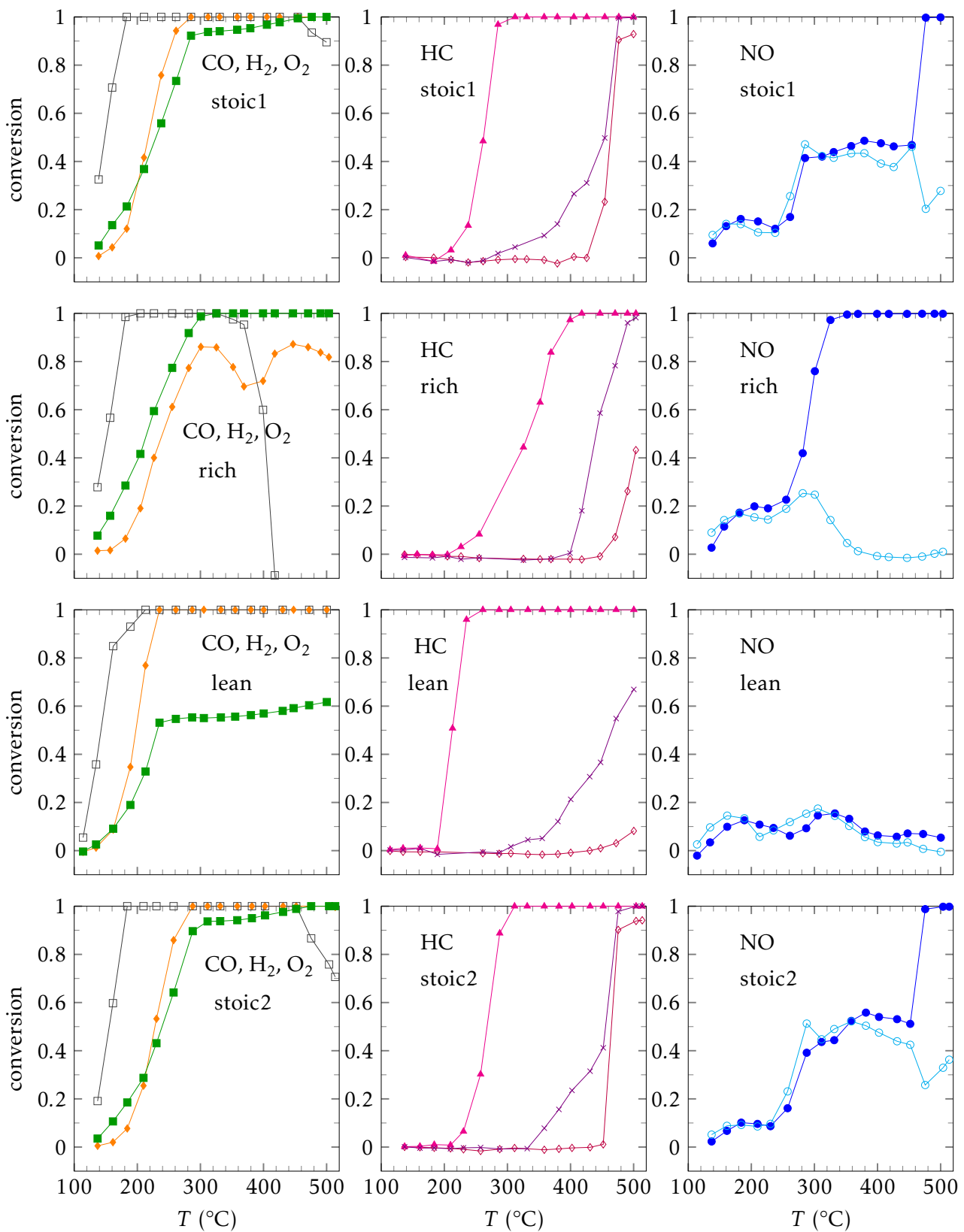
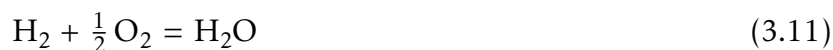


Figure 3.12 – Conversions of NO, CO, HC, H₂ and O₂ of the commercial reference TWC during the 1st test ramp under stoichiometric conditions (stoic1) and return test = 4th test ramp under stoichiometric conditions (stoic2), as well as rich and lean test ramps (Procedure B). X_{CO} (◆), X_{H_2} (□), X_{O_2} (■), $X_{\text{C}_3\text{H}_6}$ (▲), $X_{\text{C}_3\text{H}_8}$ (×), X_{CH_4} (◇), $X_{\text{NO}} = \left(1 - \frac{[\text{NO}]}{[\text{NO}]_0}\right)$ (●), $X_{\text{NO}} = \left(\frac{2[\text{N}_2] + 2[\text{N}_2\text{O}]}{[\text{NO}]_0}\right)$ (○)

In stoichiometric conditions, the examination of Fig. 3.12 (1st stoichiometric test ramp, stoic1) shows that the conversion of H_2 occurs more readily than that of CO and propylene, starting below 120 °C. Propane and methane are the most refractory reducing agents. In these conditions oxidation reactions predominate corresponding to complete conversion of oxygen above 250 °C according to the following sequence (Eq. 3.11 to Eq. 3.13).



The theoretical amount of oxygen converting inlet CO, H_2 and propylene can be estimated according to the stoichiometry of reactions 3.12 to Eq. 3.13.

To determine the selectivities of the different NO conversion products, the yields of N_2 and N_2O were monitored. Therefore, results of 2 different formulas for determining the X_{NO} (Eq. 3.14 and 3.15) are plotted in Fig. 3.12. Eq. 3.14 is based on the actual NO concentrations at the outlet, $[\text{NO}]$, compared to the inlet NO concentration, $[\text{NO}]_0$, whereas Eq. 3.15 refers to the sum of N_2 and N_2O yields.

$$X_{\text{NO}} = \left(1 - \frac{[\text{NO}]}{[\text{NO}]_0} \right) \quad (3.14)$$

$$X_{\text{NO}} = \left(\frac{2[\text{N}_2] + 2[\text{N}_2\text{O}]}{[\text{NO}]_0} \right) \quad (3.15)$$

The examination of the conversion of NO and selectivity curves vs temperature illustrates different trends depending on the operating conditions (Fig. 3.13). As seen in Fig. 3.12 (stoic1), the occurrence of parallel and sequential reactions below 450 °C leads to the production of N_2 and N_2O . The fraction of CO, H_2 and propylene non-oxidised by oxygen can explain a maximum conversion of NO which does not exceed 45%. It is worth to note that the formation of nitrous oxide predominates at low temperature. A rise in temperature induces a significant drop in $S_{\text{N}_2\text{O}}$ and correlatively an increase in S_{N_2} . Such behaviour is basically explained by a 2-step process with N_2O as intermediate species. At low conversion, Rh sites are quasi completely covered by chemisorbed NO molecules due to strong NO adsorption preventing the readsorption of N_2O once it is formed. A partial NO desorption at higher temperatures in conjunction with a greater NO dissociation will increase the density of available Rh sites for N_2O readsorption and decomposition into N_2 .

The catalytic behaviour of the commercial reference 3-way catalyst at high temperatures ($T > 450$ °C) comprises a sharp increase in NO conversion correlated to a predominant production of ammonia. In this temperature range, the conversion of methane and propane sharply increase which could a priori explain the catalytic features by the direct reduction of NO by methane and propane. However, more complex processes are likely to take place as suggested by a drop in H_2 conversion, i. e. the production of H_2 . This H_2 production is probably at the origin of the increase in NO conversion observed above 450 °C. All these trends can be explained by the involvement of additional reforming (Eq. 3.16 and 1.7) and water-gas shift reaction (WGS) (Eq. 3.17).

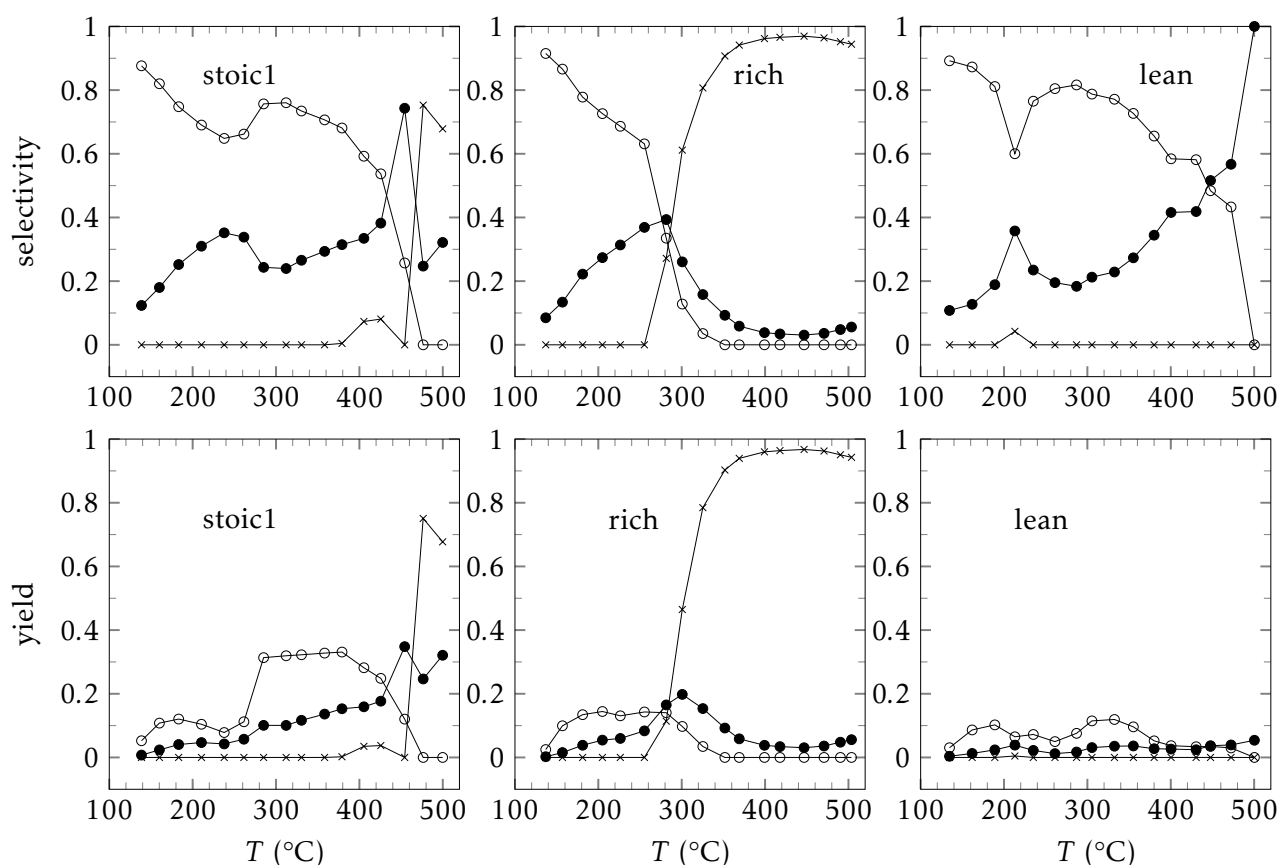


Figure 3.13 – N_2 , N_2O and NH_3 selectivities and yields of NO conversion of the commercial TWC under stoichiometric, rich and lean conditions (Procedure B). $S_{\text{N}_2}/Y_{\text{N}_2}$ (\bullet), $S_{\text{N}_2\text{O}}/Y_{\text{N}_2\text{O}}$ (\circ), $S_{\text{NH}_3}/Y_{\text{NH}_3}$ (\times)



Hence, the production of H_2 could explain the formation of ammonia through the direct $\text{NO} + \text{H}_2$ reaction (Eq. 3.18).



After sequential test ramps, a final test under the same stoichiometric conditions (Fig. 3.12, stoic2) reveals the same observations which highlights the preservation of the surface properties of the catalyst.

When the catalyst operates under rich conditions, the trends previously described in stoichiometric conditions become more accentuated (Fig. 3.12). It is noticeable that H_2 conversion sharply drops above 380°C ¹ coinciding with a minimum in the conversion profile of CO. All these observations suggest that propylene reforming and WGS reactions occur. These processes coincide more readily with a significant production of ammonia taking place

¹The drop continues to significantly negative values of X_{H_2} above 420°C . This drop is not shown to allow for the same scales in the whole Fig. 3.12.

at lower temperature, above 300 °C instead of 400 °C under stoichiometric conditions.

Finally, regarding lean conditions in the presence of an excess of oxygen, it is quite surprising to observe that the oxidative reactions are not significantly enhanced. The reverse trend compared to stoichiometric conditions is observed with lower conversion of methane and propane recorded at 500 °C, probably due to their conversion by reforming and not oxidation under stoichiometric conditions. However, the most important information is related to a strong detrimental effect on the rate of NO conversion with a maximum conversion which does not exceed 20 % in the whole temperature range. Parallel to this observation, no ammonia production is observed according to Eq. 3.18.

3.5.2 Catalytic performance of the perovskite reference catalysts

The catalytic activities of the perovskite reference solids LaFeO_3 , LaMnO_3 and the RP La_2CuO_4 were investigated according to Procedure A as described in Section 2.3. This procedure equals Procedure B except for an inversion of the rich and lean test ramps.

Table 3.11 – Temperatures corresponding to 50 % conversion of NO, CO, CH_4 , C_3H_6 , C_3H_8 , H_2 , and O_2 of the reference perovskite catalysts LaFeO_3 , LaMnO_3 , and La_2CuO_4 prepared by CCM compared to the commercial reference.

catalyst	T_{50} (°C)						
	NO	CO	CH_4	C_3H_6	C_3H_8	H_2	O_2
stoichiometric (1st test ramp)							
LaFeO_3	-	438	-	463	478	499	450
LaMnO_3	-	358	-	428	484	468	399
La_2CuO_4 ^a	-	300	-	415	-	293	330
commercial reference	456	217	464	262	455	149	230
lean							
LaFeO_3	-	436	-	449	467	484	502
LaMnO_3	-	340	-	400	454	442	470
La_2CuO_4 ^a	-	292	-	404	-	293	437
commercial reference	-	198	-	213	466	146	231
rich							
LaFeO_3	^b	442	-	-	-	-	434
LaMnO_3	^b	354	-	-	-	-	360
La_2CuO_4 ^a	479	305	-	419	-	312	307
commercial reference	286	238	-	336	440	153	215
stoichiometric (return test)							
LaFeO_3	-	443	-	469	481	496	458
LaMnO_3	-	367	-	426	476	494	401
La_2CuO_4 ^a	^b	283	-	315	-	286	298
commercial reference	351	228	465	268	457	153	240

^a The La_2CuO_4 test was performed at a GHSV of 45 000 $\text{ml h}^{-1} \text{g}^{-1}$ instead of 60 000 $\text{ml h}^{-1} \text{g}^{-1}$.

^b Conversion lower than 50 %.

These tests were conducted at a space velocity of 60 000 $\text{ml h}^{-1} \text{g}^{-1}$ except for La_2CuO_4 (45 000 $\text{ml h}^{-1} \text{g}^{-1}$). The corresponding conversion (X) versus temperature profiles under

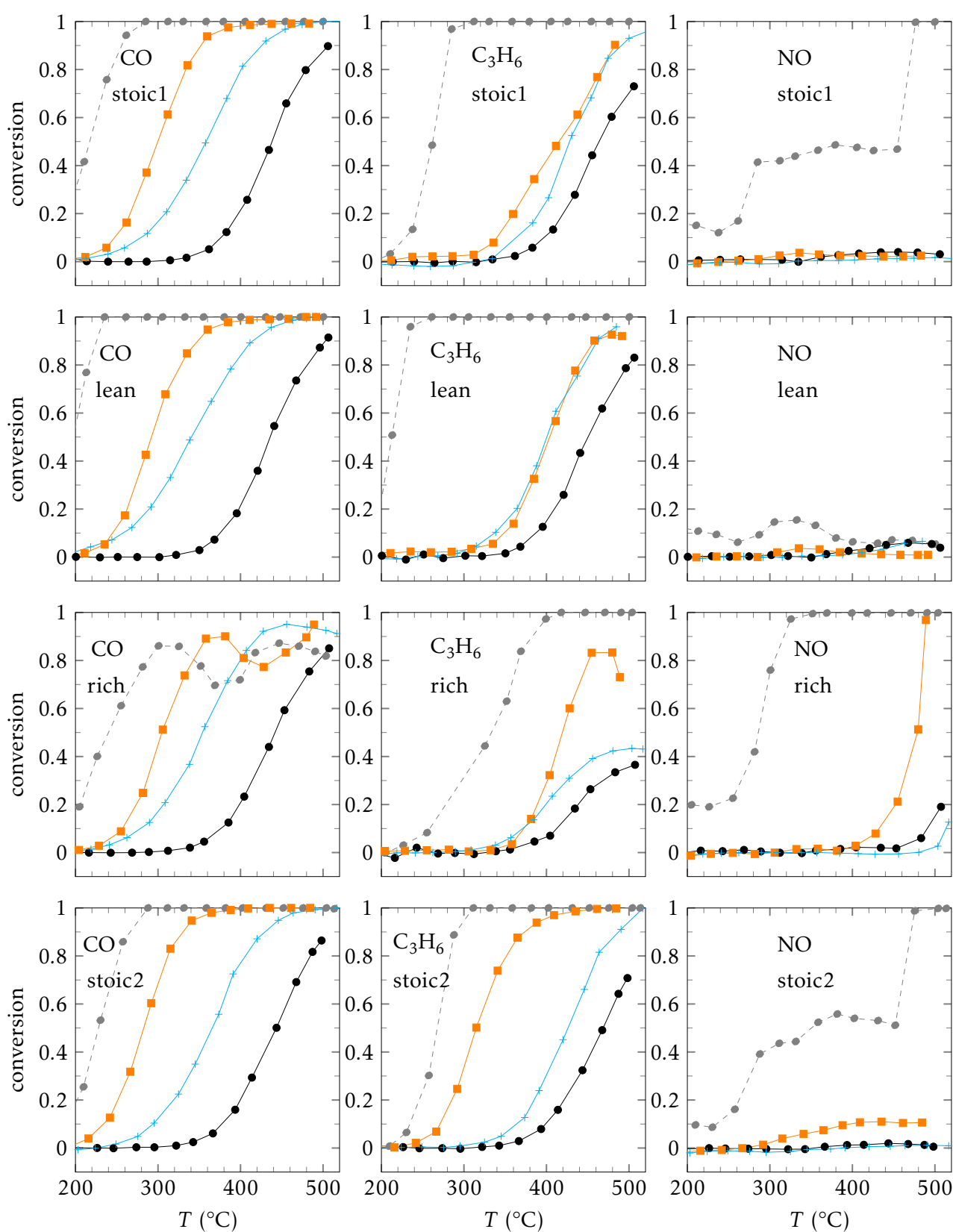


Figure 3.14 – CO, C₃H₆ and NO conversion curves of LaBO₃ (B = Fe, Mn; CCM; space velocity = 60 000 ml h⁻¹ g⁻¹) and La₂CuO₄ (CCM; space velocity = 45 000 ml h⁻¹ g⁻¹) during Procedure A. LaFeO₃ (●), LaMnO₃ (+), and La₂CuO₄ (■) compared to the commercial reference (○); 1st test ramp under stoichiometric conditions (stoic1), return test (stoic2)

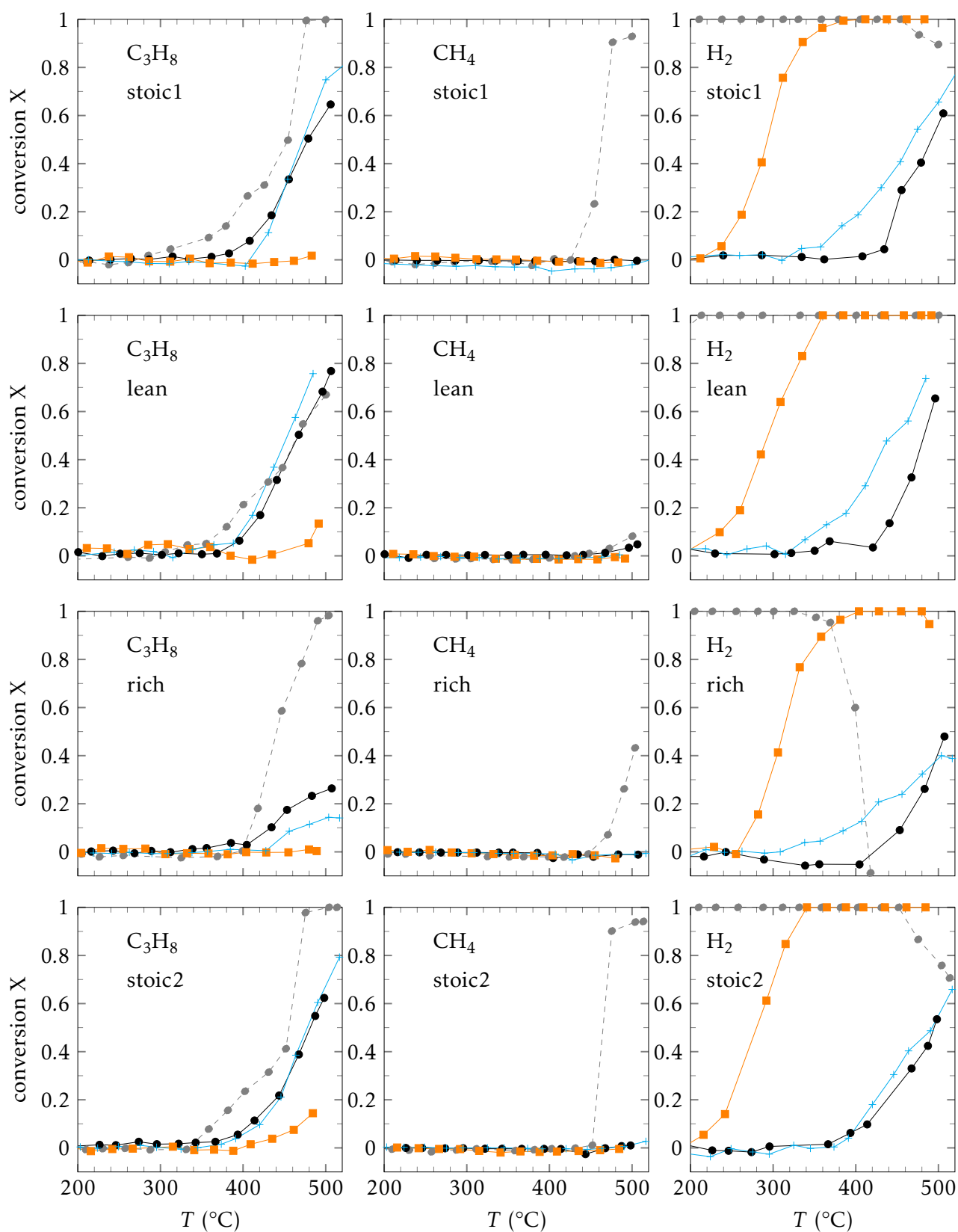


Figure 3.15 – C_3H_8 , CH_4 and H_2 conversion curves of LaBO_3 ($B = \text{Fe, Mn}$; CCM) and La_2CuO_4 (CCM) during Procedure A. LaFeO_3 (\bullet), LaMnO_3 ($+$), and La_2CuO_4 (\blacksquare) compared to the commercial reference (\circ); 1st test ramp under stoichiometric conditions (stoic1), return test (stoic2)

stoichiometric (1st test ramp: stoic1, return test: stoic2), lean and rich conditions are shown in Fig. 3.14 for CO, C₃H₆, and NO and in Fig. 3.15 for C₃H₈, CH₄, and H₂. The temperatures corresponding to 50% conversions of NO, CO, CH₄, C₃H₆, C₃H₈, H₂, and O₂ are listed in Table 3.11 for all the successively conducted test ramps and for the commercial one containing noble metals.

The examination of Fig. 3.14 and Fig. 3.15 shows that perovskite mixed oxides are less active than noble metals as expected. This is true for both – oxidative and reductive – reactions with light-off temperatures shifting to much higher values for CO, H₂ and propylene (Table 3.11).

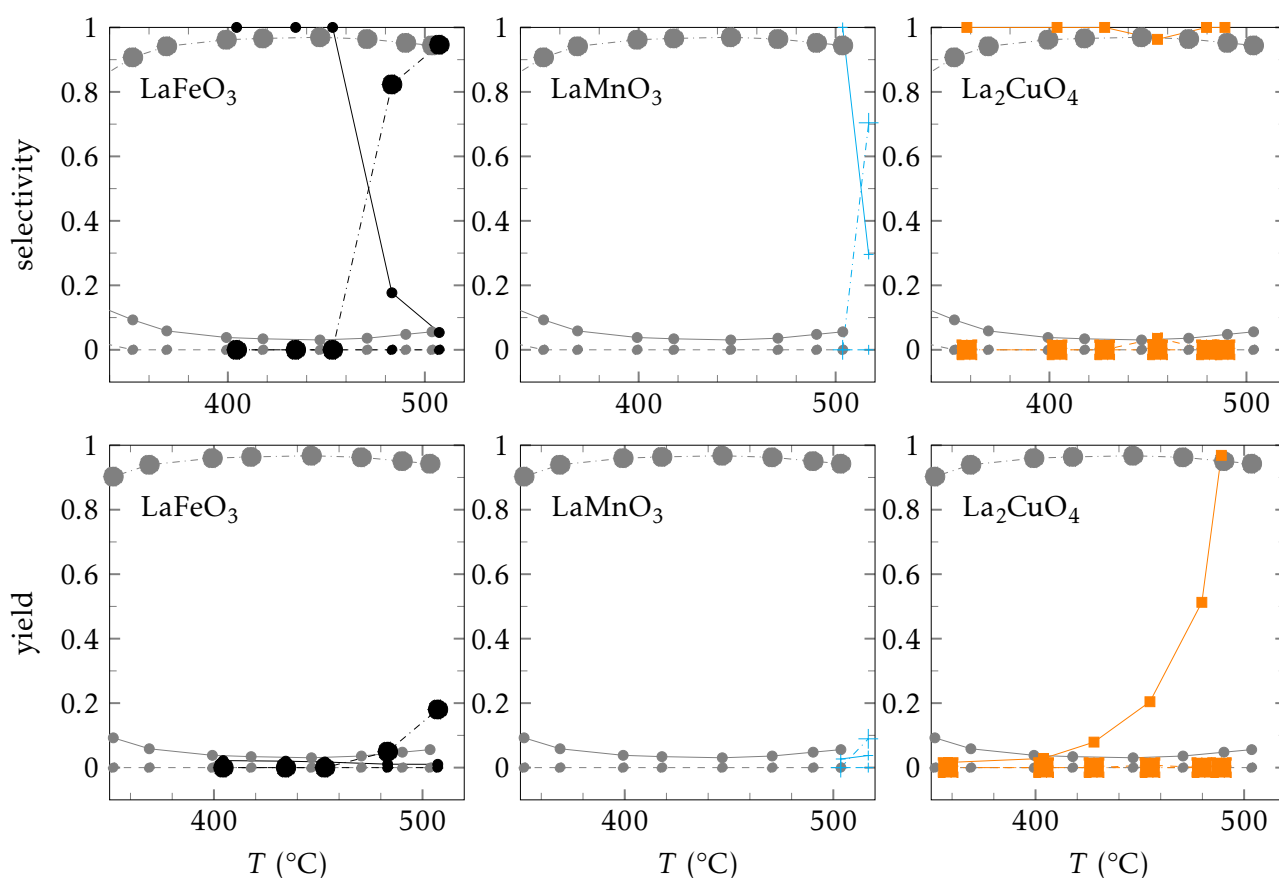


Figure 3.16 – N₂, N₂O and NH₃ selectivities and yields of NO conversion of the perovskite reference catalysts under rich conditions (Procedure A). LaFeO₃ (•), LaMnO₃ (+), and La₂CuO₄ (■) compared to the commercial reference (◐); S_{N₂}/Y_{N₂} (solid), S_{N₂O}/Y_{N₂O} (dashed), S_{NH₃}/Y_{NH₃} (dashdotted, big mark)

Among the selected mixed oxides, LaFeO₃ only displays a low but stable oxidative activity with CO and HC conversions always lower than those for the other solids. However, compared to LaMnO₃ it also shows a slightly higher reductive activity under rich conditions in line with the oxygen excess in the LaMnO₃ structure as evidenced by H₂-TPR and XPS. La₂CuO₄ seems to be the most promising catalyst of the series, being the sole solid able to convert NO above 400 °C reaching a complete conversion at 480 °C under rich conditions. It is interesting to compare this result with the conversion profiles observed for CO and H₂. As exemplified, the same trends described for the commercial reference catalyst occur underlining additional processes of H₂ and CO production attributed to reforming and WGS reactions. In contrast

to the commercial reference catalyst, however, the NO conversion observed under rich conditions leads predominantly to nitrogen (Fig. 3.16), the targeted product.

The conversion profiles recorded during the return test under stoichiometric conditions (stoic2) after the successively performed test ramps under lean and rich conditions are shown in Fig. 3.14 and Fig. 3.15. Contrarily to previous observations obtained on the commercial TWC, significant modifications are observed for the La_2CuO_4 catalyst – mainly related to a significant gain in propylene conversion with a T_{50} shift from 415 °C to 315 °C. Moreover, a broader and weak conversion of NO is observed in the temperature range of 300 to 500 °C. This NO conversion predominantly leads to nitrogen (up to $S_{\text{N}_2} = 86\%$), the remainder being nitrous oxide. These observations show an enhancement in NO conversion but not enough to compete with the commercial catalyst. A gain in activity is also observed for the conversion of the reducing agent with changes in selectivity suggested by the more pronounced drop in the H_2 conversion compared to the initial stoichiometric test (Fig. 3.15) implying an enhanced reforming and WGS reaction activity. All these modifications probably reflect surface modifications as confirmed by XRD analysis of the spent catalyst (following Section 3.5.3) showing significant phase segregation.

3.5.3 Physico-chemical properties of the spent perovskite catalysts

Solids which have been subjected to one catalytic test cycle, henceforward denoted as spent catalysts, were characterised by XRD.

The XRD patterns of the spent catalysts (Procedure A) are displayed in Fig. 3.17. The comparison of the calcined and spent catalysts did not show any significant evolution of the perovskite structure for the LaFeO_3 and LaMnO_3 catalysts whereas the RP structure is completely destroyed.

The rhombohedral manganite structure shows only slight changes. Most notably peaks are shifted to lower angles after testing and 2 additional peaks are observed at $\approx 35^\circ$ and 37° which cannot be attributed to MnO_2 (#24-0735), MnO (#07-0230), Mn_3O_4 (#24-0734), Mn_2O_3 (#41-1442), $\text{La}_2\text{O}_2\text{CO}_3$ (#48-1113), La_2O_3 (#05-0602) nor to LaOH_3 (#36-1481). The shifts to lower diffraction angles observed for its peaks could be explained by the reduction of the present Mn^{4+} fraction during the test cycle and therefore reduced oxygen content in the solid. The fact that Mn^{4+} presents a smaller ionic radius than Mn^{3+} ^[35] may contribute to a slightly increased unit cell volume², i. e. shifts to lower diffraction angles.

Contrarily to the LaFeO_3 and LaMnO_3 perovskites, the Ruddlesden-Popper phase (RP) is not retained. After testing, the La_2CuO_4 phase is nearly completely destroyed which is in agreement with literature.^[36] A mix of mainly $\text{La}_2\text{O}_2\text{CO}_3$ as well as La_2O_3 and CuO is formed. This phase destruction is in line with the results of the HTXRD measurements discussed earlier (Section 3.2). The formation of the decomposition products may account for the increasing reactivity of the solid in the course of the test cycle. Segregated and most probably finely dispersed CuO which are reduced to Cu^0 under reductive atmosphere is known to exhibit a high intrinsic catalytic activity.^[36–38] Likewise, it has been reported that $\text{La}_2\text{O}_2\text{CO}_3$ may play an important role in oxidation reactions over perovskites.^[34] Unfortunately, the catalytic activity may, however, decrease rapidly due to sintering effects if the stabilising RP phase is not reformed under reaction conditions as was reported by Peter et al. for the $\text{CO} + \text{NO}$ reaction.^[36]

²Assuming a simplified, purely steric model.

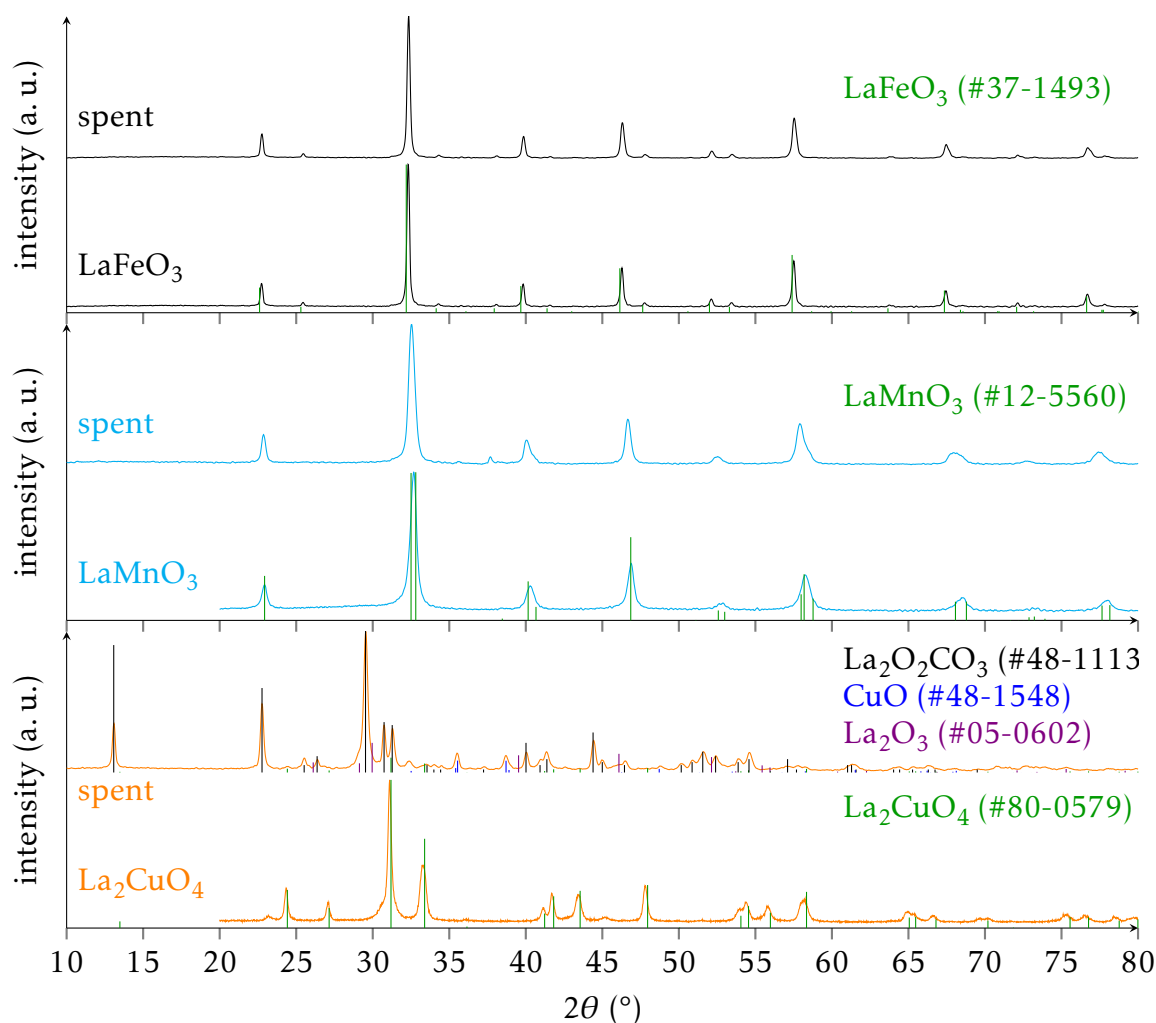


Figure 3.17 – X-ray diffractograms of calcined and spent LaBO_3 ($B = \text{Fe}, \text{Mn}; \text{CCM}$) and La_2CuO_4 (CCM) solids.

3.6 Conclusion

A commercial reference catalyst (containing noble metals and promoters) and 3 perovskite reference catalysts were studied in 3-way catalytic conditions. First, the influence of the B-site cation in perovskites was investigated for samples prepared by conventional citrate method. The choice of the B-site metal was limited to $B = \text{Mn}, \text{Fe}$ and Cu (Ruddlesden-Popper phase) as a consequence of the toxicity of Co and Ni compounds. Secondly, the catalytic performances were studied for all reference catalysts.

All perovskite solids showed the expected crystalline structure, no significant phase segregation was observed. Whereas, LaFeO_3 and La_2CuO_4 present moderate surface areas, LaMnO_3 yields the highest specific surface area. As revealed by XPS, a La enrichment at the surface is observed for all investigated solids. While the LaFeO_3 sample is stable below 700°C in H_2 atmosphere and the LaMnO_3 solid is only little more reducible, the La_2CuO_4 solid shows a high reducibility. This reduction leads to the destruction of the RP phase and the formation of Cu^0 particles (easily oxidised to CuO) and $\text{La}_2\text{O}_2\text{CO}_3$ as was confirmed by the HTXRD analysis.

3-way catalytic tests were performed in subsequent test ramps under stoichiometric,

lean and rich conditions. In general, only low NO conversion was observed under lean conditions which is mainly due to low N_2O production at low temperatures. On the other hand, the production of high amounts of ammonia at high temperature, especially under rich conditions, was observed for all catalysts except the La_2CuO_4 solid. This ammonia production can be explained by an excess H_2 formation due to occurring reforming and water-gas shift reaction.

Conventional catalysts containing noble metals and promoters are very active for oxidation and reduction in 3-way catalysis. This is in line with the known higher intrinsic catalytic activities of noble metals compared to base transition metals. The observed NO elimination is, however, achieved by the formation of mainly undesired reduction products as the greenhouse gas N_2O and toxic NH_3 . It is therefore desirable to develop catalysts which reach similar conversions while improving N_2 selectivity of the NO reduction.

For the perovskite catalysts, concerning the ability to catalyse the simultaneous oxidation of CO and HC as well as the reduction of NO, differences were observed which can be attributed to the described differing surface composition, i. e. carbonate and other adsorbed oxygen species content, and the overall reducibility of the solids. However, methane could not be converted in the investigated temperature range for any of the perovskites and propane remained difficult to activate.

Whereas the LaMnO_3 catalyst shows good performances to catalyse the oxidation reactions of CO, propylene and propane, only a very slight reductive activity was observed, probably due to the high oxygen excess in the structure. The Mn-based perovskite structure is retained with only minor phase segregation being detected after one test cycle.

On the other hand, the La_2CuO_4 sample presented the most interesting catalytic activity. The high performance on CO oxidation was accompanied by propylene reforming activity. The NO reduction performance was higher than for the other perovskite solids and yielded nearly exclusively N_2 , even under rich conditions. An activation is observed in the return test which is attributed to phase segregation, i. e. the formation of highly dispersed CuO particles on the surface of a La oxide/ La carbonate mixture mainly composed of $\text{La}_2\text{O}_2\text{CO}_3$ and La_2O_3 – much more reducible – as evidenced by ex situ XRD measurements of the spent catalyst. This phase segregation unfortunately leads to the instability of the structure under testing conditions. In contrast to the in situ HTXRD analysis, XRD ex situ analysis after one test cycle showed that the RP could not be reconstructed under the reaction conditions. The observed phase segregation initially leads to higher catalytic performances. However, it can be assumed that this high dispersion will not be maintained indefinitely. A high probability exists that sintering will occur rapidly leading to decreasing catalytic activity.

This is why this study will focus on Fe-based perovskites. The LaFeO_3 solid proved to be stable under the testing conditions with no detectable crystalline phase segregation nor any sintering being observed after one test cycle. Its moderate activity for CO, propylene and propane oxidation is accompanied by some low reduction performance under rich conditions.

Fe-based perovskites are going to be investigated as challenging but thermally stable, cheap and promising alternatives to noble metal containing conventional 3-way catalysts. The combination with substitution by Cu is taken into consideration to combine the high stability of LaFeO_3 with the higher reducibility of Cu as in La_2CuO_4 .

Bibliography

- [1] ScienceLab.com, MSDS nickel nitrate, English, <http://www.sciencelab.com/msds.php?msdsId=9926215> (visited on 2014-08-05).
- [2] ScienceLab.com, MSDS cobalt nitrate hexahydrate, English, <http://www.sciencelab.com/msds.php?msdsId=9923525> (visited on 2014-08-05).
- [3] L. Zhang, Y. Zhang, J. Deng, H. Dai, *Journal of Natural Gas Chemistry* **2012**, *21* (1), 69–75.
- [4] G. J. McCarthy, P. V. Gallagher, C. Sipe, *Materials Research Bulletin* **1973**, *8*, 1277–1284.
- [5] M. Popa, J. Frantti, M. Kakihana, *Solid State Ionics*, Proceedings of International Conference on Solid State Ionics, (Materials and Processes for Energy and Environment), Cairns, Australia, 8-13 July, 2001 **2002**, 154–155, 437–445.
- [6] B. P. Barbero, J. A. Gamboa, L. E. Cadús, *Applied Catalysis B: Environmental* **2006**, *65* (1-2), 21–30.
- [7] J.-M. Giraudon, A. Elhachimi, F. Wyrwalski, S. Siffert, A. Aboukaïs, J.-F. Lamonier, G. Leclercq, *Applied Catalysis B: Environmental* **2007**, *75*, 157–166.
- [8] J. Andreasson, J. Holmlund, R. Rauer, M. Käll, L. Börjesson, C. Knee, A. Eriksson, S.-G. Eriksson, M. Rübhausen, R. Chaudhury, *Physical Review B* **2008**, *78*, DOI 10.1103/physrevb.78.235103.
- [9] J. Bielecki, P. Svedlindh, D. T. Tibebu, S. Cai, S.-G. Eriksson, L. Börjesson, C. S. Knee, *Physical Review B* **2012**, *86*, DOI 10.1103/physrevb.86.184422.
- [10] D. L. A. de Faria, S. Venâncio Silva, M. T. de Oliveira, *Journal of Raman Spectroscopy* **1997**, *28*, 873–878.
- [11] L. J. Oblonsky, T. M. Devine, *Corrosion Science* **1995**, *37*, 17–41.
- [12] S. S. Chan, A. T. Bell, *Journal of Catalysis* **1984**, *89*, 433–441.
- [13] M. A. Peña, J. L. G. Fierro, *Chemical Reviews* **2001**, *101* (7), 1981–2018.
- [14] G. Pecchi, M. G. Jiliberto, A. Buljan, E. J. Delgado, *Solid State Ionics* **2011**, *187*, 27–32.
- [15] L. Lisi, G. Bagnasco, P. Ciambelli, S. D. Rossi, P. Porta, G. Russo, M. Turco, *Journal of Solid State Chemistry* **1999**, *146* (1), 176–183.
- [16] P. Ciambelli, S. Cimino, S. D. Rossi, M. Faticanti, L. Lisi, G. Minelli, I. Pettiti, P. Porta, G. Russo, M. Turco, *Applied Catalysis B: Environmental* **2000**, *24*, 243–253.
- [17] J. A. Anderson, J. L. G. Fierro, *Journal of Solid State Chemistry* **1994**, *108*, 305–313.
- [18] H. Taguchi, S. Matsu-ura, M. Nagao, T. Choso, K. Tabata, *Journal of Solid State Chemistry* **1997**, *129* (1), 60–65.
- [19] H. Su, L. Jing, K. Shi, C. Yao, H. Fu, *Journal of Nanoparticle Research* **2010**, *12* (3), 967–974.
- [20] Thermo Scientific, XPS Knowledge Base, English, **2014**, <http://xpssimplified.com/periodictable.php> (visited on 2014-06-11).
- [21] S. Pegoraro, M. M. Natile, A. Galenda, A. Glisenti, *Surface Science Spectra* **2009**, *16*, 75.

- [22] D. Briggs, M. P. Seah, *Practical Surface Analysis, Vol. 1*, 2nd ed., (Ed.: J. W. Crampton), Wiley-Interscience, 1993.
- [23] Z.-X. Wei, Y.-Q. Xu, H.-Y. Liu, C.-W. Hu, *Journal of Hazardous Materials* **2009**, 165 (1-3), 1056–1061.
- [24] J. Fierro, L. Tejuca, *Applied Surface Science* **1987**, 27, 453–457.
- [25] M. C. Biesinger, X-ray Photoelectron Spectroscopy (XPS) Reference Pages, English, **2014**, <http://www.xpsfitting.com/>, %20<http://www.xpsfitting.com/search/label/Carbonates> (visited on 2014-06-11).
- [26] H. Najjar, J.-F. Lamonier, O. Mentré, J.-M. Giraudon, H. Batis, *Catalysis Science & Technology* **2013**, 3, 1002.
- [27] V. Galakhov, M. Demeter, S. Bartkowski, M. Neumann, N. Ovechkina, E. Kurmaev, N. Lobachevskaya, Y. Mukovskii, J. Mitchell, D. Ederer, *Physical Review B – condensed matter and materials physics* **2002**, 65, 1131021–1131024.
- [28] J. Li, J. Zeng, L. Jia, W. Fang, *International Journal of Hydrogen Energy, Asian Hydrogen Energy Conference 2009* **2010**, 35, 12733–12740.
- [29] N. Guilhaume, S. D. Peter, M. Primet, *Applied Catalysis B: Environmental* **1996**, 10 (4), 325–344.
- [30] H. X. Dai, C. F. Ng, C. T. Au, *Journal of Catalysis* **2001**, 197, 251–266.
- [31] R. Polini, A. Falsetti, E. Traversa, O. Schäf, P. Knauth, *Journal of the European Ceramic Society, Refereed Reports ELECTROCERAMICS X 2006* **2007**, 27, 4291–4296.
- [32] J. Yuan, H. Dai, L. Zhang, J. Deng, Y. Liu, H. Zhang, H. Jiang, H. He, *Catalysis Today* **2011**, 175 (1), conference paper, 209–215.
- [33] N. Yamazoe, Y. Teraoka, *Catalysis Today* **1990**, 8 (2), 175–199.
- [34] V. G. Milt, R. Spretz, M. A. Ulla, E. A. Lombardo, J. L. G. Fierro, *Catalysis Letters* **1996**, 42, 57–63.
- [35] R. D. Shannon, *Acta Crystallographica Section A* **1976**, 32, 751–767.
- [36] S. D. Peter, É. Garbowski, V. Perrichon, M. Primet, *Comptes Rendus Chimie* **2004**, 7 (1), 57–61.
- [37] G. Centi, S. Perathoner, *Applied Catalysis A: General* **1995**, 132, 179–259.
- [38] S. D. Peter, É. Garbowski, N. Guilhaume, V. Perrichon, M. Primet, *Catalysis Letters* **1998**, 54 (1-2), 79–84.

Influence of synthesis parameters on the physico-chemical properties and catalytic performance of LaFeO_3

All synthesis protocols herein discussed were previously described in Section 2.1. They are based on the concept of complexation of precursors (metal nitrates) with citric acid to obtain a homogeneous mixed oxide after calcination. The effect of the solvent is first investigated, comparing results obtained for LaFeO_3 prepared by the conventional citrate method (CCM) with those for the hydroalcoholic method (HAM). Hereafter, the addition of a macro template (macro-structuring method (MSM)) and their influence on particle morphology and reactivity is discussed. Finally, the influence of the calcination atmosphere is explored.

4.1 Solvent effect

This work is focused on the effect of the solvent, water compared to hydroalcoholic solution, used for the citrate precursor preparation and how this solvent affects the morphology and specific surface area (SSA) of the obtained LaFeO_3 perovskite powders.

The CCM is based on a sol-gel synthesis route renowned for giving homogeneous mixed oxides with moderate specific surface area ($10 \text{ m}^2 \text{ g}^{-1} \leq \text{SSA} \leq 30 \text{ m}^2 \text{ g}^{-1}$). The main steps of this method are (i) the dissolution of the metal nitrate precursors and the complexing agent, citric acid, in aqueous medium leading to the formation of a La-Fe-citrate precursor solution under stirring, (ii) the gel-formation by slow evaporation of water under reduced pressure in a rotative evaporator, (iii) obtaining the xerogel by drying at $80 \text{ }^\circ\text{C}$, (iv) the decomposition of nitrates of the ground powder in a muffle oven, and (v) finally the calcination under air flow at $600 \text{ }^\circ\text{C}$.

The first steps, i. e. dissolution and complexation, are crucial for the homogeneity of the solid after calcination. They allow for the metal cations to be mixed statistically and close to each other in the precursor complex. The nitrates decomposition itself is done separately to spare the tubular quartz reactor employed later. In fact, this decomposition is exothermic and can proceed explosively due to the NO_x generation at rather low temperature (120 to $250 \text{ }^\circ\text{C}$).

The HAM, as already stated, is also a citrate complexing method but the synthesis takes place in hydroalcoholic medium, i. e. an EtOH-water mixture as solvent. During the synthesis

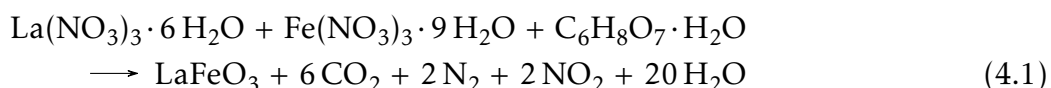
step, a minor difference may be induced by the lower temperature of the drying step of the hydroalcoholic solution to obtain the xerogel, i. e. 40 °C instead of 80 °C.

After the complete dissolution which takes a little longer than for the CCM due to the lower solubility of the precursors in the hydroalcoholic solution, the drying step is performed in an oven ($T = 40\text{ °C}$) for 2 to 3 days. The following steps are the same as for the CCM.

4.1.1 Nitrate-citrate precursor decomposition

Fig. 4.1 illustrates the thermal analysis of the dried LaFeO₃ precursor under air flow obtained by CCM and HAM methods.

Concerning the CCM precursor, 5 different zones of weight loss are observed, adding up to 82 wt.%. This is in reasonable agreement with a theoretical weight loss of about 74 wt.% for chemical transformations according to Eq. 4.1^[1] taking into account the evaporation of adsorbed water.



As shown in Fig. 4.1, after an initial weight loss of approximately 7 % up to 120 °C due to evaporation (endothermic phenomenon, 1), a major sharp and exothermic peak with a shoulder is observed in the range of 140 to 180 °C which can be attributed to the decomposition of organic and inorganic compounds such as free citrates to CO and CO₂ and nitrates to NO_x (2).^[1,2] This nearly vertical second weight loss step accounts for a about 60 % of weight loss, while the sum of subsequent weight losses does not exceed 12 %. Then, two broad exothermic peaks (3, 4) are distinguishable between 220 °C and 440 °C which can be assigned to the decomposition of the La-Fe-citrate complex probably leading to intermediary binary metal oxide and carbonate species such as La₂O₃ and La₂O₂CO₃.^[1-3] The first of these weight losses (3) sets in at 220 °C and is finished at 350 °C. At higher temperature (360 °C to 440 °C), the 4th weight loss is observed. Finally, in zone 5 burnout of any residual carbon species takes place and complete decarbonation of La₂O₂CO₃ is leading to the formation of LaFeO₃.^[2,4] Krupicka et al. detected only low amounts of NO_x formed during this whole decomposition step, probably due to a preliminary release by nitrate decomposition during the drying process.^[3] In contrast to the single oxide and mixed oxides decomposition results reported by Courty et al. which proceed in a continuous process,^[5] a fast decomposition of citrate and nitrate species, i. e. a highly exothermic and even explosive decomposition is observed in our case.

Interestingly, weight loss profiles from thermal analysis of the dried HAM precursor under air flow differ from those obtained for the CCM precursor. When decomposition of the HAM precursor is occurring, the thermogram is clearly exhibiting more complex features associated to the use of an EtOH-water mixture as solvent. In this case, a shift of the weight losses to higher temperatures is observed, the elimination of residual carbon species in the last step at 620 °C excepted. Thus, it is presumed that precursor complexes are better stabilised in hydroalcoholic medium. This stabilisation may be induced by less strong solvent-complex interactions (less hydrogen-bonding with EtOH) and therefore different interactions may occur inside the complex itself. The overall weight loss is lower than in the case of the CCM precursor and amounts to 72 wt.% which is slightly below the theoretical value mentioned above. Nonetheless, an initial solvent weight loss of the same magnitude as

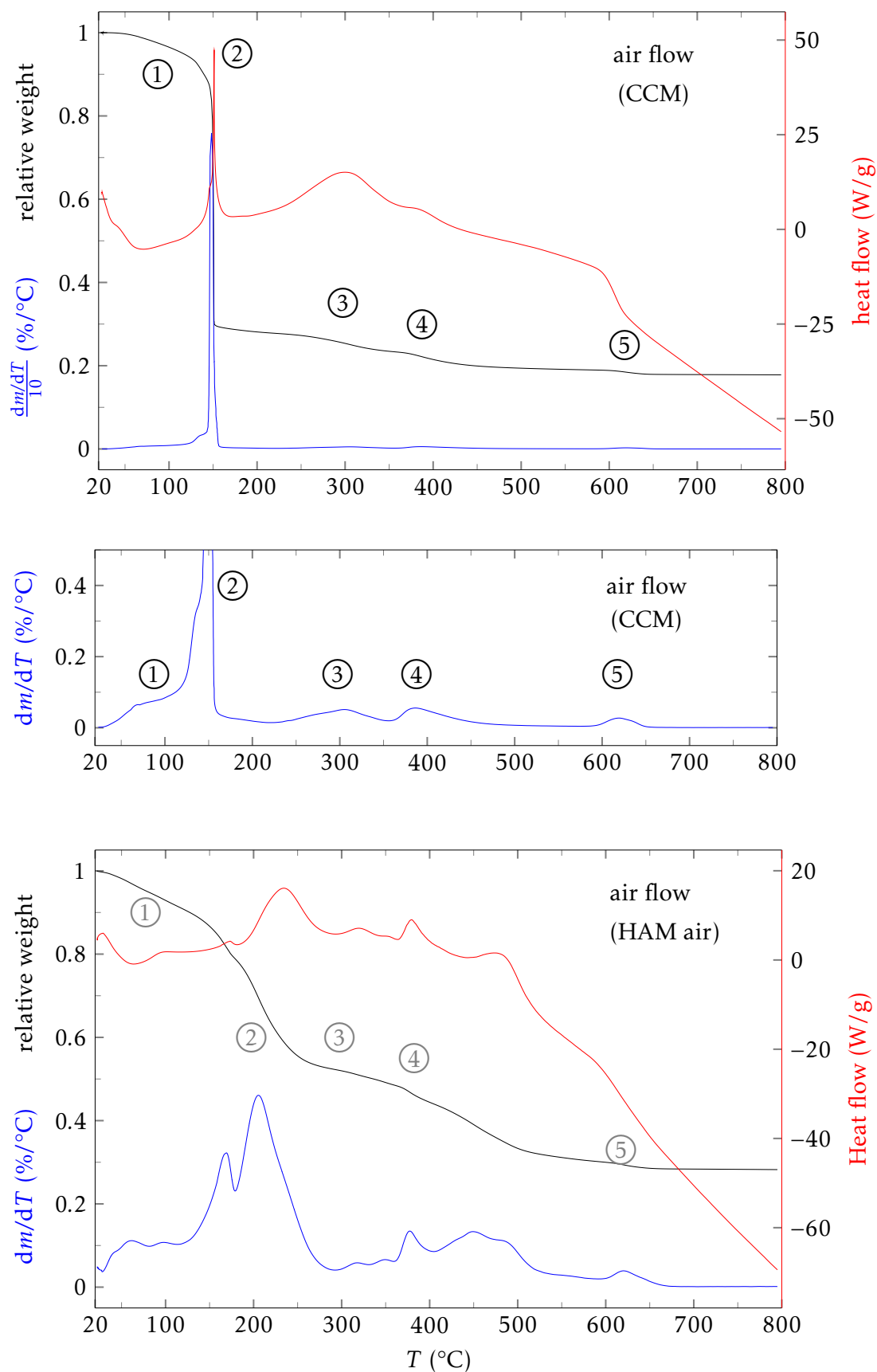


Figure 4.1 – TGA/DSC of CCM and HAM precursors of LaFeO_3 . Please note the different scales for $\frac{dm}{dT}$ and heat flow.

for the CCM precursor is observed. Thus, it is assumed, that a higher contribution of nitrates is decomposed during the drying step than for the CCM precursor. This prior decomposition of oxidising species may play an additional role in the less exothermic decomposition process as observed.

As can be seen from Fig. 4.1, the main weight loss zones are retained. They are, however, split up in more complex features. This can be well observed for zone 2 which is related to a highly exothermic and abrupt weight loss step for the CCM precursor. For the HAM precursor solid, a similar decomposition of organic compounds and nitrates takes place in a very attenuated form – attenuated regarding the weight loss and the exothermic reaction. In the CCM case the 2-step behaviour is barely visible as a shoulder (see zoom Fig. 4.1), whereas it is clearly observable for the HAM precursor. Furthermore, the temperature of decomposition of these species shifts from 140 °C and 150 °C to 170 °C and 210 °C. This is attributed to a higher stability of the complex. The processes taking place in the temperature range denoted as zone 3 and 4 for the CCM precursor previously exhibit an even higher complexity. Again temperature shifts are observed compared to the CCM precursor but they are less marked (for the first corresponding peak respectively).

Whereas the CCM nitrate/free citrate decomposition step is highly exothermic, as can be seen by the intense heat flow peak, the 1st part of the decomposition is only slightly, the 2nd part just little more exothermic in the case of the HAM precursor. The same trend of LaFeO₃ formation from a CCM precursor being more exothermic than from an HAM one is observed for the following calcination steps. Surprisingly, the exothermic behaviour in the course of the nitrate/free citrate decomposition is even shifted to slightly higher temperatures than the observed weight loss. This phenomenon may contribute to the more resolved superposed weight loss steps in zone 2 since no “chain reaction” is started by the first exothermic weight loss step.

The chosen calcination temperature in both syntheses of 600 °C is below the last weight loss step. It is generally accepted that lower calcination temperatures (and partial crystallisation) allows for lower crystallite sizes and higher specific surface areas and thereby improves the catalytic activity of the solid.^[6] Furthermore, the solids prepared by HAM are not subjected to the additional decomposition step in a muffle oven before calcination contrarily to the CCM sample since their decomposition is less explosive.

4.1.2 Structural properties

XRD measurements show that both solids are well crystallised and present the expected orthorhombic structure of LaFeO₃ (Fig. 4.2). No crystalline phase segregation is observed and relative intensities correspond to those of the reference (#37-1493). For both preparation routes, no deviation is observed despite the lower calcination temperature compared to the one indicated by the TGA/DSC analysis.

Table 4.1 – Comparison of crystallite sizes and unit cell parameters derived from full pattern matching of calcined LaFeO₃ prepared by CCM and HAM air.

synthesis method	d_{cryst} (nm)	a (Å)	b (Å)	c (Å)	$V_{\text{unit cell}}$ (Å ³)
CCM	20.1 ± 0.1	5.561	7.858	5.558	242.85 ± 0.17
HAM air	20.2 ± 0.1	5.553	7.863	5.555	242.58 ± 0.33

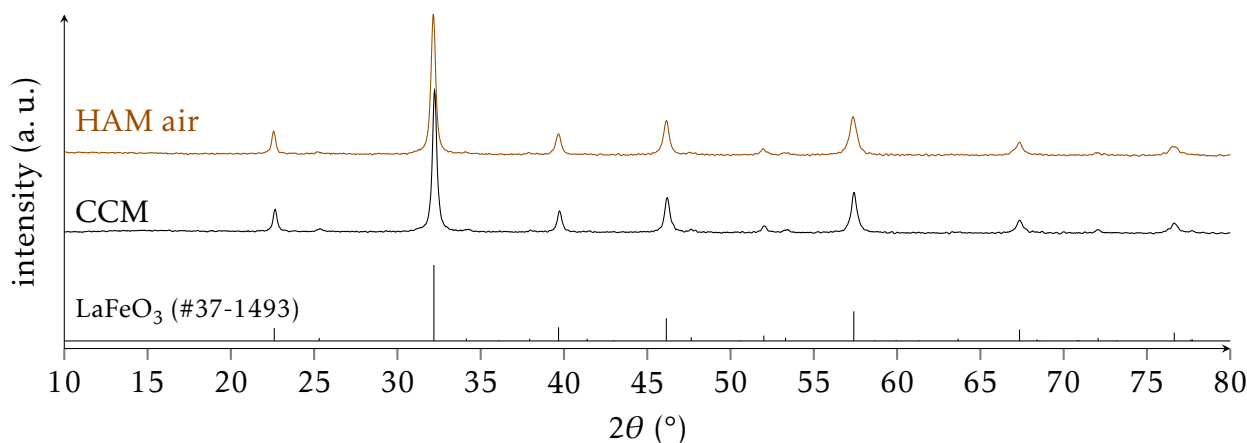


Figure 4.2 – X-ray diffractograms of calcined LaFeO_3 prepared by CCM and HAM air.

In agreement with the similar broadness of the diffraction peaks, crystallite sizes (d) of approximately 20 nm are obtained in both cases as can be seen in Table 4.1 which lists the results of full pattern matching. As expected, LaFeO_3 samples prepared by CCM and HAM air present similar unit cell parameters and unit cell volume.

4.1.3 Textural properties

Nitrogen physisorption isotherms and pore size distributions are depicted in Fig. 4.3. As illustrated, the textural properties of LaFeO_3 samples differ if prepared in different solvents. Whereas both solids display isotherms which show contributions of macroporous solids (type II) with mesopore influence (type IV), the sample prepared by CCM presents an isotherm which is mainly of type II. On the other hand, the HAM air sample shows mainly type IV behaviour. The hysteresis of the CCM solid is significantly narrower than the one of the HAM air perovskite.

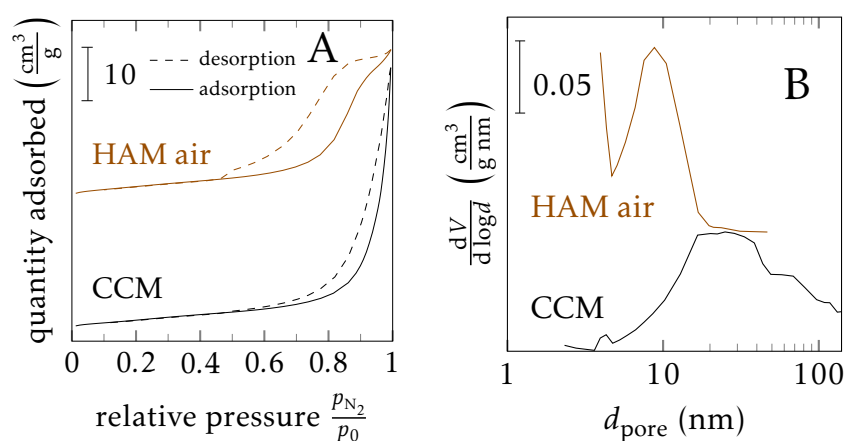


Figure 4.3 – Isotherms (A) and BJH pore size distributions from the desorption branch of the isotherm (B) of calcined LaFeO_3 prepared by CCM or HAM air.

Differences are also observed for the pore size distributions. Indeed, the CCM catalyst shows a very broad distribution in the macropore range with only a very low amount of mesopores being detected whereas the HAM air sample is characterised by a high mesopore contribution with a maximum at $d_{\text{pore}} \approx 10$ nm.

Table 4.2 – Comparison of specific surface areas, cumulative pore volume and average pore diameter of LaFeO_3 prepared by CCM and HAM air.

synthesis method	SSA ($\text{m}^2 \text{g}^{-1}$)	V_{pore} ($\text{cm}^3 \text{g}^{-1}$)	\bar{d}_{pore} (nm)
CCM	13.9	0.08	20.4
HAM air	14.0	0.06	7.5

Overall, SSA and cumulative pore volumes are similar for both synthesis methods. However, as already observed for the pore size distribution, a significantly lower \bar{d}_{pore} is observed in the case of the sample obtained by HAM air.

SEM (Fig. 4.5) reveals differences in the morphology at the micrometre level. As shown in Fig. 4.5C, the solid prepared by CCM represents a network of aggregates with macropores being mainly due to holes in this matrix. On the other hand, in agreement with the pore size distribution, the sample obtained by HAM air (Fig. 4.5D) does not show such macropores. Instead of aggregates (Fig. 4.5A) dense block-like morphologies are observed (Fig. 4.5B) which resemble the compact LaFeO_3 morphology reported by Krupicka et al.^[3] At a higher magnification (Fig. 4.5E (CCM) and Fig. 4.5F (HAM air)), differences are less marked. The presence of lower diameter mesopores for the latter solid is, however, confirmed.

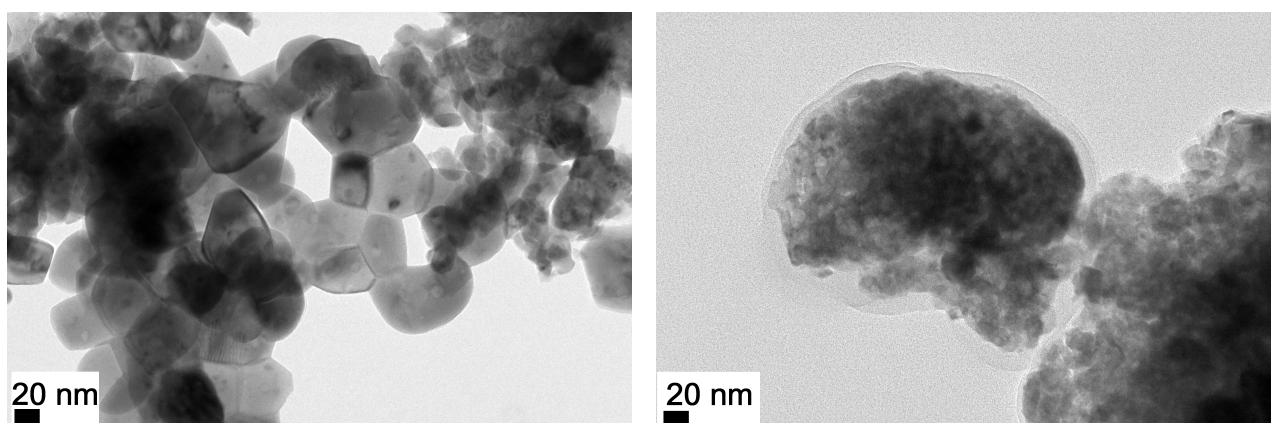


Figure 4.4 – Transmission electron micrographs of LaFeO_3 synthesized via CCM (left) and HAM air (right).

Concerning the nanometric scale, TEM analyses as displayed in Fig. 4.4 show that the structures are formed by small particles in both cases. However, the average particle size of the CCM perovskite is bigger than that obtained by HAM air. This may be caused by the very exothermic decomposition reaction leading to the sintering of different nuclei. Moreover, in the case of the HAM air solid an amorphous film is observed on the surface throughout the whole sample. This film consists of silicon oxide as evidenced by EDX. The source of this contamination remains unclear but seems to be due to the preparation of the sample before microscopy because no Si was observed by XPS.¹ This is highly unlikely to be observed if the contamination was present in the whole sample.

The loose aggregation in the case of the CCM solid compared to the dense packing of the other may be explained by the high explosiveness of the decomposition as already discussed

¹An exclusion is impossible if solely based on the Si 2p region since it overlaps with the one of La 4d. However, no adequate photopeak was detected in the range being generally attributed to Si 2s.

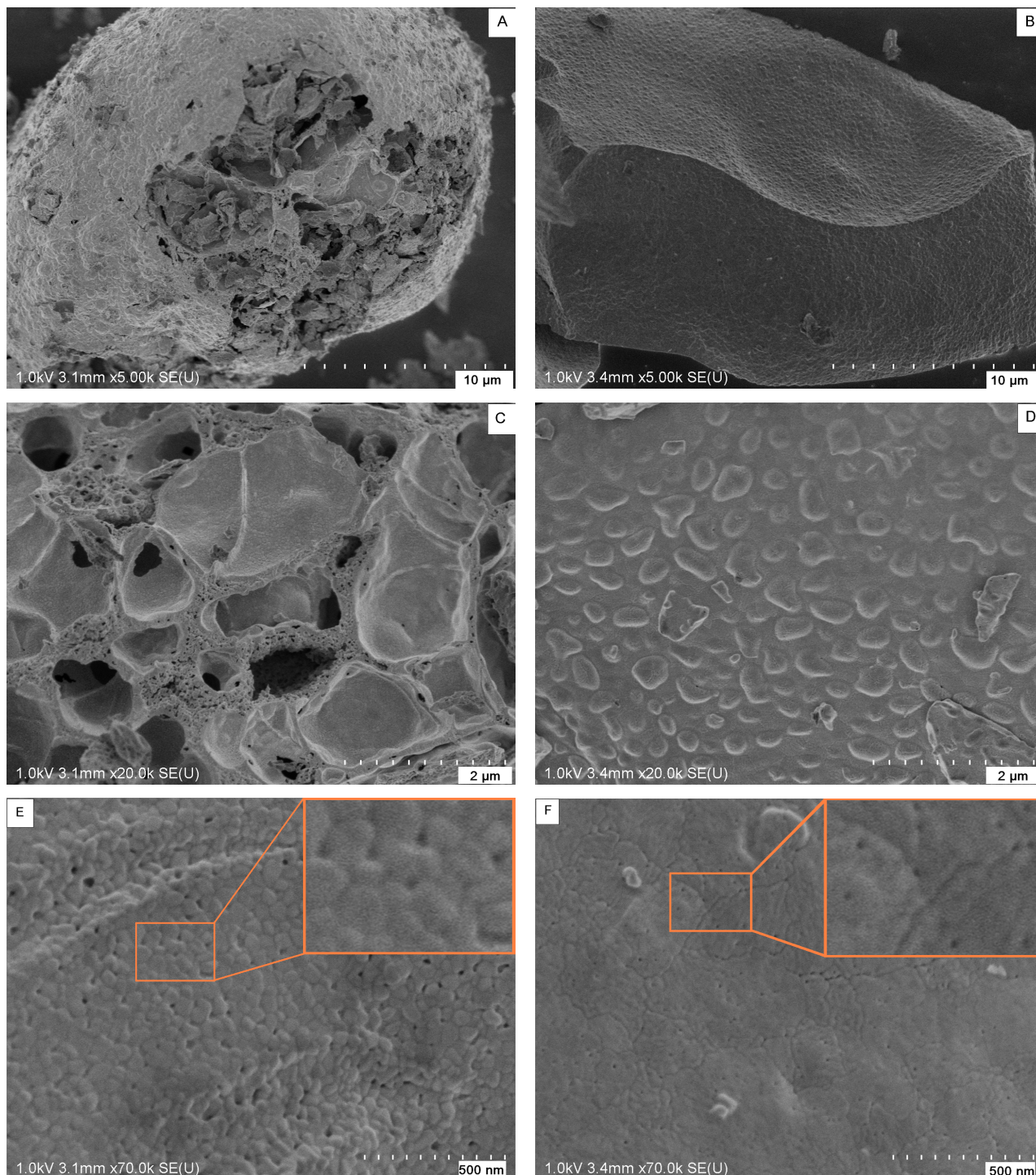


Figure 4.5 – Scanning electron micrographs of LaFeO_3 synthesized via CCM (left) and HAM air (right).

in Section 4.1.1. This leads to the high contribution of macropores and is in contrast to the slower weight loss process observed for the HAM air sample. Moreover, the smaller particles formed during HAM air are more suitable for dense packing leading to the predominance of mesopores.

4.1.4 Chemical composition at the surface

As already stated in Chapter 3, the elementary analysis confirms the nominal composition of the perovskite prepared by CCM. The chemical composition at the surface of the LaFeO_3 perovskite samples was analysed by X-ray photo-electron spectroscopy (XPS).

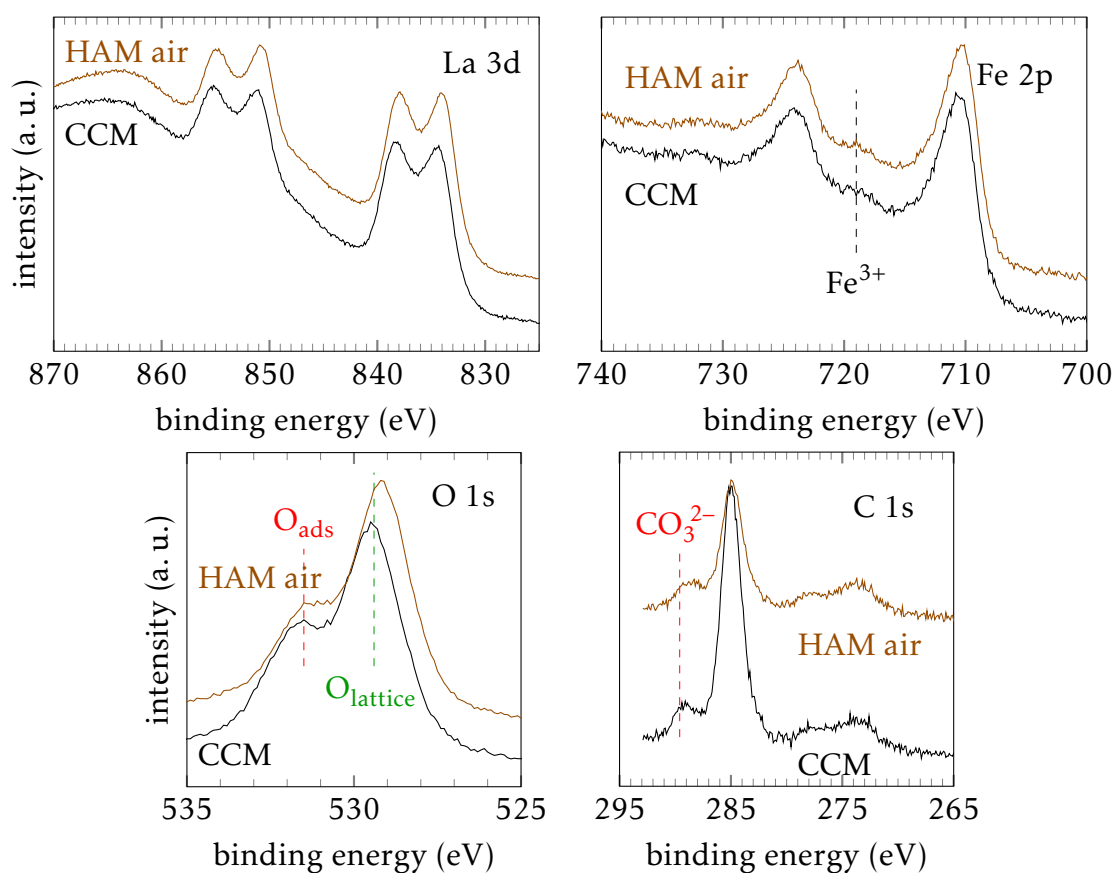


Figure 4.6 – La 3d, Fe 2p, O 1s and C 1s photopeaks of calcined LaFeO_3 prepared by CCM and HAM air.

The corresponding XPS spectra for as-synthesized catalysts are shown in Fig. 4.6. The La 3d photopeaks do not show any remarkable change in shape depending on the synthesis method. The multiplet structure is well defined for both solids. A shift of the B. E. values is discernible for the Fe 2p photopeak for the perovskite obtained by HAM air (Table 4.3). Regardless of the employed solvent, the Fe 2p photopeak envelopes of both LaFeO_3 samples show the characteristic Fe^{3+} satellite at 719 eV.

Concerning the oxygen species at the surface of the perovskite solids studied at the O 1s core level, 2 components are detected. In both cases the major contribution can be attributed to lattice oxygen ($\text{O}_{\text{lattice}}$), whereas adsorbed oxygen species (O_{ads}), i. e. surface O_2^{2-} , O_2^- , hydroxyl and carbonate species, present a lower amount. C 1s photopeaks also reveal the presence of 2 distinct components. The carbon at the surface of the solids can be

mainly classified as adventitious carbon species as they are always found. A non-negligible contribution of carbonate species is detected in addition.

Table 4.3 – Comparison of surface compositions and photopeak maxima (XPS) of calcined LaFeO₃ prepared by CCM or HAM air.

synthesis method	$x_{\text{La}}/x_{\text{Fe}}$		B. E. (eV)			at. %	
	ICP	XPS	La 3d _{5/2}	Fe 2p _{3/2}	O 1s	O _{lattice} ^a	C _{CO₃²⁻} ^b
CCM	1.01	2.13	834.3	710.8	529.5	55	13
HAM air	n. a.	2.23	834.1	710.1	529.2	65	20

^a O_{lattice} + O_{ads} = 1.

^b C_{CO₃²⁻} + C_{adventitious} = 1.

Spectral decomposition results for O 1s and C 1s core levels are reported in Table 4.3. While higher amounts of adsorbed oxygen species (O_{ads}) are detected for the LaFeO₃ sample prepared by CCM, it seems to present a lower contribution of carbonate species.

Moreover, the XPS measurements revealed a surface La enrichment (compared to Fe) for both LaFeO₃ samples as shown in Table 4.3.

4.1.5 Conclusion

The influence of the solvent used to dissolve the precursors and to allow for complexation during sol-gel synthesis, i. e. water or a hydroalcoholic solution of EtOH and water, on the physico-chemical properties of the LaFeO₃ was investigated. After calcination in air flow at 600 °C, no detectable crystalline phase segregation was observed by XRD beside the orthorhombic LaFeO₃ structure for any of the LaFeO₃ samples. Furthermore, the surface composition of the perovskite is mainly unchanged as evidenced by XPS measurements.

On the other hand, marked differences were observed concerning the textural properties. While both solids present similar specific surface areas and cumulative pore volumes, their isotherms and the respective pore size distributions differ significantly. While the CCM solid is mainly a macroporous solid with only low amounts of mesopores, the perovskite obtained by hydroalcoholic method presents a broad hysteresis due to a high contribution of mesopores in the structure. These findings were confirmed by electron microscopy.

The CCM sample is composed of in average bigger particles which form loose aggregates. This leads to the formation of the observed macropore predominance. The sample obtained by HAM air consists of lower-sized particles which are more densely packed forming compact blocks with lower-sized mesopores all over the solid.

These differences can be explained by the different behaviour during the decomposition and calcination. As evidenced by TGA/DSC measurements, the decomposition of the CCM precursor proceeds much faster with a strong exothermic reaction compared to the HAM air precursor. This could explain the formation of aggregates of bigger particles which form holes in the scale of macropores between each other. In contrast to the CCM solid, the HAM air perovskite is composed of small particles which form dense blocks with mesopores due to a slower and more controlled decomposition/calcination step.

The attenuation of the decomposition process of the perovskite precursor in the case of the HAM air synthesis is assigned to the formation of a more stable precursor complex in hydroalcoholic medium.

4.2 Influence of the template

In order to obtain perovskite catalysts with a controlled porosity and possibly higher specific surface area, a synthesis method using macro-structuring agents (MSM) was explored with quasi monodisperse polymer spheres as templates. On the one hand, they were carried out using polystyrene spheres (PS, $d = 400$ nm, 200 nm and 130 nm), on the other with smaller polymethylmethacrylate spheres (PMMA, $d = 80$ nm) (2 examples shown in Fig. 4.7).²

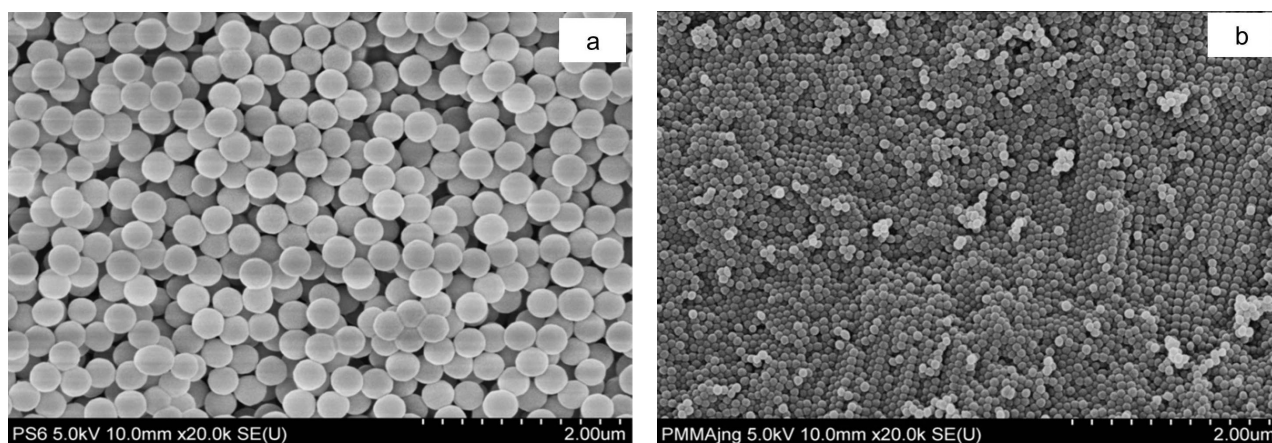


Figure 4.7 – Scanning electron micrographs of PS and PMMA spheres as used for MSM syntheses. Exemplarily shown for PS ($d = 200$ nm, a) and PMMA spheres ($d = 65$ nm, b)^[7]

This macro-structuring method (MSM) is based on the HAM synthesis route but includes a supplementary step of impregnation of dried polymer spheres before slow evaporation in a climate chamber at fixed temperature (40 °C) and relative humidity (r. h. = 30 %) (s. scheme in Appendix, Fig. A.2 and protocol in Section 2.1.3).

Calcination was performed in 2 parts, the first under inert atmosphere, the second under air flow. The reasons will be explained in the following. For further comparison, an HAM sample was prepared without using a template but under otherwise the same conditions. This sample has been labelled HAM N_2 .

Moreover, one sample, labelled MSM_{cooling}, was prepared introducing an intermediate cooling before the atmosphere switch to investigate the influence of preventing an exothermic reaction due to the switch to air flow, i. e. oxidising conditions, at high temperature.

4.2.1 Thermal analysis of the template

After the template has been impregnated by the metal-nitrate-citrate precursors, a hybrid organic-inorganic precursor is formed and needs to be transformed into a homogeneous solid-phase material. Hence, a thermal treatment is required, leading to the removal of the organic porogens and the generation of a macroporous skeleton generated by the polymer spheres' imprinting. This means that the inorganic network has to be sufficiently rigid before the decomposition of the organic template occurs to prevent it from collapsing. The polymer spheres were therefore characterised by TGA/DSC in order to determine an optimal calcination procedure to obtain the perovskite solids with controlled porosity.

²The polymer spheres were not synthesized in the framework of this PhD but provided by the UCCS laboratory (Abdelali Zaki). See [7] for synthesis details.

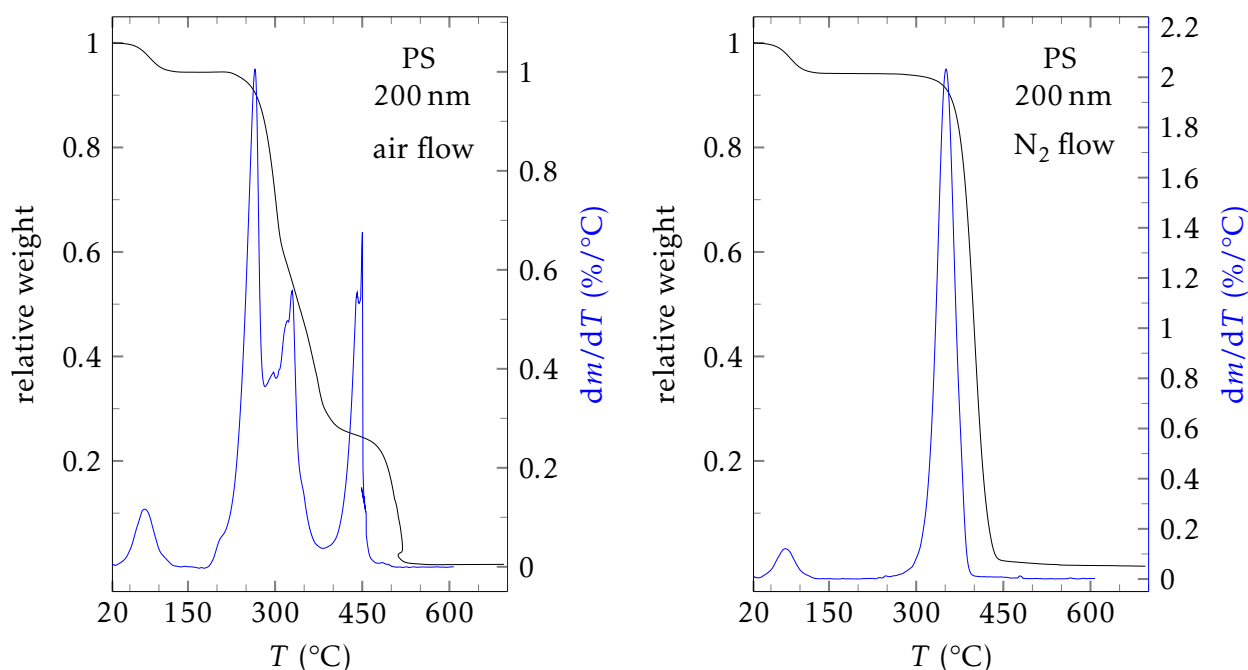


Figure 4.8 – TGA/DSC of PS spheres ($d = 200$ nm) recorded under air and N_2 flow. A problem with the highly exothermic reaction caused the last “weight loss” in the machine under air flow.

The thermograms presented in Fig. 4.8 were recorded during the decomposition of PS spheres with $d = 200$ nm under air and N_2 flow. As expected, the choice of the calcination atmosphere has an influence on the polymer decomposition mechanism. Whereas the decomposition of the spheres is taking place in a single step under inert atmosphere (N_2 flow) between 300 °C and 440 °C, several weight losses assigned to the decomposition of organic compounds were identified under oxidising atmosphere (air flow; 200 °C to 380 °C and 400 °C to 460 °C).^[7]

The observed differences in the decomposition temperature confirm the presence of 2 distinct mechanisms. Under N_2 atmosphere, the absence of oxygen does not allow the oxidation of carbon and hydrogen into CO_2 and H_2O . As a result, the polymer decomposition starts at higher temperature with the production of light hydrocarbons and carbon as reported before.^[8] On the contrary, in the presence of oxygen this step is strongly attenuated. The polymeric chains are oxidised in CO_2 and H_2O at much lower temperature. Sulfate groups (coming from the initiating agent $K_2S_2O_8$) will generate the formation of carbonaceous subproducts that will be fully decomposed during the highest temperature oxidation step.

This is the reason why, we performed the first calcination step under N_2 flow to hold off the polymer’s decomposition as long as possible until formation of a solid framework. A slow heating ramp (1 K min^{-1}) then allows for a gentle oxide formation. 5 h after reaching the final calcination temperature, the gas is switched to air resulting in the decomposition of the residual carbonaceous species and a final perovskite phase formation.

Fig. 4.9 shows the results of the thermal analysis under air or N_2 flow (corresponding to the HAM air or 1st part of HAM N_2 calcination procedure respectively) of the dried precursor of the $LaFeO_3$ perovskite prepared by HAM synthesis.³

³Corresponding TGA/DSC analyses on a MSM precursor were not performed. The non-negligible influence of the exothermic perovskite precursor decomposition on the polymer decomposition – even under inert

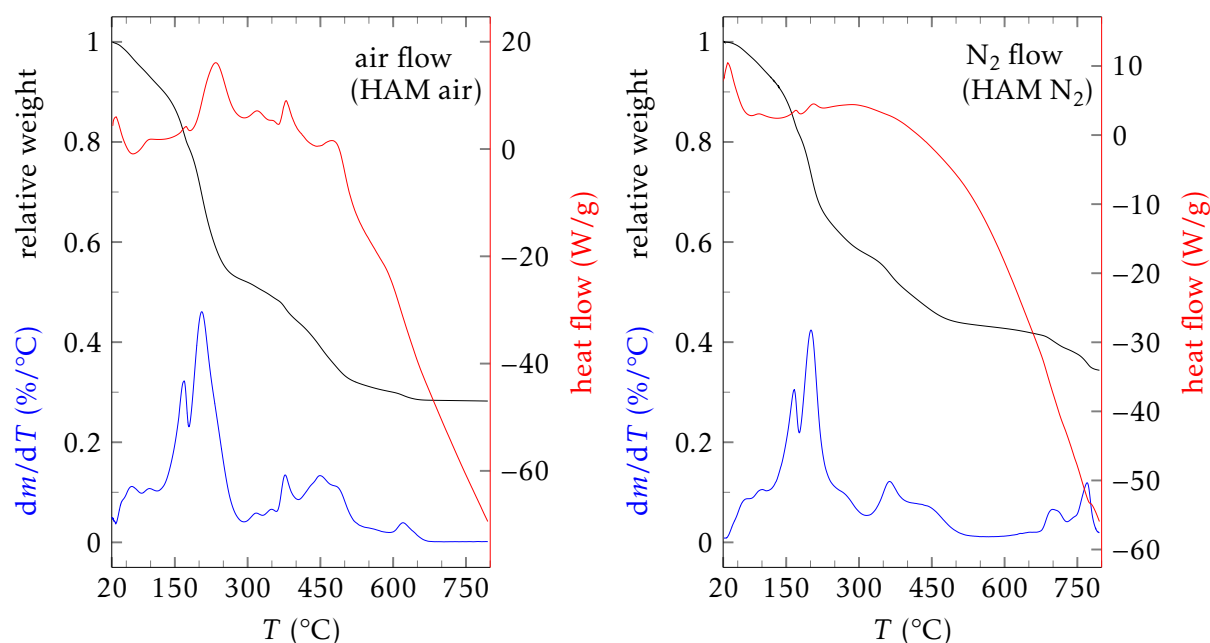


Figure 4.9 – TGA/DSC of HAM precursors of LaFeO_3 under air or N_2 flow. Please note different heat flow scales.

TGA/DSC analyses under N_2 flow reveal overall a similar weight loss behaviour as under air flow. However, weight losses are less pronounced for each step due to the attenuated decomposition under inert atmosphere. This leads to an overall 5% lower weight loss under nitrogen flow compared to the analysis conducted under air flow.

More marked differences are observed at high temperatures. For the sample subjected to N_2 flow, the delayed decomposition caused by the inert instead of oxidising atmosphere of N_2 comes mainly into play at higher temperature. Compounds which decompose at lower temperature under air flow will do so at a higher one under N_2 flow. This is why less peaks are observed under N_2 flow below 650°C . Moreover, the weight losses are decreased in the same temperature range and heat flow measurements indicate less exothermic reactions. Additional peaks are observed above 650°C under N_2 flow. They are correlated to an additional weight loss step (5%) which is not observed in the case of the sample subjected to air flow. These phenomena are attributed to the delayed combustion of residual carbonaceous species.

In order to eliminate these residual carbon species without having to increase the final calcination temperature, and thereby preventing a decrease in specific surface area, a switch to air flow was implemented as discussed above in the calcination procedure for all MSM samples as well as the HAM N_2 solid.

To improve textural properties of the perovskite materials, smaller polymer spheres ($< 100\text{ nm}$, PMMA) were investigated for the use in the macro-structuring method. Nevertheless, it is challenging to decrease the polymer size below 70 nm . In this case the decomposition of the inorganic salts and free citrate species in the precursor falls in the same temperature range as the decomposition of the polymer spheres, leading to a possible collapse of the inorganic network.

atmosphere – has, however, been considered. The use of a precursor having been prepared in hydroalcoholic medium (HAM and MSM) is, nonetheless, assumed to have less deleterious effects for the polymer stability than in the case of using a CCM precursor due to the less exothermic decomposition process (Section 4.1.1).

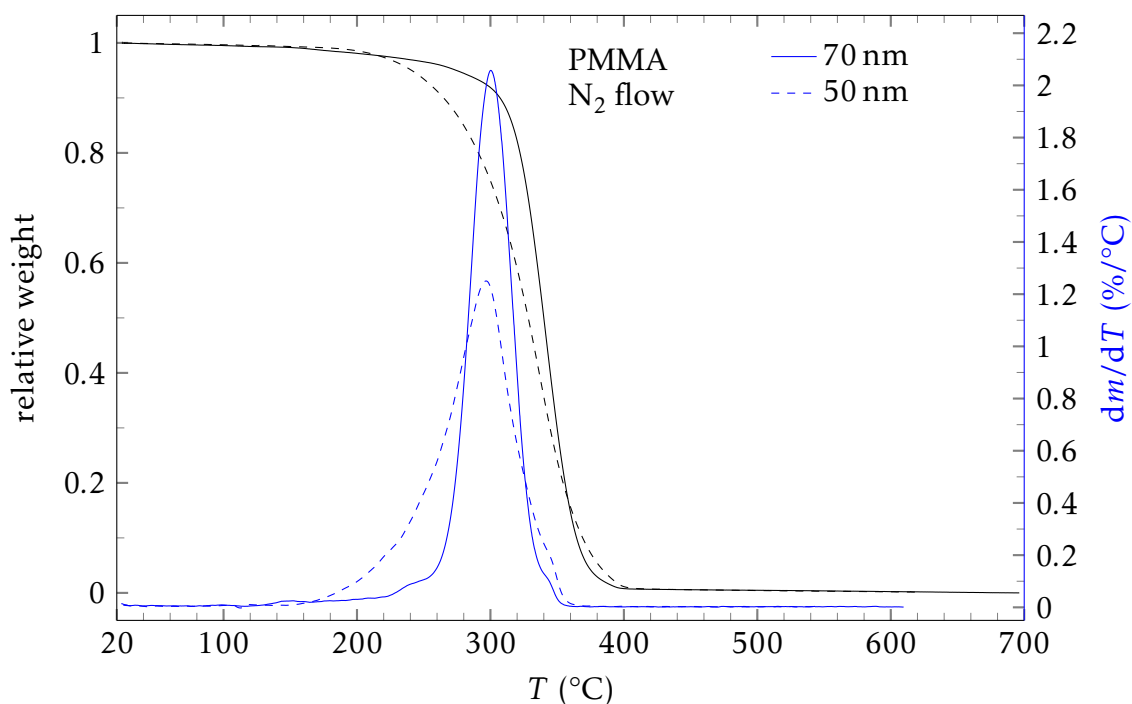


Figure 4.10 – TGA/DSC of PMMA spheres ($d = 50$ and 70 nm) under N_2 flow.

As illustrated in Fig. 4.10, the decomposition step tends to begin at lower temperature for smaller-sized spheres.

It is interesting to note that PMMA is more polar than PS. Thus, though it is easier to handle (less static), it presents the disadvantage of a lower glass temperature (T_g) and $T_{\text{decomposition}}$, e. g. 290°C for the latter in the case of 300 nm spheres (determined under air flow).^[9,10]

In fact, as shown in Fig. 4.10, PMMA spheres of 70 nm diameter are fully decomposed in a single step in a lower temperature domain (200°C to 400°C) than PS, in air (not shown) and in nitrogen atmosphere alike. Therefore, the solidification temperature of the inorganic precursor wall is more difficult using such small-sized polymers, because the decomposition of the nitrates interferes and partly hinders a gentle heating.

In conclusion, thermal analyses confirmed that, as already observed for the HAM air sample (Section 4.1.1), solids prepared by HAM-based syntheses exhibit a by far less explosive and less exothermic decomposition process than the CCM sample. In addition, MSM samples are prepared with temperature sensible templates. Therefore, they were not subjected to a preliminary decomposition step in a muffle oven before calcination.

Based on these results, it was furthermore decided to perform the calcination procedure in 2 parts up to a temperature of 600°C as for the CCM and HAM air solids. The first part of the calcination is conducted under inert atmosphere (N_2 flow), the second under air flow. This second part is implemented in order to eliminate residual carbon species after the perovskite phase generation without having to increase the maximum calcination temperature from 600°C . Additionally to the decreased heating ramp of 1 K min^{-1} , quartz sand is added to the precursor solid to further attenuate the decomposition processes by impeding the generation of hot spots. The influence of preventing an exothermic reaction due to the switch to air flow at high temperature is studied by performing an intermediate cooling before the atmosphere switch for the $\text{MSM}_{\text{cooling}}$ sample.

4.2.2 Bulk/Structural properties

Chemical composition of the bulk

The bulk chemical compositions of calcined macro-structured perovskites were exemplarily assessed by inductively coupled plasma atomic emission spectroscopy (ICP) for the LaFeO_3 sample prepared by MSM PS 200 nm. With $\text{La}_{1.02}\text{FeO}_{3\pm\delta}$, it complies with the nominal composition as expected.

XRD

The orthorhombic LaFeO_3 perovskite phase is obtained for all investigated solids as can be seen by their X-ray diffractograms shown in Fig. 4.11 and the corresponding unit cell parameters determined by full pattern matching (Table 4.4). Thus, the template addition does not prevent the perovskite phase generation.

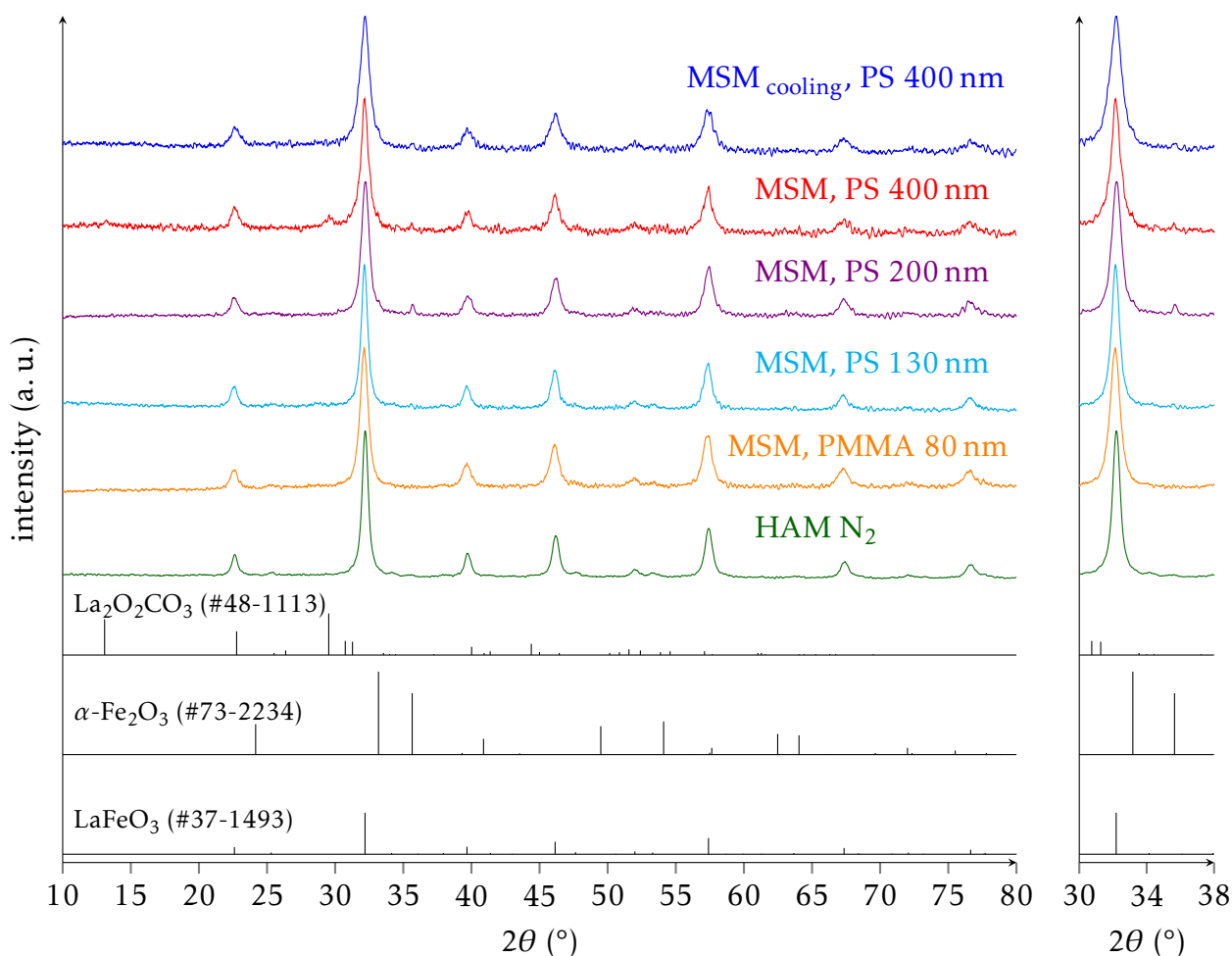


Figure 4.11 – X-ray diffractograms of calcined LaFeO_3 prepared by MSM compared to HAM N_2 .

However, XRD reveals 2 additional peaks at $2\theta = 33.2^\circ$ and 35.7° for the MSM samples using PS spheres of 200 nm and 400 nm diameter (regardless of performing an intermediate cooling or not). A much lower intensity feature at the same diffraction angle of 33.2° is observed for the HAM N_2 solid. These peaks can be attributed to a phase segregation in the form of hematite, $\alpha\text{-Fe}_2\text{O}_3$ (#73-2234).

An additional $\text{La}_2\text{O}_2\text{CO}_3$ impurity (#48-1113) was detected on the MSM PS 400 nm solid, evidenced by the diffraction peaks at 29.5° and 13.1° .

No effect on the structure was observed as a consequence of an intermediate cooling.

Table 4.4 – Comparison of crystallite sizes and unit cell parameters derived from full pattern matching of calcined LaFeO_3 prepared by MSM compared to HAM N_2 .

		d_{cryst} (nm)	a (Å)	b (Å)	c (Å)	$V_{\text{unit cell}}$ (Å ³)
HAM N_2	-	12.4 ± 0.1	5.562	7.858	5.558	242.88 ± 0.27
MSM	PMMA 80 nm	10.3 ± 0.1	5.570	7.850	5.564	243.28 ± 0.31
MSM	PS 130 nm	12.5 ± 0.1	5.562	7.856	5.558	242.86 ± 0.18
MSM	PS 200 nm	10.2 ± 0.1	5.561	7.853	5.557	242.71 ± 0.38
MSM	PS 400 nm	9.9 ± 0.1	5.575	7.826	5.555	242.37 ± 0.27
MSM _{cooling}	PS 400 nm	8.8 ± 0.1	5.567	7.820	5.554	241.79 ± 0.26

Table 4.4 also lists the crystallite sizes obtained by full pattern matching of LaFeO_3 samples prepared by MSM and HAM N_2 . No significant differences are observed between the investigated solids. Slightly lower-sized crystallites are obtained using PS template spheres with an average diameter of 400 nm.

4.2.3 Reducibility

The reducibility of the LaFeO_3 samples prepared by MSM (PS 200 nm) and the HAM N_2 solid were investigated by H_2 -TPR. Both reduction profiles are depicted in Fig. 4.12.

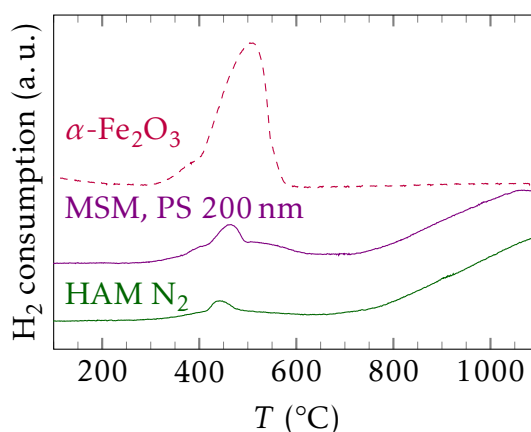


Figure 4.12 – H_2 -TPR profiles of calcined LaFeO_3 prepared by HAM N_2 and MSM PS 200 nm (both 50 mg, 50 ml min^{-1}) compared to commercial $\alpha\text{-Fe}_2\text{O}_3$ (10 mg, 50 ml min^{-1}).

The H_2 -TPR profiles reveal a weak bulk reducibility of the LaFeO_3 solids. A low intensity signal in the range of 300 to 600 °C is discernible for the HAM N_2 sample which intensifies for the solid prepared by MSM PS 200 nm and is tentatively ascribed to $\alpha\text{-Fe}_2\text{O}_3$ with respect to the H_2 -TPR measurement of a commercial hematite reference. This confirms the findings of XRD discussed above that an additional hematite phase is formed even for the HAM N_2 sample for which the XRD signal was less marked.

Table 4.5 – Comparison of H/Fe of calcined LaFeO₃ prepared by HAM N₂ and MSM PS 200 nm (both 50 mg, 50 ml min⁻¹) and commercial α -Fe₂O₃ (10 mg, 50 ml min⁻¹).

solid (synthesis method)	H ₂ consumption ^a (mmol g ⁻¹)	H/Fe ^a total	α -Fe ₂ O ₃ content ^b (wt.%)	T _{max} reduction peaks	
				(°C)	(°C)
LaFeO ₃ (HAM N ₂)	0.32	0.16	1.7	442	> 1100
LaFeO ₃ (MSM PS 200 nm)	0.79	0.39	4.3	466	> 1100
α -Fe ₂ O ₃ (commercial)	18.52	2.96	100	382	512

^a H₂ consumption was integrated over the temperature range of 200 °C to 700 °C.

^b Assuming that the H₂ is totally consumed by a hematite phase.

Table 4.5 lists the total H₂ consumption below 700 °C. An estimation of the hematite content in both samples is conducted by referring to the H/Fe ratios assuming that H₂ is completely consumed by the commercial hematite phase. This allows to roughly quantify the phase segregation. In both solids, only low amounts of this single oxide are detected with a maximum concentration of 4.3 wt.% of α -Fe₂O₃ for the MSM PS 200 nm compared to 1.7 wt.% for the HAM N₂ sample.

It therefore appears that the calcination procedure including a part under N₂ flow favours phase segregation in the form of hematite since neither the CCM nor the HAM air solid showed such segregation. This phenomenon seems to be enhanced by the use of polymer templates.

4.2.4 Textural properties

The textural properties of the templated perovskites and the HAM N₂ solid were investigated by N₂ physisorption and electron microscopy. Results of the physisorption analyses are shown in Fig. 4.13 and Table 4.6.

The reference material obtained without template (HAM N₂) is characterised by the presence of mesopores of uniform size, as indicated by the type IV adsorption isotherm accompanied by a type H1 hysteresis loop (Fig. 4.13A). No perturbation of the isotherm at high relative partial pressure is observed, suggesting that there is no textural porosity coming from particle assembly compared to the CCM sample (Fig. 4.3).

For all templated perovskite materials (MSM PS 130, 200, 400 nm and PMMA 80 nm), a combination of type IV and type II isotherms, indicating the presence of mesoporous and macroporous domains, are observed. The contribution of the type IV isotherm increases with lower macro-template size. As a consequence, the H1 hysteresis loop shape at $0.75 < \frac{p_{N_2}}{p_0} < 0.95$, assigned to the uniformly-sized mesopores of the LaFeO₃ perovskite prepared by HAM N₂, is deformed when a structuring agent is added during the synthesis.

Moreover, in the high partial pressure domain ($\frac{p_{N_2}}{p_0} > 0.95$), regardless of the polymer sphere size, adsorption isotherms are perturbed and reveal the intrinsic macroporosity of the MSM materials (Fig. 4.13A). As confirmed by SEM (Fig. 4.14), these macropores originate from the polymer sphere imprinting.

In the case of the MSM PS 130 nm sample, the hysteresis tends to a type H3 loop (Fig. 4.13A) which characterises solids with narrow slit-like pores.^[11] This may be due to a combination of the low pore sizes of approximately 65 nm (Fig. 4.13B).

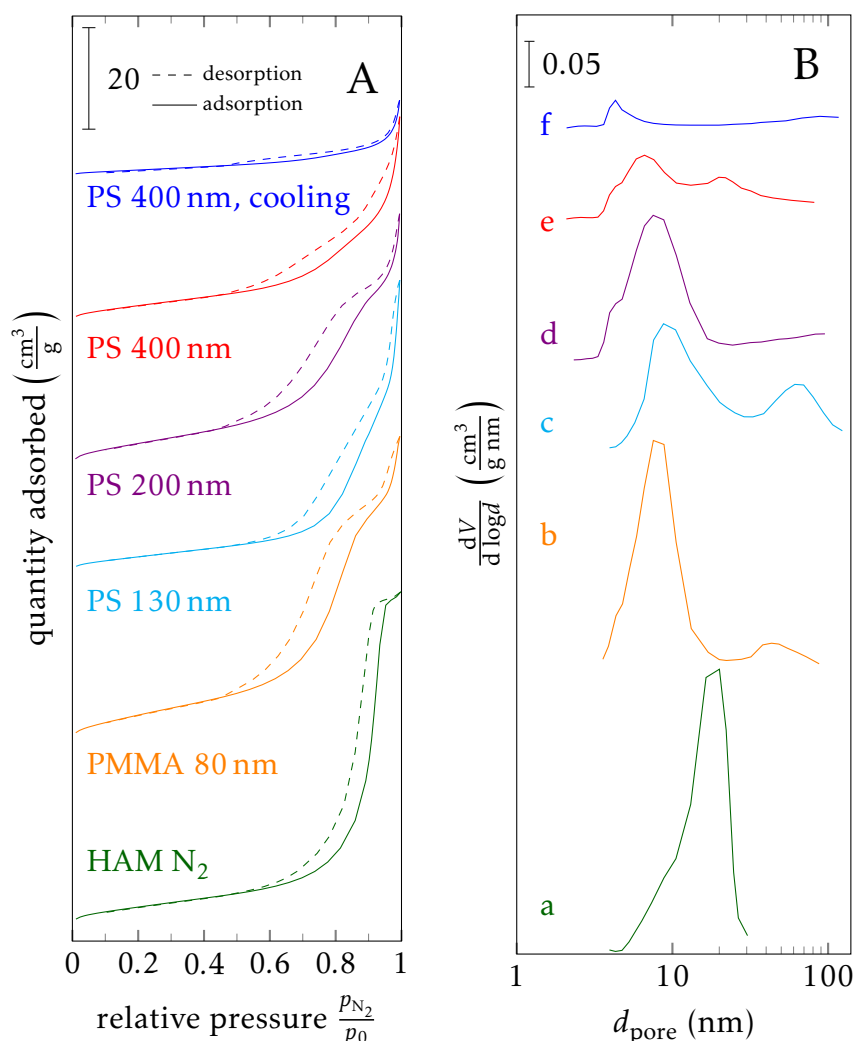


Figure 4.13 – Isotherms (A) and BJH pore size distributions from the desorption branch of the isotherm (B) of calcined LaFeO_3 prepared by MSM compared to HAM N_2 . HAM N_2 (a); MSM PMMA 80 nm (b); MSM PS 130 nm (c); MSM PS 200 nm (d); MSM PS 400 nm (e); and $\text{MSM}_{\text{cooling}}$ PS 400 nm (f)

The corresponding pore size distributions are shown in Fig. 4.13B. Compared to the HAM N_2 sample, different features are observed for all MSM solids. Except for the solid obtained by $\text{MSM}_{\text{cooling}}$ (PS 400 nm), which exhibits a pure type II isotherm (Fig. 4.13A), bimodal pore size distributions are observed. The 2nd maximum is observed in the higher pore size range: MSM PS 400 nm ($d_{\text{pore, local maximum}} \approx 20$ nm), MSM PMMA 80 nm ($d_{\text{pore, local maximum}} \approx 43$ nm) and falling in the macropore range for MSM PS 130 nm ($d_{\text{pore, local maximum}} \approx 61$ nm).

The main maximum of the pore size distribution for all MSM solids calcined without intermediate cooling is in the range of 6.6 nm to 8.7 nm.

Shoulders in the low-sized mesopore range were observed at $d_{\text{pore shoulder}} \approx 3$ nm for the PMMA 80 nm, the PS 200 nm, and PS 400 nm (both calcination procedures) samples. For the LaFeO_3 obtained by $\text{MSM}_{\text{cooling}}$, this shoulder nearly coincides with the (global) maximum of its pore size distribution.

Comparing both LaFeO_3 samples obtained using PS 400 nm templates, the solid prepared including the cooling step before the atmosphere switch presents a kind of narrowing of

the pore size distribution in the mesopore range. This narrowing is, nonetheless, difficult to interpret due to the low overall pore volume ($0.03 \text{ cm}^3 \text{ g}^{-1}$) of the MSM_{cooling} sample. This is also in agreement with its very low specific surface area of $7.1 \text{ m}^2 \text{ g}^{-1}$ as reported in Table 4.6.

Table 4.6 – Comparison of specific surface areas, cumulative pore volume and average pore diameter of LaFeO₃ prepared by MSM compared to HAM N₂.

synthesis method	template	SSA ($\text{m}^2 \text{ g}^{-1}$)	V_{pore} ($\text{cm}^3 \text{ g}^{-1}$)	\bar{d}_{pore} (nm)
HAM air	-	14.0	0.06	7.5
HAM N ₂	-	23.8	0.11	13.2
MSM	PMMA 80 nm	34.4	0.11	8.5
MSM	PS 130 nm	20.3	0.10	14.2
MSM	PS 200 nm	28.8	0.09	9.0
MSM	PS 400 nm	19.1	0.07	10.7
MSM _{cooling}	PS 400 nm	7.1	0.03	10.4

Regarding the cumulative pore volume (Table 4.6), a slight increase is observed for the MSM samples compared to the HAM air perovskite which is more marked for solids obtained using lower-sized templates. The only solid with lower cumulative pore volume is the MSM_{cooling} sample. The mesopores seem to account for the main contribution to the total pore volume. These mesopores are synonymous for interparticulate, i. e. textural, porosity.

Except for the MSM_{cooling} sample, specific surface areas are generally moderate to high (19 to $34 \text{ m}^2 \text{ g}^{-1}$) compared to the HAM N₂ sample (Table 4.6). They are not as high as initially intended if compared to the previously obtained results for LaFeO₃ with PS spheres (160 nm) by Sadakane et al. (45 to $49 \text{ m}^2 \text{ g}^{-1}$).^[12] On the other hand, the MSM PMMA 80 nm and PS 200 nm samples show SSA in the range reported by Sadakane et al. and Qin et al. (25 to $30 \text{ m}^2 \text{ g}^{-1}$) obtained with PMMA spheres of 185 nm to 415 nm diameter^[13,14] and calcined at the same temperature of 600 °C. The not as high SSA are suspected to be the consequence of the relatively big template spheres. The thereby created macropores do not yield the same increase in specific surface area as the same equivalent amount of additional smaller mesopores would provide.

Using a template during synthesis leads to structured solids but not to direct replicas of the template as already discussed by Stein et al.^[15] Using a polymer template leads to smaller pore size diameters than the initial size of the structuring agents due to the shrinkage and deformation of the polymer spheres along with inorganic wall contraction during the calcination.

For the MSM solids obtained with polymer spheres of smaller diameter, i. e. PMMA 80 nm and PS 130 nm, the second (local) maximum of the pore size distribution coincides with approximately half the diameter of the template, 43 nm and 61 nm respectively. Indeed, the shrinkage of the template during the calcination process yields pores which are about half as large as the initial polymer sphere diameter in agreement with reports in literature on PMMA spheres.^[16] This template shrinkage explains why no local maximum is observed for the MSM PS 200 nm sample since 100 nm-sized pores are out of range to be determined by N₂ physisorption. The same consideration holds true for the solids obtained using PS 400 nm templates.

By analogy, the additional pore size distribution maximum at ≈ 20 nm observed for the PS 400 nm sample obtained without intermediate cooling during calcination (Fig. 4.13B) cannot

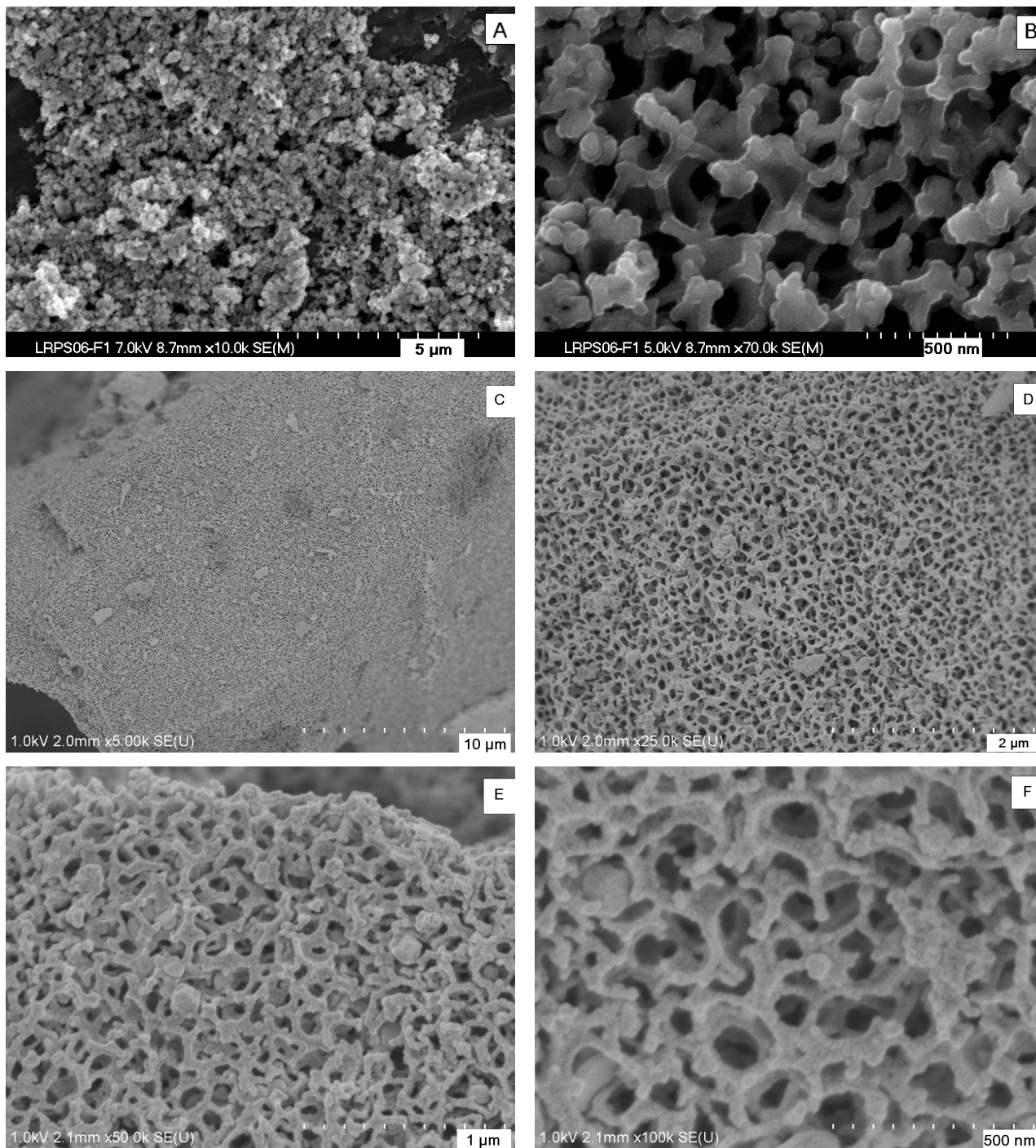


Figure 4.14 – SEM of LaFeO₃ synthesized by MSM with PS spheres: 400 nm (A, B) and 200 nm (C-F).

be explained by the diameter of the template. These pores may be so-called windows between adjacent macropores created by the close contact of neighbouring template spheres due to the compacting of the polymer spheres during the impregnated template sedimentation and drying process, followed by the shrinkage during calcination.⁴ It is, however, more probable that they are generated by partial deformation of the porous structure leading to less and especially lower-sized pores.

Complementary SEM analyses were performed for the MSM samples prepared with PS spheres of 200 and 400 nm diameter Fig. 4.14. Both solids clearly show the impact of the use of template spheres. The enhanced and more homogeneous porosity of the perovskites is evident. The MSM PS 200 nm sample presents a porous sponge-like network (Fig. 4.14). Even though no intermediate cooling step was performed a homogeneous network is obtained. The pore diameters correspond to approximately $d_{\text{template}}/2$ in agreement with the results of N_2 physisorption for the solids obtained with smaller template spheres. This phenomenon is due the progressive deformation and shrinkage of the polymer spheres during the calcination as discussed above. The MSM PS 400 nm LaFeO_3 solid shows a less homogeneous porous network. A partial collapse of the porous structure leads to strong inhomogeneities. The presence of windows is difficult to confirm. The additional maximum in the pore size distribution of the solid at 20 nm (Fig. 4.13B) could be related to a strong alteration of the macropores.

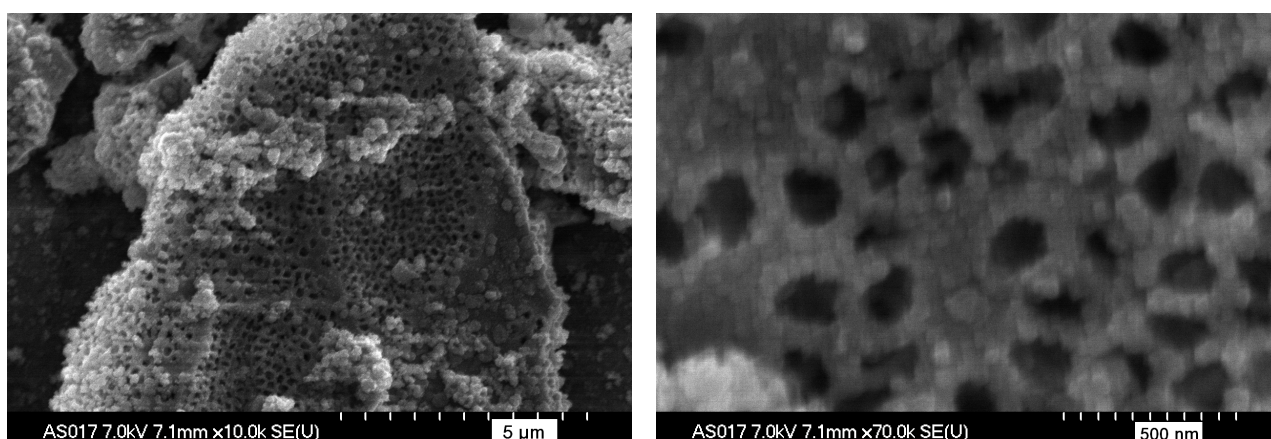


Figure 4.15 – SEM of LaFeO_3 synthesized by $\text{MSM}_{\text{cooling}}$ (PS 400 nm).

Based on these results, the influence of performing an intermediate cooling during the calcination procedure on the textural properties is dramatic (Fig. 4.13). However, instead of increasing the total (open) pore volume, it leads to its decrease as can be seen by the low quantity of adsorbed N_2 (Fig. 4.13A and Table 4.6). Comparing both samples by SEM (Fig. 4.15 compared to Fig. 4.14A and 4.14B), it is clear that the sample obtained respecting the supplementary cooling step ($\text{MSM}_{\text{cooling}}$) yields a more homogeneous porosity throughout the sample whereas partial supplemental alteration seems to have taken place in the solid obtained without this cooling step (MSM). Only small areas show the characteristic spherical pores. In the case of the $\text{MSM}_{\text{cooling}}$ sample, it is clear that pore sizes are approximately 200 nm, i. e. half the diameter of the template spheres, in line with the earlier observations on pore size distributions.

In conclusion, the formation of macroporous perovskite networks was evidenced. The gain in SSA was lower than intended which was ascribed to too big template sizes. However, lower-

⁴A scheme depicting the different pore sizes as created by the templating method can be found in [16].

sized templates are prone to decompose at too low temperatures to allow for a preliminary solidification of the inorganic framework. Therefore, other templates need to be used for this, either non-organic ones as mesoporous silica as used by different groups,^[17–19] which has, however, as already discussed in Section 1.3, the disadvantage of requiring a post-treatment of the calcined catalyst to eliminate the template, or functionalised polymers so as to elevate their decomposition temperature as exemplified by Sadakane et al.^[12] Probably, adhering to an intermediate cooling might improve the textural properties but does not lead to enhanced surface areas as can be seen by the MSM_{cooling} PS 400 nm LaFeO₃ sample which presents a surprisingly low SSA of 7 m² g⁻¹. It should therefore be combined with lower sized templates. A possible collapsing of the inorganic framework cannot, however, be prevented by the intermediate cooling since it is likely to occur before the final calcination temperature is reached, thus before the atmosphere switch.

4.2.5 Chemical composition

The chemical composition of the surface of the HAM N₂ and the MSM samples was assessed by XPS. Fig. 4.16 depicts the results for the La 3d, Fe 2p, O 1s and C 1s core levels of selected samples.

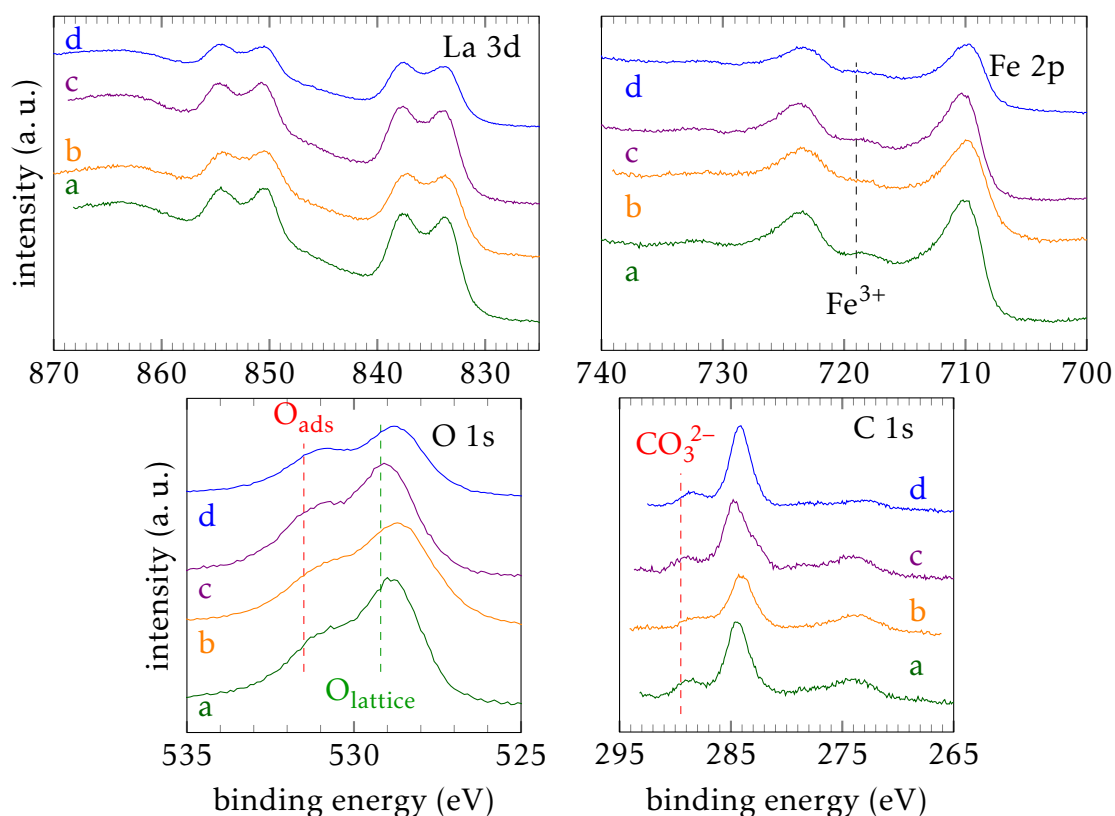


Figure 4.16 – La 3d and Fe 2p photopeaks of calcined LaFeO₃ prepared by MSM compared to HAM N₂. HAM N₂ (a); MSM PMMA 80 nm (b); MSM PS 200 nm (c) and MSM_{cooling} PS 400 nm (d). La 3d_{5/2} was used as reference at 833.7 eV (B. E.).^[20] Since the PMMA photospectra were recorded on a higher resolution XP spectrometer, i. e. present lower intensities, their intensities have been multiplied by 2.

La 3d photopeaks of all analysed perovskite samples show the characteristic multiplet

splitting. Differences in intensity are caused by the use of different XP spectrometers with different resolutions.

Similar spectral features are observed for the Fe 2p photopeaks associated to the characteristic Fe³⁺ satellite at 719 eV.

The O 1s photopeaks, as shown in Fig. 4.16, reveal again 2 components corresponding to lattice oxygen and adsorbed oxygen species. Compared to the MSM samples, a higher contribution of adsorbed species was observed for the HAM N₂ solid (Table 4.7). Lowest amounts of O_{ads} were detected for the perovskite prepared using PMMA spheres as structuring agent (45 at.%).

The B. E. of the C 1s core level are also slightly shifted. A rather asymmetric adventitious carbon component photopeak is observed for the MSM PS 200 nm sample, probably caused by the presence of other than carbonate carbon species on the surface. Spectral decomposition of the C 1s core level yields slightly increased carbonate contributions to the C 1s signal for the HAM N₂ as well as the PMMA-templated perovskite compared to the other solids.

Table 4.7 – Comparison of bulk and surface compositions and photopeak maxima (XPS) of calcined LaFeO₃ prepared by HAM N₂ and MSM. La 3d_{5/2} was used as reference at 833.7 eV (B. E.).^[20]

synthesis method	template	$x_{\text{La}}/x_{\text{Fe}}$		B. E. (eV)			at. %	
		ICP	XPS	Fe 2p _{3/2}	O 1s	C 1s	O _{lattice} ^a	C _{CO₃²⁻} ^b
HAM N ₂	-	n. a.	1.17	709.7	529.0	284.6	47	18
MSM	PMMA 80 nm	n. a.	1.41	710.0	528.7	284.3	65	18
MSM	PS 200 nm	1.02	1.23	710.3	529.1	284.8	54	13
MSM _{cooling}	PS 400 nm	n. a.	1.82	709.7	528.8	284.1	56	13

^a O_{lattice} + O_{ads} = 1.

^b C_{CO₃²⁻} + C_{adventitious} = 1.

As shown in Table 4.7, in contrast to the bulk composition, an enrichment of La at the surface is observed for all solids obtained after partial calcination under N₂ flow (all MSM samples and the HAM N₂ solid). This La excess at the surface of the perovskites is, nonetheless, much less marked than for LaFeO₃ samples prepared by CCM or HAM air ($x_{\text{La}}/x_{\text{Fe}} > 2$). The lowest La enrichment is observed at the surface of the HAM N₂ LaFeO₃ solid.

This lowered surface La enrichment in the case of the HAM N₂ and the MSM samples may be linked to the phase segregation of (finely dispersed) hematite as evidenced by XRD for all MSM solids except those with lowest template diameters and confirmed by H₂-TPR analyses for the MSM PS 200 nm and HAM N₂ samples. However, the non-detection by XRD of low amounts of a segregated hematite phase does not rule out its presence since it is barely visible for the HAM N₂ solid by this technique but was nonetheless detected by H₂-TPR.

4.2.6 Catalytic activity

The catalytic activity of LaFeO₃ samples prepared by HAM N₂ and MSM was tested according to Procedure A (Section 2.3). The corresponding light-off curves are shown in Fig. 4.17 compared to the commercial reference TWC for CO and C₃H₆ under stoichiometric and for NO under rich conditions.

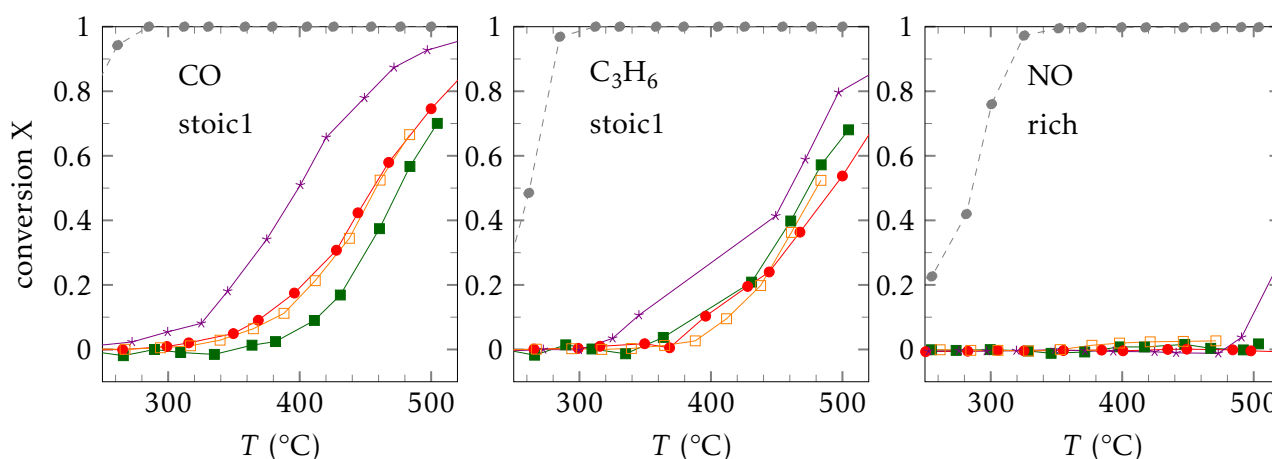


Figure 4.17 – CO, C₃H₆ and NO conversions of LaFeO₃ catalysts prepared by MSM using different templates compared to HAM N₂ under stoichiometric and rich conditions respectively. HAM N₂ (■); MSM PS 400 nm (●); MSM PS 200 nm (★); MSM PMMA 80 nm (□); compared to the commercial reference (●).

Catalysts prepared by hydro-alcoholic method but using a template (MSM), showed higher catalytic performances for CO oxidation than the corresponding sample prepared without a template (HAM N₂). The conversions are not, however, improved if compared to the CCM sample except for the MSM PS 200 nm catalyst (Table 4.8).

Table 4.8 – Temperatures corresponding to 50 % conversion of CO, C₃H₆, C₃H₈, and H₂ (stoichiometric) and NO (rich composition) of LaFeO₃ catalysts prepared by MSM compared to HAM N₂ and selectivities of NO reduction products. CCM results are given for comparison.

	condition	stoichiometric				rich	
		T ₅₀ (°C)	CO	C ₃ H ₆	C ₃ H ₈	H ₂	NO
CCM	-	-	438	463	478	501	- ^a
HAM N ₂	-	-	476	474	489	480 ^b	-
MSM	PMMA 80 nm	-	458	480	462 ^b	447 ^b	-
MSM	PS 200 nm	-	399	461	497	467	518 ^b
MSM	PS 400 nm	-	455	493	513 ^b	496 ^b	-

^a Conversion lower than 50%.

^b T₂₅.

Regarding the hydrocarbons' conversion, differences arise according to the nature of the HC. While CH₄ was not activated for any of the investigated solids in the monitored temperature range as already observed before and propane oxidation performance was decreased compared to the CCM and the HAM N₂ catalysts, propylene oxidation performance was enhanced compared to the CCM and the HAM N₂ catalysts, which also showed CO conversions at lower temperature, i. e. the MSM PS 200 nm catalyst (Table 4.8).

Likewise, no NO reduction is observed for any of the MSM samples (just as for the HAM N₂ catalyst) except for the aforementioned one prepared with PS spheres of 200 nm. At 490 °C, this solid yields a higher N₂ selectivity of 17 % than for the CCM solid. The rest of

the eliminated NO was converted to NH₃ as for the CCM solid and the commercial reference catalyst.

The best catalytic performances were achieved by the MSM PS 200 nm catalyst in agreement with the fact that it presents the best textural properties compared to the other MSM solids. This perovskite presents the highest homogeneity of the porous network and lowest pore diameters which lead to a non-collapsed, non-sintered framework. Enhanced reducibility as induced by the hematite phase segregation might play a role as well but cannot be the decisive reason since other solids prepared by MSM also show such an additional phase but not the same enhancement in catalytic performance. Different dispersions of this single oxide may, nonetheless, occur and play a role.

Generally, the catalytic performances do not seem to be much affected by the PS 400 nm and the PMMA 80 nm template. In the former case, this may be due to the non-homogeneity of the porous network as observed by SEM (Section 4.2.4) in combination with the high diameters of the pores leading to only small gains in specific surface area. The latter case is more surprising to understand since a relatively high SSA of 34 m² g⁻¹ combined with a relatively low surface La enrichment was observed. On the other hand, N₂-physisorption results hint at a partial collapse of the porous network regarding the relatively low amount of macropores compared to the mesopore contribution (Fig. 4.13).

4.2.7 Conclusion

The use of polymer spheres as macro-structuring agents for the LaFeO₃ perovskite synthesis was studied using polystyrene and polymethylmethacrylate beads of diameters in the range of 80 nm (PMMA) to 400 nm (PS) in a hydroalcoholic medium and calcination up to 600 °C in 2 parts, switching between N₂ flow in the first and air flow in the second part, i. e. under MSM conditions. An additional sample was investigated for which the gas switch during calcination was performed after an intermediate cooling (MSM_{cooling}). The obtained solids were compared to a sample obtained under the same conditions but without template, HAM N₂.

For all these samples, no change to the perovskite structure itself is observed by XRD and only minor deviations of the crystallite sizes are observed. However, nearly all solids show a hematite phase segregation as evidenced by XRD and confirmed by H₂-TPR for selected samples.

While all the MSM solids and the HAM N₂ sample analysed by XPS exhibit a surface La excess if compared to Fe, they interestingly, all show a lower La-content at the surface than was detected for the CCM and HAM air solids. This lower surface La enrichment is probably caused by the minor hematite phase segregation as evidenced by XRD (and confirmed by H₂-TPR for MSM PS 200 nm).

Concerning their textural properties, a combination of strong contributions of both macro- and mesopores is evidenced by N₂-physisorption as well as electron microscopy for MSM perovskites. Indeed, apart from the interparticulate mesopores, pores with diameters of approximately $d_{\text{template}}/2$ are evidenced by N₂ physisorption and SEM for solids obtained with smaller-sized and bigger templates respectively. Bimodal pore size distributions are observed for all except the MSM PS 200 nm and the MSM_{cooling} sample PS 400 nm. This can be explained by their higher template diameters. Likewise, the 2nd maximum in the pore size distribution observed for the MSM PS 400 nm sample cannot be assigned to the original imprints left after template decomposition but may be caused by partial sintering effects probably in consequence of the exothermic reaction after the gas switch at 600 °C during

calcination. Additionally, all samples obtained by MSM except the one prepared with PS spheres of 130 nm diameter present a shoulder to their main mesopore peak at approximately 3 nm. The contribution of mesopores is increased and shifted to lower diameters by the use of structuring agents. This is attributed to increased strain on the perovskite phase leading to smaller particles and therefore smaller-sized interparticulate voids, i. e. mesopores.

Regarding the morphology of the samples at the micrometre scale, electron microscopy revealed that homogeneous porous networks were obtained for the MSM PS 200 nm and the MSM_{cooling} sample PS 400 nm. Sintering of the network was observed for the MSM PS 400 nm solid which underlines the beneficial influence of performing an intermediate cooling before switching the calcination atmosphere on the porous network. Surprisingly, while the MSM PS 200 nm perovskite shows an enhanced SSA of $28.8 \text{ m}^2 \text{ g}^{-1}$, the specific surface area of the MSM_{cooling} sample PS 400 nm is clearly decreased ($7.1 \text{ m}^2 \text{ g}^{-1}$), even if compared to the corresponding solid obtained without intermediate cooling ($19.1 \text{ m}^2 \text{ g}^{-1}$). This cannot be explained by the surface compositions, i. e. a higher content of high surface area lanthana at the surface, since all the MSM samples present a relatively low surface La enrichment. The use of smaller-sized templates supposedly leads to the (partial) collapse of the porous inorganic network. This may explain the low catalytic performance of the solid obtained using PMMA spheres (80 nm) despite its high specific surface area.

In general, solids calcined partly under inert gas flow (HAM N₂ and MSM) yielded poor catalytic results under TWC conditions except for the MSM PS 200 nm catalyst. The macro-structured samples yield slightly better catalytic results than the HAM N₂ solid, though.

Best catalytic performances were obtained by the MSM PS 200 nm catalyst. CO oxidation performance was most enhanced for this LaFeO₃ sample. NO reduction performance was also slightly increased as was N₂ selectivity compared to the CCM catalyst.

4.3 Effect of the calcination atmosphere

Another important aspect of the synthesis method is the calcination procedure including the employed atmosphere. Recent studies made by de Jong's group on the incipient wet impregnation method (IWI) have revealed much insight in complex phenomena like migration and sintering of particles which occur during the individual thermal steps of preparation of monometallic Ni/SiO₂ or Co/SiO₂.^[21–25] For example, using model supports of mesoporous silica SBA-15-type, Sietsma et al.^[24–26] concluded that calcination in air is detrimental to obtain a high dispersion of NiO nanoparticles, when the impregnated materials are dried at 120 °C. During subsequent calcination, sintering and migration of precursor species take place, which also results in migration of NiO outside the pores and location on the external surface. The authors associated the degree of migration of oxide particles with the concentration of gaseous products (i.e. H₂O, NO₂ and O₂) evolved during the decomposition of Ni₃(NO₃)₂(OH)₄ to NiO. Interestingly, as NO₂ and O₂ display an inhibiting effect by promoting sintering and migration of NiO leading to pore blockage, H₂O vapours have the opposite effect inhibiting sintering and migration.^[24] Hence, to reach high dispersion of Ni nanoparticles throughout the support, a careful control of each thermal step (solvent impregnation, solvent evaporation, temperature of drying, calcination temperature) but also of the treatment atmosphere is needed to ensure adequate final homogeneous dispersion.

In this Section, the influence of calcining the dried precursors under so-called stagnant atmosphere during the first part of the calcination procedure, i. e. without flow in a pseudo semi-closed system (s. Section 2.1.1 for details), on the morphology of LaFeO₃ perovskites

was investigated first. An investigation was then launched to reach a better understanding of the implications of the stagnant atmosphere calcination. This study involved the preparation and characterisation of LaFeO₃ solids which were calcined under stagnant atmosphere and diluted NO flow during the first part of the calcination. They were compared to the HAM N₂ perovskite.

4.3.1 Effect of calcination under *stagnant* atmosphere

The aim of this investigation is to study the influence of calcining dried precursors obtained under varying conditions (CCM-, HAM- and MSM-based syntheses) under so-called stagnant atmosphere on the morphology and catalytic activity of LaFeO₃ perovskites. The methods will be distinguished by the employed solvent and the use of a template as before and marked by an asterisk * to designate the calcination under stagnant atmosphere, i. e. CCM* (water) and HAM* and MSM* (hydroalcoholic solvent, without and using a PS template (400 nm) respectively).⁵ These solids are compared to the corresponding samples calcined under standard conditions, i. e. air flow calcination for CCM and HAM air and N₂ flow followed by air flow for the MSM perovskite.

Nitrate-citrate precursor decomposition

Fig. 4.18 (top) shows the results of the thermal analysis under stagnant atmosphere (corresponding to the 1st part of CCM* calcination procedure), compared to those under air flow of nitrate/citrate precursor of LaFeO₃ after the drying to a xerogel according to the CCM synthesis.

For both atmospheres, the same weight loss steps as described before (Section 4.1.1) are observed. However, contrarily to the results obtained under air flow, the decomposition of the precursor solid under stagnant atmosphere occurs less abruptly in more resolved steps corresponding to different relative weight losses. After the 1st weight loss attributed to the endothermic water evaporation, under air flow a 2nd weight loss of approximately 60 % occurs corresponding to an exothermic process. A lower weight loss of 35 % is recorded under stagnant air atmosphere. A 3rd weight loss appears (≈ 20 %) which corresponds to a more exothermic process than the one observed under air flow. Less differences are observed for the final decarbonation step, i. e. the elimination of carbonates and other carbonaceous species above 600 °C.

Similar experiments were conducted for the HAM precursor of LaFeO₃. Fig. 4.18 (bottom) shows the results of the thermal analyses under stagnant air atmosphere⁶ or air flow. Results from thermal analysis of the nitrate/citrate HAM precursor subjected to air flow differ very much from the CCM results as was already discussed in Section 4.1. The comparison between the TGA/DSC analyses of the LaFeO₃ HAM precursor under air flow or stagnant atmosphere do not reveal significant changes compared to previous observations on the CCM precursor.

As could be shown, regardless of the presence or not of a gas flow during calcination, the solids prepared in hydroalcoholic medium, i. e. by HAM, present a by far less explosive

⁵The perovskite prepared by HAM* was additionally subjected to an intermediate cooling before the atmosphere switch during the calcination (subscript *cooling*). In the following it is therefore denoted as HAM*_{cooling}.

⁶It has, however, to be kept in mind that (slightly) different conditions reign in the calcination reactor under stagnant atmosphere than in the TGA/DSC analyser since the analyser cannot be operated in quasi semi-closed configuration as shown in Fig. A.1.

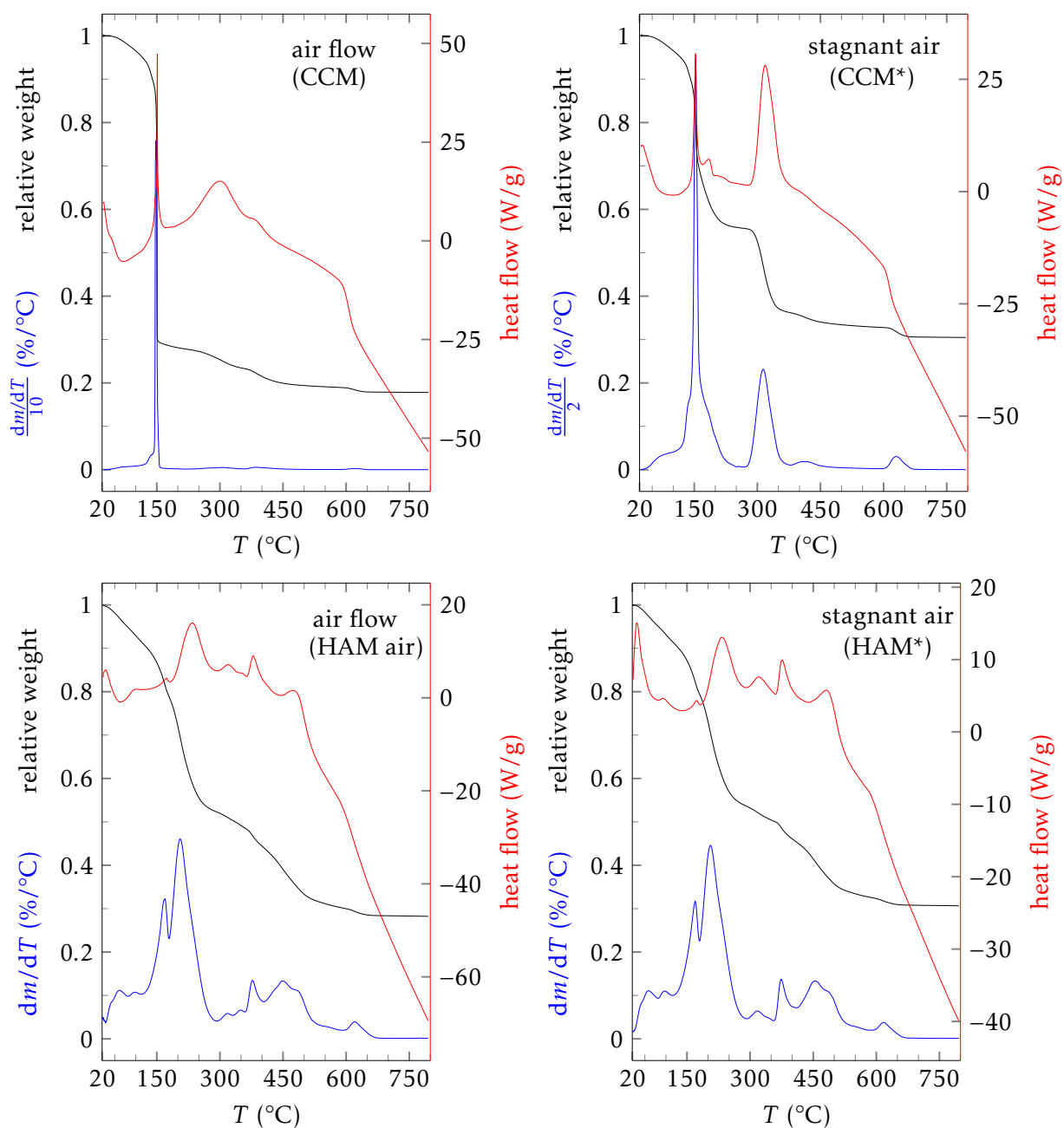


Figure 4.18 – TGA/DSC of CCM and HAM precursors of LaFeO_3 under air flow or stagnant atmosphere. Please note the different scales for dm/dT and heat flow.

and less exothermic decomposition process than the precursors obtained according to CCM synthesis (Section 4.1.1) under air flow. Therefore, they are not subjected to the additional decomposition step in a muffle oven before calcination. The same holds true for the CCM* sample.

Bulk/Structural properties

Chemical composition of the bulk The bulk chemical compositions was analysed by ICP for the LaFeO_3 sample prepared by MSM* PS 400 nm, i. e. the macro-structured perovskite calcined partly under stagnant atmosphere. As expected it is in agreement with the nominal composition ($\text{La}_{1.03}\text{FeO}_{3\pm\delta}$).

XRD XRD measurements show that all calcined catalysts present the expected orthorhombic structure of the LaFeO_3 perovskite (Fig. 4.19). Relative intensities are in line with the reference (#37-1493) and no shifts of the diffraction peaks are observed.

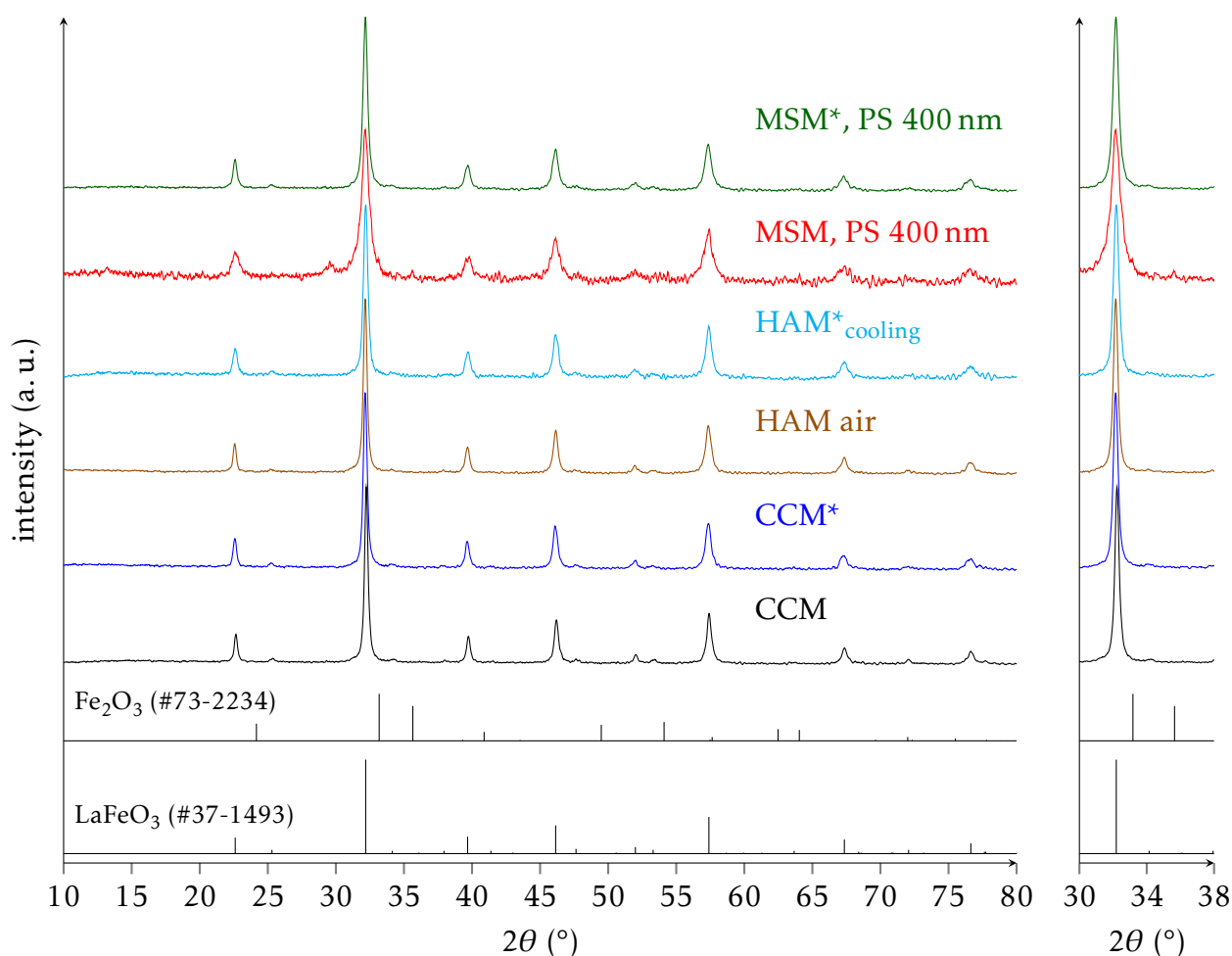


Figure 4.19 – X-ray diffractograms of calcined LaFeO_3 prepared by CCM, CCM*, HAM air, HAM*_{cooling}, MSM, and MSM*. Both samples prepared by MSM-based methods are synthesised using PS spheres of 400 nm diameter.

Apart from the already discussed additional hematite peaks in the case of the MSM sample, no phase segregation is observed. Apparently, the calcination under N_2 flow is at the

origin of the hematite phase segregation of α -Fe₂O₃ in MSM samples as it was also observed for the HAM N₂ solid but is not detected for any of the solids obtained by partially calcining under stagnant atmosphere, even the templated sample.

Table 4.9 – Comparison of crystallite sizes and unit cell parameters derived from full pattern matching of calcined LaFeO₃ prepared by CCM, CCM*, HAM air, HAM*_{cooling}, MSM, and MSM* (both PS 400 nm).

	template (<i>d</i>)	<i>d</i> _{cryst} (nm)	a (Å)	b (Å)	c (Å)	<i>V</i> _{unit cell} (Å ³)
CCM	-	20.1 ± 0.1	5.561	7.858	5.558	242.85 ± 0.17
CCM*	-	20.3 ± 0.1	5.562	7.860	5.558	243.00 ± 0.20
HAM air	-	20.2 ± 0.1	5.553	7.863	5.555	242.58 ± 0.33
HAM* _{cooling}	-	17.1 ± 0.1	5.561	7.850	5.560	242.72 ± 0.16
MSM	PS 400 nm	9.9 ± 0.1	5.575	7.825	5.554	242.29 ± 0.27
MSM*	PS 400 nm	15.8 ± 0.1	5.563	7.861	5.562	243.24 ± 0.20

Table 4.9 lists the results of full pattern matching of LaFeO₃ samples prepared by the different CCM, HAM and MSM variants calcined partly under stagnant atmosphere or completely under air flow. No significant deviations concerning the unit cell parameters or the corresponding unit cell volumes are observed for the samples calcined under stagnant atmosphere. While average crystallite sizes of solids obtained by CCM, CCM* and HAM air are similar (*d*_{cryst} = 20 nm), they are slightly decreased for the HAM*_{cooling} sample (*d*_{cryst} = 17 nm). On the other hand, higher crystallite sizes are obtained by following the MSM* than for the templated solid calcined under non-stagnant conditions (MSM).

Raman spectroscopy XRD analysis of the MSM* solid did not reveal phase segregation in the form of hematite. However, the presence of an amorphous or finely dispersed hematite phase undetectable by the XRD technique cannot be ruled out.

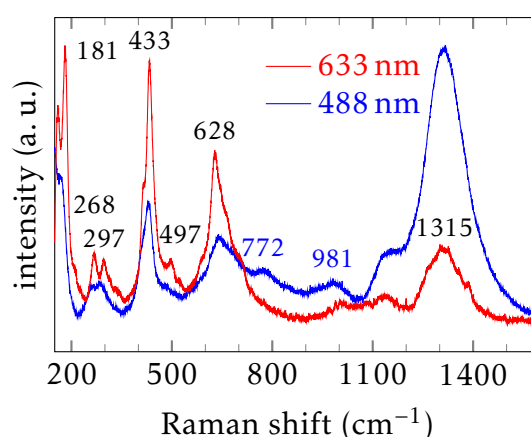


Figure 4.20 – Raman spectra of LaFeO₃ prepared by MSM* excited with $\lambda_{exc} = 488$ nm and 632 nm.

Therefore, Raman spectroscopy was performed on the MSM* solid (Fig. 4.20) in order to detect trace amounts of hematite in analogy with the MSM samples which were calcined under inert atmosphere during the first part of the calcination (Section 4.2.2).

Fig. 4.20 shows 2 Raman spectra recorded after excitation of the MSM^* sample with a blue ($\lambda_{\text{exc}} = 488 \text{ nm}$) or a red (632 nm) laser respectively. Comparing the recorded spectra to the LaFeO_3 ones already discussed in Section 3.1, only few additional lines to the perovskite's are observed. No hematite lines – which would be expected at 225 cm^{-1} , 291 cm^{-1} , 407 cm^{-1} and weaker lines at 498 cm^{-1} and 612 cm^{-1} ^[27] – are evidenced. However, a line at 497 cm^{-1} and its 2nd harmonic at approximately 1150 cm^{-1} are detected which could not be assigned to any Fe single oxide.^[28]

Furthermore, at 770 cm^{-1} and only for an excitation with a blue laser ($\lambda_{\text{exc}} = 488 \text{ nm}$) a line of minor intensity is observed. Bands in this region are generally attributed to metal–O stretch modes of perovskites.^[29] The same is true for the broader line at 981 cm^{-1} which is recorded for both excitation lasers.

In conclusion, XRD results on the absence of a segregated hematite phase were confirmed for the MSM^* sample, further affirming the hypothesis that N_2 calcination has a bigger influence on phase segregation than the use of a template.

Reducibility

The reducibility of the solid prepared by $\text{HAM}^*_{\text{cooling}}$ was investigated by H_2 -TPR, another means of estimating a hematite phase segregation as shown in Section 4.2.3. Fig. 4.21 reveals 2 very slight reduction peaks below $700 \text{ }^\circ\text{C}$. Above $700 \text{ }^\circ\text{C}$, the typical LaFeO_3 reduction occurs as already described in Section 3.2.2. The reduction peaks below $700 \text{ }^\circ\text{C}$ are very low in intensity and therefore do not enhance reducibility of the solid by much (total H_2 consumption = 0.13 mmol g^{-1}). The overall H/Fe ratio below $700 \text{ }^\circ\text{C}$ does not exceed 0.05.

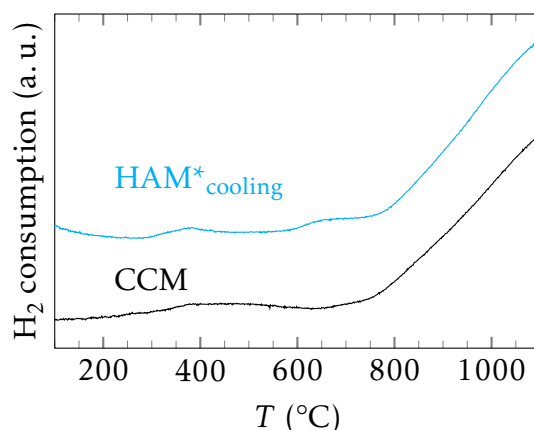


Figure 4.21 – H_2 absorption curves of calcined LaFeO_3 prepared by $\text{HAM}^*_{\text{cooling}}$ compared to the CCM sample (both 50 mg , 50 ml min^{-1}). The results of the CCM sample are given for comparison of magnitude.

The very low intensity peaks cannot be attributed to hematite which is in agreement with the XRD results. At higher temperature, the typical reduction phenomenon of the LaFeO_3 perovskite is observed.

The H_2 -TPR results of the $\text{HAM}^*_{\text{cooling}}$ sample furthermore show that calcination under stagnant atmosphere does not significantly enhance the redox properties of the LaFeO_3 perovskite.

Textural properties

As shown in Fig. 4.22, LaFeO_3 samples present different textural properties if prepared in different solvents and calcined under flow or stagnant conditions. Whereas the solids prepared by CCM and CCM^* display mainly type II isotherms (Fig. 4.22A), the HAM air and $\text{HAM}^*_{\text{cooling}}$ samples show predominantly type IV behaviour (Fig. 4.22C), especially for the perovskite prepared by $\text{HAM}^*_{\text{cooling}}$. The hysteresis is broadest in the case of the HAM air solid.

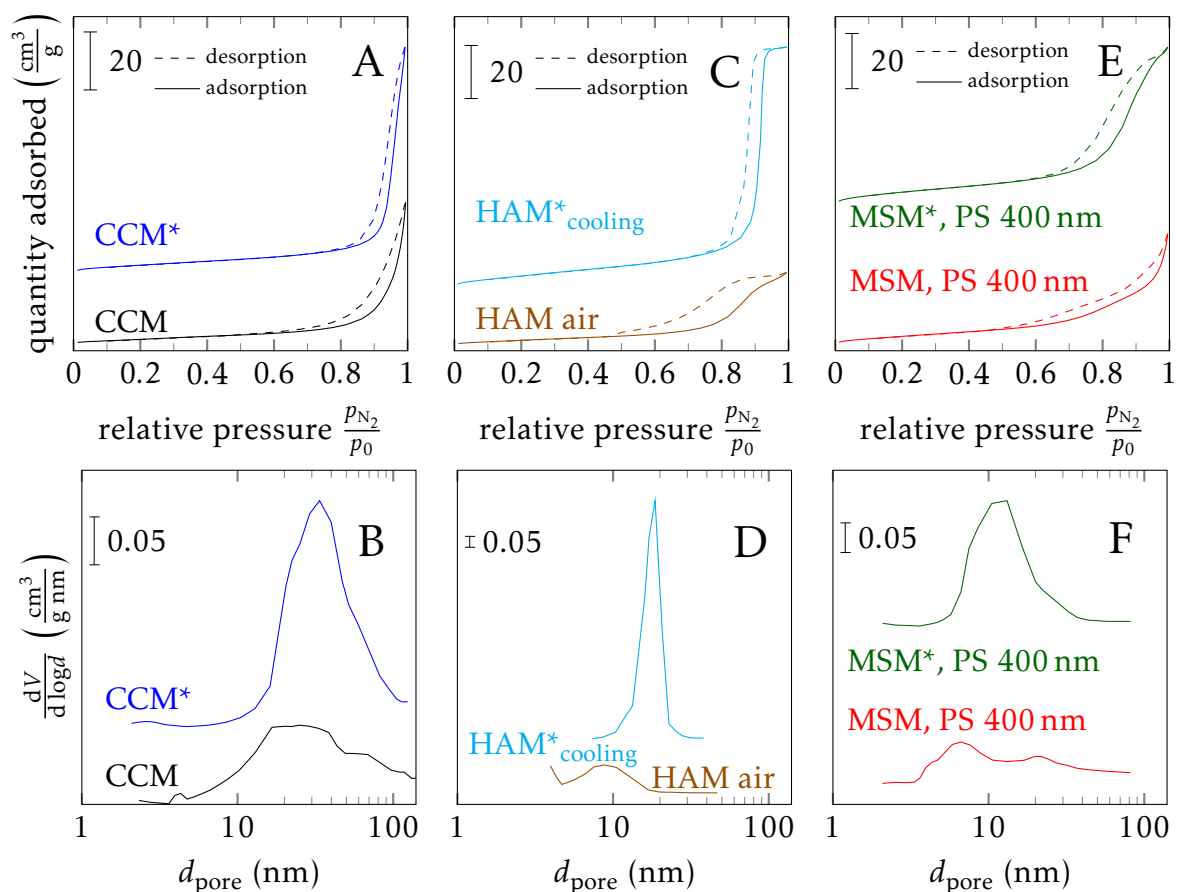


Figure 4.22 – Isotherms (A, C, E) and BJH pore size distributions from the desorption branch of the isotherm (B, D, F) of calcined LaFeO_3 prepared by CCM, CCM^* , HAM air, $\text{HAM}^*_{\text{cooling}}$, MSM, and MSM^* (both PS 400 nm).

Differences are also observed for the pore size distributions. On the one hand, the CCM catalyst shows a very broad distribution (Fig. 4.22B). It is slightly narrowed for the CCM^* perovskite. At the same time a higher total (open) pore volume is expected. This is confirmed by N_2 physisorption measurements listed in Table 4.10. While the specific surface area increases slightly, the average pore diameters are bigger for the solid obtained by CCM^* .

On the other hand, both solids obtained by HAM-based synthesis show narrower pore size distributions (Fig. 4.22D). The predominance of mesopores is evidenced for the HAM air and $\text{HAM}^*_{\text{cooling}}$ perovskites. The HAM^* synthesis method seems to favour the formation of mesopores. In fact, as already apparent from the corresponding isotherms, the $\text{HAM}^*_{\text{cooling}}$ sample shows no macropore contribution at all. In this case, the intermediate cooling before the atmosphere switch during the calcination may also contribute to the narrowing down

Table 4.10 – Comparison of specific surface areas, cumulative pore volume and average pore diameter of LaFeO₃ prepared by CCM, HAM air, HAM*_{cooling}, MSM, and MSM* (both PS 400 nm).

synthesis method	SSA (m ² g ⁻¹)	V _{pore} (cm ³ g ⁻¹)	\bar{d}_{pore} (nm)
CCM	13.9	0.08	20.4
CCM*	16.4	0.13	26.1
HAM air	14.0	0.06	7.5
HAM* _{cooling}	29.6	0.15	16.0
MSM PS 400 nm	19.1	0.07	10.7
MSM* PS 400 nm	27.3	0.10	11.1

of the distribution due to the prevention of an exothermic reaction at high temperature in response to the suddenly increased oxygen content via the air flow. Stagnant atmosphere, again induces an increase in cumulative pore volume ($V_{\text{pore}} \approx 0.15 \text{ cm}^3 \text{ g}^{-1}$, Table 4.10).

Concerning their textural properties, the solid prepared by MSM* shows intermediary behaviour between the perovskites prepared by CCM* and HAM*. As discussed in Section 4.2.4, the MSM sample shows contributions of meso- and macropores due to the use of the polymer macro-structuring agent. Regarding the perovskite prepared by partially calcining its precursor under stagnant atmosphere (MSM*), the macropore contribution is decreased as can be seen from the nearly horizontal plateau of its isotherm at high relative pressure (Fig. 4.22E) and the corresponding pore size distribution (Fig. 4.22F). Instead of these macropores, a high amount of mesopores is formed. In contrast to the MSM solids no shoulder at the lower edge of the mesopore range is observed. The disappearance of the macropores seems to indicate the collapse of the template imprinted macroporous network. This may also explain why the SSA and V_{pore} are not higher than for the HAM*_{cooling} sample (Table 4.10) whereas the MSM results are higher than those of the HAM air solid.

The SSA values of all investigated solids are listed in Table 4.10. They depend strongly on the synthesis method. The samples obtained by calcining partly under stagnant atmosphere exhibit higher SSA than the corresponding samples calcined exclusively under air flow or partially under N₂ flow. This effect is more marked in the case of the HAM*_{cooling} sample for which the highest SSA is obtained. A similar observation was made regarding the V_{pore} . The lower impact of the calcination procedure on the specific surface area of the CCM* solid, in comparison to the HAM synthesis, may be explained by a still strong exothermic decomposition step (compared to the HAM decomposition regardless of the atmosphere) and the thereby created macropores which were tentatively evidenced by N₂-physisorption. The MSM* sample exhibits a slightly lower SSA than the HAM*_{cooling} as already discussed above.

The smallest average pore diameters (\bar{d}_{pore}) are obtained for the HAM air solid ($\bar{d} \approx 8 \text{ nm}$) (Table 4.10). The largest is observed for the CCM* sample ($\bar{d} \approx 26 \text{ nm}$). The HAM*_{cooling} and MSM* solids present intermediary average pore diameters lower than the one of the CCM sample but higher than for the HAM air solid. In general, samples obtained by partial calcination under stagnant atmosphere exhibit higher average pore diameters compared to their corresponding reference solids except for the MSM* solid for which the average pore diameter is sensibly the same. This finding is biased, though, since several distinct maxima in the pore size distribution are observed for the MSM solid as shown in Fig. 4.22F.

The increase in mesopores for the solids obtained by HAM-based syntheses is also evi-

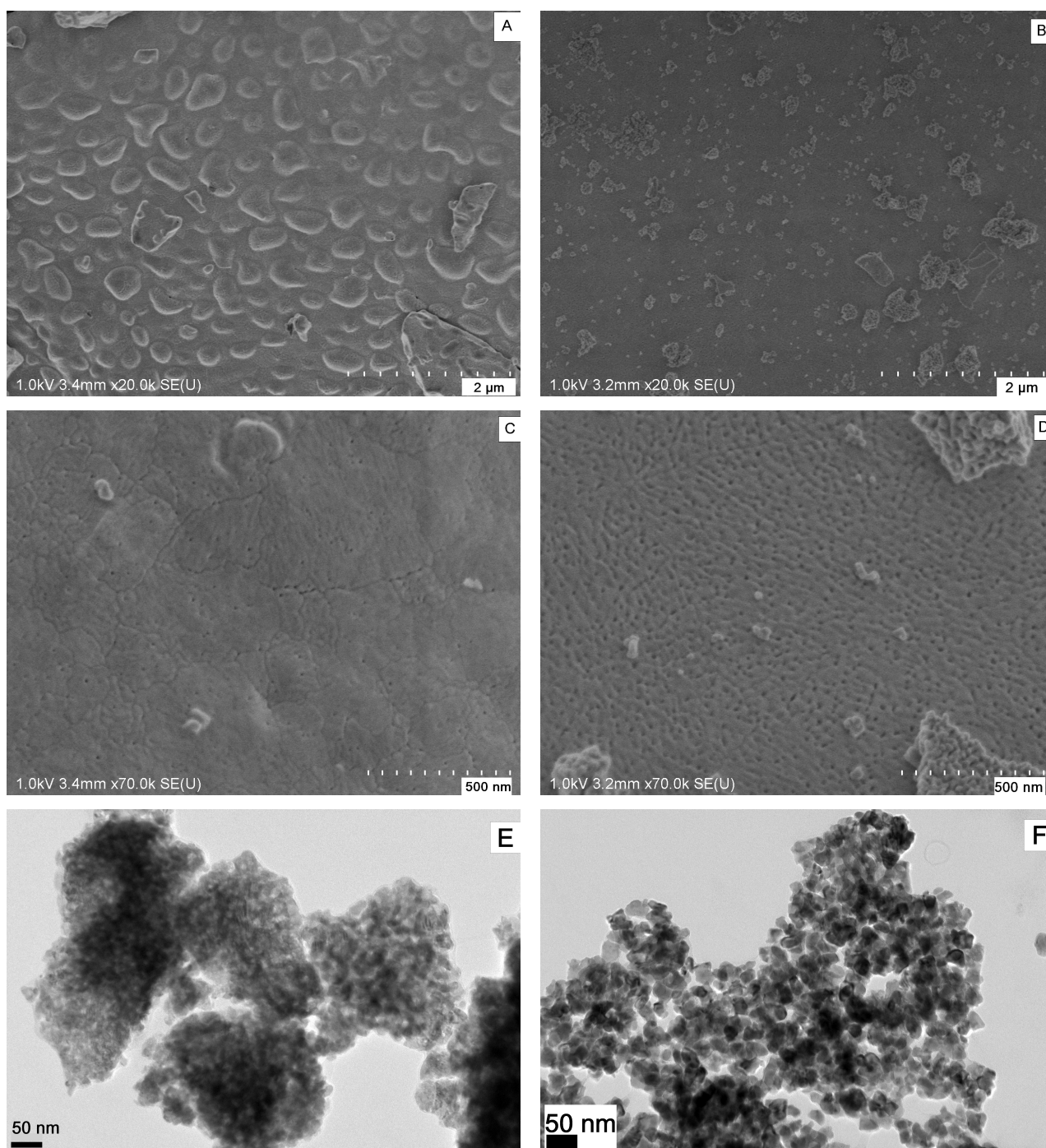


Figure 4.23 – Scanning (A-D, top, middle) and transmission electron micrographs (E, F, bottom) of LaFeO_3 synthesized via HAM air (left) and HAM*_{cooling} (right). Please refer to Section 4.1.3 for a detailed discussion of the textural properties of the HAM air solid, especially the amorphous layer observed in TEM.

denced by scanning electron microscopy (SEM). As shown in Fig. 4.23, both solids obtained by HAM-based synthesis are dense and compact structures strewn with mesopores. The HAM air solid forms little islands on its surface, whereas smaller porous blocks are observed at the surface of the $\text{HAM}^*_{\text{cooling}}$ sample. A very high density of mesopores at its surface is observed which explains its very high SSA of $29.6 \text{ m}^2 \text{ g}^{-1}$.

Transmission electron micrographs comparing the HAM air and the $\text{HAM}^*_{\text{cooling}}$ solids are also shown in Fig. 4.23. Even though crystallite sizes as estimated by XRD are similar for both solids (Section 4.3.1), bigger particles which are readily distinguishable seem to be formed under stagnant atmosphere ($\text{HAM}^*_{\text{cooling}}$) compared to the HAM air sample. The lower sintering effect observed for the $\text{HAM}^*_{\text{cooling}}$ particles may be induced by the intermediate cooling during the calcination.

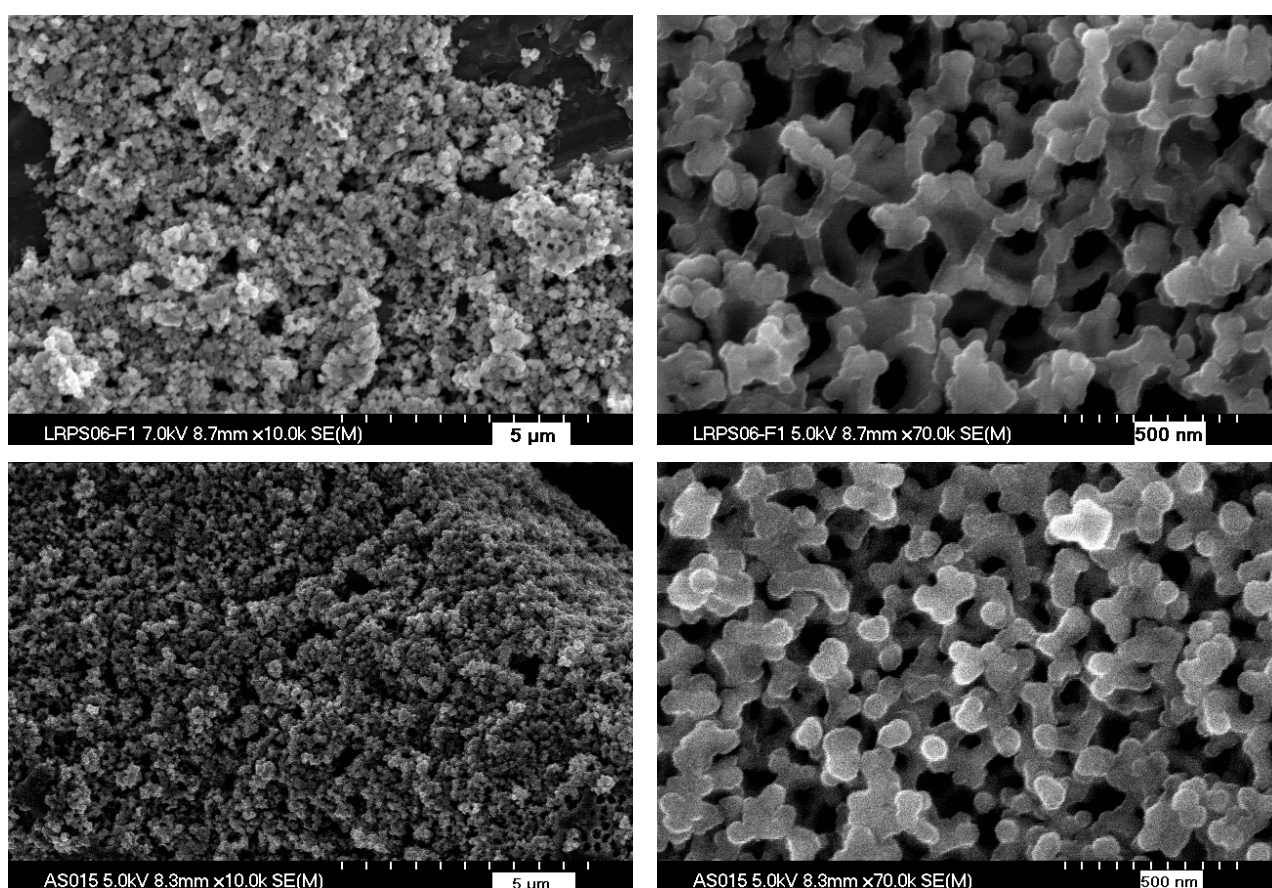


Figure 4.24 – SEM of LaFeO_3 synthesized by MSM (top) and MSM^* (bottom) (both PS 400 nm).

The morphology of the MSM^* solid at the micrometre scale, as revealed by scanning electron microscopy (Fig. 4.24), closely resembles the one of the MSM sample prepared with the same template. However, even fewer domains with truly spherical pores are encountered. Moreover, distances between the agglomerated particle strings are lower than for the MSM sample. This further sintering is probably due to limited mass and heat diffusion due to the missing gas flow creating hot spots. These hot spots lead to enhanced decomposition of the template and thereby to the (partial) collapse of the inorganic framework before its consolidation despite the use of quartz sand and the low heating ramp.

Chemical composition in the bulk and at the surface

Fig. 4.25 presents the results obtained by XPS for the samples calcined under stagnant atmosphere compared to the corresponding solids calcined under flow. In all cases, similar results are evidenced. Multiplet splitting and satellites are observed as expected for the La 3d and Fe 2p photopeaks. The trivalency of the Fe cation is again confirmed by the Fe 2p_{3/2} satellite at 719 eV.

Regarding O 1s and C 1s photopeaks, as before both can be decomposed in 2 components, i. e. O_{lattice} and O_{ads} species and adventitious carbon and carbonate species respectively (Fig. 4.25). Concerning the oxygen contributions, lattice oxygen is the predominant species at the surface of all the perovskites. Nonetheless, differences in the relative abundance of O_{ads} species are observed. As listed in Table 4.11, amounts of O_{lattice} vary from 55 at.% in the case of the CCM to 67 at.% for the CCM* solid. Apart for the CCM and CCM* solids, differences in the amounts of different oxygen species are less pronounced or non-existent between the solid pairs prepared under stagnant atmosphere or flow. The carbonate contribution to the C 1s signal of 20 at.% is the same for all solids obtained by stagnant atmosphere calcination (Table 4.11). This value is increased compared to the CCM and MSM samples.

Table 4.11 – Comparison of surface and bulk compositions, photopeak maxima and abundance of oxygen and carbon surface species (XPS) of calcined LaFeO₃ prepared by CCM, CCM*, HAM air, HAM*_{cooling}, MSM_{cooling} and MSM* (both PS 400 nm).

synthesis method	$x_{\text{La}}/x_{\text{Fe}}$		B. E. (eV)			at. %	
	(ICP)	(XPS)	La 3d _{5/2}	Fe 2p _{3/2}	O 1s	O _{lattice} ^a	C _{CO₃²⁻} ^b
CCM	1.01	2.13	834.3	710.8	529.5	55	13
CCM*	n. a.	2.30	834.4	710.6	529.4	67	20
HAM air	n. a.	2.23	834.1	710.1	529.2	65	20
HAM* _{cooling}	n. a.	2.23	834.1	710.1	529.2	65	20
MSM _{cooling} PS 400 nm	n. a.	1.82	834.6	710.6	529.7	56	13
MSM* PS 400 nm	1.03	2.18	834.1	710.2	529.3	62	19

^a O_{lattice} + O_{ads} = 1.

^b C_{CO₃²⁻} + C_{adventitious} = 1.

Table 4.11 lists the binding energies of the photopeak maxima, the spectral decomposition results of the O 1s and C 1s core levels as well as the atomic La/Fe ratios at the surface as obtained by XPS compared to the one in the bulk for the perovskite solids prepared by CCM, CCM*, HAM air, HAM*_{cooling}, MSM_{cooling} and MSM* (both PS 400 nm). Concerning the surface composition, all samples present the already observed La excess. In contrast to the partial calcination under N₂ flow (MSM and HAM N₂), stagnant atmosphere calcination seems not to induce any change in the La/Fe ratio.

Catalytic reactivity

The catalytic performance of LaFeO₃ catalysts prepared by CCM, CCM*, HAM*_{cooling}, MSM and MSM* was tested according to Procedure A (Section 2.3). The corresponding X-T profiles are shown in Fig. 4.26 for CO and C₃H₆ under stoichiometric and NO under all test conditions. Additionally, temperatures corresponding to 50 % conversion of CO, C₃H₆, C₃H₈, and H₂

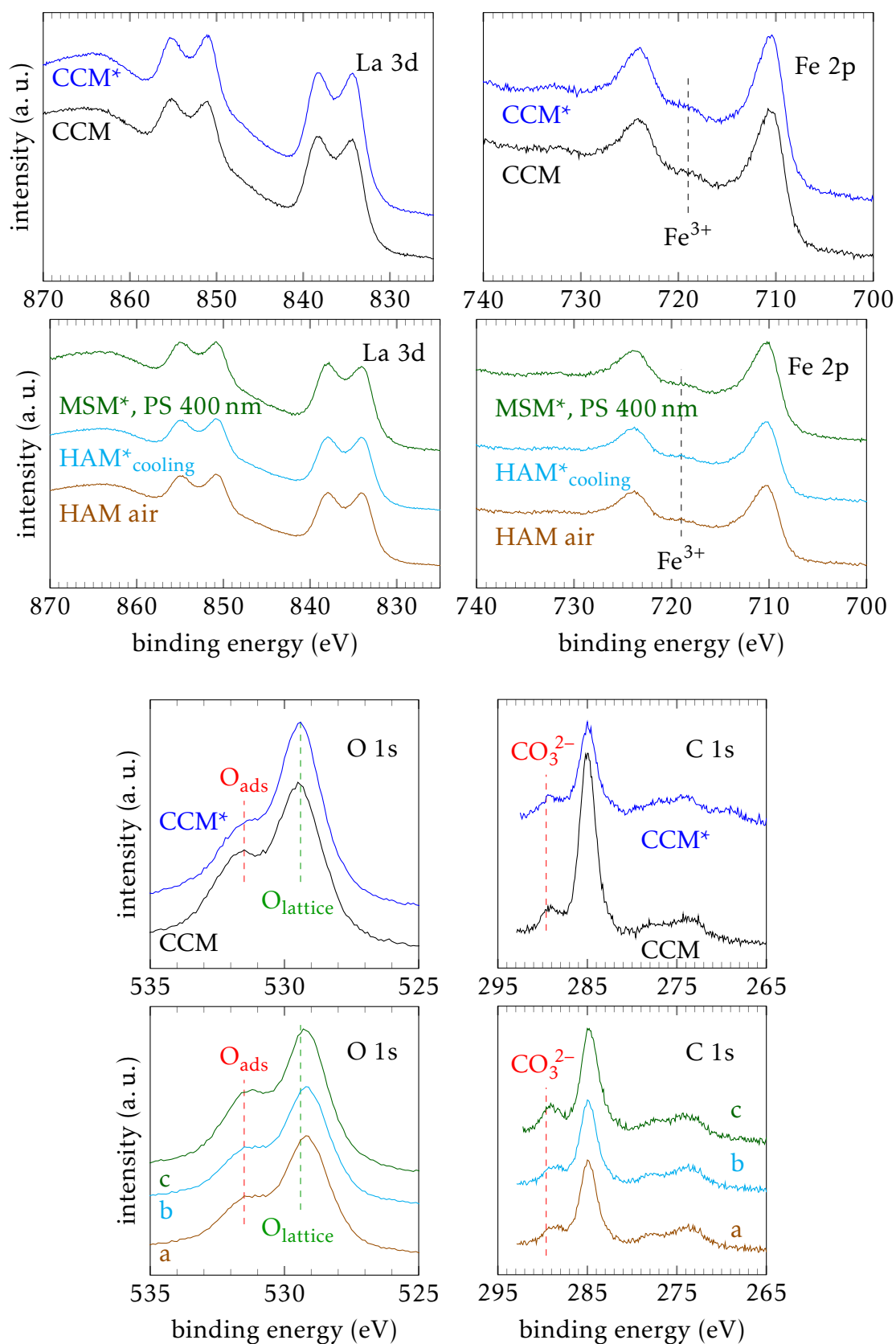


Figure 4.25 – La 3d , Fe 2p , O 1s and C 1s photopeaks of calcined LaFeO_3 prepared by prepared by CCM , CCM^* , HAM air, HAM^* cooling and MSM^* (both PS 400 nm). CCM , CCM^* , HAM air (a), HAM^* cooling (b), and MSM^* (c)

under stoichiometric conditions and NO under rich condition as well as the corresponding selectivities of NO reduction products are reported in Table 4.12.

For all investigated LaFeO₃ perovskites the aforementioned activation of CO at lower temperature than H₂ is again observed as shown in Table 4.12. Likewise, as before, no CH₄ activation is observed for any of the investigated solids in any feed composition under the described testing conditions.

Table 4.12 – Temperatures corresponding to 50 % conversion of CO, C₃H₆, C₃H₈, and H₂ (stoichiometric) and NO (rich composition) of LaFeO₃ catalysts prepared by CCM, CCM*, HAM*_{cooling}, MSM and MSM* (last both PS 400 nm) and selectivities of NO reduction products.

condition	stoichiometric				rich				
	T_{50} (°C)				selectivities at T_S				
	CO	C ₃ H ₆	C ₃ H ₈	H ₂	NO	S_{N_2}	S_{NH_3}	S_{N_2O}	T_S (°C)
CCM	438	463	478	501	- ^a	0.05	0.95	0	507
CCM*	429	463	476	485	- ^a	0.07	0.93	0	507
HAM* _{cooling}	412	446	462	466	503	0.11	0.89	0	507
MSM	455	493	513 ^b	496 ^b	-	-	-	-	-
MSM*	405	465	497	488	460 ^b	0.40	0.57	0.03	493

^a Conversion lower than 50 %.

^b T_{25} .

LaFeO₃ catalysts prepared by CCM or CCM* behave similarly for CO, propylene, and propane oxidation with CCM* being slightly more active in the case of CO. As can be seen in Fig. 4.26, for NO reduction, the sample calcined entirely under air flow presents a slightly higher performance compared to the CCM* one. However, a similarly high NH₃ selectivity during NO reduction (S_{NH_3}) is observed in both cases (Fig. 4.27). Despite the very different calcination process leading to a slightly higher specific surface area and cumulative pore volume accompanied by a changed surface composition, no major change in catalytic performance is observed.

This is in contrast to the catalytic performances observed for the HAM*_{cooling} and the MSM* catalysts. Both solids show higher CO oxidation activity than the CCM and the MSM samples. In the case of the HAM*_{cooling} catalyst, propylene and propane oxidation reactivity is also enhanced compared to both reference solids, whereas in the case of the MSM* solid this enhancement is only observed compared to the corresponding MSM solid.

The main difference observed for the solids prepared by HAM*_{cooling} and MSM* LaFeO₃ catalysts lies, however, in their markedly enhanced NO reduction. As can be seen in Fig. 4.26, NO reduction under rich conditions reaches up to 50 % and over 60 % for the MSM* and the HAM*_{cooling} solids respectively. Furthermore, a non-negligible NO conversion is detected under stoichiometric and lean conditions for both solids.

Concerning the NO reduction products, N₂, N₂O and NH₃ production are observed for the HAM*_{cooling} and MSM* perovskite catalysts. N₂ is the main product except under rich conditions under which NH₃ generation prevails at high temperature as already observed for the commercial TWC (Section 3.5.1). A limited formation of nitrous oxide is observed under all conditions for both catalysts in a limited temperature range. Its maximum concentration

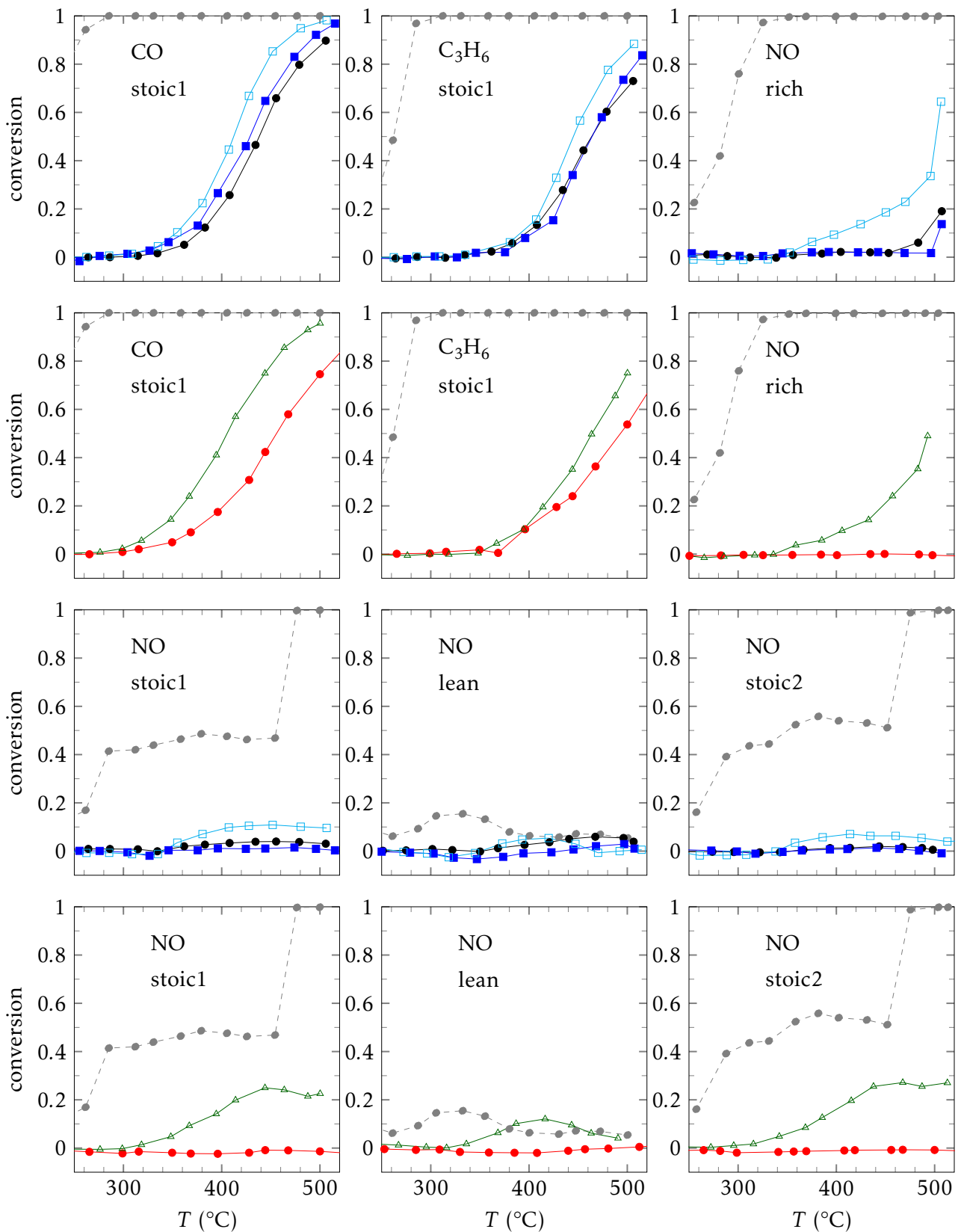


Figure 4.26 – CO, C_3H_6 and NO conversions of LaFeO_3 catalysts prepared by CCM, $\text{HAM}^*_{\text{cooling}}$, MSM and MSM^* (both PS 400 nm) under stoichiometric and all conditions respectively. CCM (●); CCM* (■); and $\text{HAM}^*_{\text{cooling}}$ (□); MSM PS 400 nm (●) and MSM^* PS 400 nm (△) compared to the commercial reference (○)

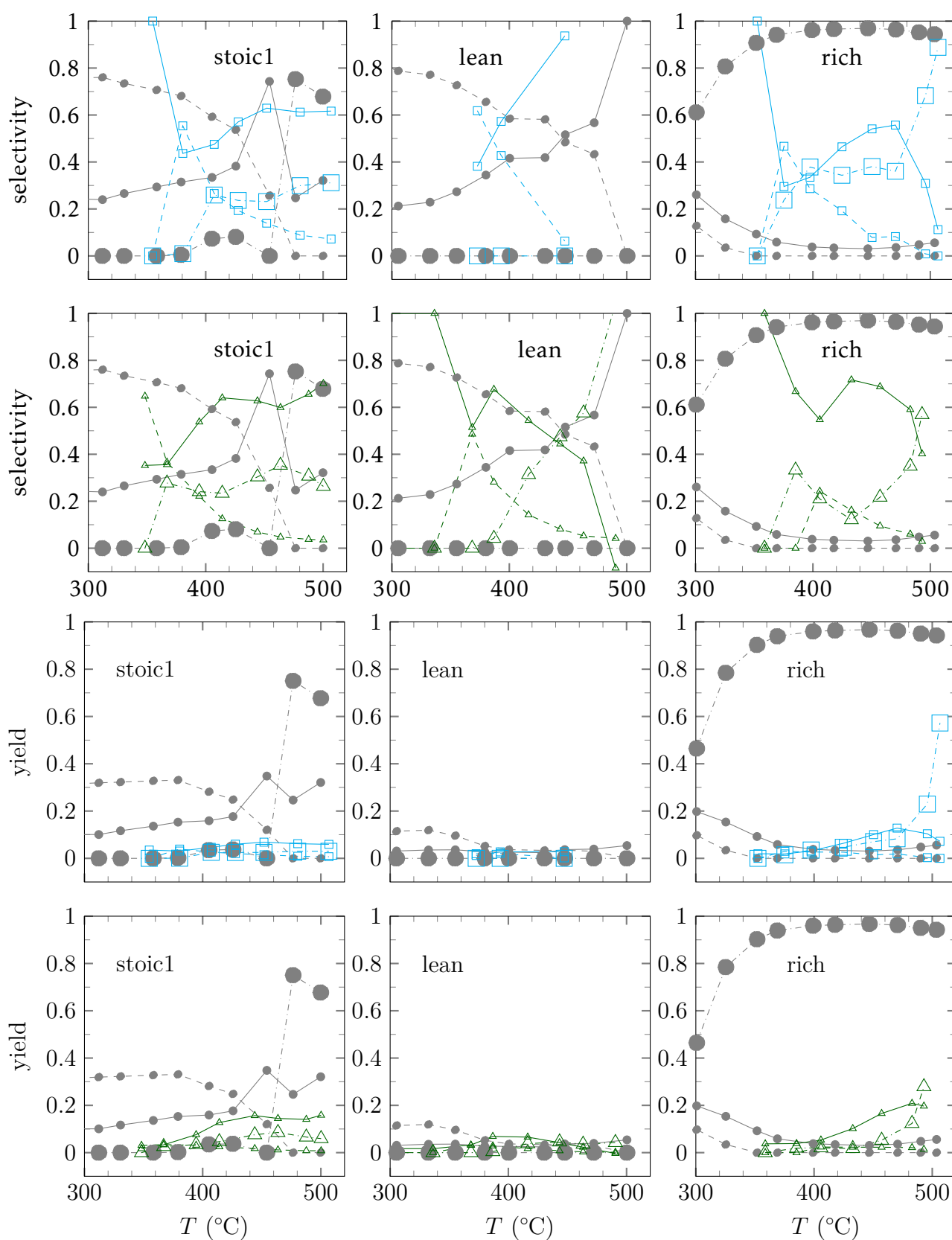


Figure 4.27 – N_2 , N_2O and NH_3 selectivities and yields of NO conversion of $LaFeO_3$ catalysts prepared by HAM*_{cooling} and MSM* (PS 400 nm) under stoichiometric, lean and rich conditions. HAM*_{cooling} (\square) and MSM* PS 400 nm (\triangle) compared to the commercial reference (\bullet); S_{N_2}/Y_{N_2} (solid), S_{N_2O}/Y_{N_2O} (dashed) and S_{NH_3}/Y_{NH_3} (dashdotted, big mark)

does not, however, exceed 12 ppm (MSM*, stoichiometric conditions at 464 °C) or 10 ppm (HAM*_{cooling}, rich conditions at 425 °C) respectively. It is difficult to determine if the NO conversion's set-off is more related to those of hydrogen and oxygen or to the one of propylene since the conversion of all these gases sets in at similar temperatures.

Fig. 4.27 depicts the N₂ yield (Y_{N₂}), N₂O yield (Y_{N₂O}) and NH₃ yield (Y_{NH₃}) of the HAM*_{cooling} and MSM* samples compared to the commercial TWC. In contrast to the latter, regarding solely the N₂ and N₂O generation, N₂ is predominantly produced under all conditions for the perovskites. Fig. 4.27 furthermore reveals that N₂ and N₂O production set in at approximately the same temperature for the HAM*_{cooling} and MSM* perovskites and this under all conditions. A single exception is observed for the MSM* solid under rich conditions for which N₂ formation starts 40 K lower than N₂O production. For both catalysts, an initially higher S_{N₂O} is observed under stoichiometric conditions which quickly decreases below the one of S_{N₂} and drops progressively to (nearly) zero. This peak is also observed under lean and rich conditions but only initially exceeds the S_{N₂} value in case of the HAM*_{cooling} catalyst. This behaviour of (initially) higher N₂O production at lower temperature being succeeded by the predominant conversion to N₂ at higher temperatures is known for the NO conversion under 3-way catalytic conditions as already discussed in Section 3.5.1.

Comparing the HAM*_{cooling} and MSM* perovskite catalysts calcined under stagnant conditions, it becomes clear that higher NO conversions as observed for the MSM* catalyst (Fig. 4.26) – compared to those of the HAM*_{cooling} perovskite – are not detrimental to the S_{N₂} (Fig. 4.27). While the HAM*_{cooling} perovskite showed higher NO conversion under rich conditions, the MSM* solid exhibited clearly higher NO conversions under stoichiometric and lean conditions.

In conclusion, a highly enhanced catalytic performance regarding oxidation and reduction is observed for LaFeO₃ perovskites prepared by an HAM-based synthesis and calcined partly under stagnant atmosphere (HAM*_{cooling} and MSM*) while the same phenomenon was not observed for the corresponding solid prepared by a CCM-based synthesis. The former solids showed promising NO reduction performances even under stoichiometric and lean conditions with relatively high S_{N₂}. The templated solid presents higher NO reduction activity under non-rich conditions, while the non-templated one which was also subjected to an intermediate cooling during calcination exhibits increased oxidation performances and higher NO conversion under rich conditions.

Conclusion

The physico-chemical properties and TWC performances of LaFeO₃ perovskites which were prepared by partly calcining under so-called stagnant atmosphere were investigated. 3 different samples were studied, distinguished by the employed solvent and the insertion of a macro-structuring agent in the synthesis or not.

The bulk perovskite structure is retained for all solids and no phase segregation in the form of hematite was detected either by XRD, Raman spectroscopy or H₂-TPR. Additional lines to the perovskite's were evidenced by Raman spectroscopy for the MSM* sample but cannot be attributed to any Fe or La single oxide. The H₂-TPR analysis of the HAM*_{cooling} perovskite showed a negligible increase in reducibility compared to the CCM solid.

Concerning the surface composition, no change is observed between the samples calcined entirely under flow and those subjected to a partial calcination under stagnant atmosphere. La is still in excess compared to Fe at the surface of all investigated LaFeO₃ perovskites, even for the MSM* solid, in contrast to results obtained for the MSM perovskites (Section 4.2.5).

The calcination under stagnant atmosphere has a high impact on the textural properties of the solids. In all cases higher SSA and cumulative pore volumes are obtained and a narrowing of the pore size distributions is observed. In the case of the CCM* solid, the higher cumulative pore volume is mainly obtained by a higher amount of macropores probably due to the highly exothermic decomposition as in the case of the HAM precursors. On the other hand, for the HAM*_{cooling} and MSM* solids mesopore formation is favoured to the detriment of macropores as could also be confirmed by SEM. Their average pore diameter is higher than for the corresponding solids obtained after calcination under flow and lies above 10 nm. For the MSM* solid, increased sintering of the perovskite network is observed compared to the MSM reference perovskite. Indeed, hot spots may occur during calcination due to the lowered heat diffusion in the absence of gas flow.

Regarding the catalytic performances, the calcination under stagnant atmosphere yielded a surprisingly beneficial effect except for the CCM* catalyst. The HAM-based syntheses modified by the stagnant atmosphere calcination (HAM* or HAM*_{cooling}) yielded promising oxidation and especially NO reduction results.

The very minor differences between CCM and CCM* and the high deviations between the activity of MSM and MSM* or HAM*_{cooling} are in stark contrast to the results of the corresponding TGA/DSC analyses which gave rise to very different decomposition/calcination processes in the former and by comparison nearly superposable ones in the case of HAM, HAM N₂ and HAM* conditions.

Best catalytic performances were obtained by the HAM* and MSM* PS 400 nm catalysts. Oxidation performance was more enhanced for the former, whereas the templated solid calcined under stagnant atmosphere was clearly more performing for NO reduction under non-rich conditions.

Based on these results, a study on the effect of different kinds of calcination atmospheres was launched as discussed in the next Subsection.

4.3.2 Effect of different calcination atmospheres on LaFeO₃ perovskites prepared by HAM

The important synthesis parameter of the calcination procedure including the employed atmosphere will be further investigated in this Subsection. In the framework of this study, 4 different procedures with varying atmospheres were explored. The calcination under air (Section 4.1, samples are denoted as CCM or HAM air) and the calcination procedure during which a switch from N₂ flow (HAM N₂ and MSM) or stagnant atmosphere to air flow is performed (Section 4.3.1, CCM*, HAM*_{cooling} and MSM*) have already been discussed. It has been shown that the hydroalcoholic method yields highly mesoporous solids. This mesoporosity is even enhanced if calcination is performed including a stagnant atmosphere step. Moreover, especially the MSM* LaFeO₃ perovskite showed interesting NO reduction performances under non-rich conditions; under stoichiometric ones NO conversions of up to about 25 % are yielded.

In this study, an attempt is made at understanding this phenomenon. The approach fixes all synthesis parameters but the atmosphere in the 1st part of the calcination process to those used for the MSM* solid, i. e. the drying step is performed under the more controlled conditions of the climate chamber at fixed temperature and humidity (40 °C) and r. h. (30 %) and quartz sand is added during calcination, during which no cooling is conducted before the atmosphere switch. The same conditions were already adhered to for the HAM N₂ solid.

2 additional LaFeO_3 samples were prepared according to this protocol denoted as HAM^* and HAM NO . The 1st part of the calcination procedure was conducted under stagnant atmosphere or diluted NO flow respectively.⁷

The use of diluted NO flow was chosen to mimic one parameter of the supposed “stagnant” atmosphere. Indeed, while the initial condition is air atmosphere, an increasing concentration of decomposition products will reign once the calcination is started. This atmosphere will therefore contain high amounts of nitric oxides, CO_2 , vapour and a decreasing content of oxygen.

Nitrate-citrate precursor decomposition

Fig. 4.28 resumes the TGA/DSC profiles recorded under stagnant air atmosphere, air and N_2 flow of the ground xerogel precursor of LaFeO_3 prepared by HAM synthesis. Results from thermal analysis of the nitrate/citrate HAM precursor exposed to air flow differ very much from the CCM results as was already discussed in Section 4.1 as do those of HAM^* from CCM and CCM^* , whereas the differences between TGA/DSC analyses of the LaFeO_3 HAM precursor under air flow and stagnant atmosphere are negligible (Section 4.3.1). TGA/DSC analyses of HAM-based precursors under air and N_2 flow reveal overall the same behaviour except at high temperatures due to the delayed decomposition of organic and inorganic compounds such as citrate and nitrate species (Section 4.2.1).

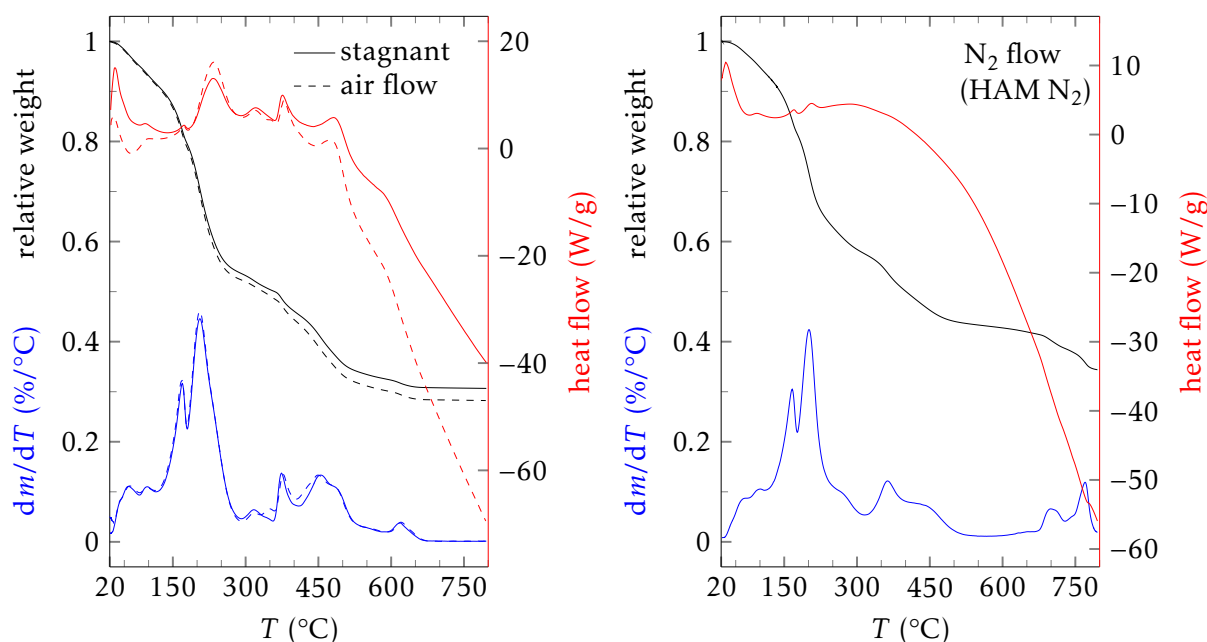


Figure 4.28 – TGA/DSC of HAM precursors of LaFeO_3 under stagnant atmosphere (no flow), air or N_2 flow.

TGA/DSC under NO atmosphere could not be performed due to the toxicity and corrosiveness of this gas. However, regardless of the investigated atmosphere, the solids prepared by HAM present a by far less explosive and less exothermic decomposition process than the CCM sample (Section 4.1.1).

⁷For comparison, the results of the $\text{HAM}^*_{\text{cooling}}$ sample will be shown in case that no analysis results for the HAM^* solid are available.

Structural properties

XRD XRD measurements show that all calcined catalysts present the expected orthorhombic structure of LaFeO_3 (Fig. 4.29). XRD patterns are in line with the reference (#37-1493). Apart from hematite ($\alpha\text{-Fe}_2\text{O}_3$), no crystalline impurities are detected. The formation of this single oxide is evidenced only for the HAM N_2 solid corresponding to ≈ 1.7 wt.% $\alpha\text{-Fe}_2\text{O}_3$ estimated by H_2 -TPR analysis (Section 4.2.3).

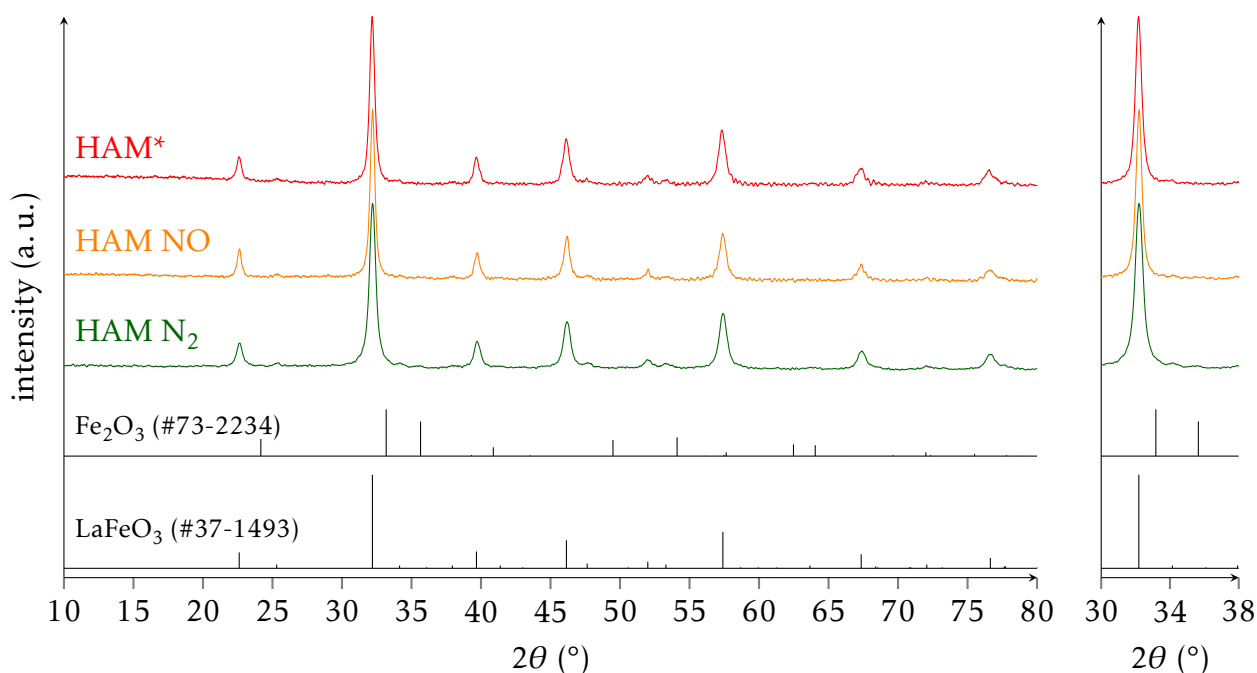


Figure 4.29 – X-ray diffractograms of calcined LaFeO_3 prepared by HAM N_2 , HAM NO and HAM*.

Table 4.13 lists the results of full pattern matching of LaFeO_3 samples prepared by HAM-based syntheses using different calcination atmospheres. No significant deviations for the unit cell parameters are observed.

Table 4.13 – Comparison of crystallite sizes and unit cell parameters derived from full pattern matching of calcined LaFeO_3 prepared by HAM N_2 , HAM NO and HAM*.

	d_{cryst} (nm)	a (Å)	b (Å)	c (Å)	$V_{\text{unit cell}}$ (Å ³)
HAM N_2	12.4 ± 0.1	5.562	7.858	5.558	242.88 ± 0.27
HAM NO	16.3 ± 0.1	5.568	7.833	5.553	242.19 ± 0.18
HAM*	15.5 ± 0.1	5.562	7.867	5.561	243.35 ± 0.21

The estimated crystallite sizes are in the range of 12 to 16 nm for the HAM N_2 , HAM NO and HAM* samples, the lowest value being observed for the HAM N_2 solid. All values are below those obtained for flow-calcined solids except the templated ones.

Raman spectroscopy The structural properties of the solids obtained by HAM NO as well as HAM* were also studied by Raman spectroscopy (Fig. 4.30 and 4.31 respectively). The

spectra were recorded after excitation with a blue (488 nm) and a red laser (632 nm). For both, no phase segregation was evidenced by XRD.

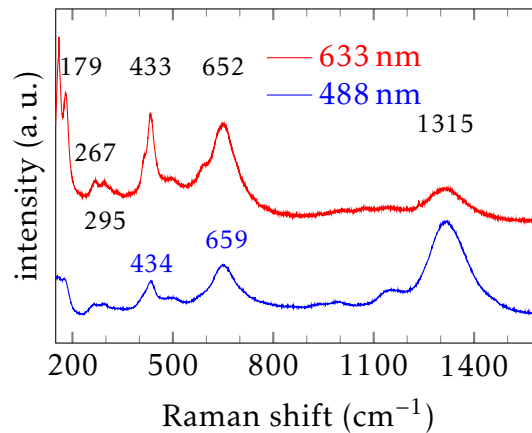


Figure 4.30 – Raman spectra of LaFeO_3 prepared by HAM NO excited with $\lambda_{\text{exc}} = 488 \text{ nm}$ and 632 nm .

As for the CCM and the MSM* sample (Sections 3.1 and 4.2.2), lines generally attributed to the orthorhombic LaFeO_3 structure are detected for both samples.^[29–33] Apart from the strongest lines which are detected at $\approx 180 \text{ cm}^{-1}$, (A-site A_g mode), 433 cm^{-1} (oxygen bending B_{1g} mode), 640 to 650 cm^{-1} (B_{1g} oxygen stretch mode), and 1315 cm^{-1} (2-phonon scattering phenomenon or an oxygen stretching vibration), less intense peaks are observed at $\approx 270 \text{ cm}^{-1}$, 295 cm^{-1} which were assigned to oxygen tilt B_{1g} and A_g modes in literature.^[29–33]

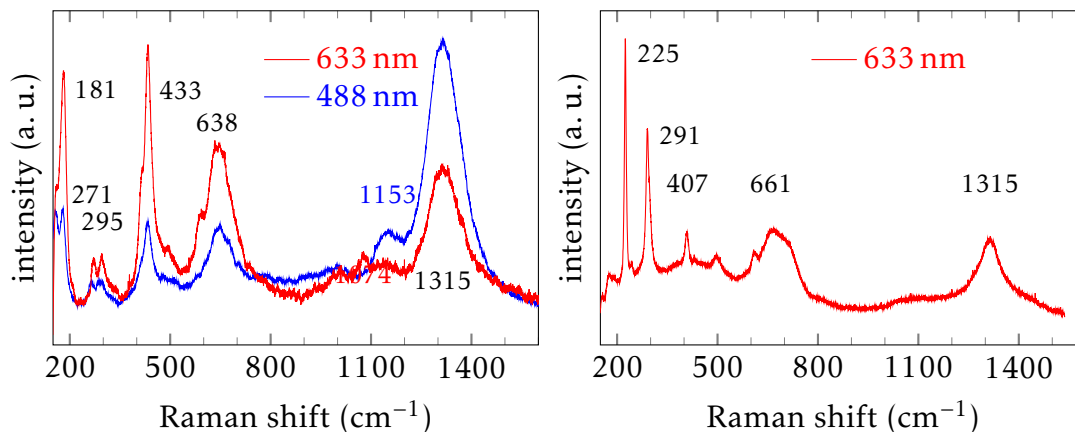


Figure 4.31 – Raman spectra of LaFeO_3 prepared by HAM* excited with $\lambda_{\text{exc}} = 488 \text{ nm}$ and 632 nm . The spectra at the left were measured for zone A while the spectrum at the right was measured for another grain of the sample, called zone B.

Similar to the CCM sample, an additional shoulder at 567 cm^{-1} and a weak line at 1153 cm^{-1} appear. As discussed before, they may be assigned to lanthanum hydroxides for which a line at 582 cm^{-1} was observed before^[34] and its 2nd harmonic.

In agreement with the XRD measurement, the sample prepared by HAM NO consists of an LaFeO_3 perovskite and does not show any significant impurities, especially no additional hematite phase.

Regarding the HAM* sample (Fig. 4.31), 2 different grains of this solid were analysed. While zone A seemingly only contains the perovskite phase as discussed above, zone B shows additional typical hematite modes, partly superposed with those of LaFeO₃. The presence of an α -Fe₂O₃ phase is characterised by Raman lines at 225 cm⁻¹ (*A_{1g}* mode), 291 cm⁻¹ (*E_g* mode), 407 cm⁻¹ (*E_g* mode) and weaker ones at 498 cm⁻¹ and 612 cm⁻¹ (both assigned to the *E_g* mode).^[27]

This finding confirms that hematite impurities may also be present if not detected by XRD. This may be due to the low concentration in the bulk solid or a high dispersion of the single oxide.

Textural properties

Fig. 4.32 depicts the results of N₂-physorption analyses of LaFeO₃ samples calcined under different atmospheres. The samples obtained by HAM N₂ and HAM* show mainly type IV behaviour. Intermediate isotherm behaviour between type II and type IV is observed for the HAM NO sample.

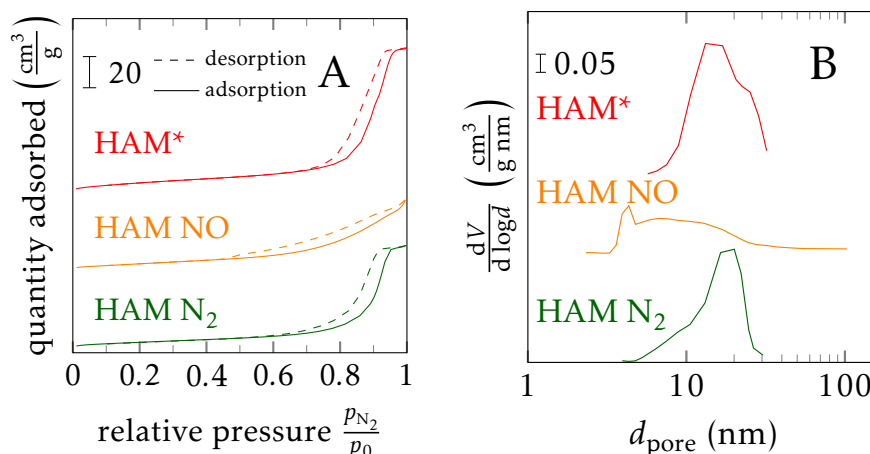


Figure 4.32 – Isotherms (A) and BJH pore size distributions from the desorption branch of the isotherm (B) of calcined LaFeO₃ prepared by HAM N₂, HAM NO and HAM*.

The difference in terms of isotherms between the HAM N₂ and the HAM* solids is less marked than expected. This resemblance may be attributed to a partly similar situation during the calcination due to the decrease in oxygen content over the time. On the other hand, NO_x which are supposed to be generated during the decomposition process are highly oxidising gases.

Table 4.14 – Comparison of specific surface areas, cumulative pore volume and average pore diameter of LaFeO₃ prepared by HAM N₂, HAM NO and HAM*.

synthesis method	SSA (m ² g ⁻¹)	V _{pore} (cm ³ g ⁻¹)	\bar{d}_{pore} (nm)
HAM N ₂	23.8	0.11	13.2
HAM NO	25.6	0.08	8.3
HAM*	33.0	0.16	14.1

In contrast to the MSM samples discussed in Section 4.2.4, a clear predominance of mesopores is observed in the case of HAM NO, HAM N₂ and HAM* perovskites (Fig. 4.32B).

The HAM NO perovskite presents a significant contribution of very low-sized mesopores which is in agreement with its low \bar{d}_{pore} (Table 4.14). The smallest average pore diameters are indeed obtained for the HAM NO solid ($\bar{d} \approx 8$ nm), whereas the HAM N_2 and HAM* solids show slightly higher ones of about 13 to 14 nm.

The HAM N_2 and the HAM* synthesis methods seem to favour the formation of mesopores. In fact, as already apparent from the corresponding isotherms, these samples show no macropore contribution at all.

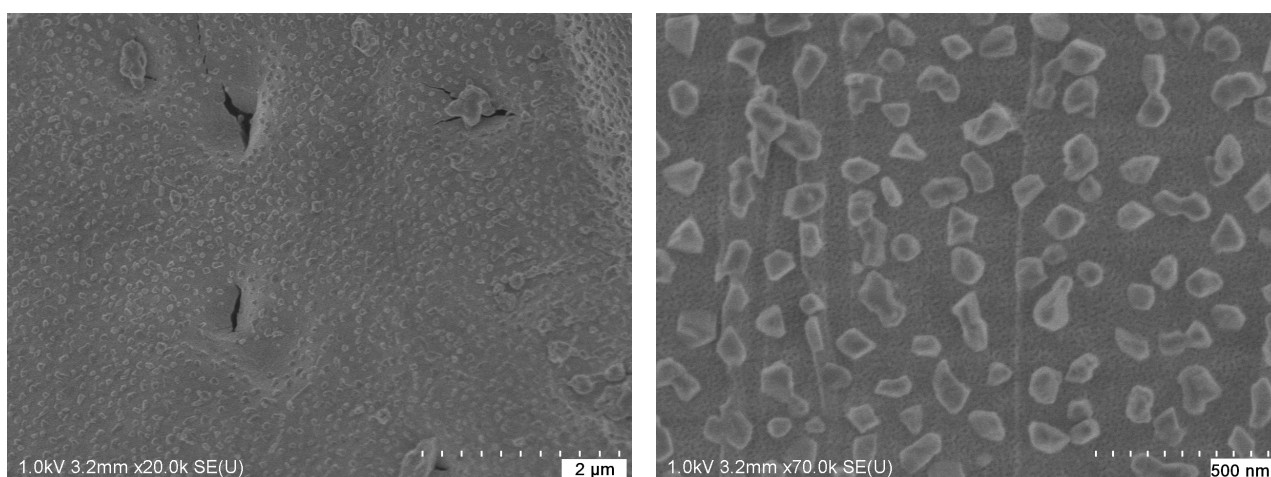


Figure 4.33 – Scanning electron micrographs of LaFeO_3 synthesized via HAM NO.

On the other hand, the HAM NO solid shows a relatively broad pore size distribution with a trailer in the macropore range and a high contribution of very small mesopores (Fig. 4.32B). This is confirmed by SEM analyses of the sample (Fig. 4.33) showing a compact structure with clearly distinguishable mesopores comparable to the HAM air solid. In addition, its whole surface is covered by smaller, non-porous blocks which was not observed for the HAM air solid. Occasional cracks are evidenced in the otherwise dense structure which may account for the macropore contribution as estimated by physisorption.

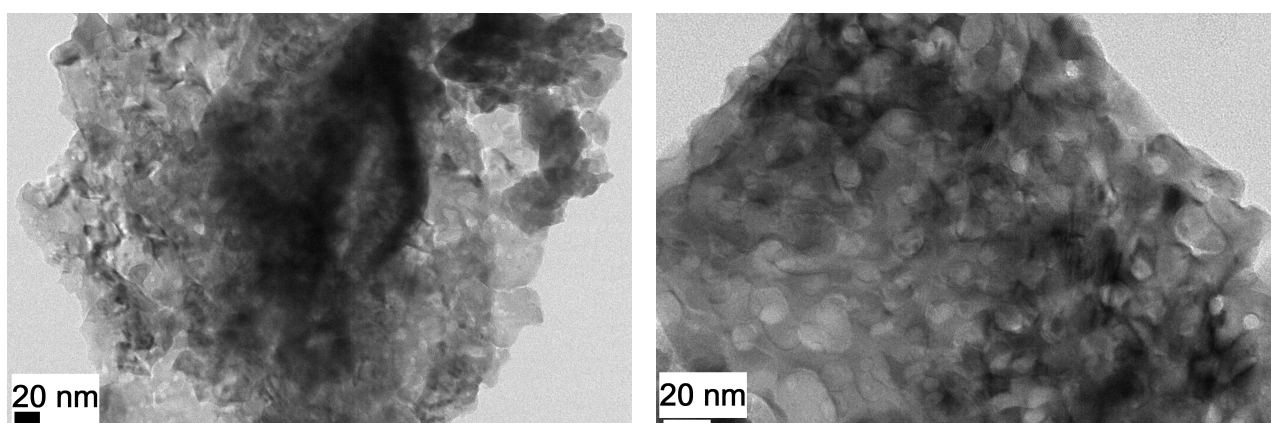


Figure 4.34 – Transmission electron micrographs of LaFeO_3 synthesized via HAM NO.

All SSA values are listed in Table 4.14. They depend strongly on the synthesis method. All HAM-based synthesis methods lead to solids with significantly higher specific surface areas than the one determined for HAM air ($14 \text{ m}^2 \text{ g}^{-1}$). Highest SSA are observed for the solid calcined under stagnant atmosphere during the first part of the calcination procedure,

followed by the HAM NO solid. A similar trend is observed regarding the V_{pore} , the HAM NO sample excepted.

Transmission electron micrographs of the HAM NO solid are shown in Fig. 4.34. The presence of interparticulate pores is evident. Individual particles seem, however, to have sintered to a complex network and are difficult to distinguish. This may also explain the low cumulative pore volume since the probability of forming closed pores is increased.

Chemical composition at the surface

The photopeaks obtained by XPS for the HAM N₂ and the HAM NO solids are shown in Fig. 4.35 for La 3d, Fe 2p, O 1s and C 1s. Regarding the position of the La 3d_{5/2} and the Fe 2p_{3/2} energy levels, the HAM NO exhibits a shift to higher B. E. However, both solids show the characteristic multiplets and the Fe 2p_{3/2} satellite attributed to trivalent Fe.

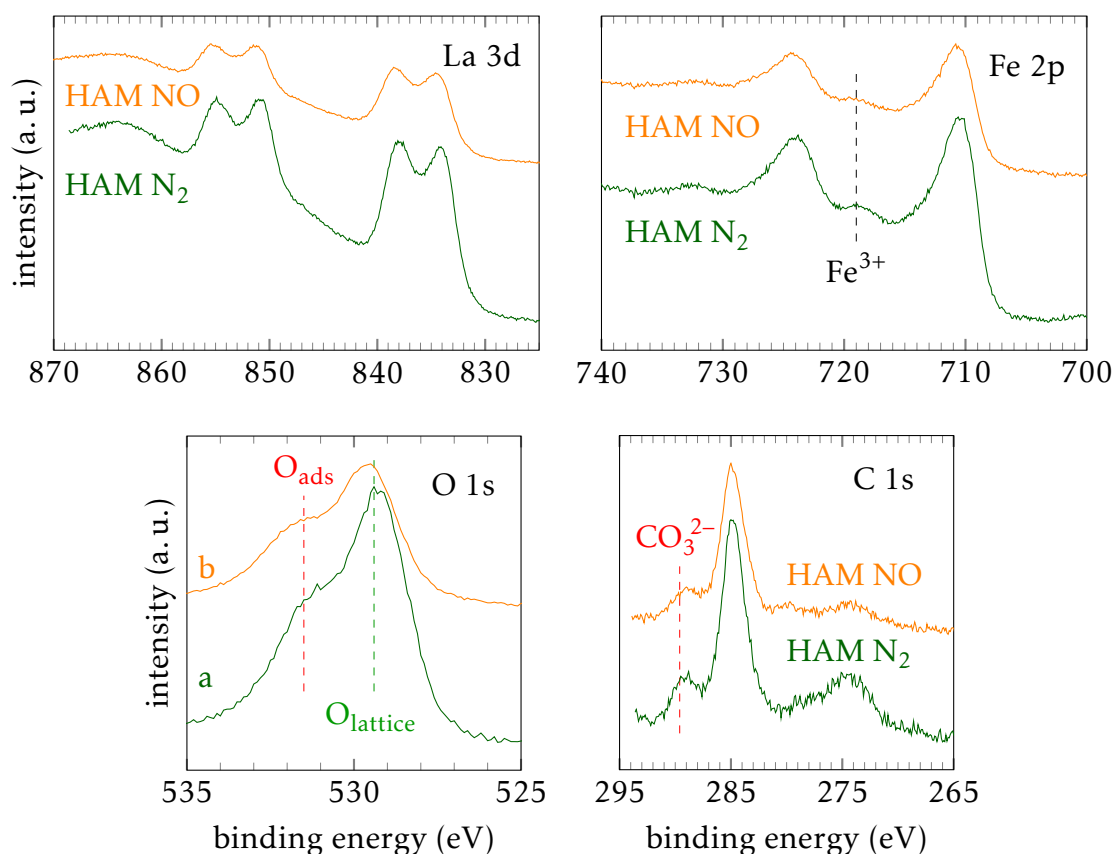


Figure 4.35 – La 3d, Fe 2p, O 1s and C 1s photopeaks of calcined LaFeO₃ prepared by prepared by HAM N₂, HAM NO and HAM*. HAM N₂ (a), HAM NO (b)

The O 1s signal reveals a high contribution of non-lattice oxygen species for the HAM N₂ perovskite of 53 at.%, whereas lower amounts of such adsorbed species were observed for the HAM NO sample (Table 4.15).

In the HAM series, for which the precursors were not subjected to a preliminary decomposition before calcination, lowest amounts of O_{ads} were detected for those solids calcined under (stagnant) air atmosphere (HAM air, HAM*_{cooling}), and similar amounts being observed for HAM NO, the rear being brought up by the HAM N₂ perovskite.

In agreement with the results obtained from O 1s spectral decomposition, a high carbonate contribution is evidenced for the HAM N₂ perovskite (Table 4.15). Slightly lower amounts of

carbonate species were detected for the solid obtained by HAM NO.

Table 4.15 – Comparison of surface compositions and photopeak maxima (XPS) of calcined LaFeO₃ prepared by HAM N₂, HAM NO and HAM*_{cooling}.

synthesis method	$x_{\text{La}}/x_{\text{Fe}}$ (XPS)	B. E. (eV)			at.%	
		La 3d _{5/2}	Fe 2p _{3/2}	O 1s	O _{lattice} ^a	C _{CO₃²⁻} ^b
HAM N ₂	1.17	834.1	710.1	529.4	47	18
HAM NO	1.40	834.6	710.8	529.5	60	15
HAM* _{cooling}	2.23	834.1	710.1	529.2	65	20

^a O_{lattice} + O_{ads} = 1.

^b C_{CO₃²⁻} + C_{adventitious} = 1.

Table 4.15 lists the surface properties as obtained by XPS for the different solids prepared by hydroalcoholic method (HAM)-based syntheses calcined under NO or N₂ flow⁸. Concerning the surface composition, all samples present the already observed La excess. However, the discrepancy is less important for the solids obtained by HAM NO and especially HAM N₂ with $x_{\text{La}}/x_{\text{Fe}} = 1.40$ and 1.17 respectively compared to 2.23 that was obtained for the HAM*_{cooling} sample previously.

Catalytic reactivity

The catalytic performance of LaFeO₃ catalysts prepared by HAM under different calcination atmospheres was tested according to Procedure A (Section 2.3). The corresponding light-off curves are shown in Fig. 4.36 for CO, C₃H₆ and NO under all test conditions, including the return test (stoic2). The temperatures corresponding to 50 % conversion of CO, C₃H₆, C₃H₈, and H₂ under stoichiometric conditions and rich condition for NO, as well as the selectivities are reported in Table 4.16. Light-off curves of C₃H₈, O₂ and H₂ of the HAM* and HAM NO solids are reported in Appendix D (Fig. D.1).

As shown in Table 4.16, the conversion of CO on LaFeO₃ still occurs at lower temperature than H₂. Likewise, as already discussed before, no CH₄ activation is achieved for any of the investigated solids in any feed composition under the described testing conditions.

The HAM N₂ solid exhibits a low activity towards oxidation reactions and no reduction of NO is observed in the whole temperature range. As already stated in Section 4.2.6, the HAM N₂ perovskite is less active than the CCM one even though differences in propylene and propane oxidation are less marked than for CO between the catalysts prepared by CCM and HAM N₂.

Under stoichiometric conditions, no NO conversion is observed for the HAM NO solid. The HAM* catalyst, on the other hand, converts NO above 300 °C with a maximum conversion of 23 % at 440 °C. 3 different reaction products, N₂, N₂O and NH₃, are formed (Fig. 4.37). Interestingly, the 1st part of the NO reduction (up to 320 °C) leads selectively to N₂ formation. The production of N₂O is delayed exhibiting a typical volcano-type curve reflecting a 2-step process (Eq. 4.3 and Eq. 4.4) as usually described over noble metals. Indeed, especially on Rh, N₂O readsorption is generally inhibited on Rh by a strong NO adsorption. In the case of the HAM* sample, N₂O production only sets in at 320 °C and then follows the generally observed behaviour to increase to a maximum (S_{N₂O} = 58 % at 350 °C) before gradually decreasing

⁸The values of HAM*_{cooling} are given for comparison with a solid calcined under stagnant atmosphere.

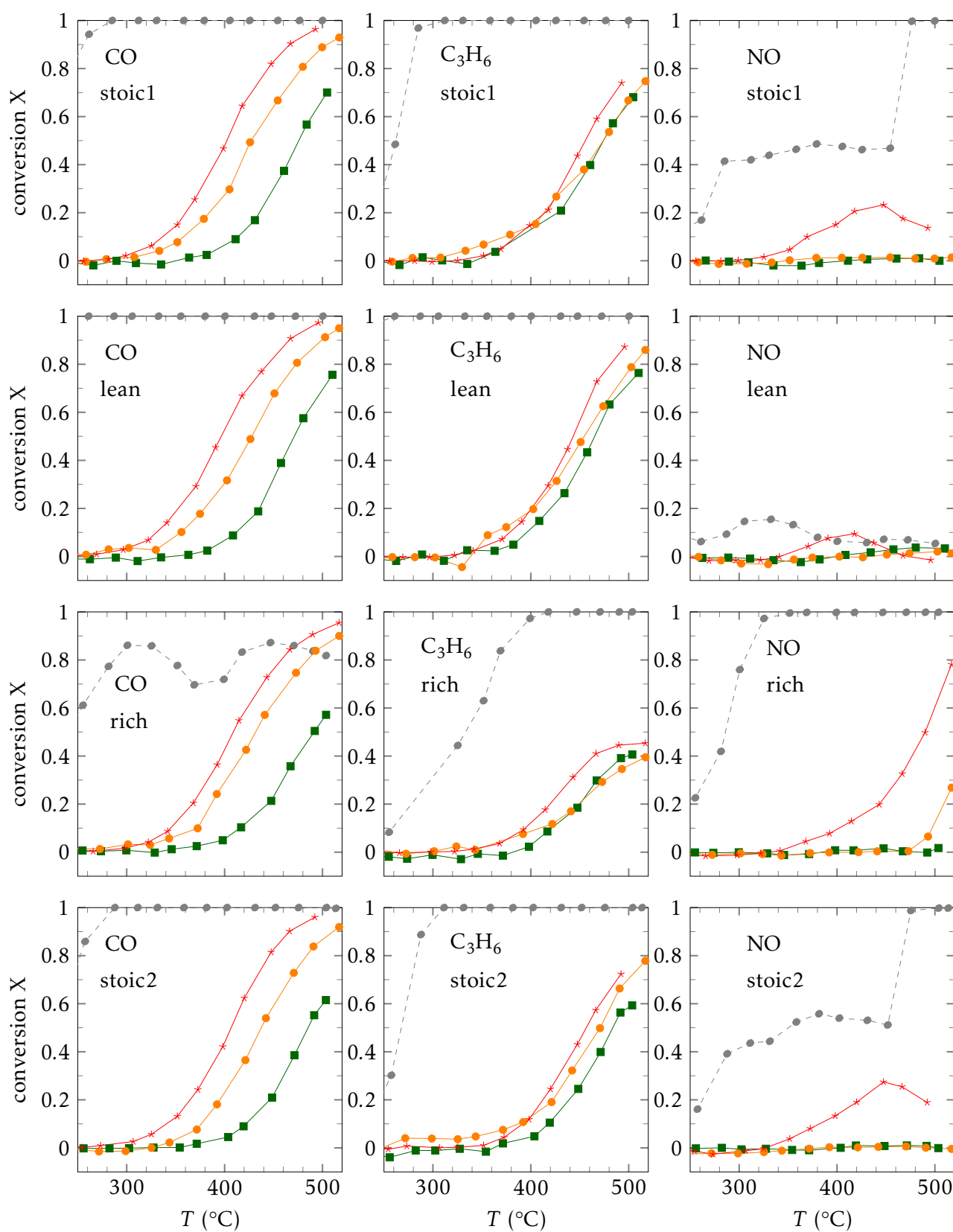


Figure 4.36 – CO , C_3H_6 and NO conversions of LaFeO_3 catalysts prepared by HAM N_2 , HAM NO and HAM*. HAM N_2 (\blacksquare), HAM NO (\bullet), and HAM* (\star) compared to the commercial reference (\circ)

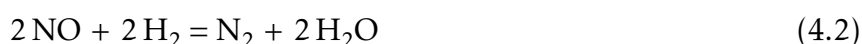
Table 4.16 – Temperatures corresponding to 50 % conversion of CO, C₃H₆, C₃H₈, and H₂ (stoichiometric) and NO (rich composition) of LaFeO₃ catalysts prepared by HAM N₂, HAM NO, HAM* and HAM*_{cooling} and selectivities of NO reduction products.

condition	stoichiometric				rich				
	T ₅₀ (°C)				selectivities at T _S				
	CO	C ₃ H ₆	C ₃ H ₈	H ₂	NO	S _{N₂}	S _{NH₃}	S _{N₂O}	T _S (°C)
CCM	438	463	478	501	- ^a	0.05	0.95	0	507
HAM N ₂	476	474	489	480 ^b	-	-	-	-	-
HAM NO	427	475	501	482	516 ^b	0.30	0.70	0	493
HAM*	402	456	487	474	490	0.32	0.68	0	491
HAM* _{cooling}	412	446	462	466	503	0.11	0.89	0	507

^a Conversion lower than 50 %.

^b T₂₅.

to nearly zero selectivity again. This decrease in S_{N₂O} is accompanied by an increase in NH₃ selectivity during NO reduction (S_{NH₃}) – for which production sets in at 350 °C – and an increase in N₂ formation. This selectivity behaviour reflects a faster NO dissociation. Chemisorbed N atoms can then be hydrogenated or recombine to produce NH₃ and N₂ respectively. Contrarily to the commercial reference catalyst, S_{N₂} remains higher than S_{NH₃} regardless of the temperature. After reaching a maximum of 40 % at 480 °C, NH₃ production decreases. At 350 °C only 24 % of H₂ are estimated to be consumed for the reduction of NO according to the reactions shown in Eq. 4.2, Eq. 4.3 and 4.5. This contribution increases to up to 51 % at 467 °C before decreasing again at higher temperatures.



Concerning CO oxidation under stoichiometric conditions, the typical S-shaped light-off curves are observed (Fig. 4.36). While the HAM* solid yields nearly complete CO conversion below 500 °C, the HAM NO and the HAM N₂ solids yield maximum conversions of 92 % and 70 % respectively. Propylene and propane conversions under stoichiometric conditions are similar (Fig. 4.36 and Table 4.16) except that slightly higher performances are observed for the HAM* catalyst. No reforming activity could be evidenced but H₂ and O₂ conversions are incomplete (Fig. D.1).

Under lean conditions, only minor NO reduction is observed for the perovskite catalysts (Fig. 4.36). In the case of the HAM* solid, maximum conversion is yielded at 420 °C. This reduction in the range of 320 to 470 °C results in the formation of N₂O and N₂ (Fig. 4.37). The oxidation behaviour is similar to the one observed under stoichiometric conditions.

Under rich conditions, NO reduction is observed for the HAM NO and the HAM* catalysts (Fig. 4.36). While the HAM NO sample yields a maximum conversion of 28 % above 500 °C, the HAM* solid reaches 78 % at the same temperature. Again, a reduction route following the same behaviour as under stoichiometric conditions is observed, i. e. N₂ represents the primary

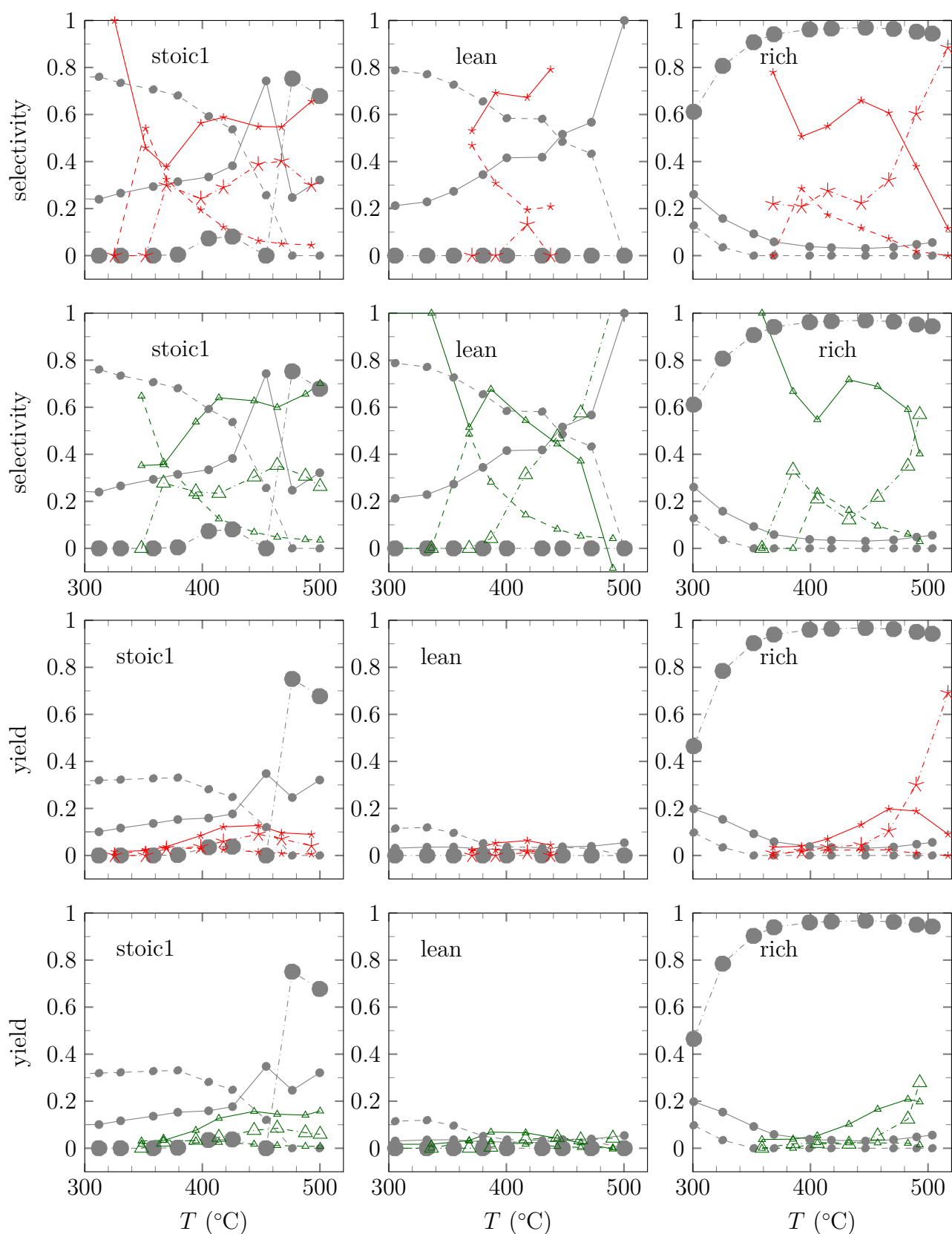


Figure 4.37 – N_2 , N_2O and NH_3 selectivities and yields of NO conversion of LaFeO_3 catalyst prepared by HAM* compared to the solid obtained by MSM* PS 400 nm under stoichiometric, lean and rich conditions. HAM* (\star) compared to MSM* PS 400 nm (\triangle) and the commercial reference (\bullet); $S_{\text{N}_2}/Y_{\text{N}_2}$ (solid), $S_{\text{N}_2\text{O}}/Y_{\text{N}_2\text{O}}$ (dashed), $S_{\text{NH}_3}/Y_{\text{NH}_3}$ (dashdotted, big mark)

reduction product and NH₃ production is observed above 370 °C. At this temperature 34 % of the fed hydrogen are converted by NO reduction (Eq. 4.2 to 4.5). In contrast to the results obtained under stoichiometric conditions, higher S_{NH₃} of up to 90 % are observed at high temperatures under rich conditions, though. The high conversion can be correlated to a higher contribution of hydrogen to the reduction, i. e. up to 69 %. Concerning oxidation activity, slightly lower CO conversions are observed than under stoichiometric conditions. As under stoichiometric conditions, no reforming processes can be evidenced and incomplete H₂ conversion is observed. Propylene conversion remains below 50 % for all investigated samples and propane conversion below 20 % except for the HAM N₂ sample.

Regarding the return test under stoichiometric conditions, stable results are obtained. NO reduction is even slightly enhanced for the HAM* solid yielding up to 30 % conversion. The observed trends in NO reduction product selectivities remain unchanged (s. Appendix D, Fig. D.2 and D.3). However, overall N₂ selectivity and yield increase.

The NO reduction under stoichiometric and lean conditions of the HAM* sample closely resembles the one already discussed of the MSM* perovskite. While the overall NO conversions are nearly superposable under lean and stoichiometric conditions – except for temperatures close to 500 °C for which the MSM* sample shows higher performances – a maximum NO conversion of about 80 % is yielded for the HAM* solid under rich conditions, probably due to the higher recorded maximum temperature. Concerning the selectivities (Fig. 4.37), only minor differences are observed between the HAM* and the MSM* catalysts under stoichiometric conditions. The order of formation of N₂ and N₂O is unchanged as is the observation that N₂ is predominantly formed with respect to N₂O. However, NH₃ remains the main product under rich conditions. Selectivities differ mainly under lean conditions for which higher S_{N₂} are observed above 400 °C for the HAM* catalyst.

Conclusion

The impact of the calcination step under different atmospheres during the first part of the calcination procedure was investigated using diluted NO flow (HAM NO) and stagnant atmosphere (HAM*) in comparison to the already discussed influence of N₂ flow (HAM N₂).

Different calcination atmospheres do not prevent the generation of the perovskite structure as evidenced by ex situ XRD. Minor phase segregation, 2 wt.% in the case of HAM N₂, in the form of hematite (α -Fe₂O₃) is observed for the HAM N₂ and the HAM* samples. The hematite formation minimises the usual surface La enrichment in the case of the HAM N₂ sample but not for the HAM* solid. For the HAM NO sample, the absence of hematite as revealed by XRD was confirmed by Raman spectroscopy despite the observation that this sample also presents a lowered surface La enrichment.

Varying the calcination atmospheres leads to the formation of solids with different textural properties. The solids obtained under N₂ flow and under stagnant atmosphere present a relatively broad mesopore size distribution but no macropores. On the other hand, the HAM NO sample exhibits a broad distribution which reaches into the macropore range with a distinct non-centered maximum at very low mesopore diameters, lower than 5 nm, leading to a much decreased average pore diameter. SEM confirmed the presence of such mesopores which are densely distributed over the whole solid. The overall morphology for the HAM NO solid resembles closely the one of the HAM*_{cooling} sample. However, a main difference is the formation of smaller, non-porous blocks on the compact solid surface. Furthermore, cracks in this surface are evidenced by SEM which might account for the macropore contribution as found by N₂-physisorption. Further studies need to be done to understand this behaviour.

An increase in specific surface area is observed for all investigated solids. The HAM* sample exhibits the highest SSA of $33 \text{ m}^2 \text{ g}^{-1}$.

Concerning the catalytic performances of these solids, the beneficial effect of calcination under stagnant atmosphere is confirmed. Surprisingly, the HAM* LaFeO₃ solid generally outperforms the HAM*_{cooling} perovskite which was subjected to an intermediate cooling before the switch to air during calcination. The HAM* catalyst even reaches comparable results as the MSM* solid for NO reduction ($X_{\text{max}} = 23 \%$ (stoichiometric) and 80% (rich)) while at the same time exceeding its oxidative activity reaching nearly complete CO conversion under stoichiometric conditions. The use of a template, therefore, appears to be unnecessary for the reproduction of the phenomenon which excludes the influence of decomposition residues of polymer synthesis initiators and the template itself as key parameters for the surprisingly high NO reduction performance.

The sample calcined partly under diluted NO flow, does show higher catalytic performances than the HAM N₂ (and CCM) solid but does not exhibit a similar reduction behaviour as the solids calcined under stagnant atmosphere. It is therefore concluded that NO atmosphere cannot be the decisive or at least not the sole parameter leading to the high catalytic performances as observed the HAM* solid. Likewise, an at best limited effect of the revealed hematite segregation can be presumed due to its absence in the MSM* sample which showed similar NO reduction activity.

4.3.3 Conclusion

The influence of varying calcination procedures and atmospheres, namely air, N₂ or diluted NO flow or stagnant atmosphere, on the physico-chemical properties and catalytic activities of LaFeO₃ perovskites was studied in this Section.

The investigation of the effect of calcination under stagnant atmosphere for differently prepared precursors (CCM-, HAM- and MSM-based syntheses) lead to the result that so-calcined solids obtained following an HAM* or MSM* synthesis route yielded high specific surface areas and pore volumes and gave interesting catalytic results, especially concerning NO reduction under rich feed but also under stoichiometric and lean conditions in the case of the MSM* and the HAM* catalysts. Interestingly, only minor enhancement of the catalytic performance of the CCM catalyst was observed for the solid obtained by CCM*. This is in contrast to the results of the corresponding TGA/DSC analyses which gave rise to very different decomposition/calcination processes in the case of the CCM precursor and by comparison nearly superposable ones in the case of the HAM precursor.

To further understand the origin of the high NO reduction performance of LaFeO₃ perovskites calcined under stagnant atmosphere, the properties and catalytic performances of perovskites calcined under NO or N₂ instead of the stagnant atmosphere were studied and compared to a HAM* catalyst.

Modifying the calcination procedure of LaFeO₃ catalysts lead to significant changes of the surface composition and the textural properties of some solids.

N₂ atmosphere does not lead to enhanced catalytic activities, neither for oxidation nor reduction, which is not surprising since stagnant atmosphere is not an inert atmosphere due to the initial oxygen content but also as a consequence of the presence of decomposition products of the precursor solid.

Indeed, NO atmosphere (HAM NO) leads to a solid with a broad pore size distribution. However, the HAM NO sample shows a distinct maximum for low-sized mesopores explaining the observation of the lowest average pore diameter of 8 nm of all studied solids. Its

morphology at the micrometre scale resembles the one of the HAM air solid, i. e. a dense structure permeated by many fine mesopores. Additionally, however, approximately 100 nm-sized, non-porous blocks are sprinkled all over the surface of the bigger blocks. At the nanometre scale, an intense sintering of the particles is observed which is not the case for the HAM*_{cooling} sample. This sintering may be the reason for the altogether low catalytic performance comparable to the CCM* solid.

Comparing the HAM*_{cooling}, the HAM* and the MSM* LaFeO₃ catalysts, the overall enhanced catalytic activity for oxidation is highest for the HAM* solid, which was not subjected to a cooling during the calcination procedure, and which therefore presents a slightly broader pore size distribution than the HAM*_{cooling} sample. On the other hand, NO reduction performance is most enhanced for the MSM* and the HAM* LaFeO₃ perovskites. The most important feature of these catalysts is the observed NO reduction under stoichiometric and lean conditions. At the same time, the N₂ selectivity of both solids is generally higher than the one of the commercial reference TWC in the same temperature range.

It is assumed that the presence of high amounts of evenly distributed mesopores of about 10 nm to 25 nm diameter is beneficial for the NO reduction since these are observed for all solids prepared under stagnant atmosphere. Other samples generally presented either low mesopore contributions or in other size ranges, especially in the one below 10 nm.

4.4 Conclusion

Influence of the solvent A sample of LaFeO₃ perovskite was prepared by HAM air to investigate the influence of the solvent on the solid's properties. Apart from the textural properties, no significant variations were observed. Neither structural properties nor the surface composition are affected by using an EtOH/water mixture instead of water as the solvent during synthesis.

However, since the solvent seems to change significantly the interactions in the precursor complex, the decomposition of nitrates and organic compounds during the preliminary decomposition step and the calcination process is strongly influenced. The hydroalcoholic medium leads to improved textural properties after calcination of the precursor. This is probably due to the attenuated exothermic process recognised as detrimental in the case of CCM.

Therefore, differences arise concerning its morphology at the micrometre scale. As evidenced by N₂-physisorption and electron microscopy, the solid prepared by CCM is mainly macroporous due to the fast, highly exothermic and explosive decomposition. The perovskite obtained by HAM air, on the other hand, is formed via a slower and less exothermic decomposition. It therefore consists of compact blocks which are densely scattered by low-sized mesopores. Surprisingly, this does not affect the overall specific surface area and the cumulative pore volume, which are similar for both cases.

Template-assisted synthesis To further control the porosity of the perovskite, the use of polymer templates of different sizes was investigated. PS spheres of 130, 200 and 400 nm as well as PMMA spheres of 80 nm diameter were used. The employed synthesis method, MSM, was based on the hydroalcoholic method to prevent the premature decomposition of the template and thereby the collapse of the inorganic framework. Due to the same consideration, calcination was conducted in 2 parts. The first part was performed under N₂ flow, the second under air flow.

N₂ flow seems to favour low phase segregation in the perovskite, observed for nearly all investigated solids. This segregation seems to occur in slightly higher amounts for the MSM samples than for HAM N₂ as can be deduced from XRD and H₂-TPR analyses. At the same time, a lower La enrichment is observed at the surface of these solids which is in agreement with the hypothesis of a correlation between the lower surface La enrichment and hematite segregation.

It was shown that MSM leads to LaFeO₃ perovskites with bimodal pore size distributions. The main maximum falls in the mesopore-size range, whereas the 2nd maximum corresponds to macropores. The latter are induced directly by the imprint of the template spheres. The macroporous network is formed with pore diameters which measure approximately half the diameter of the employed template spheres as evidenced by N₂ physisorption and SEM due to the shrinking/deformation process of the polymer spheres during heat treatment.

The formation of the regular porous network does not forcibly lead to an increased specific surface area as was shown by the example of the MSM_{cooling} perovskite (PS 400 nm) with the lowest observed SSA of 7 m² g⁻¹. On the other hand, the MSM sample prepared with PS 200 nm showed an increased SSA of 29 m² g⁻¹.

A partial collapse of the inorganic network was observed for the solid obtained with small PMMA spheres (80 nm) which may explain its low catalytic performance.

Furthermore, it was proven that an intermediate cooling during the calcination helps to prevent sintering of the particles in the network.

Overall, the solid with the most regular porous network (MSM PS 200 nm) also showed the most promising catalytic performances of the MSM perovskites even though NO reduction leads mainly to ammonia. Hematite segregation was evidenced for this sample but does not seem to be at the origin of the enhanced catalytic performances since other solids with lower catalytic performances also presented phase segregation in the form of α -Fe₂O₃.

Influence of the calcination procedure The influence of the calcination procedure on the perovskite's properties was investigated for precursors obtained by CCM, HAM and MSM. For this study, all perovskites which were not exclusively calcined under air flow, were subjected to a calcination in 2 parts as already described for the MSM solids. The difference between the compared procedures consisted in the employed atmosphere during the 1st part of this calcination procedure. The investigated atmospheres consisted of N₂ flow (HAM N₂), NO flow (HAM NO) and no flow (stagnant atmosphere, HAM*, HAM*_{cooling}, CCM*, MSM*). Results thereof were compared to those obtained under continuous flow (HAM air, CCM and MSM (same template) respectively).

Minor phase segregation of α -Fe₂O₃ is observed (by XRD or Raman spectroscopy) for HAM N₂ and HAM* solids. A correlation to the observed decrease in surface La enrichment was observed for some solids but cannot be generalised.

Interestingly, using stagnant atmosphere during calcination of HAM- or MSM-precursors gives rise to LaFeO₃ perovskites with very enhanced NO reduction performance under rich, stoichiometric and lean conditions and likewise enhanced CO oxidation compared to the other LaFeO₃ perovskite samples presented in this Chapter. This is not the case for the CCM* perovskite which shows only slightly enhanced catalytic performances compared to the CCM perovskite.

The phenomenon that NO reduction is observed over non-substituted, non-doped LaFeO₃ perovskites is not yet completely understood. While the increase in oxidation and reduction performance might be due to the increase in specific surface area, it seems unlikely that it is

at the source of the reduction activity in non-rich conditions.

First steps were ventured to narrow down the possibly intervening parameters leading to this extraordinary reduction behaviour. First of all, the higher SSA are observed for all perovskites calcined under stagnant atmosphere is outruled in comparison to the catalytic activity of the MSM sample templated by 80 nm PMMA spheres which also yielded SSA above $30 \text{ m}^2 \text{ g}^{-1}$ but showed but poor catalytic activity. Secondly, the contribution of non-perovskite phases to the NO reduction performances under non-rich conditions was excluded since only 1 of the catalysts in question shows a hematite phase segregation while many other solids likewise present such a hematite phase – especially the MSM ones even in higher amounts. Moreover, lower La surface enrichment is not at the origin of this increase in catalytic reduction activity. In addition, it could be shown that the HAM* and MSM* catalysts show comparable NO reduction behaviour under stoichiometric and lean conditions, thereby outruling the possibility that residues of the polymer synthesis initiator containing K may be at the origin. Thirdly, the use of the template itself could be excluded as a key parameter for the same reason. Fourthly, and in analogy to the idea just pointed out, it could be shown that perovskites obtained from CCM precursors subjected to the same calcination procedure do not yield the same catalytic activity as such which are prepared in hydroalcoholic medium, i. e. that the employed solvent plays a key role in this respect in contrast to the results obtained for continuous air flow calcination. Fifthly, inert flow calcination leads to perovskites with poor catalytic performances. Finally, tests on the HAM NO solid could demonstrate that the phenomenon of enhanced NO reduction is not (exclusively) based on the long-term presence of NO_x during the whole temperature ramp of calcination.

In conclusion, precursors prepared in hydroalcoholic medium, i. e. forming more stable complexes and which are therefore decomposing in a more controlled way, are suitable to generate LaFeO₃ perovskites which show outstanding reduction performances under 3-way catalytic conditions if calcined under conditions of a non-air, non-inert, non-(solely)-NO flow resembling stagnant air atmosphere conditions. This may be explained in part by the high amount of well-distributed and therefore more easily accessible > 10 nm- and < 30 nm-sized mesopores.

Concerning the non-templated synthesis route, an intensified investigation into the reasons for the high catalytic performances of the perovskites obtained after (partial) calcination under stagnant atmosphere is necessary. Since NO atmosphere was outruled as being the key parameter, the next step should be the investigation of a calcination under humid and/or CO₂ atmosphere and once the key parameter is found an optimisation of the synthesis. Then, depending on the key parameter, a transfer to other perovskite or non-perovskite systems should be envisaged.

In the framework of this study, the enhancement of the Fe-based perovskite's catalytic performance is further studied by making use of its high tolerance regarding the incorporation of different metal cations into the structure (bulk composition) and by investigating the influence of the surface composition. For these composition optimisations the CCM method was chosen as synthesis mode to allow for comparability.

Bibliography

- [1] G. Shabbir, A. Qureshi, K. Saeed, *Materials Letters* **2006**, *60*, 3706–3709.
- [2] E. Magnone, E. Traversa, M. Miyayama, *Journal of the Ceramic Society of Japan* **2007**, *115*, 402–408.
- [3] E. Krupicka, A. Reller, A. Weidenkaff, *Crystal Engineering* **2002**, *5* (3-4 SPEC), Crystal Chemistry of Functional Materials II, Proceedings of Symposium L, E-MRS, 195–202.
- [4] H. Fjellvåg, O. H. Hansteen, B. G. Tilset, A. Olafsen, N. Sakai, H. Seim, *Thermochimica Acta* **1995**, *256*, 75–89.
- [5] P. Courty, H. Ajoy, C. Marcilly, B. Delmon, *Powder Technology* **1973**, *7*, 21–38.
- [6] J. Zhu, H. Li, L. Zhong, P. Xiao, X. Xu, X. Yang, Z. Zhao, J. Li, *ACS Catalysis* **2014**, *4*, 2917–2940.
- [7] A. Zaki, J. Xu, G. Stoclet, S. Casale, J.-P. Dacquin, P. Granger, *Microporous and Mesoporous Materials* **2015**, *208*, 140–151.
- [8] S. Vaudreuil, PhD thesis, Université Laval, Québec, **2003**.
- [9] H. Li, L. Zhang, H. Dai, H. He, *Inorganic Chemistry* **2009**, *48*, 4421–4434.
- [10] J. Yuan, H. Dai, L. Zhang, J. Deng, Y. Liu, H. Zhang, H. Jiang, H. He, *Catalysis Today* **2011**, *175* (1), conference paper, 209–215.
- [11] K. S. W. Sing, *Pure and Applied Chemistry* **1985**, *57*, DOI 10.1351/pac198557040603.
- [12] M. Sadakane, T. Asanuma, J. Kubo, W. Ueda, *Chemistry of Materials* **2005**, *17* (13), 3546–3551.
- [13] M. Sadakane, T. Horiuchi, N. Kato, K. Sasaki, W. Ueda, *Journal of Solid State Chemistry* **2010**, *183* (6), 1365–1371.
- [14] J. Qin, Z. Cui, X. Yang, S. Zhu, Z. Li, Y. Liang, *Sensors and Actuators B: Chemical* **2015**, *209*, 706–713.
- [15] A. Stein, *Microporous and Mesoporous Materials* **2001**, *44-45*, 227–239.
- [16] M. Sadakane, T. Horiuchi, N. Kato, C. Takahashi, W. Ueda, *Chemistry of Materials* **2007**, *19* (23), 5779–5785.
- [17] T. Valdés-Solís, G. Marbán, A. B. Fuertes, *Chemistry of Materials* **2005**, *17* (8), 1919–1922.
- [18] H. Su, L. Jing, K. Shi, C. Yao, H. Fu, *Journal of Nanoparticle Research* **2010**, *12* (3), 967–974.
- [19] M. M. Nair, F. Kleitz, S. Kaliaguine, *ChemCatChem* **2012**, *4* (3), 387–394.
- [20] I. Twagirashema, M. Engelmann-Pirez, M. Frere, L. Burylo, L. Gengembre, C. Dujardin, P. Granger, *Catalysis Today* **2007**, *119* (1-4), 100–105.
- [21] J. R. Sietsma, H. Friedrich, A. Broersma, M. Versluijs-Helder, A. J. van Dillen, P. E. de Jongh, K. P. de Jong, *Journal of Catalysis* **2008**, *260*, 227–235.
- [22] J. R. A. Sietsma, J. D. Meeldijk, J. P. den Breejen, M. Versluijs-Helder, A. J. van Dillen, P. E. de Jongh, K. P. de Jong, *Angewandte Chemie International Edition* **2007**, *119*, 4631–4633.

- [23] H. Friedrich, J. R. A. Sietsma, P. E. de Jongh, A. J. Verkleij, K. P. de Jong, *Journal of the American Chemical Society* **2007**, *129*, 10249–10254.
- [24] J. R. A. Sietsma, J. D. Meeldijk, M. Versluijs-Helder, A. Broersma, A. J. v. Dillen, P. E. de Jongh, K. P. de Jong, *Chemistry of Materials* **2008**, *20*, 2921–2931.
- [25] M. Wolters, P. Munnik, J. H. Bitter, P. E. de Jongh, K. P. de Jong, *The Journal of Physical Chemistry C* **2011**, *115*, 3332–3339.
- [26] M. Wolters, L. J. van Grotel, T. M. Eggenhuisen, J. R. Sietsma, K. P. de Jong, P. E. de Jongh, *Catalysis Today* **2011**, *163*, 27–32.
- [27] D. L. A. de Faria, S. Venâncio Silva, M. T. de Oliveira, *Journal of Raman Spectroscopy* **1997**, *28*, 873–878.
- [28] L. J. Oblonsky, T. M. Devine, *Corrosion Science* **1995**, *37*, 17–41.
- [29] J. Bielecki, P. Svedlindh, D. T. Tibebe, S. Cai, S.-G. Eriksson, L. Börjesson, C. S. Knee, *Physical Review B* **2012**, *86*, DOI 10.1103/physrevb.86.184422.
- [30] M. Popa, J. Frantti, M. Kakihana, *Solid State Ionics*, Proceedings of International Conference on Solid State Ionics, (Materials and Processes for Energy and Environment), Cairns, Australia, 8-13 July, 2001 **2002**, *154–155*, 437–445.
- [31] B. P. Barbero, J. A. Gamboa, L. E. Cadús, *Applied Catalysis B: Environmental* **2006**, *65* (1-2), 21–30.
- [32] J.-M. Giraudon, A. Elhachimi, F. Wyrwalski, S. Siffert, A. Aboukaïs, J.-F. Lamonier, G. Leclercq, *Applied Catalysis B: Environmental* **2007**, *75*, 157–166.
- [33] J. Andreasson, J. Holmlund, R. Rauer, M. Käll, L. Börjesson, C. Knee, A. Eriksson, S.-G. Eriksson, M. Rübhausen, R. Chaudhury, *Physical Review B* **2008**, *78*, DOI 10.1103/physrevb.78.235103.
- [34] S. S. Chan, A. T. Bell, *Journal of Catalysis* **1984**, *89*, 433–441.

Enhancement of catalytic activity by composition optimisation of Fe-based perovskites

As described before many investigations pointed out the high variability of the perovskite properties with various possible substitutions in the A- and B-sites by which catalytic activity and stability can be modulated (Section 1.2). As described in Chapter 3, the redox properties of the B sites strongly influence the level of conversion of NO_x . La_2CuO_4 was found to be more active compared to LaFeO_3 but its high reducibility destabilises the structure leading to extensive segregation. In contrast, LaFeO_3 was found to be more stable but exhibiting a very low activity in NO conversion. Based on this, a combined approach can be envisaged consisting in partial substitution of Fe by Cu. Optimisation of the LaFeO_3 surface was also investigated by purposely lowering the La-content of perovskite samples.

5.1 Surface composition optimisation

As evidenced by XPS experiments in Chapter 3 (Section 3.4), the surface of LaFeO_3 usually presents La enrichment which may hinder the accessibility to the suggested Fe^{3+} active sites. To increase the density of Fe species at the surface, a series of perovskite catalysts was prepared by purposely reducing the lanthanum content, $\text{La}_{1-y}\text{FeO}_3$ ($y = 0, 0.1, 0.2, 0.33$). The solids were all synthesized by CCM. The employed nomenclature is based on the nominal composition, i. e. the La/Fe atomic ratio of the precursors used during synthesis.

A commercial hematite ($\alpha\text{-Fe}_2\text{O}_3$) sample (Merck (p. A.)) was used for comparison. Furthermore, a mechanic mixture of hematite (12.4 wt.%) and LaFeO_3 (87.6 wt.%) was tested for comparison of catalytic performance with a so-called $\text{La}_{0.7}\text{FeO}_3$ ¹ solid.

5.1.1 Chemical composition in the bulk and at the surface

Elementary analysis (ICP) was performed first in order to check the nominal composition of calcined LaFeO_3 and $\text{La}_{1-y}\text{FeO}_3$ solids. As expected, the atomic La/Fe ratio is confirming the nominal composition for the LaFeO_3 and $\text{La}_{0.67}\text{FeO}_3$ solids (Table 5.1).

¹The notation of $\text{La}_{1-y}\text{FeO}_3$ is used for the sake of simplicity and based on the nominal composition of the employed precursor amounts – not the postulation of a structure with as many cationic defects.

Table 5.1 – Bulk and surface atomic ratios $x_{\text{La}}/x_{\text{Fe}}$ and photopeak maxima of $\text{La}_{1-y}\text{FeO}_3$ ($y = 0, 0.1, 0.2, 0.33$; CCM).

nominal composition	$x_{\text{La}}/x_{\text{Fe}}$		B. E. (eV)		
	ICP	XPS	La 3d _{5/2}	Fe 2p _{3/2}	O 1s
LaFeO_3	1.01	2.13	834.3	710.8	529.5
$\text{La}_{0.9}\text{FeO}_3$	n. a.	1.64	834.3	710.5	529.5
$\text{La}_{0.8}\text{FeO}_3$	n. a.	1.31	834.3	710.4	529.7
$\text{La}_{0.67}\text{FeO}_3$	0.66	0.88	834.3	710.6	529.6

Next, surface atomic compositions were investigated by X-ray photo-electron spectroscopy (XPS) on the $\text{La}_{1-y}\text{FeO}_3$ series (Table 5.1). All samples exhibit an excess of La at the surface. This non-stoichiometric behaviour at the surface of LaFeO_3 was already reported before.^[1–3] In the investigated series, the extent of La excess at the surface decreases with the purposely decreased La-content.

As shown in Fig. 5.1, the atomic surface La to Fe ratio varies linearly with the nominal composition. In fact, the decreasing La-content in the bulk correlatively leads to a similarly decreasing surface La concentration. The intended impact of La-deficient synthesis to control surface composition was confirmed.

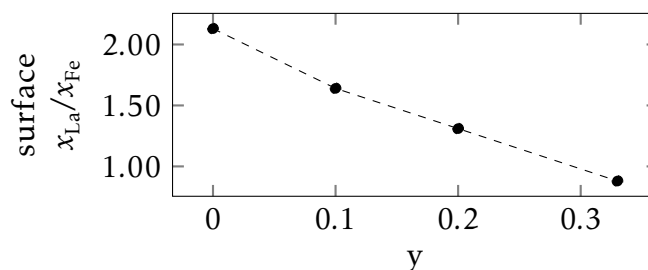


Figure 5.1 – Evolution of surface atomic ratio La/Fe (XPS) on the calcined $\text{La}_{1-y}\text{FeO}_3$ ($y = 0, 0.1, 0.2, 0.33$) series.

Fig. 5.2 shows the La 3d, Fe 2p, O 1s, and C 1s XPS spectra of the series of lanthanum orthoferrites. The binding energies (B. E.) of the La 3d peaks remain constant whatever the La-content (Table 5.1). For all perovskites prepared with decreased La-content, $\text{La}_{1-y}\text{FeO}_3$, the characteristic multiplet splitting and satellites for Fe 2p are observed (Fig. 5.2). The overall positions of the photopeaks (≈ 710.7 eV for Fe 2p_{3/2} and ≈ 719 eV for its satellite) are in agreement with trivalent Fe.^[4,5] This is in accordance with the supposed co-existence of LaFeO_3 and $\alpha\text{-Fe}_2\text{O}_3$. As reported before,^[1,4,6] the shake-up photopeak of the LaFeO_3 perovskite is relatively broader and less intense than for the Fe_2O_3 solid. The satellite's intensity increases slightly with decreasing La-content in the bulk which may indicate the presence of Fe_2O_3 in the samples prepared with lower La-content. However, it is very difficult to differentiate between Fe^{3+} in LaFeO_3 and hematite, $\alpha\text{-Fe}_2\text{O}_3$, because the chemical environment is very similar, i. e. Fe^{3+} octahedrally coordinated by oxygen anions.

Differences between the LaFeO_3 solid and the samples obtained by synthesis with lower La-content are mainly observed for the C 1s and O 1s photopeaks (Fig. 5.2). C 1s photo-

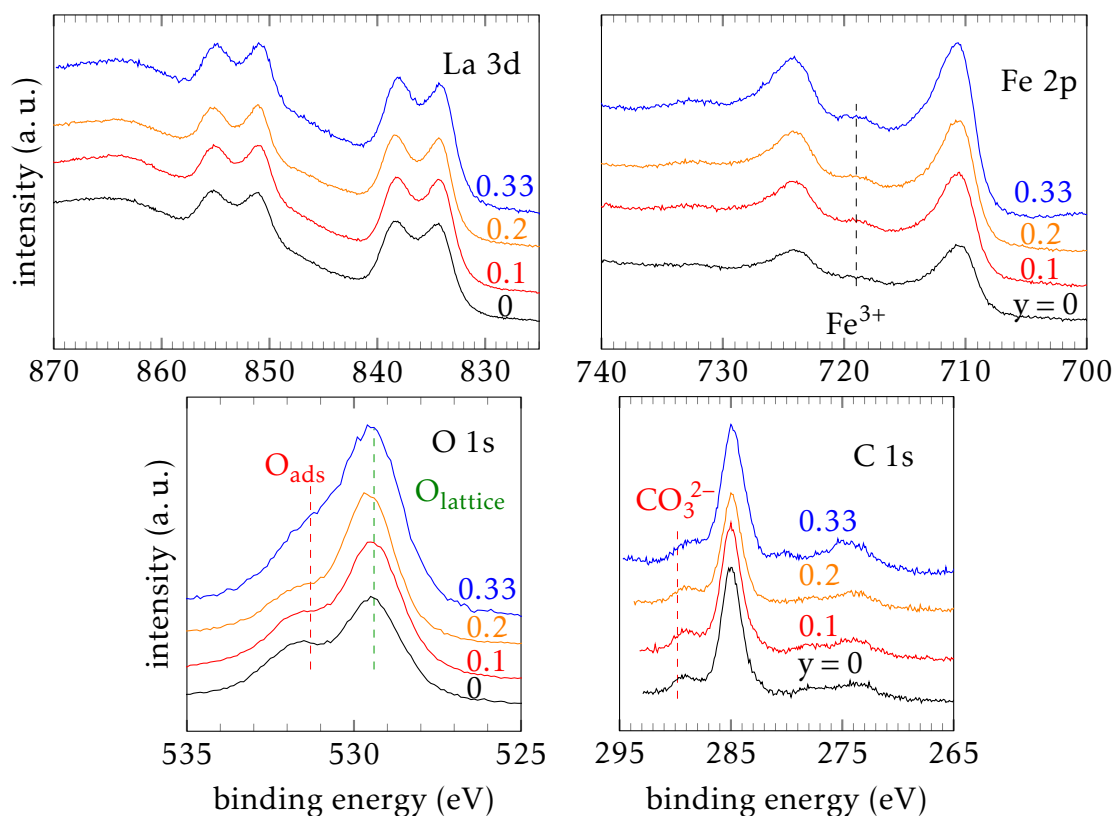


Figure 5.2 – La 3d, Fe 2p, O 1s and C 1s photopeaks of calcined $\text{La}_{1-y}\text{FeO}_3$ ($y = 0, 0.1, 0.2, 0.33$; CCM).

peaks reveal the presence of adventitious carbon (285.0 eV) and adsorbed carbonate species (289.9 eV). The relative intensity of carbonates decreases for the catalysts presenting lower La-content. This is also the case for non-lattice oxygen species (≈ 531.5 eV) which can be associated to hydroxyls or carbonates.

5.1.2 Structural properties

X-ray diffraction analyses

Table 5.2 – Comparison of crystallite sizes and unit cell parameters derived from full pattern matching of calcined $\text{La}_{1-y}\text{FeO}_3$ ($y = 0, 0.1, 0.2, 0.33$; CCM).

	d_{cryst} (nm)	a (Å)	b (Å)	c (Å)	$V_{\text{unit cell}}$ (Å ³)
LaFeO_3	20.1 ± 0.1	5.561	7.858	5.558	242.85 ± 0.17
$\text{La}_{0.9}\text{FeO}_3$	16.4 ± 0.1	5.558	7.861	5.560	242.91 ± 0.25
$\text{La}_{0.8}\text{FeO}_3$	18.2 ± 0.1	5.558	7.863	5.558	242.88 ± 0.23
$\text{La}_{0.67}\text{FeO}_3$	12.6 ± 0.1	5.556	7.851	5.558	242.43 ± 0.27

The orthorhombic perovskite structure of LaFeO_3 is obtained for all solids of the $\text{La}_{1-y}\text{FeO}_3$ series (Fig. 5.3). Only minor phase segregation of hematite, $\alpha\text{-Fe}_2\text{O}_3$, is observed in the diffractogram for solids with lower La-content. A higher extent of phase segregation than estimated

from the diffractograms is to be expected for the solids which show the characteristic diffraction peak at $2\theta = 33.2^\circ$.

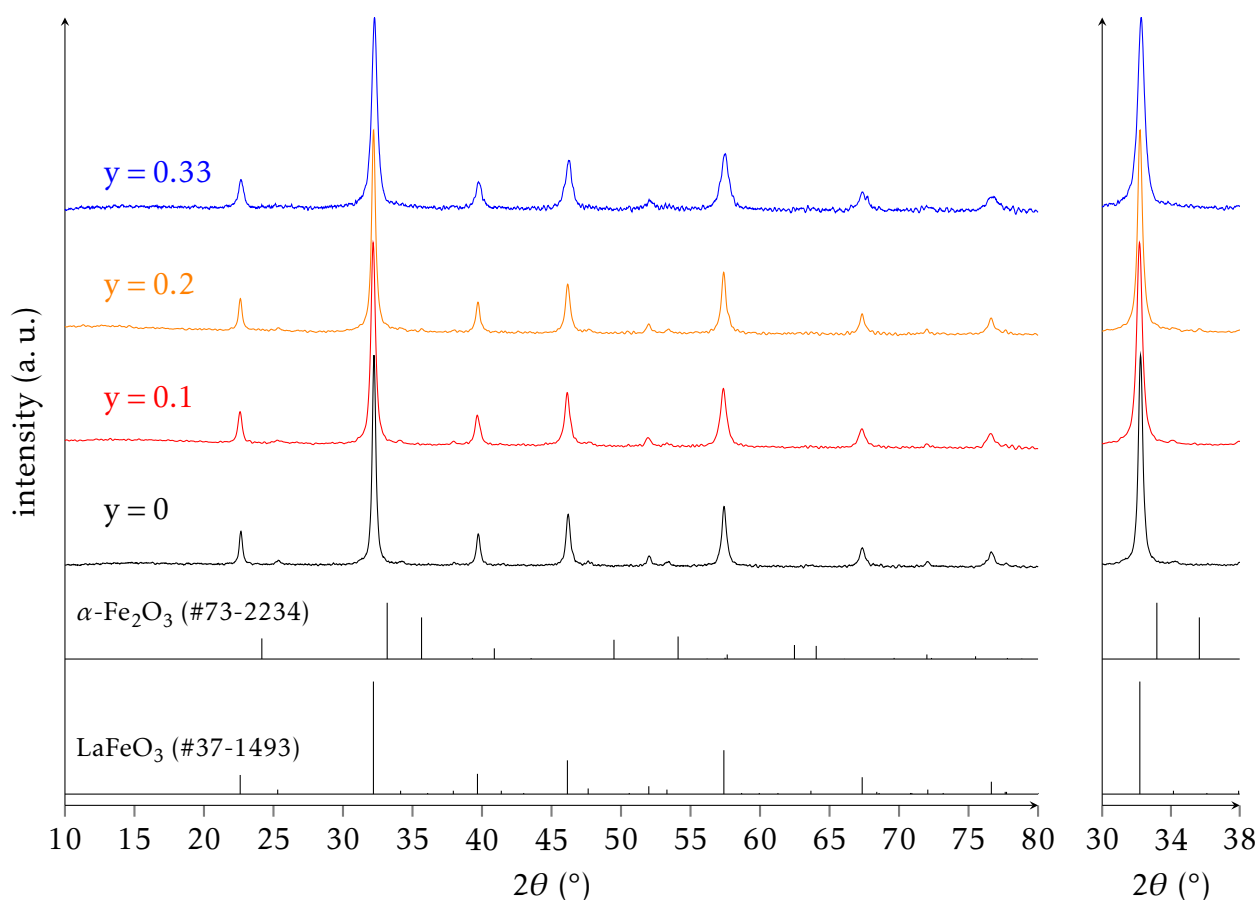


Figure 5.3 – X-ray diffraction patterns of calcined $\text{La}_{1-y}\text{FeO}_3$ ($y = 0, 0.1, 0.2, 0.33$; CCM).

Relative intensities of the diffraction peaks are in agreement with the perovskite reference (#37-1493), i. e. no preferential growth of the crystallites is observed. Furthermore, as can be seen in Table 5.2 listing the unit cell parameters obtained by the full pattern matching method of the calcined $\text{La}_{1-y}\text{FeO}_3$ catalysts, samples with lower La-content show no significant deviation from the parameters of LaFeO_3 . This is in agreement with the relative intensities which remained constant in the series of $\text{La}_{1-y}\text{FeO}_3$ solids. This means that the perovskite structure is nearly unaffected by decreased La-content. The thereby created Fe excess in the bulk seems to be consumed by the separate phase of $\alpha\text{-Fe}_2\text{O}_3$.

In the series of $\text{La}_{1-y}\text{FeO}_3$, except for the $\text{La}_{0.9}\text{FeO}_3$ sample, the crystallite sizes of the perovskite phase, as reported in Table 5.2 and seen by the broadening of the diffraction peaks in Fig. 5.3, decrease for lower La-content.

Raman spectroscopy

Fig. 5.4 shows the Raman spectra of 2 different zones of the $\text{La}_{0.67}\text{FeO}_3$ solid. In zone A characteristic perovskite lines are observed at 175 cm^{-1} (assigned to the A-site A_g mode), at 267 and 291 cm^{-1} oxygen tilt B_{1g} and A_g modes' lines overlap, and at 430 cm^{-1} (oxygen bending B_{1g} mode).^[4,7-10] Furthermore, the characteristic intense oxygen stretch mode at

641 cm^{-1} (B_{1g} mode) is present, as well as a broad line at 1320 cm^{-1} generally attributed to either a 2-phonon scattering phenomenon or an oxygen stretching vibration.^[4,7-10]

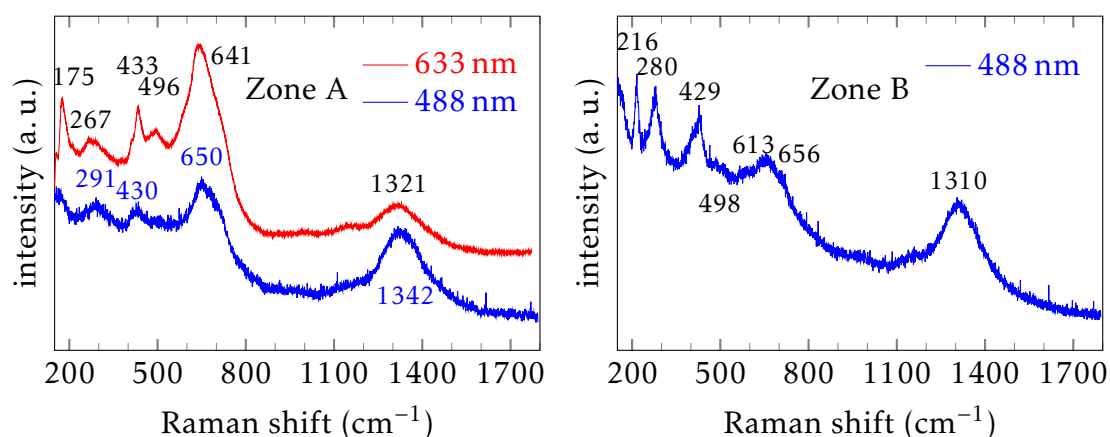


Figure 5.4 – **Raman spectra of $\text{La}_{0.67}\text{FeO}_3$ excited with $\lambda_{\text{exc}} = 488\text{ nm}$ and 632 nm .** The spectra at the left were measured for zone A while the spectrum at the right was measured for another grain of the sample, called zone B.

In zone B, typical hematite modes additionally occur, even though with low intensity, and are partly superposed with those of the perovskite. Hematite lines are observed at 216 cm^{-1} (A_{1g} mode), 412 cm^{-1} (E_g mode) and with less intensity at 498 cm^{-1} and 613 cm^{-1} (both assigned to the E_g mode).^[11] The line at 280 cm^{-1} may be attributed to either the perovskite (B_{1g} mode)^[7,9] or the hematite (E_g mode).^[11] Equally the line at 1310 cm^{-1} may be assigned to the 2-magnon or the 2-phonon scattering of the hematite or the perovskite.^[9,11]

The presence of modes of both oxides comforts the assumption that excess Fe is consumed by phase segregation into $\alpha\text{-Fe}_2\text{O}_3$. This is in agreement with the findings previously discussed for XRD.

5.1.3 Thermal stability and reducibility

High temperature XRD

As for the sample prepared with stoichiometric amounts of La and Fe precursors (Section 3.2), high temperature X-ray diffraction (HTXRD) analyses were performed on calcined $\text{La}_{0.68}\text{FeO}_3$ to determine its stability under reductive atmosphere and humid air. The procedure has been presented in Section 2.2.5 (Fig. 2.5). It follows 6 consecutive steps corresponding to a reductive followed by a humid oxidative thermal treatment.

Regarding the stability of the $\text{La}_{0.68}\text{FeO}_3$ solid under H_2 atmosphere (Fig. 5.5 and 5.6), the perovskite structure is retained during the whole procedure including the heating ramp (step 1), the plateau (step 2) and the cooling under N_2 (step 3). Slight shifts of the diffraction peaks to lower angles attributed to thermal expansion of the unit cell during the analysis are observed. The same trends were observed under humid atmosphere.

As shown in Table 5.3, no deviation of the photoppeak maxima of the $\text{La}_{0.68}\text{FeO}_3$ sample before and after completion of the whole HTXRD procedure, labelled post-HTXRD, are observed. Changes of the surface composition of the $\text{La}_{0.68}\text{FeO}_3$ sample are observed after HTXRD analysis compared to the calcined solid. Apparently successive reductive and

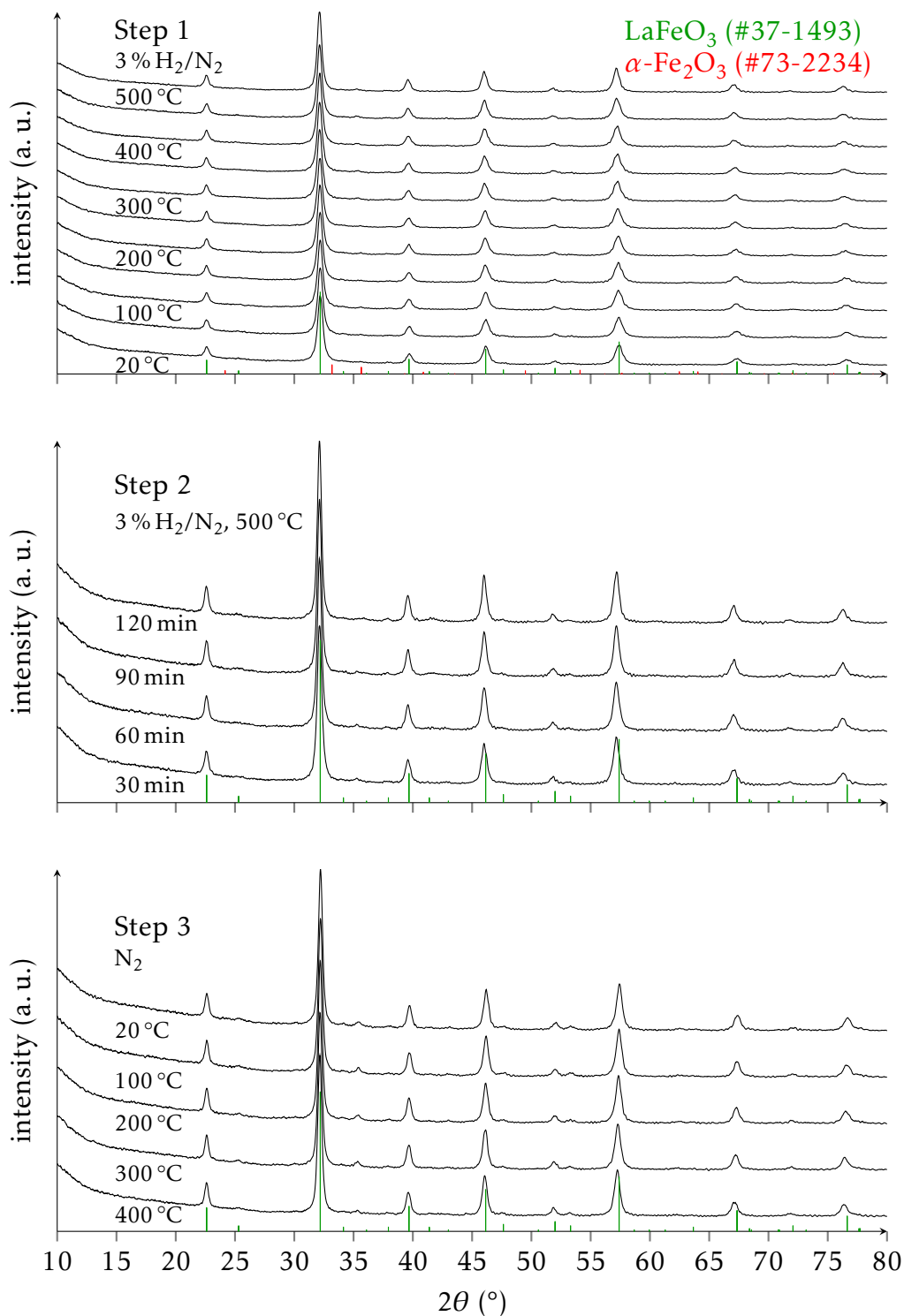


Figure 5.5 – High Temperature X-ray diffractograms of $\text{La}_{0.68}\text{FeO}_3$ prepared by CCM. Step 1 corresponds to a heating ramp under reductive atmosphere (3 Vol.% H_2/N_2), Step 2 to the corresponding plateau and Step 3 to the subsequent cooling under inert atmosphere. Scheme in Section 2.2.5 Fig. 2.5.

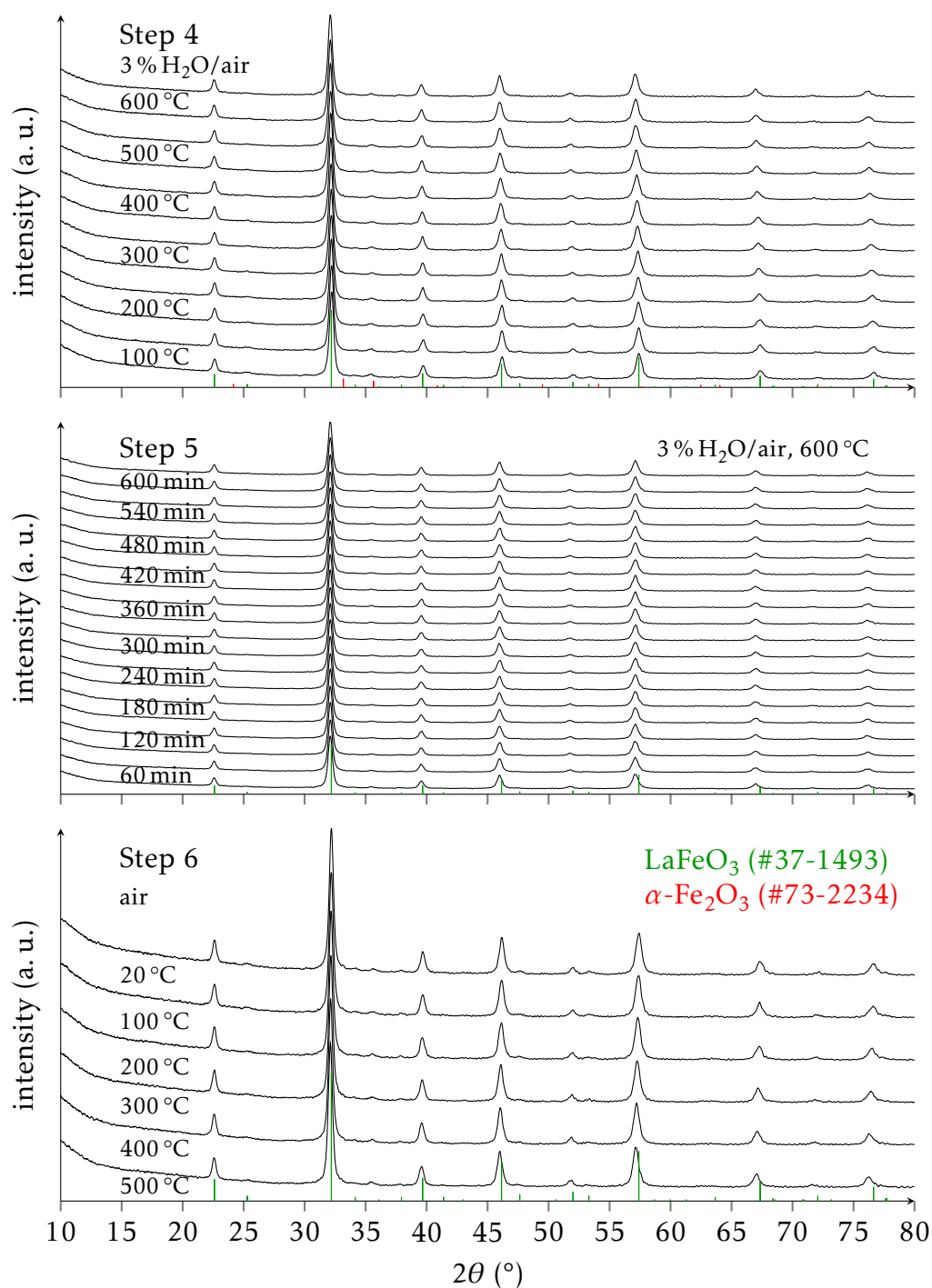


Figure 5.6 – High Temperature X-ray diffractograms of $\text{La}_{0.68}\text{FeO}_3$ prepared by CCM. Step 4 corresponds to a heating ramp under humid air flow up to 600 °C, Step 5 to the corresponding plateau and Step 6 to the subsequent cooling under dry air flow. Scheme in Section 2.2.5 Fig. 2.5.

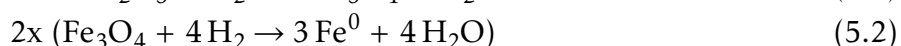
Table 5.3 – Comparison of photopeak maxima and surface compositions of calcined $\text{La}_{1-y}\text{FeO}_3$ ($y = 0, 0.32$; CCM), and the corresponding post-HTXRD samples. Post-HTXRD samples were analysed after step 6 after exposition to air.

nominal composition		B. E. (eV)			surface composition based on Fe
		La 3d _{5/2}	Fe 2p _{3/2}	O 1s	
LaFeO ₃	calcined	834.3	710.8	529.5	La _{2.13} FeO _{4.63} (C _{3.66})
LaFeO ₃	post-HTXRD	834.4	710.4	529.6	La _{1.64} FeO _{5.20} (C _{9.36})
La _{0.68} FeO ₃	calcined	834.6	710.6	529.7	La _{0.68} FeO _{2.98} (C _{3.19})
La _{0.68} FeO ₃	post-HTXRD	834.1	710.8	529.6	La _{1.02} FeO _{3.42} (C _{3.02})

oxidative thermal treatments do not accentuate the lower La content at the surface. On the contrary, the surface compositions seem to converge towards an equilibrated composition.

H₂-TPR

The results of H₂-TPR on La-deficient samples are shown in Fig. 5.7 compared to those of LaFeO₃ and the hematite sample. The reduction of LaFeO₃ starts only above 700 °C suggesting that LaFeO₃ is not reducible in the temperature range studied for the catalytic test. α -Fe₂O₃, on the other hand, is reduced at lower temperatures (< 600 °C). The H/Fe value of 2.96 (H/Fe_{max} = 3) indicates a complete reduction of Fe³⁺ to metallic Fe. As reported by Zielinski et al.,^[12] the overall reduction process involves successive steps as shown in Eq. 5.1 and 5.2.



Herein, the reduction corresponding to Eq. 5.2 can occur split in two reduction steps passing by the intermediate of wüstite, FeO, in certain cases as for example high water content in the system.^[12]

For samples with purposely decreased La-content, H₂-TPR curves reveal H₂ consumption in the same temperature range than that observed for α -Fe₂O₃ with 2 apparent maxima which could be explained by a reduction following the steps 5.1 and 5.2. At the same time, the H₂ uptake increases. Both findings are in agreement with an increasing hematite phase segregation. It is noticeable that the temperature of the apparent maximum shifts to higher values converging to that recorded for α -Fe₂O₃. This trend is particularly accentuated for La_{0.67}FeO₃ for which a greater extraction of Fe takes place. This could be indicative of the extent of dispersion and interaction of hematite on perovskites with lower La-content. In the case of the La_{0.8}FeO₃ solid an additional peak is observed, which can be attributed to the reduction of magnetite, Fe₃O₄, to wüstite, FeO, as an intermediate step for the reduction to Fe⁰.^[12]

As stated above, the total H₂-consumption at temperatures below 700 °C is increased with the decreasing La-content in the solid. An estimation of the hematite content was conducted on the basis of the H₂ consumption in this temperature range. The results are shown in Table 5.4. Thereby a maximum content of 9.9 wt.% of hematite was found for La_{0.67}FeO₃,

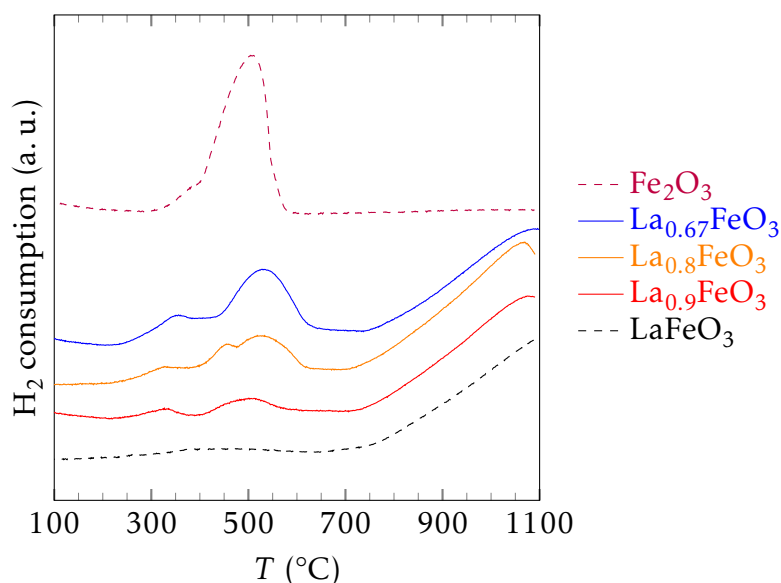


Figure 5.7 – H_2 -TPR of calcined $\text{La}_{1-y}\text{FeO}_3$ ($y = 0, 0.1, 0.2, 0.33$; 50 mg, 50 ml min^{-1}) compared to commercial $\alpha\text{-Fe}_2\text{O}_3$ (10 mg, 50 ml min^{-1}).

slightly lower compared to the theoretical value of 13.9 wt.% assuming a complete uptake in the solid of excess Fe in the form of hematite. A better agreement is observed for $\text{La}_{0.8}\text{FeO}_3$ and $\text{La}_{0.9}\text{FeO}_3$ accounting for the margin of error.

Table 5.4 – Comparison of H_2 -TPR results of $\text{La}_{1-y}\text{FeO}_3$ ($y = 0, 0.1, 0.2, 0.33$; 50 mg, 50 ml min^{-1}) and commercial $\alpha\text{-Fe}_2\text{O}_3$ (10 mg, 50 ml min^{-1}).

nominal composition	H_2 consumption ^a (mmol g^{-1})	Fe_2O_3 content		T_{max} reduction peaks			
		exp. (wt.%)	theo. ^b (wt.%)	(°C)	(°C)	(°C)	(°C)
LaFeO_3	-	-	-	-	-	-	> 1100
$\text{La}_{0.9}\text{FeO}_3$	0.49	2.6	3.6	328	-	504	1075
$\text{La}_{0.8}\text{FeO}_3$	1.39	7.5	7.6	327	457	521	1065
$\text{La}_{0.67}\text{FeO}_3$	1.83	9.9	13.9	354	-	527	1090
$\alpha\text{-Fe}_2\text{O}_3$	18.52	100	100	382	-	512	-

^a H_2 consumption was integrated over the temperature range of 200 °C to 700 °C.

^b Assuming that all excess Fe in the perovskite (based on the La-content) is consumed by a hematite phase (with $\text{H}/\text{Fe} = 2.96$).

5.1.4 Textural properties

The textural properties of the solids with decreased La-content are differing from LaFeO_3 . In both cases, isotherms are a composite of type II, indicating a low affinity toward the adsorbate such as in macroporous solids, and type IV, indicating the additional presence of mesoporosity. This latter trend is favoured for lower La-content as highlighted by the broad opening of the hysteresis compared to the LaFeO_3 sample (Fig. 5.8). Hence, the broadest

hysteresis showing mesoporosity has been observed for the sample prepared with the lowest La-content.

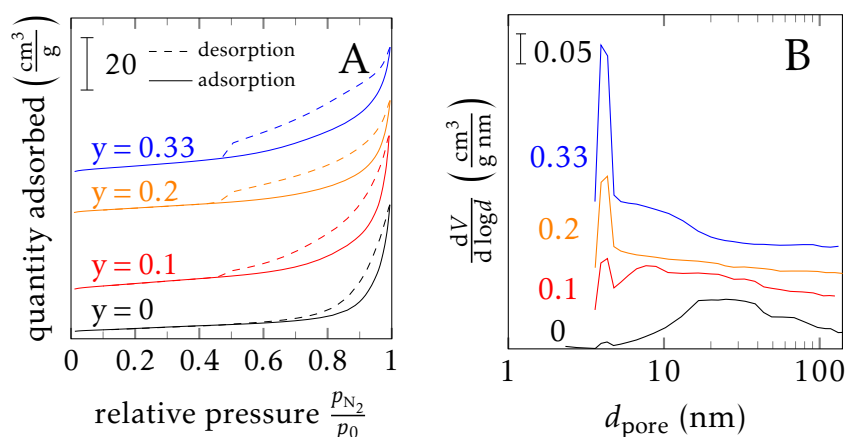


Figure 5.8 – Isotherms (A) and BJH pore size distributions from the desorption branch of the isotherm (B) of calcined $\text{La}_{1-y}\text{FeO}_3$ ($y = 0, 0.1, 0.2, 0.33$; CCM).

Cumulative pore volumes are very slightly increased for the samples with lower La-content (Table 5.5). The pore size distributions show an increased share of very low diameter mesopores ($d_{\text{pore}} < 5$ nm) for decreasing La-content, confirming the growing contribution of type IV in the isotherms. This happens at the expense of the macropores ($d_{\text{pore}} > 50$ nm). However, the microstructure morphology does not seem to evolve among all investigated samples as can be observed by scanning electron microscopy (SEM). Fig. 5.9 shows the SE micrographs of calcined LaFeO_3 and $\text{La}_{0.67}\text{FeO}_3$. In both cases porosity is only based on texture, pores are formed as holes between perovskite particles, typical for CCM solids as already discussed in Section 4.1. However, it can be seen that the macropores observed are slightly smaller for $\text{La}_{0.67}\text{FeO}_3$. This is in agreement with the evolution previously underlined for the pore size distributions (Fig. 5.8B).

Table 5.5 – Comparison of textural properties and crystallite sizes of $\text{La}_{1-y}\text{FeO}_3$ ($y = 0, 0.1, 0.2, 0.33$; CCM). Crystallite sizes (d_{cryst}) were estimated from XRD analyses (Section 5.1.2).

composition	SSA ($\text{m}^2 \text{g}^{-1}$)	V_{pore} ($\text{cm}^3 \text{g}^{-1}$)	d_{cryst} (nm)
LaFeO_3	13.9	0.08	20.1
$\text{La}_{0.9}\text{FeO}_3$	22.0	0.11	16.4
$\text{La}_{0.8}\text{FeO}_3$	17.6	0.08	18.2
$\text{La}_{0.67}\text{FeO}_3$	23.8	0.10	12.6

The data in Table 5.5 reveals that the specific surface areas are higher for all solids with decreased La-content compared to the LaFeO_3 sample. This increase was already observed before for Fe- and Mn-based perovskites.^[13,14] However, no clear correlation appears by comparing changes in the specific surface area and the extent of hematite segregation. Even though, in general, crystallite sizes are different from particle sizes, there seems to be a relation between the crystallite sizes of the perovskites and their specific surface area, the lower the former, the higher the latter. This has also been reported by Delmastro et al.^[13]

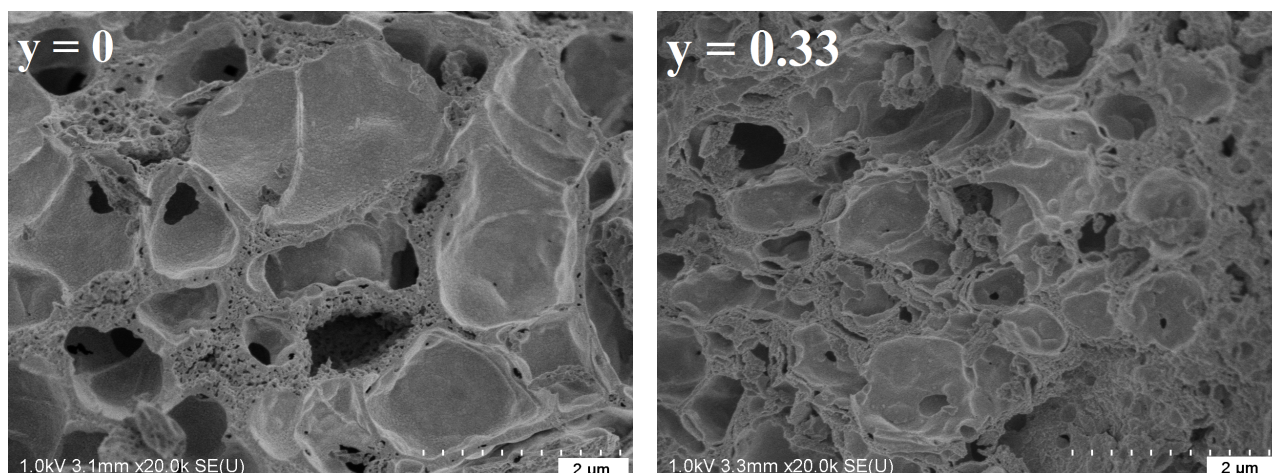


Figure 5.9 – Scanning electron micrographs of $\text{La}_{1-y}\text{FeO}_3$ ($y = 0, 0.33$; CCM).

5.1.5 Catalytic activity

The catalytic activity of the $\text{La}_{1-y}\text{FeO}_3$ samples was tested according to Procedure A by successive temperature-programmed reactions under stoichiometric (stoic1), lean and rich conditions, concluded by a return test under stoichiometric conditions (stoic2) performed after an activation under stoichiometric conditions at 600 °C (Section 2.3). CO, propylene, NO, propane, oxygen and hydrogen conversions during the test ramps are presented in Fig. 5.10 and 5.11 for the series of Fe-based perovskite catalysts. Additionally, temperatures corresponding to 50 % conversion (T_{50}) of CO, C_3H_6 and C_3H_8 under stoichiometric (1st run) and NO under rich conditions are reported in Table 5.6, additional ones in Appendix D (Table D.1).

The reference catalyst LaFeO_3 exhibited poor catalytic performances. By contrast, a significant enhancement of CO, propylene and NO conversion is observed for the samples containing less La, especially for $\text{La}_{0.67}\text{FeO}_3$.

For the whole perovskite series, H_2 is activated at temperatures above 300 °C (Fig. 5.11), higher than those corresponding to CO (Fig. 5.10) in agreement with the results obtained for the aforementioned LaFeO_3 solids prepared by different synthesis methods (Chapter 4). NO conversion is more closely linked to the residual O_2 concentration. Due to the high concentration of reductants (CO, hydrocarbons, and H_2), complete O_2 consumption is only reached at high temperatures under rich conditions. In all the other conditions, it is not achieved in the investigated temperature range. However, NO conversion only sets in after all O_2 is consumed, suggesting the low selectivity of H_2 , CO and propylene towards NO reduction.

Concerning the reductants, the enhancement of propylene conversion seems to be directly related to the degree of La-deficiency of the catalyst. This is not the case for the CO oxidation for which $\text{La}_{0.9}\text{FeO}_3$ is nearly as performing as $\text{La}_{0.67}\text{FeO}_3$. This may be due to the similar specific surface areas of the solids, and following the trend already seen for the crystallite sizes. Since differences in specific surface area are not very high, they should not be the decisive reason for the enhancement of catalytic performance. As stated earlier, propane conversion sets off at relatively high temperatures compared to CO and propylene. Propane's conversion is enhanced for a low La-decrease in the bulk ($\text{La}_{0.9}\text{FeO}_3$) compared to LaFeO_3 but decreased for samples with higher La-deficiency imposed during synthesis. On the other hand, NO reduction is significantly enhanced. While the stoichiometric LaFeO_3 sample does

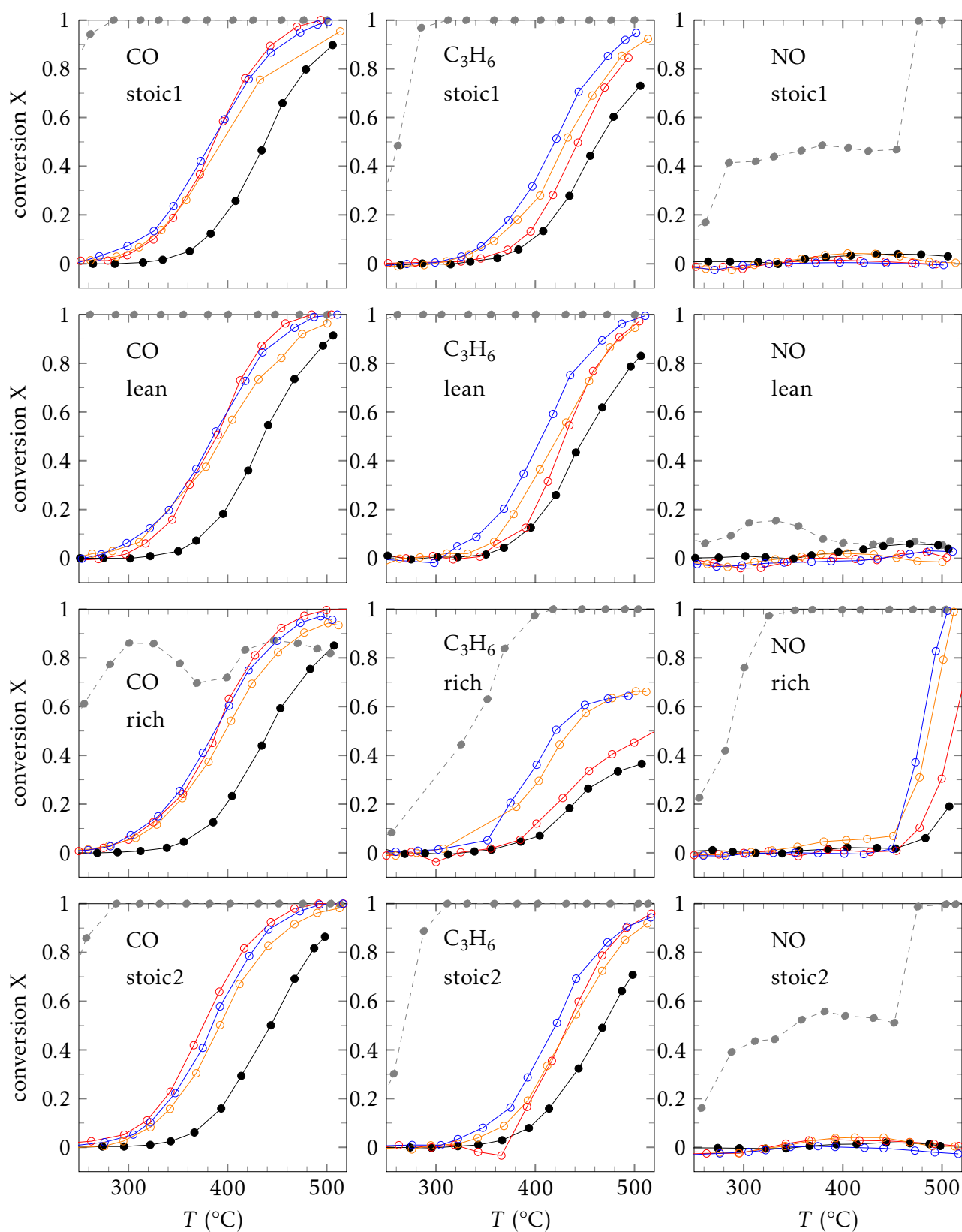


Figure 5.10 – CO, C₃H₆ and NO conversions of Fe-based perovskite catalysts (Procedure A). LaFeO₃ (●), La_{0.9}FeO₃ (◊), La_{0.8}FeO₃ (◐), and La_{0.67}FeO₃ (◑) compared to the commercial reference TWC (◉)

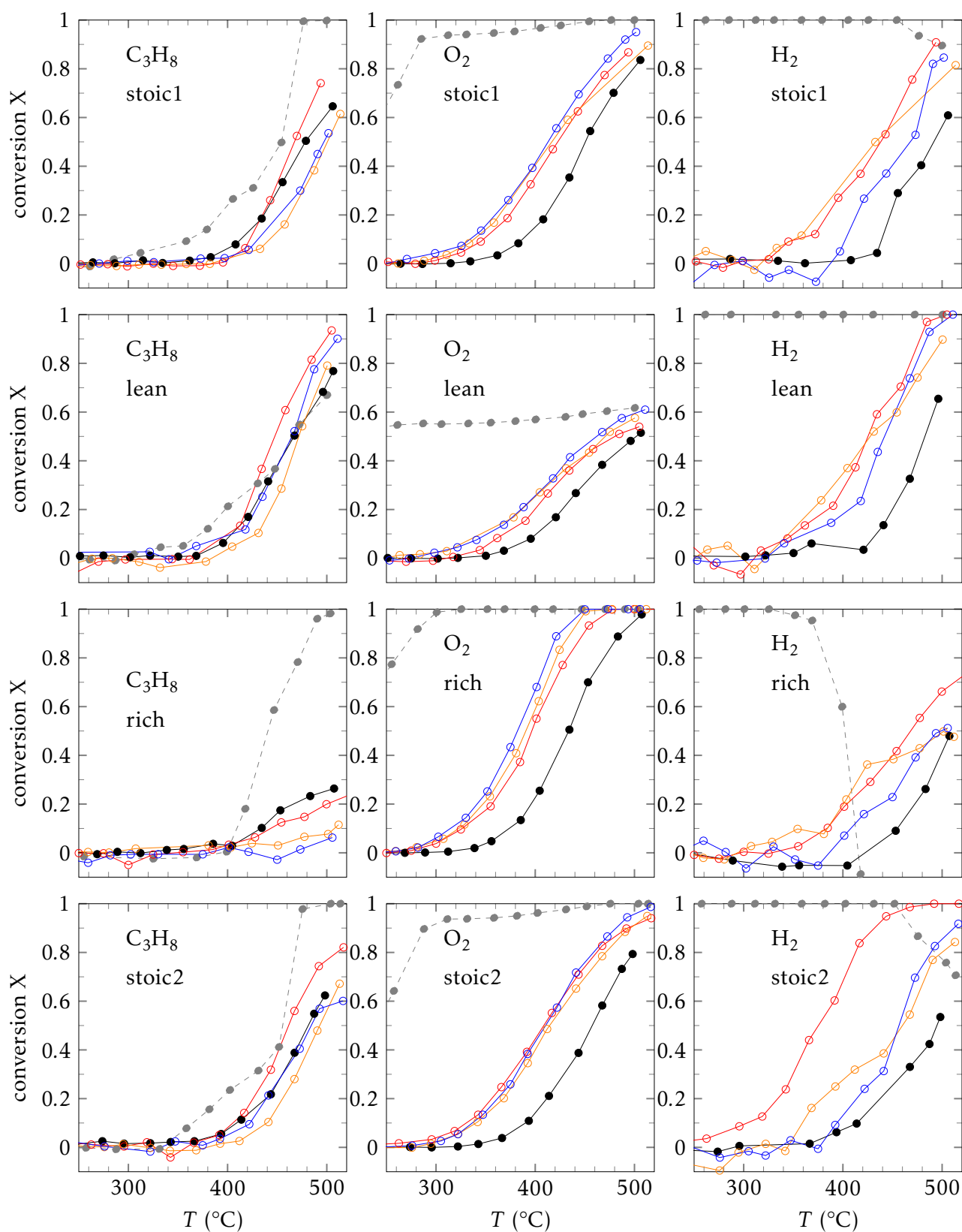


Figure 5.11 – C_3H_8 , O_2 and H_2 conversions of Fe-based perovskite catalysts (Procedure A). LaFeO_3 (●), $\text{La}_{0.9}\text{FeO}_3$ (◊), $\text{La}_{0.8}\text{FeO}_3$ (◐), and $\text{La}_{0.67}\text{FeO}_3$ (◑) compared to the commercial reference TWC (◐)

not even reach 50 % conversion below 510 °C, lower La-content clearly leads to activation at lower temperatures. Overall best results for all pollutants are obtained by $\text{La}_{0.67}\text{FeO}_3$. The main product, however, remains ammonia as already observed for the LaFeO_3 solid.

Table 5.6 – Temperatures corresponding to 50 % conversion of CO, C_3H_6 , C_3H_8 , and H_2 (stoichiometric) and NO (rich composition) of $\text{La}_{1-y}\text{FeO}_3$ catalysts ($y = 0, 0.1, 0.2, 0.33$; CCM) compared to hematite and a mechanic mixture of LaFeO_3 and Fe_2O_3 .

condition	stoichiometric				rich
	CO	C_3H_6	C_3H_8	H_2	NO
T_{50} (°C)					
LaFeO_3	438	463	478	501	^{-a}
$\text{La}_{0.9}\text{FeO}_3$	386	443	467	439	510
$\text{La}_{0.8}\text{FeO}_3$	398	431	499	433	488
$\text{La}_{0.67}\text{FeO}_3$	384	420	497	471	479
Fe_2O_3	459	490	^{-a}	493	^{-a}
$\text{Fe}_2\text{O}_3 + \text{LaFeO}_3$	436	465	486	482	^{-a}

^a Conversion lower than 50 %.

The solids prove stable under the test conditions as suggested by the similar conversion profiles obtained during the return tests (Fig. 5.10 and 5.11, stoic2). Interestingly, a much enhanced H_2 activation is observed for the $\text{La}_{0.9}\text{FeO}_3$ solid, and to a lesser extent for the $\text{La}_{0.8}\text{FeO}_3$ sample.

Table 5.7 – Comparison of specific reaction rates r_{specific} at 350 °C, apparent activation energies $E_{A,\text{app}}$ and pre-exponential factors A of CO and C_3H_6 oxidation for $\text{La}_{1-y}\text{FeO}_3$ catalysts ($y = 0, 0.1, 0.2, 0.33$; CCM) under stoichiometric conditions (1st test ramp). Arrhenius parameters were determined by Arrhenius plots (Fig. D.4).

	SSA ($\text{m}^2 \text{g}^{-1}$)	r_{specific}^a ($\text{mol s}^{-1} \text{g}^{-1}$)		$E_{A,\text{app}}$ (kJ mol^{-1})		A ($10^3 \text{ m}^3 \text{ s}^{-1} \text{g}^{-1}$)	
		CO	C_3H_6	CO	C_3H_6	CO	C_3H_6
$\text{La}_{0.9}\text{FeO}_3$	22.0	$4.4 \cdot 10^{-7}$	$4.1 \cdot 10^{-9}$	119	127	40.1	20.4
$\text{La}_{0.8}\text{FeO}_3$	17.6	$4.4 \cdot 10^{-7}$	$10.4 \cdot 10^{-9}$	101	111	1.2	2.5
$\text{La}_{0.67}\text{FeO}_3$	21.5	$5.2 \cdot 10^{-7}$	$12.3 \cdot 10^{-9}$	81	119	0.03	12.7

^a Specific reaction rates were calculated from conversions at 350 °C.

Interestingly, some differences arise in the kinetic behaviour of $\text{La}_{1-y}\text{FeO}_3$ ($y = 0, 0.1, 0.2, 0.33$) for CO and propylene oxidation by oxygen. This can be seen by comparing the values of the pre-exponential factor and the apparent activation energy. As illustrated in Table 5.7, the numerical values for A obtained for propylene oxidation are of the same order of magnitude with no significant variation. The gradual increase of the specific activity can be simply explained by slight changes observed on the activation barriers. On the other hand, a sharp decrease on A values is recorded on La-deficient perovskites for CO oxidation and an apparent compensation effect is also noticeable with a parallel sharp decrease in the apparent activation energy values. These comparisons would suggest that propylene

oxidation would be much less sensitive to surface modifications than CO oxidation. In this case, activity changes might be partly related to a partial segregation of Fe^{3+} in the form of hematite. Hence, the intrinsic activity related to changes of the apparent activation energy would be likely explained by the segregation of Fe_2O_3 intrinsically more active than LaFeO_3 (commercial hematite sample: $1.8 \text{ m}^2 \text{ g}^{-1}$). On the other hand, the discontinuity observed on the specific activities from LaFeO_3 to $\text{La}_{0.9}\text{FeO}_3$ with no variation recorded for lower y composition suggests that the degree of clustering is an outstanding parameter. An optimal value would be obtained for $y = 0.9$ while below 0.9 aggregation of Fe_2O_3 clusters would lower the density of active sites compensated by the decrease observed on the activation barriers. This explanation seems to be in agreement with the shift observed of the H_2 -TPR curves showing that the reducibility of the hematite phase may be related to the extent of dispersion.

A comparative test was conducted on α - Fe_2O_3 . It is clearly less performing than the perovskites, even the stoichiometric LaFeO_3 solid (Table 5.6). The mechanical mixture of $\text{Fe}_2\text{O}_3 + \text{LaFeO}_3$ – containing the same atomic distribution of Fe in perovskite and simple oxide as assumed for $\text{La}_{0.7}\text{FeO}_3$ – yields similar results concerning temperatures corresponding to 50 % conversion to the ones of the stoichiometric LaFeO_3 perovskite sample. Temperatures corresponding to 50 % conversion are listed in Table 5.6. They are similar to those of LaFeO_3 or higher except for hydrogen. Therefore, the increase in activity of the perovskites with lower La-content cannot be directly attributed to increasing amounts of hematite in itself, but may be due to a stronger interaction of hematite and perovskite phases in the solids.

The enhancement of catalytic performance is related to the higher Fe surface concentration previously evidenced by XPS measurements, the B cation being considered as the catalytically active one in the perovskite structure.^[15] Higher specific surface areas of the solids prepared with decreased La-content as well as lower crystallite sizes leading to enhanced exposure of active sites further intensify the impact on the pollutants' conversions. Nonetheless, from the estimations of the specific surface rates and Arrhenius parameters it is evident that not only the increased specific surface area but the quality of the surface, i. e. the active sites, enhances catalytic activity for Fe-based perovskites with lowered La-content.

5.1.6 Conclusion

The catalytic activity of a series of perovskite-based $\text{La}_{1-y}\text{FeO}_3$ was investigated for application in 3-way catalysis. The decrease of La involved in the synthesis was successfully used to reduce the initial La enrichment at the surface. The increase of specific surface area with a corresponding decrease of crystallite size was accompanied by the development of mesopores with a typical diameter range of 3 to 5 nm. The co-existence of hematite in strong interaction with the orthorhombic LaFeO_3 perovskite structure was evidenced by H_2 -TPR and Raman spectroscopy on solids with lower La-content. Comparing the respective XRD and H_2 -TPR results, the dispersion of the hematite phase on $\text{La}_{1-y}\text{FeO}_3$ solids appears to be higher than on the LaFeO_3 perovskites prepared by MSM.

Surface composition optimisation strongly enhances the catalytic activity of the perovskite by increasing the accessibility of the active Fe^{3+} sites. This increase in performance is not only due to higher specific surface areas as could be shown by estimations of the specific reaction rates and the Arrhenius parameters. It was found that CO and propylene oxidation proceed on different sites. Furthermore, the increase in performance cannot be explained by the hematite itself but may be due to the stronger interaction of low concentrations of dispersed hematite with the perovskite phase due to the in situ synthesis.

Fe-based perovskites with controlled surface composition are a good basis in order to partly replace noble metals in conventional 3-way catalysts. This further step could be achieved by combining this approach with partial substitution by a divalent cation in A or by more reducible cations in B.

5.2 Influence of substitution in A-site

Herein, the partial A-site substitution in order to optimise the bulk composition of the perovskites has been investigated. Substituting LaFeO_3 in the A-site by divalent cations such as Ca^{2+} can be relevant because to fulfil the electronic neutrality B-site cations can be stabilised in unusual oxidation states or anionic vacancies can be created. These processes must be controlled in order to prevent a destabilisation of the structure. In order to study this effect, a series of $\text{La}_{1-x}\text{Ca}_x\text{FeO}_3$ ($x = 0, 0.1, 0.2$) prepared by CCM was investigated.

5.2.1 Structural properties

Fig. 5.12 displays the XRD patterns of the $\text{La}_{1-x}\text{Ca}_x\text{FeO}_3$ series. The substituted catalysts retain the orthorhombic LaFeO_3 perovskite structure. Slight shifts to higher angles are discernible but no crystalline phase segregation is observed.

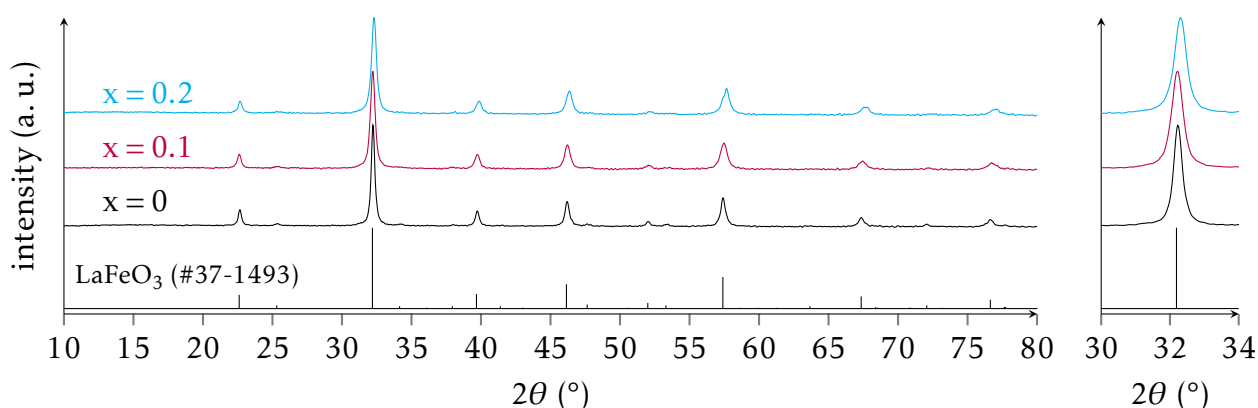


Figure 5.12 – X-ray diffractograms of calcined $\text{La}_{1-x}\text{Ca}_x\text{FeO}_3$ ($x = 0, 0.1, 0.2$; CCM).

Such shifts to higher angles originate from the contraction of the perovskite lattice, confirmed by the evolution of unit cell volume which decreases nearly linearly with the Ca-content as illustrated in Fig. 5.13.

Assuming the behaviour of a simple steric model, such decrease in lattice parameters (listed in Table 5.8) cannot arise from the difference of the ionic radii of La^{3+} and Ca^{2+} , being nearly equal in a 12-coordinate environment ($r_{\text{Ca}^{2+}} = 1.34 \text{ \AA}$, $r_{\text{La}^{3+}} = 1.36 \text{ \AA}$)^[16]. The partial oxidation of Fe^{3+} to Fe^{4+} can be assumed to account for part of the decreasing unit cell volume induced by the substitution of La by Ca as reported by Ciambelli et al. and Pecchi et al.^[17,18] The difference in effective ionic radii in 6-coordinate environment ($r_{\text{Fe}^{3+}} = 0.645 \text{ \AA}$, $r_{\text{Fe}^{4+}} = 0.585 \text{ \AA}$)^[16] could indeed be partly at the origin of the shrinkage of the unit cell. Ciambelli et al. did extensive studies on this subject for $\text{La}_{1-x}\text{Ca}_x\text{FeO}_3$ ($x = 0, 0.1, 0.2, 0.3, 0.4, 0.5$; CCM; calcined at $800 \text{ }^\circ\text{C}$) including Fe^{4+} titration and thereby confirmed the presence of low amounts of this Fe species.^[17] However, they also reported that the ratio of $\text{Fe}^{4+}/\text{Ca}^{2+}$

²effective ionic radii

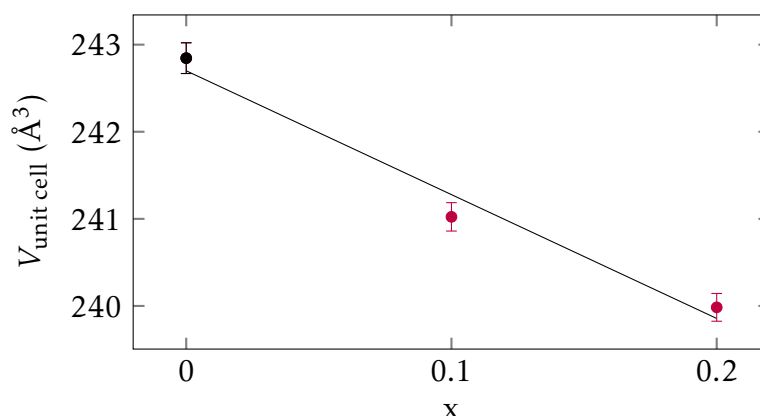


Figure 5.13 – Evolution of the unit cell volume of calcined $\text{La}_{1-x}\text{Ca}_x\text{FeO}_3$ ($x = 0, 0.1, 0.2$; CCM).

was always lower than 1^[17] – the value which would be necessary to reach electroneutrality – i. e. it has to be supposed that oxygen vacancies are present as well. Since oxygen anions with an effective radius of $r_{\text{O}^{2-}} = 1.40 \text{ \AA}$ ^[16] are even larger than Ca^{2+} and La^{3+} , their influence on the unit cell parameters can be assumed to be stronger than the partial oxidation of the B-site cation.

Table 5.8 – Comparison of crystallite sizes and unit cell parameters derived from full pattern matching of calcined $\text{La}_{1-x}\text{Ca}_x\text{FeO}_3$ ($x = 0, 0.1, 0.2$; CCM).

	d_{cryst} (nm)	a (Å)	b (Å)	c (Å)	$V_{\text{unit cell}}$ (Å ³)
LaFeO_3	20.1 ± 0.1	5.561	7.858	5.558	242.85 ± 0.17
$\text{La}_{0.9}\text{Ca}_{0.1}\text{FeO}_3$	17.6 ± 0.1	5.556	7.825	5.543	241.02 ± 0.16
$\text{La}_{0.8}\text{Ca}_{0.2}\text{FeO}_3$	15.9 ± 0.1	5.550	7.806	5.539	239.98 ± 0.16

Table 5.8 also reports apparent crystallite sizes of the $\text{La}_{1-x}\text{Ca}_x\text{FeO}_3$ ($x = 0, 0.1, 0.2$) samples. A decrease in crystallite size is observed for samples with higher Ca-content.

5.2.2 Reducibility

The reducibility of the solids was studied by H_2 -TPR analyses. As illustrated in Fig. 5.14, the differences between LaFeO_3 and the Ca-substituted samples are of a minor extent. The LaFeO_3 bulk reduction starts above $700 \text{ }^\circ\text{C}$. 3 additional reduction peaks with very low intensity are observed for the Ca-substituted solids in the temperature range below $700 \text{ }^\circ\text{C}$ (Table 5.9).

In the low temperature domain, 2 hydrogen consumption ranges ($200 \text{ }^\circ\text{C} < T < 340 \text{ }^\circ\text{C}$, $340 \text{ }^\circ\text{C} < T < 400 \text{ }^\circ\text{C}$) have been reported before for $\text{La}_{1-x}\text{Ca}_x\text{FeO}_3$ ($x = 0.1, 0.2$).^[18,19] As reported by Pecchi et al., the 1st peak can be attributed to the reduction of Fe^{4+} species while the 2nd peak and 3rd peak (just below $700 \text{ }^\circ\text{C}$) have also been observed before, however, no clear evidence as to the origin was found.^[18]

The Fe^{4+} content of the $\text{La}_{1-x}\text{Ca}_x\text{FeO}_3$ samples was estimated assuming the complete reduction of this species to Fe^{3+} in the temperature range corresponding to the 1st reduction peak.^[18,19] As shown in Table 5.9, the $\text{Fe}^{4+}/\text{Fe}_{\text{total}}$ ratio increases proportionally to the Ca-content. Nonetheless, the atomic ratio of $\text{Fe}^{4+}/\text{Ca}^{2+}$ diverge from the theoretical value of 1

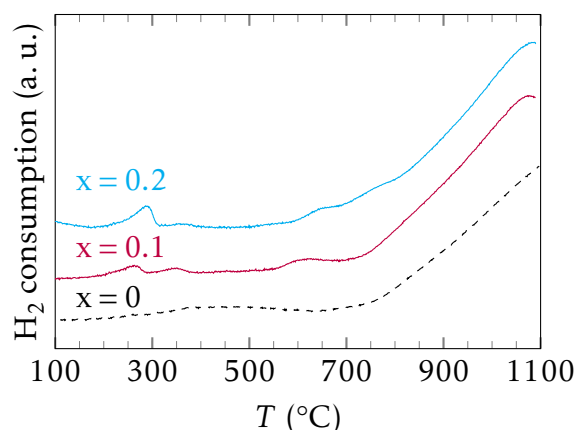


Figure 5.14 – H_2 uptake curves recorded during H_2 -TPR of calcined $\text{La}_{1-x}\text{Ca}_x\text{FeO}_3$ ($x = 0, 0.1, 0.2$; CCM, 50 ml min^{-1}).

assuming that electroneutrality is achieved exclusively by the variation of the oxidation state of Fe. This suggests the generation of anionic vacancies.

Table 5.9 – Comparison of H_2 -TPR results of $\text{La}_{1-x}\text{Ca}_x\text{FeO}_3$ ($x = 0, 0.1, 0.2$; CCM; 50 mg, 50 ml min^{-1}).

nominal composition	H_2 consumption		$\text{Fe}^{4+}/\text{Fe}_{\text{total}}^{bc}$ (at.%)	$\text{Fe}^{4+}/\text{Ca}^{2+}$ (at.%)	T_{max} (°C)	reduction peaks		
	total ^a (mmol g^{-1})	Fe^{4+} ^b				(°C)	(°C)	(°C)
LaFeO_3	-	-	-	-	-	-	-	> 1100
$\text{La}_{0.9}\text{Ca}_{0.1}\text{FeO}_3$	0.17	0.07	3.2	0.32	261	349	600	1075
$\text{La}_{0.8}\text{Ca}_{0.2}\text{FeO}_3$	0.18	0.15	6.6	0.33	290	370	642	1084

^a H_2 consumption was integrated over the temperature range of 200 °C to 700 °C.

^b H_2 consumption of 1st peak was attributed to the reduction of Fe^{4+} .

^c Assuming that Fe^{4+} is completely reduced to Fe^{3+} ($\text{H}/\text{Fe} = 1$).

Overall, these additional reduction phenomena lead to only slightly more reducible solids with respect to LaFeO_3 .

5.2.3 Textural properties

The textural properties of the Ca-substituted solids were studied by N_2 -physisorption. As shown in Fig. 5.15A, all $\text{La}_{1-x}\text{Ca}_x\text{FeO}_3$ solids ($x = 0, 0.1, 0.2$) present similar textural properties of perovskites with respect to LaFeO_3 , exhibiting a combination between a dominant type II (weakly porous or macroporous) and type IV (mesoporous) isotherm.

Textural porosity of the solids is confirmed by the broad pore size distributions ranging from 5 to more than 100 nm (Fig. 5.15B). Similar pore size distribution profiles are observed for all materials and higher specific surface area and cumulative pore volume are obtained on $\text{La}_{1-x}\text{Ca}_x\text{FeO}_3$ solids with respect to LaFeO_3 (Table 5.10).

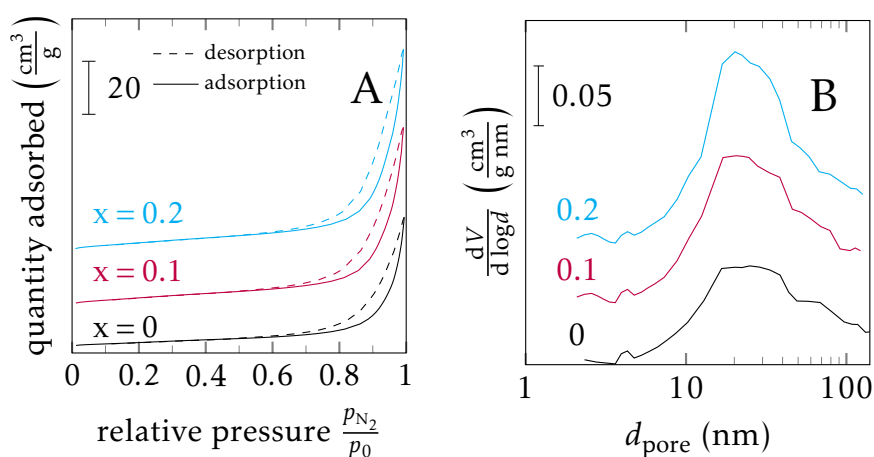


Figure 5.15 – N_2 adsorption and desorption isotherms and pore size distributions of calcined $La_{1-x}Ca_xFeO_3$ ($x = 0, 0.1, 0.2$; CCM).

Table 5.10 – Comparison of specific surface areas and cumulative pore volume of $La_{1-x}Ca_xFeO_3$ ($x = 0, 0.1, 0.2$; CCM).

composition	SSA ($m^2 g^{-1}$)	V_{pore} ($cm^3 g^{-1}$)
$LaFeO_3$	13.9	0.08
$La_{0.9}Ca_{0.1}FeO_3$	20.8	0.11
$La_{0.8}Ca_{0.2}FeO_3$	23.4	0.13

5.2.4 Chemical composition at the surface

The chemical composition at the surface of the solids was studied by XPS. Photopeak maxima of the La $3d_{5/2}$ core level (Table 5.11) are shifted to slightly lower B. E. This is also observed for the Fe $2p_{3/2}$ maxima. Furthermore, the La $3d$ and Fe $2p$ photopeaks (Fig. 5.16) of the whole $La_{1-x}Ca_xFeO_3$ series show the typical multiplet splitting and satellite positions of La^{3+} and Fe^{3+} . The Fe $2p$ photopeaks show broad but low intensity Fe $2p$ satellites at ≈ 719 eV characteristic of Fe^{3+} . Low amounts of Fe^{4+} species may be generated to yield electroneutrality as a consequence of the destabilisation of the structure by the introduction of the divalent A-site cation. Fe^{4+} cations would be expected at 711.6 eV.^[20] However, since Fe^{3+} and Fe^{4+} are so close in B. E. no meaningful spectral decomposition can be performed by using only these 2 components. Another way to achieve electroneutrality in the perovskite structure is the generation of oxygen vacancies whose presence, however, cannot be confirmed or denied by XPS.

The maximum positions of Ca $2p_{3/2}$ are close but a slightly higher value is observed for the sample with higher Ca-content. Ca $2p$ photopeaks (Fig. 5.16) of the substituted samples show the characteristic multiplet splitting and very low intensity satellite features at B. E. > 353 eV.

O $1s$ and C $1s$ photopeaks of the $La_{1-x}Ca_xFeO_3$ series are also shown in Fig. 5.16. Photopeak maxima of O $1s$ are shifted to lower B. E. for the substituted samples. Spectral decomposition of the O $1s$ photopeaks confirmed a high contribution of non-lattice oxygen species (about 44 at.%) as already observed for the non-substituted perovskite (46 at.%). The relative intensity of carbonates is increased (17 to 21 at.%) compared to the non-substituted perovskite sample (13 at.%). This is in agreement with the potential formation and stabilisa-

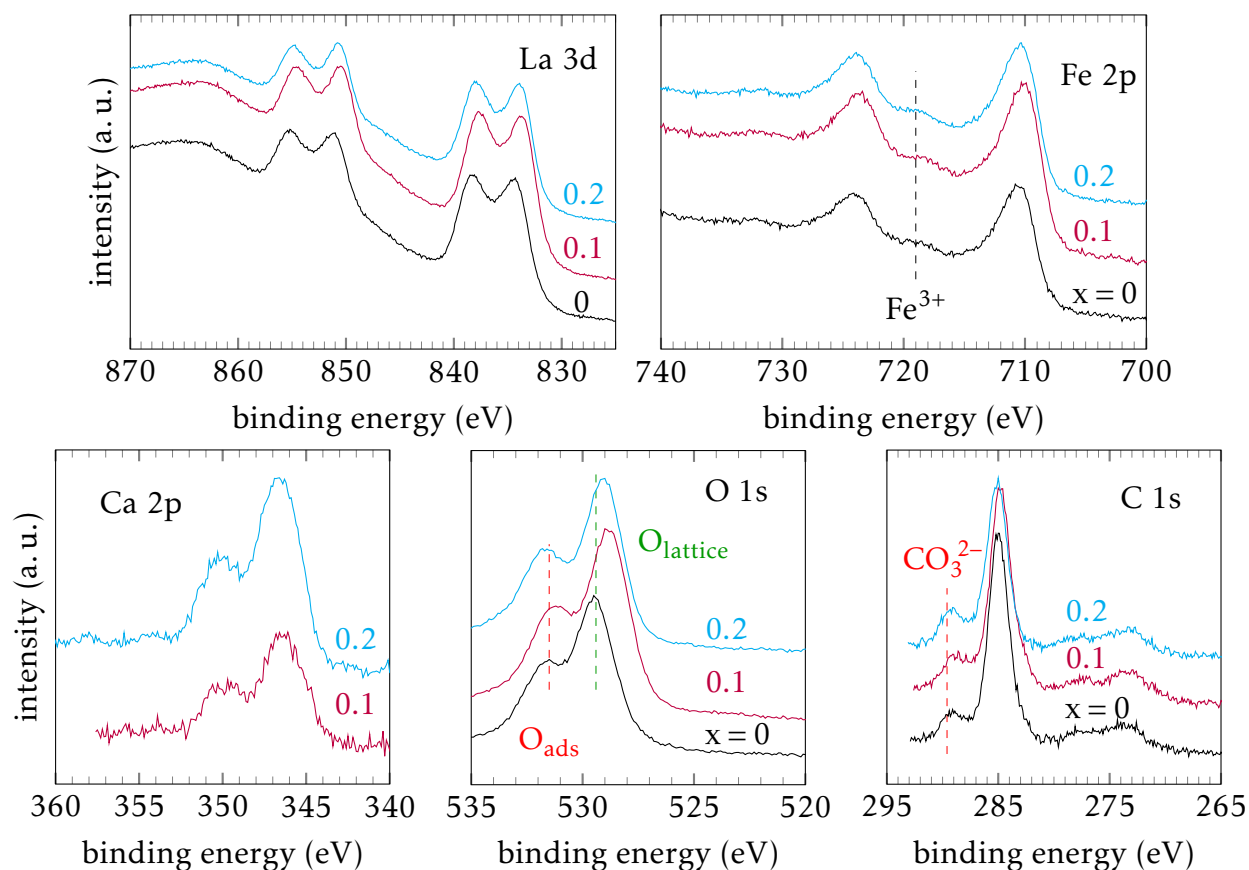


Figure 5.16 – La 3d, Fe 2p, Ca 2p, O 1s and C 1s photopeaks of calcined $\text{La}_{1-x}\text{Ca}_x\text{FeO}_3$ ($x = 0, 0.1, 0.2$; CCM).

tion of calcium carbonate on the surface.

As expected the atomic La/Fe ratio decreases with increasing La substitution by Ca (Table 5.11). However, the A^3/Fe ratios of Ca-substituted perovskites remain close to that of the LaFeO_3 solid suggesting that A-site enrichment on the $\text{La}_{1-x}\text{Ca}_x\text{FeO}_3$ surface is maintained.

³A = La + Ca

Table 5.11 – **Surface atomic ratios $x_{\text{La}}/x_{\text{Fe}}$ and $x_{\text{Ca}}/x_{\text{La}}$, photopeak maxima and abundance of selected surface species of calcined $\text{La}_{1-x}\text{Ca}_x\text{FeO}_3$ ($x = 0, 0.1, 0.2$; CCM). Atomic abundances of $\text{O}_{\text{lattice}}$ and $\text{C}_{\text{CO}_3^{2-}}$ were obtained by spectral decomposition of O 1s and C 1s photopeaks. Complete surface compositions are reported in Table B.2 in the Appendix.**

x	XPS			B. E. (eV)				at. %	
	$x_{\text{La}}/x_{\text{Fe}}$	$x_{\text{A}}/x_{\text{Fe}}$	$x_{\text{Ca}}/x_{\text{La}}$	La 3d _{5/2}	Ca 2p _{3/2}	Fe 2p _{3/2}	O 1s	$\text{O}_{\text{lattice}}^a$	$\text{C}_{\text{CO}_3^{2-}}^b$
0	2.13	2.13	-	834.3	-	710.8	529.5	55	13
0.1	1.77	1.94	0.10	833.7	346.1	709.9	529.0	57	17
0.2	1.71	2.08	0.21	833.9	346.6	710.3	529.0	56	21

^a $\text{O}_{\text{lattice}} + \text{O}_{\text{ads}} = 1$.

^b $\text{C}_{\text{CO}_3^{2-}} + \text{C}_{\text{adventitious}} = 1$.

5.2.5 Catalytic performance

The catalytic activity of the Ca-substituted samples was tested according to Procedure A (Section 2.3). CO, propylene and NO conversions during temperature-programmed reactions are presented in Fig. 5.17. Additionally, T_{50} values are reported in Table 5.12 and in Appendix D (Table D.2).

Oxidation reactions of CO, propylene and propane are enhanced for a Ca-substitution degree of $x = 0.1$. This is most notable for the CO conversion which is complete under lean and stoichiometric conditions and above 90 % under rich conditions. Propylene and propane yield up to 10 % higher maximum conversions for this sample compared to LaFeO_3 (CCM) under stoichiometric and lean conditions. On the other hand, a higher Ca-substitution degree seems to lead to an inverse trend. In the context of the complexity of the involved reaction pathways in the employed gas feed, this may be due to either the slightly enhanced reducibility due to an increased substitution degree leading to higher amounts of Fe^{4+} species or the higher amount of oxygen vacancies. On the other hand, a higher A-site cation excess and a higher surface carbonate contribution blocking the catalytically active Fe cation is observed for higher Ca-content.

Table 5.12 – Temperatures corresponding to 50 % conversion of CO, C_3H_6 , C_3H_8 , and H_2 (stoichiometric) and NO (rich composition) of $\text{La}_{1-x}\text{Ca}_x\text{FeO}_3$ catalysts ($x = 0, 0.1, 0.2$; CCM) and selectivities of NO reduction products at T_S .

condition	stoichiometric				rich				
	T_{50} (°C)				selectivities at T_S				
	CO	C_3H_6	C_3H_8	H_2	NO	S_{N_2}	S_{NH_3}	$S_{\text{N}_2\text{O}}$	T_S (°C)
LaFeO_3	438	463	478	501	^a	0.05	0.95	0	507
$\text{La}_{0.9}\text{Ca}_{0.1}\text{FeO}_3$	414	446	461	463	499 ^b	0.86	0	0.14	498
$\text{La}_{0.8}\text{Ca}_{0.2}\text{FeO}_3$	449	482	499	482	510 ^b	1.00	0	0	500

^a Conversion lower than 50 %.

^b T_{25} .

As was already discussed for other CCM solids before, NO reduction only occurs at very high temperatures under rich conditions. Even though the reduction performance is slightly enhanced by the Ca-substitution of La (even for $x = 0.2$), it is still very low. It is clearly lower than for the samples prepared with lower La-content. The main advantage of substitution in this respect is a higher N_2 selectivity. Whereas only 5 % of NO are converted to N_2 for the non-substituted LaFeO_3 , the rest leading to NH_3 production, the $\text{La}_{0.8}\text{Ca}_{0.2}\text{FeO}_3$ solid yields an N_2 selectivity of 25 %.

The return test yields similar results for the $\text{La}_{1-x}\text{Ca}_x\text{FeO}_3$ samples suggesting stability under test conditions.

In conclusion, $\text{LaFe}_{0.9}\text{Ca}_{0.1}\text{O}_3$ showed similar or better results than LaFeO_3 under all conditions (Table D.2), whereas the sample with higher Ca-content yielded generally lower conversions of the pollutants compared to both solids. This is in agreement with results on methane combustion reported by Ciambelli et al. who found that a higher Fe^{4+} concentration does not enhance catalytic activity for methane oxidation.^[17] While NO conversion remains low, a higher S_{N_2} is observed. However, no correlation between the Fe^{4+} or oxygen vacancy amount and the catalytic performance can be established.

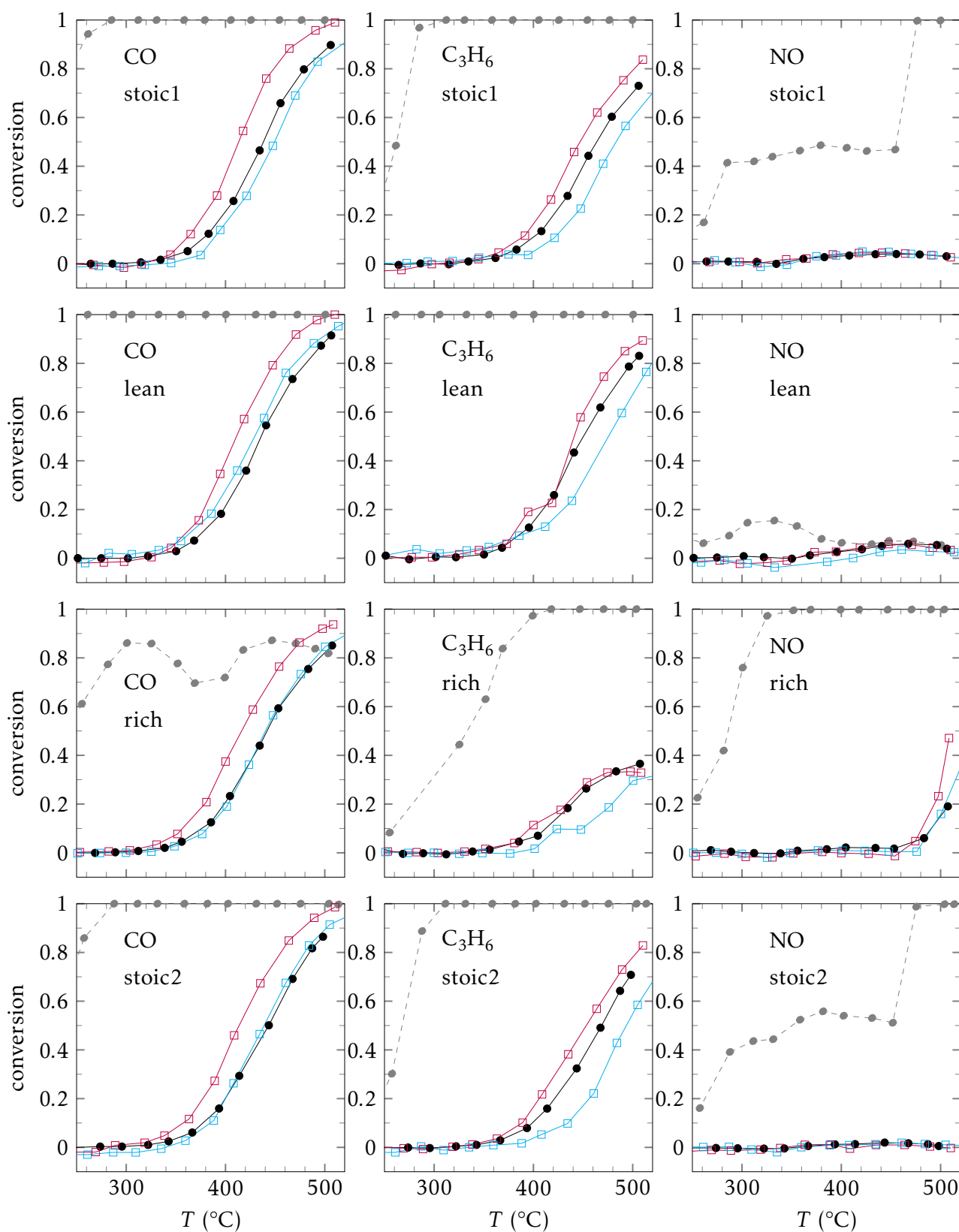


Figure 5.17 – CO, C_3H_6 and NO conversions of $La_{1-x}Ca_xFeO_3$ catalysts (Procedure A). $LaFeO_3$ (\bullet), $LaCa_{0.1}Fe_{0.9}O_3$ (\square), and $LaCa_{0.2}Fe_{0.8}O_3$ (\square) compared to the commercial reference TWC (\bullet)

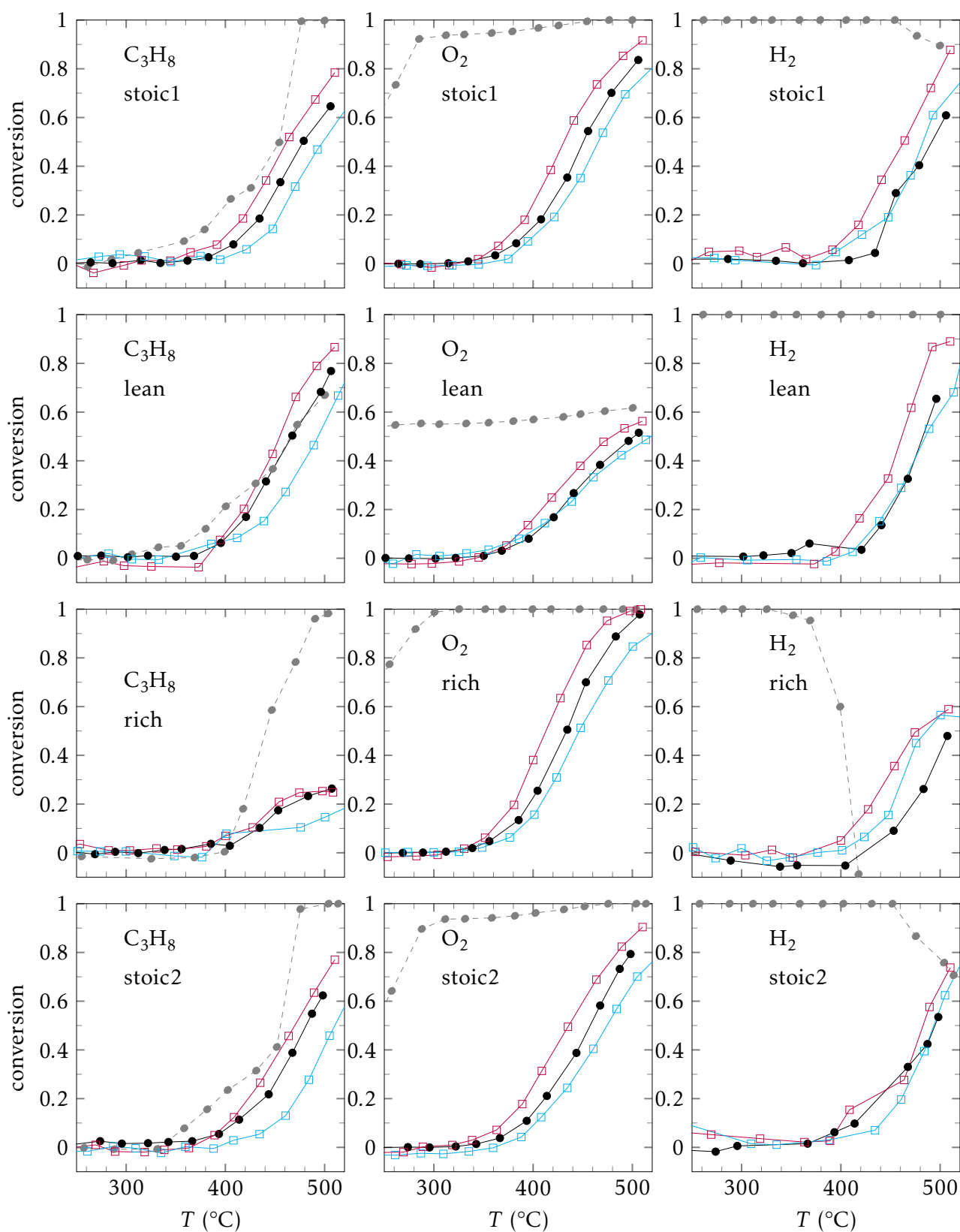


Figure 5.18 – C_3H_8 , O_2 and H_2 conversions of $La_{1-x}Ca_xFeO_3$ catalysts (Procedure A). $LaFeO_3$ (●), $LaCa_{0.1}Fe_{0.9}O_3$ (◻), and $LaCa_{0.2}Fe_{0.8}O_3$ (◻) compared to the commercial reference TWC (●)

5.2.6 Conclusion

The influence of Ca-substitution in A of Fe-based perovskites on the catalytic activity in 3-way catalytic conditions was investigated comparing $\text{La}_{1-x}\text{Ca}_x\text{FeO}_3$ catalysts ($x = 0, 0.1, 0.2$) prepared by CCM. In this substitution degree range a solid solution within the perovskite structure is obtained without any detectable crystalline segregation. XRD analyses evidenced that the insertion of the divalent cation causes a contraction of the unit cell due to the generation of low amounts of Fe^{4+} species and higher contributions of anionic defects as confirmed by H_2 -TPR analyses. The absolute amounts of Fe^{4+} species as oxygen vacancies increase for higher substitution degrees.

Textural properties of the $\text{La}_{1-x}\text{Ca}_x\text{FeO}_3$ solids ($x = 0.1, 0.2$) are similar to those of the LaFeO_3 sample prepared by CCM. A slight narrowing of the pore size distribution accompanied by a higher specific surface area is observed.

Concerning the surface of the Ca-substituted solids, an A-site cation enrichment of similar magnitude as for the non-substituted LaFeO_3 sample was revealed. This is attributed to a Ca enrichment at the surface in analogy to the already known La enrichment. Furthermore, due to the high basicity of Ca^{2+} a higher contribution of carbonate species is detected on the surface of the $\text{La}_{1-x}\text{Ca}_x\text{FeO}_3$ solids ($x = 0.1, 0.2$).

The insertion of low amounts of Ca ($x = 0.1$) into the LaFeO_3 perovskite structure yields moderate catalytic performance enhancements especially concerning oxidation of CO and HC. While NO reduction improvement is lower than for the $\text{La}_{1-y}\text{FeO}_3$ solids, a higher N_2 selectivity than for the non-substituted orthoferrites is observed. Increasing the substitution degree in Ca to 0.2 leads to decreased catalytic performances compared to the LaFeO_3 and $\text{LaFe}_{0.9}\text{Ca}_{0.1}\text{O}_3$ catalysts. It is therefore concluded, that increasing amounts of Fe^{4+} species do not improve the catalytic performances of Fe-based perovskites.

5.3 Influence of substitution in B-site

As illustrated in the previous section, the partial substitution in the A-site by Ca has no significant effect on the catalytic properties. This is consistent with previous statements demonstrating that catalytic properties of perovskites are mainly influenced by the nature of the B-site cation.^[15] Therefore, the influence of substitution of Fe by a more reductive and therefore more active metal was investigated. Cu was chosen as substituting cation due to its high reducibility and reactivity in the RP structure (Chapter 3). The goal of its incorporation in the perovskite structure was to profit from its catalytic properties while stabilising it inside the LaFeO_3 lattice. As discussed for the Ca substitution before, the incorporation of this generally divalent cation destabilises the electroneutrality of the structure and thereby should lead to the formation of Fe^{4+} species and/or oxygen vacancies.^[21] The latter are generally accepted to play an important role in the process of NO adsorption and desorption.^[21,22] Therefore, an enhanced reduction performance is expected. The investigation was performed on a series of $\text{LaFe}_{1-x}\text{Cu}_x\text{O}_3$ ($x = 0, 0.05, 0.1, 0.2$) catalysts prepared by CCM.

5.3.1 Bulk/Structural properties

Chemical composition of the bulk

The atomic ratios of the metal cations in the bulk of the $\text{LaFe}_{0.8}\text{Cu}_{0.2}\text{FeO}_3$ catalyst was determined exemplarily for the whole series by ICP. As reported in Table 5.13, the elementary

analysis confirms the nominal composition for the bulk of this Cu-substituted perovskite sample.

Table 5.13 – **Bulk atomic ratios $x_{\text{La}}/x_{\text{B}}$ and $x_{\text{Cu}}/x_{\text{Fe}}$ of calcined $\text{LaFe}_{1-x}\text{Cu}_x\text{O}_3$ ($x = 0, 0.2$; CCM).**

nominal composition	$x_{\text{La}}/x_{\text{Fe}}$	$x_{\text{La}}/x_{\text{B}}$	$x_{\text{Cu}}/x_{\text{Fe}}$
LaFeO_3	1.01	1.01	-
$\text{LaFe}_{0.8}\text{Cu}_{0.2}\text{FeO}_3$	1.26	1.03	0.23

XRD

The structural properties of all $\text{LaFe}_{1-x}\text{Cu}_x\text{O}_3$ ($x = 0, 0.05, 0.1, 0.2$) materials have been assessed by XRD. As shown in Fig. 5.19, the orthorhombic LaFeO_3 structure is obtained for all materials and no crystalline phase segregation is evidenced. In addition, the relative intensities of the diffraction peaks are unchanged compared to the reference (#37-1493), indicating that no preferential growth of the crystallites is observed.

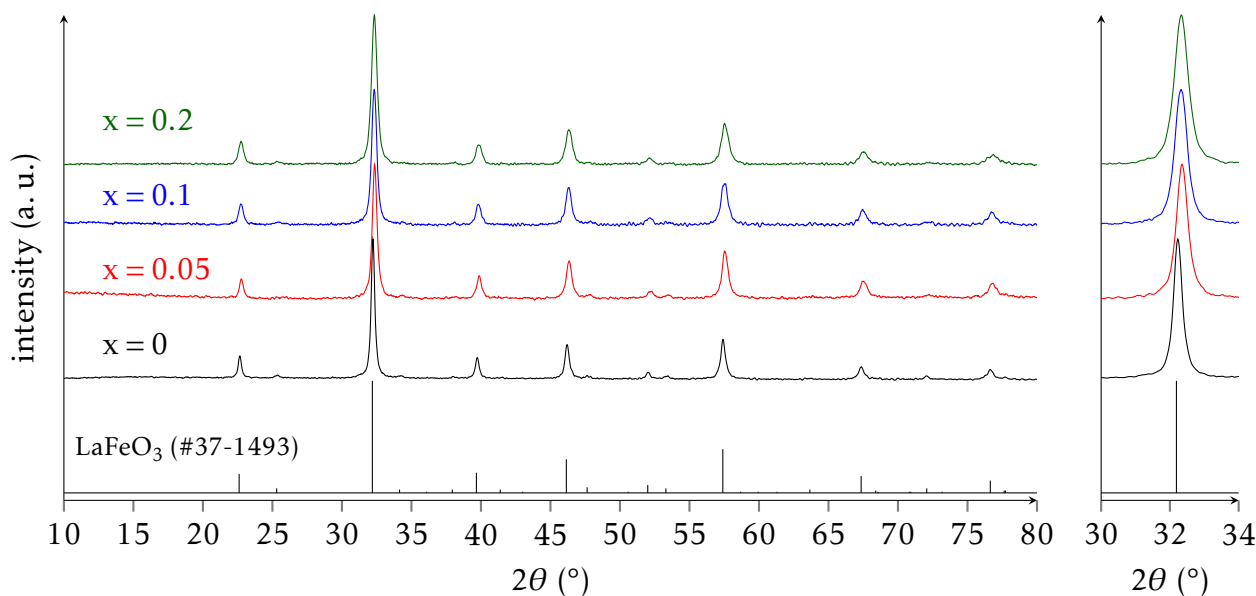


Figure 5.19 – **X-ray diffractograms of calcined $\text{LaFe}_{1-x}\text{Cu}_x\text{O}_3$ ($x = 0, 0.05, 0.1, 0.2$; CCM).**

Previous studies investigating the structural modifications due to Cu-substitution in the B-site of LaFeO_3 concluded that a solid solution is formed for Cu substitution degrees up to $x = 0.2$.^[22] Based on this statement, the evolution of the unit cell parameters reported in Table 5.14 with the Cu-substitution degree x can be studied. It is worthwhile to note that the volume of the unit cell decreases linearly for increasing Cu-content (Fig. 5.20). Assuming a simple steric model, the observed unit cell contraction cannot be explained by comparing the ionic radii of Cu^{2+} and Fe^{3+} of 0.73 \AA ^[16] and 0.645 \AA (high-spin)^[16] in 6-coordinate environment respectively. In this case, a unit cell expansion would have to be expected. Such an apparent discrepancy emphasises that charge compensation has to be accounted for – associated with the generation of anionic vacancies and the stabilisation of Fe in the unusual tetravalent oxidation state. The difference in ionic radii between Cu^{2+} and Fe^{3+} of 0.085 \AA is

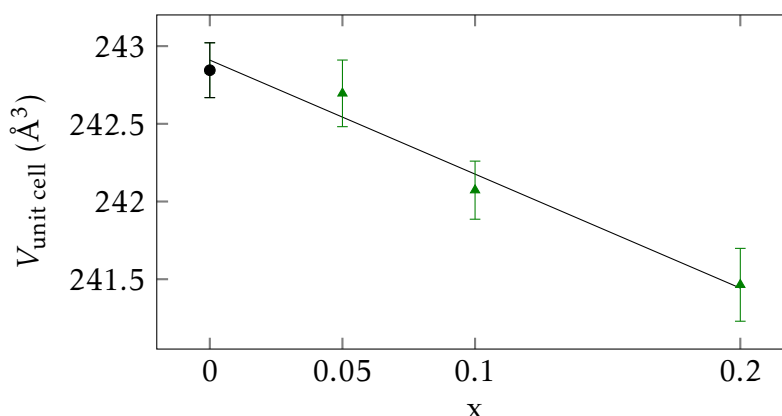


Figure 5.20 – Evolution of the unit cell volume of calcined $\text{LaFe}_{1-x}\text{Cu}_x\text{O}_3$ ($x = 0, 0.05, 0.1, 0.2$; CCM).

not counterbalanced by the difference in radii between Fe^{3+} and Fe^{4+} (0.06 \AA). This suggests that a large amount of defects in the form of anionic vacancies is required to ensure the electroneutrality of this system.

Similar results have been reported in literature backing up a negligible amount of Fe^{4+} species by titration.^[22] The less marked unit cell contraction compared to the $\text{La}_{1-x}\text{Ca}_x\text{FeO}_3$ samples can be explained by the interference of the generated anion defects and the substitution of Fe^{3+} by Cu^{2+} , creating on the one hand a considerable unit cell contraction and leading on the other hand to a unit cell expansion respectively.

Table 5.14 – Comparison of crystallite sizes and unit cell parameters derived from full pattern matching of calcined $\text{LaFe}_{1-x}\text{Cu}_x\text{O}_3$ ($x = 0, 0.05, 0.1, 0.2$; CCM).

	d_{cryst} (nm)	a (Å)	b (Å)	c (Å)	$V_{\text{unit cell}}$ (Å ³)
LaFeO_3	20.1 ± 0.1	5.561	7.858	5.558	242.85 ± 0.17
$\text{LaFe}_{0.95}\text{Cu}_{0.05}\text{O}_3$	15.7 ± 0.1	5.557	7.861	5.556	242.70 ± 0.21
$\text{LaFe}_{0.9}\text{Cu}_{0.1}\text{O}_3$	15.3 ± 0.1	5.560	7.842	5.552	242.07 ± 0.20
$\text{LaFe}_{0.8}\text{Cu}_{0.2}\text{O}_3$	13.5 ± 0.1	5.559	7.829	5.548	241.46 ± 0.22

Crystallite sizes (Table 5.14) are slightly lower for the Cu-substituted samples compared to LaFeO_3 .

Raman spectroscopy

Fig. 5.21 shows the Raman spectra of $\text{LaFe}_{0.8}\text{Cu}_{0.2}\text{O}_3$. Characteristic perovskite lines assigned to the A-site A_g mode (150 cm^{-1}), to the overlapping oxygen tilt B_{1g} and A_g modes (285 cm^{-1}), and to the oxygen bending B_{1g} mode ($422 - 428 \text{ cm}^{-1}$) are observed though decreased in relative intensity.^[4,7-10] Furthermore, the line at 1310 cm^{-1} already observed before and generally attributed to a 2-phonon scattering phenomenon or an oxygen stretching vibration is discernible.^[4,7-10]

Generally, only slight downshifts of the $\text{LaFe}_{0.8}\text{Cu}_{0.2}\text{O}_3$ solid's Raman shifts are observed compared to those of LaFeO_3 . Only the characteristic and normally very intense oxygen stretch mode at 640 cm^{-1} (B_{1g} mode) is considerably downshifted to 612 cm^{-1} for the Cu-

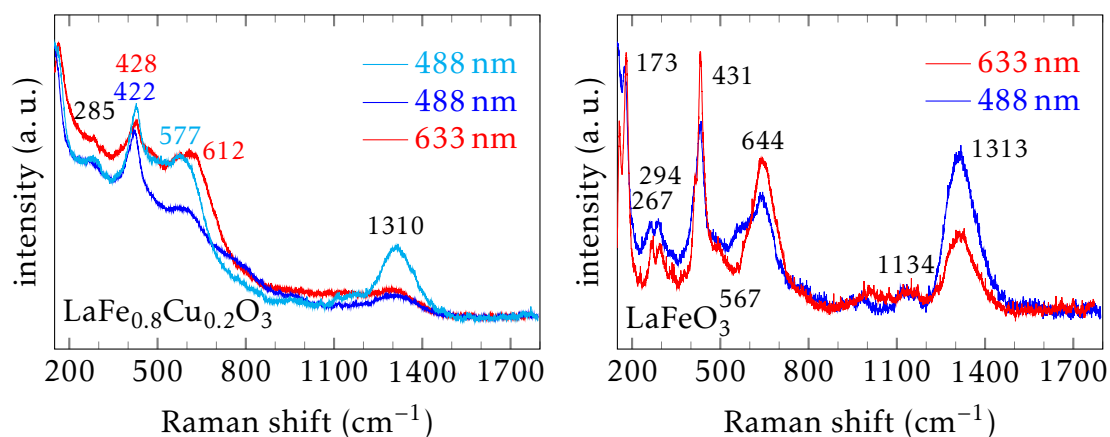


Figure 5.21 – Raman spectra of $\text{LaFe}_{0.8}\text{Cu}_{0.2}\text{O}_3$ compared to those of LaFeO_3 (CCM) excited with $\lambda_{\text{exc}} = 488 \text{ nm}$ and 632 nm .

substituted sample compared to 640 cm^{-1} for LaFeO_3 . This behaviour may be due to the assumed high abundance of anionic defects impacting on oxygen modes. Likewise, relative line intensities differ from the LaFeO_3 solid. Additionally, an intense shoulder to this line is discernible at 577 cm^{-1} which may correspond to a mode of lanthanum hydroxide normally observed at about 582 cm^{-1} .^[23] This shoulder was already observed for the non-substituted LaFeO_3 sample (Section 3.1). However, the intensity is increased in the case of the Cu-substituted solid. This is in agreement with the higher amount of adsorbed oxygen species found by XPS (Section 5.2.4).

5.3.2 Thermal stability and reducibility

High temperature XRD analyses (HTXRD)

As for LaFeO_3 and La_2CuO_4 the thermal stability under reductive atmosphere of the solids was investigated by HTXRD (procedure scheme in Section 2.2.5 Fig. 2.5). All solids of the $\text{LaFe}_{1-x}\text{Cu}_x\text{O}_3$ series ($x = 0, 0.05, 0.1, 0.2$) show the same behaviour. Therefore, only the HTXRD diffractograms recorded for $\text{LaFe}_{0.8}\text{Cu}_{0.2}\text{O}_3$ are reported in Fig. 5.22 and 5.23 and discussed, whereas those of $\text{LaFe}_{1-x}\text{Cu}_x\text{O}_3$ ($x = 0.05, 0.1$) are depicted in Appendix C.

Returning to $\text{LaFe}_{0.8}\text{Cu}_{0.2}\text{O}_3$, no change in the diffractograms is observed for any of the imposed conditions either under reductive atmosphere (Fig. 5.22) or humid air (Fig. 5.23) apart from thermal dilatation effects. This is in agreement with findings reported by Zhang et al. who investigated the stability of $\text{LaFe}_{0.8}\text{Cu}_{0.2}\text{O}_3$ prepared by reactive grinding under reducing atmosphere up to $900 \text{ }^\circ\text{C}$.^[24] The authors did not observe crystalline phase segregation. The examination of Fig. 5.24 shows the same trend for the calcined sample compared to the solid obtained after exposure to successive reductive and oxidative thermal treatment (Fig. 5.22 and 5.23). The most significant observation is related to the increased unit cell parameters after HTXRD analysis, especially for the $\text{LaFe}_{0.8}\text{Cu}_{0.2}\text{O}_3$ solid. According to previous observations, a greater amount of anionic vacancies during reductive thermal treatment locally destabilises the structure inducing partial extraction of Cu stabilised in B-sites. These Cu species would not diffuse back into the perovskite lattice during the oxidative step remaining segregated at the surface.

The atomic compositions at the surface of the $\text{LaFe}_{1-x}\text{Cu}_x\text{O}_3$ ($x = 0, 0.05, 0.1, 0.2$) catalysts after HTXRD analysis were determined by XPS. Results are discussed in Section 5.3.4.

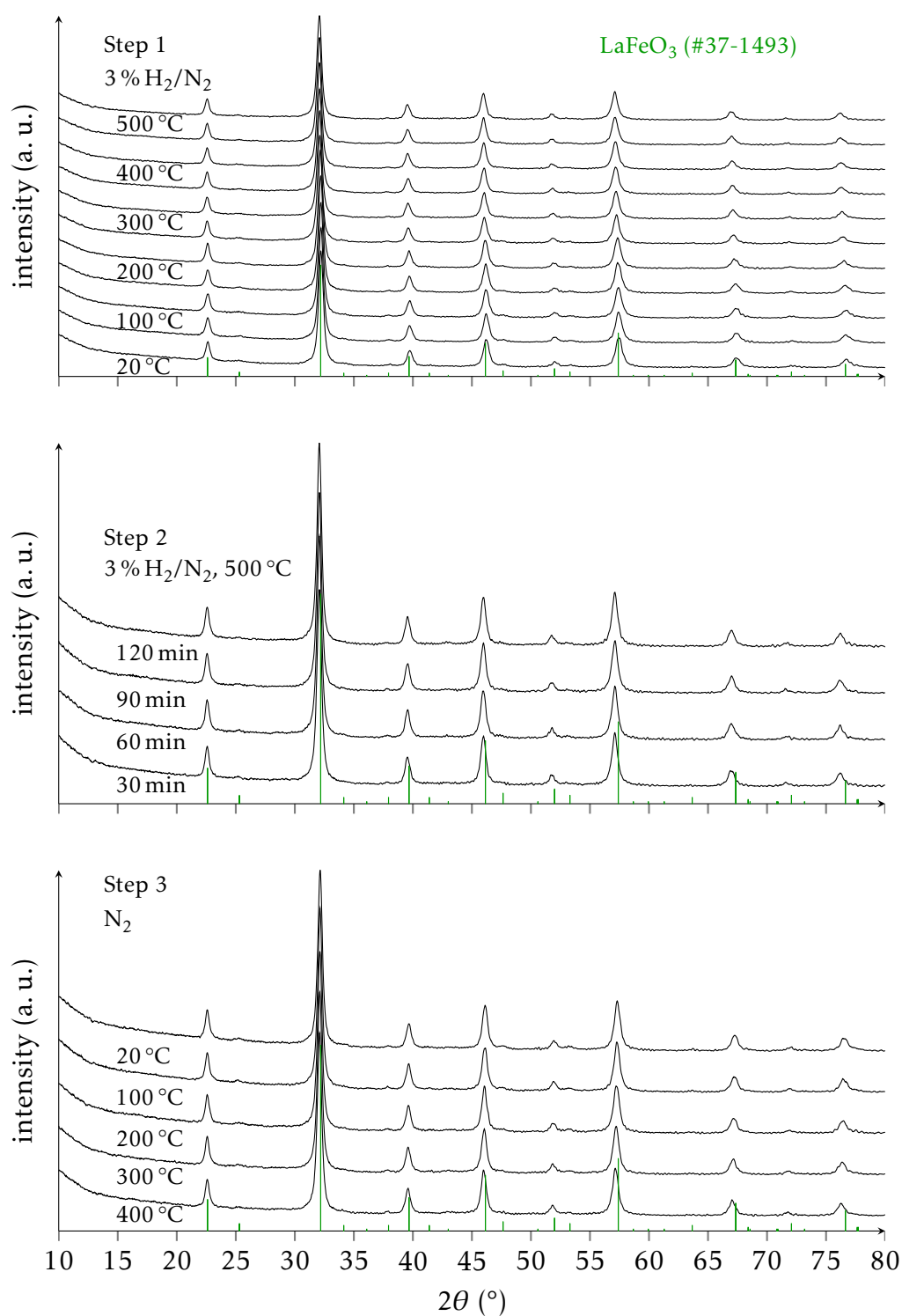


Figure 5.22 – High Temperature X-ray diffractograms of $\text{LaFe}_{0.8}\text{Cu}_{0.2}\text{O}_3$ prepared by CCM. Step 1 corresponds to a heating ramp under reductive atmosphere (3 Vol.% H_2/N_2), Step 2 to the corresponding plateau and Step 3 to the subsequent cooling under inert atmosphere.

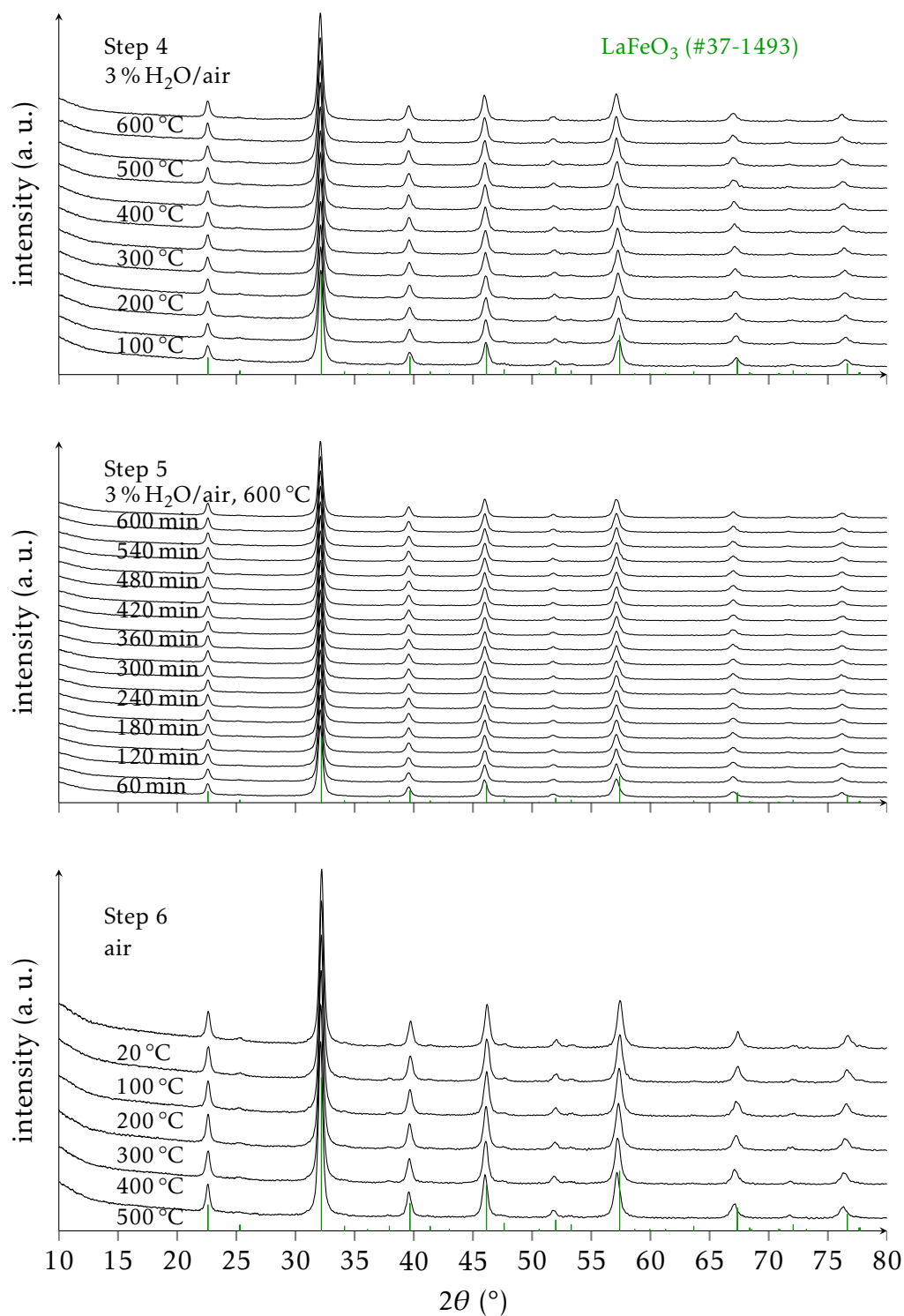


Figure 5.23 – High Temperature X-ray diffractograms of $\text{LaFe}_{0.8}\text{Cu}_{0.2}\text{O}_3$ prepared by CCM. Step 4 corresponds to a heating ramp under humid air flow up to 600 °C, Step 5 to the corresponding plateau and Step 6 to the subsequent cooling under dry air flow.

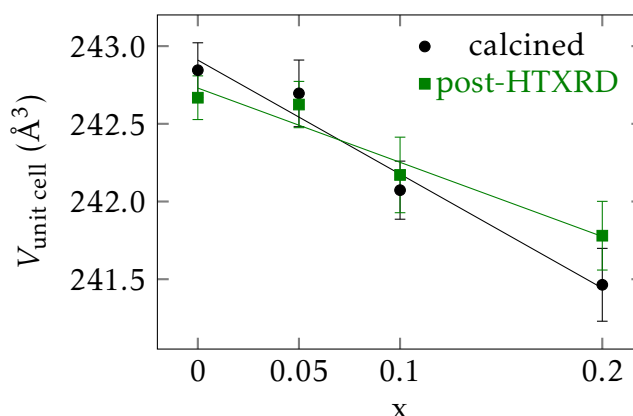


Figure 5.24 – Evolution of unit cell volumes of calcined and post-HTXRD $\text{LaFe}_{1-x}\text{Cu}_x\text{O}_3$ samples ($x = 0, 0.05, 0.1, 0.2$; CCM).

H_2 -TPR

To further investigate the reducibility of the Cu-substituted perovskites H_2 -TPR analyses were performed. The profiles are shown in Fig. 5.25. Contrarily to the LaFeO_3 solid, which is only reducible at temperatures above 700°C (Section 3.2.2), the Cu-substituted samples clearly show an additional low temperature reduction peak with its maximum at $\approx 240^\circ\text{C}$ in accordance with literature.^[21] As expected, the H_2 consumption increases with increasing Cu-content. This peak consists of 2 overlapping peaks, the 1st forming a shoulder of the second which is more intense. The sample with the lowest substitution degree, contrarily to the other Cu-substituted samples, also shows a weak 3rd reduction peak at 390°C which was not possible to assign.

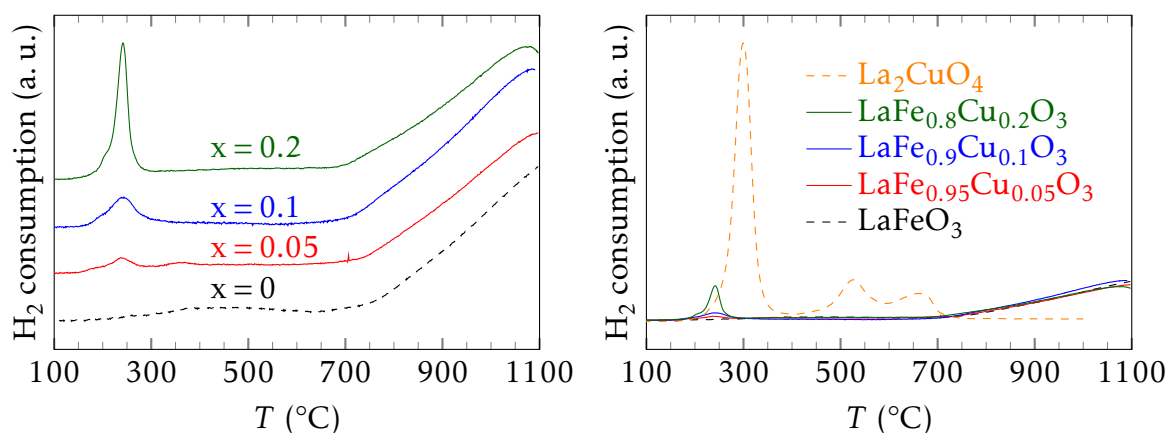


Figure 5.25 – H_2 absorption curves of calcined $\text{LaFe}_{1-x}\text{Cu}_x\text{O}_3$ ($x = 0, 0.05, 0.1, 0.2$; CCM; $50\text{ mg}, 50\text{ ml min}^{-1}$) compared to La_2CuO_4 (CCM; $100\text{ mg}, 25\text{ ml min}^{-1}$).

A comparison with the H_2 -TPR profile of La_2CuO_4 is also shown in Fig. 5.25. It confirms that the additional peaks observed for $\text{LaFe}_{1-x}\text{Cu}_x\text{O}_3$ ($x = 0.05, 0.1, 0.2$) can be attributed to the Cu^{2+} reduction in the perovskite structure. For all Cu-substituted perovskites, Cu^{2+} reduction is stopped in a lower temperature range (up to 280°C) compared to the Ruddlesden-Popper phase (up to 350°C). Clearly, the reduction peaks can unlikely be attributed to Fe^{4+} species since their maximum temperatures are lower than the 1st reduction peak of the $\text{La}_{1-x}\text{Ca}_x\text{FeO}_3$ samples regardless of the substitution degree. This is in agreement with

literature^[22] and confirms as previously discussed (Subsection 5.3.1) that anion defects contribute to compensate for the lower oxidation state of the substituting Cu cation in the perovskite lattice.

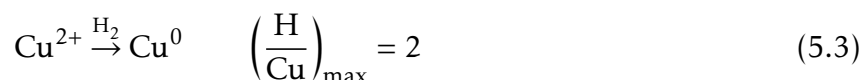
Table 5.15 – Comparison of H₂-TPR results of LaFe_{1-x}Cu_xO₃ (x = 0, 0.05, 0.1, 0.2; CCM).

nominal composition	H ₂ consumption ^a (mmol g ⁻¹)	total ^a H/Cu	extracted Cu ⁰ ^b (wt.%)	T _{max} reduction peaks		
				(°C)	(°C)	(°C)
LaFeO ₃	-	-	-	-	-	> 1100
LaFe _{0.95} Cu _{0.05} O ₃	0.24	1.07	1.1	237	(368)	> 1100
LaFe _{0.9} Cu _{0.1} O ₃	0.29	1.40	1.8	245	-	1084
LaFe _{0.8} Cu _{0.2} O ₃	0.67	1.64	4.3	241	-	1080
La ₂ CuO ₄	2.51	2.03	15.7	300	525	667

^a H₂ consumption was integrated over the temperature range of 150 °C to 400 °C.

^b After H₂-TPR analysis, estimated according to 100 wt.% Cu⁰ corresponding to H/Cu = 2 for T < 280 °C.

According to Eq. 5.3, the complete reduction of the divalent Cu cations proceeds with a maximum H/Cu ratio of 2. At temperatures below 700 °C the maximum H/Cu ratio should equal this theoretical H/Cu ratio, since only Cu is reduced in this temperature range.



As shown in Table 5.15, the total H/Cu ratio increases with higher Cu concentration in the sample. Cu²⁺ is only partially reduced in the substituted Fe-based perovskites whereas complete reduction occurred for La₂CuO₄. While the reduction of Cu²⁺ to Cu⁺ is completed for all solids, the reduction to metallic Cu only partially proceeds. This is in agreement with the enhanced stability of the structure. Nevertheless, the higher the Cu-content in the perovskite the higher the fraction of formed Cu⁰. The highest amount of segregated Cu⁰ of 4.3 wt.% is obtained for the LaFe_{0.8}Cu_{0.2}O₃ solid. This value is expectedly lower compared to the La₂CuO₄ sample (16 wt.%) due to the lower Cu-content in the sample itself.

5.3.3 Textural properties

Table 5.16 – Comparison of specific surface areas and cumulative pore volume of LaFe_{1-x}Cu_xO₃ (x = 0, 0.05, 0.1, 0.2; CCM).

composition	SSA (m ² g ⁻¹)	V _{pore} (cm ³ g ⁻¹)
LaFeO ₃	13.9	0.08
LaFe _{0.95} Cu _{0.05} O ₃	15.0	0.09
LaFe _{0.9} Cu _{0.1} O ₃	18.4	0.09
LaFe _{0.8} Cu _{0.2} O ₃	13.8	0.07

The textural properties of the Cu-substituted perovskites, studied by N₂-physisorption, are typical of CCM solids. As can be seen in Fig. 5.26A, all solids of the LaFe_{1-x}Cu_xO₃ series (x = 0, 0.05, 0.1, 0.2; CCM) present isotherms which are partly indicative of macroporous or

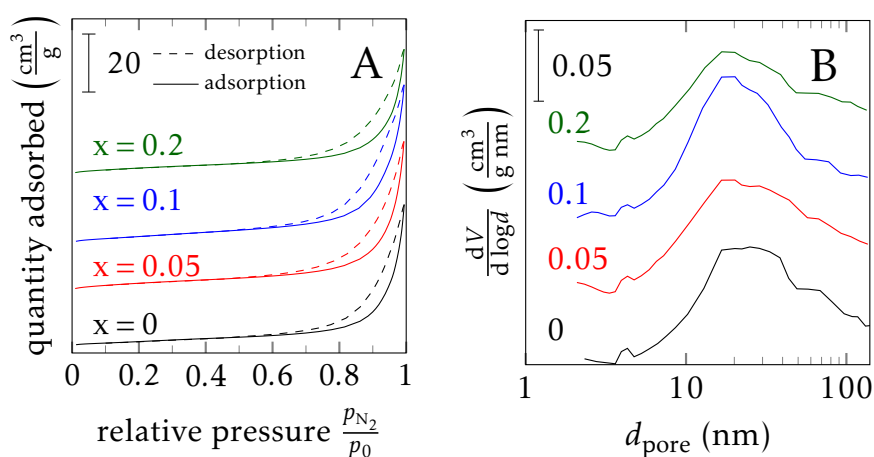


Figure 5.26 – N_2 adsorption and desorption isotherms and pore size distributions of calcined $\text{LaFe}_{1-x}\text{Cu}_x\text{O}_3$ ($x = 0, 0.05, 0.1, 0.2$; CCM).

weakly porous solids (type II) with a low additional contribution of mesopores (type IV). No significant changes in hysteresis are observed.

The pore size distributions, as plotted in Fig. 5.26B, are very broad. They show an unchanging high contribution of high diameter mesopores and macropores regardless of the substitution degree. This is attributed to the fact that porosity is mainly due to holes formed by perovskite particles during crystallisation. This is known for solids obtained by CCM as discussed in Chapter 4 (Section 4.1) and no change is observed due to Cu substitution.

Table 5.16 shows the specific surface areas and the cumulative pore volumes of the Cu-substituted perovskites. As expected from the isotherms and the corresponding pore size distributions, both properties are very similar to those of the LaFeO_3 solid. Only slight increases in specific surface area are observed for $\text{LaFe}_{0.95}\text{Cu}_{0.05}\text{O}_3$ and $\text{LaFe}_{0.9}\text{Cu}_{0.1}\text{O}_3$.

5.3.4 Chemical composition at the surface

XPS analyses were conducted on the $\text{LaFe}_{1-x}\text{Cu}_x\text{O}_3$ series. Results are shown in Fig. 5.27 and Table 5.17. The photopeaks of La 3d, Fe 2p and Cu 2p energy levels are illustrated in Fig. 5.27. All spectra exhibit the characteristic multiplet splitting and satellites of trivalent La and Fe and divalent Cu cations. In the case of Fe, this is confirmed by the positions of the satellite (≈ 719 eV as for the non-substituted perovskite). The presence of Cu^{2+} cations is confirmed by the positions of the photopeaks at approximately 933.1 eV and the presence of the characteristic satellites. For all samples the area of the Cu 2p_{3/2} satellite is approximately equal to half the area of the main peak which confirms that contributions of Cu species other than Cu^{2+} are negligible. Indeed only 0 to 8 at.% of Cu^+ species were estimated by spectral decomposition of the Cu 2p_{3/2} core level. No clear trend with the substitution degree is observed (Table 5.17).

The examination of the O 1s photopeak (Fig. 5.27) reveals 2 contributions at 531.5 eV and 529.5 eV previously ascribed to adsorbed oxygen-containing species and lattice oxygen species (O^{2-}) respectively. As shown in Table 5.17, the high relative intensity of the higher B. E. contribution increases correlated to the development of the 289.9 eV contribution of the C 1s core level attributed to carbonate species. Compared to the La_2CuO_4 sample, lower amounts of adsorbed oxygen (La_2CuO_4 : 75 at.%) and carbonate species (La_2CuO_4 : 33 at.%) are observed on the surface of the $\text{LaFe}_{1-x}\text{Cu}_x\text{O}_3$ samples ($x = 0.05, 0.1, 0.2$).

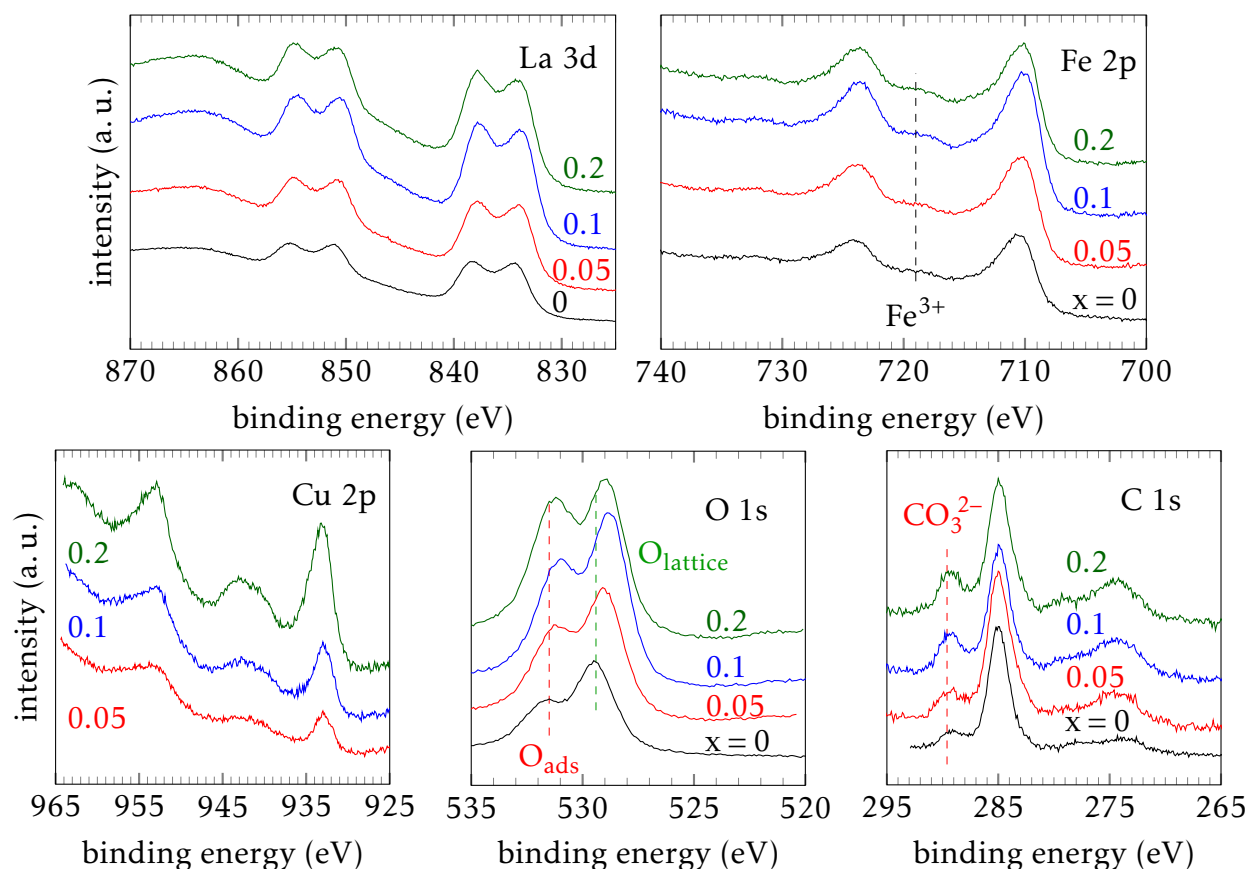


Figure 5.27 – La 3d, Fe 2p, Ca 2p, O 1s and C 1s photopeaks of calcined $\text{LaFe}_{1-x}\text{Cu}_x\text{O}_3$ ($x = 0, 0.05, 0.1, 0.2$; CCM).

Table 5.17 – Comparison of photopeak maxima and spectral decomposition results of calcined $\text{LaFe}_{1-x}\text{Cu}_x\text{O}_3$ ($x = 0, 0.05, 0.1, 0.2$; CCM) compared to La_2CuO_4 (CCM).

	B. E. (eV)				at. %		
	La 3d _{5/2}	Fe 2p _{3/2}	Cu 2p _{3/2}	O 1s	O _{lattice} ^a	C _{CO₃²⁻} ^b	Cu ⁺ ^c
LaFeO ₃	834.3	710.8	-	529.5	55	13	-
LaFe _{0.95} Cu _{0.15} O ₃	833.9	710.1	933.0	529.1	52	15	5
LaFe _{0.9} Cu _{0.1} O ₃	833.9	710.3	933.0	528.9	51	23	0
LaFe _{0.8} Cu _{0.2} O ₃	833.9	710.1	933.2	528.9	47	23	8
La ₂ CuO ₄	835.2	-	933.1	531.7	25	25	15

^a O_{lattice} + O_{ads} = 1.

^b C_{CO₃²⁻} + C_{adventitious} = 1.

^c Cu⁺ + Cu²⁺ = 1.

Table 5.18 – Surface atomic ratios $x_{\text{La}}/x_{\text{B}}$ and $x_{\text{Cu}}/x_{\text{Fe}}$ of calcined $\text{LaFe}_{1-x}\text{Cu}_x\text{O}_3$ ($x = 0, 0.05, 0.1, 0.2$; CCM) and La_2CuO_4 (CCM). Results of the La_2CuO_4 sample are given for comparison.

nominal composition	$x_{\text{La}}/x_{\text{Fe}}(\text{Cu})$	$x_{\text{La}}/x_{\text{B}}$	$x_{\text{Cu}}/x_{\text{Fe}}$	surface composition based on nominal Fe (Cu) content
LaFeO_3	2.13	2.13	-	$\text{La}_{2.13}\text{FeO}_{4.63}$ ($\text{C}_{3.66}$)
$\text{LaFe}_{0.95}\text{Cu}_{0.05}\text{O}_3$	2.08	1.94	0.08	$\text{La}_{1.98}\text{Fe}_{0.95}\text{Cu}_{0.07}\text{O}_{5.57}$ ($\text{C}_{4.26}$)
$\text{LaFe}_{0.9}\text{Cu}_{0.1}\text{O}_3$	2.36	2.08	0.14	$\text{La}_{2.12}\text{Fe}_{0.90}\text{Cu}_{0.13}\text{O}_{5.39}$ ($\text{C}_{2.81}$)
$\text{LaFe}_{0.8}\text{Cu}_{0.2}\text{FeO}_3$	2.52	1.82	0.39	$\text{La}_{1.62}\text{Fe}_{0.80}\text{Cu}_{0.24}\text{O}_{4.53}$ ($\text{C}_{2.61}$)
La_2CuO_4	(2.98)	2.98	-	$(\text{La}_{4.75}\text{CuO}_{10.10})$ ($\text{C}_{6.08}$)

Table 5.19 – Surface compositions and spectral decomposition results (XPS) of $\text{LaFe}_{1-x}\text{Cu}_x\text{O}_3$ ($x = 0, 0.05, 0.1, 0.2$; CCM) perovskites, before (calcined) and after (post-HTXRD) the HTXRD procedure.

nominal composition		surface composition based on nominal Fe content	at. %	
			$\text{O}_{\text{lattice}}^a$	$\text{C}_{\text{CO}_3^{2-}}^b$
LaFeO_3	calcined	$\text{La}_{2.13}\text{FeO}_{4.63}$ ($\text{C}_{3.66}$)	55	13
LaFeO_3	post-HTXRD	$\text{La}_{1.64}\text{FeO}_{5.20}$ ($\text{C}_{9.36}$)	34	11
$\text{LaFe}_{0.95}\text{Cu}_{0.15}\text{O}_3$	calcined	$\text{La}_{1.98}\text{Fe}_{0.95}\text{Cu}_{0.07}\text{O}_{5.57}$ ($\text{C}_{4.26}$)	52	15
$\text{LaFe}_{0.95}\text{Cu}_{0.15}\text{O}_3$	post-HTXRD	$\text{La}_{2.29}\text{Fe}_{0.95}\text{Cu}_{0.13}\text{O}_{6.25}$ ($\text{C}_{3.60}$)	50	18
$\text{LaFe}_{0.9}\text{Cu}_{0.1}\text{O}_3$	calcined	$\text{La}_{2.12}\text{Fe}_{0.90}\text{Cu}_{0.13}\text{O}_{5.39}$ ($\text{C}_{2.81}$)	51	23
$\text{LaFe}_{0.9}\text{Cu}_{0.1}\text{O}_3$	post-HTXRD	$\text{La}_{1.69}\text{Fe}_{0.90}\text{Cu}_{0.13}\text{O}_{6.11}$ ($\text{C}_{3.45}$)	47	21
$\text{LaFe}_{0.8}\text{Cu}_{0.2}\text{O}_3$	calcined	$\text{La}_{1.62}\text{Fe}_{0.80}\text{Cu}_{0.24}\text{O}_{4.53}$ ($\text{C}_{2.61}$)	47	23
$\text{LaFe}_{0.8}\text{Cu}_{0.2}\text{O}_3$	post-HTXRD	$\text{La}_{1.41}\text{Fe}_{0.80}\text{Cu}_{0.33}\text{O}_{4.99}$ ($\text{C}_{2.67}$)	42	25

^a $\text{O}_{\text{ads}} + \text{O}_{\text{lattice}} = 1$. For LaFeO_3 post-HTXRD: $\text{O}_{\text{ads}} + \text{O}_{\text{lattice}} + \text{O}_{\text{ads H}_2\text{O}} = 1$. ($\text{O}_{\text{ads H}_2\text{O}} = 12$ at.%)

^b $\text{C}_{\text{CO}_3^{2-}} + \text{C}_{\text{adventitious}} = 1$.

The atomic ratios of the metal cations at the surface of the $\text{LaFe}_{1-x}\text{Cu}_x\text{O}_3$ ($x = 0, 0.05, 0.1, 0.2$) catalysts were also determined by XPS. Results are shown in Table 5.18. A surface La enrichment is observed compared to the B-site cations for all samples in the series $\text{LaFe}_{1-x}\text{Cu}_x\text{O}_3$ ($x = 0, 0.05, 0.1, 0.2$). This La excess is only slightly attenuated by the Cu substitution. Comparing the atomic Cu/Fe ratios for the Cu-substituted samples to the theoretical ones, a slight Cu enrichment at the surface is observed.

Ex situ XPS measurements were also performed on the samples previously exposed to the HTXRD procedure. The quantification results are reported in Table 5.19. The solids show a slight decrease in the La excess at the surface. Slight Cu extraction towards the surface is detected in agreement with the discussed unit cell expansion observed after the heat treatments. However, no major photopeak shifts were observed (Table B.4). At the same time, the contribution of non-lattice oxygen species is increased after the HTXRD procedure. The same is true for the carbonate contribution as was already observed for the LaFeO_3 solid (Section 3.2).

5.3.5 Catalytic activity

The catalytic performance reacts sensibly with the Cu substitution degree. Especially the CO oxidation and to a lesser extent the NO reduction performance are enhanced by higher Cu-content in the perovskites. However, $\text{LaFe}_{1-x}\text{Cu}_x\text{O}_3$ samples present similar HC oxidation performance as the non-substituted LaFeO_3 catalyst up to temperatures of 420 °C and lower ones at higher temperatures in the case of $x = 0.05$ and 0.2. No indications for propylene reforming reactions are observed in contrast to the La_2CuO_4 catalyst (Section 3.5.2).

The catalytic performances of the Cu-substituted samples were tested as before in 3-way catalytic conditions according to Procedure A (Section 2.3). CO, propylene, NO, propane, oxygen and hydrogen conversions during temperature-programmed reactions are presented in Fig. 5.28 and 5.29. Additionally, T_{50} values are reported in Table 5.20 and in Appendix D (Table D.3).

Table 5.20 – Temperatures corresponding to 50 % conversion of CO, C_3H_6 , C_3H_8 , and H_2 (stoichiometric) and NO (rich composition) of $\text{LaFe}_{1-x}\text{Cu}_x\text{O}_3$ catalysts ($x = 0, 0.05, 0.1, 0.2$; CCM) and selectivities of NO reduction products.

condition	stoichiometric					rich ^a			
	T_{50} (°C)					selectivities at T_S			
	CO	C_3H_6	C_3H_8	H_2	NO	S_{N_2}	S_{NH_3}	$S_{\text{N}_2\text{O}}$	T_S (°C)
LaFeO_3	438	463	478	501	^b	0.05	0.95	0	507
$\text{LaFe}_{0.95}\text{Cu}_{0.05}\text{O}_3$	328	510	n. a.	440	485	0.85	0.11	0.03	499
$\text{LaFe}_{0.9}\text{Cu}_{0.1}\text{O}_3$	305	469	467 ^c	444	489	0.51	0.43	0.07	493
$\text{LaFe}_{0.8}\text{Cu}_{0.2}\text{O}_3$	294	497	505 ^c	421	501 ^c	0.94	0	0.06	513

^a Space velocity ($\text{LaFe}_{0.95}\text{Cu}_{0.05}\text{O}_3$, rich) = 59 400 ml h⁻¹ g⁻¹

^b Conversion lower than 50 %.

^c T_{25} .

As shown in Fig. 5.28 and Table 5.20, best CO oxidation results are obtained by the sample with the highest Cu-substitution degree, $\text{LaFe}_{0.8}\text{Cu}_{0.2}\text{O}_3$, which is also the most reducible

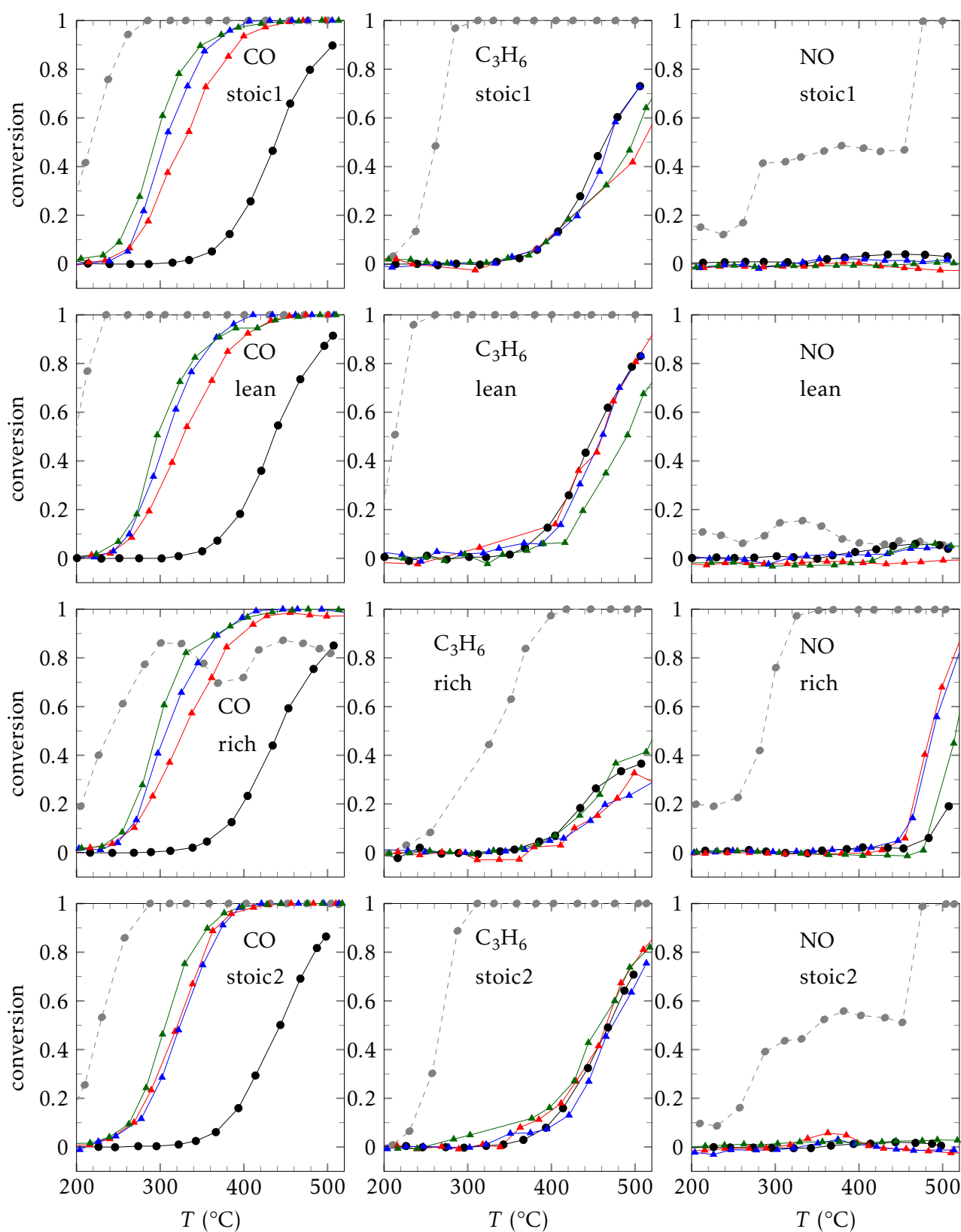


Figure 5.28 – CO, C₃H₆ and NO conversions of LaFe_{1-x}Cu_xO₃ catalysts under stoichiometric and rich conditions respectively. LaFeO₃ (•), LaFe_{0.95}Cu_{0.05}O₃ (▲), LaFe_{0.9}Cu_{0.1}O₃ (▲), and LaFe_{0.8}Cu_{0.2}O₃ (▲) compared to the commercial reference TWC (•)

solid and which contains the highest amounts of anionic defects of the $\text{LaFe}_{1-x}\text{Cu}_x\text{O}_3$ perovskite series as evidenced by H_2 -TPR and XRD. Its performance even exceeds the one of La_2CuO_4 ($T_{50}(\text{CO, stoic1}) = 300\text{ }^\circ\text{C}^4$). The CO oxidation performance enhancement follows the trend of increasing substitution degree.

For NO reduction under rich conditions, all samples show enhanced performance. The enhancement is most marked for $\text{LaFe}_{0.95}\text{Cu}_{0.05}\text{O}_3$ and $\text{LaFe}_{0.9}\text{Cu}_{0.1}\text{O}_3$, in contrast to the results obtained for CO oxidation. The samples substituted with lower amounts of Cu show similar performances. Concerning the reduction products differences are observed as shown in Fig. 5.30. While all samples show low N_2O production in the temperature range of 440 to about $500\text{ }^\circ\text{C}$, differences in the N_2 and NH_3 selectivity are detected. Contrarily to LaFeO_3 , the main product of reduction catalysed by Cu-substituted perovskites is N_2 . No NH_3 production and an N_2 selectivity close to 1 are observed for $\text{LaFe}_{0.8}\text{Cu}_{0.2}\text{O}_3$ around $500\text{ }^\circ\text{C}$. The catalyst with lowest Cu substitution degree shows a minor contribution of NH_3 production of 11 %, a high N_2 selectivity of 85 % and the lowest amount of produced N_2O of the substituted solids at this temperature. The $\text{LaFe}_{0.9}\text{Cu}_{0.1}\text{O}_3$ solid, on the other hand, shows a significant NH_3 contribution (43 %). The high N_2 selectivity of the Cu-substituted orthoferrites and the high catalytic activity of the $\text{LaFe}_{0.8}\text{Cu}_{0.2}\text{O}_3$ catalyst are in agreement with previous reports on the catalytic reduction of NO by propylene over $\text{LaFe}_{0.8}\text{Cu}_{0.2}\text{O}_3$ in the presence of O_2 by Zhang et al.^[25]

Whereas no NO conversion was observed for $\text{La}_{1-y}\text{FeO}_3$ and $\text{La}_{1-x}\text{Ca}_x\text{FeO}_3$ solids under other than rich conditions, low amounts of reduction products are detected for the $\text{LaFe}_{1-x}\text{Cu}_x\text{O}_3$ catalysts under stoichiometric and lean conditions. However, the conversion is marginal accounting for a maximum of 5 % at temperatures above $430\text{ }^\circ\text{C}$ under lean and in the temperature range of 360 to $380\text{ }^\circ\text{C}$ under stoichiometric conditions. Up to 10 % of NO conversion were obtained for $\text{LaFe}_{0.95}\text{Cu}_{0.05}\text{O}_3$ during the return test with an S_{N_2} of 70 % vs. 30 % of $S_{\text{N}_2\text{O}}$. Generally, the sole reduction product observed under lean conditions is N_2 , whereas nitrous oxide is formed as a side product under stoichiometric conditions.

Different mechanisms for NO reduction were proposed for the $\text{LaFe}_{0.8}\text{Cu}_{0.2}\text{O}_3$ catalyst depending on the reductive agent. According to Zhang et al., nitrosyl (NO^-) species are the main adsorbed reactants during NO reduction by CO^[21] whereas the NO reduction by propylene in the presence of oxygen involved the formation of nitrates (NO_3^-) at the perovskite surface.^[25] The key role of the presence and fast regeneration of oxygen vacancies for NO reduction was emphasized. Studies under more complex feed gas mixtures such as the combination of CO, propylene and NO have not been conducted, however. Regarding the light-off curves depicted in Fig. 5.28, it appears unlikely that CO + NO reaction occurs under 3-way catalytic conditions. The NO reduction by propylene or hydrogen is more probable in this case.

All $\text{LaFe}_{1-x}\text{Cu}_x\text{O}_3$ catalysts ($x = 0.05, 0.1, 0.2$; CCM) show higher specific reaction rates for CO and C_3H_6 oxidation under stoichiometric conditions than LaFeO_3 as shown in Table 5.21. The increase in r_{specific} for the latter is slight and the catalytic activity does not change for different substitution degrees as can also be seen for the Arrhenius parameters in Table 5.21 (estimated by linear regression as shown in Fig. D.5). On the other hand, catalytic performance of CO oxidation is markedly increased for Cu-substituted samples. In agreement with this trend, the specific reaction rates at $250\text{ }^\circ\text{C}$ increase with increasing Cu-content. The catalytic activity is enhanced for the samples with the lowest and the highest Cu-content respectively as reflected by the estimated Arrhenius parameters. However, a marked decrease

⁴Space velocity (La_2CuO_4) = $45\ 000\ \text{ml h}^{-1}\ \text{g}^{-1}$ instead of $60\ 000\ \text{ml h}^{-1}\ \text{g}^{-1}$

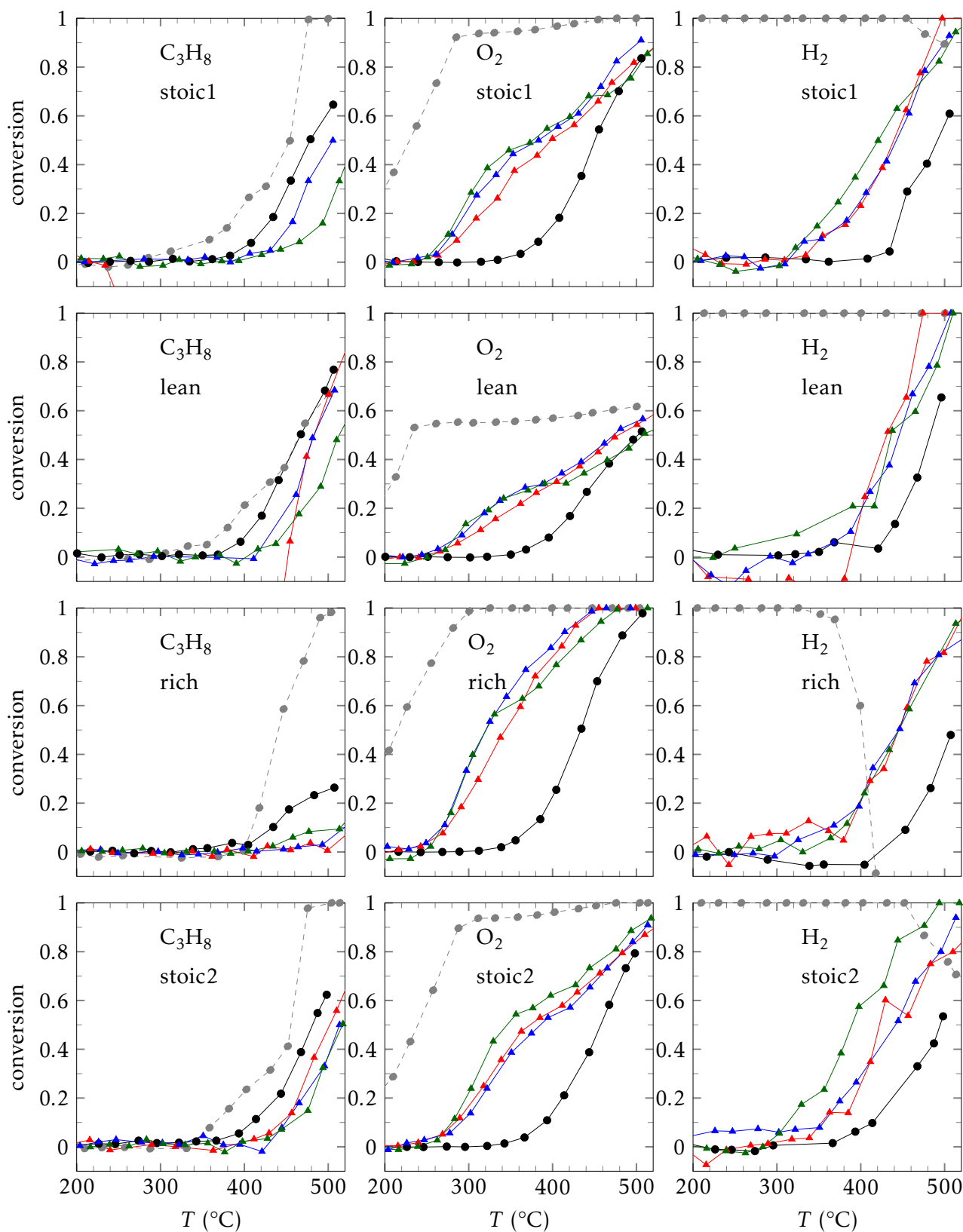


Figure 5.29 – C_3H_8 , O_2 and H_2 conversions of $\text{LaFe}_{1-x}\text{Cu}_x\text{O}_3$ catalysts under stoichiometric and rich conditions respectively. LaFeO_3 (\bullet), $\text{LaFe}_{0.95}\text{Cu}_{0.05}\text{O}_3$ (\blacktriangle), $\text{LaFe}_{0.9}\text{Cu}_{0.1}\text{O}_3$ (\blacktriangle), and $\text{LaFe}_{0.8}\text{Cu}_{0.2}\text{O}_3$ (\blacktriangle) compared to the commercial reference TWC (\bullet)

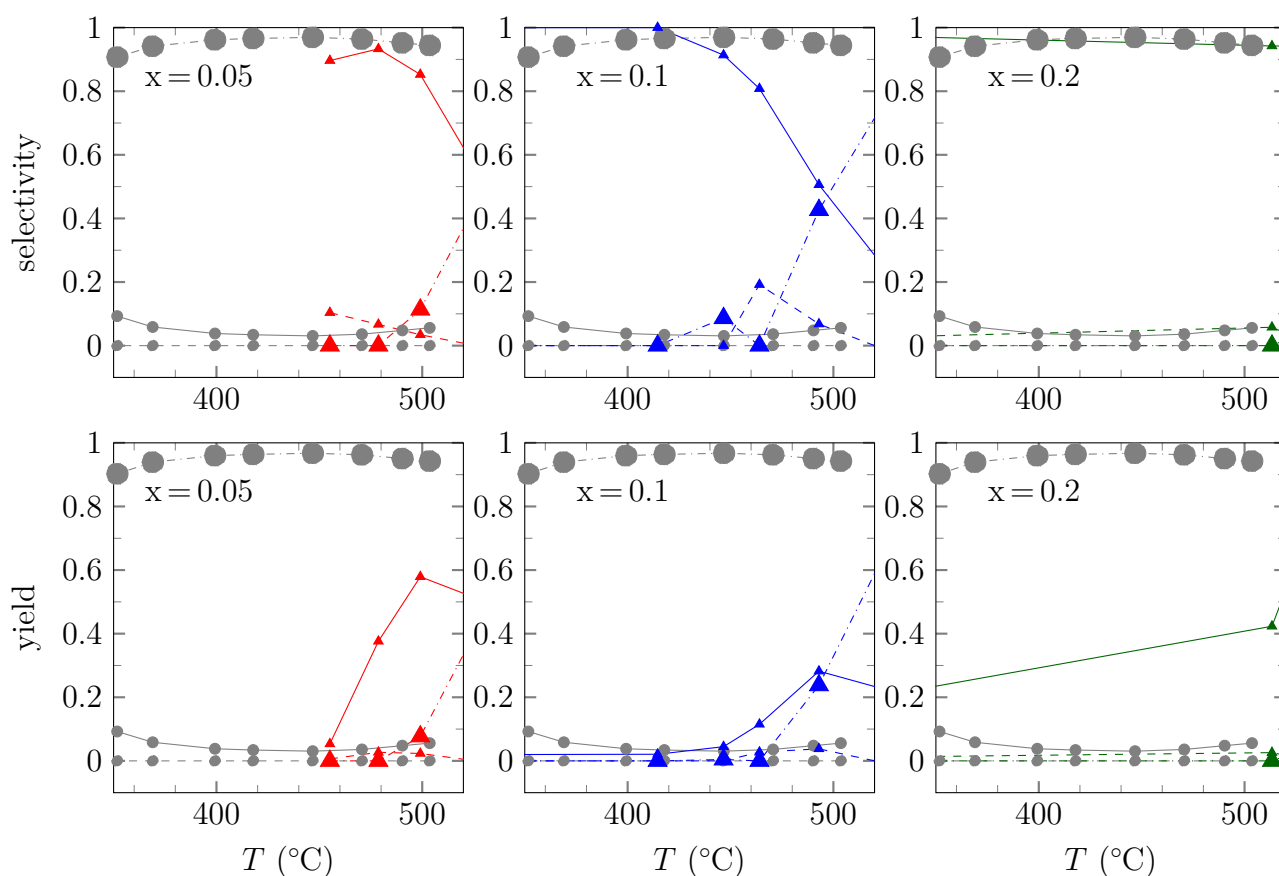


Figure 5.30 – N_2 , N_2O and NH_3 selectivities and yields of NO conversion of $LaFe_{1-x}Cu_xO_3$ catalysts ($x=0.05, 0.1, 0.2$; CCM) under rich conditions. $LaFe_{0.95}Cu_{0.05}O_3$ (\blacktriangle), $LaFe_{0.9}Cu_{0.1}O_3$ (\blacktriangle), and $LaFe_{0.8}Cu_{0.2}O_3$ (\blacktriangle) compared to the commercial reference TWC (\bullet); S_{N_2}/Y_{N_2} (solid), S_{N_2O}/Y_{N_2O} (dashed), S_{NH_3}/Y_{NH_3} (dashdotted, big mark)

in activity is observed for the $LaFe_{0.9}Cu_{0.1}O_3$ solid as can be seen by its high pre-exponential factor.

In conclusion, $LaFe_{1-x}Cu_xO_3$ catalysts ($x = 0.05, 0.1, 0.2$) present interesting catalytic properties mainly with respect to CO oxidation, NO reduction in rich conditions and N_2 selectivities. Except in the case of $LaFe_{0.9}Cu_{0.1}O_3$, the Cu-substitution leads not only to lower T_{50} values but also enhanced activity for CO oxidation. This can be attributed to the higher reducibility of the solid as evidenced earlier by H_2 -TPR and the high amount of oxygen vacancies as confirmed by XRD results in agreement with earlier reports on the catalytic performance of $LaFe_{0.8}Cu_{0.2}O_3$.^[21,25] Catalytic activity toward propylene oxidation is also slightly enhanced. This is, however, not reflected by the performances. The higher NO reduction activity is in agreement with the intended influence of introducing Cu into the perovskite structure. While NO reduction performance is less marked than for La_2CuO_4 , it is in the range of $La_{1-y}FeO_3$ catalysts with the clear advantage of leading to N_2 as the major reduction product. Interestingly, a higher amount of Cu did not lead to increased NO reduction performances, whereas this was observed for CO oxidation. This affirms the already discussed hypothesis that CO and propylene oxidation are catalysed on different active sites of the (substituted) orthoferrites.

Table 5.21 – Comparison of specific reaction rates r_{specific} , apparent activation energies $E_{A,\text{app}}$ and pre-exponential factors A of CO and C₃H₆ oxidation for LaFe_{1-x}Cu_xO₃ catalysts (x = 0, 0.05, 0.1, 0.2) under stoichiometric conditions (1st test ramp). Arrhenius parameters were determined by Arrhenius plots (Fig. D.5)

	SSA (m ² g ⁻¹)	r_{specific}^a (mol s ⁻¹ g ⁻¹)		$E_{A,\text{app}}$ (kJ mol ⁻¹)		A (10 ³ m ³ s ⁻¹ g ⁻¹)	
		CO	C ₃ H ₆	CO	C ₃ H ₆	CO	C ₃ H ₆
LaFeO ₃	13.9	≈ 0	2.5 · 10 ⁻⁹	142	128	424.4	15.2
LaFe _{0.95} Cu _{0.05} O ₃	15.0	1.1 · 10 ⁻⁸	n. a.	107	n. a.	33.9	n. a.
LaFe _{0.9} Cu _{0.1} O ₃	18.4	8.4 · 10 ⁻⁸	3.7 · 10 ⁻⁹	171	100	55351179	0.112
LaFe _{0.8} Cu _{0.2} O ₃	13.8	22.5 · 10 ⁻⁸	3.7 · 10 ⁻⁹	112	103	216.8	0.130

^a Specific reaction rates were calculated from conversions at 250 °C for CO and 350 °C for C₃H₆.

5.3.6 Conclusion

A series of Cu-substituted orthoferrites was prepared by CCM. While LaFe_{1-x}Cu_xO₃ catalysts (x = 0.05, 0.1, 0.2) present similar textural properties as the LaFeO₃ solid, their unit cells are slightly decreased as evidenced by XRD in agreement with the formation of a solid solution by incorporation of the Cu ions into the perovskite lattice. The insertion of divalent Cu in the B-site is mainly compensated by the generation of anionic defects.

The thermal stability of the LaFe_{1-x}Cu_xO₃ catalysts (x = 0.05, 0.1, 0.2) was preliminarily tested by HTXRD analyses. The in situ measurements as well as analyses performed after the heat treatments confirmed the stability of the structure. No crystalline phase segregation was detected and only slight Cu extraction at the surface of the samples after the HTXRD analysis may be deduced from XRD and ex situ XPS results. Nonetheless, all Cu-substituted solids show enhanced reducibility as evidenced by H₂-TPR. The solid's reducibility increases for higher substitution degree and so does the reducibility of the Cu cations inside the structure.

The higher reducibility and the abundance of oxygen vacancies accompanied by the ease of their regeneration is assumed to be at the origin of the enhanced catalytic performances and activities of the Cu-substituted orthoferrites. XPS revealed higher amounts of adsorbed oxygen and carbonate species on the surface of the Cu-substituted perovskites, similar to the observations with respect to the La₂CuO₄ solid – even though in a lower proportion.

The coupling of high CO oxidation and high NO reduction performances with high N₂ selectivities of the Cu-substituted orthoferrites constitutes a potential to be further explored. Substitution degrees in the Fe-based perovskite of 0.05 and 0.1 lead to similar T₅₀ for NO reduction, even though S_{N₂} was higher for the perovskite with lower Cu-content. However, LaFe_{0.9}Cu_{0.1}O₃ yielded more interesting results concerning HC and CO oxidation while highest catalytic activity for CO oxidation was observed for LaFe_{0.8}Cu_{0.2}O₃. Therefore, the substitution degrees of x = 0.1 and 0.2 were retained for the following study combining A- and B-site substitution.

5.4 Influence of substitution in A- and B-site

Taking into account the positive results of catalytic performances of La_{1-x}Ca_xFeO₃ and LaFe_{1-x}Cu_xO₃ (Sections 5.2 and 5.3), an investigation of the substitution in A- and B-site

of Fe-based perovskites was performed by studying a series of $\text{La}_{1-x}\text{Ca}_x\text{Fe}_{1-x}\text{Cu}_x\text{O}_3$ ($x = 0, 0.1, 0.2$) solids. This series was prepared by CCM. The conjunction of positive effects due to individual substitution or detrimental effects due to higher charge imbalances leading to phase segregation was studied.

5.4.1 Bulk/Structural properties

Chemical composition of the bulk

As shown in Table 5.22, elementary analyses of $\text{La}_{1-x}\text{Ca}_x\text{Fe}_{1-x}\text{Cu}_x\text{O}_3$ solids ($x = 0, 0.1, 0.2$) are in agreement with the theoretical compositions.

Table 5.22 – **Bulk atomic ratios x_A/x_B , $x_{\text{Cu}}/x_{\text{Fe}}$ and $x_{\text{Ca}}/x_{\text{La}}$ of calcined $\text{La}_{1-x}\text{Ca}_x\text{Fe}_{1-x}\text{Cu}_x\text{O}_3$ ($x = 0, 0.1, 0.2$; CCM).**

nominal composition	$x_{\text{La}}/x_{\text{Fe}}$	x_A/x_B	$x_{\text{Cu}}/x_{\text{Fe}}$	$x_{\text{Ca}}/x_{\text{La}}$
LaFeO_3	1.01	1.01	-	-
$\text{La}_{0.9}\text{Ca}_{0.1}\text{Fe}_{0.9}\text{Cu}_{0.1}\text{O}_3$	1.00	1.01	0.10	0.11
$\text{La}_{0.8}\text{Ca}_{0.2}\text{Fe}_{0.8}\text{Cu}_{0.2}\text{O}_3$	1.00	1.02	0.23	0.25

XRD

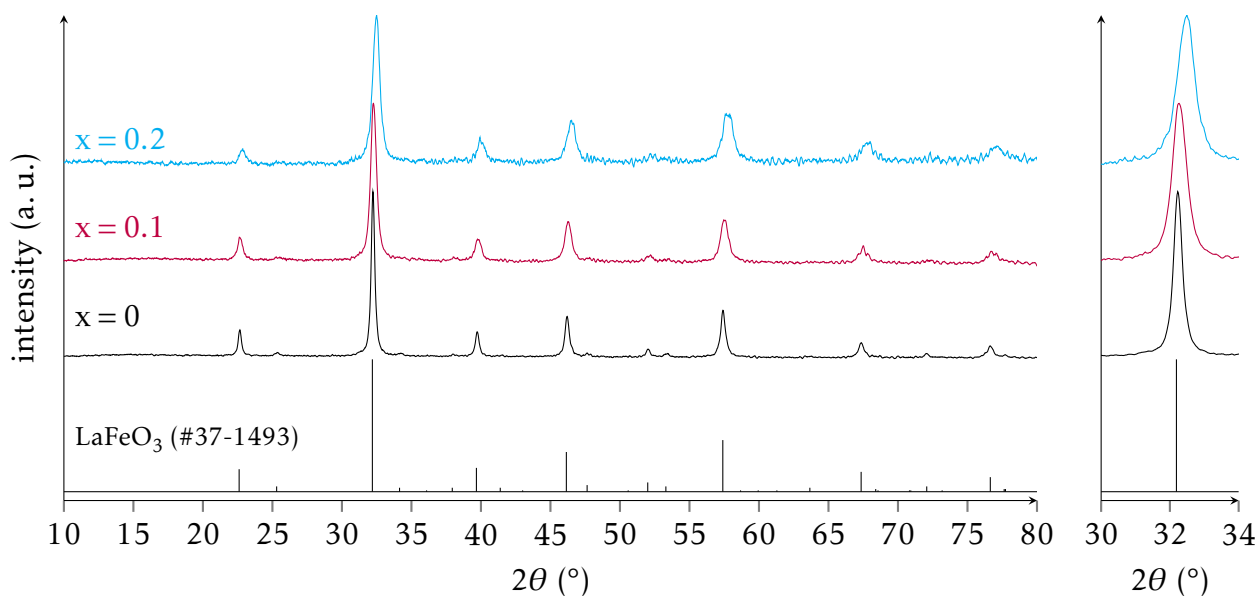


Figure 5.31 – **X-ray diffractograms of calcined $\text{La}_{1-x}\text{Ca}_x\text{Fe}_{1-x}\text{Cu}_x\text{O}_3$ ($x = 0, 0.1, 0.2$; CCM).**

All $\text{La}_{1-x}\text{Ca}_x\text{Fe}_{1-x}\text{Cu}_x\text{O}_3$ ($x = 0, 0.1, 0.2$) samples are characterised by an orthorhombic perovskite structure as evidenced by XRD patterns (Fig. 5.31). Significant shifts of 2θ values depending on the Ca and Cu substitution degree were observed but no additional X-ray peaks suggesting phase segregation are evidenced. Relative intensities remain unchanged compared to the reference. Thus, the simultaneous substitution by divalent cations in A- and B-sites does not prevent the generation of the orthorhombic perovskite phase. However,

diffraction peaks are significantly less intense and broadened with increasing substitution in the LaFeO_3 structure. Likewise, increased distortion of the structure is observed.

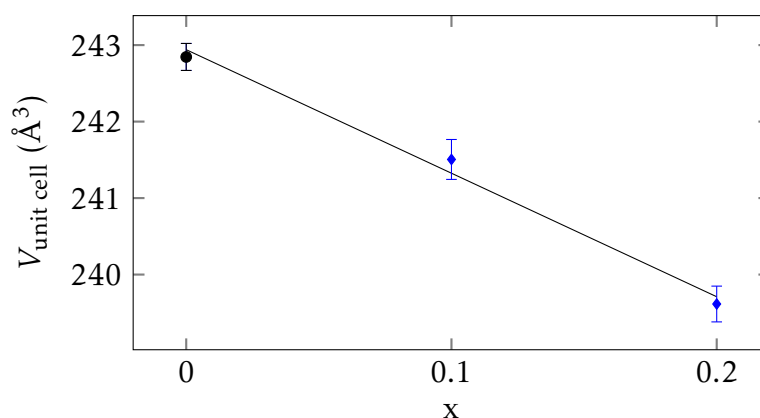


Figure 5.32 – Evolution of the unit cell volume of calcined $\text{La}_{1-x}\text{Ca}_x\text{Fe}_{1-x}\text{Cu}_x\text{O}_3$ ($x = 0, 0.1, 0.2$; CCM).

By plotting the unit cell volume evolution, as depicted in Fig. 5.32, a nearly continuous decrease is observed with increasing substitution degree in A- and B-sites. A similar trend was observed and explained earlier for $\text{La}_{1-x}\text{Ca}_x\text{FeO}_3$ solids (Section 5.2.1). This is in agreement with the lower impact of Cu substitution on the unit cell parameters already seen for the $\text{LaFe}_{1-x}\text{Cu}_x\text{O}_3$ solids (Section 5.3.1).

However, as discussed before (Sections 5.2.1 and 5.3.1), the decrease of the unit cell volume cannot be easily explained by neither the size of the Ca^{2+} nor the one of the Cu^{2+} cation. Hence, additional charge compensation is necessary for $\text{La}_{1-x}\text{Ca}_x\text{Fe}_{1-x}\text{Cu}_x\text{O}_3$ solids compared to the parent substituted samples in A- or B-site since both substituting cations are divalent creating an even stronger charge imbalance in the perovskite structure. Even though this destabilising effect does not lead to the destruction of the orthoferrite structure, it nonetheless should generate a high amount of defects. As discussed earlier, these defects may consist of the partial oxidation of Fe^{3+} to Fe^{4+} species and the creation of oxygen vacancies, leading to a unit cell contraction.

Apparent crystallite sizes and unit cell parameters as obtained by full pattern matching are reported in Table 5.23. Crystallite sizes of the doubly substituted series are significantly lower with respect to the LaFeO_3 solid. This is already apparent from the significant peak broadening observed in the diffractogram (Fig. 5.31). Among all materials already prepared by CCM, crystallites' sizes seem to generally follow the trend $\text{LaFeO}_3 > \text{La}_{1-x}\text{Ca}_x\text{FeO}_3 > \text{LaFe}_{1-x}\text{Cu}_x\text{O}_3 > \text{La}_{1-x}\text{Ca}_x\text{Fe}_{1-x}\text{Cu}_x\text{O}_3$. This decrease is more marked and following the same order when x is increased.

Table 5.23 – Comparison of crystallite sizes and unit cell parameters derived from full pattern matching of calcined $\text{La}_{1-x}\text{Ca}_x\text{Fe}_{1-x}\text{Cu}_x\text{O}_3$ ($x = 0, 0.1, 0.2$; CCM).

	d_{cryst} (nm)	a (Å)	b (Å)	c (Å)	$V_{\text{unit cell}}$ (Å ³)
LaFeO_3	20.1 ± 0.1	5.561	7.858	5.558	242.85 ± 0.17
$\text{La}_{0.9}\text{Ca}_{0.1}\text{Fe}_{0.9}\text{Cu}_{0.1}\text{O}_3$	13.3 ± 0.1	5.551	7.845	5.546	241.51 ± 0.26
$\text{La}_{0.8}\text{Ca}_{0.2}\text{Fe}_{0.8}\text{Cu}_{0.2}\text{O}_3$	10.4 ± 0.1	5.552	7.801	5.532	239.62 ± 0.23

5.4.2 Reducibility

The reducibility of the $\text{La}_{1-x}\text{Ca}_x\text{Fe}_{1-x}\text{Cu}_x\text{O}_3$ solids was investigated by H_2 -TPR. The profiles are displayed in Fig. 5.33. For all samples, the growing H_2 consumption above 700°C is attributed to the progressive bulk reduction of LaFeO_3 . Remarkable differences compared to LaFeO_3 are observed at lower temperatures ($150^\circ\text{C} < T < 300^\circ\text{C}$). An additional asymmetric reduction peak is observed for the substituted solids at 223°C and 247°C for $x = 0.1$ and $x = 0.2$ respectively as observed earlier for $\text{LaFe}_{1-x}\text{Cu}_x\text{O}_3$ (Section 5.3.2).

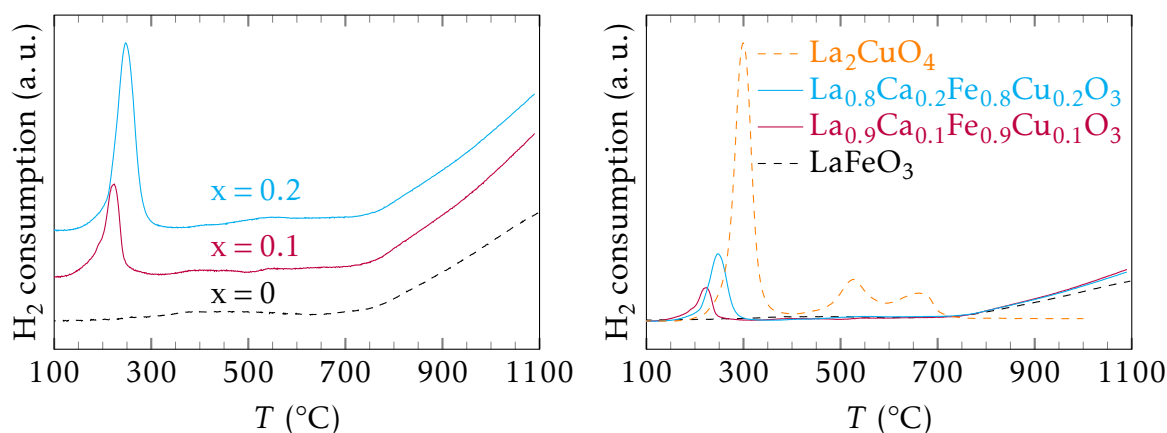


Figure 5.33 – H_2 absorption curves of calcined $\text{La}_{1-x}\text{Ca}_x\text{Fe}_{1-x}\text{Cu}_x\text{O}_3$ ($x = 0.1, 0.2$; CCM; $50\text{ mg}, 25\text{ ml min}^{-1}$) compared to LaFeO_3 (CCM; $50\text{ mg}, 50\text{ ml min}^{-1}$) and La_2CuO_4 (CCM; $100\text{ mg}, 25\text{ ml min}^{-1}$).

By analogy with the $\text{LaFe}_{1-x}\text{Cu}_x\text{O}_3$ solids (Subsection 5.3.2), the 1st peak must of course be mainly attributed to Cu^{2+} . A significant increase in the normalised H_2 uptake is noticeable which could be ascribed to a greater extraction of Cu^{2+} and/or the stabilisation of Fe^{4+} species as discussed for the $\text{La}_{1-x}\text{Ca}_x\text{FeO}_3$ samples (Section 5.2.2).

Table 5.24 – Comparison of H_2 -TPR results of $\text{La}_{1-x}\text{Ca}_x\text{Fe}_{1-x}\text{Cu}_x\text{O}_3$ ($x = 0.1, 0.2$; CCM; $50\text{ mg}, 25\text{ ml min}^{-1}$) compared to LaFeO_3 (CCM; $50\text{ mg}, 50\text{ ml min}^{-1}$).

x	H ₂ consumption		H/B		H/Cu ^c extracted Cu ⁰ ^d	T _{max}	reduction peaks			
	total ^a	low T ^b	total	low T ^b			(°C)	(°C)	(°C)	(°C)
0	-	-	-	-	-	-	-	-	-	> 1100
0.1	0.49	0.45	0.22	0.20	1.00	2.8	223	386	544	> 1100
0.2	1.03	0.98	0.44	0.44	2.19	6.2	247	401	536	> 1100

^a H_2 consumption was integrated over the temperature range of 150°C to 700°C .

^b Temperature domain up to 300°C .

^c Assuming that H_2 consumption of the 1st peak could be fully attributed to the reduction of Cu^{2+} .

^d After H_2 -TPR analysis, estimated by H_2 consumption in temperature range up to 300°C .

Calculating the ratio of H/Cu from the H_2 consumption assigned to the 1st peak a value of H/Cu > 2 has been obtained for the $\text{La}_{0.8}\text{Ca}_{0.2}\text{Fe}_{0.8}\text{Cu}_{0.2}\text{O}_3$ sample. It can be deduced that at least as much Fe^{4+} as can be calculated by the excess, i. e. 0.173 mmol , has to be present.

This represents 4.8 at.% of the Fe in the perovskite structure, slightly less than what was estimated for $\text{La}_{1-x}\text{Ca}_x\text{FeO}_3$ ($x = 0.2$).

The behaviour of the $\text{La}_{0.9}\text{Ca}_{0.1}\text{Fe}_{0.9}\text{Cu}_{0.1}\text{O}_3$ solid differs from the above mentioned explanation since the reduction of Cu^{2+} is incomplete. In this case the H/Cu ratio of 1 underlines that Cu^+ species are not further reduced in agreement with the H_2 -TPR results of the $\text{LaFe}_{1-x}\text{Cu}_x\text{O}_3$ solids, i. e. increasing reducibility of the Cu cations inside the structure is observed for higher substitution degree.

5.4.3 Textural properties

N_2 physisorption isotherms (Fig. 5.34A) present the typical CCM feature of type II and type IV isotherms. However, a broadening of the hysteresis towards low relative pressure domains is occurring for substituted samples and is increased with the substitution degree.

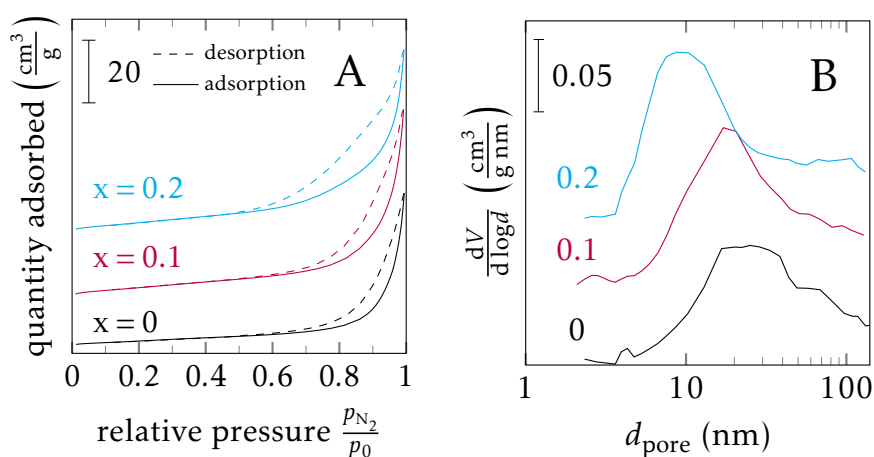


Figure 5.34 – N_2 adsorption and desorption isotherms and pore size distributions of calcined $\text{La}_{1-x}\text{Ca}_x\text{Fe}_{1-x}\text{Cu}_x\text{O}_3$ ($x = 0, 0.1, 0.2$; CCM).

The corresponding pore diameter distributions are shown in Fig. 5.34B. While the LaFeO_3 solid presents a broad distribution of mainly large macropores the $\text{La}_{1-x}\text{Ca}_x\text{Fe}_{1-x}\text{Cu}_x\text{O}_3$ solids ($x = 0.1, 0.2$) show narrower pore size distributions, the maximum being shifted to lower pore sizes.

Table 5.25 – Comparison of specific surface areas and cumulative pore volume of $\text{La}_{1-x}\text{Ca}_x\text{Fe}_{1-x}\text{Cu}_x\text{O}_3$ ($x = 0, 0.1, 0.2$; CCM).

composition	SSA ($\text{m}^2 \text{g}^{-1}$)	V_{pore} ($\text{cm}^3 \text{g}^{-1}$)
LaFeO_3	13.9	0.08
$\text{La}_{0.9}\text{Ca}_{0.1}\text{Fe}_{0.9}\text{Cu}_{0.1}\text{O}_3$	21.4	0.10
$\text{La}_{0.8}\text{Ca}_{0.2}\text{Fe}_{0.8}\text{Cu}_{0.2}\text{O}_3$	24.0	0.10

Regarding their specific surface area, the doubly substituted catalysts present significantly higher values than the non-substituted LaFeO_3 or the corresponding individually substituted samples. A bigger difference is observed compared to the Cu-substituted samples than for the Ca-substituted ones. Cumulative pore volumes are again slightly increased by a constant amount regardless of the substitution degree. Overall, the insertion of Ca and Cu in the perovskite structure is leading to higher specific surface area and slightly more porous solids.

5.4.4 Chemical composition at the surface

XPS analyses were performed to investigate the surface composition. Fig. 5.35 shows the La 3d and Fe 2p photopeaks of $\text{La}_{1-x}\text{Ca}_x\text{Fe}_{1-x}\text{Cu}_x\text{O}_3$. As for the other orthoferrites, they show the characteristic spectral features of trivalent La and Fe, including the broad and low intensity Fe 2p satellite at 719 eV.

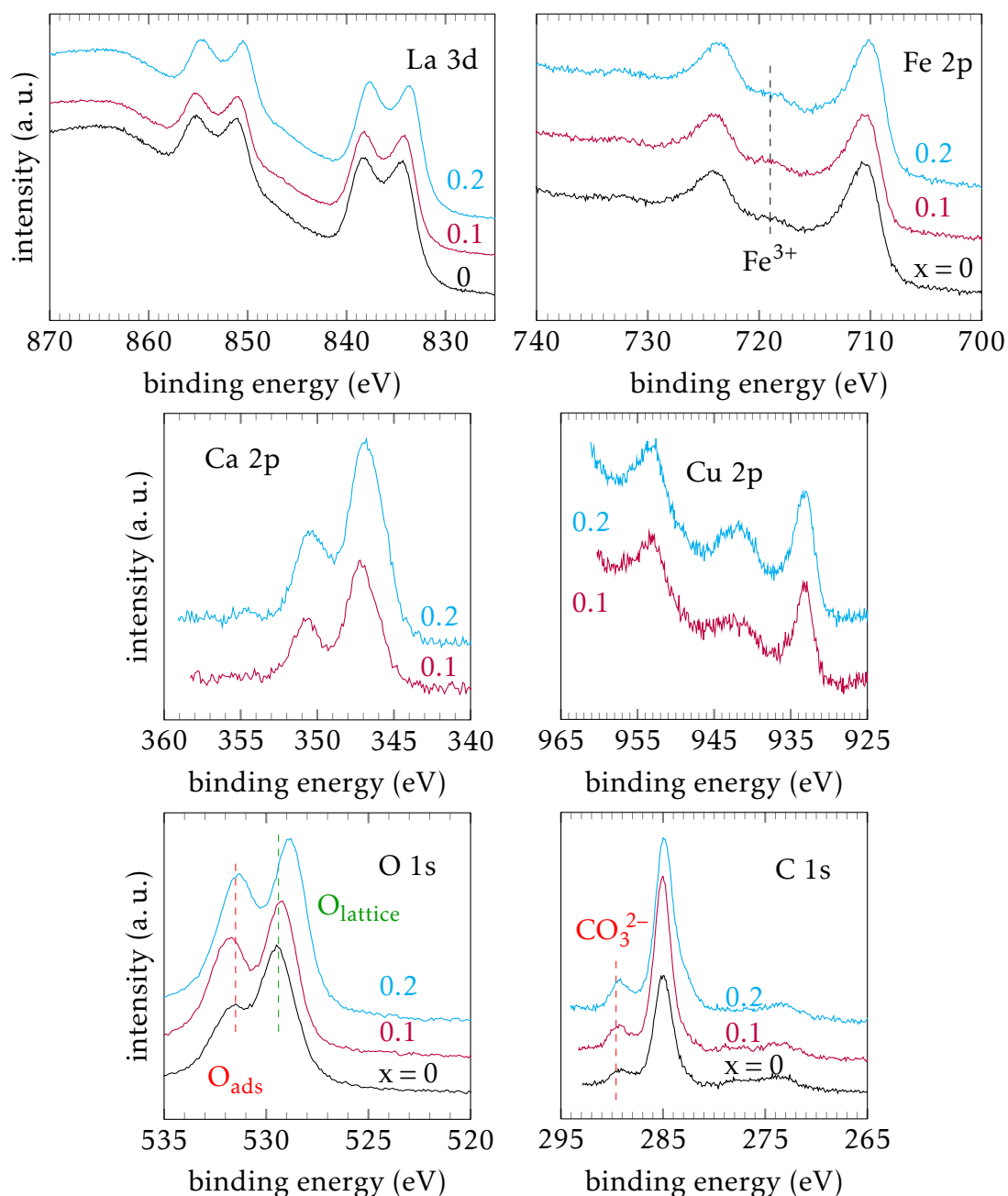


Figure 5.35 – La 3d, Fe 2p, Ca 2p, Cu 2p, O 1s and C 1s photopeaks of calcined $\text{La}_{1-x}\text{Ca}_x\text{Fe}_{1-x}\text{Cu}_x\text{O}_3$ ($x = 0, 0.1, 0.2$; CCM).

The photopeaks of the substituting cations are also shown in Fig. 5.35. The weakly intense Ca 2p satellites at B. E. > 353 eV are slightly discernible as for $\text{La}_{1-x}\text{Ca}_x\text{FeO}_3$. Therefore, the presence of high amounts of CaCO_3 is improbable.^[5] Spectral decomposition of the Cu 2p_{3/2} core level shows once again the predominance of Cu^{2+} species yielding a contribution of

only 3 at.% of Cu^+ for the $\text{La}_{0.8}\text{Ca}_{0.2}\text{Fe}_{0.8}\text{Cu}_{0.2}\text{O}_3$ and none for the less substituted solid in agreement with the observed intense satellite.

Table 5.26 – Comparison of photopeak maxima of calcined $\text{La}_{1-x}\text{Ca}_x\text{Fe}_{1-x}\text{Cu}_x\text{O}_3$ ($x = 0, 0.1, 0.2$; CCM).

x	B. E. (eV)					at. %	
	La 3d _{5/2}	Ca 2p _{3/2}	Fe 2p _{3/2}	Cu 2p _{3/2}	O 1s	O _{lattice} ^a	C _{CO₃²⁻} ^b
0	834.3	-	710.8	-	529.5	55	13
0.1	834.1	347.2	710.2	932.9	529.2	50	14
0.2	833.6	346.8	710.2	933.1	528.8	48	14

^a O_{lattice} + O_{ads} = 1.

^b C_{CO₃²⁻} + C_{adventitious} = 1.

Most distinct differences between LaFeO_3 and substituted solids are observed for the O 1s photopeaks (Fig. 5.35). An increase of adsorbed oxygen species is occurring with increasing substitution degree. This phenomenon can be attributed to the Cu-content, similar observations having been made for the photopeaks of $\text{LaFe}_{1-x}\text{Cu}_x\text{O}_3$.

C 1s photopeaks show again a main peak at 285 eV assigned to adventitious carbon species and a weaker contribution at 289.9 eV attributed to carbonates. The carbonate contribution seems to be independent of the substitution degree for all studied $\text{La}_{1-x}\text{Ca}_x\text{Fe}_{1-x}\text{Cu}_x\text{O}_3$ solids which is in contrast to the observations made for solids individually substituted in A- or B-site.

Concerning La 3d and O 1s photopeaks (Fig. 5.35), gradual decreases in binding energies of the apparent maxima are observed, as can be seen in Table 5.26. The positions of the Ca 2p_{3/2} photopeak are slightly higher for $\text{La}_{1-x}\text{Ca}_x\text{Fe}_{1-x}\text{Cu}_x\text{O}_3$ compared to $\text{La}_{1-x}\text{Ca}_x\text{FeO}_3$ samples, whereas Cu 2p_{3/2} photopeak maxima of $\text{La}_{1-x}\text{Ca}_x\text{Fe}_{1-x}\text{Cu}_x\text{O}_3$ solids do not show significant shifts. As for the solids obtained by substitution in A- or B-site only, Fe 2p_{3/2} maxima are shifted to constantly lower B. E. No clear explanation can be given regarding the origins of this phenomenon.

XPS measurements also revealed surface enrichment of A-site cations to the detriment of especially Fe in all solids (Table 5.27). However, this surface enhancement is attenuated with increasing Ca- and Cu-content. As can be seen from comparing the atomic ratios of Cu/Fe and Ca/La at the surface to the bulk values obtained by elementary analysis confirming the nominal values (Section 5.4.1), an enrichment of the substituting cations at the surface is observed for both sites.

Table 5.27 – Surface atomic ratios x_A/x_B , $x_{\text{Cu}}/x_{\text{Fe}}$ and $x_{\text{Ca}}/x_{\text{La}}$ of calcined $\text{La}_{1-x}\text{Ca}_x\text{Fe}_{1-x}\text{Cu}_x\text{O}_3$ ($x = 0, 0.1, 0.2$; CCM).

nominal composition	x_A/x_B	$x_{\text{Cu}}/x_{\text{Fe}}$	$x_{\text{Ca}}/x_{\text{La}}$	surface composition based on the nominal Fe content
LaFeO_3	2.13	-	-	$\text{La}_{2.13}\text{FeO}_{4.63}$ (C _{3.66})
$\text{La}_{0.9}\text{Ca}_{0.1}\text{Fe}_{0.9}\text{Cu}_{0.1}\text{O}_3$	1.74	0.26	0.21	$\text{La}_{1.63}\text{Ca}_{0.34}\text{Fe}_{0.90}\text{Cu}_{0.23}\text{O}_{4.91}$ (C _{4.82})
$\text{La}_{0.8}\text{Ca}_{0.2}\text{Fe}_{0.8}\text{Cu}_{0.2}\text{O}_3$	1.65	0.34	0.34	$\text{La}_{1.32}\text{Ca}_{0.45}\text{Fe}_{0.80}\text{Cu}_{0.27}\text{O}_{4.62}$ (C _{4.06})

5.4.5 Catalytic activity

The catalytic activity of the Ca- and Cu-substituted samples was tested according to Procedure A (Section 2.3). CO, propylene, NO, propane, oxygen and hydrogen conversions during temperature-programmed reactions are presented in Fig. 5.36 and 5.37. Additionally, T_{50} values are reported in Table 5.28 and in Appendix D (Table D.4).

Conversion profiles vs temperature reproduce the same trends as described earlier for $\text{LaFe}_{1-x}\text{Cu}_x\text{O}_3$. Again, the catalytic activity can be ascribed to the presence of Cu ions in the B-site compared to the lower activity recorded for $\text{La}_{1-x}\text{Ca}_x\text{FeO}_3$. The most prominent observations are related to CO oxidation to CO_2 and NO reduction which is only observed in rich conditions and usually accompanied by a predominant production of ammonia (Fig. 5.38). Such an ammonia production – also observed over noble metals – has been previously explained by a production of excess H_2 coming from reforming or WGS reactions. The same behaviour is observed for $\text{La}_{1-x}\text{Ca}_x\text{Fe}_{1-x}\text{Cu}_x\text{O}_3$ as exemplified in Fig. 5.36 and 5.37. However, a significant S_{N_2} enhancement is observable compared to the LaFeO_3 catalyst.

Regarding CO conversion, it is obvious that Ca and Cu insertion lead to significant activity enhancement. The comparison of the temperature at half conversion (Table 5.28) shows the lowest value of 279 °C for the $\text{La}_{0.8}\text{Ca}_{0.2}\text{Fe}_{0.8}\text{Cu}_{0.2}\text{O}_3$ perovskite compared to those recorded on $\text{La}_{0.8}\text{Ca}_{0.2}\text{FeO}_3$ (449 °C) and $\text{LaFe}_{0.8}\text{Cu}_{0.2}\text{O}_3$ (294 °C). The same observation can be made regarding NO.

Table 5.28 – Temperatures corresponding to 50 % conversion of CO, C_3H_6 , C_3H_8 , and H_2 (stoichiometric) and NO (rich composition) of $\text{La}_{1-x}\text{Ca}_x\text{Fe}_{1-x}\text{Cu}_x\text{O}_3$ catalysts ($x = 0, 0.1, 0.2$; CCM) and selectivities of NO reduction products at T_S . Values of the $\text{La}_{1-x}\text{Ca}_x\text{FeO}_3$ and $\text{LaFe}_{1-x}\text{Cu}_x\text{O}_3$ series are given for comparison.

condition	stoichiometric				rich				
	T_{50} (°C)				selectivities at T_S				
	CO	C_3H_6	C_3H_8	H_2	NO	S_{N_2}	S_{NH_3}	$S_{\text{N}_2\text{O}}$	T_S (°C)
LaFeO_3	438	463	478	501	^a	0.05	0.95	0	507
$\text{La}_{0.9}\text{Ca}_{0.1}\text{Fe}_{0.9}\text{Cu}_{0.1}\text{O}_3$	288	456	488	437	478	0.45	0.54	0.01	504
$\text{La}_{0.8}\text{Ca}_{0.2}\text{Fe}_{0.8}\text{Cu}_{0.2}\text{O}_3$	279	449	487	399	469	0.36	0.64	0	506
$\text{La}_{0.9}\text{Ca}_{0.1}\text{FeO}_3$	414	446	461	463	499 ^b	0.86	0	0.14	498
$\text{La}_{0.8}\text{Ca}_{0.2}\text{FeO}_3$	449	482	499	482	510 ^b	1.00	0	0	500
$\text{LaFe}_{0.9}\text{Cu}_{0.1}\text{O}_3$	305	469	467 ^c	444	489	0.51	0.43	0.07	493
$\text{LaFe}_{0.8}\text{Cu}_{0.2}\text{O}_3$	294	497	505 ^c	421	501 ^b	0.94	0	0.06	513

^a Conversion lower than 50 %.

^b T_{25} .

As shown in Table 5.29, both $\text{La}_{1-x}\text{Ca}_x\text{Fe}_{1-x}\text{Cu}_x\text{O}_3$ catalysts ($x = 0.1, 0.2$) show higher specific reaction rates for CO and C_3H_6 oxidation than LaFeO_3 . CO oxidation activity is markedly increased for doubly substituted perovskite samples. In agreement with the trend observed for the performances and the $\text{LaFe}_{1-x}\text{Cu}_x\text{O}_3$ samples, the specific reaction rates at 200 °C increase with higher Ca- and Cu-content. The increase in specific reaction rates for the C_3H_6 oxidation is less marked and only slight changes are observed for different substitution degrees. On the other hand, regarding the Arrhenius parameters shown in Table 5.29 (derived

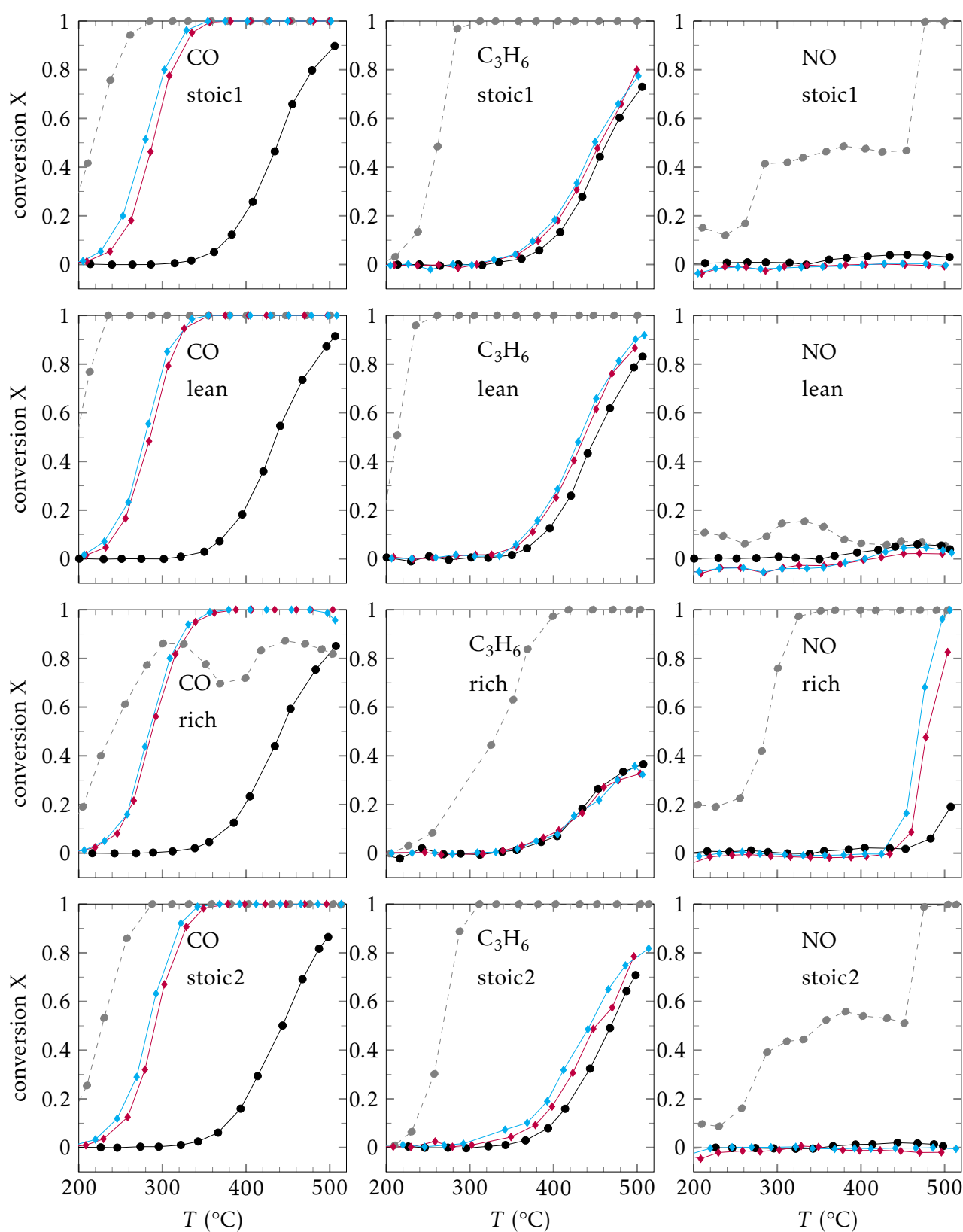


Figure 5.36 – CO, C₃H₆ and NO conversions of La_{1-x}Ca_xFe_{1-x}Cu_xO₃ catalysts (x = 0, 0.1, 0.2; CCM) under stoichiometric and rich conditions respectively. LaFeO₃ (•), La_{0.9}Ca_{0.1}Fe_{0.9}Cu_{0.1}O₃ (♦), and La_{0.8}Ca_{0.2}Fe_{0.8}Cu_{0.2}O₃ (◆) compared to the commercial reference TWC (○)

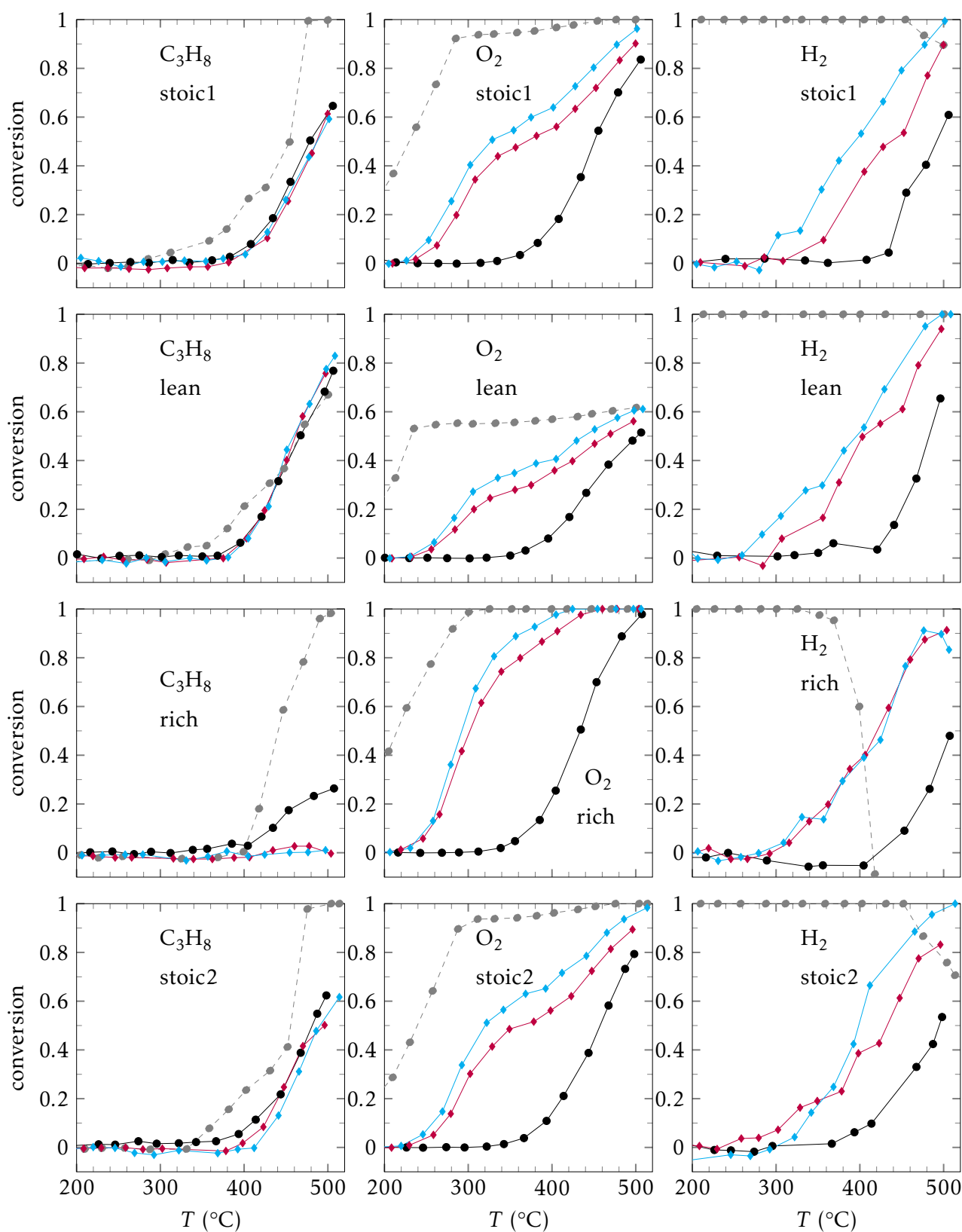


Figure 5.37 – C₃H₈, O₂ and H₂ conversions of La_{1-x}Ca_xFe_{1-x}Cu_xO₃ catalysts (x = 0, 0.1, 0.2; CCM) under stoichiometric and rich conditions respectively. LaFeO₃ (•), La_{0.9}Ca_{0.1}Fe_{0.9}Cu_{0.1}O₃ (♦), and La_{0.8}Ca_{0.2}Fe_{0.8}Cu_{0.2}O₃ (♦) compared to the commercial reference TWC (•)

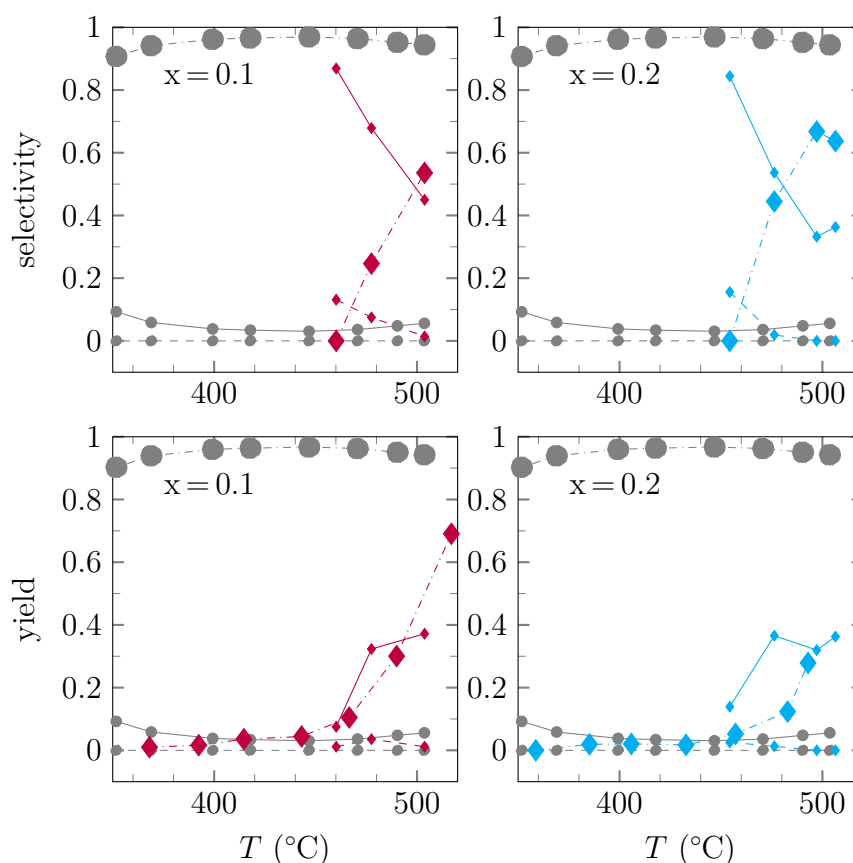


Figure 5.38 – N_2 , N_2O and NH_3 selectivities and yields of NO conversion of $\text{La}_{1-x}\text{Ca}_x\text{Fe}_{1-x}\text{Cu}_x\text{O}_3$ catalysts ($x=0.1, 0.2$; CCM) under rich conditions. $\text{La}_{0.9}\text{Ca}_{0.1}\text{Fe}_{0.9}\text{Cu}_{0.1}\text{O}_3$ (\blacklozenge), and $\text{La}_{0.8}\text{Ca}_{0.2}\text{Fe}_{0.8}\text{Cu}_{0.2}\text{O}_3$ (\blacklozenge) compared to the commercial reference TWC (\bullet); $S_{\text{N}_2}/Y_{\text{N}_2}$ (solid), $S_{\text{N}_2\text{O}}/Y_{\text{N}_2\text{O}}$ (dashed), $S_{\text{NH}_3}/Y_{\text{NH}_3}$ (dashdotted, big mark). Please note different T scales compared to the conversion profiles.

from linear regression of straight lines in Fig. D.6), catalytic activity for C_3H_6 oxidation is enhanced with increasing substitution degree, i. e. apparent activation energies and pre-exponential factors decrease. Regarding the CO oxidation, no such significant decreases in A are observed. Whereas both doubly substituted solids present lower $E_{A,\text{app}}$ than LaFeO_3 , the numerical values of A differ. While similar ones are observed for the $\text{La}_{0.9}\text{Ca}_{0.1}\text{Fe}_{0.9}\text{Cu}_{0.1}\text{O}_3$ and LaFeO_3 samples, a higher value (with the same order of magnitude) is obtained for the $\text{La}_{0.8}\text{Ca}_{0.2}\text{Fe}_{0.8}\text{Cu}_{0.2}\text{O}_3$ catalyst. Propylene oxidation seems to be less affected by the increase of reducibility and/or anionic defects in the structure. This leads once again to the conclusion that CO and propylene oxidation proceed on different active sites.

Comparing the results of the $\text{La}_{1-x}\text{Ca}_x\text{Fe}_{1-x}\text{Cu}_x\text{O}_3$ catalysts ($x=0.1, 0.2$) to those of the $\text{La}_{1-y}\text{FeO}_3$ solids ($x=0.1, 0.2, 0.33$) propylene oxidation was further enhanced by the solids obtained by purposely decreasing the La-content. However, higher performances with respect to CO and propane oxidation as well as NO reduction were achieved by the Cu- and Ca-substituted Fe-based perovskites.

Moreover, the stability of the doubly substituted solids was confirmed by unchanged conversion profiles comparing the initial with the return test under stoichiometric conditions.

Table 5.29 – Comparison of specific reaction rates r_{specific} , apparent activation energies $E_{A, \text{app}}$ and pre-exponential factors A of CO and C_3H_6 oxidation for $\text{La}_{1-x}\text{Ca}_x\text{Fe}_{1-x}\text{Cu}_x\text{O}_3$ catalysts ($x = 0, 0.1, 0.2$) under stoichiometric conditions (1st test ramp). Arrhenius parameters were determined by Arrhenius plots (Fig. D.6). Values of the $\text{La}_{1-x}\text{Ca}_x\text{FeO}_3$ and $\text{LaFe}_{1-x}\text{Cu}_x\text{O}_3$ series are given for comparison.

	SSA ($\text{m}^2 \text{g}^{-1}$)	r_{specific}^a ($\text{mol s}^{-1} \text{g}^{-1}$)		$E_{A, \text{app}}$ (kJ mol^{-1})		A ($10^3 \text{ m}^3 \text{s}^{-1} \text{g}^{-1}$)	
		CO	C_3H_6	CO	C_3H_6	CO	C_3H_6
LaFeO_3	13.9	≈ 0	$2.5 \cdot 10^{-9}$	142	128	424.4	15.2
$\text{La}_{0.9}\text{Ca}_{0.1}\text{Fe}_{0.9}\text{Cu}_{0.1}\text{O}_3$	21.4	$2.7 \cdot 10^{-8}$	$5.0 \cdot 10^{-9}$	113	116	364.2	2.9
$\text{La}_{0.8}\text{Ca}_{0.2}\text{Fe}_{0.8}\text{Cu}_{0.2}\text{O}_3$	24.0	$3.6 \cdot 10^{-8}$	$5.5 \cdot 10^{-9}$	115	107	895.6	0.690
$\text{La}_{0.9}\text{Ca}_{0.1}\text{FeO}_3$	20.8	≈ 0	$3.7 \cdot 10^{-9}$	144	148	1064	1004
$\text{La}_{0.8}\text{Ca}_{0.2}\text{FeO}_3$	23.4	≈ 0	$3.9 \cdot 10^{-9}$	273	145	$6.1 \cdot 10^{12}$	132
$\text{LaFe}_{0.9}\text{Cu}_{0.1}\text{O}_3$	18.4	≈ 0	$3.7 \cdot 10^{-9}$	171	100	55351179	0.112
$\text{LaFe}_{0.8}\text{Cu}_{0.2}\text{O}_3$	13.8	$5.4 \cdot 10^{-8}$	$3.7 \cdot 10^{-9}$	112	103	216.8	0.130

^a Specific reaction rates were calculated from conversions at 200 °C for CO and 350 °C for C_3H_6 .

5.4.6 Conclusion

The investigation of the simultaneous substitution in the A- and B-site of the LaFeO_3 perovskite was conducted by preparing a series of $\text{La}_{1-x}\text{Ca}_x\text{Fe}_{1-x}\text{Cu}_x\text{O}_3$ solids ($x = 0, 0.1, 0.2$) by CCM. Modifications in the textural properties are moderate, i. e. a shift to slightly lower-sized pores combined with a narrowing of the pore size distribution and increased specific surface areas are observed.

Likewise, the orthorhombic LaFeO_3 structure is retained – even though distorted – despite the high charge imbalance caused by the substitution with aliovalent cations. The compensation of this charge balance is mainly achieved by the generation of anionic defects as for the individually substituted solids. The existence of low amounts of Fe^{4+} species could be tentatively deduced from H_2 -TPR analyses results.

In addition, doubly substituted orthoferrites present a high reducibility due to the presence of Cu^{2+} and probably to a lesser extent of Fe^{4+} . Moreover, a slightly less stable structure is assumed due to the high lattice distortions.

Finally, enhancements were observed for catalytic performances regarding CO oxidation as well as NO reduction and catalytic activities for CO oxidation. The combination of Ca- and Cu-substitution lead to markedly lower light-off temperatures and increased conversions, especially of CO and NO. The N_2 selectivities of NO reduction were observed to be lower than for the $\text{LaFe}_{1-x}\text{Cu}_x\text{O}_3$ samples but are still significantly improved compared to the LaFeO_3 solid and the commercial reference catalyst.

5.5 Combining surface and bulk composition optimisation approaches

Since bulk and surface composition optimisation of Fe-based perovskites independently yielded enhanced catalytic activity, a combination of these approaches was studied. Hence, a

solid with lowered La-content and partial substitution in A- and B-sites was prepared by CCM with the following nominal composition: $\text{La}_{0.6}\text{Ca}_{0.2}\text{Fe}_{0.8}\text{Cu}_{0.2}\text{O}_3$. Since the lattice is assumed to be already rather distorted due to the high substitution degree of Ca and Cu, only a lower decrease in La-content was investigated than the one which gave highest performances ($\text{La}_{0.67}\text{FeO}_3$). On the other hand, a solid was prepared which was only substituted in the B-site combined with a lower La-content, its nominal composition: $\text{La}_{0.67}\text{Fe}_{0.83}\text{Cu}_{0.17}\text{O}_3$. Since the insertion of Cu into the perovskite lattice induced less distortion, an attempt at combining high Cu-substitution ($x = 0.2$) and the lowest investigated La-content ($y = 0.33$) was studied.

5.5.1 Bulk/Structural properties

Chemical composition of the bulk

The bulk chemical composition of the $\text{La}_{0.67}\text{Fe}_{0.83}\text{Cu}_{0.17}\text{O}_3$ solid obtained by combining surface and bulk composition optimisation approaches was studied by ICP. Elementary analysis confirms the nominal composition of the $\text{La}_{0.67}\text{Fe}_{0.83}\text{Cu}_{0.17}\text{O}_3$ sample. The obtained value for the bulk La to B⁵ ratio complies as well for the $\text{La}_{0.67}\text{Fe}_{0.83}\text{Cu}_{0.17}\text{O}_3$ sample as shown in Table 5.30.

Table 5.30 – Bulk atomic ratios x_A/x_B and $x_{\text{Cu}}/x_{\text{Fe}}$ of calcined $\text{La}_{1-y}\text{Fe}_{1-x}\text{Cu}_x\text{O}_3$ ($x = 0, 0.17, 0.2$; $y = 0, 0.33$; CCM).

nominal composition	$x_{\text{La}}/x_{\text{Fe}}$	x_A/x_B	$x_{\text{Cu}}/x_{\text{Fe}}$
$\text{LaFe}_{0.8}\text{Cu}_{0.2}\text{O}_3$	1.26	1.03	0.23
$\text{La}_{0.67}\text{FeO}_3$	0.66	0.66	-
$\text{La}_{0.67}\text{Fe}_{0.83}\text{Cu}_{0.17}\text{O}_3$	0.82	0.68	0.19

XRD

Fig. 5.39 shows the X-ray diffractograms of the $\text{La}_{1-x-y}\text{Ca}_x\text{Fe}_{1-x}\text{Cu}_x\text{O}_3$ ($x = 0, 0.2$; $y = 0, 0.2$) and $\text{La}_{1-y}\text{Fe}_{1-x}\text{Cu}_x\text{O}_3$ ($x = 0, 0.17, 0.2$; $y = 0, 0.33$) solids. The derived $\text{La}_{0.6}\text{Ca}_{0.2}\text{Fe}_{0.8}\text{Cu}_{0.2}\text{O}_3$ and $\text{La}_{0.67}\text{Fe}_{0.83}\text{Cu}_{0.17}\text{O}_3$ catalysts retain the orthorhombic perovskite structure and the relative intensities of the diffraction peaks as for LaFeO_3 . While the $\text{La}_{0.6}\text{Ca}_{0.2}\text{Fe}_{0.8}\text{Cu}_{0.2}\text{O}_3$ sample shows slight shifts to higher 2θ values, none are observed for the $\text{La}_{0.67}\text{Fe}_{0.83}\text{Cu}_{0.17}\text{O}_3$ sample. Minor crystalline phase segregation in the form of hematite is observed for both solids in agreement with the results discussed in Section 5.1.

In Fig. 5.40, the unit cell volumes ($V_{\text{unit cell}}$) of the derived substituted and La-deficient solid series are compared to LaFeO_3 . Since the lowering of the La-content in LaFeO_3 does not have an impact on the perovskite structure itself (Section 5.1.2), the unit cell volumes of $\text{La}_{1-y}\text{FeO}_3$ are not displayed and those of the optimised solids would depend only on the substitution degree in A- and B-site. Regarding the evolution of the unit cell volume of $\text{La}_{1-x}\text{Ca}_x\text{FeO}_3$, $\text{La}_{1-x}\text{Ca}_x\text{Fe}_{1-x}\text{Cu}_x\text{O}_3$ and $\text{LaFe}_{1-x}\text{Cu}_x\text{O}_3$ solids with respect to LaFeO_3 , a slight decrease in unit cell is obtained for the B-site substitution by Cu, whereas a marked decrease is noticed for the samples substituted with Ca. This behaviour is retained for the optimised solids. The $\text{La}_{0.67}\text{Fe}_{0.83}\text{Cu}_{0.17}\text{O}_3$ sample shows a similar unit cell volume to the one

⁵B = Fe + Cu

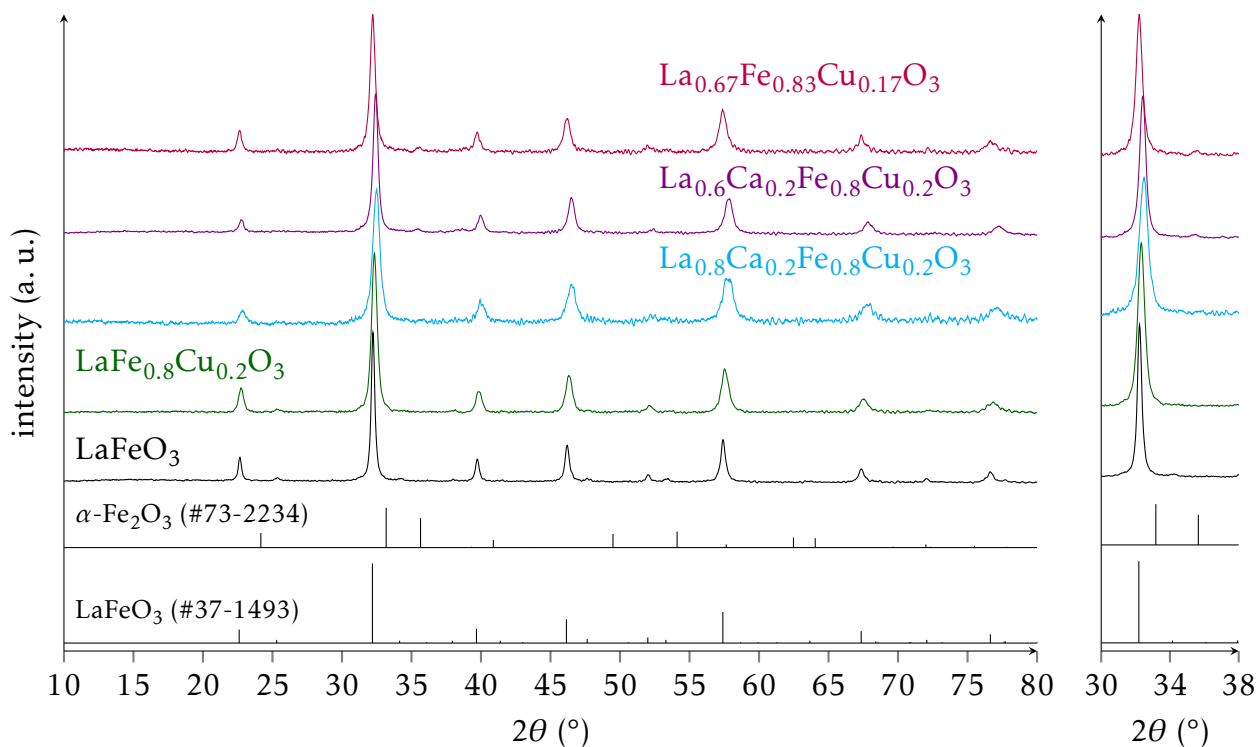


Figure 5.39 – X-ray diffractograms of calcined $\text{La}_{1-x-y}\text{Ca}_x\text{Fe}_{1-x}\text{Cu}_x\text{O}_3$ ($x = 0, 0.2$; $y = 0, 0.2$; CCM) and $\text{La}_{1-y}\text{Fe}_{1-x}\text{Cu}_x\text{O}_3$ ($x = 0, 0.17, 0.2$; $y = 0, 0.33$; CCM).

of the LaFeO_3 and $\text{LaFe}_{1-x}\text{Cu}_x\text{O}_3$ ($x = 0.05$) solids. In contrast, the $\text{La}_{0.6}\text{Ca}_{0.2}\text{Fe}_{0.8}\text{Cu}_{0.2}\text{O}_3$ solid clearly shows a significant supplementary decrease in unit cell volume compared to LaFeO_3 and even the $\text{La}_{0.8}\text{Ca}_{0.2}\text{Fe}_{0.8}\text{Cu}_{0.2}\text{O}_3$ sample. One has to keep in mind that the substitution degree x in the nominal formula is probably different from the actual substitution degree inside the perovskite structure. This difference is a consequence of the purposely lowered La-content. The employed notation for these samples does not reflect the real composition of the perovskite since phase segregation in form of hematite occurs, as was seen in the diffractograms (Fig. 5.39). Therefore, the presence of higher amounts of Ca and Cu in the perovskite are probable. This should therefore, as already discussed in Sections 5.2.1, 5.3.1 and 5.4.1, lead to a higher amount of created (anionic) defects to allow for electroneutrality throughout the perovskite structure. This is of course also true for $\text{La}_{0.67}\text{Fe}_{0.83}\text{Cu}_{0.17}\text{O}_3$. However, in this case the effect is partly compensated by the sole substitution by the bigger Cu^{2+} cation.⁶

Unit cell parameters and volume as well as apparent crystallite sizes are reported in Table 5.31. Interestingly, even if the $\text{La}_{0.6}\text{Ca}_{0.2}\text{Fe}_{0.8}\text{Cu}_{0.2}\text{O}_3$ catalyst presents a smaller unit cell volume and lattice parameters, the average crystallite size is higher than for the $\text{La}_{0.8}\text{Ca}_{0.2}\text{Fe}_{0.8}\text{Cu}_{0.2}\text{O}_3$ solid. The B-site substituted solid seem to be less affected by the lowered La-content, the average crystallite diameter remaining similar.

⁶The same simplified assumption of a purely steric model applies as for the discussions in Sections 5.2.1, 5.3.1 and 5.4.1.

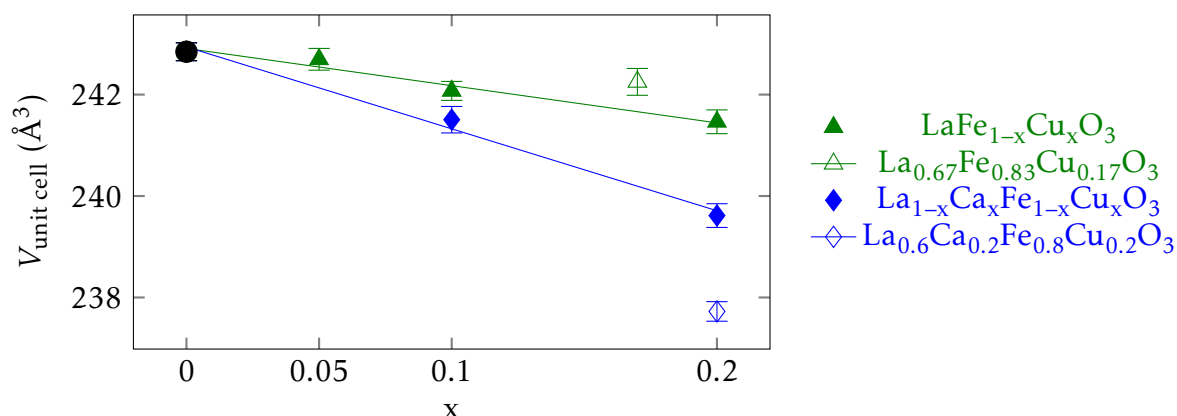


Figure 5.40 – Evolution of the unit cell volumes of calcined perovskites prepared by CCM. x corresponds to the *nominal* substitution degree.

Table 5.31 – Comparison of crystallite sizes, unit cell parameters and volume derived from full pattern matching of calcined $\text{La}_{1-x-y}\text{Ca}_x\text{Fe}_{1-x}\text{Cu}_x\text{O}_3$ ($x = 0, 0.2$; $y = 0, 0.2$; CCM) and $\text{La}_{1-y}\text{Fe}_{1-x}\text{Cu}_x\text{O}_3$ ($x = 0, 0.17, 0.2$; $y = 0, 0.33$; CCM).

nominal composition	d_{cryst} (nm)	a (Å)	b (Å)	c (Å)	$V_{\text{unit cell}}$ (Å ³)
LaFeO_3	20.1 ± 0.1	5.561	7.858	5.558	242.85 ± 0.17
$\text{La}_{0.8}\text{FeO}_3$	18.2 ± 0.1	5.558	7.863	5.558	242.88 ± 0.23
$\text{La}_{0.8}\text{Ca}_{0.2}\text{Fe}_{0.8}\text{Cu}_{0.2}\text{O}_3$	10.4 ± 0.1	5.552	7.801	5.532	239.62 ± 0.23
$\text{La}_{0.6}\text{Ca}_{0.2}\text{Fe}_{0.8}\text{Cu}_{0.2}\text{O}_3$	15.6 ± 0.1	5.537	7.782	5.518	237.73 ± 0.19
$\text{La}_{0.67}\text{FeO}_3$	12.6 ± 0.1	5.556	7.851	5.558	242.43 ± 0.27
$\text{LaFe}_{0.8}\text{Cu}_{0.2}\text{O}_3$	13.5 ± 0.1	5.559	7.829	5.548	241.46 ± 0.22
$\text{La}_{0.67}\text{Fe}_{0.83}\text{Cu}_{0.17}\text{O}_3$	13.3 ± 0.1	5.564	7.833	5.558	242.25 ± 0.26

5.5.2 Reducibility

The reducibility of the $\text{La}_{0.67}\text{Fe}_{0.83}\text{Cu}_{0.17}\text{O}_3$ and $\text{La}_{0.6}\text{Ca}_{0.2}\text{Fe}_{0.8}\text{Cu}_{0.2}\text{O}_3$ solids has been investigated by H_2 -TPR experiments. The H_2 consumption profiles are reported in Fig. 5.41. The main observations are related to 2 different temperature domains: The 1st, below 280 °C, is ascribed to the reduction of Cu^{2+} species, in the 2nd above 280 °C a 2-step reduction of hematite, $\alpha\text{-Fe}_2\text{O}_3$, is assumed to occur.

As observed, the high temperature H_2 uptake occurs only for the La-deficient solids. In that case, excess Fe is partially extracted and aggregates. 2 observations are, however, made for the $\text{La}_{0.6}\text{Ca}_{0.2}\text{Fe}_{0.8}\text{Cu}_{0.2}\text{O}_3$ (Fig. 5.41d) and $\text{La}_{0.67}\text{Fe}_{0.83}\text{Cu}_{0.17}\text{O}_3$ (Fig. 5.41g) catalysts. First, for the $\text{La}_{0.6}\text{Ca}_{0.2}\text{Fe}_{0.8}\text{Cu}_{0.2}\text{O}_3$ solid the reduction peak attributed to hematite presents but a negligible intensity. In addition, both optimised solids show 2 distinct reduction peaks below 280 °C corresponding to an overestimated H/Cu ratio (Table 5.32) assuming a complete reduction of Cu^{2+} to metallic Cu^0 species. This phenomenon is most marked for the $\text{La}_{0.67}\text{Fe}_{0.83}\text{Cu}_{0.17}\text{O}_3$ solid. IR analysis of the outlet gas did not reveal the presence of decomposition products of the reduction of carbonate species.

Concerning the first observation, on $\text{La}_{0.67}\text{Fe}_{0.83}\text{Cu}_{0.17}\text{O}_3$ only the 1st peak of hematite reduction (300 °C < T < 450 °C) is observed and this with a lower intensity than for the corresponding non-substituted sample. According to this peak only 4.1 wt.% of the sample

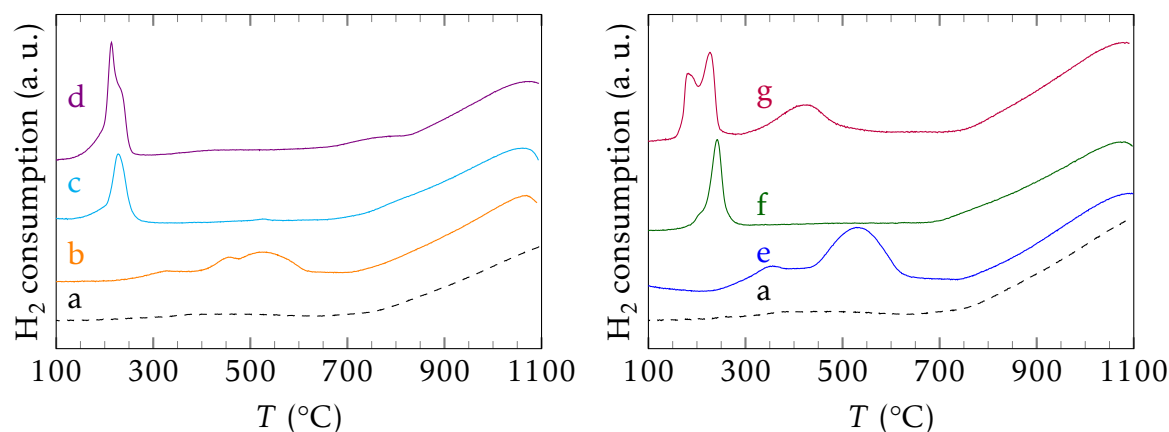


Figure 5.41 – H_2 absorption curves of calcined $\text{La}_{1-x-y}\text{Ca}_x\text{Fe}_{1-x}\text{Cu}_x\text{O}_3$ ($x = 0, 0.2$; $y = 0, 0.2$; CCM) and $\text{La}_{1-y}\text{Fe}_{1-x}\text{Cu}_x\text{O}_3$ ($x = 0, 0.17, 0.2$; $y = 0, 0.33$; CCM). LaFeO_3 (a), $\text{La}_{0.8}\text{FeO}_3$ (b), $\text{La}_{0.8}\text{Ca}_{0.2}\text{Fe}_{0.8}\text{Cu}_{0.2}\text{O}_3$ (c), $\text{La}_{0.6}\text{Ca}_{0.2}\text{Fe}_{0.8}\text{Cu}_{0.2}\text{O}_3$ (d), $\text{La}_{0.67}\text{FeO}_3$ (e), $\text{LaFe}_{0.8}\text{Cu}_{0.2}\text{O}_3$ (f), $\text{La}_{0.67}\text{Fe}_{0.83}\text{Cu}_{0.17}\text{O}_3$ (g) (50 mg, 50 ml min^{-1}).

are estimated to correspond to $\alpha\text{-Fe}_2\text{O}_3$ (Table 5.32). This value is far below the one which would be expected if all excess Fe in the solid was consumed by a hematite phase but higher than for the $\text{La}_{0.6}\text{Ca}_{0.2}\text{Fe}_{0.8}\text{Cu}_{0.2}\text{O}_3$ solid (0.4 wt.%). Such low amounts of hematite suggest that Cu is preferentially extracted from the perovskite lattice compared to Fe by lowering the La-content, thereby attenuating the La-deficiency. This phenomenon seems to be amplified for the Ca-substituted solid.

Regarding the appearance of a 2nd reduction peak below 300 °C for both optimised solids, it has to be noticed that this behaviour was already observed for the corresponding Cu-containing samples – however only as a shoulder to the main peak (Fig. 5.41c and 5.41f). 2 possible hypotheses can be suggested to explain this pronounced phenomenon on the optimised solids. On the one hand, a splitting in the reduction process from Cu^{2+} over Cu^+ to metallic Cu^0 as reported by Anderson et al. for CuO ^[26] may be induced by the lowered La-content. On the other hand, the appearance of a more reducible Cu^{2+} species, i. e. residing in a different chemical environment, can be envisaged. Such a Cu^{2+} species may be segregated CuO in which Cu^{2+} is less stabilised than in the perovskite lattice. Due to the lowered La-content such a Cu segregation is probable. This may also explain the absence of the typical hematite reduction peak(s) in the case of the $\text{La}_{0.6}\text{Ca}_{0.2}\text{Fe}_{0.8}\text{Cu}_{0.2}\text{O}_3$ solid which presents a lower La-deficiency. As stated before, this deficiency may be compensated by Cu segregation instead of the formation of a separate hematite phase. Assuming $\text{H}/\text{Cu} = 2$ to correspond to 100 wt.% of Cu^0 formed during H_2 -TPR analysis, an only slightly higher metallic Cu-content ($+ \approx 1 \text{ wt.}\%$) after reduction is present for both optimised solids compared to the parent Cu-substituted samples. Depending on the real oxygen content, the Cu contribution may, however, be higher than expected from the nominal composition in line with the higher H/Cu values based on the nominal composition.

As shown in Table 5.32, the overall H_2 consumption (integrated up to 700 °C) of the $\text{La}_{0.6}\text{Ca}_{0.2}\text{Fe}_{0.8}\text{Cu}_{0.2}\text{O}_3$ solid is lower than the $\text{La}_{0.67}\text{Fe}_{0.83}\text{Cu}_{0.17}\text{O}_3$ catalyst's 1.76 mmol g^{-1} which is lower than for the $\text{La}_{0.67}\text{FeO}_3$ solid. This is in agreement with the lower hematite content already discussed since the Cu contribution is high in both cases.

Regarding, the H_2 consumption up to 700 °C, the solids obtained by combining surface and bulk composition optimisation approaches show higher reducibility, especially at tem-

Table 5.32 – Comparison of H₂-TPR results of La_{1-x-y}Ca_xFe_{1-x}Cu_xO₃ (x = 0, 0.2; y = 0, 0.2; CCM) and La_{1-y}Fe_{1-x}Cu_xO₃ (x = 0, 0.17, 0.2; y = 0, 0.33; CCM). (50 mg, 50 ml min⁻¹)

nominal composition	low T H ₂ uptake ^a				high T H ₂ uptake ^b				
	T_{\max}		H/Cu ^c	Cu ⁰ ^d	T_{\max}			H/Fe ^e	Fe ₂ O ₃ ^f
	(°C)	(°C)			(°C)	(°C)	(°C)		
LaFeO ₃	-	-	-	-	-	-	-	-	-
La _{0.8} FeO ₃	-	-	-	-	327	457	521	0.60	7.5
La _{0.8} Ca _{0.2} Fe _{0.8} Cu _{0.2} O ₃	^g	228	2.00	5.5	-	-	525	0.01	-
La _{0.6} Ca _{0.2} Fe _{0.8} Cu _{0.2} O ₃	214	230	2.48	6.5	-	425	(750)	0.03	0.4
La _{0.67} FeO ₃	-	-	-	-	354	-	527	0.72	9.9
LaFe _{0.8} Cu _{0.2} O ₃	^g	241	1.64	4.3	-	-	-	-	-
La _{0.67} Fe _{0.83} Cu _{0.17} O ₃	182	227	2.33	5.4	422	-	-	0.36	4.1

^a 150 °C to 280 °C.

^b 250 °C to 650 °C.

^c H/Cu_{max} = 2 according to CuO + H₂ = Cu⁰ + H₂O.

^d Extracted Cu⁰ after H₂-TPR analysis, estimated according to 100 wt.% Cu⁰ corresponding to H/Cu = 2 for T < 280 °C.

^e H/Fe_{max} = 3 according to process described in Section 5.1.4.

^f Fe₂O₃ content assuming Fe³⁺ (hematite phase) reduction with H/Fe = 2.96.

^g Unresolved shoulder of the 2nd peak.

peratures below 300 °C. As can be seen by the H/Cu values > 2 for these peaks, they cannot be solely attributed to the Cu²⁺ reduction to Cu⁰. Therefore, non-Cu contributions like Fe⁴⁺ may be assumed.

5.5.3 Textural properties

The results of N₂-physisorption of the La_{0.6}Ca_{0.2}Fe_{0.8}Cu_{0.2}O₃ and La_{0.67}Fe_{0.83}Cu_{0.17}O₃ solids compared to the corresponding samples with either lowered La-content or containing the same substitution are displayed in Fig. 5.42. As for the other CCM solids, all isotherms present a combination of type II and type IV behaviour (Fig. 5.42A and 5.42C). The solids combining surface and bulk composition optimisation show isotherms which represent textural properties which lie in between those of the samples for which surface or bulk compositions were “individually” optimised, i. e. a broader hysteresis is observed than for the samples with Cu or Ca and Cu substitution. However, the hysteresis are less broad than for the samples obtained by purposely lowering the La-content.

This intermediate behaviour is confirmed by their pore size distributions (Fig. 5.42B and 5.42D). As for the samples which were prepared lowering the La-content, an increased contribution of low-sized mesopores is observed. However, this trend is far more distinct for the La_{0.67}Fe_{0.83}Cu_{0.17}O₃ than for the La_{0.6}Ca_{0.2}Fe_{0.8}Cu_{0.2}O₃ solid. However, the pore size distribution maxima are clearly shifted to lower diameters for both solids.

The catalysts combining surface and bulk optimisation approaches present the highest surface area with respect to all perovskites derived from LaFeO₃. Both solids yield specific surface areas of about 26 m² g⁻¹ (Table 5.33) accompanied by slightly increased cumulative pore volumes.

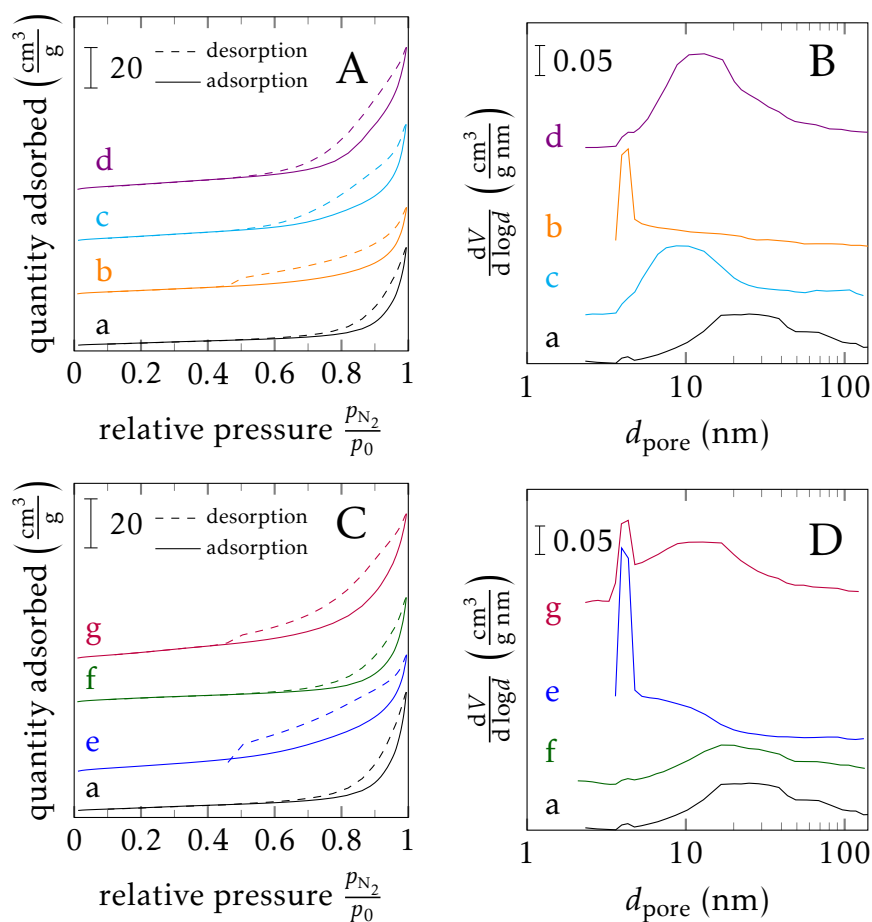


Figure 5.42 – N_2 adsorption and desorption isotherms and pore size distributions of calcined $\text{La}_{1-x-y}\text{Ca}_x\text{Fe}_{1-x}\text{Cu}_y\text{O}_3$ ($x = 0, 0.2$; $y = 0, 0.2$; CCM) and $\text{La}_{1-y}\text{Fe}_{1-x}\text{Cu}_x\text{O}_3$ ($x = 0, 0.17, 0.2$; $y = 0, 0.33$; CCM). LaFeO_3 (a), $\text{La}_{0.8}\text{FeO}_3$ (b), $\text{La}_{0.8}\text{Ca}_{0.2}\text{Fe}_{0.8}\text{Cu}_{0.2}\text{O}_3$ (c), $\text{La}_{0.6}\text{Ca}_{0.2}\text{Fe}_{0.8}\text{Cu}_{0.2}\text{O}_3$ (d), $\text{La}_{0.67}\text{FeO}_3$ (e), $\text{LaFe}_{0.8}\text{Cu}_{0.2}\text{O}_3$ (f), $\text{La}_{0.67}\text{Fe}_{0.83}\text{Cu}_{0.17}\text{O}_3$ (g)

Table 5.33 – Comparison of specific surface areas and cumulative pore volume of $\text{La}_{1-x-y}\text{Ca}_x\text{Fe}_{1-x}\text{Cu}_y\text{O}_3$ ($x = 0, 0.2$; $y = 0, 0.2$; CCM) and $\text{La}_{1-y}\text{Fe}_{1-x}\text{Cu}_x\text{O}_3$ ($x = 0, 0.17, 0.2$; $y = 0, 0.33$; CCM).

composition	SSA ($\text{m}^2 \text{g}^{-1}$)	V_{pore} ($\text{cm}^3 \text{g}^{-1}$)
LaFeO_3	13.9	0.08
$\text{La}_{0.8}\text{FeO}_3$	17.6	0.08
$\text{La}_{0.8}\text{Ca}_{0.2}\text{Fe}_{0.8}\text{Cu}_{0.2}\text{O}_3$	24.0	0.10
$\text{La}_{0.6}\text{Ca}_{0.2}\text{Fe}_{0.8}\text{Cu}_{0.2}\text{O}_3$	26.4	0.12
$\text{La}_{0.67}\text{FeO}_3$	23.8	0.10
$\text{LaFe}_{0.8}\text{Cu}_{0.2}\text{O}_3$	13.8	0.07
$\text{La}_{0.67}\text{Fe}_{0.83}\text{Cu}_{0.17}\text{O}_3$	26.5	0.11

5.5.4 Chemical composition at the surface

Regarding the photopeaks obtained by XPS of La 3d and Fe 2p for all the samples (Fig. 5.43), the characteristic multiplets are observed. Fe 2p photopeaks also show the already discussed broad and not very intense satellite at 719 eV. Trivalent La and Fe are therefore again evidenced. Photopeak maxima, reported in Table 5.34, show slight shifts to higher B. E. of La 3d_{5/2} for La_{0.6}Ca_{0.2}Fe_{0.8}Cu_{0.2}O₃ compared to La_{0.6}Ca_{0.2}Fe_{0.8}Cu_{0.2}O₃. With 833.9 eV, the La 3d_{5/2} position of the solid obtained combining the approach of lower La-content and double substitution (in A and B) is situated between the samples prepared according to the individual approaches. This is not the case for Fe 2p_{3/2} for which the maximum of 710.1 eV is even slightly lower than for La_{0.8}Ca_{0.2}Fe_{0.8}Cu_{0.2}O₃.

La_{0.67}Fe_{0.83}Cu_{0.17}O₃ also shows a shift to higher B. E. as observed for the La_{0.67}FeO₃ sample concerning the photopeak maximum of La 3d_{5/2}. Contrarily to the observation of La_{0.6}Ca_{0.2}Fe_{0.8}Cu_{0.2}O₃, the Fe 2p_{3/2} maximum is shifted in the same way to 710.9 eV.

Table 5.34 – Comparison of photopeak maxima of calcined La_{1-x-y}Ca_xFe_{1-x}Cu_xO₃ (x = 0, 0.2; y = 0, 0.2; CCM) and La_{1-y}Fe_{1-x}Cu_xO₃ (x = 0, 0.17, 0.2; y = 0, 0.33; CCM).

nominal composition	B. E. (eV)					at. %	
	La 3d _{5/2}	Ca 2p _{3/2}	Fe 2p _{3/2}	Cu 2p _{3/2}	O 1s	O _{lattice} ^a	C _{CO₃²⁻} ^b
LaFeO ₃	834.3	-	710.8	-	529.5	55	13
La _{0.8} FeO ₃	834.3	-	710.4	-	529.7	67	14
La _{0.8} Ca _{0.2} Fe _{0.8} Cu _{0.2} O ₃	833.6	346.8	710.2	933.1	528.8	48	14
La _{0.6} Ca _{0.2} Fe _{0.8} Cu _{0.2} O ₃	833.9	346.0	710.1	933.4	529.2	56	27
La _{0.67} FeO ₃	834.3	-	710.6	-	529.6	34	14
LaFe _{0.8} Cu _{0.2} O ₃	833.9	-	710.1	933.2	528.9	47	20
La _{0.67} Fe _{0.83} Cu _{0.17} O ₃	834.5	-	710.9	933.1	530.0	65	17

^a O_{lattice} + O_{ads} = 1.

^b C_{CO₃²⁻} + C_{adventitious} = 1.

Comparing the Ca 2p_{3/2} photopeak maxima of La_{0.6}Ca_{0.2}Fe_{0.8}Cu_{0.2}O₃ and the corresponding sample prepared with stoichiometric La amount, a shift to lower B. E. is observed (Fig. 5.44, Table 5.34). Apart from the mentioned shift, no significant differences due to the lowered La-content are observed.

The photopeak maxima of Cu 2p_{3/2} of all the studied perovskites are similar (933.1 to 933.4 eV). However, concerning their photopeaks (Fig. 5.44), significant differences are observed. Whereas La_{0.6}Ca_{0.2}Fe_{0.8}Cu_{0.2}O₃ shows the intense characteristic satellites of Cu²⁺ just as La_{0.8}Ca_{0.2}Fe_{0.8}Cu_{0.2}O₃ and LaFe_{0.8}Cu_{0.2}O₃, La_{0.67}Fe_{0.83}Cu_{0.17}O₃ only shows satellites in very low intensity. Therefore, even though the predominance of Cu²⁺ species already observed for the other samples is confirmed for this solid by spectral decomposition, a significant contribution of Cu⁺ species of 39 at.% at the surface is estimated. This phenomenon may be explained by a partial reduction under irradiation of a segregated CuO phase as suggested by H₂-TPR results (Section 5.5.2). Assuming that the contribution of Cu⁺ species at the surface corresponded to the bulk contribution of a segregated CuO phase, an estimate of 2.7 wt.% CuO would be present in the La_{0.67}Fe_{0.83}Cu_{0.17}O₃ sample. On the other hand, a distinct satellite is observed for the La_{0.6}Ca_{0.2}Fe_{0.8}Cu_{0.2}O₃ solid for which only 1 at.% of the total Cu 2p_{3/2} signal can be attributed to Cu⁺ based on spectral decomposition of the Cu

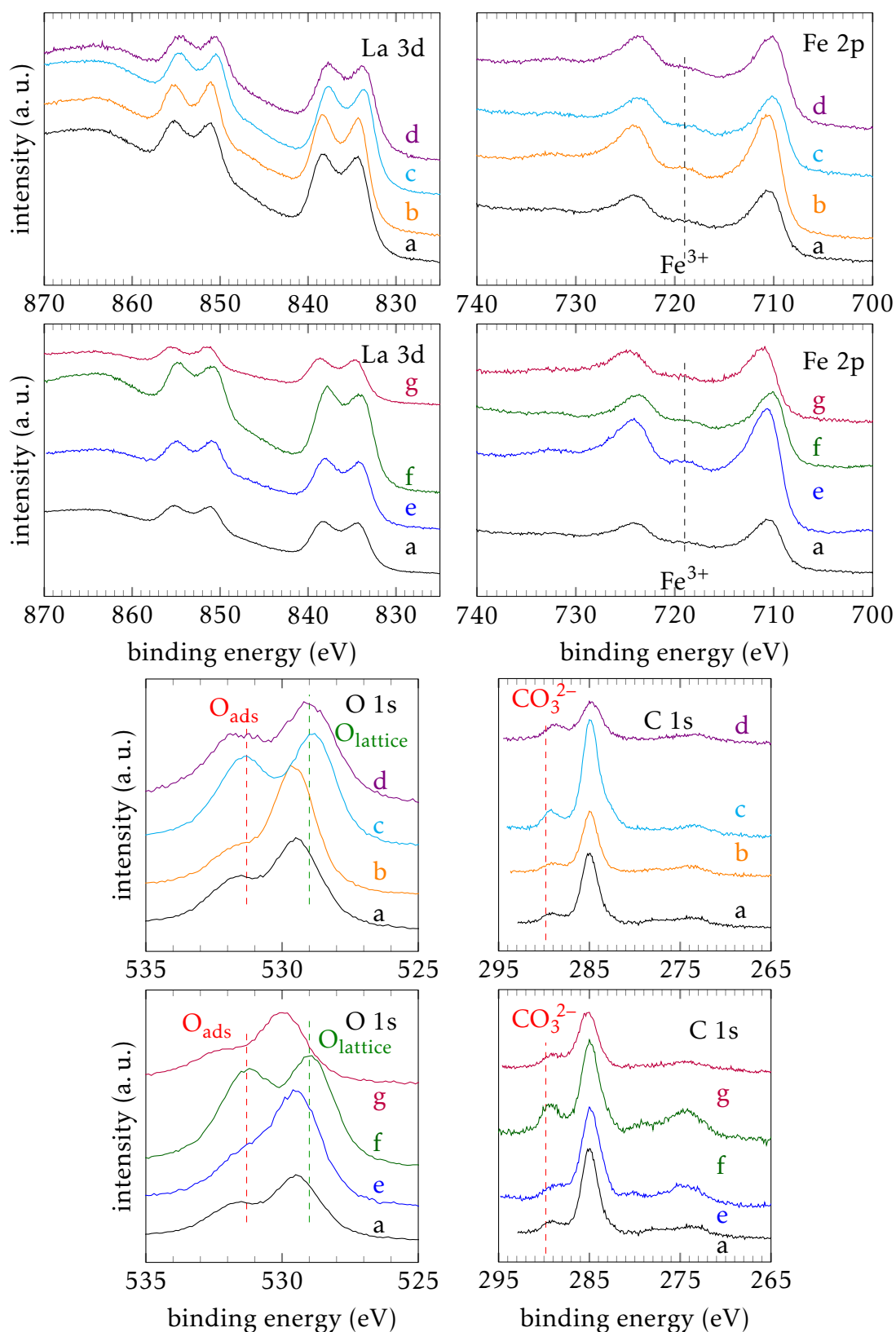


Figure 5.43 – La 3d, Fe 2p, O 1s and C 1s photopeaks of calcined $\text{La}_{1-x-y}\text{Ca}_x\text{Fe}_{1-x}\text{Cu}_x\text{O}_3$ ($x = 0, 0.2$; $y = 0, 0.2$; CCM) and $\text{La}_{1-y}\text{Fe}_{1-x}\text{Cu}_x\text{O}_3$ ($x = 0, 0.17, 0.2$; $y = 0, 0.33$; CCM). LaFeO_3 (a), $\text{La}_{0.8}\text{FeO}_3$ (b), $\text{La}_{0.8}\text{Ca}_{0.2}\text{Fe}_{0.8}\text{Cu}_{0.2}\text{O}_3$ (c), $\text{La}_{0.6}\text{Ca}_{0.2}\text{Fe}_{0.8}\text{Cu}_{0.2}\text{O}_3$ (d), $\text{La}_{0.67}\text{FeO}_3$ (e), $\text{LaFe}_{0.8}\text{Cu}_{0.2}\text{O}_3$ (f), $\text{La}_{0.67}\text{Fe}_{0.83}\text{Cu}_{0.17}\text{O}_3$ (g)

2p_{3/2} photopeak in line with the less pronounced changes compared to La_{0.67}Fe_{0.83}Cu_{0.17}O₃ with respect to their H₂-TPR profiles.

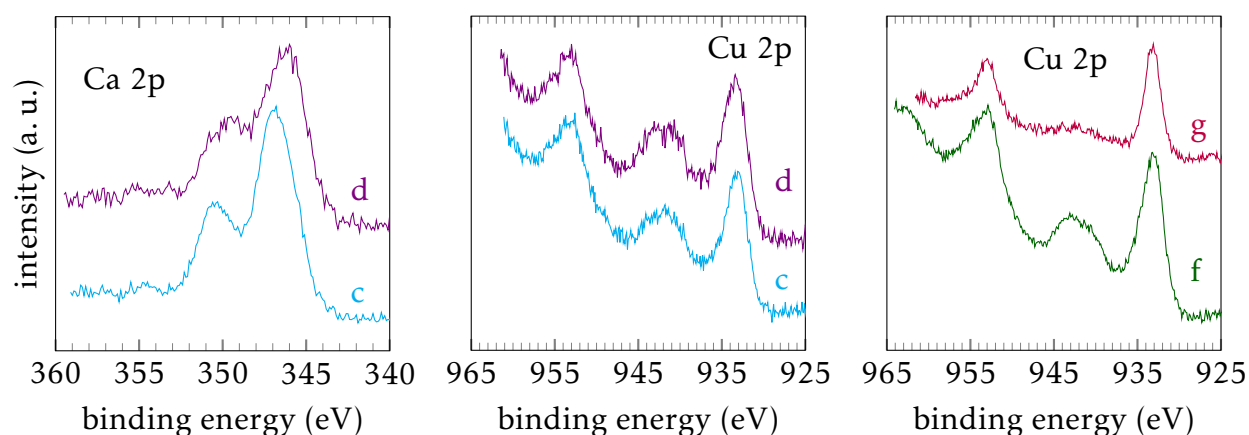


Figure 5.44 – Ca 2p and Cu 2p photopeaks of calcined La_{1-x-y}Ca_xFe_{1-x}Cu_xO₃ (x = 0.2; y = 0, 0.2; CCM) and La_{1-y}Fe_{1-x}Cu_xO₃ (x = 0, 0.17, 0.2; y = 0, 0.33; CCM). La_{0.8}Ca_{0.2}Fe_{0.8}Cu_{0.2}O₃ (c), La_{0.6}Ca_{0.2}Fe_{0.8}Cu_{0.2}O₃ (d), LaFe_{0.8}Cu_{0.2}O₃ (f), La_{0.67}Fe_{0.83}Cu_{0.17}O₃ (g)

The apparent maxima of the O 1s photopeaks, as reported in Table 5.34, generally slightly increase in B. E. for samples with purposely lowered La-content and are significantly decreased for the substituted samples compared to LaFeO₃. As can be seen from Fig. 5.43, a decrease in the contribution of adsorbed oxygen species (O_{ads}: 44 at.%) is detected for La_{0.6}Ca_{0.2}Fe_{0.8}Cu_{0.2}O₃ compared to the corresponding “stoichiometric” sample (Table 5.34). Similar results are obtained for the La_{0.67}Fe_{0.83}Cu_{0.17}O₃ solid (O_{ads}: 35 at.%). Especially, compared to LaFe_{0.8}Cu_{0.2}O₃ the tendency observed that more O_{ads} is found for higher Cu substitution is clearly reversed by the lower La-content. Equally, a lower carbonate contribution to C 1s is observed contrarily to the La_{0.6}Ca_{0.2}Fe_{0.8}Cu_{0.2}O₃ solid as can be seen in Fig. 5.43. The latter shows a considerably higher carbonate contribution of 27 at.%.

The lower contributions of adsorbed surface species are in agreement with the relatively low amounts of oxygen and carbon as seen in the surface compositions (Table 5.35).

Table 5.35 – Surface atomic ratios x_A/x_B , x_{Cu}/x_{Fe} and x_{Ca}/x_{La} of calcined La_{1-x-y}Ca_xFe_{1-x}Cu_xO₃ (x = 0, 0.2; y = 0, 0.2; CCM) and La_{1-y}Fe_{1-x}Cu_xO₃ (x = 0, 0.17, 0.2; y = 0, 0.33; CCM).

nominal composition	x_A/x_B	x_{Cu}/x_{Fe}	x_{Ca}/x_{La}	surface composition based on nominal Fe content
LaFeO ₃	2.13	-	-	La _{2.13} FeO _{4.63} (C _{3.66})
La _{0.8} Ca _{0.2} Fe _{0.8} Cu _{0.2} O ₃	1.65	0.34	0.34	La _{1.32} Ca _{0.45} Fe _{0.80} Cu _{0.27} O _{4.62} (C _{4.06})
La _{0.8} FeO ₃	1.31	-	-	La _{1.31} FeO _{2.70} (C _{1.48})
La _{0.6} Ca _{0.2} Fe _{0.8} Cu _{0.2} O ₃	1.27	0.35	0.33	La _{0.62} Ca _{0.20} Fe _{0.73} Cu _{0.17} O _{1.92} (C _{0.86})
LaFe _{0.8} Cu _{0.2} FeO ₃	1.82	0.39	-	La _{1.62} Fe _{0.80} Cu _{0.24} O _{4.53} (C _{2.61})
La _{0.67} FeO ₃	0.88	-	-	La _{0.88} FeO _{3.08} (C _{1.84})
La _{0.67} Fe _{0.83} Cu _{0.17} O ₃	1.03	0.22	-	La _{1.05} Fe _{0.83} Cu _{0.18} O _{2.42} (C _{1.50})

As can be seen from Table 5.35, the La_{0.6}Ca_{0.2}Fe_{0.8}Cu_{0.2}O₃ solid shows a clearly decreased A-site excess at the surface compared to the sample prepared without lower La-content.

However, the atomic A to B ratio is still beyond a surface stoichiometry between A- and B-site cations. Ca enrichment with respect to La is only observed for the “stoichiometric” $\text{La}_{0.8}\text{Ca}_{0.2}\text{Fe}_{0.8}\text{Cu}_{0.2}\text{O}_3$ sample, whereas the value obtained for $\text{La}_{0.6}\text{Ca}_{0.2}\text{Fe}_{0.8}\text{Cu}_{0.2}\text{O}_3$ complies with the theoretical one of 0.33.

On the other hand, the $\text{La}_{0.67}\text{Fe}_{0.83}\text{Cu}_{0.17}\text{O}_3$ sample presents a marked decrease of A-site excess – to the point that surface stoichiometry between La and B-site cations is achieved at the surface. This is assumed to be due to the even lower La-content of the solid. Surprisingly, a lower Cu enrichment at the surface is observed for the $\text{La}_{0.67}\text{Fe}_{0.83}\text{Cu}_{0.17}\text{O}_3$ solid comparing the obtained value of the atomic Cu/Fe ratio of 0.22 to the theoretical one of 0.20. Surface Cu enrichment therefore seems to be attenuated by the lowered La-content compared to the $\text{LaFe}_{0.8}\text{Cu}_{0.2}\text{FeO}_3$ sample for which $x_{\text{Cu}}/x_{\text{Fe}} = 0.39$ instead of 0.25.

5.5.5 Catalytic activity

The catalytic activity was evaluated according to Procedure A (Section 2.3). Conversion profiles are reported in Fig. 5.45 and 5.46, complementary results in Table 5.36 and in Appendix D (Table D.5).

Table 5.36 – Temperatures corresponding to 50 % conversion of CO, C_3H_6 , C_3H_8 , and H_2 (stoichiometric) and NO (rich composition) of $\text{La}_{1-x-y}\text{Ca}_x\text{Fe}_{1-x}\text{Cu}_y\text{O}_3$ ($x = 0, 0.2$; $y = 0, 0.2$; CCM) and $\text{La}_{1-y}\text{Fe}_{1-x}\text{Cu}_x\text{O}_3$ ($x = 0, 0.17, 0.2$; $y = 0, 0.33$; CCM) catalysts and selectivities of NO reduction products at T_S .

condition	stoichiometric				rich				
	T_{50} (°C)				selectivities at T_S				
	CO	C_3H_6	C_3H_8	H_2	NO	S_{N_2}	S_{NH_3}	$S_{\text{N}_2\text{O}}$	T_S (°C)
LaFeO_3	438	463	478	501	^a	0.05	0.95	0	507
$\text{La}_{0.8}\text{FeO}_3$	398	431	499	433	488	0.02	0.98	0	501
$\text{La}_{0.8}\text{Ca}_{0.2}\text{Fe}_{0.8}\text{Cu}_{0.2}\text{O}_3$	279	449	487	399	469	0.36	0.64	0	506
$\text{La}_{0.6}\text{Ca}_{0.2}\text{Fe}_{0.8}\text{Cu}_{0.2}\text{O}_3$	311	444	465	407	477	0.54	0.45	0.01	487
$\text{La}_{0.67}\text{FeO}_3$	384	420	497	471	479	0.03	0.97	0	506
$\text{LaFe}_{0.8}\text{Cu}_{0.2}\text{O}_3$	294	497	505 ^b	421	501 ^b	0.94	0	0.06	513
$\text{La}_{0.67}\text{Fe}_{0.83}\text{Cu}_{0.17}\text{O}_3$	232	386	458 ^b	344	438	0.32	0.68	0	491

^a Conversion lower than 50 %.

^b T_{25} .

The comparison between $\text{La}_{0.67}\text{Fe}_{0.83}\text{Cu}_{0.17}\text{O}_3$ and the reference noble metal-based catalyst shows for the first time comparable performances for CO conversion and even better ones under rich conditions with a complete conversion of CO above 350 °C whereas the maximum observed on the commercial TWC is below 85 %. Based on the temperature at half-conversion the following classification can be established: $\text{La}_{0.67}\text{Fe}_{0.83}\text{Cu}_{0.17}\text{O}_3 > \text{La}_{0.8}\text{Ca}_{0.2}\text{Fe}_{0.8}\text{Cu}_{0.2}\text{O}_3 > \text{La}_{0.6}\text{Ca}_{0.2}\text{Fe}_{0.8}\text{Cu}_{0.2}\text{O}_3 > \text{LaFe}_{0.8}\text{Cu}_{0.2}\text{O}_3 > \text{La}_{0.67}\text{FeO}_3 \approx \text{La}_{0.8}\text{FeO}_3$. This comparison reveals that Ca addition can have a promoting effect on the catalytic activity in CO oxidation. However, it is also worth to note that the most active catalyst does not contain Ca. Clearly, non-stoichiometry can also be considered as an important factor inducing a beneficial effect on the catalytic activity. However, the most prominent observation is likely related to the rate

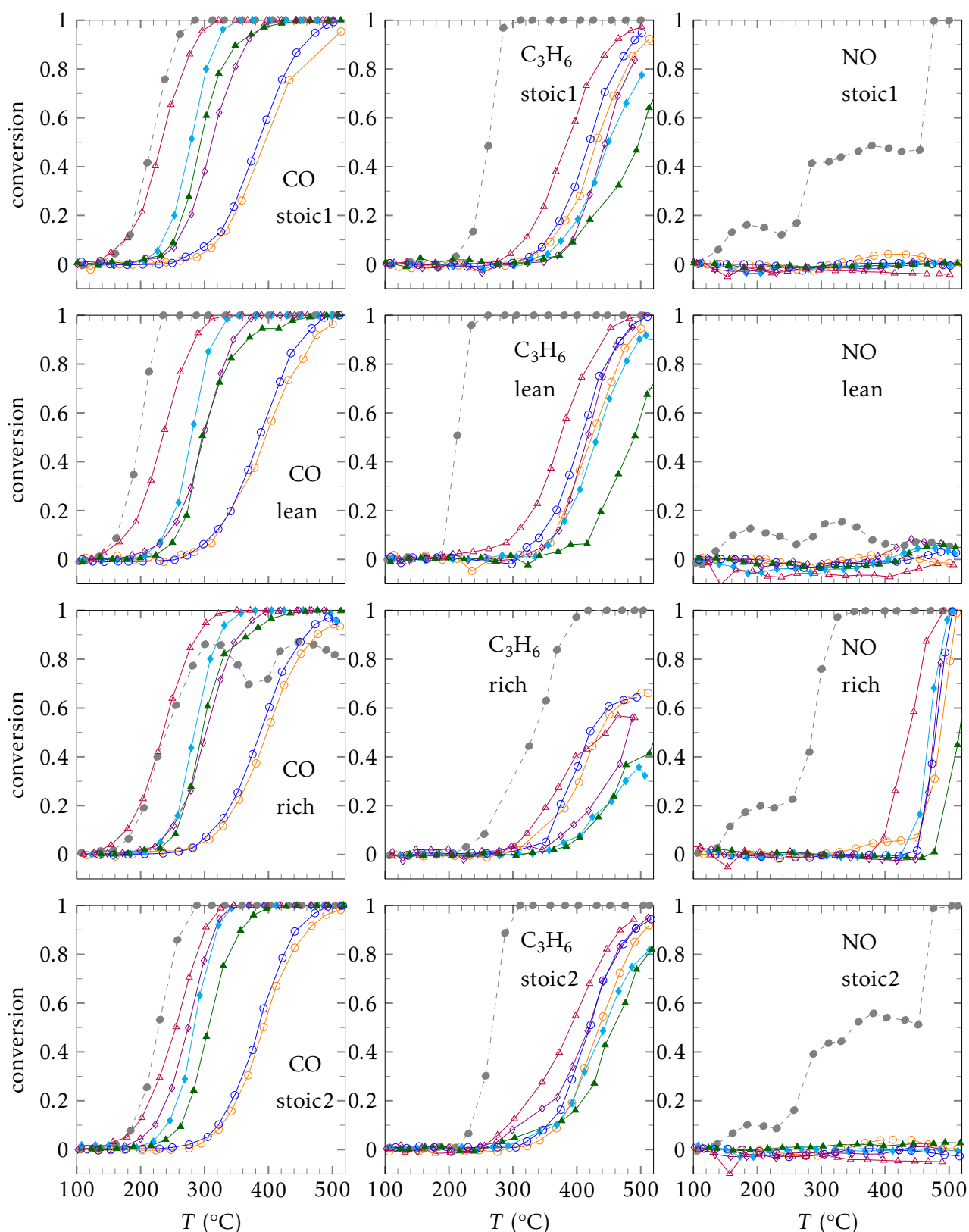


Figure 5.45 – CO, C₃H₆ and NO conversions of La_{1-x-y}Ca_xFe_{1-x}Cu_yO₃ (x = 0, 0.2; y = 0, 0.2; CCM) and La_{1-y}Fe_{1-x}Cu_xO₃ (x = 0, 0.17, 0.2; y = 0, 0.33; CCM) catalysts (Procedure A). La_{0.8}FeO₃ (○), and La_{0.67}FeO₃ (◐), LaFe_{0.8}Cu_{0.2}O₃ (▲), La_{0.8}Ca_{0.2}Fe_{0.8}Cu_{0.2}O₃ (◆), La_{0.6}Ca_{0.2}Fe_{0.8}Cu_{0.2}O₃ (◇), and La_{0.67}Fe_{0.83}Cu_{0.17}O₃ (△) compared to the commercial reference TWC (●)

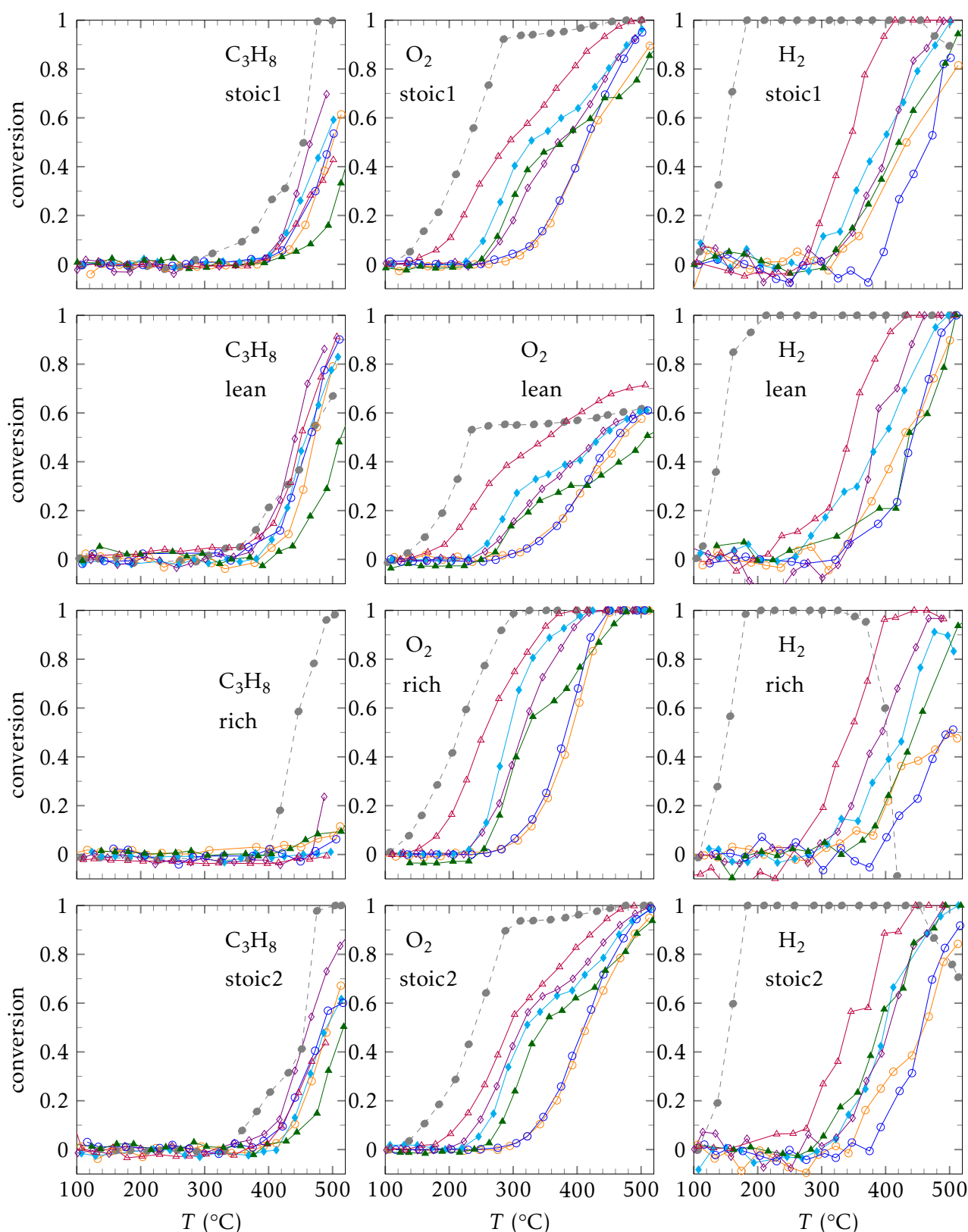


Figure 5.46 – CO, C₃H₆ and NO conversions of La_{1-x-y}Ca_xFe_{1-x}Cu_yO₃ (x = 0, 0.2; y = 0, 0.2; CCM) and La_{1-y}Fe_{1-x}Cu_xO₃ (x = 0, 0.17, 0.2; y = 0, 0.33; CCM) catalysts (Procedure A). La_{0.8}FeO₃ (○), and La_{0.67}FeO₃ (◐), LaFe_{0.8}Cu_{0.2}O₃ (▲), La_{0.8}Ca_{0.2}Fe_{0.8}Cu_{0.2}O₃ (◆), La_{0.6}Ca_{0.2}Fe_{0.8}Cu_{0.2}O₃ (◇), and La_{0.67}Fe_{0.83}Cu_{0.17}O₃ (△) compared to the commercial reference TWC (•)

enhancement in CO conversion induced by Cu addition in conjunction with La-deficiency in the solid. A different behaviour from the commercial reference catalyst's under rich conditions for CO conversion is observed for most of the perovskite-based catalysts. The observation of two ranges of CO conversion on PGM previously explained by the occurrence of light hydrocarbon reforming and water-gas shift reaction (WGS) is generally not observed. The involvement of both reactions can easily explain the sharp drop in H₂ conversion on the noble metal containing commercial reference (Fig. 5.46). The absence of similar observations on perovskite-based catalysts suggests that the relative rates of these reactions under rich conditions are much slower than that of the oxidation of CO to CO₂. This may reflect the presence of a more active segregated phase formed during the activation of the catalyst, especially on the La-deficient La_{0.67}Fe_{0.83}Cu_{0.17}O₃ sample, as well as an improvement in the OSC properties due to improved redox properties. As a general trend, further addition of Ca and Cu enhances the oxidative properties of the perovskite solids. As seen, propane conversion occurs slightly more readily on Ca- and Cu-modified samples than on the commercial reference. This is also true for the reductive properties but only under rich conditions with a shift of the light-off curves for NO conversion to lower temperatures. Unfortunately, ammonia remains the main conversion product except on the stoichiometric La_{0.8}Ca_{0.2}Fe_{0.8}Cu_{0.2}O₃ sample (Fig. 5.47). Likewise, no significant conversion of NO is detected under lean and stoichiometric conditions compared to the commercial reference containing PGM. Again the examination of the selectivity at 100 % NO conversion on La_{0.67}Fe_{0.83}Cu_{0.17}O₃ highlights the best compromise with selectivities towards N₂ and NH₃ of respectively 0.32 and 0.68.

Kinetic data obtained from the exploitation of conversion profiles is reported in Table 5.37. Particular attention was paid to the oxidation of CO and propylene into CO₂ and H₂O. Rate values were roughly estimated for low conversions. Pre-exponential and apparent activation energy values were estimated by linear regression from the Arrhenius plot $\ln k$ vs. $1/T$. The same observations as those previously discussed are observed regarding the beneficial effect of Cu and Ca on the rate of CO conversion. Indeed, the parent stoichiometric and non-stoichiometric LaFeO₃-based samples are inactive at 200 °C compared to the Ca- and Cu-modified samples. The specific rate calculated on La_{0.67}Fe_{0.83}Cu_{0.17}O₃ is one order of magnitude higher than the estimates obtained on the other samples emphasising the remarkable effect of non-stoichiometry combined with Cu addition. Fe is inactive for the CO/O₂ reaction at the selected temperature of 200 °C. As a general trend, such an improvement in activity can be correlated to a significant lowering of the apparent activation energy.

Regarding the catalytic properties towards propylene conversion, it is obvious that the rate of propylene oxidation does not seem sensitive to Ca- and Cu-substitution. There is no clear correlation neither on the specific rates nor on the apparent activation energies. Moreover, contrarily to the CO/O₂ reaction, Fe is active for propylene conversion. An additional important information is associated to the role played by La-deficient catalysts with the highest activity recorded on La_{0.8}FeO₃, La_{0.67}FeO₃ and La_{0.67}Fe_{0.83}Cu_{0.17}O₃. Finally, it is obvious that no significant correlation can be established with changes in specific surface areas for both reactions emphasising the fact that the catalytic activity is mostly governed by the surface composition with the possible formation of defective sites or Cu or Fe segregation under reaction conditions, especially under rich conditions as suggested by H₂-TPR experiments and catalytic tests.

Table 5.37 also reports kinetic data estimated after successive ramps under lean and rich conditions (stoic2). As exemplified in this Table, significant changes are discernible which can be induced by surface changes taking place during the temperature cycle under rich conditions. The following tendencies appear: (i) a stable activity in stoichiometric condi-

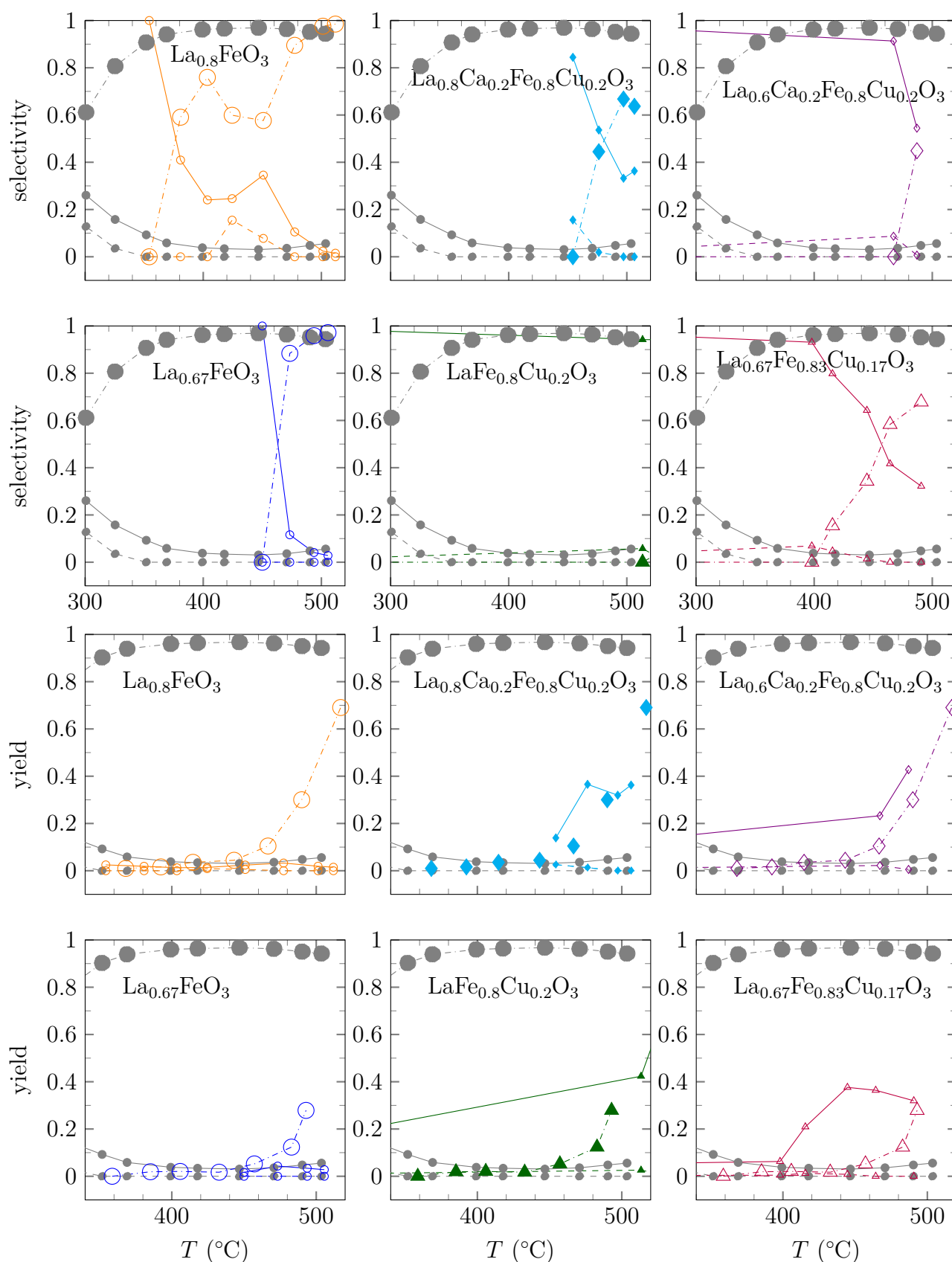


Figure 5.47 – N_2 , N_2O and NH_3 selectivities and yields of NO conversion of $\text{La}_{1-x}\text{Ca}_x\text{Fe}_{1-x}\text{Cu}_x\text{O}_3$ catalysts ($x=0.1, 0.2$; CCM) under rich conditions. $\text{La}_{0.8}\text{FeO}_3$ (\circ), and $\text{La}_{0.67}\text{FeO}_3$ (\diamond), $\text{LaFe}_{0.8}\text{Cu}_{0.2}\text{O}_3$ (\blacktriangle), $\text{La}_{0.8}\text{Ca}_{0.2}\text{Fe}_{0.8}\text{Cu}_{0.2}\text{O}_3$ (\blacklozenge), $\text{La}_{0.6}\text{Ca}_{0.2}\text{Fe}_{0.8}\text{Cu}_{0.2}\text{O}_3$ (\blacklozenge), and $\text{La}_{0.67}\text{Fe}_{0.83}\text{Cu}_{0.17}\text{O}_3$ (\blacktriangle) compared to the commercial reference TWC (\bullet); $S_{\text{N}_2}/Y_{\text{N}_2}$ (solid), $S_{\text{N}_2\text{O}}/Y_{\text{N}_2\text{O}}$ (dashed), $S_{\text{NH}_3}/Y_{\text{NH}_3}$ (dashdotted, big mark)

Table 5.37 – Comparison of specific reaction rates r_{specific} , apparent activation energies $E_{A,\text{app}}$ and pre-exponential factors A of CO and C₃H₆ oxidation for La_{1-x-y}Ca_xFe_{1-x}Cu_xO₃ (x = 0, 0.2; y = 0, 0.2; CCM) and La_{1-y}Fe_{1-x}Cu_xO₃ (x = 0, 0.17, 0.2; y = 0, 0.33; CCM) catalysts (x = 0, 0.1, 0.2). Arrhenius parameters were determined by Arrhenius plots (Fig. D.7).

	SSA (m ² g ⁻¹)	r_{specific}^a (mol s ⁻¹ g ⁻¹)		$E_{A,\text{app}}$ (kJ mol ⁻¹)		A (10 ³ m ³ s ⁻¹ g ⁻¹)	
		CO	C ₃ H ₆	CO	C ₃ H ₆	CO	C ₃ H ₆
stoichiometric - initial test (stoic1)							
LaFeO ₃	13.9	≈ 0	2.5 · 10 ⁻⁹	142	128	424	15.2
La _{0.8} FeO ₃	17.6	≈ 0	10.4 · 10 ⁻⁹	101	111	1.2	2.5
La _{0.8} Ca _{0.2} Fe _{0.8} Cu _{0.2} O ₃	24.0	0.4 · 10 ⁻⁷	5.5 · 10 ⁻⁹	115	107	896	0.7
La _{0.6} Ca _{0.2} Fe _{0.8} Cu _{0.2} O ₃	26.4	0.5 · 10 ⁻⁷	1.7 · 10 ⁻⁹	100	172	11.5	56395
La _{0.67} FeO ₃	21.5	≈ 0	12.3 · 10 ⁻⁹	81	119	0.03	12.7
LaFe _{0.8} Cu _{0.2} O ₃	13.8	0.5 · 10 ⁻⁷	3.7 · 10 ⁻⁹	112	103	217	0.1
La _{0.67} Fe _{0.83} Cu _{0.17} O ₃	26.5	5.4 · 10 ⁻⁷	31.5 · 10 ^{-9^b}	59	142	11.6	5925
stoichiometric - return test (stoic2)							
LaFeO ₃	13.9	≈ 0	≈ 0	129	136	34.8	62.8
La _{0.8} FeO ₃	17.6	≈ 0	1.5 · 10 ⁻⁹	118	115	31.9	3.4
La _{0.8} Ca _{0.2} Fe _{0.8} Cu _{0.2} O ₃	24.0	0.4 · 10 ⁻⁷	3.9 · 10 ⁻⁹	103	107	42.5	0.9
La _{0.6} Ca _{0.2} Fe _{0.8} Cu _{0.2} O ₃	26.4	1.3 · 10 ⁻⁷	12.6 · 10 ⁻⁹	80	65	0.5	0.0008
La _{0.67} FeO ₃	21.5	≈ 0	1.4 · 10 ⁻⁹	93	105	0.3	0.9
LaFe _{0.8} Cu _{0.2} O ₃	13.8	0.4 · 10 ⁻⁷	7.3 · 10 ⁻⁹	106	83	40.9	0.01
La _{0.67} Fe _{0.83} Cu _{0.17} O ₃	26.5	3.5 · 10 ⁻⁷	18.0 · 10 ⁻⁹	82	67	1.4	0.003

^a Unless specified otherwise r_{specific} were calculated from conversions at 200 °C (CO) and for C₃H₆ at 350 °C (1st test run) and 300 °C (return test).

^b At 300 °C the corresponding r_{specific} equals 8.2 · 10⁻⁹ mol s⁻¹ g⁻¹.

tions and a loss of activity on La-deficient samples in the CO/O₂ reaction correlated to an increase in $E_{A,\text{app}}$ and (ii) a loss of conversion in propylene oxidation on all samples except for La_{0.6}Ca_{0.2}Fe_{0.8}Cu_{0.2}O₃. Again, this observation seems mainly related to changes in the apparent activation energy shifting from 172 kJ mol⁻¹ to 65 kJ mol⁻¹ on La_{0.6}Ca_{0.2}Fe_{0.8}Cu_{0.2}O₃. Anyway, it is obvious that iron exhibits an intrinsic activity for propylene conversion. However, the coexistence of defective sites can probably explain the improvement observed on the rate values. However, one cannot rule out that an extensive formation of defective sites locally destabilises the surface structure inducing migration and aggregation of inactive Fe species as previously shown. Regarding this latter point, Ca incorporation seems to play the role of a stabiliser because no significant hematite segregation was observed for the La_{0.6}Ca_{0.2}Fe_{0.8}Cu_{0.2}O₃ solid by H₂-TPR. At the same time the comparison of the specific reaction rate and $E_{A,\text{app}}$ values does not reveal significant changes between the initial (stoic1) and the return test (stoic2).

5.5.6 Conclusion

This Section was dedicated to the influence of combined approaches consisting in substituting the A- and B- sites of a parent LaFeO_3 structure and optimising the extent of La-deficiency in the solid. Previous results reported in this Chapter showed a rate enhancement through an increase in the density of Fe sites at the surface. It was found that the substitution in the B-site is essential for developing the catalytic performance rather than substitution in the A-site since Ca incorporation has quasi no effect on the rate of oxidative and reductive reactions. On the other hand, Cu incorporation promotes both the activity and the selectivity of NO conversion towards nitrogen as well as CO oxidation. Based on this, significant improvements can still be obtained by optimising both factors. This is particularly true for the $\text{La}_{0.67}\text{Fe}_{0.83}\text{Cu}_{0.17}\text{O}_3$ solid. Again, it is interesting to note that this catalyst is the most active towards CO, propylene and NO conversion especially under rich conditions but not the most stable. As a matter of fact, the stoichiometric $\text{La}_{0.8}\text{Ca}_{0.2}\text{Fe}_{0.8}\text{Cu}_{0.2}\text{O}_3$ sample seems to be the most stable with regard to only slight changes observed on the kinetic parameters between the initial and the return catalytic test ramps and it can be speculated that it would likely have a longer lifetime than $\text{La}_{0.67}\text{Fe}_{0.83}\text{Cu}_{0.17}\text{O}_3$. At that time, however, we have no isotherm measurements during a significant period of time which could confirm this statement. On the other hand, physico-chemical characterisation clearly evidenced that La-deficient samples are unstable at rather low temperature under reductive atmosphere as shown during H_2 -TPR experiments. By way of illustration, partial extraction of isolated oxidic Fe species from the perovskite structure, segregating into more reducible α - Fe_2O_3 aggregates was observed on $\text{La}_{1-y}\text{FeO}_3$ ($y = 0.1, 0.2, 0.33$). It is noticeable that this process is strongly attenuated in the Ca-substituted sample, i. e. the La-deficient $\text{La}_{0.6}\text{Ca}_{0.2}\text{Fe}_{0.8}\text{Cu}_{0.2}\text{O}_3$ solid. On the other hand, the H_2 -TPR profile recorded on $\text{La}_{0.67}\text{Fe}_{0.83}\text{Cu}_{0.17}\text{O}_3$ reveals significant segregation processes. Indeed, a high temperature H_2 uptake was ascribed to the reduction of α - Fe_2O_3 and a lower temperature one to the reduction of Cu species. However, the 2 reduction peaks located at 182 °C and 227 °C observed for $\text{La}_{0.67}\text{Fe}_{0.83}\text{Cu}_{0.17}\text{O}_3$ cannot be simply related to a 2-step reduction process of single isolated Cu^{2+} species inside the perovskite structure but may reflect the presence of more reducible oxidic Cu species extracted from the perovskite structure and segregating into CuO clusters according to the same process as described for α - Fe_2O_3 . XPS analysis results seem consistent with this latter assumption with the observation of a strong attenuation of the satellite shake-up structure characteristic of Cu^{2+} . Hence, under irradiation segregated CuO could be partially reduced to Cu^+ or metallic Cu^0 species. All these observations – even if they have been obtained in different atmospheres than those corresponding to rich conditions during catalytic testing – may have to be considered, especially to explain the highest activity observed in CO oxidation and also in NO reduction for $\text{La}_{0.67}\text{Fe}_{0.83}\text{Cu}_{0.17}\text{O}_3$. These surface modifications, especially the possible stabilisation of metallic species, can also influence the NO conversion selectivity as suggested by the comparison between $\text{La}_{0.67}\text{Fe}_{0.83}\text{Cu}_{0.17}\text{O}_3$ and $\text{La}_{0.6}\text{Ca}_{0.2}\text{Fe}_{0.8}\text{Cu}_{0.2}\text{O}_3$, the latter developing a higher selectivity towards the production of nitrogen.

5.6 Conclusion

In this Chapter, 2 different composition optimisation approaches for Fe-based perovskites were investigated. The first approach followed aimed at increasing the Fe accessibility on the surface of the solid. The high surface La excess was successfully reduced by decreasing the La-content during synthesis. The increased accessibility of the active Fe^{3+} sites of

the perovskite as a consequence of surface composition optimisation ($\text{La}_{1-y}\text{FeO}_3$) leads to markedly enhanced catalytic activities and performances. Estimations of the specific reaction rates and the Arrhenius parameters confirmed that the increased performance is not caused by the higher specific surface areas. They also revealed that CO and propylene oxidation proceed on different sites. A well dispersed hematite phase with strong interactions with the perovskite, as formed by this in situ synthesis, is assumed to play a key role for the enhanced catalytic activity.

The second approach consisted in the gentle destabilisation of the perovskite structure promoting defects such as anionic vacancies but retaining the stability of the catalysts. Partial substitution of LaFeO_3 perovskites was investigated substituting in the A-site by Ca, in the B-site by Cu and combining both substitution approaches. All substituted perovskites retained the orthorhombic LaFeO_3 structure without any detectable crystalline phase segregation. However, all solids show a unit cell contraction as a consequence of charge destabilisation leading to the generation of oxygen vacancies and to a lesser extent the partial oxidation of trivalent Fe. The reducibility of the perovskite was increased by substitution, especially for the Cu-substituted samples.

All these physicochemical properties lead to generally increased catalytic activity. Ca-substitution showed a lower impact than Cu-substitution but proved promoting in the combination with Cu-substitution. As for the surface composition optimisation, CO oxidation seems to profit most of the bulk composition optimisation approach. NO reduction performance was mainly increased by the incorporation of Cu into the perovskite structure. In parallel, S_{N_2} was increased to yield N_2 as the main reduction product. Combining Ca- and Cu-substitution lead to a further increase in NO conversion, unfortunately linked to slightly lower N_2 selectivity.

Finally, the combination of both approaches lead to preliminarily optimised catalyst compositions. Both solids, $\text{La}_{0.6}\text{Ca}_{0.2}\text{Fe}_{0.8}\text{Cu}_{0.2}\text{O}_3$ and $\text{La}_{0.67}\text{Fe}_{0.83}\text{Cu}_{0.17}\text{O}_3$, retained the orthorhombic LaFeO_3 perovskite structure as evidenced by XRD. Their specific surface areas of $26 \text{ m}^2 \text{ g}^{-1}$ correspond to the highest of all substituted samples. XPS measurements confirmed the lowered A-site excess at the surface for both solids, even reaching A- to B-site stoichiometry for the $\text{La}_{0.67}\text{Fe}_{0.83}\text{Cu}_{0.17}\text{O}_3$ solid. H_2 -TPR measurements revealed a lower hematite segregation than expected for both solids. This is most marked for the $\text{La}_{0.6}\text{Ca}_{0.2}\text{Fe}_{0.8}\text{Cu}_{0.2}\text{O}_3$ solid. At the same time, the presence of Cu^{2+} species outside the perovskite lattice was suggested by a distinct additional reduction peak at lower temperature. XPS affirmed this hypothesis for the $\text{La}_{0.67}\text{Fe}_{0.83}\text{Cu}_{0.17}\text{O}_3$ solid showing a marked decrease in intensity for the Cu 2p satellite which is ascribed to the presence of highly reducible Cu^{2+} species on the surface of the perovskite, reducible by the irradiation. It was therefore concluded that Cu segregation is favoured compared to Fe for La-deficient solids, especially in the presence of Ca.

Combining the aforementioned composition optimisation approaches lead to significantly enhanced catalytic activities. The increase in NO conversion lead to a reduced N_2 selectivity for the $\text{La}_{0.67}\text{Fe}_{0.83}\text{Cu}_{0.17}\text{O}_3$ catalyst (main product: NH_3), whereas it is increased for the $\text{La}_{0.6}\text{Ca}_{0.2}\text{Fe}_{0.8}\text{Cu}_{0.2}\text{O}_3$ solid (main product: N_2) compared to the corresponding substituted solids in agreement with the predominant segregated phases. Again, catalytic activities of CO and propylene oxidation were found not to follow the same trends, which is in concert with their supposed proceeding on different sites. CO oxidation activity seems to be more affected by the combined composition optimisation whereas Fe shows a high intrinsic activity towards propylene conversion which is not much affected by composition optimisation. Furthermore, deactivation phenomena were observed for the $\text{La}_{0.67}\text{Fe}_{0.83}\text{Cu}_{0.17}\text{O}_3$ solid. However, even

after one test cycle it remained the most performing catalyst. On the other hand, the activity of the $\text{La}_{0.6}\text{Ca}_{0.2}\text{Fe}_{0.8}\text{Cu}_{0.2}\text{O}_3$ catalyst increased during the test cycle, making it closely follow the lead of the $\text{La}_{0.67}\text{Fe}_{0.83}\text{Cu}_{0.17}\text{O}_3$ sample in the return test.

Bibliography

- [1] Z.-X. Wei, Y.-Q. Xu, H.-Y. Liu, C.-W. Hu, *Journal of Hazardous Materials* **2009**, 165 (1-3), 1056–1061.
- [2] A. Eyssler, A. Winkler, P. Mandaliev, P. Hug, A. Weidenkaff, D. Ferri, *Applied Catalysis B: Environmental* **2011**, 106, 494–502.
- [3] J.-P. Dacquain, C. Lancelot, C. Dujardin, C. Cordier-Robert, P. Granger, *Journal of Physical Chemistry C* **2011**, 115 (5), 1911–1921.
- [4] J.-M. Giraudon, A. Elhachimi, F. Wyrwalski, S. Siffert, A. Aboukaïs, J.-F. Lamonier, G. Leclercq, *Applied Catalysis B: Environmental* **2007**, 75, 157–166.
- [5] Thermo Scientific, XPS Knowledge Base, English, **2014**, <http://xpssimplified.com/periodictable.php> (visited on 2014-06-11).
- [6] D. Briggs, M. P. Seah, *Practical Surface Analysis, Vol. 1*, 2nd ed., (Ed.: J. W. Crampton), Wiley-Interscience, **1993**.
- [7] M. Popa, J. Frantti, M. Kakihana, *Solid State Ionics*, Proceedings of International Conference on Solid State Ionics, (Materials and Processes for Energy and Environment), Cairns, Australia, 8-13 July, 2001 **2002**, 154–155, 437–445.
- [8] B. P. Barbero, J. A. Gamboa, L. E. Cadús, *Applied Catalysis B: Environmental* **2006**, 65 (1-2), 21–30.
- [9] J. Andreasson, J. Holmlund, R. Rauer, M. Käll, L. Börjesson, C. Knee, A. Eriksson, S.-G. Eriksson, M. Rübhausen, R. Chaudhury, *Physical Review B* **2008**, 78, DOI 10.1103/physrevb.78.235103.
- [10] J. Bielecki, P. Svedlinth, D. T. Tibebu, S. Cai, S.-G. Eriksson, L. Börjesson, C. S. Knee, *Physical Review B* **2012**, 86, DOI 10.1103/physrevb.86.184422.
- [11] D. L. A. de Faria, S. Venâncio Silva, M. T. de Oliveira, *Journal of Raman Spectroscopy* **1997**, 28, 873–878.
- [12] J. Zieliński, I. Zglinicka, L. Znak, Z. Kaszukur, *Applied Catalysis A: General* **2010**, 381, 191–196.
- [13] A. Delmastro, D. Mazza, S. Ronchetti, M. Vallino, R. Spinicci, P. Brovotto, M. Salis, *Materials Science and Engineering: B* **2001**, 79 (2), 140–145.
- [14] G. Qi, W. Li, X. Wang, M. Shen, Chinese, *Patent Application*, US2012304624 (A1), DE102012209204 (A1) (CN, DE, US), **2011**.
- [15] M. A. Peña, J. L. G. Fierro, *Chemical Reviews* **2001**, 101 (7), 1981–2018.
- [16] R. D. Shannon, *Acta Crystallographica Section A* **1976**, 32, 751–767.
- [17] P. Ciambelli, S. Cimino, L. Lisi, M. Faticanti, G. Minelli, I. Pettiti, P. Porta, *Applied Catalysis B: Environmental* **2001**, 33 (3), 193–203.
- [18] G. Pecchi, M. G. Jiliberto, A. Buljan, E. J. Delgado, *Solid State Ionics* **2011**, 187, 27–32.
- [19] G. Pecchi, P. Reyes, R. Zamora, C. Campos, L. E. Cadús, B. P. Barbero, *Catalysis Today* **2008**, 133-135, 420–427.
- [20] S. Phokha, S. Pinitsoontorn, S. Maensiri, S. Rujirawat, *Journal of Sol-Gel Science and Technology* **2014**, 71, 333–341.

- [21] R. Zhang, H. Alamdari, S. Kaliaguine, *Journal of Catalysis* **2006**, *242*, 241–253.
- [22] T. Caronna, F. Fontana, I. N. Sora, R. Pelosato, *Materials Chemistry and Physics* **2009**, *116*, 645–648.
- [23] S. S. Chan, A. T. Bell, *Journal of Catalysis* **1984**, *89*, 433–441.
- [24] R. Zhang, H. Alamdari, S. Kaliaguine, *Applied Catalysis A: General* **2008**, *340*, 140–151.
- [25] R. Zhang, A. Villanueva, H. Alamdari, S. Kaliaguine, *Journal of Catalysis* **2006**, *237*, 368–380.
- [26] J. A. Anderson, J. L. G. Fierro, *Journal of Solid State Chemistry* **1994**, *108*, 305–313.

Fe-based perovskites doped with low loadings of Platinum Group Metals (PGM)

Partial substitution and surface composition optimisation strategies were implemented in Chapter 5. Best catalytic performances were obtained for the $\text{La}_{0.8}\text{Ca}_{0.2}\text{Fe}_{0.8}\text{Cu}_{0.2}\text{O}_3$ and $\text{La}_{0.67}\text{Fe}_{0.83}\text{Cu}_{0.17}\text{O}_3$ catalysts respectively. These promising perovskite solids were impregnated with low loadings of platinum group metals (PGM). The influence on the reducibility and the catalytic performance of the nature of the noble metal (Pd, Pt or Rh) was investigated using a loading of 0.1 wt.%. Furthermore, the influence of a reductive pretreatment instead of an activation under air and stoichiometric feed on the catalytic performance was investigated. Finally, the Rh-doped $\text{La}_{0.67}\text{Fe}_{0.83}\text{Cu}_{0.17}\text{O}_3$ catalyst was tested under modified stoichiometric conditions accounting for the generally low methane conversion and therefore adjusting the oxygen content accordingly.

6.1 Influence of the nature of the doping noble metal on $\text{La}_{0.8}\text{Ca}_{0.2}\text{Fe}_{0.8}\text{Cu}_{0.2}\text{O}_3$

It is known that different precious metals behave differently in 3-way catalytic reactions (Section 1.1.1). Therefore, the influence of the nature of doping noble metal in interaction with one of the most promising perovskites was investigated. The loading with commonly used 3-way catalyst metals Pd, Pt, Rh will be compared. To do so, 0.1 wt.% of the corresponding PGM was loaded on $\text{La}_{0.8}\text{Ca}_{0.2}\text{Fe}_{0.8}\text{Cu}_{0.2}\text{O}_3$ using an incipient wet impregnation method (IWI) technique as described in Section 2.1.

6.1.1 Physico-chemical properties

Bulk/Structural properties

Elementary analysis by inductively coupled plasma atomic emission spectroscopy (ICP) was performed for the Pd-doped $\text{La}_{0.8}\text{Ca}_{0.2}\text{Fe}_{0.8}\text{Cu}_{0.2}\text{O}_3$ revealing a slightly lower Pd loading of 0.08 wt.% compared to the theoretical value. The bulk composition of the perovskite is confirmed to be in agreement with the nominal composition.

Likewise, XRD revealed no changes to the crystalline orthorhombic perovskite structure after impregnation with the PGM including a calcination at 400 °C. No additional diffraction

peaks attributable to the corresponding PGM or its oxides were observed by XRD. This is easily explained with the very low loadings.

Reducibility

The influence of the PGM-doping on the overall reducibility of the solid was investigated by H₂-TPR in comparison to the non-doped La_{0.8}Ca_{0.2}Fe_{0.8}Cu_{0.2}O₃ sample (Fig. 6.1). Pt-, Rh- and Pd-doped La_{0.8}Ca_{0.2}Fe_{0.8}Cu_{0.2}O₃ perovskites showed a different behaviour.

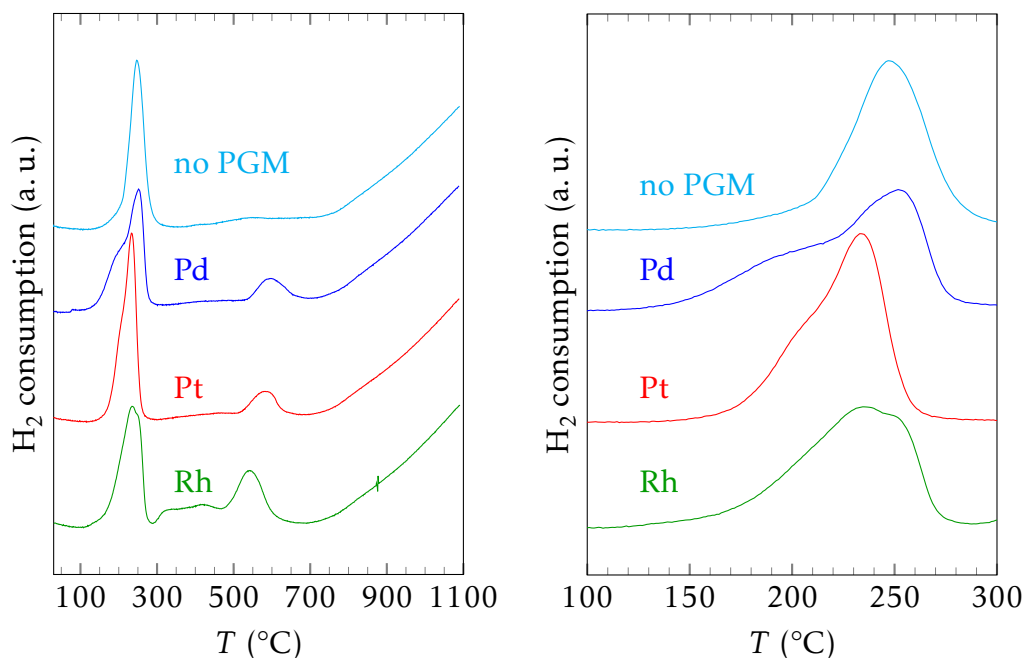


Figure 6.1 – H₂ absorption curves of calcined non-doped and PGM-doped La_{0.8}Ca_{0.2}Fe_{0.8}Cu_{0.2}O₃ (0.1 wt.% Pd, Pt or Rh; CCM).

All samples show the typical perovskite Fe³⁺ (> 700 °C) and the Cu²⁺ reduction (at approximately 250 °C) as already discussed earlier (Chapter 5).

The sample loaded with Pd shows an additional very slight reduction phenomenon at lower temperature (79 °C), a differently shaped Cu²⁺ reduction peak and an additional peak at about 600 °C. According to literature,^[1-4] Pd generally is reduced at near ambient temperature, i. e. below 100 °C. The H₂ uptake in the temperature range of the reduction peak at 79 °C peak corresponds to a H/Pd of 0.66. Therefore, the rest of the presumed PdO has to be reduced at lower temperature or in the same temperature range as the Cu²⁺. The low amount of Pd explains the low increase in overall H₂ consumption of 1.16 mmol g⁻¹ integrated over the temperature range of 70 °C to 700 °C (Table 6.1). The corresponding H/M¹ value of 2.57 is remarkably higher than expected keeping in mind the low Pd loading and that the maximum H/Cu is 2. Having a look at the H/M value of the overlapping peaks in the temperature range of 150 °C to 300 °C of 2.12 (H/Cu = 2.14), it is clear that Cu²⁺ is fully reduced to Cu⁰ in this temperature domain. Therefore, the additionally observed peak at 597 °C has to be attributed to an impurity, possibly in the form of carbonates.

Regarding the reduction phenomenon below 300 °C, an overlap of 2 different peaks is seen for the Pd-doped solid. For bulk CuO, the Cu reduction in the temperature range up to

¹M = Cu + PGM, i. e. Cu + Pd.

350 °C takes place in 2 steps via the formation of Cu_2O , and the reduction of Cu^+ is delayed until all Cu^{2+} is reduced to Cu^+ .^[5] In the case of the Pd-doped perovskite, it seems that the presence of Pd mainly induces a shift of the Cu^{2+} to Cu^+ reduction to lower temperature, thereby splitting the contributions of both reduction phenomena leading to the broadening of the observed peak. The Cu^+ to Cu^0 reduction seemingly remains unaffected since the maximum temperature is unchanged. Such a peak shift was already observed for other materials such as Pd-doped LaMnO_3 , LaFeO_3 and LaCoO_3 perovskites and was attributed to so-called H_2 spillover effects.^[1,6] This effect relies on the adsorption of H_2 on reduced Pd which then allows for the reduction of the support at lower temperature.

Table 6.1 – Comparison of H_2 -TPR results of calcined non-doped and PGM-doped $\text{La}_{0.8}\text{Ca}_{0.2}\text{Fe}_{0.8}\text{Cu}_{0.2}\text{O}_3$. 0.1 wt.% Pd, Pt or Rh; CCM; all 50 mg, 25 ml min^{-1}

loading	H_2 consumption ^a (mmol g^{-1})	H/M^b		T_{max} reduction peaks			
		total ^a	low T^c	(°C)	(°C)	(°C)	(°C)
non-doped	1.03	2.30	2.19	247	401	536	> 1100
+ Pd	1.16	2.57	2.12	251	-	597	> 1100
+ Pt	1.22	2.72	2.26	234	-	586	> 1100
+ Rh	1.80	3.99	2.04	236	broad	543	> 1100

^a H_2 consumption was integrated over the temperature range of 70 °C to 700 °C.

^b $\text{M} = \text{Cu} + \text{PGM}$ (Pd, Pt or Rh respectively).

^c Temperature range of 150 °C to 300 °C.

This splitting of the low temperature reduction peaks below 300 °C of the Cu-containing perovskite is observed for all doped solids (Fig. 6.1). The Pt-impregnated sample shows a still discernible shoulder. This shoulder appears just below 200 °C in agreement with previous findings in literature attributing a reduction peak at 197 °C to PtO_2 species ($\text{H}/\text{Pt} = 4$).^[7] Compared to the Pd-doped solid, the H_2 spillover effect also seems to affect the Cu^+ to Cu^0 reduction step leading to the lowest maximum temperature observed for all doped solids. Concerning the overall H_2 uptake, the Pt-doped perovskite shows a slight increase compared to the non-doped $\text{La}_{0.8}\text{Ca}_{0.2}\text{Fe}_{0.8}\text{Cu}_{0.2}\text{O}_3$ perovskite (Table 6.1) for the 1st reduction peaks ($\text{H}/(\text{Pt}+\text{Cu}) = 2.26$) affirming an overlap of the Pt reduction peak with those of the Cu reduction. Again, the high temperature peak is ascribed to a contamination since Cu and Pt reductions are completed below 300 °C.

In the case of the Rh-impregnated perovskite, the Cu reduction peaks overlap to a broad but asymmetric peak between 150 °C and 270 °C. An attribution of a possible Rh contribution and the assignment to a specific Rh species is difficult. If Rh^{3+} reduction occurs in this temperature range, it is incomplete as can be concluded from the H/M value of 2.04 of these peaks ($\text{H}/\text{Cu} = 2.06$). Moreover, an additional broad reduction phenomenon is observed between 300 and 500 °C which may be ascribable partly to Rh reduction. However, the corresponding H_2 uptake is too high for Rh^{3+} reduction only ($\text{H}/\text{Rh} = 28$). The high temperature reduction peak at 543 °C, on the other hand, may be attributed to a similar contamination as for the other doped solids since the temperature domain is similar and H_2 uptake too high for the low PGM loadings. The Rh-impregnated sample shows a highly increased overall H_2 consumption of 1.80 mmol g^{-1} corresponding to an H/M value of 3.99. Even its lower molar mass compared to Pt and the probably higher oxidation state compared to Pd cannot explain this high value affirming the already mentioned hypothesis of a surface contamination in form of carbonates.

A similar reduction behaviour in the temperature range of 380 °C to 580 °C – even though more intense in its H₂ uptake – was observed for Pt-containing perovskites, i. e. LaFe_{0.95}Pt_{0.05}O₃, prepared by sol-gel technique by Dacquín et al. In this case, however, no such reduction behaviour was evidenced for the corresponding impregnated perovskites.^[7,8]

Textural properties

No major deviations from the textural properties of the non-doped La_{0.8}Ca_{0.2}Fe_{0.8}Cu_{0.2}O₃ perovskite, neither for the isotherms nor the pore size distributions, are observed. Compared to the Pd-doped sample which surprisingly shows a slightly higher SSA of 28.7 m² g⁻¹, the Rh- and Pt-doped samples show similar ones as the non-doped solid of about 24 m² g⁻¹.

Chemical composition

Table 6.2 lists the photopeak maxima of La 3d, Ca 2p, Fe 2p, Cu 2p, O 1s as well as the corresponding PGM. The positions of the perovskite peaks remain mainly unchanged compared to the non-doped solid. The B. E. correspond to La³⁺, Ca²⁺, Fe³⁺ and Cu²⁺ as described in Chapter 5. Similar contributions of lattice oxygen as for the non-doped sample are detected. The carbonate content, however, is significantly increased for all doped solids (about 31 at.% compared to 14 at.% in the case of the non-doped sample) regardless of the dopant nature. This is surprising keeping in mind that the A-site cations are less abundant at the surface than in the non-doped solid. On the other hand, this may explain the high temperature reduction peak evidenced for all doped perovskites by H₂-TPR.

Table 6.2 – Comparison of photopeak maxima of calcined PGM-doped La_{0.8}Ca_{0.2}Fe_{0.8}Cu_{0.2}O₃ (0.1 wt.% Pd, Pt or Rh; CCM).

	B. E. (eV)					PGM ^c	at.%	
	La 3d _{5/2}	Ca 2p _{3/2}	Fe 2p _{3/2}	Cu 2p _{3/2}	O 1s		O _{lattice} ^a	C _{CO₃²⁻} ^b
non-doped	833.6	346.8	710.2	933.1	528.8	-	48	14
+ Pd	833.7	347.2	710.2	933.9	529.0	337.1	50	31
+ Pt	833.6	346.7	710.3	933.6	529.1	n. a. ^d	49	30
+ Rh	833.5	346.8	709.8	933.1	528.8	309.2	51	31

^a O_{lattice} + O_{ads} = 1.

^b C_{CO₃²⁻} + C_{adventitious} = 1.

^c Pd 3d_{5/2}, Pt 4f and Rh 3d_{5/2} respectively.

^d The Pt 4f signal overlaps with the Cu 3p region.

Fig. 6.2 shows the spectra of the Pd 3d, Pt 4f and Rh 3d photopeaks. The Pd 3d_{5/2} photopeak maximum of 337.1 eV (Table 6.2) is in agreement with the presence of PdO.^[6,9-11] The full width at half maximum (FWHM) of the Pd 3d_{5/2} core level was determined. With 1.5 eV for Pd, this FWHM below 2.5 eV confirms that Pd is present as a single species only at the surface of the doped perovskite. The Rh 3d photopeak is noisy due to the low loading and corresponds to the expected multiplet for Rh₂O₃ with the Rh 3d_{5/2} photopeak maximum at 309.2 eV.^[9,12,13] The FWHM of 2.1 eV for Rh is again below 2.5 eV confirming that Rh is present as a single species only as well. The Pt 4f region, on the other hand, does not show the characteristic multiplet. Since the energy region of Pt 4f overlaps with the Cu 3p core level. The low sensibility obtained for Pt is also related to its higher molar mass of 195 g mol⁻¹

compared to Rh (102.9 g mol^{-1}) and Pd (106.4 g mol^{-1}). It is assumed that Pt is present in one of its oxidic forms, probably PtO_2 , as the other precious metals.

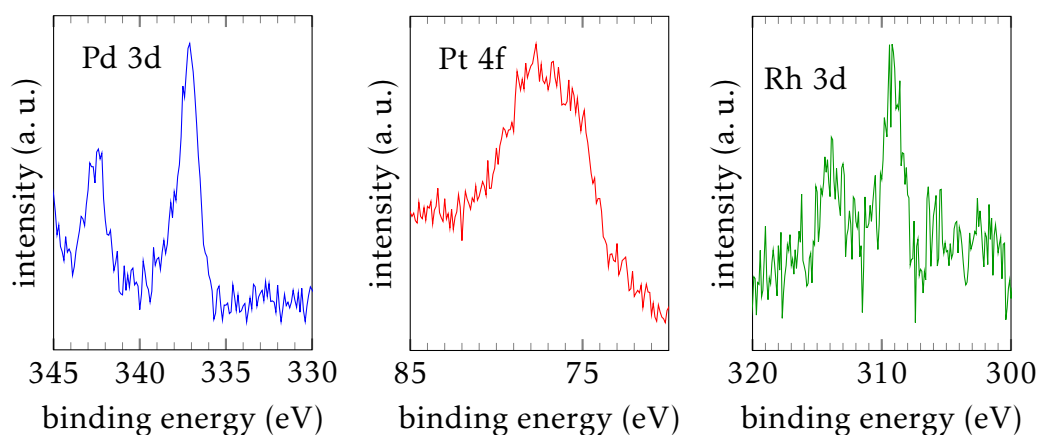


Figure 6.2 – Pd 3d, Pt 4f and Rh 3d photopeaks of PGM-doped $\text{La}_{0.8}\text{Ca}_{0.2}\text{Fe}_{0.8}\text{Cu}_{0.2}\text{O}_3$ (0.1 wt.% Pd, Pt or Rh; CCM).

Concerning the loadings evidenced at the surface of the catalysts, the atomic La to PGM ratios were determined for the Pd- and Rh-doped solids by XPS (Table 6.2). Comparing the values of the Pd- and the Rh-doped perovskite, the Pd-loading at the atomic scale is double as high than for the Rh-doped solid. Moreover, both values are significantly higher than the theoretical value of about 0.002. This finding suggests a good dispersion of the doping metal on the surface of the solids, and a higher accessibility of the Pd than the Rh.

Table 6.3 – Surface ratios of the $\text{La}_{0.8}\text{Ca}_{0.2}\text{Fe}_{0.8}\text{Cu}_{0.2}\text{O}_3$ perovskite catalysts (CCM), doped with 0.1 wt.% of Pd, Rh, or Pt as determined by XPS analyses.

PGM loading (wt.%)	x_A/x_B (at.%)	$x_{\text{Cu}}/x_{\text{Fe}}$	$x_{\text{Ca}}/x_{\text{La}}$	$x_{\text{Pd}}/x_{\text{La}}$
theoretical values	1	0.25	0.25	0.002
non-doped	1.65	0.34	0.34	-
+ 0.1 Pd	1.36	0.13	0.13	0.017
+ 0.1 Pt	1.38	0.12	0.15	n. a.
+ 0.1 Rh	1.36	0.12	0.13	0.008

XPS analysis again puts into evidence a deviation between bulk and surface composition of the doped perovskites. As previously discussed, the surface atomic ratio A/B is higher than 1 in line with surface enrichment in La and Ca. A decrease of the A-site cation enrichment at the surface of the PGM-doped samples is observed after addition of PGM (Table 6.3). Another aspect which stands out is that the surface atomic ratios of the substituting, Ca and Cu, to the substituted cations in both sites, La and Fe respectively, are lower than the nominal values for all doped solids, whereas the bulk ratios comply with the nominal ones as shown by elementary analysis for the $\text{La}_{0.8}\text{Ca}_{0.2}\text{Fe}_{0.8}\text{Cu}_{0.2}\text{O}_3$ samples doped with 0.1 wt.% Pd compared to the non-doped perovskite. The impact seems to be independent of the nature of the PGM, however.

6.1.2 Catalytic performance

Catalytic performance tested according to Procedure A

The catalytic performances of the 0.1 wt.% Pd-, Pt- and Rh-doped $\text{La}_{0.8}\text{Ca}_{0.2}\text{Fe}_{0.8}\text{Cu}_{0.2}\text{O}_3$ perovskites were tested according to Procedure A (Section 2.3). Selected test results are listed in Table 6.4 and depicted in Fig. 6.3 and 6.4 for CO, propylene, NO, propane, O_2 and H_2 conversion and are compared to the commercial reference TWC and $\text{La}_{0.8}\text{Ca}_{0.2}\text{Fe}_{0.8}\text{Cu}_{0.2}\text{O}_3$ catalyst.

The influence of PGM addition on $\text{La}_{0.8}\text{Ca}_{0.2}\text{Fe}_{0.8}\text{Cu}_{0.2}\text{O}_3$ can be observed only for the oxidation of C_3H_6 and H_2 in stoichiometric conditions (stoic1). On the other hand, CO, propane, methane and NO conversions are not significantly modified after Pt, Pd or Rh impregnation. Best performances for propylene and H_2 oxidation are obtained by the Pd-doped sample whereas Pt- and Pd-doped samples showed similar propylene conversion curves. It should be mentioned that H_2 is activated at higher temperature than CO on Pt- and Rh-doped catalysts as previously observed on the bare $\text{La}_{0.8}\text{Ca}_{0.2}\text{Fe}_{0.8}\text{Cu}_{0.2}\text{O}_3$ support. Another remark concerns the absence of propylene reforming in this series of PGM-doped perovskites during the 1st stoichiometric test ramp after activation according to Procedure A (stabilisation in stoichiometric conditions at 600 °C during 2 h).

Similar trends were obtained during the 2nd test ramp in lean conditions. Pd- and Pt-doped solids exhibited almost the same catalytic performances except for H_2 oxidation. Surprisingly, results of the Rh-doped catalyst cannot be distinguished from those of the bare $\text{La}_{0.67}\text{Fe}_{0.83}\text{Cu}_{0.17}\text{O}_3$ support.

Table 6.4 – Temperatures corresponding to 50% conversion of CO, C_3H_6 , C_3H_8 , and H_2 (stoichiometric) and NO (rich composition) of PGM-doped $\text{La}_{0.8}\text{Ca}_{0.2}\text{Fe}_{0.8}\text{Cu}_{0.2}\text{O}_3$ (0.1 wt.% Pd, Pt or Rh; CCM) and selectivities of NO reduction products at T_S .

condition	stoichiometric				rich				
	T_{50} (°C)				selectivities at T_S				
	CO	C_3H_6	C_3H_8	H_2	NO	S_{N_2}	S_{NH_3}	$S_{\text{N}_2\text{O}}$	T_S (°C)
non-doped	279	449	487	399	469	0.36	0.64	0	506
+ 0.1 wt.% Pd	287	377	495	287	430	0.38	0.62	0	493
+ 0.1 wt.% Pt	279	381	504	329	473	0.40	0.60	0	509
+ 0.1 wt.% Rh	289	460	485	484	423	0.39	0.61	0	504

Concerning the catalytic performances under rich conditions, 2 deviations stand out. On the one hand, the Pd-impregnated solid clearly presents an enhancement of NO reduction activity towards lower temperature compared to the other solids. The main NO reduction product at approximately 500 °C is NH_3 for all doped samples (Table 6.4). The N_2 selectivity (S_{N_2}) values at 500 °C are, however, slightly higher for the Pd-doped $\text{La}_{0.8}\text{Ca}_{0.2}\text{Fe}_{0.8}\text{Cu}_{0.2}\text{O}_3$ compared to the non-doped perovskite. Higher activity is also observed for H_2 oxidation for Pd/ $\text{La}_{0.8}\text{Ca}_{0.2}\text{Fe}_{0.8}\text{Cu}_{0.2}\text{O}_3$. On the other hand, the Rh-doped solid shows the highest maximum conversion of propylene at 500 °C, even though conversions over the Pd-doped perovskite are higher in the temperature range of 300 °C to 470 °C.

The most interesting changes are observed during the return tests under stoichiometric conditions (stoic2) after the rich test ramp. A significant improvement of catalytic perfor-

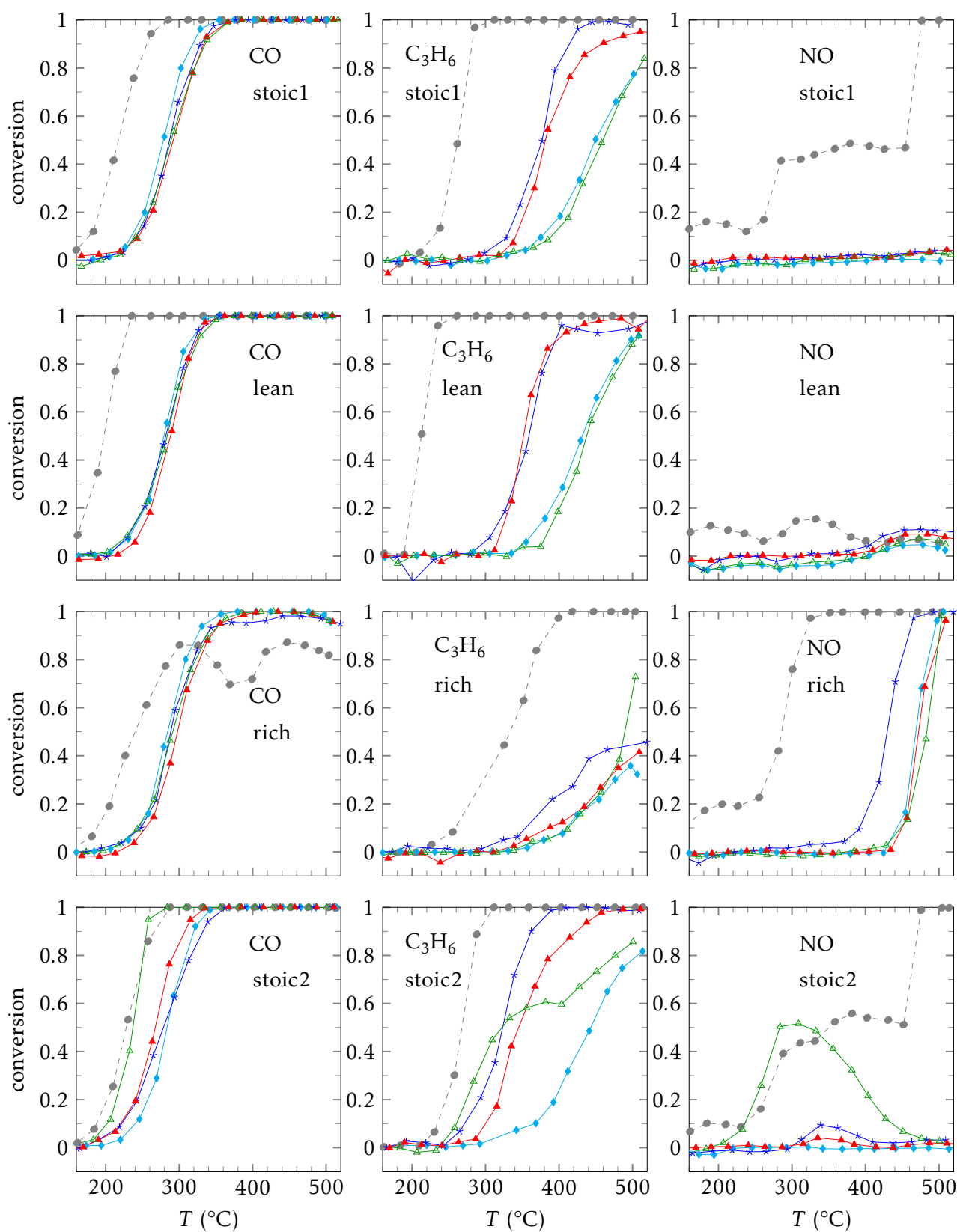


Figure 6.3 – CO, C₃H₆ and NO conversions of PGM-doped $\text{La}_{0.8}\text{Ca}_{0.2}\text{Fe}_{0.8}\text{Cu}_{0.2}\text{O}_3$ (0, 0.1 wt.% Pd, Pt or Rh; CCM) catalysts during Procedure A. $\text{La}_{0.8}\text{Ca}_{0.2}\text{Fe}_{0.8}\text{Cu}_{0.2}\text{O}_3$ (◆), doped with 0.1 wt.% Pd (★), Pt (▲), or Rh (△) compared to the commercial reference TWC (●)

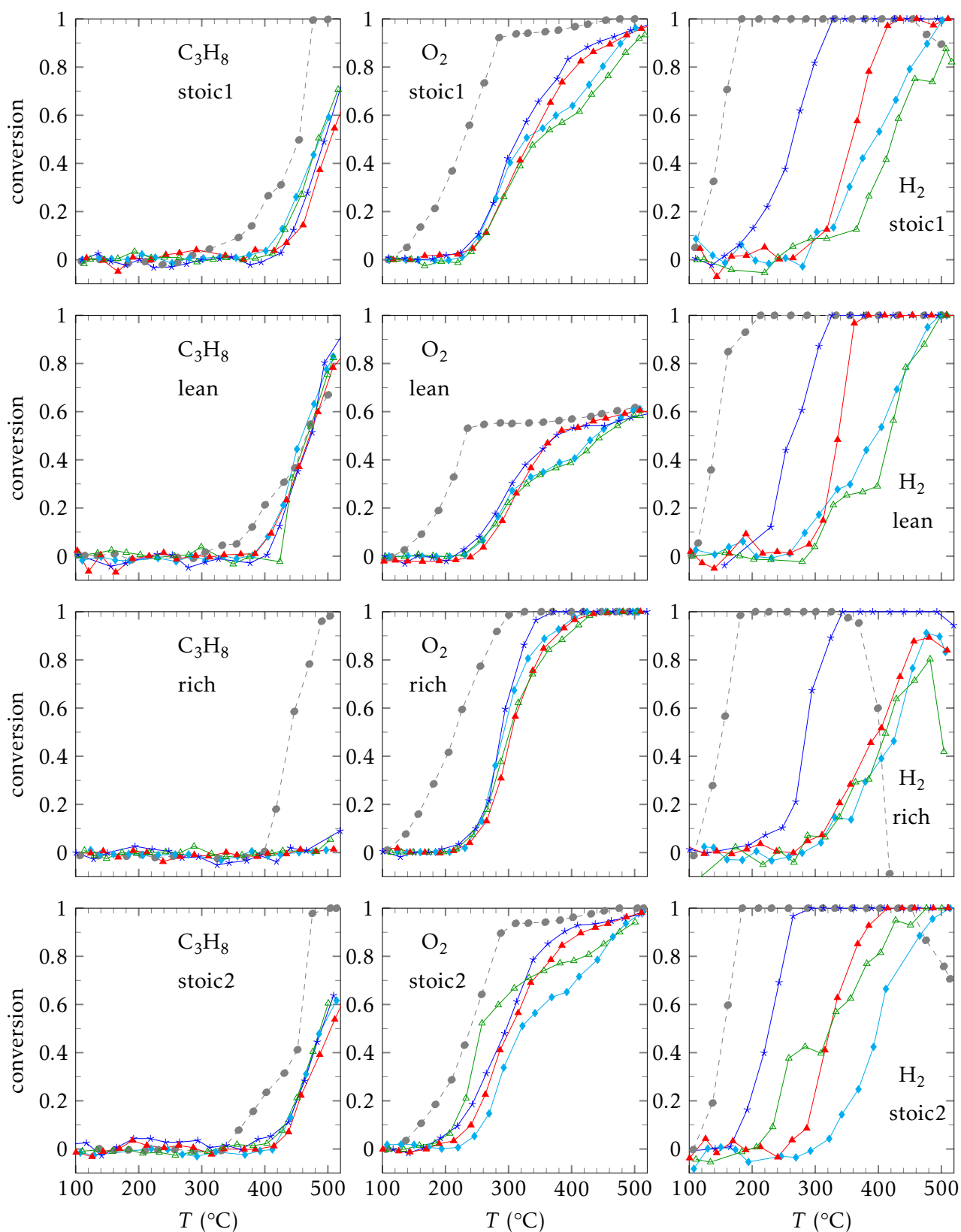


Figure 6.4 – C_3H_8 , O_2 and H_2 conversions of PGM-doped $\text{La}_{0.8}\text{Ca}_{0.2}\text{Fe}_{0.8}\text{Cu}_{0.2}\text{O}_3$ (0, 0.1 wt.% Pd, Pt or Rh; CCM) catalysts during catalytic performance test procedure A conducted for perovskites, s. Fig. 2.7 (Procedure A). $\text{La}_{0.8}\text{Ca}_{0.2}\text{Fe}_{0.8}\text{Cu}_{0.2}\text{O}_3$ (\blacklozenge), doped with 0.1 wt.% Pd (\blackstar), Pt (\blacktriangle), or Rh (\blacktriangledown)

mances is observed, mainly for NO reduction and H_2 , C_3H_6 and CO oxidation reactions on PGM-doped $\text{La}_{0.8}\text{Ca}_{0.2}\text{Fe}_{0.8}\text{Cu}_{0.2}\text{O}_3$ solids compared to the initial catalytic measurements (stoic1). This is most remarkable for the Rh-impregnated sample which shows 50 % conversion of NO. The main product of NO reduction during the return test for the Rh-doped perovskite as well as other PGM-doped solids is nitrous oxide. At 285 °C, $S_{\text{N}_2\text{O}}$ of the Rh-impregnated sample yields 80 %. N_2O selectivity decreases to 43 % at 355 °C due to the successive reduction of N_2O to N_2 . Only few NH_3 is formed during the whole temperature ramp. The conversion-temperature-profile of NO does not follow the typical S-shape but conversion declines gradually after reaching its maximum at about 300 °C. This phenomenon is well known for Rh catalysts and explained by a $\text{CO} + \text{NO}$ reaction which stops due to increased competition of oxygen suppliers such as O_2 and N_2O at temperatures where NO desorption is facilitated.^[14] The $\text{CO} + \text{NO}$ reaction in the low temperature range favours N_2O production as already discussed in Section 3.5.1. The reduction of NO on the Rh-doped catalyst started at approximately 200 °C which is close to the temperatures of CO, C_3H_6 and H_2 activation. Therefore, a significant enhancement of CO, C_3H_6 and H_2 oxidation reactions with ΔT_{50} of 52 K, 140 K and ≈ 100 K respectively is observed compared to the initial stoichiometric test. This enhancement on Rh/ $\text{La}_{0.8}\text{Ca}_{0.2}\text{Fe}_{0.8}\text{Cu}_{0.2}\text{O}_3$ should be related to a change of active site nature due to the previous exposure to rich conditions which precede the last stoichiometric test. It should be underlined that this catalyst exhibits a similar activity for CO oxidation compared to the commercial reference. Minor NO reduction is observed for the Pt- and the Pd-doped perovskites. The Pd-impregnated sample also shows a marked propylene performance enhancement.

The Pt-impregnated sample shows the lowest differences between both tests in stoichiometric conditions. The Rh-impregnated catalyst seems to be activated by the test ramp undergone under rich, i. e. reductive, conditions. The difference between both stoichiometric tests is in agreement with the presence of the PGM in their oxide forms in the initial solids as evidenced (Pd, Rh) or assumed (Pt) by XPS and H_2 -TPR results.

Influence of a reductive pretreatment (Procedure C) on the catalytic performance

Results of the previous section suggest that PGM-doped perovskites became more active after contact with a reducing mixture. Based on these results, a reductive pretreatment (Procedure C) was introduced in the procedure for the PGM-doped solids as alternative to the activation with stoichiometric feed at 600 °C as conducted in Procedure A. The reduction step was performed at 300 °C. At this temperature, as suggested by H_2 -TPR, all Cu species should be reduced as well as the impregnated PGM oxides, i. e. PdO, PtO_2 and Rh_2O_3 .

Results of the corresponding catalytic tests are shown in Fig. 6.5 and 6.6 and Table 6.5 for the 0.1 wt.% PGM-doped solids.

The reductive pretreatment leads to significantly enhanced catalytic performances during the 1st stoichiometric test ramp for all PGM-doped solids as well as for all investigated pollutants except methane. In stoichiometric conditions, different behaviour is observed for oxidations reactions and NO reduction depending on the nature of the PGM. The conversion curves for CO and C_3H_6 oxidation are shifted to lower temperature over Pt/ $\text{La}_{0.8}\text{Ca}_{0.2}\text{Fe}_{0.8}\text{Cu}_{0.2}\text{O}_3$ compared to the commercial TWC reference despite the lower PGM loading (0.1 wt.% Pt vs 0.55 wt.% PGM). This underlines the beneficial interaction of Pt on the perovskite. Pd- and Rh-doped perovskites exhibited lower activity than Pt/ $\text{La}_{0.8}\text{Ca}_{0.2}\text{Fe}_{0.8}\text{Cu}_{0.2}\text{O}_3$ for oxidative reactions.

It should be mentioned that perovskite-based catalysts are less selective than the commer-

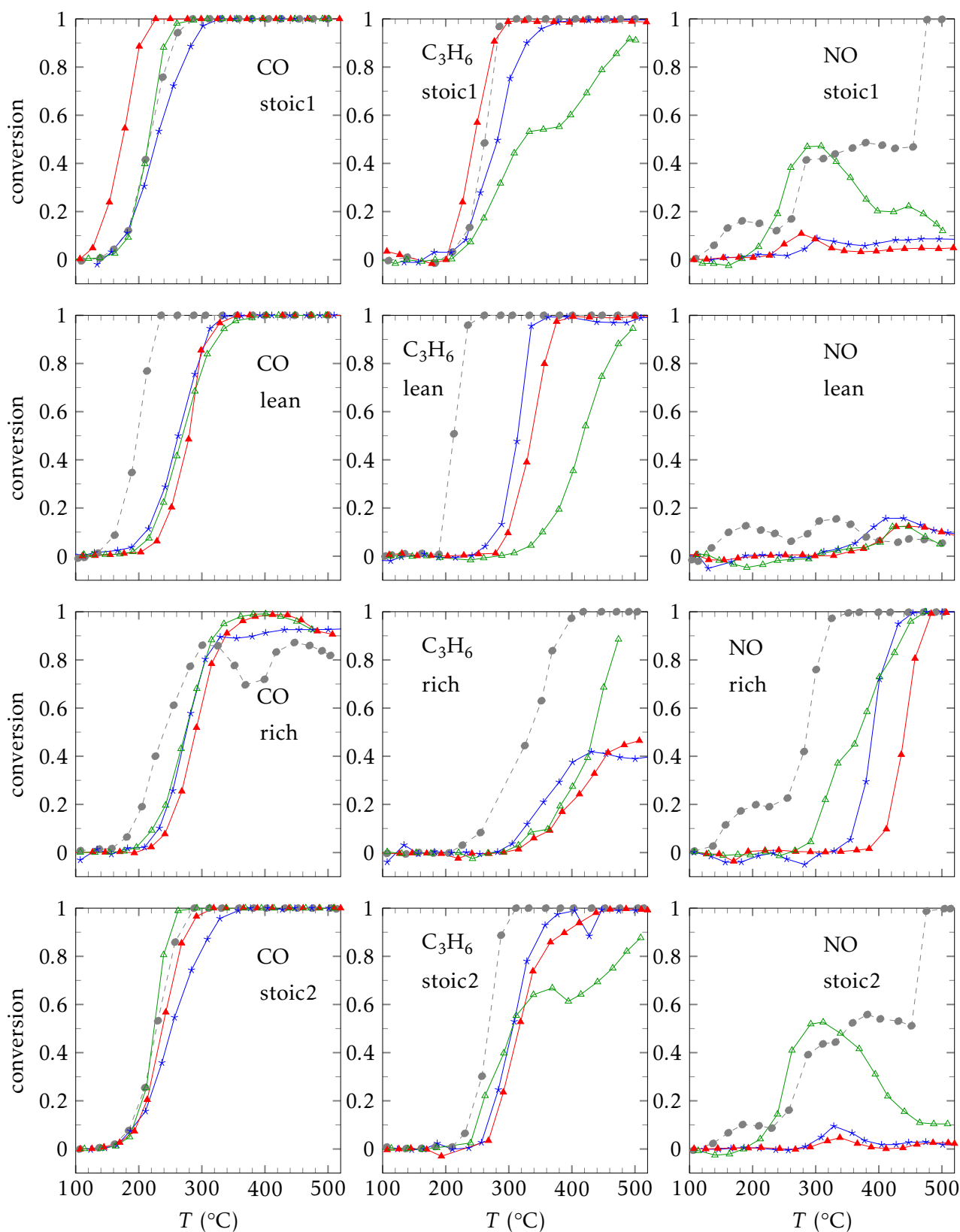


Figure 6.5 – CO, C₃H₆ and NO conversions of PGM-doped La_{0.8}Ca_{0.2}Fe_{0.8}Cu_{0.2}O₃ (0, 0.1 wt.% Pd, Pt or Rh; CCM) catalysts after a reductive pretreatment (Procedure C). La_{0.8}Ca_{0.2}Fe_{0.8}Cu_{0.2}O₃ doped with 0.1 wt.% Pd (★), Pt (▲), or Rh (△) compared to the commercial reference TWC (•, Procedure B)

Table 6.5 – Temperatures corresponding to 50% conversion of CO , C_3H_6 , C_3H_8 , and H_2 (stoichiometric) and NO (rich composition) of PGM-doped $\text{La}_{0.8}\text{Ca}_{0.2}\text{Fe}_{0.8}\text{Cu}_{0.2}\text{O}_3$ (0.1 wt.% Pd, Pt or Rh; CCM) and selectivities of NO reduction products at T_S after a reductive pretreatment (Procedure C).

condition	stoichiometric				rich				
	T_{50} (°C)				selectivities at T_S				
	CO	C_3H_6	C_3H_8	H_2	NO	S_{N_2}	S_{NH_3}	$S_{\text{N}_2\text{O}}$	T_S (°C)
+ 0.1 wt.% Pd	228	283	457	169	390	0.43	0.57	0	500
+ 0.1 wt.% Pt	175	245	473	198	441	0.49	0.51	0	507
+ 0.1 wt.% Rh	215	321	463	266	370	0.28	0.72	0	474

cial reference catalyst for H_2 oxidation compared to CO oxidation as previously evidenced for LaBO_3 catalysts (Chapter 3). On the other hand, $\text{Rh}/\text{La}_{0.8}\text{Ca}_{0.2}\text{Fe}_{0.8}\text{Cu}_{0.2}\text{O}_3$ is able to convert NO between 200 °C and 500 °C with a maximum conversion of about 50%. This is in line with previous results observed after one test cycle (return test of Procedure A, Fig. 6.3, stoic2). Subsequent enhancement of NO reduction on $\text{Rh}/\text{La}_{0.8}\text{Ca}_{0.2}\text{Fe}_{0.8}\text{Cu}_{0.2}\text{O}_3$ is observed at high temperature above 400 °C. This phenomenon may be explained by the stepwise reduction as discussed in Section 3.5.1 as induced by the Rh content.

As shown in Fig. 6.7, under stoichiometric conditions, a high $S_{\text{N}_2\text{O}}$ is observed for all PGM-doped solids, including the commercial reference TWC. Nitrous oxide is produced at low temperature for the doped perovskite whereas at higher temperatures (> 400 °C), only the Rh-doped perovskite shows NO conversion with high N_2 selectivity and only little ammonia formation compared to the commercial reference catalyst.

Propylene conversion on the Pt-doped sample is enhanced by pre-reduction ($\Delta T_{50}(\text{C}_3\text{H}_6) = 136 \text{ K}$). The Rh-doped solid for which $\Delta T_{50}(\text{C}_3\text{H}_6)$ is equal to 139 K presents a 2-step conversion profile hinting at 2 different elimination mechanisms at different temperatures. The process at higher temperature may be caused by propylene reforming even though CO and H_2 conversion remain complete in the corresponding temperature range.

Under lean conditions, conversion curves are less influenced by the reductive pretreatment. A very slight enhancement for NO conversion is observed between 400 °C and 500 °C compared to the non pre-reduced solids.

Regarding the results of the test ramp being conducted under rich conditions, an enhancement of NO reduction is observed. All PGM-doped perovskites show enhanced performances by pre-reduction, $\Delta T_{50}(\text{NO})$ ranging from 32 K for the Pt- over 40 K for the Pd- to 53 K for the Rh-impregnated catalyst. The latter also shows the highest overall NO reduction performance. The Rh-doped perovskite yields the highest S_{NH_3} at 500 °C (Table 6.5). High amounts of N_2 and to a lesser extent of N_2O (only in the temperature range of 280 °C to 440 °C) are produced below 500 °C (Fig. 6.7). The drop in N_2 production above 420 °C is most likely correlated to the in situ H_2 formation, explaining the suddenly high NH_3 selectivity of NO reduction. This behaviour is comparable to the one of the commercial reference catalyst as discussed in Section 3.5.1. Similar observations are also made for the Pd- and Pt-doped solids although at higher temperature leading to a lower S_{NH_3} . The N_2 selectivity at high temperature remains, nonetheless, higher than for the commercial reference catalyst over a wide temperature range. Furthermore, H_2 production due to HC reforming is observed at temperatures above 420 °C leading to a H_2 conversion drop for all pre-reduced solids. The

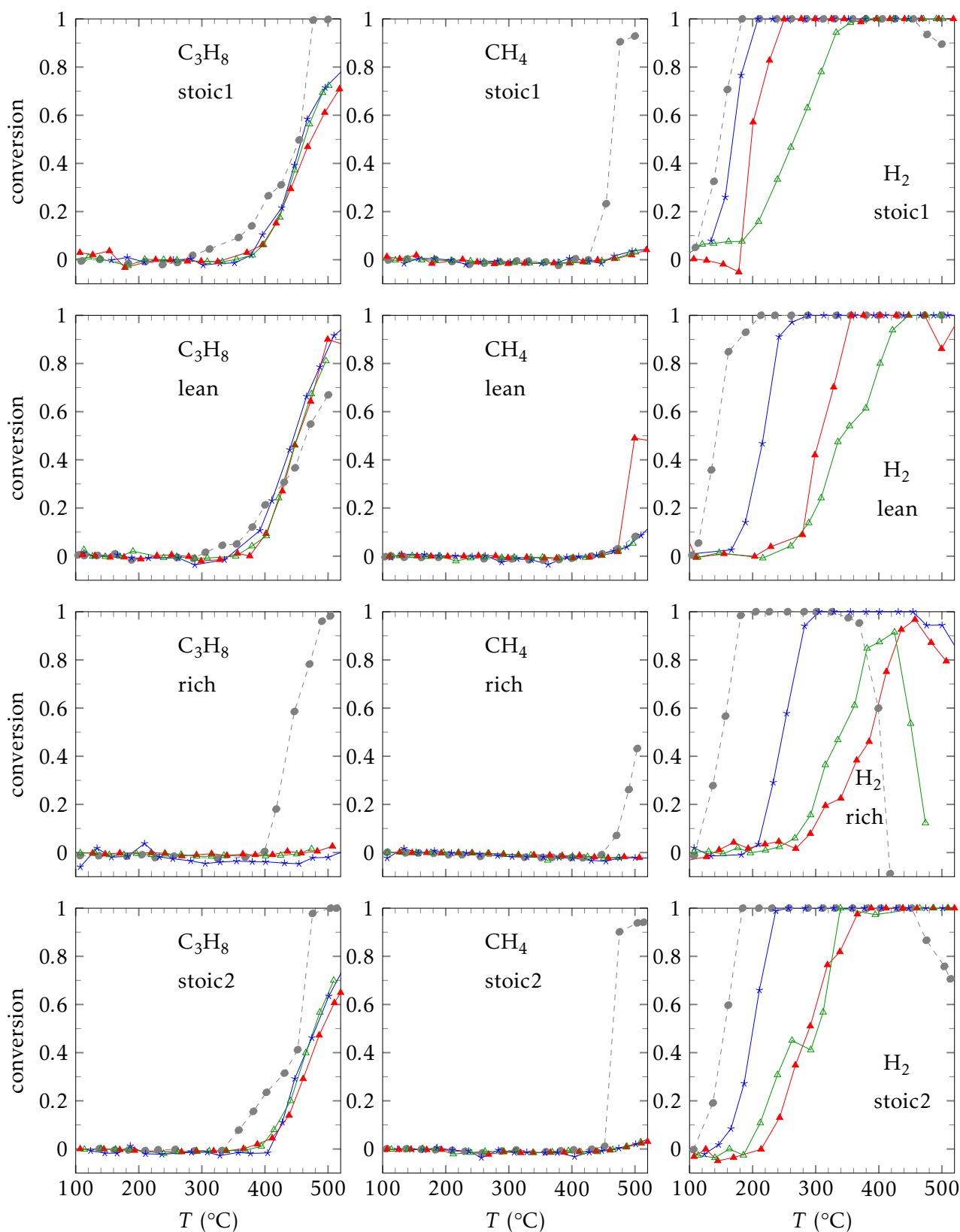


Figure 6.6 – C_3H_8 , CH_4 and H_2 conversions of PGM-doped $La_{0.8}Ca_{0.2}Fe_{0.8}Cu_{0.2}O_3$ (0, 0.1 wt.% Pd, Pt or Rh; CCM) catalysts after a reductive pretreatment (Procedure C). $La_{0.8}Ca_{0.2}Fe_{0.8}Cu_{0.2}O_3$ doped with 0.1 wt.% Pd (★), Pt (▲), or Rh (△) compared to the commercial reference TWC (•, Procedure B)

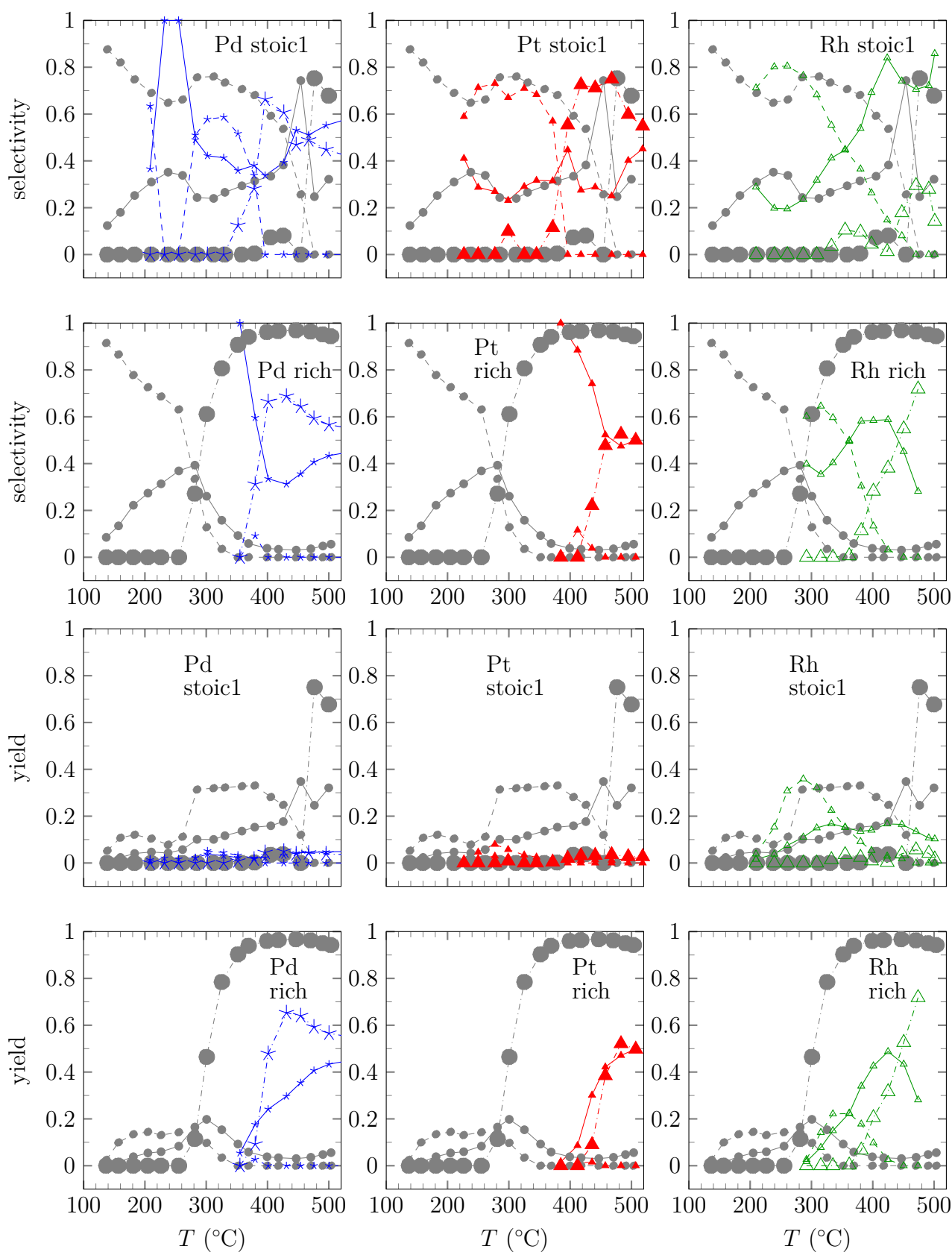


Figure 6.7 – N_2 , N_2O and NH_3 selectivities and yields of NO conversion of PGM-doped $\text{La}_{0.8}\text{Ca}_{0.2}\text{Fe}_{0.8}\text{Cu}_{0.2}\text{O}_3$ (0.1 wt.% Pd, Pt or Rh; CCM) after a reductive pretreatment (Procedure C) under stoichiometric and rich conditions. $\text{La}_{0.8}\text{Ca}_{0.2}\text{Fe}_{0.8}\text{Cu}_{0.2}\text{O}_3$ doped with 0.1 wt.% Pd (\star), Pt (\blacktriangle), or Rh (\triangle) compared to the commercial reference TWC (\bullet , Procedure B); $S_{\text{N}_2}/Y_{\text{N}_2}$ (solid), $S_{\text{N}_2\text{O}}/Y_{\text{N}_2\text{O}}$ (dashed), $S_{\text{NH}_3}/Y_{\text{NH}_3}$ (dashdotted, big mark)

drop in H_2 conversion is observed at the same temperature as the drop in CO conversion and the enhanced propylene oxidation pointing to a C_3H_6 reforming process.

Comparing the return test to the 1st stoichiometric ramp, the Rh/ $La_{0.8}Ca_{0.2}Fe_{0.8}Cu_{0.2}O_3$ catalyst shows stable catalytic performances after one test cycle. The Pd-impregnated perovskite shows similar conversions while the Pt-doped catalyst presents a decrease in performance during the return test. The main product of NO reduction over the Rh-doped catalyst up to 400 °C is nitrous oxide, completed by N_2 . No significant NH_3 production is observed. While NO reduction over the Pd-doped catalyst leads to equal amounts of nitrous oxide and N_2 , the NO reduction observed for the Pt-doped solid is mainly due to nitrous oxide.

6.2 Rh-doped $La_{0.67}Fe_{0.83}Cu_{0.17}O_3$

The results of the combination of partial substitution and surface composition optimisation highlighted the catalytic performances of the La-deficient $La_{0.67}Fe_{0.83}Cu_{0.17}O_3$ solid (Chapter 5). Among the pre-reduced doped catalysts investigated in the previous section, the Pt- and Rh-doped $La_{0.8}Ca_{0.2}Fe_{0.8}Cu_{0.2}O_3$ solids yielded the most interesting results. Since the performance of the Rh-doped perovskite was more stable during the test, Rh was chosen as the dopant for tests on the $La_{0.67}Fe_{0.83}Cu_{0.17}O_3$ catalyst. Moreover, the Rh-doped catalyst was revealed to be more active especially for NO reduction. Based on these results, a sample of the most promising perovskite containing no noble metals, $La_{0.67}Fe_{0.83}Cu_{0.17}O_3$, was impregnated with 0.1 wt.% Rh by incipient wet impregnation method (IWI) to be tested under 3-way catalytic conditions.

6.2.1 Physico-chemical properties

Structural properties

As already seen for the PGM-doped $La_{0.8}Ca_{0.2}Fe_{0.8}Cu_{0.2}O_3$ solids, the Rh/ $La_{0.67}Fe_{0.83}Cu_{0.17}O_3$ solid shows no additional crystalline phases compared to the orthorhombic corresponding non-doped perovskite due to the very low amount of Rh. No deviations from the parent perovskite crystalline structure were detected.

Reducibility

The reducibility of the solid was investigated by H_2 -TPR as for the corresponding non-doped perovskite. Results are shown in Fig. 6.8 and Table 6.6.

Comparing the H_2 -TPR profiles of the non-doped with the Rh-doped $La_{0.67}Fe_{0.83}Cu_{0.17}O_3$ sample (Fig. 6.8), the same behaviour is observed for temperatures above 250 °C, i. e. the hematite contribution remains unchanged. The doping with Rh mainly affects the low temperature reduction domain. In comparison with the Rh-doped $La_{0.8}Ca_{0.2}Fe_{0.8}Cu_{0.2}O_3$ solid, no additional reduction peaks or intensity increases are observed at temperatures > 300 °C. On the other hand, as for the $La_{0.8}Ca_{0.2}Fe_{0.8}Cu_{0.2}O_3$ solid, the Rh reduction influences the Cu^{2+} to Cu^0 reduction leading to one unresolved peak with a maximum at about 180 °C. This may either be due to an overlap with the Rh^{3+} reduction, a H_2 spillover effect or indicative of the disappearance of the Cu segregation phenomenon observed for the non-doped solid (Section 5.5.2). As shown in Table 6.6, the reducibility of the solid, i. e. its overall H_2 consumption, is similar for the Rh- and non-doped solids. The hematite phase segregation seems to be unaffected by the Rh-impregnation.

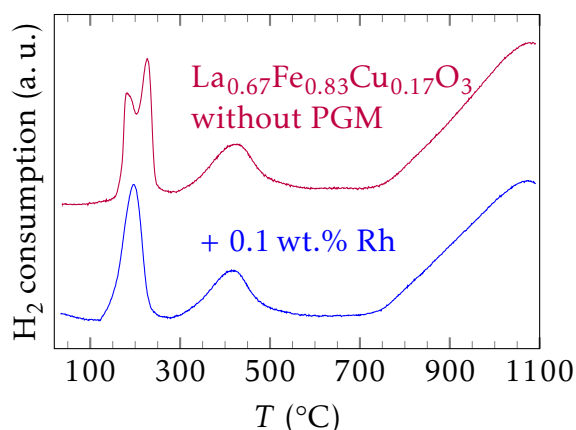


Figure 6.8 – H_2 absorption curves of the calcined non-doped and Rh-doped $\text{La}_{0.67}\text{Fe}_{0.83}\text{Cu}_{0.17}\text{O}_3$ samples (0.1 wt.% Rh; CCM; 50 mg, 50 ml min^{-1}).

Table 6.6 – Comparison of H_2 -TPR results of non-doped and Rh-doped $\text{La}_{0.67}\text{Fe}_{0.83}\text{Cu}_{0.17}\text{O}_3$ (0.1 wt.% Rh; CCM; both 50 mg, 50 ml min^{-1}).

nominal composition	H_2 consumption ^a (mmol g^{-1})	H/M^b		T_{max} reduction peaks (°C)			
		low T^c	high T^d				
$\text{La}_{0.67}\text{Fe}_{0.83}\text{Cu}_{0.17}\text{O}_3$	1.76	2.33	0.36	182	227	422	1080
+ 0.1 wt.% Rh	1.79	2.28	0.38	196	417	1097	

^a H_2 consumption was integrated over the T range of 100 °C to 700 °C.

^b $\text{M} = \text{Cu} + \text{Rh}$.

^c 100 °C $\leq T <$ 290 °C.

^d 290 °C $\leq T <$ 550 °C.

Reduction of Cu^{2+} species and Rh_2O_3 is confirmed to take place below 300 °C validating the temperature of 300 °C for the reductive pre-treatment conducted in Procedure C.

Textural properties

The textural properties of the non-doped and the Rh-doped $\text{La}_{0.67}\text{Fe}_{0.83}\text{Cu}_{0.17}\text{O}_3$ are similar. Neither the isotherms nor the pore size distributions differ. Likewise, the SSA of both perovskite samples are about 27 $\text{m}^2 \text{g}^{-1}$.

Chemical composition

The surface composition of the 0.1 wt.% Rh-doped $\text{La}_{0.67}\text{Fe}_{0.83}\text{Cu}_{0.17}\text{O}_3$ was investigated by XPS. The results are shown in Table 6.7.

Regarding the positions of the photopeaks (Table 6.7), La^{3+} and Fe^{3+} are again obtained. Concerning the Cu 2p core level, an intense satellite is observed in contrast to the bare support (not shown) suggesting that either less segregated CuO is present on the surface or that it is less easily reduced to Cu^+ due to the irradiation. The Rh 3d signal being too weak, it is lost in the noise. Therefore, it can only be assumed that it is present in its trivalent oxide form (Rh_2O_3).

Table 6.7 – Comparison of binding energies of calcined non-doped and Rh-doped $\text{La}_{0.67}\text{Fe}_{0.83}\text{Cu}_{0.17}\text{O}_3$ (0.1 wt.% Rh; CCM).

	B. E. (eV)					at. %	
	La 3d _{5/2}	Fe 2p _{3/2}	Cu 2p _{3/2}	O 1s	Rh 3d _{5/2}	O _{lattice} ^a	C _{CO₃²⁻} ^b
$\text{La}_{0.67}\text{Fe}_{0.83}\text{Cu}_{0.17}\text{O}_3$	834.5	710.9	933.1	530.0	-	65	17
+ 0.1 wt.% Rh	834.1	710.4	932.7	529.3	n. a. ^c	43	20

^a O_{lattice} + O_{ads} = 1.

^b C_{CO₃²⁻} + C_{adventitious} = 1.

^c The Rh 3d signal is lost in the noise due to its low loading.

In contrast to the PGM-doped $\text{La}_{0.8}\text{Ca}_{0.2}\text{Fe}_{0.8}\text{Cu}_{0.2}\text{O}_3$ solids, the carbonate content remains about the same as for the non-doped $\text{La}_{0.67}\text{Fe}_{0.83}\text{Cu}_{0.17}\text{O}_3$. On the other hand, the contribution of non-lattice oxygen species (O_{ads}) is increased after the impregnation with Rh.

Table 6.8 – Surface compositions of the $\text{La}_{0.67}\text{Fe}_{0.83}\text{Cu}_{0.17}\text{O}_3$ perovskite catalyst doped with 0.1 wt.% Rh compared to the non-doped sample.

nominal composition	$x_{\text{La}}/x_{\text{B}}$	$x_{\text{Cu}}/x_{\text{Fe}}$	S. S. A. (m ² g ⁻¹)
$\text{La}_{0.67}\text{Fe}_{0.83}\text{Cu}_{0.17}\text{O}_3$	1.03	0.22	26.5
+ 0.1 wt.% Rh	1.00	0.12	27.5

The ratio of La to B-site cations remains constant compared to the bare support. On the other hand, the Cu to Fe ratio is reduced as was already observed for the PGM-doped $\text{La}_{0.8}\text{Ca}_{0.2}\text{Fe}_{0.8}\text{Cu}_{0.2}\text{O}_3$.

6.2.2 Catalytic performance

The catalytic performance of the Rh-impregnated $\text{La}_{0.67}\text{Fe}_{0.83}\text{Cu}_{0.17}\text{O}_3$ catalyst was first tested according to different procedures (Section 2.3) in order to investigate the influence of the oxidation states of the Rh and Cu (Procedure A and Procedure C). Alternatively, another gas mixture was finally studied in which the oxygen content during stoichiometric test runs was reduced by 450 ppm (Procedure D).

Catalytic performance tested according to Procedure A

The Rh/ $\text{La}_{0.67}\text{Fe}_{0.83}\text{Cu}_{0.17}\text{O}_3$ solid was tested after activation at 600 °C under stoichiometric conditions. XPS analysis previously suggested the presence of an oxidic form for Rh (Rh₂O₃) on perovskites. Fig. 6.9 and 6.10 present the comparison of catalytic performances of $\text{La}_{0.67}\text{Fe}_{0.83}\text{Cu}_{0.17}\text{O}_3$, Rh/ $\text{La}_{0.67}\text{Fe}_{0.83}\text{Cu}_{0.17}\text{O}_3$ and the commercial reference TWC.

The conversion curves are almost similar for the 1st stoichiometric test and the Rh addition does not lead to the expected enhancement of catalytic performances. This behaviour is mainly due to the presence of Rh in its oxidic form as previously observed in the case of Rh/ $\text{La}_{0.8}\text{Ca}_{0.2}\text{Fe}_{0.8}\text{Cu}_{0.2}\text{O}_3$.

Similar observations are made for the lean run concerning CO, propylene and propane oxidation and NO reduction (S_{N₂} = 100 %) with no clear additional effect of the Rh-doping.

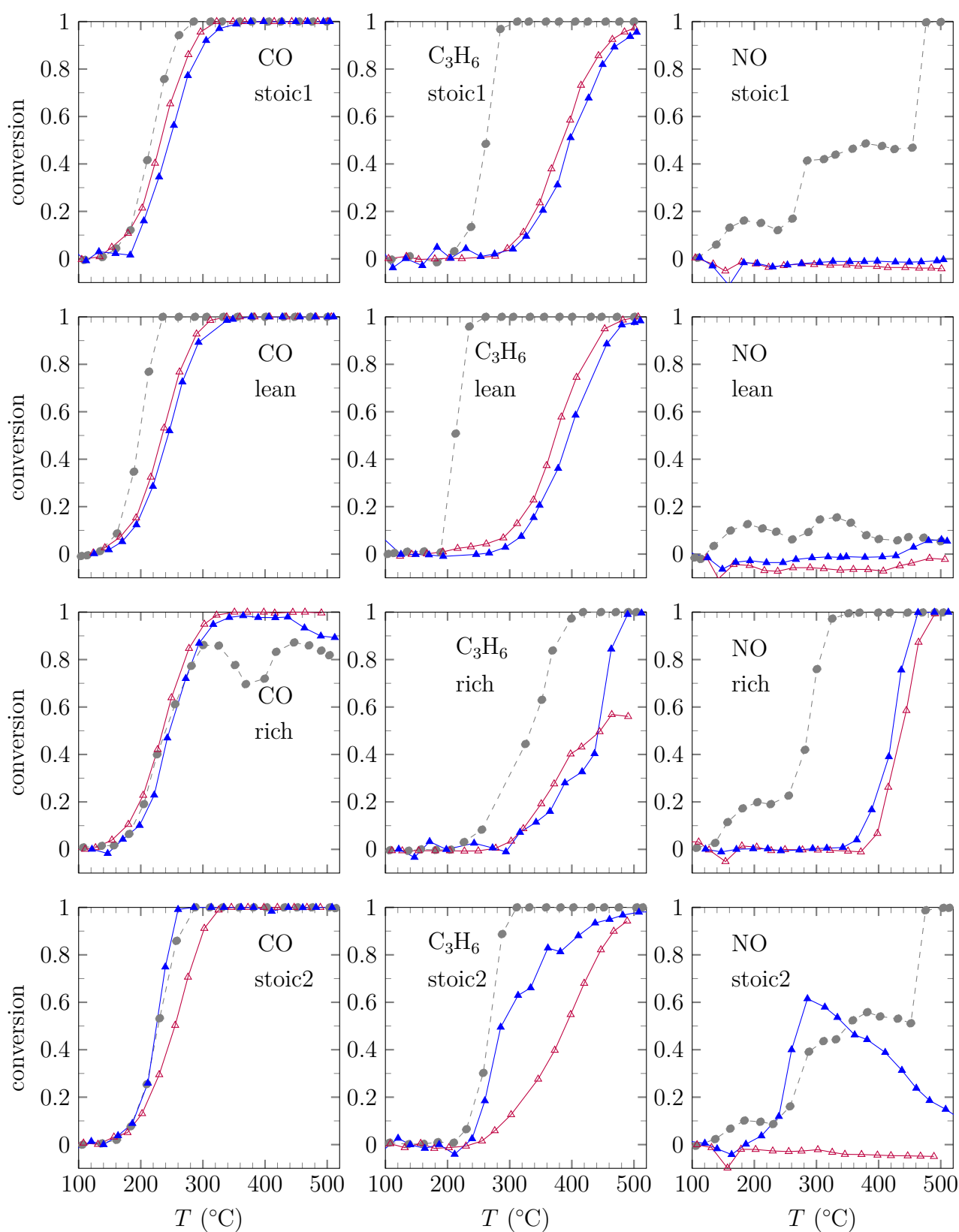


Figure 6.9 – CO, C_3H_6 and NO conversions of non-doped and Rh-doped $\text{La}_{0.67}\text{Fe}_{0.83}\text{Cu}_{0.17}\text{O}_3$ (0.1 wt.% Rh; CCM) catalysts during Procedure A. $\text{La}_{0.67}\text{Fe}_{0.83}\text{Cu}_{0.17}\text{O}_3$ (Δ), doped with 0.1 wt.% Rh (\blacktriangle) compared to the commercial reference TWC (\bullet)

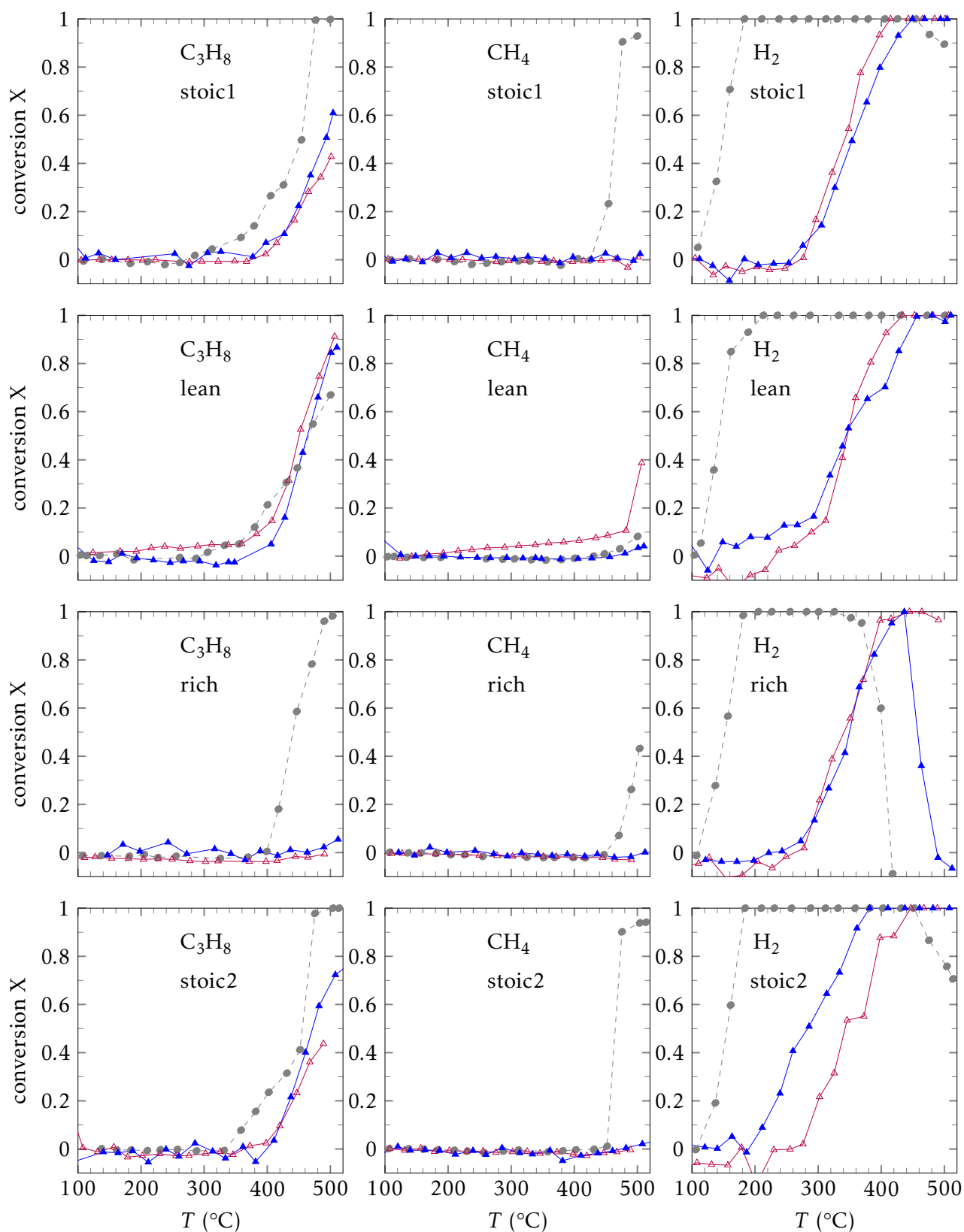


Figure 6.10 – C_3H_8 , CH_4 and H_2 conversions of non-doped and Rh-doped $\text{La}_{0.67}\text{Fe}_{0.83}\text{Cu}_{0.17}\text{O}_3$ (0.1 wt.% Rh; CCM) catalysts during Procedure A. $\text{La}_{0.67}\text{Fe}_{0.83}\text{Cu}_{0.17}\text{O}_3$ (Δ), doped with 0.1 wt.% Rh (\blacktriangle) compared to the commercial reference TWC (\bullet)

In rich conditions, the catalytic performances of $\text{Rh}/\text{La}_{0.67}\text{Fe}_{0.83}\text{Cu}_{0.17}\text{O}_3$ are very similar to the bare support. However, the behaviour of the Rh-doped solid is modified at high temperatures. H_2 and CO conversion decrease above 440 °C, whereas propylene conversion is enhanced. This enhancement may be due to propylene reforming leading to CO and H_2 production. Furthermore, a slightly enhanced NO reduction performance ($T_{50} = 423$ °C) is observed. Due to the high amounts of H_2 , a high NH_3 selectivity of 83 % is observed at 512 °C (as shown in Table 6.9).

Major differences occur if comparing the return tests in stoichiometric conditions. As in the case of the $\text{Rh}/\text{La}_{0.8}\text{Ca}_{0.2}\text{Fe}_{0.8}\text{Cu}_{0.2}\text{O}_3$ catalyst, CO, propylene, propane and NO conversions increase after the rich test ramp for the $\text{Rh}/\text{La}_{0.67}\text{Fe}_{0.83}\text{Cu}_{0.17}\text{O}_3$ perovskite. An activation of H_2 at lower temperature is also observed. Especially the NO reduction performance is enhanced. The light-off curve presents the same shape as already observed for the Rh-doped $\text{La}_{0.8}\text{Ca}_{0.2}\text{Fe}_{0.8}\text{Cu}_{0.2}\text{O}_3$ perovskite. A higher maximum conversion of 62 % is yielded, however, and the conversion only drops down to about 12 % above 500 °C. The NO products are mainly nitrous oxide ($S_{\text{N}_2\text{O}}(260$ °C) = 84 %) and N_2 (Fig. D.8 and D.9). While both are formed at lower temperature, the N_2O production yields its maximum at 285 °C and then drops to nearly zero at about 500 °C. Indeed, N_2 presents the major NO reduction product above 360 °C.

Table 6.9 – Temperatures corresponding to 50 % conversion of CO, C_3H_6 , C_3H_8 , and H_2 (stoichiometric) and NO (rich composition) of non- or 0.1 wt.% Rh-doped $\text{La}_{0.67}\text{Fe}_{0.83}\text{Cu}_{0.17}\text{O}_3$ (CCM) and selectivities of NO reduction products at T_S ; (Procedure A, Procedure C and Procedure D). Tests were conducted according to Procedure A or after a reductive pretreatment including stoichiometric (Procedure C) or modified stoichiometric conditions (Procedure D) in the following sections.

Test procedure	condition	stoichiometric ^a				rich				
		T_{50} (°C)				selectivities at T_S				
		CO	C_3H_6	C_3H_8	H_2	NO	S_{N_2}	S_{NH_3}	$S_{\text{N}_2\text{O}}$	T_S (°C)
A	non-doped	232	386	458 (T_{25})	344	438	0.32	0.68	0	491
A	Rh-doped	247	397	493	355	423	0.17	0.83	0	512
C	Rh-doped	218	305	458	276	392	0.48	0.52	0	508
D	Rh-doped	219	287	464	262	389	0.31	0.69	0	514

^a 1st stoichiometric test ramp (stoic1), in the case of Procedure D modified stoichiometric conditions.

Due to the activation of the catalyst observed after the rich test ramp, the influence of a reducing thermal pretreatment of the Rh-doped $\text{La}_{0.67}\text{Fe}_{0.83}\text{Cu}_{0.17}\text{O}_3$ on its catalytic performances was investigated next.

Influence of a reductive pretreatment (Procedure C) on the catalytic performance

The $\text{Rh}/\text{La}_{0.67}\text{Fe}_{0.83}\text{Cu}_{0.17}\text{O}_3$ catalyst was activated in 5 % H_2/He flow at 300 °C during 5 h (Procedure C) in order to study the catalytic performances after reduction. H_2 -TPR suggested that both Rh and Cu are reduced after reduction at 300 °C.

As shown in the Fig. 6.11 and 6.12, the test of the Rh-impregnated $\text{La}_{0.67}\text{Fe}_{0.83}\text{Cu}_{0.17}\text{O}_3$ (CCM) according to Procedure C leads to an improved catalytic performance during the 1st stoichiometric test ramp. In parallel to an activation of H_2 at lower temperature, especially

propylene and NO conversions were enhanced. Propane and CO oxidation performances were also increased, even though to a lesser extent. Concerning the NO reduction, contrarily to the Rh-doped $\text{La}_{0.8}\text{Ca}_{0.2}\text{Fe}_{0.8}\text{Cu}_{0.2}\text{O}_3$ sample, a significant increase in conversion above 420°C is observed. This performance increase is mainly selective towards N_2 ($S_{\text{N}_2} = 75\%$ at 495°C) contrarily to the 1st domain of NO conversion (200 to 400°C) which is accompanied by the production of nitrous oxide ($S_{\text{N}_2\text{O}, \text{max}} = 76\%$ at 275°C , Fig. D.8 and D.9). In both domains, only low amounts of NH_3 are formed. Propylene shows a stepwise conversion profile pointing at the succession of 2 different processes. The process at temperatures above 300°C might include C_3H_6 reforming even though no CO nor H_2 conversion drops are observed. Surprisingly, Rh/ $\text{La}_{0.67}\text{Fe}_{0.83}\text{Cu}_{0.17}\text{O}_3$ seems incapable to catalyse NO + H_2 reaction between 100 and 200°C as observed in the case of the commercial TWC reference. The presence of (higher loadings of) Pd on the commercial reference catalyst may explain the promotion of NO + H_2 reaction which was not even observed on Pd/ $\text{La}_{0.8}\text{Ca}_{0.2}\text{Fe}_{0.8}\text{Cu}_{0.2}\text{O}_3$.

During the lean test ramp, propylene and CO performances of the pre-reduced (Procedure C) and the non-reduced solid (Procedure A) are similar. A minor enhancement of propane and methane oxidation and NO reduction is observed as well as a slightly lower activation temperature of H_2 .

NO reduction and propylene oxidation were also slightly improved under rich conditions, whereas the conversions of all other pollutants remained similar to those of the test performed without reductive pre-reduction. Whereas only low amounts of nitrous oxide were formed in both tests, N_2 is the predominant product formed without pre-reduction ($S_{\text{N}_2} = 82\%$ at 490°C , Procedure A).

Finally, the catalytic activity of pre-reduced Rh/ $\text{La}_{0.67}\text{Fe}_{0.83}\text{Cu}_{0.17}\text{O}_3$ is stable after a complete test cycle leading to similar performances compared to non-reduced Rh-doped $\text{La}_{0.67}\text{Fe}_{0.83}\text{Cu}_{0.17}\text{O}_3$.

Influence of the oxygen content under stoichiometric conditions (Procedure D) on the catalytic performance

From the results discussed above, it is evident that methane is not converted in the investigated temperature range under stoichiometric testing conditions. It can therefore be assumed, that the so-called “stoichiometric” runs were more likely being conducted under lean conditions because the O_2 concentration for “stoichiometry” was adjusted to allow for the CH_4 oxidation. But this part of the O_2 (450 ppm) was not consumed.

In order to verify this assumption a test was conducted under modified stoichiometric conditions (Section 2.3 Table 2.2), subtracting the part of O_2 concentration which had been included to allow for the methane oxidation. This test run was conducted in a full test cycle as part of Procedure D. This means that all stoichiometric runs were performed under hereafter denoted “modified stoichiometric” conditions.

Resulting performances are depicted in Fig. 6.11 and 6.12 in comparison to the results obtained according to Procedure A and Procedure C. Selected T_{50} values and NO reduction selectivities are reported in Table 6.9.

For the 1st test ramp, i. e. under stoichiometric (Procedure A, Procedure C) or modified stoichiometric conditions (Procedure D), a clearly enhanced performance of the pre-reduced Rh-doped $\text{La}_{0.67}\text{Fe}_{0.83}\text{Cu}_{0.17}\text{O}_3$ catalyst is observed. An additional enhancement is seen for the sample if the test is conducted under modified stoichiometric conditions. While H_2 and CO conversions are similar, propylene oxidation and especially NO reduction performances are enhanced. The C_3H_6 and NO conversion light-off curves follow the same behaviour as

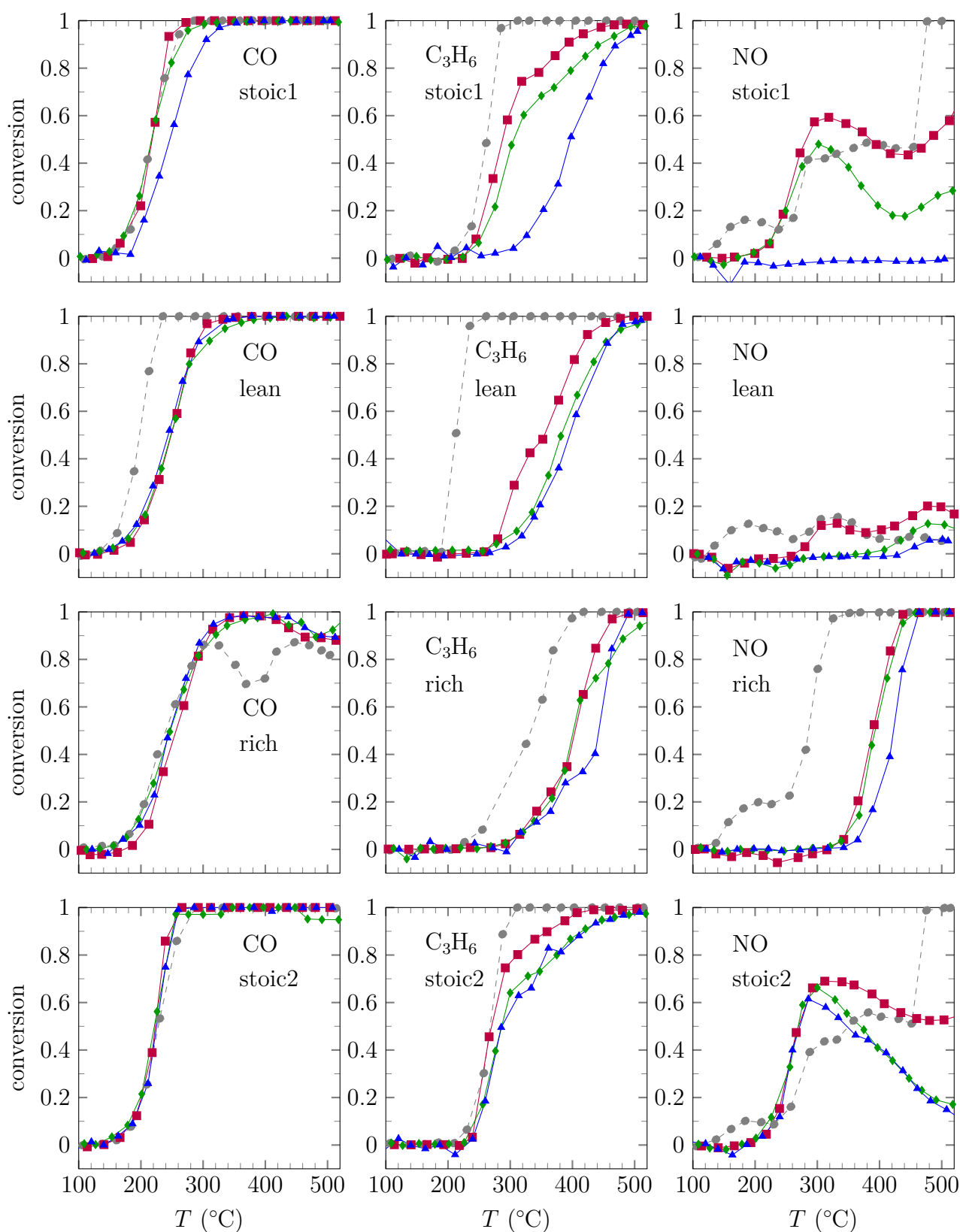


Figure 6.11 – CO, C₃H₆ and NO conversions of 0.1 wt.% Rh-doped $\text{La}_{0.67}\text{Fe}_{0.83}\text{Cu}_{0.17}\text{O}_3$ (CCM) catalysts tested according to Procedure A or after a reductive pretreatment (Procedure C or Procedure D). $\text{La}_{0.67}\text{Fe}_{0.83}\text{Cu}_{0.17}\text{O}_3$ doped with 0.1 wt.% Rh tested by Procedure A (\blacktriangle) or pre-reduced including tests under “stoichiometric” (Procedure C, \blacklozenge) or “modified stoichiometric” conditions (Procedure D, \blacksquare) compared to the commercial reference TWC (\bullet , Procedure B)

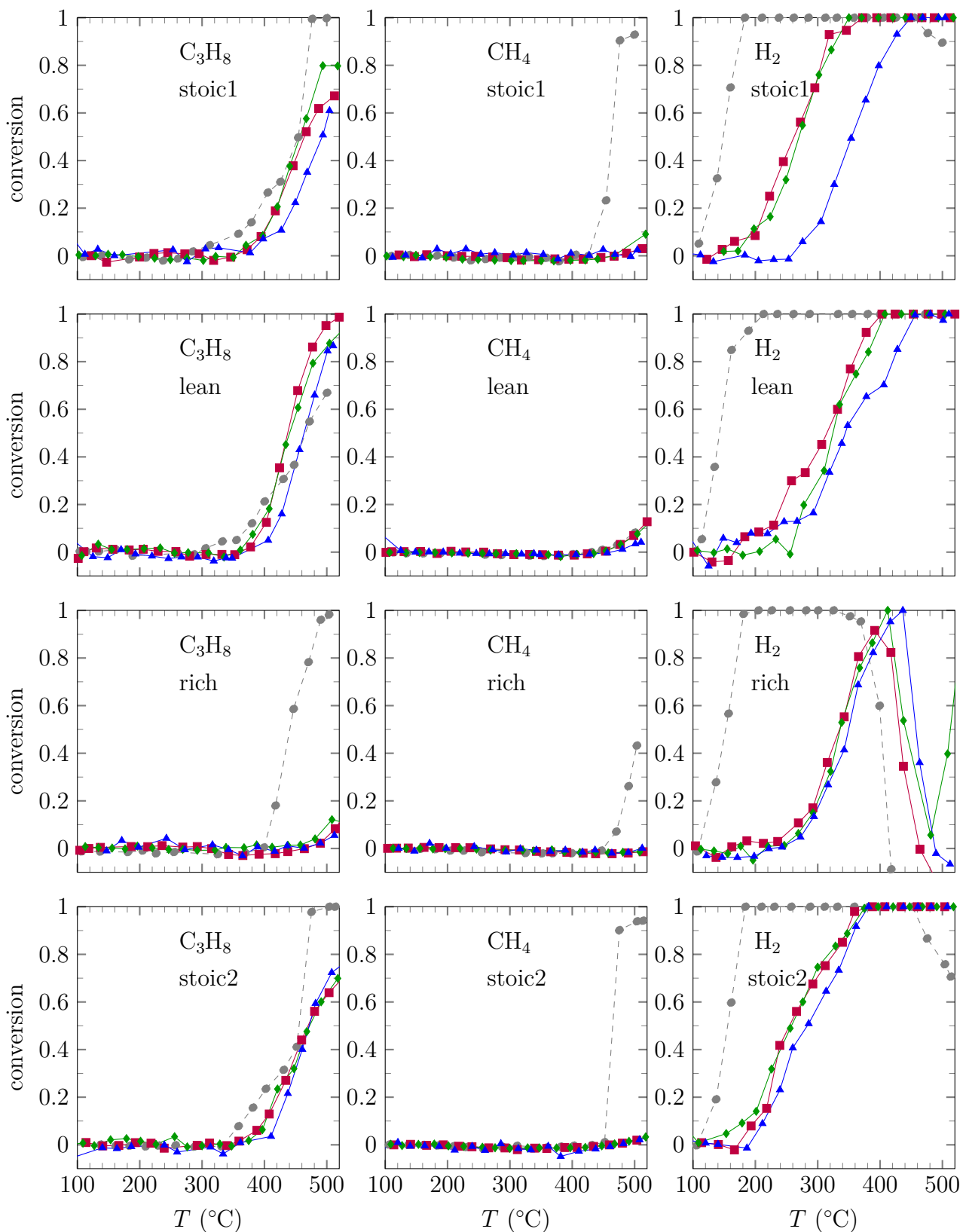


Figure 6.12 – C_3H_8 , CH_4 and H_2 conversion conversions of 0.1 wt.% Rh-doped $\text{La}_{0.67}\text{Fe}_{0.83}\text{Cu}_{0.17}\text{O}_3$ (CCM) tested according to Procedure A or after a reductive pretreatment (Procedure C or Procedure D). $\text{La}_{0.67}\text{Fe}_{0.83}\text{Cu}_{0.17}\text{O}_3$ doped with 0.1 wt.% Rh tested by Procedure A (\blacktriangle) or pre-reduced including tests under “stoichiometric” (Procedure C, \blacklozenge) or “modified stoichiometric” conditions (Procedure D, \blacksquare) compared to the commercial reference TWC (\bullet , Procedure B)

already seen for Procedure C. However, both show an enhanced performance with respect to this test. NO reduction proceeds via 2 different processes between 180 °C – 420 °C and 420 °C – 520 °C respectively (Fig. D.8 and D.9). The 1st domain corresponds to the production of N₂O (S_{N_2O} up to 77 % and $S_{N_2} = 23$ % at 245 °C) while during the 2nd domain mainly N₂ and to a lesser extent NH₃ (S_{N_2} up to 69 % and $S_{NH_3} = 31$ % at 512 °C) are formed.

Interestingly, the conversions of propylene and NO are enhanced for the test performed according to Procedure D compared to Procedure C under lean and rich conditions even though the gas feed was the same. This behaviour could be ascribed to the less oxidising atmosphere during the initial stoichiometric test ramp, i. e. the prevention of too intense oxidation of the perovskite and/or the segregated phases, especially Cu.

In the Procedure D, the NO reduction under lean conditions takes place in 2 temperature domains as already seen for the commercial reference catalyst (Chapter 3). The lowest temperature domain below 270 °C attributed to the presence of Pd in the commercial reference TWC is not observed. In the 1st domain for which reduction is observed for the Rh/La_{0.67}Fe_{0.83}Cu_{0.17}O₃, only nitrous oxide and N₂ are detected with S_{N_2O} up to 80 % and $S_{N_2} = 20$ % at 280 °C. This ratio is reversed for the 2nd domain leading to a S_{N_2} of 75 % and a S_{N_2O} up to 7 % at 477 °C. Moreover, up to 20 % NO conversion are achieved over the Rh/La_{0.67}Fe_{0.83}Cu_{0.17}O₃ catalyst at 480 °C.

Under rich conditions, nitrous oxide is only formed in a limited temperature range of 300 °C to 420 °C. While up to 390 °C N₂ is the main reduction product ($S_{N_2} = 76$ %), it is superseded by ammonia at higher temperature. This NH₃ formation is again promoted by extra H₂ production due to propylene reforming activity which occurs at 390 °C during Procedure D instead of 440 °C (Procedure C).

The return test shows similar results as the 1st test ramp under modified stoichiometric conditions. The performance enhancements if compared to results of Procedure C for propylene and NO are maintained and even improved in the case of the maximum NO conversion. However, the high temperature reduction close to 500 °C is slightly decreased. This behaviour is combined with a less marked stepwise conversion. Having a look at the corresponding NO conversion products, both steps are still distinguishable, though. During the 1st temperature domain (200 to 350 °C), nitrous oxide represents the main product (S_{N_2O} up to 82 % and $S_{N_2} = 18$ % at 240 °C). On the other hand, the 2nd step is governed by the production of N₂ (S_{N_2} of 69 %, $S_{N_2O} = 6$ % and $S_{NH_3} = 24$ % at 503 °C). Overall, the domain of NO reduction activity is observed in a wider temperature range from 200 °C to 520 °C combined with high conversions of up to 70 %.

6.3 Conclusion

The monometallic Pt-, Pd- and Rh-impregnated La_{0.8}Ca_{0.2}Fe_{0.8}Cu_{0.2}O₃ perovskites and Rh-doped La_{0.67}Fe_{0.83}Cu_{0.17}O₃ were compared to the bare supports and to the commercial TWC reference. Investigations on PGM-doped perovskites generally showed that the orthorhombic perovskite structure as well as the textural properties of the corresponding non-doped perovskites were maintained after PGM impregnation. The doping with PGM on these 2 types of solids leads to remarkable changes in the catalytic performances despite the low loadings (0.1 wt.%). The influence of introducing a reductive thermal pretreatment was also investigated for the PGM-doped solids. The reducibility results obtained by H₂-TPR suggested a complete reduction of Cu as well as Pd, Pt and Rh after a reductive pretreatment at 300 °C. On the other hand, XPS put into evidence the stabilisation of oxidic Pd and Rh as

PdO and Rh₂O₃ respectively, Pt being presumably in PtO_x form. The reactivity of the doped perovskite in absence of a reductive pretreatment was investigated first for both series of catalysts.

The doping with the highly reducible Pd on La_{0.8}Ca_{0.2}Fe_{0.8}Cu_{0.2}O₃ leads to the most interesting catalytic performances, especially concerning CO, propylene and NO conversion. Interestingly an enhancement of catalytic performance was observed during the stoichiometric test performed after the rich test ramp suggesting a reduction of PGM at the surface of the perovskite. The Rh/La_{0.8}Ca_{0.2}Fe_{0.8}Cu_{0.2}O₃ catalyst exhibited NO reduction between 200 °C and 500 °C in stoichiometric conditions with approximately 50 % conversion at 300 °C. It should be mentioned that hydrocarbon reforming as well as WGS reactions were not clearly observed while PGM prevailed in their oxidic forms. The reductive thermal pretreatment induced a significant enhancement of catalytic performances compared to an activation under stoichiometric feed at 600 °C for 2 h (Procedure A).

The pre-reduced Pt-impregnated catalyst shows a much more enhanced catalytic performance (ΔT_{50} (CO) = 104 K, ΔT_{50} (C₃H₆) = 136 K for the stoichiometric test run). It is decreasing over the test cycle but still higher during the return test than for the stoichiometric feed-activated solid. The NO light-off temperature under rich conditions is also decreased (ΔT_{50} (NO) = 32 K) and higher N₂ selectivity is observed. Furthermore, this is the only perovskite-based catalyst to clearly show CH₄ conversion except for the La_{0.6}Ca_{0.2}Fe_{0.8}Cu_{0.2}O₃ sample discussed in Section 5.5 (lean conditions at high temperature).

Pre-reduced Rh-impregnated La_{0.8}Ca_{0.2}Fe_{0.8}Cu_{0.2}O₃ equally shows interesting results with ΔT_{50} (CO) = 74 K and ΔT_{50} (C₃H₆) = 139 K under stoichiometric conditions. The results are stable over the test cycle or improve. Its NO reduction performance surpasses the one of all other doped perovskites, under rich (ΔT_{50} (NO) = 114 K) and especially under stoichiometric conditions. One drawback seems to be that NO conversion under stoichiometric conditions is decreasing gradually again at temperatures over 340 °C.

Similar investigations were conducted on the 0.1 wt.% Rh/La_{0.67}Fe_{0.83}Cu_{0.17}O₃ catalyst. Even though mainly similar or slightly lower conversions are observed during the initial test ramps in stoichiometric conditions, promising results were obtained during the return test. A marked enhancement in conversions – as a consequence of the exposure to reductive conditions of the rich test ramp – is observed as in the case of Rh/La_{0.8}Ca_{0.2}Fe_{0.8}Cu_{0.2}O₃. Propylene oxidation and NO reduction performances are most enhanced.

In analogy to the La_{0.8}Ca_{0.2}Fe_{0.8}Cu_{0.2}O₃ catalysts doped with PGM, the Rh-impregnated La_{0.67}Fe_{0.83}Cu_{0.17}O₃ perovskite was exposed to a catalytic test including a pre-reduction step. As a result, enhanced CO, propylene, propane and NO conversions were observed under stoichiometric and to a lesser extent under lean and rich conditions. In contrast to the Rh-doped La_{0.8}Ca_{0.2}Fe_{0.8}Cu_{0.2}O₃ perovskite, the NO conversion under stoichiometric conditions remains ≥ 20 % even above 420 °C. During the return test, NO conversion increases up to 70 %. Moreover, the stability of the catalyst is confirmed by comparing return tests according to Procedure A and Procedure C.

Due to the non-conversion of methane under stoichiometric conditions for all investigated perovskites, another catalytic test including the reductive pretreatment was conducted. The feed stream composition was modified during the stoichiometric test ramps subtracting the O₂ amount corresponding to the intended full combustion of methane. This lowered O₂ content did lead to similar CO conversions. Furthermore, the propylene oxidation and as expected the NO reduction performances were enhanced. The return test mainly confirmed the stability of Rh/La_{0.67}Fe_{0.83}Cu_{0.17}O₃ after one test cycle.

Comparing the Rh/La_{0.8}Ca_{0.2}Fe_{0.8}Cu_{0.2}O₃ and the Rh/La_{0.67}Fe_{0.83}Cu_{0.17}O₃ catalysts, the

latter is clearly more active in its unreduced form. After reductive pretreatment, differences in performances are less pronounced but the Rh/La_{0.67}Fe_{0.83}Cu_{0.17}O₃ still yields higher N₂ selectivities.

On pre-reduced doped perovskites, similar or even better CO oxidation performances (Pt-doped La_{0.8}Ca_{0.2}Fe_{0.8}Cu_{0.2}O₃) as for the commercial reference TWC were obtained. Likewise propane and propylene conversion results are close to the reference despite the significantly lower PGM content. Among the 0.1 wt.% PGM-doped perovskites, the Rh-doped catalysts (especially after pre-reduction) show the most promising results. This is particularly true for the NO reduction under rich and stoichiometric conditions. Concerning the NO conversion products, even though ammonia presents still the main product at high temperatures under rich conditions, a significantly higher N₂ selectivity is observed in the case of the doped Cu-substituted perovskites than for the commercial reference. The formation of nitrous oxide is also detected in a limited temperature range but drops to zero at temperatures below 500 °C.

Bibliography

- [1] W.-J. Shen, M. Okumura, Y. Matsumura, M. Haruta, *Applied Catalysis A: General* **2001**, *213*, 225–232.
- [2] R. Zhang, H. Alamdari, S. Kaliaguine, *Journal of Catalysis* **2006**, *242*, 241–253.
- [3] J.-M. Giraudon, A. Elhachimi, F. Wyrwalski, S. Siffert, A. Aboukaïs, J.-F. Lamonier, G. Leclercq, *Applied Catalysis B: Environmental* **2007**, *75*, 157–166.
- [4] A. Eyssler, P. Mandaliev, A. Winkler, P. Hug, O. Safonova, R. Figi, A. Weidenkaff, D. Ferri, *The Journal of Physical Chemistry C* **2010**, *114*, 4584–4594.
- [5] J. A. Anderson, J. L. G. Fierro, *Journal of Solid State Chemistry* **1994**, *108*, 305–313.
- [6] C.-L. Li, C.-L. Wang, Y.-C. Lin, *Catalysis Today* **2011**, *174* (1), Conference Paper, 135–140.
- [7] J.-P. Dacquin, C. Lancelot, C. Dujardin, C. Cordier-Robert, P. Granger, *Journal of Physical Chemistry C* **2011**, *115* (5), 1911–1921.
- [8] J.-P. Dacquin, M. Cabié, C. R. Henry, C. Lancelot, C. Dujardin, S. Raouf, P. Granger, *Journal of Catalysis* **2010**, *270* (2), 299–309.
- [9] Thermo Scientific, XPS Knowledge Base, English, **2014**, <http://xpssimplified.com/periodictable.php> (visited on 2014-06-11).
- [10] P. Miquel, PhD thesis, Université de Lille 1, **2009**.
- [11] Y. Lu, K. A. Michalow, S. K. Matam, A. Winkler, A. E. Maegli, S. Yoon, A. Heel, A. Weidenkaff, D. Ferri, *Applied Catalysis B: Environmental* **2014**, *144*, 631–643.
- [12] P. S. Lambrou, A. M. Efstathiou, *Journal of Catalysis* **2006**, *240* (2), 182–193.
- [13] Y. Renème, F. Dhainaut, M. Trentesaux, B. Ravanbakhsh, P. Granger, C. Dujardin, L. Gengembre, P. L. De Cola, *Surface and Interface Analysis* **2010**, *42*, 530–535.
- [14] N. W. Cant, D. E. Angove, D. C. Chambers, *Applied Catalysis B: Environmental* **1998**, *17*, 63–73.

Conclusion and Prospects

The objective of this study was the development of alternative perovskite catalysts for the exhaust gas treatment of petrol fuelled automotive vehicles. These catalysts were supposed to meet the criteria of 3-way catalysis (TWC), in particular

- high performances on CO, hydrocarbons and NO_x removal according to the Euro 6 regulation for petrol fuelled engines
- simultaneous conversions of all 3 kinds of pollutants at conditions close to the stoichiometry
- high selectivities of non-noxious NO conversion products (N₂)
- high thermal stability

and additionally, of being constituted of available, non-toxic and low-cost materials. The partial replacement of noble metals in 3-way catalysis by optimised Fe-based perovskites was the intention of this study.

The investigation of a commercial TWC and Mn-, Cu- and Fe-based perovskite reference catalysts confirmed the significantly higher intrinsic activity of noble metals emphasizing the challenge of finding a suitable alternative. Among the perovskite catalysts, best catalytic performances were observed for the La₂CuO₄ solid due to its high reducibility leading to Cu segregation. This led to the promotion of specifically metal-like reactions such as propylene reforming which was not clearly observed for LaFeO₃ and LaMnO₃ solids. Furthermore high NO reduction performances were achieved which lead quasi entirely to nitrogen production. However, this catalyst proved unstable under test conditions due to too pronounced phase segregation. LaFeO₃-based perovskites were therefore retained for this study because of their high thermal stability under reducing atmosphere as well as their potential for oxidation *and* reduction catalytic activity. As a consequence of the very interesting catalytic results of La₂CuO₄, the partial substitution of Fe by Cu was investigated later on.

Two main strategies were followed during this study to improve the catalytic performances of Fe-based perovskites, namely the control of the textural properties by investigating the influence of synthesis parameters and the optimisation of the catalysts composition.

Concerning the first approach, it could be shown that the choice of the solvent during sol-gel synthesis has a dramatic impact on the textural properties of the LaFeO₃ perovskite. It was revealed that the use of a hydroalcoholic solution (HAM) instead of water (CCM) has a beneficial impact on the control of the porosity of the resulting perovskite. The attenuated decomposition step ascribed to stronger interactions in the precursor complex lead to more compact samples with a high density of mesopores instead of the broad distribution of macropore sizes observed for the solid prepared in aqueous medium.

A second aspect of this approach consisted in studying the impact of the use of polymer spheres of different sizes (80 nm to 400 nm) during synthesis. The use of soft templates

yielded the intended control of morphology, leading to perovskites with homogeneous macroporous networks with macropores of approximately half the size of the employed template spheres. Merely the use of template spheres lower than 100 nm lead to the partial collapse of the created network during the calcination step attributed to a too low decomposition temperature of the polymer spheres. Occasionally, sintering effects were observed. A remedy for such phenomena was proposed in the form of observing an intermediate cooling. Concerning the 3-way catalytic performances, best results were obtained for the solid with the most regular macroporous network. The good performances, especially for CO oxidation, could not be attributed to the presence of a segregated hematite phase.

Finally, the influence of the calcination procedure and especially the calcination atmosphere was investigated. For all HAM-based solids calcined under *stagnant* atmosphere surprisingly high NO reduction performances under rich and non-rich conditions (HAM*, MSM*) were revealed. In this study, a narrowing down of the crucial parameters was attempted to understand the origins of this catalytic performance enhancement. It could be shown that neither the obtained higher specific surface area, nor any segregated phase or additive coming from the polymer template synthesis could be at the source of this increase in reduction performance under non-rich conditions. Furthermore, only solids prepared from HAM-based precursors – not CCM-based ones – yielded the observed enhanced reduction behaviour confirming the importance of the employed solvent. Finally, the comparison with other calcination atmospheres such as inert gas flow (N₂) and diluted NO flow revealed a detrimental effect on catalytic performances by calcining under inert gas flow, while the solid calcined under NO flow did not yield the same reduction behaviour as the ones calcined under stagnant conditions. Therefore, it was concluded that HAM-based precursors are leading to LaFeO₃ perovskites with extraordinary NO reduction performances under stoichiometric conditions if calcined under conditions of stagnant air atmosphere, probably due to the high humidity. A correlation with the presence of high amounts of better accessible medium-sized mesopores (10 nm < *d* < 30 nm) is assumed.

On the other hand, composition optimisation of the Fe-based perovskites was conducted. Three main approaches were investigated: the composition optimisation of the perovskite surface, partial substitution of the perovskite cations (bulk composition optimisation) and the impregnation with low loadings of noble metals.

Surface composition optimisation, i. e. the lowering of the nominal La-content in LaFeO₃, yielded the intended higher accessibility of catalytically active Fe³⁺ sites on the surface of the perovskites. Low amounts of a probably finely dispersed hematite phase were detected. The co-existence of both phases in strong interaction is supposed to be at the origin of the enhanced catalytic activity of the La_{1-y}FeO₃ solids.

Partial substitution was investigated for A- and B-site cations. The insertion of Ca and Cu cations lead to perovskites which exhibited unit cell contractions attributed mainly to the generation of anionic defects in line with the formation of solid solutions. As expected, the A-site substitution by Ca lead to only minor enhancement of catalytic oxidation performances. On the other hand, B-site substitution by Cu lead to much enhanced oxidation and reduction performances and especially high N₂ selectivities. The high catalytic performances of the Cu-substituted samples was attributed to a higher amount of oxygen vacancies and the higher reducibility of the Cu-substituted perovskites. Despite the high reducibility, the stabilisation of the Cu in the perovskite lattice leading to a good thermal stability of the Cu-containing perovskites was confirmed. The combination of A- and B-site substitution by Ca and Cu showed especially promising results. The bulk composition optimisation approach mainly lead to higher CO oxidation activity. However, NO conversion was also influenced positively,

especially by substitution with Cu – with respect to performance and N₂ selectivity.

The combination of both composition optimisation approaches lead to much enhanced catalytic activities, close to those of the commercial reference for CO oxidation. This was attributed to the simultaneous phase segregation of hematite and copper oxide due to the lowered La-content. Best results were obtained for the La_{0.67}Fe_{0.83}Cu_{0.17}O₃ solid. Performances were higher than for any other CCM perovskite prepared in the framework of this study. Under rich conditions, N₂ selectivity was much higher than for the LaFeO₃ and the commercial TWC. Whereas the La_{0.6}Ca_{0.2}Fe_{0.8}Cu_{0.2}O₃ catalyst showed a remarkable activation over the test cycle leading to performances close to those of the La_{0.67}Fe_{0.83}Cu_{0.17}O₃ solid in the return test, slight deactivation was observed for the La_{0.67}Fe_{0.83}Cu_{0.17}O₃ catalyst which remained, nonetheless, the most catalytically active. In general, CO and C₃H₆ oxidation processes appear to proceed on different sites since the corresponding catalytic activities were found to follow different trends regardless of the followed optimisation approach.

The most promising catalysts obtained by the composition optimisation approaches were finally impregnated with low loadings of noble metals. It was shown that a reductive pretreatment lead to enhanced performances since the noble metals were present in their oxidic forms. Thanks to the high reducibility of the doped solid, the high intrinsic activity of the noble metals and a possibly segregated CuO phase as well as the beneficial interactions with the perovskite support, marked increases in catalytic activity were obtained, especially for Rh/La_{0.8}Ca_{0.2}Fe_{0.8}Cu_{0.2}O₃ and Rh/La_{0.67}Fe_{0.83}Cu_{0.17}O₃ yielding generally high CO and propylene conversions but also high NO reduction performances under rich and stoichiometric conditions. Finally, a test with modified stoichiometric conditions accounting for the residual oxygen due to difficult methane activation was performed for the Rh/La_{0.67}Fe_{0.83}Cu_{0.17}O₃. NO reduction performance increased and occurred over a wide temperature range from 300 °C up to 520 °C – even under stoichiometric conditions, conversions of up to 70 % were achieved under these conditions. Interestingly, even propylene conversion was enhanced and CO oxidation performance remained constantly high. Moreover, the stability of the catalyst was confirmed by return tests for the Rh-doped solids.

Concluding, the high potential of Fe-based perovskites for use in 3-way catalysis could be ascertained using complex feed compositions. While NO and hydrocarbon conversions still need boosting by low amounts of PGM to meet regulations in effect, optimisation of the composition lead to CO conversions in the range of those observed for the commercial reference catalyst. Doping with a low amount of 0.1 wt.% of Rh lead to comparable propylene and propane results as well. Indeed, NO and propylene conversions could also be dramatically improved by combining surface and bulk optimisation approaches for the Fe-based perovskites. Even though NO conversion remains a major challenge under 3-way catalytic conditions, it could be shown that perovskites, especially Cu-substituted ones, are capable of increasing the desired N₂ selectivity.

Prospects This study opens new perspectives for the continuation on many different aspects. Concerning the synthesis parameters, the optimisation of the drying conditions as well as the calcination parameters should be pursued. Understanding the underlying conditions which reign under stagnant atmosphere is the key for understanding the high catalytic activity towards NO reduction of the LaFeO₃ sample. A first step would be to investigate the calcination under humid and/or CO₂-containing flow conditions. After comprehension is reached, this method should also be extended to other compositions and solids. This transfer would allow to further understand whether the process is the same for different compounds. The final goal would be to establish a more easily up-scalable method.

Improving results by the MSM approach could be achieved by conducting the described intermediate cooling step during calcination. Furthermore, the prevention of the collapse of smaller-sized template spheres is important to descend in pore diameter of the final solid. This may be achieved by using functionalised polymer spheres with higher glass and decomposition temperatures. Macroporous perovskites prepared by MSM may be more suited for soot oxidation than for TWC. A combination of this synthesis method with more promising perovskite compositions such as $\text{La}_{0.67}\text{Fe}_{0.83}\text{Cu}_{0.17}\text{O}_3$ could be interesting for the upcoming particulate matter regulations for spark-ignition engines.

In general, a promising prospect would be to further combine different approaches such as the hydroalcoholic method (HAM) and the composition optimisation approach. A more detailed study on different compositions developed from the surface and bulk optimisation approaches would also be helpful to better discern the influence of different parameters on the final composition.

Ageing studies need to be performed in order to confirm the assumption of thermal stability of Fe-based perovskites which was only preliminarily tested by return tests. A critical point to address is the drop in NO conversion at high temperatures under stoichiometric conditions. As shown, this drop could be dampened by a more realistic (modified) stoichiometric feed stream. However, a study on a (low loading) bi-metallic impregnation might help to overcome this problem. Additionally, the influence of adding promoters to the catalytic system should be examined, as should be the influence of the dispersion on a monolith on the catalytic behaviour. Investigating the resistance to sulphur poisoning may also be of interest for the Cu-substituted solids. Finally, before considering the commercialisation of such a system, an up-scaling study would have to be performed.

Synthesis schemes

Concerning the calcination atmosphere, selected syntheses were conducted including a calcination part under so-called stagnant atmosphere (Fig. A.1). This describes a system which is not confined, i. e. pressure compensation is possible, but for which no gas inlet and henceforth no gas flow is imposed.

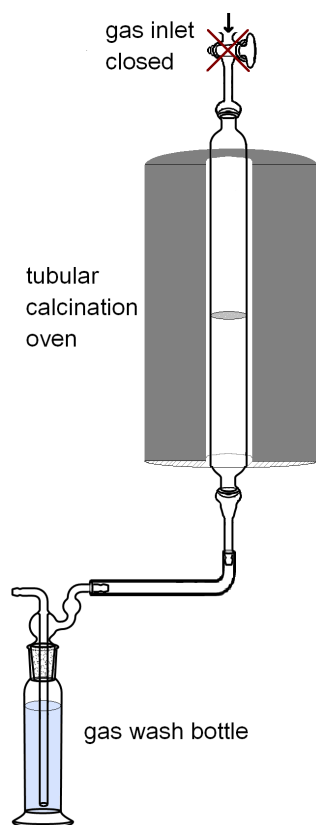


Figure A.1 – **Stagnant conditions scheme.** During calcination under stagnant conditions, no gas inlet exists but pressure compensation is possible via the gas wash bottle.

The basic synthesis steps of the conventional citrate method (CCM), the hydroalcoholic method (HAM) and the macro-structuring method (MSM) are shown in Fig. A.2.

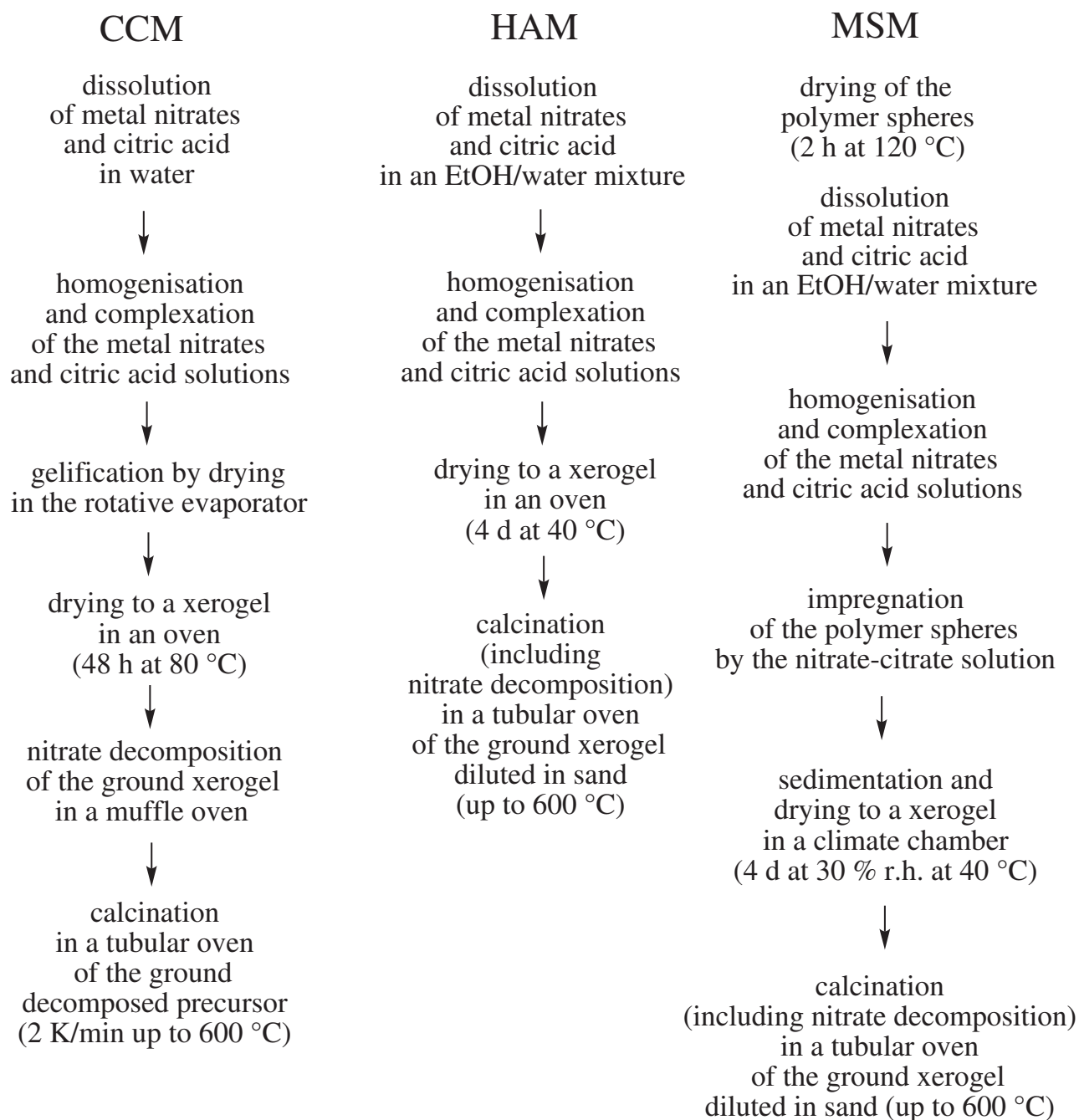


Figure A.2 – The conventional citrate method (CCM), hydroalcoholic method (HAM) and macro-structuring method (MSM).

Appendix B

ICP and XPS results

Table B.1 – Bulk and surface atomic ratios x_A/x_B of calcined perovskite catalysts.

	synthesis method	x_A/x_B	
		ICP	XPS
LaFeO ₃	CCM	1.01	2.13
LaFeO ₃	CCM*	n. a.	2.30
LaFeO ₃	HAM air	n. a.	2.23
LaFeO ₃	HAM N ₂	n. a.	1.17
LaFeO ₃	HAM NO	n. a.	1.40
LaFeO ₃	HAM*	n. a.	n. a.
LaFeO ₃	HAM* _{cooling}	n. a.	2.23
LaFeO ₃	MSM PMMA 80 nm	n. a.	1.41
LaFeO ₃	MSM PS 200 nm	1.02	1.23
LaFeO ₃	MSM _{cooling} PS 400 nm	n. a.	1.82
LaFeO ₃	MSM* PS 400 nm	n. a.	2.18
LaMnO ₃	CCM	n. a.	1.91
La ₂ CuO ₄	CCM	n. a.	2.98
La _{0.67} FeO ₃	CCM	0.66	0.88
LaFe _{0.95} Cu _{0.05} O ₃	CCM	n. a.	1.94
LaFe _{0.9} Cu _{0.1} O ₃	CCM	n. a.	2.08
LaFe _{0.8} Cu _{0.2} FeO ₃	CCM	1.03	1.82
La _{0.9} Ca _{0.1} FeO ₃	CCM	n. a.	1.94
La _{0.8} Ca _{0.2} FeO ₃	CCM	n. a.	2.08
La _{0.9} Ca _{0.1} Fe _{0.9} Cu _{0.1} O ₃	CCM	1.01	1.74
La _{0.8} Ca _{0.2} Fe _{0.8} Cu _{0.2} O ₃	CCM	1.02	1.65
La _{0.6} Ca _{0.2} Fe _{0.8} Cu _{0.2} O ₃	CCM	n. a.	1.27
La _{0.67} Fe _{0.83} Cu _{0.17} O ₃	CCM	0.68	1.03
La _{0.8} Ca _{0.2} Fe _{0.8} Cu _{0.2} O ₃ + 0.1 wt.% Pd	CCM	1.01	1.36

Table B.2 – Comparison of surface compositions derived from XPS of perovskite catalysts prepared by CCM, and post-HTXRD samples.

nominal composition		surface composition based on nominal Fe content
LaFeO ₃	calcined	La _{2.13} FeO _{4.63} (C _{3.66})
LaFeO ₃	post-HTXRD	La _{1.64} FeO _{5.20} (C _{9.36})
LaMnO ₃	calcined	La _{1.91} MnO _{3.88} (C _{2.24})
La ₂ CuO ₄	calcined	La _{2.98} CuO _{9.69} (C _{7.39})
La ₂ CuO ₄	post-HTXRD	La _{4.75} CuO _{10.10} (C _{6.08})
La _{0.9} FeO ₃	calcined	La _{1.64} FeO _{3.48} (C _{2.32})
La _{0.8} FeO ₃	calcined	La _{1.31} FeO _{2.70} (C _{1.48})
La _{0.67} FeO ₃	calcined	La _{0.88} FeO _{3.08} (C _{1.84})
LaFe _{0.95} Cu _{0.15} O ₃	calcined	La _{1.98} Fe _{0.95} Cu _{0.07} O _{5.57} (C _{4.26})
LaFe _{0.95} Cu _{0.15} O ₃	post-HTXRD	La _{2.29} Fe _{0.95} Cu _{0.13} O _{6.25} (C _{3.60})
LaFe _{0.9} Cu _{0.1} O ₃	calcined	La _{2.12} Fe _{0.90} Cu _{0.13} O _{5.39} (C _{2.81})
LaFe _{0.9} Cu _{0.1} O ₃	post-HTXRD	La _{1.69} Fe _{0.90} Cu _{0.13} O _{6.11} (C _{3.45})
LaFe _{0.8} Cu _{0.2} O ₃	calcined	La _{1.62} Fe _{0.80} Cu _{0.24} O _{4.53} (C _{2.61})
LaFe _{0.8} Cu _{0.2} O ₃	post-HTXRD	La _{1.41} Fe _{0.80} Cu _{0.33} O _{4.99} (C _{2.67})
La _{0.9} Ca _{0.1} FeO ₃	calcined	La _{1.77} Ca _{0.17} Fe _{1.00} O _{4.04} (C _{2.69})
La _{0.8} Ca _{0.2} FeO ₃	calcined	La _{1.71} Ca _{0.37} Fe _{1.00} O _{4.10} (C _{2.38})
La _{0.9} Ca _{0.1} Fe _{0.9} Cu _{0.1} O ₃	calcined	La _{1.63} Ca _{0.34} Fe _{0.90} Cu _{0.23} O _{4.91} (C _{4.82})
La _{0.8} Ca _{0.2} Fe _{0.8} Cu _{0.2} O ₃	calcined	La _{1.32} Ca _{0.45} Fe _{0.80} Cu _{0.27} O _{4.62} (C _{4.06})
La _{0.6} Ca _{0.2} Fe _{0.8} Cu _{0.2} O ₃	calcined	La _{0.62} Ca _{0.20} Fe _{0.73} Cu _{0.17} O _{1.92} (C _{0.86})
La _{0.67} Fe _{0.83} Cu _{0.17} O ₃	calcined	La _{1.05} Fe _{0.83} Cu _{0.18} O _{2.42} (C _{1.50})

Table B.3 – Comparison of surface compositions derived from XPS of LaFeO₃ catalysts.

synthesis method	surface composition based on Fe
CCM	La _{2.13} FeO _{4.63} (C _{3.66})
CCM*	La _{2.30} FeO _{4.06} (C _{1.80})
HAM air	La _{2.23} FeO _{3.91} (C _{1.88})
HAM N ₂	La _{1.17} FeO _{4.12} (C _{2.08})
HAM NO	La _{1.40} FeO _{3.11} (C _{1.80})
HAM* _{cooling}	La _{2.23} FeO _{4.04} (C _{1.90})
MSM PMMA 80 nm	La _{3.70} FeO _{3.10} (C _{1.09})
MSM PS 200 nm	La _{1.22} FeO _{4.08} (C _{1.93})
MSM _{cooling} PS 400 nm	La _{1.82} FeO _{4.49} (C _{3.17})
MSM* PS 400 nm	La _{2.18} FeO _{4.25} (C _{1.92})

Table B.4 – Comparison of photopeak maxima of perovskites prepared by CCM.

B. E. (eV)		La 3d _{5/2}	Ca 2p _{3/2}	Fe 2p _{3/2}	Cu 2p _{3/2}	O 1s
LaFeO ₃	calcined	834.3	-	710.8	-	529.5
LaFeO ₃	post-HTXRD	834.4	-	710.4	-	529.6
La ₂ CuO ₄	calcined	835.2	-	-	933.1	531.7
La ₂ CuO ₄	post-HTXRD	837.7	-	-	932.7	531.3
La _{0.9} FeO ₃	calcined	834.3	-	710.5	-	529.5
La _{0.8} FeO ₃	calcined	834.3	-	710.4	-	529.7
La _{0.67} FeO ₃	calcined	834.3	-	710.6	-	529.6
LaFe _{0.95} Cu _{0.15} O ₃	calcined	833.9	-	710.1	933.0	529.1
LaFe _{0.95} Cu _{0.15} O ₃	post-HTXRD	834.2	-	710.3	932.9	529.0
LaFe _{0.9} Cu _{0.1} O ₃	calcined	833.9	-	710.3	933.0	528.9
LaFe _{0.9} Cu _{0.1} O ₃	post-HTXRD	834.2	-	710.2	932.9	529.2
LaFe _{0.8} Cu _{0.2} O ₃	calcined	833.9	-	710.1	933.2	528.9
LaFe _{0.8} Cu _{0.2} O ₃	post-HTXRD	833.9	-	709.7	933.5	528.8
La _{0.9} Ca _{0.1} FeO ₃	calcined	833.7	346.1	709.9	-	529.0
La _{0.8} Ca _{0.2} FeO ₃	calcined	833.9	346.6	710.3	-	529.0
La _{0.9} Ca _{0.1} Fe _{0.9} Cu _{0.1} O ₃	calcined	834.1	347.2	710.2	932.9	529.2
La _{0.8} Ca _{0.2} Fe _{0.8} Cu _{0.2} O ₃	calcined	833.6	346.8	710.2	933.1	528.8
La _{0.67} Fe _{0.83} Cu _{0.17} O ₃	calcined	834.5	-	710.9	933.1	530.0
La _{0.6} Ca _{0.2} Fe _{0.8} Cu _{0.2} O ₃	calcined	833.9	346.0	710.1	933.4	529.2

Table B.5 – Comparison of photopeak maxima of calcined LaFeO₃ catalysts prepared by different synthesis methods.

B. E. (eV)	La 3d _{5/2}	Fe 2p _{3/2}	O 1s	C 1s
CCM	834.3	710.8	529.5	285.0
CCM*	834.4	710.6	529.4	285.0
HAM air	834.1	710.1	529.2	285.0
HAM N ₂	834.1	710.1	529.4	285.0
HAM NO	834.6	710.8	529.5	285.0
HAM* _{cooling}	834.1	710.1	529.2	285.0
MSM PMMA 80 nm	833.7	710.0	528.7	284.3
MSM PS 200 nm	833.7	710.3	529.1	284.8
MSM _{cooling} PS 400 nm	833.7	709.7	528.8	284.1
MSM* PS 400 nm	834.1	710.2	529.3	285.0

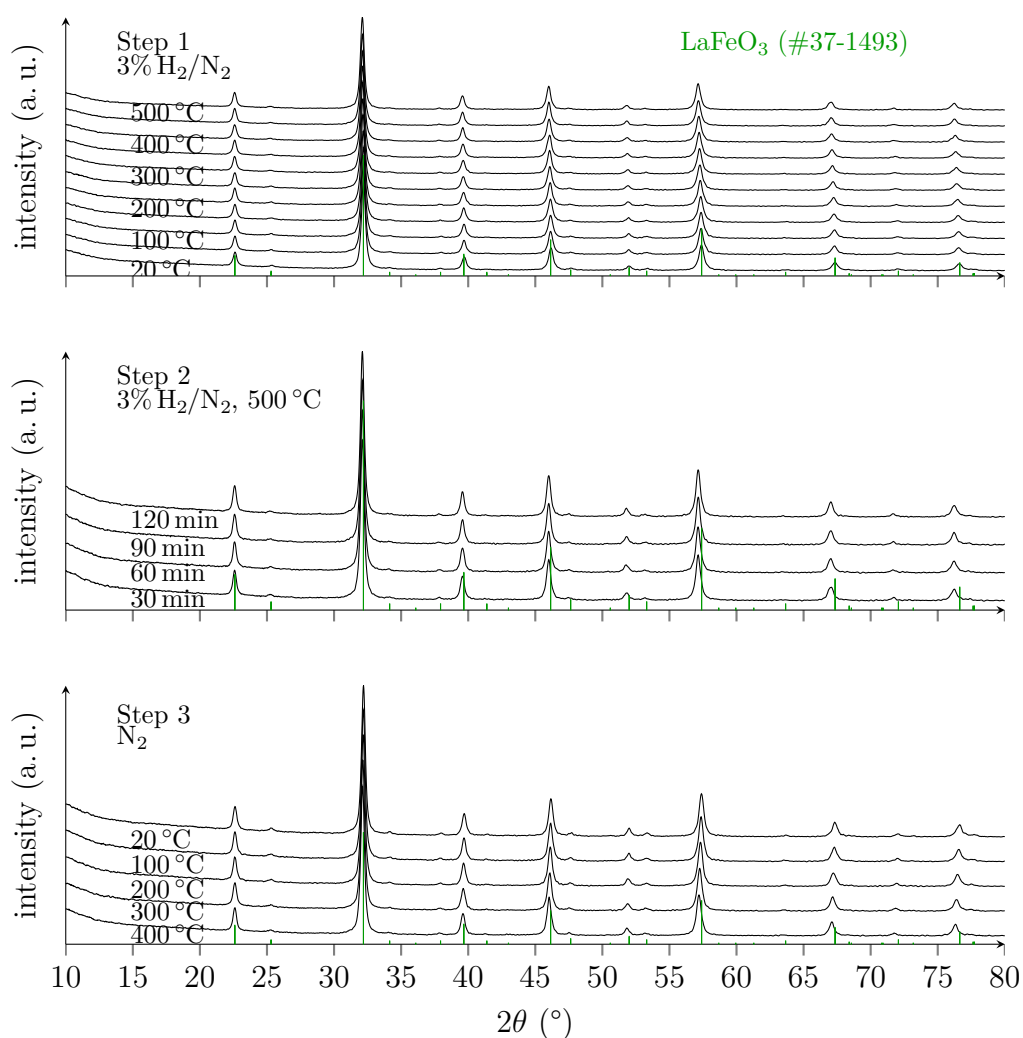
HTXRD results $\text{LaFe}_{1-x}\text{Cu}_x\text{O}_3$ ($x = 0.05, 0.1$)

Figure C.1 – High Temperature X-ray diffractograms of $\text{LaFe}_{0.95}\text{Cu}_{0.2}\text{O}_3$ (CCM). Step 1 corresponds to a heating ramp under reductive atmosphere (3 Vol.% H_2/N_2), Step 2 to the corresponding plateau and Step 3 to the subsequent cooling under inert atmosphere. Scheme in Fig. 2.5.

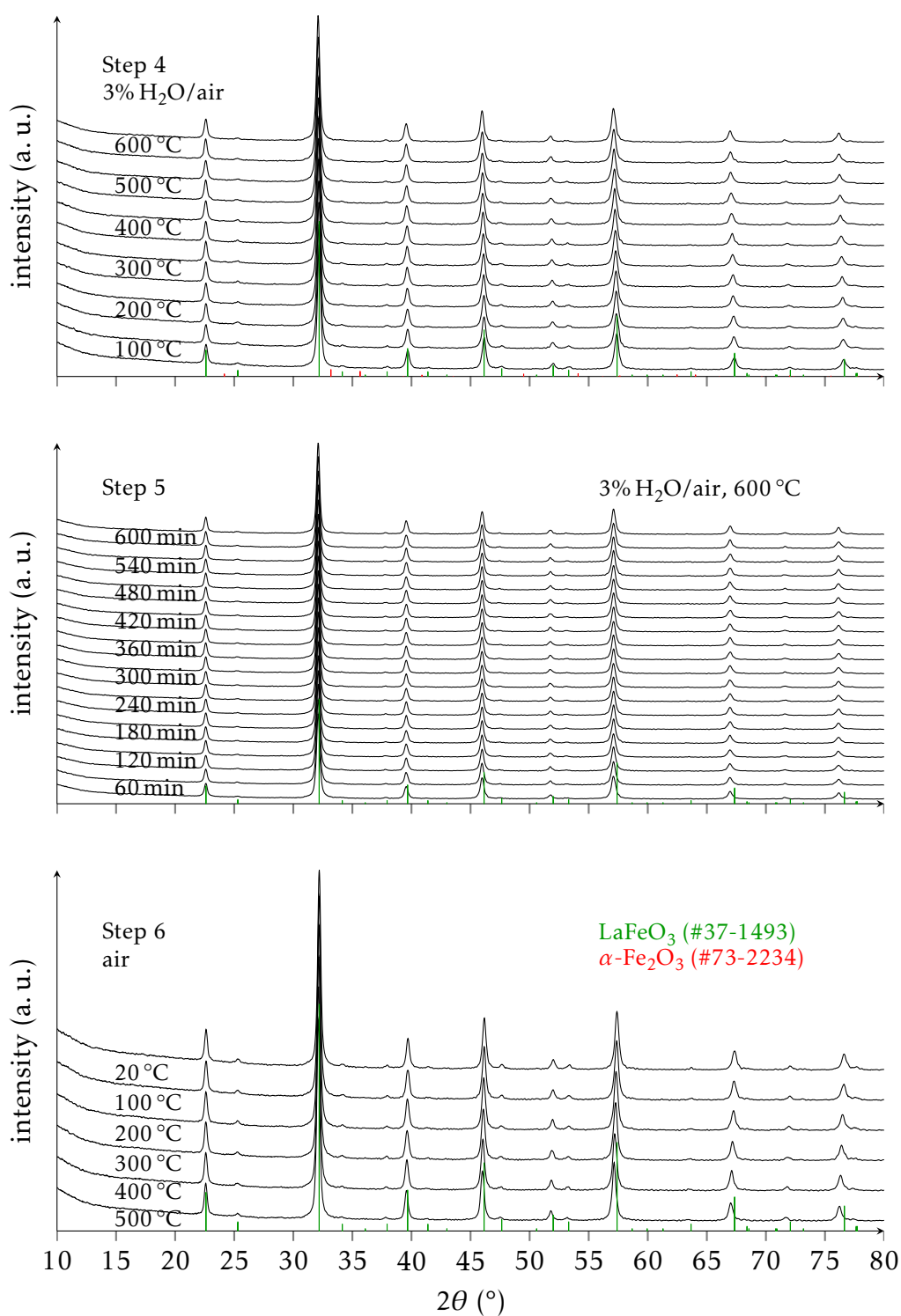


Figure C.2 – High Temperature X-ray diffractograms of $\text{LaFe}_{0.95}\text{Cu}_{0.2}\text{O}_3$ (CCM). Step 4 corresponds to a heating ramp under humid air flow up to 600 °C, Step 5 to the corresponding plateau and Step 6 to the subsequent cooling under dry air flow. Scheme in Fig. 2.5.

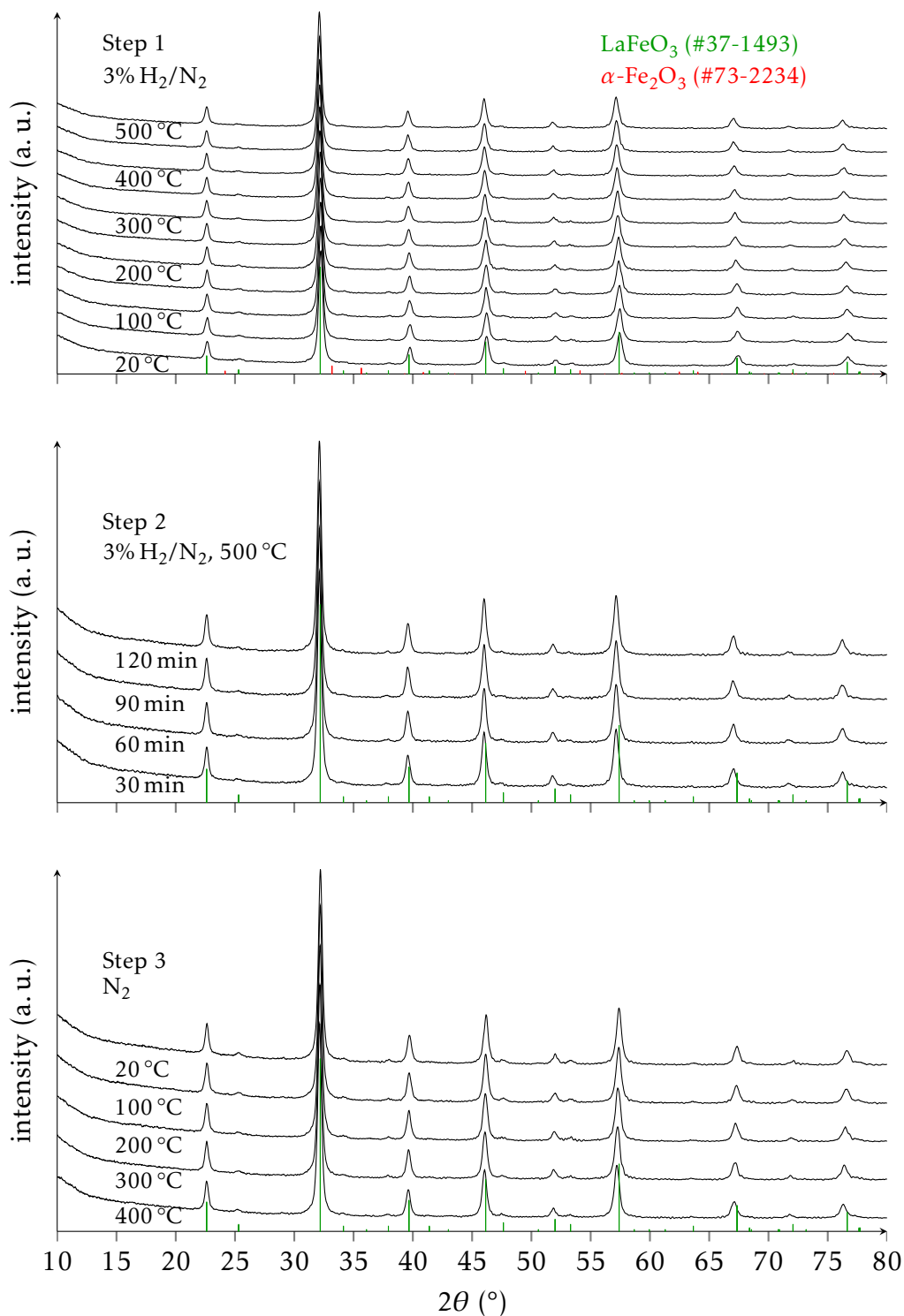


Figure C.3 – High Temperature X-ray diffractograms of $\text{LaFe}_{0.9}\text{Cu}_{0.1}\text{O}_3$ (CCM). Step 1 corresponds to a heating ramp under reductive atmosphere (3 Vol.% H_2/N_2), Step 2 to the corresponding plateau and Step 3 to the subsequent cooling under inert atmosphere. Scheme in Fig. 2.5.

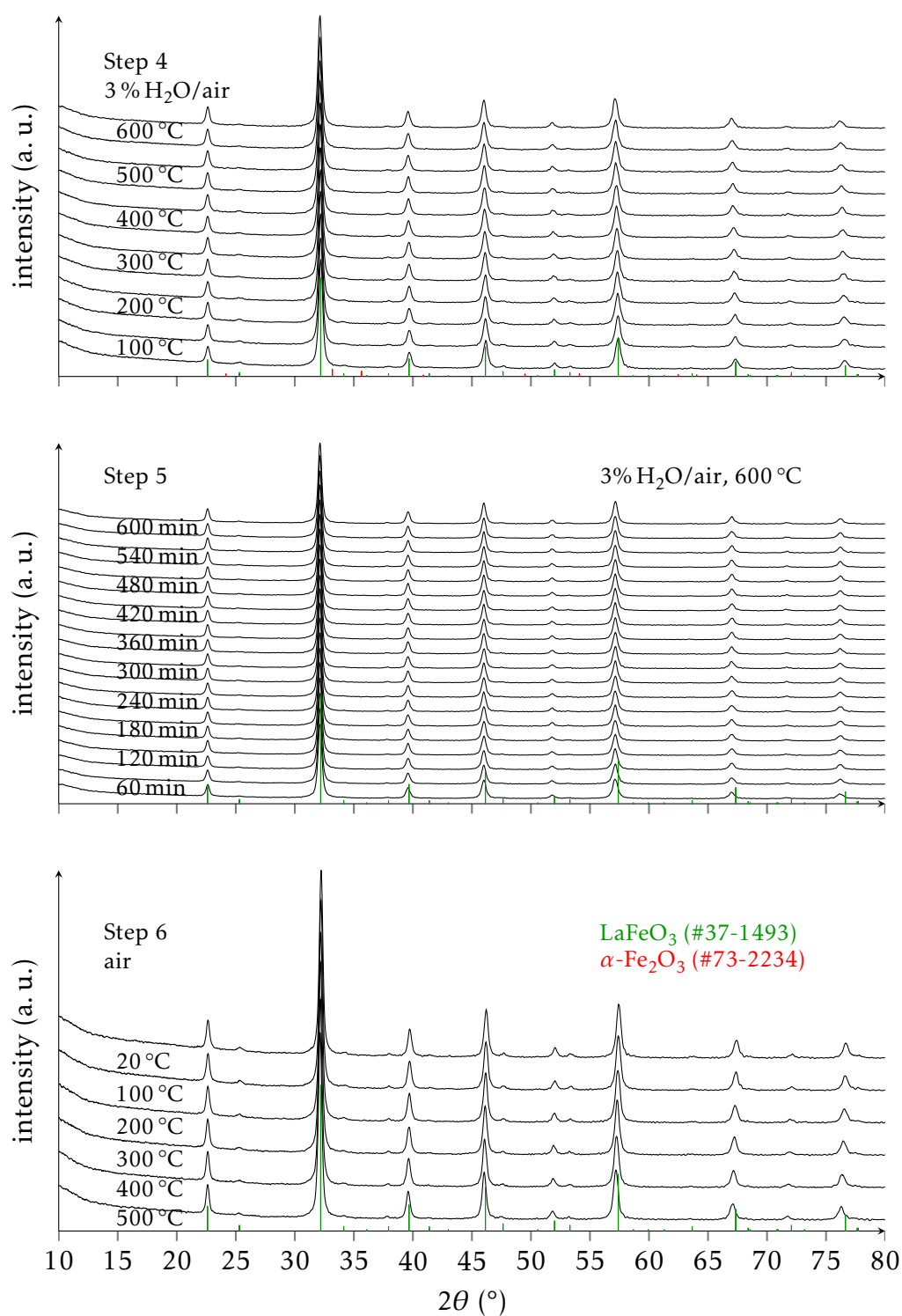


Figure C.4 – High Temperature X-ray diffractograms of $\text{LaFe}_{0.9}\text{Cu}_{0.1}\text{O}_3$ (CCM). Step 4 corresponds to a heating ramp under humid air flow up to 600 °C, Step 5 to the corresponding plateau and Step 6 to the subsequent cooling under dry air flow. Scheme in Fig. 2.5.

Additional catalytic activity test results

D.1 Influence of synthesis parameters on properties of LaFeO₃

C₃H₈, O₂ and H₂ conversions of LaFeO₃ catalysts prepared by HAM NO and HAM* are reported in Fig. D.1.

N₂, N₂O and NH₃ selectivities and yields of LaFeO₃ catalyst prepared by HAM* and MSM* (PS 400 nm) compared to the commercial reference catalyst are depicted in Fig. D.2 and D.3.

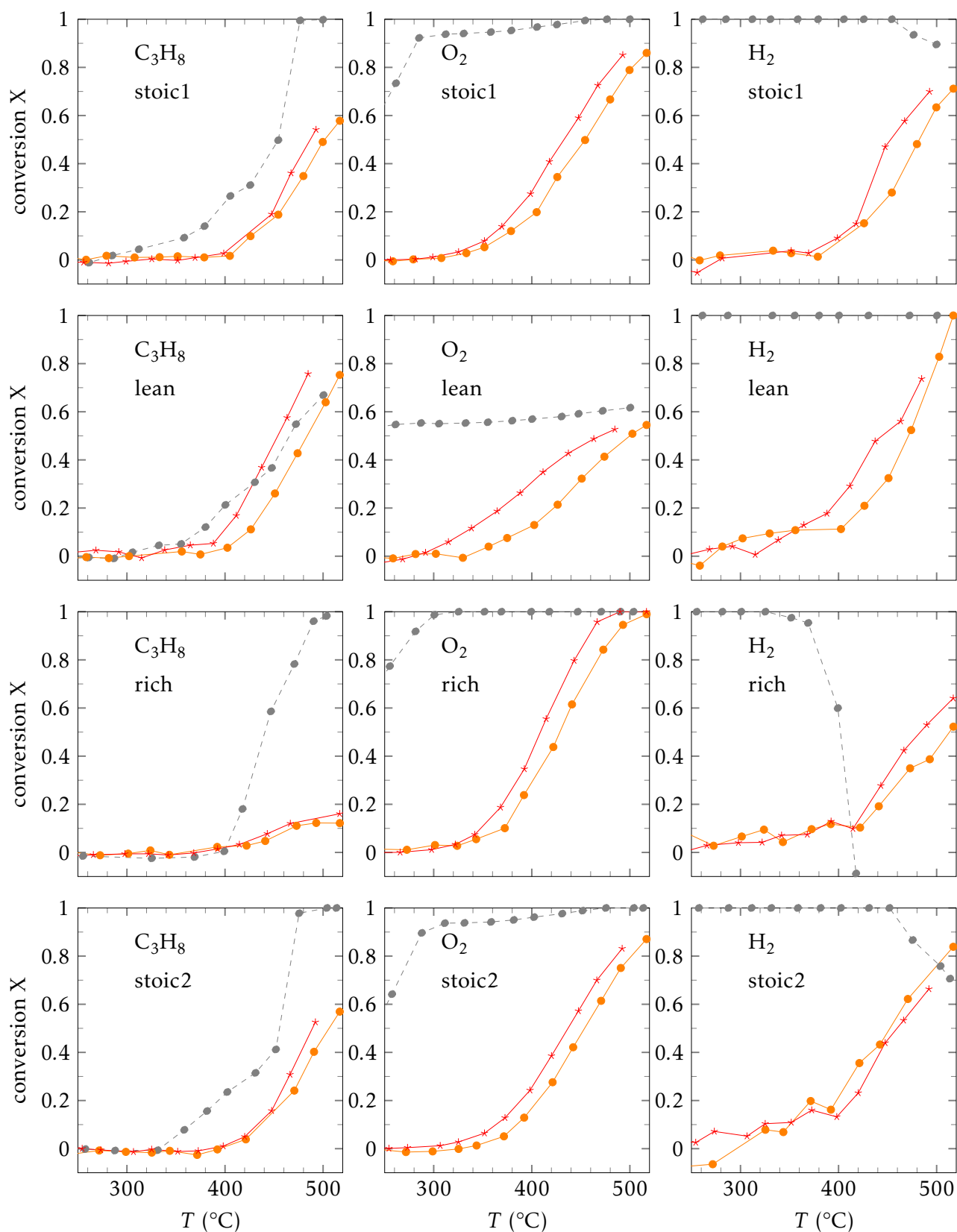


Figure D.1 – C_3H_8 , O_2 and H_2 conversions of $LaFeO_3$ catalysts prepared by HAM NO and HAM*. HAM NO (\bullet), and HAM* (\star) compared to the commercial reference (\circ)

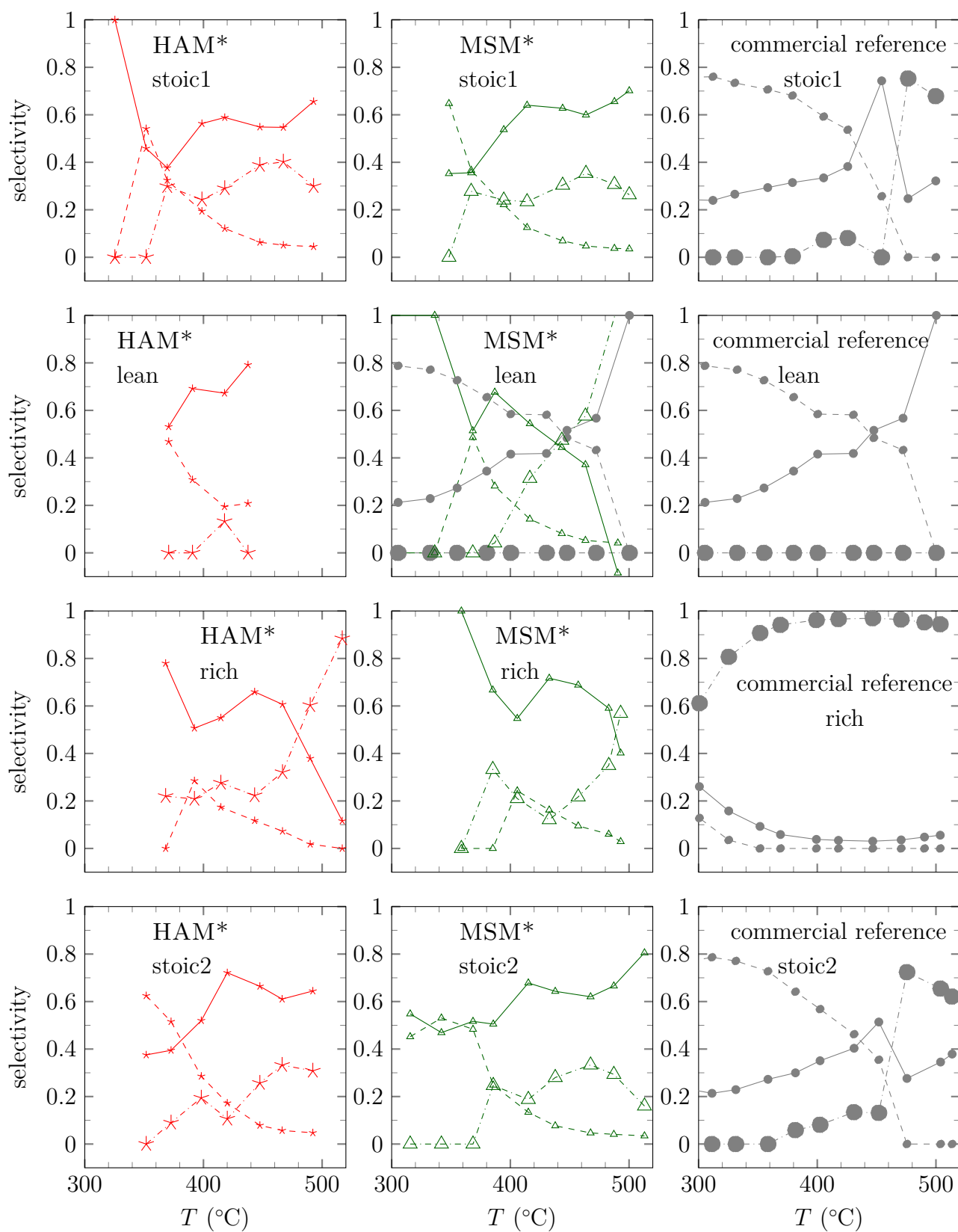


Figure D.2 – N_2 , N_2O and NH_3 selectivities of NO conversion of LaFeO_3 catalyst prepared by HAM* compared to the solid obtained by MSM* (PS 400 nm). HAM* (★) compared to MSM* PS 400 nm (△) and the commercial reference (●); S_{N_2} (solid), $S_{\text{N}_2\text{O}}$ (dashed), S_{NH_3} (dashdotted, big mark)

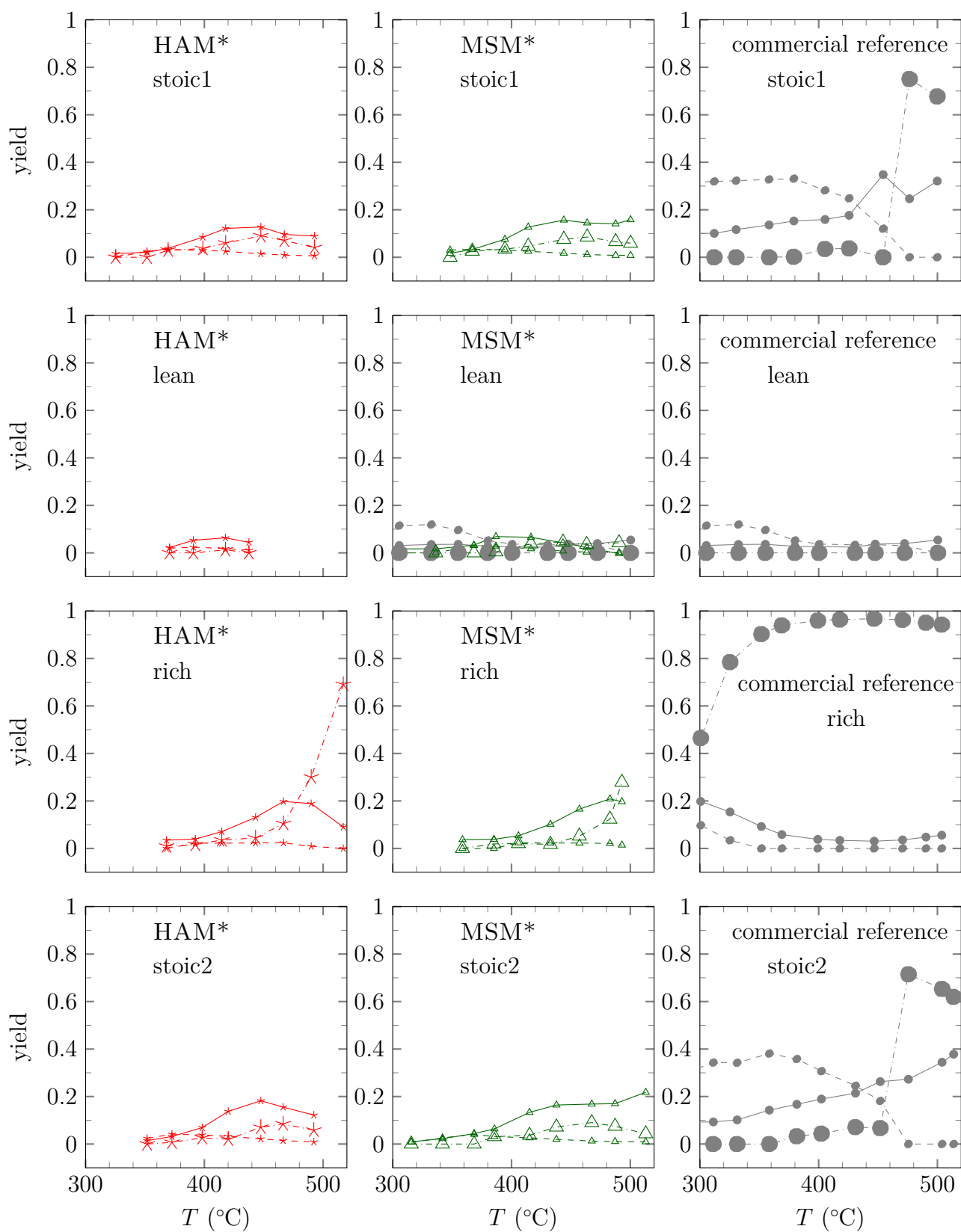


Figure D.3 – N_2 , N_2O and NH_3 yields of NO conversion of LaFeO_3 catalyst prepared by HAM* compared to the solid obtained by MSM* (PS 400 nm). HAM* (\star) compared to MSM* PS 400 nm (\triangle) and the commercial reference (\bullet); Y_{N_2} (solid), $Y_{\text{N}_2\text{O}}$ (dashed), Y_{NH_3} (dashdotted, big mark)

D.2 Composition optimisation

Temperatures corresponding to 50 % conversions of NO, CO, CH₄, C₃H₆, C₃H₈, H₂, and O₂ for all the successively conducted test conditions – stoichiometric, lean, and rich concluded by a return test under stoichiometric conditions – for

- La_{1-y}FeO₃ prepared by CCM are listed in Table D.1. The Arrhenius plots corresponding to the initial stoichiometric test ramps are depicted in Fig. D.4.
- La_{1-x}Ca_xFeO₃ prepared by CCM are listed in Table D.2
- LaFe_{1-x}Cu_xO₃ prepared by CCM are listed in Table D.3. The Arrhenius plots corresponding to the initial stoichiometric test ramps are depicted in Fig. D.5.
- La_{1-x}Ca_xFe_{1-x}Cu_xO₃ prepared by CCM are listed in Table D.4. The Arrhenius plots corresponding to the initial stoichiometric test ramps are depicted in Fig. D.6.
- for La_{0.67}Fe_{0.83}Cu_{0.17}O₃ and La_{0.6}Ca_{0.2}Fe_{0.8}Cu_{0.2}O₃ prepared by CCM are listed in Table D.5. The Arrhenius plots corresponding to the stoichiometric test ramps are depicted in Fig. D.7.

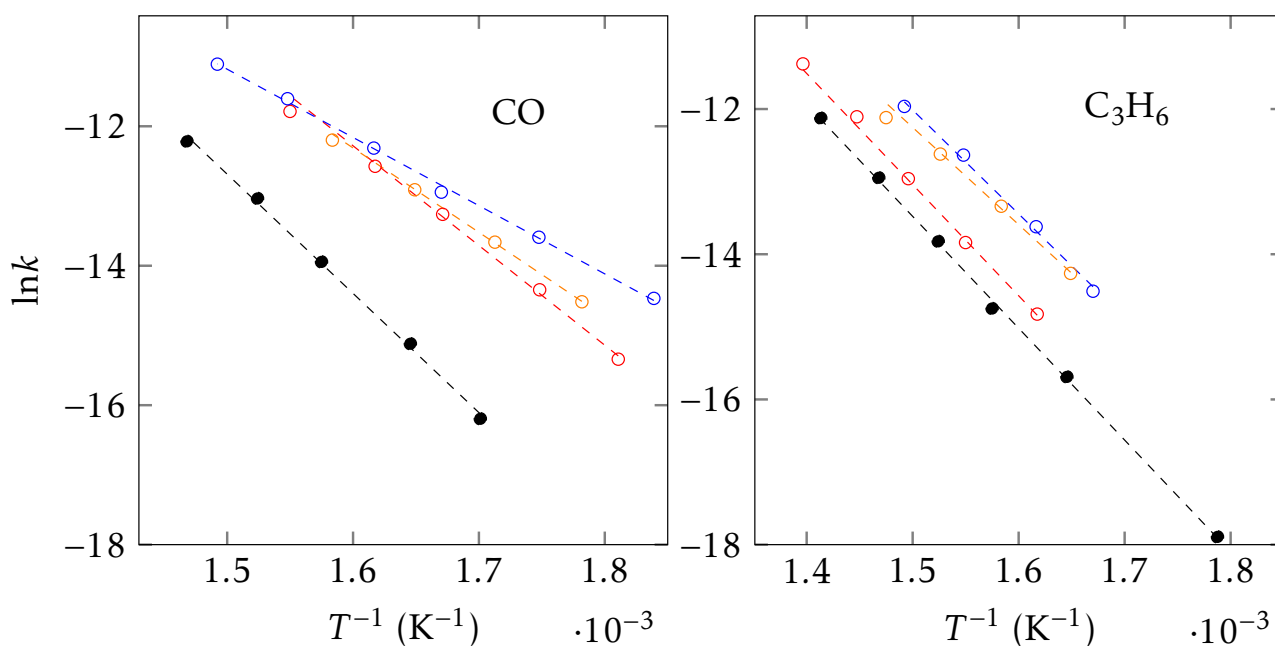


Figure D.4 – Arrhenius plots of CO and C₃H₆ conversion under stoichiometric conditions for LaFeO₃ (•), La_{0.9}FeO₃ (◦), La_{0.8}FeO₃ (◦), and La_{0.67}FeO₃ (◦).

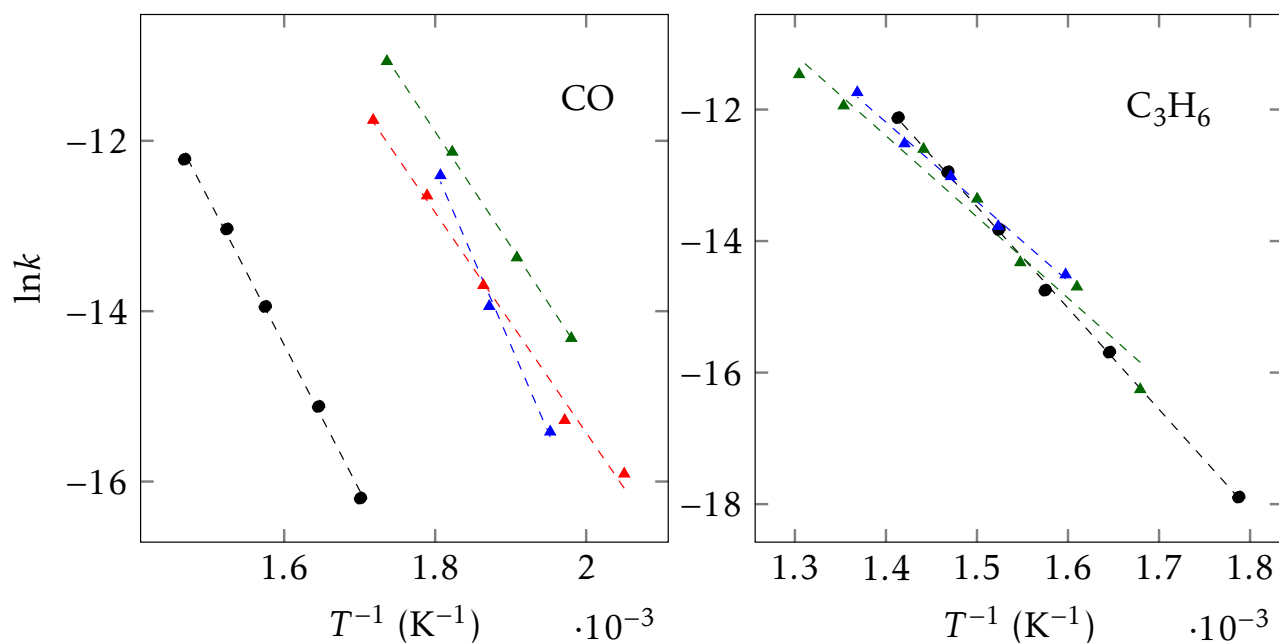


Figure D.5 – Arrhenius plots of CO and C_3H_6 conversion under stoichiometric conditions for $LaFe_{1-x}Cu_xO_3$ ($x = 0, 0.05, 0.1, 0.2$; CCM). $LaFeO_3$ (\bullet), $LaFe_{0.95}Cu_{0.05}O_3$ (\blacktriangle), $LaFe_{0.9}Cu_{0.1}O_3$ (\blacktriangle), and $LaFe_{0.8}Cu_{0.2}O_3$ (\blacktriangle)

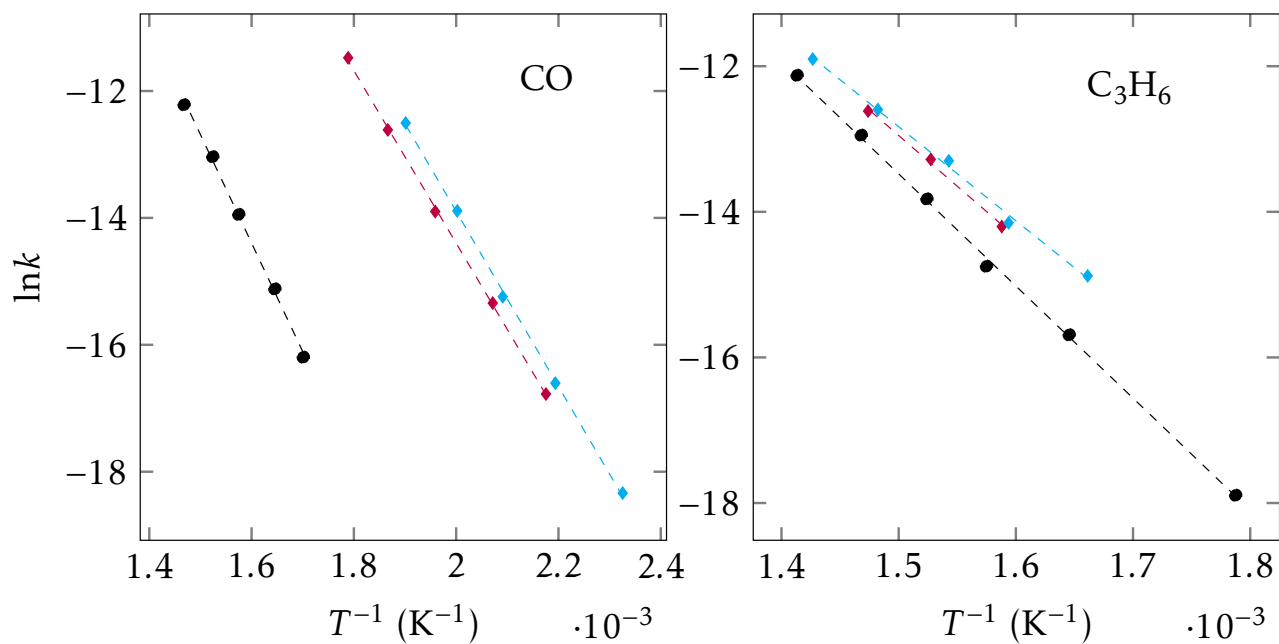


Figure D.6 – Arrhenius plots of CO and C_3H_6 conversion under stoichiometric conditions for $La_{1-x}Ca_xFe_{1-x}Cu_xO_3$ ($x = 0, 0.1, 0.2$; CCM). $LaFeO_3$ (\bullet), $La_{0.9}Ca_{0.1}Fe_{0.9}Cu_{0.1}O_3$ (\blacklozenge), and $La_{0.8}Ca_{0.2}Fe_{0.8}Cu_{0.2}O_3$ (\blacklozenge)

Table D.1 – Temperatures corresponding to 50 % conversion of NO, CO, CH₄, C₃H₆, C₃H₈, H₂, and O₂ of La_{1-y}FeO₃ catalysts (y = 0, 0.1, 0.2, 0.33) compared to hematite and a mechanical mixture of LaFeO₃ and Fe₂O₃.

solid	T ₅₀ (°C)						
	NO	CO	CH ₄	C ₃ H ₆	C ₃ H ₈	H ₂	O ₂
stoichiometric 1st run							
LaFeO ₃	-	438	-	463	478	499	450
La _{0.9} FeO ₃	-	386	-	443	467	439	423
La _{0.8} FeO ₃	-	414	-	431	499	433	424
La _{0.67} FeO ₃	-	384	-	420	497	471	413
Fe ₂ O ₃	-	460	-	490	-	493	483
mixture ^a	-	436	-	465	482	486	454
lean							
LaFeO ₃	-	436	-	449	467	484	502
La _{0.9} FeO ₃	-	389	-	430	446	424	479
La _{0.8} FeO ₃	-	392	-	423	474	426	471
La _{0.67} FeO ₃	-	386	-	408	465	441	461
Fe ₂ O ₃	-	462	-	485	-	511	-
mixture ^a	-	432	-	454	471	485	495
rich							
LaFeO ₃	^{-b}	442	-	-	-	-	434
La _{0.9} FeO ₃	512	389	-	-	-	474	397
La _{0.8} FeO ₃	488	398	-	434	328	-	391
La _{0.67} FeO ₃	479	387	-	420	-	497	383
Fe ₂ O ₃	^{-b}	463	-	492	-	-	452
mixture ^a	^{-b}	443	-	-	-	512	438
stoichiometric return test							
LaFeO ₃	-	443	-	469	481	496	458
La _{0.9} FeO ₃	-	375	-	433	461	375	409
La _{0.8} FeO ₃	-	392	-	435	493	462	414
La _{0.67} FeO ₃	-	384	-	421	484	457	411
Fe ₂ O ₃	-	405	-	486	-	484	485
mixture ^a	-	439	-	470	488	497	458

^a Mechanical mixture of LaFeO₃ and Fe₂O₃.

^b Conversion lower than 50 %.

Table D.2 – Temperatures corresponding to 50 % conversion of NO, CO, CH₄, C₃H₆, C₃H₈, H₂, and O₂ of La_{1-x}Ca_xFeO₃ catalysts (x = 0, 0.1, 0.2).

solid	T ₅₀ (°C)						
	NO	CO	CH ₄	C ₃ H ₆	C ₃ H ₈	H ₂	O ₂
stoichiometric 1st run							
LaFeO ₃	-	438	-	463	478	499	450
La _{0.9} Ca _{0.1} FeO ₃	-	414	-	446	461	463	430
La _{0.8} Ca _{0.2} FeO ₃	-	449	-	482	499	482	466
lean							
LaFeO ₃	-	436	-	449	467	484	502
La _{0.9} Ca _{0.1} FeO ₃	-	411	-	441	455	462	478
La _{0.8} Ca _{0.2} FeO ₃	-	430	-	484	494	485	-
rich							
LaFeO ₃	- ^a	442	-	-	-	-	434
La _{0.9} Ca _{0.1} FeO ₃	499 ^b	416	-	-	-	500	413
La _{0.8} Ca _{0.2} FeO ₃	510 ^b	440	-	-	-	510	446
stoichiometric return test							
LaFeO ₃	-	443	-	469	481	496	458
La _{0.9} Ca _{0.1} FeO ₃	-	413	-	453	470	484	436
La _{0.8} Ca _{0.2} FeO ₃	-	439	-	493	510	494	474

^a Conversion lower than 50 %.

^b T₂₅.

Table D.3 – Temperatures corresponding to 50 % conversion of NO, CO, CH₄, C₃H₆, C₃H₈, H₂, and O₂ of LaFe_{1-x}Cu_xO₃ catalysts (x = 0, 0.1, 0.2).

solid	T ₅₀ (°C)						
	NO	CO	CH ₄	C ₃ H ₆	C ₃ H ₈	H ₂	O ₂
stoichiometric 1st run							
LaFeO ₃	-	438	-	463	478	499	450
LaFe _{0.95} Cu _{0.05} O ₃	-	328	-	510	n. a.	440	398
LaFe _{0.9} Cu _{0.1} O ₃	-	305	-	469	467 ^b	444	384
LaFe _{0.8} Cu _{0.2} O ₃	-	294	-	497	505 ^b	421	377
lean							
LaFeO ₃	-	436	-	449	467	484	502
LaFe _{0.95} Cu _{0.05} O ₃	-	327	-	461	484	430	477
LaFe _{0.9} Cu _{0.1} O ₃	-	308	-	461	482	444	479
LaFe _{0.8} Cu _{0.2} O ₃	-	296	-	490	512	436	472
rich							
LaFeO ₃	- ^a	442	-	-	-	-	434
LaFe _{0.95} Cu _{0.05} O ₃	485	328	-	484 ^b	-	447	344
LaFe _{0.9} Cu _{0.1} O ₃	489	306	-	510 ^b	-	446	319
LaFe _{0.8} Cu _{0.2} O ₃	501 ^b	296	-	459 ^b	-	449	318
stoichiometric return test							
LaFeO ₃	-	443	-	469	481	496	458
LaFe _{0.95} Cu _{0.05} O ₃	-	321	-	466	501	421	371
LaFe _{0.9} Cu _{0.1} O ₃	-	324	-	472	513	443	385
LaFe _{0.8} Cu _{0.2} O ₃	-	306	-	455	487 ^b	388	342

^a Conversion lower than 50 %.^b T₂₅.

Table D.4 – Temperatures corresponding to 50 % conversion of NO, CO, CH₄, C₃H₆, C₃H₈, H₂, and O₂ of La_{1-x}Ca_xFe_{1-x}Cu_xO₃ catalysts (x = 0, 0.1, 0.2).

solid	T ₅₀ (°C)						
	NO	CO	CH ₄	C ₃ H ₆	C ₃ H ₈	H ₂	O ₂
stoichiometric 1st run							
LaFeO ₃	-	438	-	463	478	499	450
La _{0.9} Ca _{0.1} Fe _{0.9} Cu _{0.1} O ₃	-	288	-	456	488	437	369
La _{0.8} Ca _{0.2} Fe _{0.8} Cu _{0.2} O ₃	-	279	-	449	487	399	326
lean							
LaFeO ₃	-	436	-	449	467	484	502
La _{0.9} Ca _{0.1} Fe _{0.9} Cu _{0.1} O ₃	-	285	-	437	461	404	465
La _{0.8} Ca _{0.2} Fe _{0.8} Cu _{0.2} O ₃	-	280	-	432	458	402	436
rich							
LaFeO ₃	- ^a	442	-	-	-	-	434
La _{0.9} Ca _{0.1} Fe _{0.9} Cu _{0.1} O ₃	478	288	-	-	-	423	301
La _{0.8} Ca _{0.2} Fe _{0.8} Cu _{0.2} O ₃	469	284	-	-	-	429	291
stoichiometric return test							
LaFeO ₃	-	443	-	469	481	496	458
La _{0.9} Ca _{0.1} Fe _{0.9} Cu _{0.1} O ₃	-	291	-	450	491	435	359
La _{0.8} Ca _{0.2} Fe _{0.8} Cu _{0.2} O ₃	-	284	-	443	489	398	319

^a Conversion lower than 50 %.Table D.5 – Temperatures corresponding to 50 % conversion of NO, CO, CH₄, C₃H₆, C₃H₈, H₂, and O₂ of La_{1-x}Ca_xFe_{1-x}Cu_xO₃ catalysts (x = 0, 0.1, 0.2).

solid	T ₅₀ (°C)						
	NO	CO	CH ₄	C ₃ H ₆	C ₃ H ₈	H ₂	O ₂
stoichiometric 1st run							
LaFeO ₃	-	438	-	463	478	499	450
La _{0.6} Ca _{0.2} Fe _{0.8} Cu _{0.2} O ₃	-	311	-	444	465	407	370
La _{0.67} Fe _{0.83} Cu _{0.17} O ₃	-	232	-	386	458 ^b	344	293
lean							
LaFeO ₃	-	436	-	449	467	484	502
La _{0.6} Ca _{0.2} Fe _{0.8} Cu _{0.2} O ₃	-	298	-	417	441	382	432
La _{0.67} Fe _{0.83} Cu _{0.17} O ₃	-	235	-	374	450	346	354
rich							
LaFeO ₃	- ^a	442	-	-	-	-	434
La _{0.6} Ca _{0.2} Fe _{0.8} Cu _{0.2} O ₃	477	302	-	484	-	394	314
La _{0.67} Fe _{0.83} Cu _{0.17} O ₃	438	235	-	446	-	341	254
stoichiometric return test							
LaFeO ₃	-	443	-	469	481	496	458
La _{0.6} Ca _{0.2} Fe _{0.8} Cu _{0.2} O ₃	-	274	-	419	462	345	311
La _{0.67} Fe _{0.83} Cu _{0.17} O ₃	-	255	-	390	449 ^b	341	293

^a Conversion lower than 50 %.^b T₂₅.

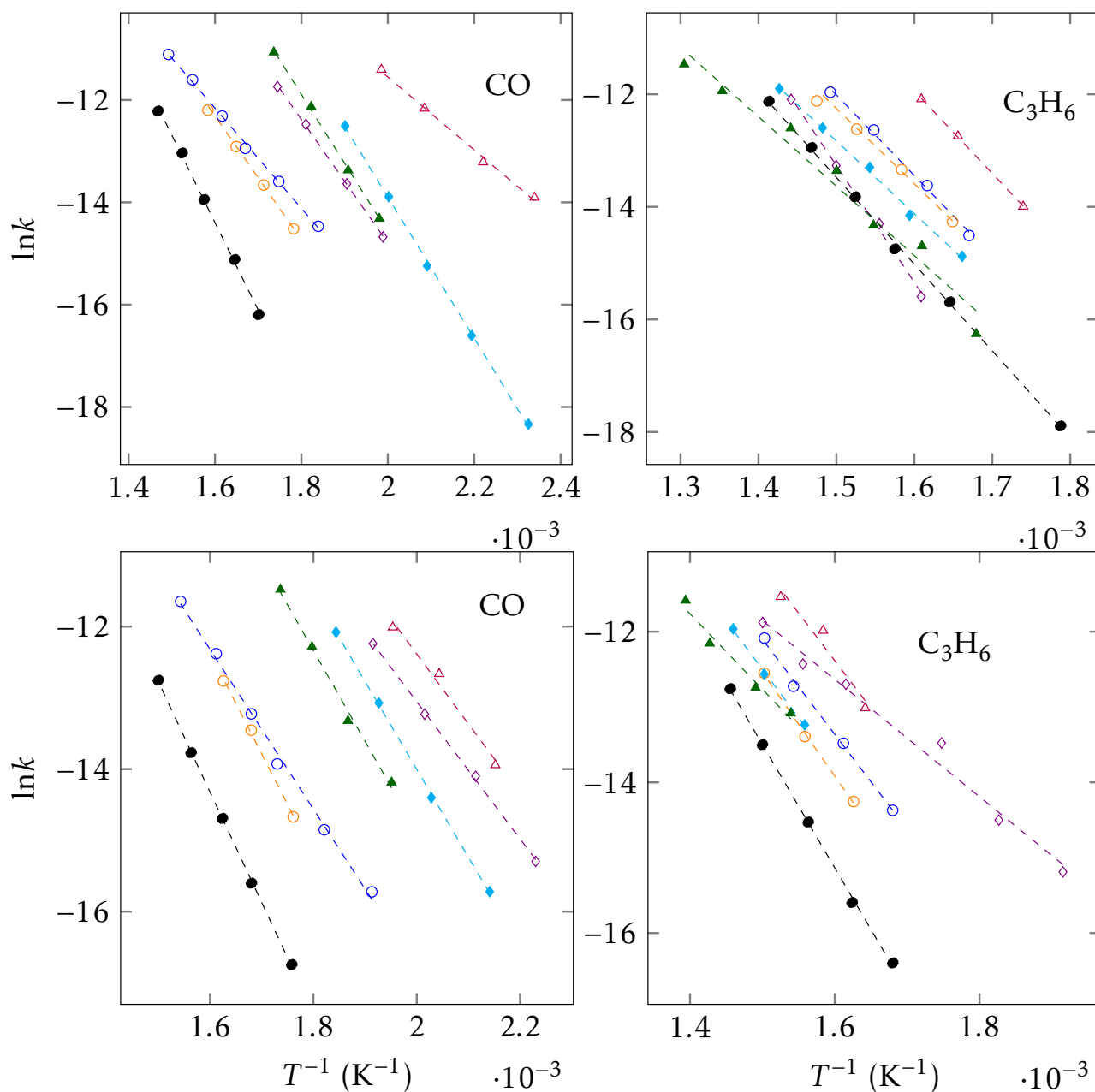


Figure D.7 – Arrhenius plots of CO and C_3H_6 conversion under stoichiometric conditions for $La_{1-x-y}Ca_xFe_{1-x}Cu_xO_3$ ($x = 0, 0.2$; $y = 0, 0.2$; CCM) and $La_{1-y}Fe_{1-x}Cu_xO_3$ ($x = 0, 0.17, 0.2$; $y = 0, 0.33$; CCM). $LaFeO_3$ (\bullet), $La_{0.8}FeO_3$ (\circ), and $La_{0.67}FeO_3$ (\circ), $LaFe_{0.8}Cu_{0.2}O_3$ (\blacktriangle), $La_{0.8}Ca_{0.2}Fe_{0.8}Cu_{0.2}O_3$ (\blacklozenge), $La_{0.6}Ca_{0.2}Fe_{0.8}Cu_{0.2}O_3$ (\blacklozenge), and $La_{0.67}Fe_{0.83}Cu_{0.17}O_3$ (\blacktriangle)

D.3 PGM-doped perovskites prepared by CCM

Temperatures corresponding to 50 % conversions of CO, C₃H₆, C₃H₈, H₂ under stoichiometric (stoic1) and NO under rich conditions, evaluated during Procedure A, Procedure C and Procedure D, for PGM-doped La_{0.8}Ca_{0.2}Fe_{0.8}Cu_{0.2}O₃ and La_{0.67}Fe_{0.83}Cu_{0.17}O₃ catalysts are listed in Table D.6.

Table D.6 – Temperatures corresponding to 50 % conversion of CO, C₃H₆, C₃H₈, and H₂ (stoichiometric) and NO (rich composition) of PGM-doped perovskite catalysts (CCM) and selectivities of NO reduction products at T_S, compared to the commercial reference catalyst. Tests were conducted according to Procedure A, Procedure C and Procedure D.

Test procedure	condition	stoichiometric (stoic1)				rich				
		T ₅₀ (°C)				selectivities at T _S				
		CO	C ₃ H ₆	C ₃ H ₈	H ₂	NO	S _{N₂}	S _{NH₃}	S _{N₂O}	T _S (°C)
La _{0.8} Ca _{0.2} Fe _{0.8} Cu _{0.2} O ₃										
A	+ 0.1 wt.% Pd	287	377	495	287	430	0.38	0.62	0	493
C	+ 0.1 wt.% Pd	228	283	457	169	390	0.43	0.57	0	500
A	+ 0.1 wt.% Pt	279	381	504	329	473	0.40	0.60	0	509
C	+ 0.1 wt.% Pt	175	245	473	198	441	0.49	0.51	0	507
A	+ 0.1 wt.% Rh	289	460	485	484	423	0.39	0.61	0	504
C	+ 0.1 wt.% Rh	215	321	463	266	370	0.28	0.72	0	474
La _{0.67} Fe _{0.83} Cu _{0.17} O ₃										
A	+ 0.1 wt.% Rh	247	397	493	355	423	0.17	0.83	0	512
C	+ 0.1 wt.% Rh	218	305	458	276	392	0.48	0.52	0	508
D	+ 0.1 wt.% Rh	219	287	464	262	389	0.31	0.69	0	514
commercial reference										
B	0.55 wt.% PGM	217	262	455	149	286	0.06	0.94	0	504

The selectivities and yields of NO conversion products of the Rh-doped La_{0.67}Fe_{0.83}Cu_{0.17}O₃ solid are depicted in Fig. D.8 and D.9 for all investigated test procedures (Procedure A, Procedure C and Procedure D).

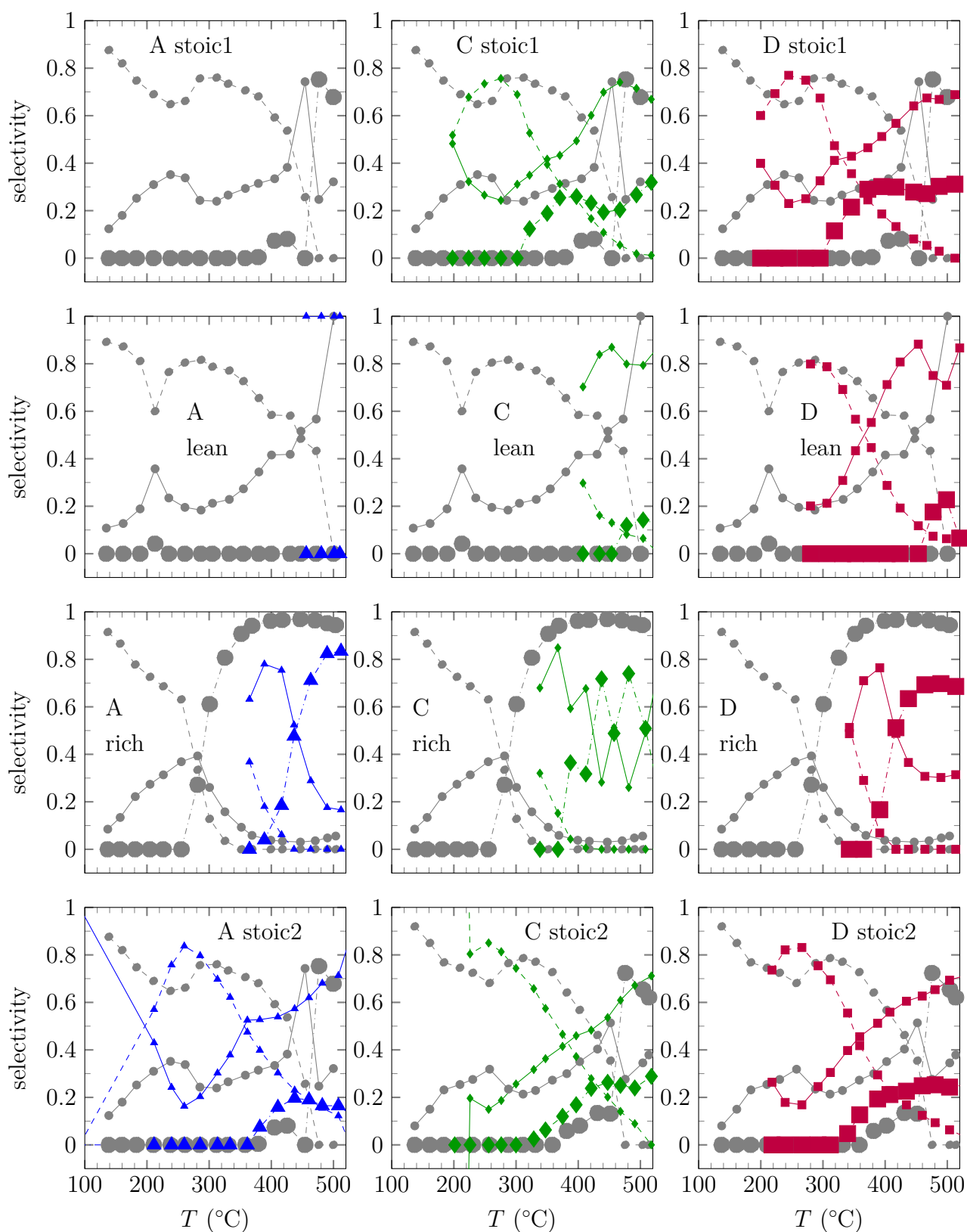


Figure D.8 – N_2 , N_2O and NH_3 selectivities of NO conversion of 0.1 wt.% Rh-doped $\text{La}_{0.67}\text{Fe}_{0.83}\text{Cu}_{0.17}\text{O}_3$ (CCM) catalysts tested according to Procedure A or after a reductive pretreatment (Procedure C or Procedure D). $\text{La}_{0.67}\text{Fe}_{0.83}\text{Cu}_{0.17}\text{O}_3$ doped with 0.1 wt.% Rh tested by Procedure A (\blacktriangle) or pre-reduced including tests under “stoichiometric” (Procedure C, \blacklozenge) or “modified stoichiometric” conditions (Procedure D, \blacksquare) compared to the commercial reference TWC (\bullet , Procedure B); S_{N_2} (solid), $S_{\text{N}_2\text{O}}$ (dashed), S_{NH_3} (dashdotted, big mark)

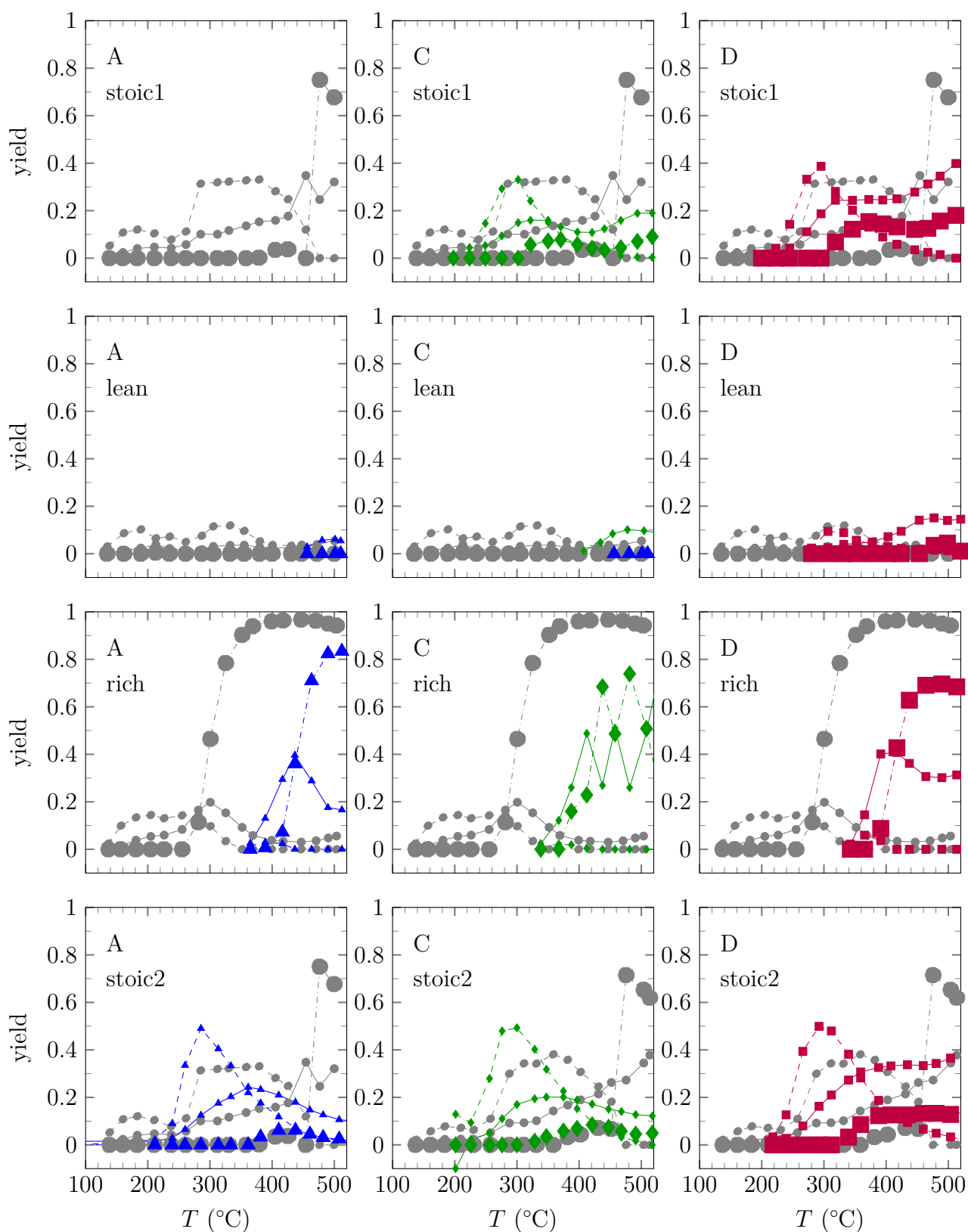


Figure D.9 – N_2 , N_2O and NH_3 yields of NO conversion of 0.1 wt.% Rh-doped $La_{0.67}Fe_{0.83}Cu_{0.17}O_3$ (CCM) catalysts tested according to Procedure A or after a reductive pretreatment (Procedure C or Procedure D). $La_{0.67}Fe_{0.83}Cu_{0.17}O_3$ doped with 0.1 wt.% Rh tested by Procedure A (\blacktriangle) or pre-reduced including tests under “stoichiometric” (Procedure C, \blacklozenge) or “modified stoichiometric” conditions (Procedure D, \blacksquare) compared to the commercial reference TWC (\bullet , Procedure B); Y_{N_2} (solid), Y_{N_2O} (dashed), Y_{NH_3} (dashdotted, big mark)

List of Tables

1.1	Euro 5 and 6 regulations for petrol fuelled cars	4
1.2	Current market prices of TWC-relevant PGM	8
1.3	Comparison of SSA of LaFeO ₃ perovskites obtained by different synthesis methods	38
2.1	Syntheses by parameters	54
2.2	Feed compositions for catalytic tests	58
3.1	Crystallite sizes, unit cell parameters and volumes of LaBO ₃ (B = Fe, Mn) and La ₂ CuO ₄ (CCM) derived from full pattern matching	67
3.2	Crystallite sizes, unit cell parameters and volumes of LaFeO ₃ and La ₂ CuO ₄ (CCM) derived from full pattern matching	73
3.3	H ₂ -TPR results of LaBO ₃ (B = Fe, Mn) and La ₂ CuO ₄ (CCM)	74
3.4	SSA of LaBO ₃ (B = Fe, Mn) and La ₂ CuO ₄ (CCM)	75
3.5	Photopeak maxima (XPS) of LaBO ₃ (B = Fe, Mn; CCM) and La ₂ CuO ₄ (CCM)	76
3.6	Deconvolution results (XPS) of LaBO ₃ (B = Fe, Mn) and La ₂ CuO ₄ (CCM)	78
3.7	Atomic ratios x_{La}/x_B (ICP, XPS) and surface compositions of LaBO ₃ (B = Fe, Mn) and La ₂ CuO ₄ (CCM)	79
3.8	Photopeak maxima (XPS) of fresh and post-HTXRD LaFeO ₃ and La ₂ CuO ₄ (CCM) and spectral decomposition results	81
3.9	Atomic ratios x_{La}/x_B (XPS) and surface compositions of LaFeO ₃ and La ₂ CuO ₄ (CCM)	82
3.10	T_{50} of NO, CO, CH ₄ , C ₃ H ₆ , C ₃ H ₈ , H ₂ , and O ₂ of the commercial reference.	82
3.11	T_{50} of NO, CO, CH ₄ , C ₃ H ₆ , C ₃ H ₈ , H ₂ , and O ₂ of LaFeO ₃ , LaMnO ₃ , and La ₂ CuO ₄ (CCM) compared to the commercial reference.	86
4.1	Crystallite sizes and unit cell parameters of calcined LaFeO ₃ prepared by CCM and HAM air derived from full pattern matching	98
4.2	Textural properties of LaFeO ₃ prepared by CCM and HAM air	100
4.3	Surface compositions and photopeak maxima (XPS) of calcined LaFeO ₃ prepared by CCM or HAM air	103
4.4	Crystallite sizes and unit cell parameters of calcined LaFeO ₃ prepared by MSM compared to HAM N ₂ derived from full pattern matching	109
4.5	H ₂ -TPR results of calcined LaFeO ₃ prepared by HAM N ₂ and MSM PS 200 nm	110
4.6	Textural properties of LaFeO ₃ prepared by MSM compared to HAM N ₂	112
4.7	Bulk and surface compositions and photopeak maxima (XPS) of calcined LaFeO ₃ prepared by HAM N ₂ and MSM	116
4.8	T_{50} of CO, C ₃ H ₆ , C ₃ H ₈ , H ₂ and NO of LaFeO ₃ catalysts prepared by MSM compared to HAM N ₂ and selectivities of NO reduction products.	117

4.9	Crystallite sizes and unit cell parameters of calcined LaFeO_3 prepared by CCM, CCM*, $\text{HAM}^*_{\text{cooling}}$, MSM, and MSM^* derived from full pattern matching . . .	123
4.10	Textural properties of LaFeO_3 prepared by CCM, HAM air, $\text{HAM}^*_{\text{cooling}}$, MSM and MSM^*	126
4.11	Surface compositions, photopeak maxima and abundance of O and C surface species (XPS) of calcined LaFeO_3 prepared by CCM, CCM*, HAM air, $\text{HAM}^*_{\text{cooling}}$, $\text{MSM}_{\text{cooling}}$ and MSM^* (PS 400 nm)	129
4.12	T_{50} of CO, C_3H_6 , C_3H_8 , H_2 and NO of LaFeO_3 catalysts prepared by CCM, CCM*, $\text{HAM}^*_{\text{cooling}}$, MSM and MSM^* and selectivities of NO reduction products.	131
4.13	Crystallite sizes and unit cell parameters of calcined LaFeO_3 prepared by HAM N_2 , HAM NO and HAM^* derived from full pattern matching	137
4.14	Textural properties of LaFeO_3 prepared by HAM N_2 , HAM NO and HAM^* .	139
4.15	Surface compositions and photopeak maxima (XPS) of calcined LaFeO_3 prepared by HAM N_2 , HAM NO and $\text{HAM}^*_{\text{cooling}}$	142
4.16	T_{50} of CO, C_3H_6 , C_3H_8 , H_2 and NO of LaFeO_3 catalysts prepared by HAM N_2 , HAM NO, HAM^* and $\text{HAM}^*_{\text{cooling}}$ and selectivities of NO reduction products.	144
5.1	Bulk and surface $x_{\text{La}}/x_{\text{Fe}}$ and photopeak maxima of $\text{La}_{1-y}\text{FeO}_3$ ($y = 0, 0.1, 0.2, 0.33$; CCM)	154
5.2	Crystallite sizes and unit cell parameters of $\text{La}_{1-y}\text{FeO}_3$ ($y = 0, 0.1, 0.2, 0.33$; CCM) derived from full pattern matching	155
5.3	Photopeak maxima and surface compositions (XPS) of calcined and post-HTXRD $\text{La}_{1-y}\text{FeO}_3$ ($y = 0, 0.32$; CCM)	160
5.4	H_2 -TPR results of $\text{La}_{1-y}\text{FeO}_3$ ($y = 0, 0.1, 0.2, 0.33$) compared to $\alpha\text{-Fe}_2\text{O}_3$	161
5.5	Textural properties of $\text{La}_{1-y}\text{FeO}_3$ ($y = 0, 0.1, 0.2, 0.33$; CCM)	162
5.6	T_{50} of CO, C_3H_6 , C_3H_8 , and H_2 and NO of $\text{La}_{1-y}\text{FeO}_3$ catalysts ($y = 0, 0.1, 0.2, 0.33$; CCM) compared to hematite and a mechanic mixture of LaFeO_3 and the Fe_2O_3	166
5.7	Comparison of r_{specific} at 350°C , $E_{\text{A,app}}$ and A of CO and C_3H_6 oxidation for $\text{La}_{1-y}\text{FeO}_3$ catalysts ($y = 0, 0.1, 0.2, 0.33$; CCM) compared to hematite.	166
5.8	Crystallite sizes and unit cell parameters of calcined $\text{La}_{1-x}\text{Ca}_x\text{FeO}_3$ ($x = 0, 0.1, 0.2$; CCM) derived from full pattern matching	169
5.9	H_2 -TPR results of $\text{La}_{1-x}\text{Ca}_x\text{FeO}_3$ ($x = 0, 0.1, 0.2$; CCM)	170
5.10	Textural properties of $\text{La}_{1-x}\text{Ca}_x\text{FeO}_3$ ($x = 0, 0.1, 0.2$; CCM)	171
5.11	Surface $x_{\text{A}}/x_{\text{Fe}}$ and $x_{\text{Ca}}/x_{\text{La}}$, photopeak maxima and spectral decomposition results of calcined $\text{La}_{1-x}\text{Ca}_x\text{FeO}_3$ ($x = 0, 0.1, 0.2$; CCM)	173
5.12	T_{50} of CO, C_3H_6 , C_3H_8 , and H_2 and NO of $\text{La}_{1-x}\text{Ca}_x\text{FeO}_3$ catalysts ($x = 0, 0.1, 0.2$; CCM).	174
5.13	Bulk $x_{\text{La}}/x_{\text{B}}$ and $x_{\text{Cu}}/x_{\text{Fe}}$ of $\text{LaFe}_{1-x}\text{Cu}_x\text{O}_3$ ($x = 0, 0.2$; CCM)	178
5.14	Crystallite sizes and unit cell parameters of calcined $\text{LaFe}_{1-x}\text{Cu}_x\text{O}_3$ ($x = 0, 0.05, 0.1, 0.2$; CCM) derived from full pattern matching	179
5.15	H_2 -TPR results of $\text{LaFe}_{1-x}\text{Cu}_x\text{O}_3$ ($x = 0, 0.05, 0.1, 0.2$; CCM) compared to La_2CuO_4 (CCM)	184
5.16	Textural properties of $\text{LaFe}_{1-x}\text{Cu}_x\text{O}_3$ ($x = 0, 0.05, 0.1, 0.2$; CCM)	184
5.17	Photopeak maxima and spectral decomposition results (XPS) of calcined $\text{LaFe}_{1-x}\text{Cu}_x\text{O}_3$ ($x = 0, 0.05, 0.1, 0.2$; CCM) compared to La_2CuO_4 (CCM)	186
5.18	Surface $x_{\text{La}}/x_{\text{B}}$ and $x_{\text{Cu}}/x_{\text{Fe}}$ of $\text{LaFe}_{1-x}\text{Cu}_x\text{O}_3$ ($x = 0, 0.05, 0.1, 0.2$; CCM) and La_2CuO_4 (CCM).	187

5.19	Surface compositions and spectral decomposition results (XPS) of calcined and post-HTXRD $\text{LaFe}_{1-x}\text{Cu}_x\text{O}_3$ ($x = 0, 0.05, 0.1, 0.2$; CCM)	187
5.20	T_{50} of CO, C_3H_6 , C_3H_8 , H_2 and NO of $\text{LaFe}_{1-x}\text{Cu}_x\text{O}_3$ catalysts ($x = 0, 0.05, 0.1, 0.2$; CCM) and selectivities of NO reduction products.	188
5.21	Comparison of r_{specific} , $E_{A, \text{app}}$ and A of CO and C_3H_6 oxidation for $\text{LaFe}_{1-x}\text{Cu}_x\text{O}_3$ catalysts ($x = 0, 0.05, 0.1, 0.2$; CCM).	193
5.22	Bulk x_A/x_B , $x_{\text{Cu}}/x_{\text{Fe}}$ and $x_{\text{Ca}}/x_{\text{La}}$ of $\text{La}_{1-x}\text{Ca}_x\text{Fe}_{1-x}\text{Cu}_x\text{O}_3$ ($x = 0, 0.1, 0.2$; CCM) .	194
5.23	Crystallite sizes and unit cell parameters of calcined $\text{La}_{1-x}\text{Ca}_x\text{Fe}_{1-x}\text{Cu}_x\text{O}_3$ ($x = 0, 0.1, 0.2$; CCM) derived from full pattern matching	195
5.24	H_2 -TPR results of $\text{La}_{1-x}\text{Ca}_x\text{Fe}_{1-x}\text{Cu}_x\text{O}_3$ ($x = 0, 0.1, 0.2$; CCM)	196
5.25	Textural properties of $\text{La}_{1-x}\text{Ca}_x\text{Fe}_{1-x}\text{Cu}_x\text{O}_3$ ($x = 0, 0.1, 0.2$; CCM)	197
5.26	Photopeak maxima (XPS) of calcined $\text{La}_{1-x}\text{Ca}_x\text{Fe}_{1-x}\text{Cu}_x\text{O}_3$ ($x = 0, 0.1, 0.2$; CCM)	199
5.27	Surface x_A/x_B , $x_{\text{Cu}}/x_{\text{Fe}}$ and $x_{\text{Ca}}/x_{\text{La}}$ of $\text{La}_{1-x}\text{Ca}_x\text{Fe}_{1-x}\text{Cu}_x\text{O}_3$ ($x = 0, 0.1, 0.2$; CCM)	199
5.28	T_{50} of CO, C_3H_6 , C_3H_8 , and H_2 and NO of $\text{La}_{1-x}\text{Ca}_x\text{Fe}_{1-x}\text{Cu}_x\text{O}_3$ catalysts ($x = 0, 0.1, 0.2$; CCM) and selectivities of NO reduction products.	200
5.29	Comparison of r_{specific} , $E_{A, \text{app}}$ and A of CO and C_3H_6 oxidation for $\text{La}_{1-x}\text{Ca}_x\text{Fe}_{1-x}\text{Cu}_x\text{O}_3$ catalysts ($x = 0, 0.1, 0.2$; CCM).	204
5.30	Bulk x_A/x_B of $\text{La}_{1-y}\text{Fe}_{1-x}\text{Cu}_x\text{O}_3$ ($x = 0, 0.17, 0.2$; $y = 0, 0.33$; CCM)	205
5.31	Crystallite sizes, unit cell parameters and volume of calcined $\text{La}_{1-x-y}\text{Ca}_x\text{Fe}_{1-x}\text{Cu}_x\text{O}_3$ ($x = 0, 0.2$; $y = 0, 0.2$; CCM) and $\text{La}_{1-y}\text{Fe}_{1-x}\text{Cu}_x\text{O}_3$ ($x = 0, 0.17, 0.2$; $y = 0, 0.33$; CCM) derived from full pattern matching	207
5.32	H_2 -TPR results of $\text{La}_{1-x-y}\text{Ca}_x\text{Fe}_{1-x}\text{Cu}_x\text{O}_3$ ($x = 0, 0.2$; $y = 0, 0.2$; CCM) and $\text{La}_{1-y}\text{Fe}_{1-x}\text{Cu}_x\text{O}_3$ ($x = 0, 0.17, 0.2$; $y = 0, 0.33$; CCM)	209
5.33	Textural properties of $\text{La}_{1-x-y}\text{Ca}_x\text{Fe}_{1-x}\text{Cu}_x\text{O}_3$ ($x = 0, 0.2$; $y = 0, 0.2$; CCM) and $\text{La}_{1-y}\text{Fe}_{1-x}\text{Cu}_x\text{O}_3$ ($x = 0, 0.17, 0.2$; $y = 0, 0.33$; CCM)	210
5.34	Photopeak maxima (XPS) of calcined $\text{La}_{1-x-y}\text{Ca}_x\text{Fe}_{1-x}\text{Cu}_x\text{O}_3$ ($x = 0, 0.2$; $y = 0, 0.2$; CCM) and $\text{La}_{1-y}\text{Fe}_{1-x}\text{Cu}_x\text{O}_3$ ($x = 0, 0.17, 0.2$; $y = 0, 0.33$; CCM)	211
5.35	Surface x_A/x_B , $x_{\text{Cu}}/x_{\text{Fe}}$ and $x_{\text{Ca}}/x_{\text{La}}$ of $\text{La}_{1-x-y}\text{Ca}_x\text{Fe}_{1-x}\text{Cu}_x\text{O}_3$ ($x = 0, 0.2$; $y = 0, 0.2$; CCM) and $\text{La}_{1-y}\text{Fe}_{1-x}\text{Cu}_x\text{O}_3$ ($x = 0, 0.17, 0.2$; $y = 0, 0.33$; CCM)	213
5.36	T_{50} of CO, C_3H_6 , C_3H_8 , and H_2 and NO of $\text{La}_{1-x-y}\text{Ca}_x\text{Fe}_{1-x}\text{Cu}_x\text{O}_3$ ($x = 0, 0.2$; $y = 0, 0.2$; CCM) and $\text{La}_{1-y}\text{Fe}_{1-x}\text{Cu}_x\text{O}_3$ ($x = 0, 0.17, 0.2$; $y = 0, 0.33$; CCM) and selectivities of NO reduction products.	214
5.37	Comparison of r_{specific} , $E_{A, \text{app}}$ and A of CO and C_3H_6 oxidation for $\text{La}_{1-x-y}\text{Ca}_x\text{Fe}_{1-x}\text{Cu}_x\text{O}_3$ ($x = 0, 0.2$; $y = 0, 0.2$; CCM) and $\text{La}_{1-y}\text{Fe}_{1-x}\text{Cu}_x\text{O}_3$ ($x = 0, 0.17, 0.2$; $y = 0, 0.33$; CCM).	219
6.1	H_2 -TPR results of PGM-doped $\text{La}_{0.8}\text{Ca}_{0.2}\text{Fe}_{0.8}\text{Cu}_{0.2}\text{O}_3$ (CCM)	227
6.2	Photopeak maxima (XPS) of calcined PGM-doped $\text{La}_{0.8}\text{Ca}_{0.2}\text{Fe}_{0.8}\text{Cu}_{0.2}\text{O}_3$ (0.1 wt.% Pd, Pt or Rh; CCM)	228
6.3	Surface ratios of PGM-doped $\text{La}_{0.8}\text{Ca}_{0.2}\text{Fe}_{0.8}\text{Cu}_{0.2}\text{O}_3$ (0.1 wt.% Pd, Pt or Rh; CCM)	229
6.4	T_{50} of CO, C_3H_6 , C_3H_8 , and H_2 and NO of PGM-doped $\text{La}_{0.8}\text{Ca}_{0.2}\text{Fe}_{0.8}\text{Cu}_{0.2}\text{O}_3$ (0.1 wt.% Pd, Pt or Rh; CCM) and selectivities of NO reduction products.	230
6.5	T_{50} of CO, C_3H_6 , C_3H_8 , and H_2 and NO of PGM-doped $\text{La}_{0.8}\text{Ca}_{0.2}\text{Fe}_{0.8}\text{Cu}_{0.2}\text{O}_3$ (0.1 wt.% Pd, Pt or Rh; CCM) and selectivities of NO reduction products after a reductive pretreatment (Procedure C).	235
6.6	H_2 -TPR results of non-doped and Rh-doped $\text{La}_{0.67}\text{Fe}_{0.83}\text{Cu}_{0.17}\text{O}_3$ (0.1 wt.% Rh; CCM)	239

6.7	Photopeak maxima (XPS) of non-doped and Rh-doped $\text{La}_{0.67}\text{Fe}_{0.83}\text{Cu}_{0.17}\text{O}_3$ (0.1 wt.% Rh; CCM)	240
6.8	Surface compositions of non-doped and Rh-doped $\text{La}_{0.67}\text{Fe}_{0.83}\text{Cu}_{0.17}\text{O}_3$ (0.1 wt.% Rh; CCM)	240
6.9	T_{50} of CO, C_3H_6 , C_3H_8 , and H_2 and NO of non- or 0.1 wt.% Rh-doped $\text{La}_{0.67}\text{Fe}_{0.83}\text{Cu}_{0.17}\text{O}_3$ (CCM) and selectivities of NO reduction products, tests conducted according to Procedure A or after a reductive pretreatment (Procedure C and Procedure D).243	
B.1	Bulk and surface x_A/x_B of calcined perovskite catalysts.	259
B.2	Surface compositions (XPS) of perovskite catalysts prepared by CCM	260
B.3	Surface compositions (XPS) of LaFeO_3 catalysts	260
B.4	Photopeak maxima (XPS) of perovskite catalysts (CCM)	261
B.5	Photopeak maxima (XPS) of LaFeO_3 catalysts	261
D.1	T_{50} of NO, CO, CH_4 , C_3H_6 , C_3H_8 , H_2 , and O_2 of $\text{La}_{1-y}\text{FeO}_3$ catalysts ($y = 0, 0.1, 0.2, 0.33$) compared to hematite and a mechanic mixture of LaFeO_3 and Fe_2O_3 . 273	
D.2	T_{50} of NO, CO, CH_4 , C_3H_6 , C_3H_8 , H_2 , and O_2 of $\text{La}_{1-x}\text{Ca}_x\text{FeO}_3$ catalysts ($x = 0, 0.1, 0.2$).	274
D.3	T_{50} of NO, CO, CH_4 , C_3H_6 , C_3H_8 , H_2 , and O_2 of $\text{LaFe}_{1-x}\text{Cu}_x\text{O}_3$ catalysts ($x = 0, 0.1, 0.2$).	275
D.4	T_{50} of NO, CO, CH_4 , C_3H_6 , C_3H_8 , H_2 , and O_2 of $\text{La}_{1-x}\text{Ca}_x\text{Fe}_{1-x}\text{Cu}_x\text{O}_3$ catalysts ($x = 0, 0.1, 0.2$).	276
D.5	T_{50} of NO, CO, CH_4 , C_3H_6 , C_3H_8 , H_2 , and O_2 of $\text{La}_{1-x}\text{Ca}_x\text{Fe}_{1-x}\text{Cu}_x\text{O}_3$ catalysts ($x = 0, 0.1, 0.2$).	276
D.6	T_{50} of CO, C_3H_6 , C_3H_8 , and H_2 and NO of PGM-doped perovskite catalysts (CCM) and selectivities of NO reduction products; Procedure A, Procedure C, Procedure D, compared to the commercial reference catalyst.	278

List of Figures

1.1	Ideal operation A/F in TWC	5
1.2	Conventional TWC converter	7
1.3	Parameters influencing the performances of TWC	9
1.4	Light-off curves for Rh/alumina	10
1.5	Perovskite structure	13
1.6	Changes to the perovskite structure during redox reactions	15
1.7	O ₂ and isobutene adsorption on LaBO ₃	15
1.8	CO and NO adsorption on LaBO ₃	16
1.9	Catalytic activity of ABO ₃ for propane oxidation	18
1.10	Catalytic activity of lanthanum and yttrium ferrites and manganites and the corresponding Pd-doped perovskites compared to a conventional TWC catalyst under TWC conditions	24
1.11	Self-regenerative function of the <i>intelligent</i> catalyst	27
1.12	PGM segregation on ageing	27
1.13	Ageing dependence of CO–NO _x cross-over point conversion	28
1.14	Generic scheme of macro-structuring methods	34
1.15	Scheme of CCT	36
2.1	Syntheses overview	50
2.2	SEM of polymer spheres employed as structuring agent	51
2.3	<i>T</i> profiles of calcination (CCM and CCM*)	52
2.4	<i>T</i> profile of calcination (MSM and MSM _{cooling})	53
2.5	<i>T</i> profile of the HTXRD analysis	55
2.6	Catalytic test setup scheme	59
2.7	Procedure A	60
2.8	Procedure B	61
2.9	Procedure C	62
3.1	XRD of calcined LaBO ₃ (B = Fe, Mn) and La ₂ CuO ₄	66
3.2	Raman spectra of LaFeO ₃	67
3.3	HTXRD of LaFeO ₃ Steps 1-3	69
3.4	HTXRD of LaFeO ₃ Steps 4-6	70
3.5	HTXRD of La ₂ CuO ₄ (CCM) Steps 1-3	71
3.6	HTXRD of La ₂ CuO ₄ (CCM) Steps 4-6	72
3.7	H ₂ -TPR profiles of calcined LaFeO ₃ , LaMnO ₃ and La ₂ CuO ₄ (CCM)	74
3.8	Isotherms of calcined LaFeO ₃ , LaMnO ₃ , and La ₂ CuO ₄ (CCM)	75
3.9	XPS: La 3d, Fe 2p, Mn 2p, Cu 2p, O 1s and C 1s photopeaks of calcined LaFeO ₃ , LaMnO ₃ , La ₂ CuO ₄ (CCM)	77

3.10 XPS: La 3d, Fe 2p, O 1s and C 1s photopeaks of calcined and post-HTXRD LaFeO ₃ (CCM)	80
3.11 XPS: La 3d, Cu 2p, O 1s and C 1s photopeaks of La ₂ CuO ₄ (CCM)	81
3.12 $X_{\text{NO,CO,HC,H}_2\text{O}_2}$ over the commercial reference during Procedure B	83
3.13 S_{N_2} , $S_{\text{N}_2\text{O}}$, S_{NH_3} and Y_{N_2} , $Y_{\text{N}_2\text{O}}$ and Y_{NH_3} of commercial TWC during Procedure B	85
3.14 X_{CO} , $X_{\text{C}_3\text{H}_6}$ and X_{NO} of LaBO ₃ (B = Fe, Mn; CCM) and La ₂ CuO ₄ (CCM) during Procedure A under stoichiometric, lean and rich conditions	87
3.15 $X_{\text{C}_3\text{H}_8}$, X_{CH_4} and X_{H_2} of LaBO ₃ (B = Fe, Mn; CCM) and La ₂ CuO ₄ (CCM) during Procedure A under stoichiometric, lean and rich conditions	88
3.16 S_{N_2} , $S_{\text{N}_2\text{O}}$, S_{NH_3} , Y_{N_2} , $Y_{\text{N}_2\text{O}}$ and Y_{NH_3} of perovskite reference catalysts during Procedure A	89
3.17 XRD of calcined and spent LaBO ₃ (B = Fe, Mn; CCM) and La ₂ CuO ₄ (CCM) solids	91
4.1 TGA/DSC of CCM and HAM precursors of LaFeO ₃	97
4.2 XRD of calcined LaFeO ₃ prepared by CCM and HAM air	99
4.3 Isotherms and pore size distributions of calcined LaFeO ₃ prepared by CCM or HAM air	99
4.4 TEM of LaFeO ₃ synthesized via CCM and HAM air	100
4.5 SEM of LaFeO ₃ synthesized via CCM and HAM air	101
4.6 XPS spectra of La 3d, Fe 2p, O 1s and C 1s core levels of LaFeO ₃ (CCM, HAM air)	102
4.7 SEM of PS ($d = 200$ nm) and PMMA spheres ($d = 65$ nm)	104
4.8 TGA/DSC of PS spheres ($d = 200$ nm)	105
4.9 TGA/DSC of HAM precursors of LaFeO ₃ recorded under stagnant atmosphere, air or N ₂ flow	106
4.10 TGA/DSC of PMMA spheres ($d = 50$ and 70 nm) under N ₂ flow	107
4.11 XRD of calcined LaFeO ₃ prepared by MSM compared to HAM N ₂	108
4.12 H ₂ -TPR curves of calcined LaFeO ₃ prepared by HAM N ₂ and MSM PS 200 nm compared to commercial α -Fe ₂ O ₃	109
4.13 Isotherms and pore size distributions of calcined LaFeO ₃ prepared by MSM compared to HAM N ₂	111
4.14 SEM of LaFeO ₃ synthesized by MSM (PS 200 nm)	113
4.15 SEM of LaFeO ₃ synthesized by MSM _{cooling} (PS 400 nm)	114
4.16 XPS spectra of La 3d, Fe 2p, O 1s and C 1s energy levels of LaFeO ₃ prepared by MSM compared to HAM N ₂	115
4.17 CO, C ₃ H ₆ and NO conversions of LaFeO ₃ catalysts prepared by MSM using different templates compared to HAM N ₂ under stoichiometric and rich conditions	117
4.18 TGA/DSC of CCM and HAM precursors of LaFeO ₃ under air flow or stagnant atmosphere	121
4.19 XRD of calcined LaFeO ₃ prepared by CCM, CCM*, HAM air, HAM* _{cooling} , MSM, and MSM*	122
4.20 Raman spectra of LaFeO ₃ prepared by MSM*	123
4.21 H ₂ -TPR curves of calcined LaFeO ₃ prepared by HAM* _{cooling} compared to the CCM sample	124
4.22 Isotherms and pore size distributions of calcined LaFeO ₃ prepared by CCM, CCM*, HAM air, HAM* _{cooling} , MSM, and MSM*	125
4.23 SEM and TEM of LaFeO ₃ synthesized via HAM air and HAM* _{cooling}	127
4.24 SEM of LaFeO ₃ synthesized by MSM and MSM* (PS 400 nm)	128

4.25 XPS spectra of La 3d, Fe 2p, O 1s and C 1s levels of LaFeO ₃ prepared by CCM, CCM*, HAM air, HAM* _{cooling} and MSM*	130
4.26 CO, C ₃ H ₆ and NO conversions of LaFeO ₃ catalysts prepared by CCM, HAM* _{cooling} , MSM and MSM* (both PS 400 nm) under stoichiometric or all conditions	132
4.27 S _{N₂} , S _{N₂O} , S _{NH₃} , Y _{N₂} , Y _{N₂O} and Y _{NH₃} of LaFeO ₃ catalysts prepared by HAM* _{cooling} and MSM* (PS 400 nm)	133
4.28 TGA/DSC of HAM precursors of LaFeO ₃ under stagnant atmosphere, air or N ₂ flow	136
4.29 XRD of calcined LaFeO ₃ prepared by HAM N ₂ , HAM NO and HAM*	137
4.30 Raman spectra of LaFeO ₃ prepared by HAM NO	138
4.31 Raman spectra of LaFeO ₃ prepared by HAM*	138
4.32 Isotherms and pore size distributions of calcined LaFeO ₃ prepared by HAM N ₂ , HAM NO and HAM*	139
4.33 SEM of LaFeO ₃ synthesized via HAM NO	140
4.34 TEM of LaFeO ₃ synthesized via HAM NO	140
4.35 XPS spectra of La 3d, Fe 2p, O 1s and C 1s levels of LaFeO ₃ prepared by HAM N ₂ , HAM NO	141
4.36 CO, C ₃ H ₆ and NO conversions of LaFeO ₃ catalysts prepared by HAM N ₂ , HAM NO and HAM*	143
4.37 S _{N₂} , S _{N₂O} , S _{NH₃} , Y _{N₂} , Y _{N₂O} and Y _{NH₃} of LaFeO ₃ catalysts prepared by HAM* and MSM* (PS 400 nm)	145
5.1 Evolution of surface atomic ratio La/Fe (XPS) on La _{1-y} FeO ₃ (y = 0, 0.1, 0.2, 0.33)	154
5.2 XPS spectra of La 3d, Fe 2p, O 1s and C 1s levels of La _{1-y} FeO ₃ (y = 0, 0.1, 0.2, 0.33; CCM)	155
5.3 XRD patterns of calcined La _{1-y} FeO ₃ (y = 0, 0.1, 0.2, 0.33; CCM)	156
5.4 Raman spectra of La _{0.67} FeO ₃	157
5.5 HTXRD of La _{0.68} FeO ₃ (CCM) Steps 1-3	158
5.6 HTXRD of La _{0.68} FeO ₃ (CCM) Steps 4-6	159
5.7 H ₂ -TPR curves of calcined La _{1-y} FeO ₃ (y = 0, 0.1, 0.2, 0.32; CCM) and Fe ₂ O ₃	161
5.8 Isotherms and pore size distributions of calcined La _{1-y} FeO ₃ (y = 0, 0.1, 0.2, 0.33; CCM)	162
5.9 SEM of La _{1-y} FeO ₃ (y = 0, 0.33; CCM)	163
5.10 CO, C ₃ H ₆ and NO conversions of La _{1-y} FeO ₃ catalysts (Procedure A)	164
5.11 C ₃ H ₈ , O ₂ and H ₂ conversions of La _{1-y} FeO ₃ catalysts (Procedure A)	165
5.12 XRD of calcined La _{1-x} Ca _x FeO ₃ (x = 0, 0.1, 0.2; CCM)	168
5.13 Evolution of the unit cell volume of calcined La _{1-x} Ca _x FeO ₃ (x = 0, 0.1, 0.2; CCM)	169
5.14 H ₂ -TPR curves of calcined La _{1-x} Ca _x FeO ₃ (x = 0, 0.1, 0.2; CCM)	170
5.15 Isotherms and pore size distributions of calcined La _{1-x} Ca _x FeO ₃ (x = 0, 0.1, 0.2; CCM)	171
5.16 XPS: La 3d, Fe 2p, Ca 2p, O 1s and C 1s photopeaks of calcined La _{1-x} Ca _x FeO ₃ (x = 0, 0.1, 0.2; CCM)	172
5.17 CO, C ₃ H ₆ and NO conversions of La _{1-x} Ca _x FeO ₃ catalysts (Procedure A)	175
5.18 C ₃ H ₈ , O ₂ and H ₂ conversions of La _{1-x} Ca _x FeO ₃ catalysts (Procedure A)	176
5.19 XRD of calcined LaFe _{1-x} Cu _x O ₃ (x = 0, 0.05, 0.1, 0.2; CCM)	178
5.20 Evolution of the unit cell volume of calcined LaFe _{1-x} Cu _x O ₃ (x = 0, 0.05, 0.1, 0.2; CCM)	179
5.21 Raman spectra of LaFe _{0.8} Cu _{0.2} O ₃ and LaFeO ₃ (CCM)	180

5.22 HTXRD of $\text{LaFe}_{0.8}\text{Cu}_{0.2}\text{O}_3$ (CCM) Steps 1-3	181
5.23 HTXRD of $\text{LaFe}_{0.8}\text{Cu}_{0.2}\text{O}_3$ (CCM) Steps 4-6	182
5.24 Evolution of unit cell volumes of calcined and post-HTXRD $\text{LaFe}_{1-x}\text{Cu}_x\text{O}_3$ ($x = 0, 0.05, 0.1, 0.2$; CCM)	183
5.25 H_2 -TPR profiles of calcined $\text{LaFe}_{1-x}\text{Cu}_x\text{O}_3$ ($x = 0, 0.05, 0.1, 0.2$; CCM) compared to La_2CuO_4 (CCM)	183
5.26 Isotherms and pore size distributions of calcined $\text{LaFe}_{1-x}\text{Cu}_x\text{O}_3$ ($x = 0, 0.05,$ $0.1, 0.2$; CCM)	185
5.27 XPS: La 3d, Fe 2p, Cu 2p, O 1s and C 1s photopeaks of calcined $\text{LaFe}_{1-x}\text{Cu}_x\text{O}_3$ ($x = 0, 0.05, 0.1, 0.2$; CCM)	186
5.28 CO, C_3H_6 and NO conversions of $\text{LaFe}_{1-x}\text{Cu}_x\text{O}_3$ catalysts under stoichiometric and rich conditions	189
5.29 C_3H_8 , O_2 and H_2 conversions of $\text{LaFe}_{1-x}\text{Cu}_x\text{O}_3$ catalysts under stoichiometric and rich conditions	191
5.30 S_{N_2} , $S_{\text{N}_2\text{O}}$, S_{NH_3} , Y_{N_2} , $Y_{\text{N}_2\text{O}}$ and Y_{NH_3} of $\text{LaFe}_{1-x}\text{Cu}_x\text{O}_3$ catalysts ($x=0.05, 0.1,$ 0.2 ; CCM)	192
5.31 XRD of calcined $\text{La}_{1-x}\text{Ca}_x\text{Fe}_{1-x}\text{Cu}_x\text{O}_3$ ($x = 0, 0.1, 0.2$; CCM)	194
5.32 Evolution of the unit cell volume of calcined $\text{La}_{1-x}\text{Ca}_x\text{Fe}_{1-x}\text{Cu}_x\text{O}_3$ ($x = 0, 0.1,$ 0.2 ; CCM)	195
5.33 H_2 -TPR curves of calcined $\text{La}_{1-x}\text{Ca}_x\text{Fe}_{1-x}\text{Cu}_x\text{O}_3$ ($x = 0, 0.1, 0.2$; CCM) and La_2CuO_4 (CCM)	196
5.34 Isotherms and pore size distributions of calcined $\text{La}_{1-x}\text{Ca}_x\text{Fe}_{1-x}\text{Cu}_x\text{O}_3$ ($x = 0,$ $0.1, 0.2$; CCM)	197
5.35 XPS: La 3d, Fe 2p, Ca 2p, Cu 2p, O 1s and C 1s photopeaks of calcined $\text{La}_{1-x}\text{Ca}_x\text{Fe}_{1-x}\text{Cu}_x\text{O}_3$ ($x = 0, 0.1, 0.2$; CCM)	198
5.36 CO, C_3H_6 and NO conversions of $\text{La}_{1-x}\text{Ca}_x\text{Fe}_{1-x}\text{Cu}_x\text{O}_3$ catalysts ($x = 0, 0.1, 0.2$; CCM) under stoichiometric and rich conditions	201
5.37 C_3H_8 , O_2 and H_2 conversions of $\text{La}_{1-x}\text{Ca}_x\text{Fe}_{1-x}\text{Cu}_x\text{O}_3$ catalysts ($x = 0, 0.1, 0.2$; CCM) under stoichiometric and rich conditions	202
5.38 S_{N_2} , $S_{\text{N}_2\text{O}}$, S_{NH_3} , Y_{N_2} , $Y_{\text{N}_2\text{O}}$ and Y_{NH_3} of $\text{La}_{1-x}\text{Ca}_x\text{Fe}_{1-x}\text{Cu}_x\text{O}_3$ catalysts ($x=0.1,$ 0.2 ; CCM)	203
5.39 XRD of calcined $\text{La}_{1-x-y}\text{Ca}_x\text{Fe}_{1-x}\text{Cu}_x\text{O}_3$ ($x = 0, 0.2$; $y = 0, 0.2$; CCM) and $\text{La}_{1-y}\text{Fe}_{1-x}\text{Cu}_x\text{O}_3$ ($x = 0, 0.17, 0.2$; $y = 0, 0.33$; CCM)	206
5.40 Evolution of the unit cell volumes of calcined perovskite samples (CCM)	207
5.41 H_2 -TPR curves of calcined $\text{La}_{1-x-y}\text{Ca}_x\text{Fe}_{1-x}\text{Cu}_x\text{O}_3$ ($x = 0, 0.2$; $y = 0, 0.2$; CCM) and $\text{La}_{1-y}\text{Fe}_{1-x}\text{Cu}_x\text{O}_3$ ($x = 0, 0.17, 0.2$; $y = 0, 0.33$; CCM)	208
5.42 Isotherms and pore size distributions of calcined $\text{La}_{1-x-y}\text{Ca}_x\text{Fe}_{1-x}\text{Cu}_x\text{O}_3$ ($x = 0,$ 0.2 ; $y = 0, 0.2$; CCM) and $\text{La}_{1-y}\text{Fe}_{1-x}\text{Cu}_x\text{O}_3$ ($x = 0, 0.17, 0.2$; $y = 0, 0.33$; CCM)	210
5.43 XPS: La 3d, Fe 2p, O 1s and C 1s photopeaks of calcined $\text{La}_{1-x-y}\text{Ca}_x\text{Fe}_{1-x}\text{Cu}_x\text{O}_3$ ($x = 0, 0.2$; $y = 0, 0.2$; CCM) and $\text{La}_{1-y}\text{Fe}_{1-x}\text{Cu}_x\text{O}_3$ ($x = 0, 0.17, 0.2$; $y = 0, 0.33$; CCM)	212
5.44 XPS: Ca 2p and Cu 2p photopeaks of calcined $\text{La}_{1-x-y}\text{Ca}_x\text{Fe}_{1-x}\text{Cu}_x\text{O}_3$ ($x = 0.2$; $y = 0, 0.2$; CCM) and $\text{La}_{1-y}\text{Fe}_{1-x}\text{Cu}_x\text{O}_3$ ($x = 0, 0.17, 0.2$; $y = 0, 0.33$; CCM)	213
5.45 CO, C_3H_6 and NO conversions of $\text{La}_{1-x-y}\text{Ca}_x\text{Fe}_{1-x}\text{Cu}_x\text{O}_3$ ($x = 0, 0.2$; $y = 0, 0.2$; CCM) and $\text{La}_{1-y}\text{Fe}_{1-x}\text{Cu}_x\text{O}_3$ ($x = 0, 0.17, 0.2$; $y = 0, 0.33$; CCM) catalysts (Proce- dure A)	215

5.46	CO, C ₃ H ₆ and NO conversions of La _{1-x-y} Ca _x Fe _{1-x} Cu _x O ₃ (x = 0, 0.2; y = 0, 0.2; CCM) and La _{1-y} Fe _{1-x} Cu _x O ₃ (x = 0, 0.17, 0.2; y = 0, 0.33; CCM) catalysts (Procedure A)	216
5.47	S _{N₂} , S _{N₂O} , S _{NH₃} , Y _{N₂} , Y _{N₂O} and Y _{NH₃} of La _{1-x} Ca _x Fe _{1-x} Cu _x O ₃ catalysts (x, = 0.1, 0.2; CCM)	218
6.1	H ₂ -TPR curves of calcined PGM-doped La _{0.8} Ca _{0.2} Fe _{0.8} Cu _{0.2} O ₃ (0.1 wt.% Pd, Pt or Rh; CCM)	226
6.2	XPS: Pd 3d, Pt 4f and Rh 3d photopeaks of PGM-doped La _{0.8} Ca _{0.2} Fe _{0.8} Cu _{0.2} O ₃ (0.1 wt.% Pd, Pt or Rh; CCM)	229
6.3	X _{CO} , X _{C₃H₆} and X _{NO} of PGM-doped La _{0.8} Ca _{0.2} Fe _{0.8} Cu _{0.2} O ₃ (0.1 wt.% Pd, Pt or Rh; CCM) during Procedure A	231
6.4	X _{C₃H₈} , X _{O₂} and X _{H₂} of PGM-doped La _{0.8} Ca _{0.2} Fe _{0.8} Cu _{0.2} O ₃ (0.1 wt.% Pd, Pt or Rh; CCM) during Procedure A	232
6.5	X _{CO} , X _{C₃H₆} and X _{NO} of PGM-doped La _{0.8} Ca _{0.2} Fe _{0.8} Cu _{0.2} O ₃ (0.1 wt.% Pd, Pt or Rh; CCM) after a reductive pretreatment (Procedure C)	234
6.6	X _{C₃H₈} , X _{CH₄} and X _{H₂} of PGM-doped La _{0.8} Ca _{0.2} Fe _{0.8} Cu _{0.2} O ₃ (0.1 wt.% Pd, Pt or Rh; CCM) after a reductive pretreatment (Procedure C)	236
6.7	S _{N₂} , S _{N₂O} , S _{NH₃} , Y _{N₂} , Y _{N₂O} and Y _{NH₃} of PGM-doped La _{0.8} Ca _{0.2} Fe _{0.8} Cu _{0.2} O ₃ (0.1 wt.% Pd, Pt or Rh; CCM) after a reductive pretreatment (Procedure C)	237
6.8	H ₂ -TPR curves of calcined non-doped and Rh-doped La _{0.67} Fe _{0.83} Cu _{0.17} O ₃ (0.1 wt.% Rh; CCM)	239
6.9	X _{CO} , X _{C₃H₆} and X _{NO} of non-doped and Rh-doped La _{0.67} Fe _{0.83} Cu _{0.17} O ₃ (0.1 wt.% Rh; CCM) during Procedure A	241
6.10	X _{C₃H₈} , X _{CH₄} and X _{H₂} of non-doped and Rh-doped La _{0.67} Fe _{0.83} Cu _{0.17} O ₃ (0.1 wt.% Rh; CCM) during Procedure A	242
6.11	X _{CO} , X _{C₃H₆} and X _{NO} of Rh-doped La _{0.67} Fe _{0.83} Cu _{0.17} O ₃ (0.1 wt.% Rh; CCM) tested according to Procedure A or after a reductive pretreatment (Procedure C or Procedure D)	245
6.12	X _{C₃H₈} , X _{CH₄} and X _{H₂} of Rh-doped La _{0.67} Fe _{0.83} Cu _{0.17} O ₃ (0.1 wt.% Rh; CCM) tested according to Procedure A or after a reductive pretreatment (Procedure C or Procedure D)	246
A.1	Stagnant conditions scheme	257
A.2	Synthesis schemes of CCM, hydroalcoholic method (HAM) and macro-structuring method (MSM)	258
C.1	HTXRD LaFe _{0.95} Cu _{0.2} O ₃ (CCM) Steps 1-3	263
C.2	HTXRD LaFe _{0.95} Cu _{0.2} O ₃ (CCM) Steps 4-6	264
C.3	HTXRD LaFe _{0.9} Cu _{0.1} O ₃ (CCM) Steps 1-3	265
C.4	HTXRD LaFe _{0.9} Cu _{0.1} O ₃ (CCM) Steps 4-6	266
D.1	C ₃ H ₈ , O ₂ and H ₂ conversions of LaFeO ₃ catalysts prepared by HAM NO and HAM*	268
D.2	S _{N₂} , S _{N₂O} and S _{NH₃} of LaFeO ₃ catalysts prepared by HAM* and MSM* (PS 400 nm)	269
D.3	N ₂ yield (Y _{N₂}), Y _{N₂O} and Y _{NH₃} of LaFeO ₃ catalysts prepared by HAM* and MSM* (PS 400 nm)	270

D.4	Arrhenius plots of CO and C ₃ H ₆ conversion under stoichiometric conditions for La _{1-y} FeO ₃	271
D.5	Arrhenius plots of CO and C ₃ H ₆ conversion under stoichiometric conditions for LaFe _{1-x} Cu _x O ₃ (x = 0, 0.05, 0.1, 0.2; CCM)	272
D.6	Arrhenius plots of CO and C ₃ H ₆ conversion under stoichiometric conditions for La _{1-x} Ca _x Fe _{1-x} Cu _x O ₃ (x = 0, 0.1, 0.2; CCM)	272
D.7	Arrhenius plots of CO and C ₃ H ₆ conversion under stoichiometric conditions for La _{1-x-y} Ca _x Fe _{1-x} Cu _x O ₃ (x = 0, 0.2; y = 0, 0.2; CCM) and La _{1-y} Fe _{1-x} Cu _x O ₃ (x = 0, 0.17, 0.2; y = 0, 0.33; CCM)	277
D.8	S _{N₂} , S _{N₂O} and S _{NH₃} of Rh-doped La _{0.67} Fe _{0.83} Cu _{0.17} O ₃ (0.1 wt.% Rh; CCM) tested according to Procedure A or after a reductive pretreatment (Procedure C or Procedure D)	279
D.9	Y _{N₂} , Y _{N₂O} and Y _{NH₃} of Rh-doped La _{0.67} Fe _{0.83} Cu _{0.17} O ₃ (0.1 wt.% Rh; CCM) tested according to Procedure A or after a reductive pretreatment (Procedure C or Procedure D)	280